



HAL
open science

Développement de nouvelles stratégies de lutte contre les biofilms de *Providencia stuartii*, un pathogène humain multi-résistant

Julie Lopes

► **To cite this version:**

Julie Lopes. Développement de nouvelles stratégies de lutte contre les biofilms de *Providencia stuartii*, un pathogène humain multi-résistant. Sciences agricoles. Université Grenoble Alpes, 2019. Français. NNT : 2019GREAV025 . tel-02464435

HAL Id: tel-02464435

<https://theses.hal.science/tel-02464435v1>

Submitted on 3 Feb 2020

HAL is a multi-disciplinary open access archive for the deposit and dissemination of scientific research documents, whether they are published or not. The documents may come from teaching and research institutions in France or abroad, or from public or private research centers.

L'archive ouverte pluridisciplinaire **HAL**, est destinée au dépôt et à la diffusion de documents scientifiques de niveau recherche, publiés ou non, émanant des établissements d'enseignement et de recherche français ou étrangers, des laboratoires publics ou privés.

THÈSE

Pour obtenir le grade de

DOCTEUR DE LA COMMUNAUTE UNIVERSITE GRENOBLE ALPES

Spécialité : **Biologie Structurale et Nanobiologie**

Arrêté ministériel : 25 mai 2016

Présentée par

« Julie LOPES »

Thèse dirigée par **Jacques Philippe COLLETIER, CNRS**

préparée au sein du **Laboratoire Institut de Biologie Structurale**
dans **l'École Doctorale Chimie et Science du Vivant**

Développement de nouvelles stratégies de lutte contre les biofilms de *Providencia stuartii*, un pathogène humain multi- résistant

Development of new strategies to fight biofilms of *Providencia stuartii*, a multi- resistant human pathogen

Thèse soutenue publiquement le **16 octobre 2019**,
devant le jury composé de :

Madame Ina ATTREE

Directeur de Recherche, Institut de Biologie Structurale (Présidente)

Madame Lydie PLOUX

Directeur de Recherche, Institut de Science des Matériaux de Mulhouse,
(Rapporteur)

Monsieur Jean-Marc GHIGO

Professeur, Institut Pasteur de Paris (Rapporteur)

Monsieur Pierre-Yves RENARD

Professeur, Unité Cobra de l'Université de Rouen (Examineur)

Monsieur Jean-Michel BOLLA

Directeur de Recherche, Laboratoire Membranes et Cibles Thérapeutiques de
Marseille (Examineur)

Monsieur Jacques-Philippe COLLETIER

Directeur de Recherche, Institut de Biologie Structurale (Encadrant)



Remerciements

Je tiens dans un premier temps à remercier très sincèrement le professeur Pierre-Yves RENARD de l'unité Cobra à l'Université de Rouen, le docteur Jean-Michel BOLLA, directeur de recherche INSERM au Laboratoire Membranes et Cibles thérapeutiques de Marseille, la docteure Ina ATTREE, directrice de recherche au CNRS à l'Institut de Biologie Structurale de Grenoble, le professeur Jean-Marc GHIGO de l'Institut Pasteur de Paris et la docteure Lydie PLOUX, directrice de recherche du CNRS à l'Institut de Science des Matériaux de Mulhouse, de m'avoir fait l'honneur d'accepter de faire partie des membres du jury et de juger mon travail de thèse.

Je remercie le professeur Winfried WEISSENHORN, directeur de l'Institut de Biologie Structurale de Grenoble, de m'avoir donné l'opportunité de réaliser cette thèse au sein de l'institut.

Je tiens à exprimer ma gratitude envers le docteur Martin WEIK, directeur du groupe DYNAMOP (Dynamique et cinétique des processus moléculaires) de m'avoir accueilli dans son équipe. Martin, tu apportes beaucoup de bonne humeur dans l'équipe et tu t'assures toujours que l'ambiance scientifique et humaine est au rendez-vous. Merci pour ta patience et ton investissement.

Merci au Docteur Jacques-Philippe COLLETIER de m'avoir donné l'opportunité de commencer un sujet de thèse sous sa direction et de m'avoir encadré pendant ces trois années. Jacques, merci de m'avoir fait confiance. Sache que tu m'as fait grandir professionnellement et personnellement : tu m'as poussée dans mes retranchements, rendu autonome, tu m'as fait réaliser la difficulté des relations humaines au travail et appris à comment les surpasser ; puis surtout tu m'as aidé et rassuré dans mon projet professionnel. Pour tout cela, tout simplement : Merci.

Je tiens bien évidemment à remercier tous nos collaborateurs qui ont permis de mener à bien ce projet de thèse. Merci au professeur Pierre-Yves RENARD, au maître de conférences Ludovic JEAN et à l'ancien thésard Pierrick BRUYAT de l'unité Cobra de l'université de Rouen pour votre écoute, vos idées et nos visioconférences très enrichissantes. A l'Institut de Biologie Structurale, je remercie l'ingénieur-chercheur Jean-Philippe KLEMAN et l'ingénieure d'étude Françoise LACROIX de la plateforme de microscopie conventionnelle, Daphna Fenel de son accompagnement en microscopie électronique, la technicienne Aline LEROY de son aide en caractérisation biophysique, ainsi que l'ingénieur d'études Anne-Marie VILLARD, concernant les expériences de biologie moléculaire.

Je suis profondément reconnaissante envers Guillaume TETREAU, post-doctorant dans l'équipe, avec qui j'ai beaucoup travaillé et échangé au cours de la thèse. Guillaume, tu as été un pilier, sans toi je n'aurais pas vécu ces trois années de la même manière. Je te remercie de ton écoute, de ton soutien et de ta sagesse dans les moments difficiles. Tu as su me canaliser et à me faire voir sous un autre angle chaque problème que je pouvais rencontrer. Je suis heureuse que nos chemins se soient croisés car tu es une personne en or.

J'aimerai ensuite remercier très sincèrement tous les collègues de laboratoire et de bureau, et plus particulièrement Kévin POUNOT – doctorant en 3^{ème} année, Ninon ZALA – notre chère technicienne à qui nous devons l'organisation formidable du laboratoire, Kyprianos HADJIDEMETRIOU ainsi qu' Elena ANDREVVA – doctorants en 2^{ème} année de thèse, de toutes nos discussions agréables et qui font du bien.

Je remercie les docteurs Andrea DESSEN, Cécile MORLOT et Patricia RENESTO d'avoir accepté de faire partie de mon comité de suivi de thèse pendant ces trois ans, et d'avoir pris du temps pour m'écouter et m'accompagner au cours de ce projet. Merci pour toutes vos remarques, vos conseils et surtout vos encouragements.

Je tiens de tout cœur à remercier la docteure et amie Christine GABORIAUD de nos discussions scientifiques, de son aide, des ses idées, de son investissement... Christine, merci de ces pauses café auxquelles je pouvais me confier à toi. Tu m'as été d'un grand soutien.

Un grand Merci à ma famille : ma maman Ariel, mon papa Antonio, ma belle-mère Valérie, mes frères et sœurs Stéphanie, Thomas, Lucie et Raphael, ainsi que toute ma belle-famille. Je suis éternellement reconnaissante de votre soutien.

Cendric, merci est un mot loin d'être suffisant pour te faire parvenir toute la gratitude que je ressens envers toi. Tu m'as soutenue, encouragée, poussée à ne rien lâcher. C'est de toi que je dégage ma force et mon envie d'aller toujours plus loin chaque jour. Tu m'as offert un environnement idéal pour assurer la réussite de ce travail et c'est pour cela que je te le dédie.

A mon amour

Table des matières

I- INTRODUCTION.....	2
1- Les microorganismes	2
2- Les biofilms.....	3
A. Un biofilm, c'est quoi ?	3
B. Quels bénéfices ?	4
C. Où les retrouve-on?	5
D. Comment se développent-ils ?	6
a. L'attachement à une surface	7
b. La formation de micro-colonies.....	7
c. La synthèse d'une MEC	8
d. La maturation	10
e. La dispersion	10
E. Comment communiquent-ils ?	11
F. Quels impacts ?	12
a. Les effets négatifs	12
b. Les effets positifs	14
c. Nécessité de trouver un équilibre	14
d. Les thérapies anti-biofilms	14
3- Les porines.....	15
A. Les bactéries Gram-négatif.....	15
a. Le périplasme	16
b. Les membranes interne et externe	16
c. Les LPS	16
B. Structure des porines.....	18
C. Rôles des porines générales non spécifiques	20
a. Diffusion générale.....	20
b. Activité immunologique	21
c. Signalisation transmembranaire	21
d. Survie bactérienne	21
e. Résistance aux antibiotiques	22
f. Fonction non diffusive des porines.....	23
4- <i>Providencia stuartii</i>.....	23
A. Description.....	23
B. Impact des biofilms de <i>P. stuartii</i>	24
C. Les porines de <i>P. stuartii</i>	24
II - OBJECTIFS DE LA THESE	28
III – Méthodologies	34
1- Biologie moléculaire.....	34
A. PCR.....	34
B. RT-qPCR	35
C. Clonage	39
2- Biochimie des protéines membranaires	42
A. Détergents	43
B. Liposomes et incorporation de protéines membranaires	44
C. Diffusion dynamique de lumière.....	46
3- Imagerie cellulaire	47
A. Microscopie de fluorescence conventionnelle	48
B. Microscopie électronique.....	51
4- Cristallographie aux rayons X.....	52
A. La cristallogénèse	54
B. La diffraction	56
C. La pratique	58
D. Le traitement de données	59
IV – Matériels et méthodes.....	64
1- Les souches bactériennes.....	64
2- Biologie moléculaire.....	64

A. Les plasmides.....	64
B. RT-qPCR	65
3- Etude de la croissance et de la socialisation bactérienne	69
A. Transformation bactérienne	69
B. Etude des effets environnementaux, ou de l'addition de peptides et d'acides aminés, sur la formation de communautés flottantes et de biofilms adhérents par <i>P. stuartii</i>	70
C. Etude des effets environnementaux ou de l'ajout d'acides aminés sur les communautés flottantes et biofilms adhérents de <i>P. stuartii</i> déjà développées	71
4- Imagerie des bactéries	72
A. Microscopie d'épifluorescence.....	72
B. Microscopie électronique.....	73
5- Etudes <i>in vivo</i> des porines de <i>P. stuartii</i>	74
A. Etude des effets environnementaux sur les porines	74
B. Observation des porines.....	74
6- Biochimie des protéines membranaires	76
A. Purification des protéines membranaires.....	76
a. Expression et extraction.....	76
b. Purification des porines de <i>P. stuartii</i> par chromatographie échangeuse d'ion et d'exclusion stérique.....	78
B. Etude <i>in vitro</i> des capacités d'auto-association des porines de <i>P. stuartii</i> par DLS.....	78
a. La formation des liposomes	79
b. La DLS.....	79
c. Visualisation des protéoliposomes	80
C. Cristallographie aux rayons X.....	81
a. La cristallisation.....	81
b. La collecte et le traitement de données	81
V – Résultats	84
1- Article n°1 – <i>Providencia stuartii</i> form biofilms and floating communities of cells that display high resistance to environmental insults	84
2- Article n°2 – Porin self-association enables cell-to-cell contact in <i>Providencia stuartii</i> floating communities of cells.....	85
3- Article n°3 – Socialization of <i>Providencia stuartii</i> enables resistance to environmental insults	86
4- Article n°4 – Targeting bacterial porins : a possible alternative strategy for disrupting biofilms to combat infections from the human pathogen <i>Providencia stuartii</i>	87
VI - Conclusions et perspectives	89
1- Objectif n°1 : Etude du rôle des porines dans l'établissement et la résistance des communautés microbiennes de <i>P. stuartii</i>.....	90
A. Socialisation microbienne : un moyen de survie pour <i>P. stuartii</i>	91
B. Porines : rôles dans la résistance de <i>P. stuartii</i> aux métabolites du tractus urinaire, ainsi que dans l'établissement des deux types de communautés microbiennes	91
C. Protection des bactéries de <i>P. stuartii</i> : l'importance d'une MEC ?.....	91
2- Objectif n°2 : Inhibition des DOTs de porines pour lutter contre le caractère social de <i>P. stuartii</i>.....	93
A. Lien direct entre la formation de DOTs et la socialisation bactérienne chez <i>P. stuartii</i>	93
B. Intégration d'un fragment de coumarine au sein des peptides synthétisés : Une stratégie prometteuse pour le développement d'outils diagnostiques contre les infections à <i>P. stuartii</i>	94
C. Combinaison des peptides avec les antibiotiques à des buts thérapeutiques ?	95
3- Perspectives	96
A. Porines et pompes à efflux : implication corrélée dans la résistance élevée des biofilms aux antibiotiques ?.....	96
B. Les phages : une alternative aux antibiotiques ?.....	97
VII – Références	100
VIII – Annexes.....	118

Tables des illustrations

Figure 1. Illustration de différentes formes bactériennes.....	2
Figure 2. Biofilm de <i>Pseudomonas aeruginosa</i> recouvert de sa MEC observé en microscopie électronique à balayage.....	3
Figure 3. Abondance des bactéries et archées comparée au nombre total de biofilms dans les habitats les plus pertinents de notre planète.....	5
Figure 4. Les biofilms sont omniprésents.	6
Figure 5. Représentation schématique des différentes étapes conduisant à la formation d'un biofilm bactérien.	6
Figure 6. Les biofilms distants synchronisent leur dynamique de croissance	12
Figure 7. Les biofilms affectent profondément la productivité industrielle et la santé humaine	13
Figure 8. Schéma représentant la double membrane d'une bactérie Gram-négatif.....	18
Figure 9. Comparaison de la structure monomérique de différentes porines d' <i>E. coli</i>	19
Figure 10. Structure du trimère d'OmpF présentant les principales caractéristiques communes aux porines	19
Figure 11. Omp-Pst1 et Omp-Pst2, les deux porines de <i>P. stuartii</i>	25
Figure 12. Représentation schématique des différentes étapes de développement de <i>P. stuartii</i> en communautés flottantes et en biofilms adhérents	28
Figure 13. Les porines Omp-Pst1 et Omp-Pst2 de <i>P. stuartii</i> s'auto-associent en DOTs à travers leurs boucles extracellulaires.	29
Figure 14. Illustration de la stratégie établie pour étudier les communautés flottantes et les biofilms adhérents, ainsi que les porines de <i>P. stuartii</i> , en présence d'urée, d'ammonium, de créatinine, de bicarbonate ou soumis à une variation de pH.....	30
Figure 15. Les huit classes de stérique zipper.....	31
Figure 16. L'interface des DOTs d'Omp-Pst1 et d'Omp-Pst2 est médiée par des interfaces stérique zipper différentes	32
Figure 17. Les différentes étapes d'une PCR.....	35
Figure 18. Schéma explicatif de la RT-qPCR.....	36
Figure 19. Schéma explicatif de la détection d'ADN cible par SYBR Green	36
Figure 20. Profil d'une réaction de qPCR.....	37
Figure 21. Schéma d'un plasmide double brin	40
Figure 22. Schémas illustrant les différences entre le clonage par ER et par assemblage de Gibson.....	42
Figure 23. Représentation schématique de l'assemblage spontané de molécules de détergent monomériques en micelle, au dessus de la concentration micellaire critique (CMC).....	44
Figure 24. Représentation schématique d'une micelle (gauche) comparé à un liposome de type LUV (droite)	45
Figure 25. Schéma des différentes étapes de préparation des LUVs	46
Figure 26. Schéma explicatif de la méthode de DLS.....	47
Figure 27. Illustration d'images de points à imager limitées ou non en résolution	49
Figure 28. Structure générale des protéines fluorescentes	50
Figure 29. Simplification du diagramme d'énergie de Jablonski	51
Figure 30. Echelle représentative des différentes tailles d'objets biologiques avec les techniques permettant de les observer et de les étudier.	53

Figure 31. Proportion des structures protéiques publiées dans la PDB (Protein DataBase) en 2018, résolues par cristallographie aux rayons X (bleu), par cryo-ME (vert) ou par RMN (jaune).	53
Figure 32. Schéma représentatif du diagramme de phase.....	54
Figure 33. Schéma illustratif de la méthode de cristallogénèse par diffusion de vapeur.....	56
Figure 34. Illustration de la loi de Bragg	57
Figure 35. Présentation des éléments constituant le synchrotron de Grenoble.....	58
Figure 36. Schéma illustratif de la diffraction des rayons X à travers un cristal	59
Figure 37. Représentation schématique des premières étapes du protocole d'extraction d'ARN total sur les communautés flottantes et biofilms adhérents.....	66
Figure 38. Protocoles d'étude des communautés flottantes et biofilms adhérents en conditions de stress environnementaux	71
Figure 39. Illustration d'une lame GelZan.....	72
Figure 40. Illustration du protocole de préparation d'échantillon bactérien par coloration négative sur une grille de microscopie électronique.....	73
Figure 41. Représentation schématique illustrant le protocole d'expression et d'extraction de protéines membranaires	78
Figure 42. Présentation schématique du mini-extruder et de ses composants	79

Abréviations

3D	Tridimensionnelle
AcUr	Acétate d'uranyle
ADN	Acide désoxyribonucléique
ADNc	ADN complémentaire
ANSM	Agence National de Sécurité du Médicament et des produits de santé
ARN	Acide ribonucléique
ARNm	ARN messenger
BAC	Bacteria Artificial Chromosome
BEt	Bromure d'éthydiuim
BLSE	β -lactamase à spectre étendu
CC	Coefficient de corrélation de Pearson
CCD	Charge Coupled Devices
CMC	Concentration Micellaire Critique
CMI	Concentration Minimale Inhibitrice
cou	Fragment de coumarine
Cryo-ME	Cryo-microscopie électronique
Ct	Seuil de cycle
Da	Dalton
DLS	Diffusion dynamique de lumière (Dynamic Light Scattering)
DMP	Dimethylpimelimidate
dNTP	Désoxyribonucléotide triphosphate
DO	Densité Optique
DOT	Dimère de trimère intercellulaire (Dimer Of Trimer)
DTSSP	3,3'-dithiobis(sulfosuccinimidylpropionate))
DTT	Dithiothéitol
EDTA	Acide d'éthylène diamine tétraacétique
EggPC	L- α -phosphatidylcholine
EPS	Exopolysaccharide
ER	Enzymes de Restriction
ESRF	European Synchrotron Radiation Facility
F	Facteurs de structures
FCCs	Floating communities of cells

FRET	Fluorescence Resonance Energy Transfer
GADPH	Glycéraldéhyde-3-phosphate déshydrogénase
GUV	Giant Unilamellar Vesicle
HAC	Human Artificial Chromosome
IBS	Institut de Biologie Structurale
ICU	Intensive Care Unit
IM	Inner Membrane
INU	Infections Nosocomiales Urinaires
InVS	Institut de Veille Sanitaire
IPTG	Isopropyl β -D-1-thiogalactopyranose
ITIS	Integrated Taxonomic Information System
LARKS	Low-complexity aromatic-rich kinked segments
LB	Luria-Bertani
LDAO	Lauryldimethylamine oxide
LPS	Lipopolysaccharide
LUV	Large Unilamellar Vesicle
MAD	Multi-wavelength Anomalous Diffraction
MBBR	Moving Bed Biofilm Reactor
MCS	Site de clonage multiple (Multiple Cloning Site)
MDR	Multi-drug resistant
ME	Microscopie électronique
MEC	Matrice extracellulaire (ou ECM pour extracellular matrix)
MIR	Multiple Isomorphous Replacement
MLV	Multi-Lamellar Vesicle
OM	Membrane externe (ou OM pour Outer Membrane)
OMP	Protéine de la membrane externe (Outer Membrane Protein)
OPOE	n-Octyl-oligo-oxyethylene
pb	Paires de bases
PBS	Phosphate Buffered Saline
PCR	Polymerase Chain Reaction
PDB	Protein DataBase
PEG	Polyéthylène glycol
PFA	Para-formaldéhyde
PG	Peptidoglycane
PMT	Tubes photomultiplicateurs

PSF	Point Spread Function
PTA	Acide phosphotungstique
qPCR	PCR quantitative
QS	Quorum Sensing
qsp	Quantité suffisante pour
REM	Reflection Electron Microscope
Rh	Rayon hydrodynamique
Rhod PE	1,2-dioleoyl-sn-glycero-3-phosphoethanolamine-N-(lissamine rhodamine B sulfonyl)
RMN	Résonance Magnétique Nucléaire
Rmsd	Déviations standard des liaisons covalentes
RNB	Réseau National Biofilm
rpm	Rotations par minute
RT-qPCR	Reverse Transcriptase PCR quantitative
SABs	Surface-attached biofilms
SAD	Single-wavelength anomalous dispersion
SDS	Sodium Dodecyl Sulfate
SDS-PAGE	SDS-Polyacrylamide gel electrophoresis
SEC	Size Exclusion Chromatography
SEM	Scanning Electron Microscope
SIR	Single Isomorphous Replacement
SST	Sodium Silico Tungstate
STEM	Scanning Transmission Electron Microscope
SUV	Small Unilamellar Vesicle
TEM	Transmission Electron Microscope
TLR	Toll-like receptors
UV	Unilamellar Vesicle
YAC	Yeast Artificial Chromosome
WT	Wild-type
λ	Longueur d'onde

I - INTRODUCTION

I- INTRODUCTION

1- Les microorganismes

Pendant presque un milliard d'années, les seuls habitants de notre planète ont été les microorganismes¹. Ces derniers sont des organismes uni- ou multicellulaires (constitués d'une ou plusieurs cellules, respectivement) complexes et organisés, invisibles à l'œil nu². Les microorganismes procaryotes, comme les bactéries et les archées, se distinguent des eucaryotes par l'absence d'un noyau.

Les bactéries peuvent prendre de nombreuses formes : sphériques (coques), en bâtonnets (bacilles), en formes plus ou moins spiralées (Figure 1). Elles sont pour la plupart inoffensives et/ou bénéfiques pour l'organisme, mais il existe de nombreuses espèces pathogènes à l'origine de maladies infectieuses. Jusqu'à la découverte des antibiotiques, ces infections étaient la première cause de décès naturel pour l'Homme.



Figure 1. Illustration de différentes formes bactériennes. Cette image est adaptée du site *SanofiConnect (antibio-responsable.fr)*

Une caractéristique importante, car distinctive, des bactéries est leur paroi cellulaire. Cette dernière donne la forme de la cellule et la protège contre un potentiel éclatement dû à la forte pression osmotique du cytoplasme³. Elle permet de diviser structurellement les bactéries en deux groupes:

- les bactéries Gram-positif, constituées d'une paroi à une seule membrane, la membrane plasmidique⁴ ;
- les bactéries Gram-négatif, constituées d'une paroi à deux membranes, la membrane interne et la membrane externe⁵.

Certains appendices extracellulaires peuvent être présents à la paroi cellulaire, comme par exemple les flagelles qui assurent la mobilité bactérienne⁶.

La plupart des espèces bactériennes ne vivent pas individuellement en suspension, c'est à dire à l'état planctonique, mais en communautés complexes adhérentes à des surfaces et enrobées d'un gel muqueux, appelées biofilms⁷.

2- Les biofilms

C'est au 17^{ème} siècle que le biologiste néerlandais Antoni van Leeuwenhoek observe pour la première fois des formes de vies minuscules sur ses propres dents⁸. Ces dernières ont été caractérisées par la suite comme étant la plaque dentaire, un biofilm naturel multi-espèces. En 1943, Claude E. Zobell, professeur émérite de microbiologie marine, constate que « l'eau de mer environnante contient moins de bactéries qu'à sa surface »⁹. Ce résultat ne sera expliqué qu'en 1978 lorsque le microbiologiste John W. Costerton démontra pour la première fois l'existence des biofilms, ceux-ci étant définis comme des communautés bactériennes multicellulaires adhérentes à une surface ou à une interface, et enrobées d'une matrice environnante protectrice^{10,11}. Grâce à l'utilisation de la microscopie électronique à balayage et à transmission, un biofilm a pour la première fois été visualisé dans le détail en 1989, provenant de filtres à ruissellement d'une usine de traitement des eaux usées. Le biofilm était multi-espèces, autrement dit regroupant une variété de micro-organismes¹².

Pour plusieurs raisons développées plus bas, les biofilms posent des problèmes en industrie et en santé publique. Ceci explique qu'il existe aujourd'hui en France le Réseau National Biofilm (RNB), qui regroupe plusieurs laboratoires privés et publics, tels que le CNRS et l'INRA, focalisés sur l'étude des biofilms en milieux alimentaire, médical et naturel. Le but de ce réseau est de permettre une synergie de l'ensemble des acteurs par le biais d'échanges scientifiques et méthodologiques.

A. Un biofilm, c'est quoi ?

Les biofilms correspondent à une organisation de bactéries en communautés adhérentes à des surfaces et enveloppées d'une matrice extracellulaire (MEC)¹³ (Figure 2).

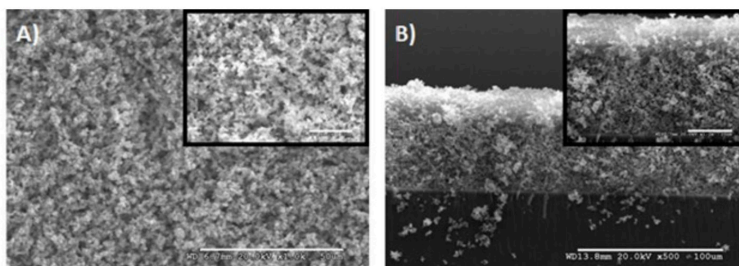


Figure 2. Biofilm de *Pseudomonas aeruginosa* recouvert de sa MEC observé en microscopie électronique à balayage. Des images de surface (A) et de tranche (B) d'un biofilm de *P. aeruginosa* dévoilent la présence d'une matrice polymérique qui l'enrobe. Les barres d'échelle sont respectivement 25 et 50 μm pour les images A et B et de 25 μm pour celles incrustées. Cette figure est tirée de l'article de Wilson et al¹⁴.

Quatre facteurs sont nécessaires à l'établissement des biofilms:

- les microorganismes,
- un milieu humide,
- une surface (ou une interface),
- des nutriments.

La variété de ces quatre éléments est à l'origine de la diversité et de la prévalence des biofilms, les rendant spécifiques aux conditions dans lesquelles ils apparaissent. Les biofilms peuvent être désignés comme homogènes ou hétérogènes selon qu'ils soient composés d'une ou de plusieurs espèces, respectivement. Au sein de ces structures supracellulaires, les bactéries optent pour un comportement coopératif, où chacune participe à, et profite de, l'établissement du biofilm. Au niveau des couches internes, la concentration en nutriments est très faible et les bactéries sont dites « en dormance ». La consommation nutritive se réalise donc par les cellules des couches plus externes, établissant un gradient de nutriments, de catabolites et de pH à l'intérieur du biofilm¹⁵.

B. Quels bénéfices ?

Le biofilm fournit un environnement complet pour le développement d'une association syntrophique, c'est à dire une relation symbiotique entre deux espèces, telles que des bactéries métaboliquement différentes, l'une se nourrissant et éliminant de fait les catabolites de l'autre¹⁶. Cette socialisation syntrophique permet aux microorganismes de survivre à des conditions environnementales hostiles telles que la température, le pH et le rayonnement U.V¹⁷, ainsi qu'à des concentrations très élevées d'antibiotiques¹⁸, diminuant jusqu'à 1 000 fois leur susceptibilité¹⁹. La promiscuité des cellules dans le biofilm favorise le transfert horizontal de gènes entre bactéries, leur assurant cette résistance accrue. Il est en effet estimé que ce transfert de gènes est jusqu'à 700 fois plus important à l'intérieur d'un biofilm qu'entre individus planctoniques²⁰.

Les stress environnementaux, la densité cellulaire des micro-colonies et le manque de nutriments font partie des facteurs pouvant déclencher le passage de l'état planctonique à l'état de biofilm. Cette transition phénotypique permet aux bactéries d'économiser leur énergie et d'assurer leur survie. Un biofilm est d'autant plus stable et résistant face aux contraintes environnementales lorsqu'il abrite une diversité d'espèces et de groupe de microorganismes²¹. Dans des conditions optimales de croissance, le biofilm peut rapidement devenir macroscopique, jusqu'à atteindre le mètre d'épaisseur si l'environnement le permet.

C. Où les retrouve-on?

Les biofilms sont omniprésents du fait de leur résistance élevée aux conditions environnantes variées (Figure 3). L'estimation actuelle est que notre planète est composée de $1,2 \times 10^{30}$ bactéries pour $3,5 \times 10^{29}$ développées en biofilm.

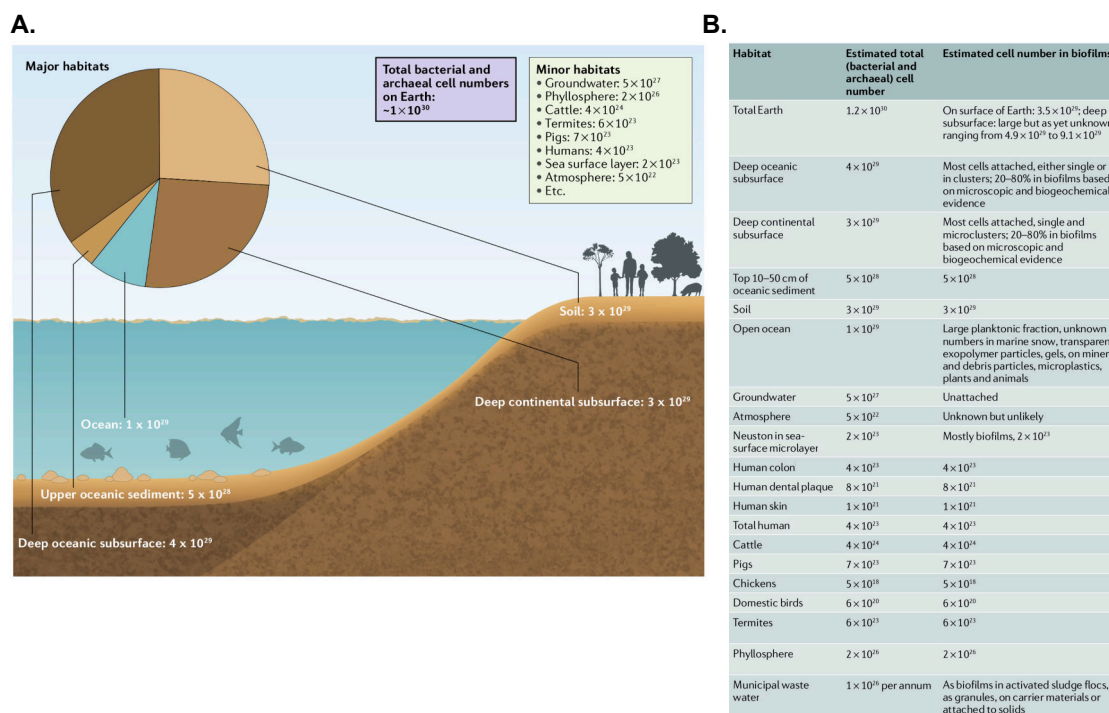


Figure 3. Abondance des bactéries et archées comparée au nombre total de biofilms dans les habitats les plus pertinents de notre planète. A. Illustration de l'abondance microbienne sur Terre. Les cinq principaux habitats des bactéries et des archées sont les océans, les sédiments océaniques supérieurs, les fonds océaniques profonds, les sols et les sous-sols continentaux profonds. Au total, environ $1,2 \times 10^{30}$ de cellules bactériennes et archéennes sont estimées. B. Tableau récapitulatif du nombre approximatif de bactéries et d'archées présentes dans les divers habitats de notre planète (les eaux souterraines, les eaux usées, les animaux et les plantes), comparé au nombre de cellules estimées au sein de biofilms. Les figures A et B sont extraites de l'article de Flemming et Wuertz²².

Les biofilms sont capables de coloniser des surfaces aussi bien biotiques qu'abiotiques (Figure 4). Il est commun de les retrouver sur les racines et feuilles de plantes, les cours d'eau (fleuve du Tagliamento en Italie²³), les rochers hydrothermaux (Pilbara en Australie²⁴), les surfaces glaciaires (Antarctique²⁵), le sable humique, ou bien sur les navires, les vases, les rideaux de douches, les tuyaux d'eau chaude^{26,27}, les matériaux de plomberie^{28,29}, mais encore sur les surfaces dentaires, les tissus humains et les implants prothétiques³⁰.

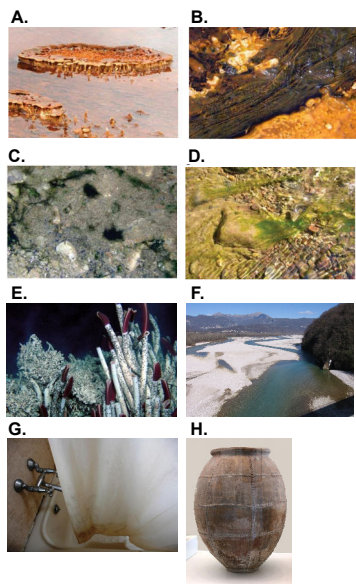


Figure 4. Les biofilms sont omniprésents. Les biofilms peuvent se développer dans les sources hydrothermales (A et B), les rivières d'eau douce (C et D) et les fonds marins (E). Le fleuve du Tagliamento (Italie) est un bel exemple de colonisation de biofilms (F). Les rideaux de douche ainsi que les vases sont tout autant des « nids » à biofilms (G et H).

D. Comment se développent-ils ?

Le modèle actuel supporte que les biofilms s'établissent en 5 étapes (Figure 5) :

- l'attachement à une surface,
- la formation de micro-colonies,
- la synthèse d'une MEC,
- la maturation,
- la dispersion.

Ci-après, nous développons plus avant ces étapes.

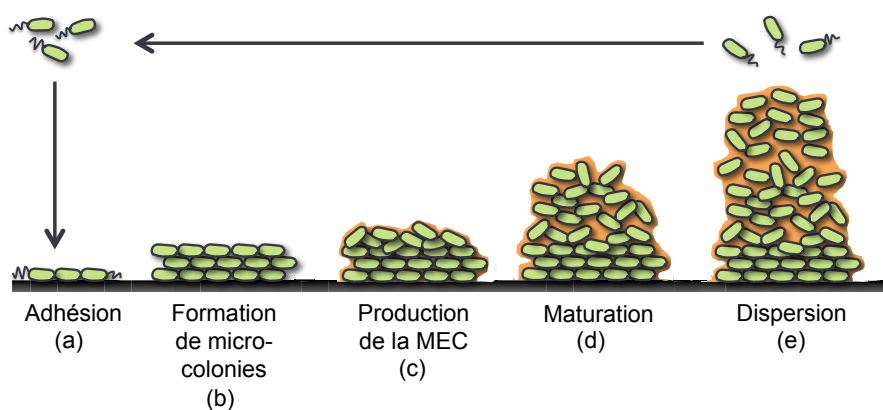


Figure 5. Représentation schématique des différentes étapes conduisant à la formation d'un biofilm bactérien. Les cinq étapes du développement d'un biofilm bactérien sont représentées de gauche à droite. (a) Les bactéries planctoniques adhèrent à une surface, (b) et forment des micro-colonies par différenciation cellulaire et recrutement de nouvelles bactéries planctoniques. (c) La production d'une MEC confère au biofilm une résistance face à son environnement, (d) lui permettant de passer à un état mature. (e) Les bactéries finissent par se détacher du biofilm, entraînant sa dispersion. La figure est adaptée du modèle proposé par Vlamakis et al¹³.

a. L'attachement à une surface

La première étape est l'adhésion des bactéries planctoniques à une surface, déclenchant leur passage d'un état unicellulaire nomadique à un état multicellulaire sédentaire grâce à plusieurs changements phénotypiques. Les cellules planctoniques initient les interactions avec la surface en réponse à divers signaux, tels que l'état nutritionnel de l'environnement³¹. Des forces physiques, telles que les forces van der Waals et les interactions électrostatiques, contribuent à cette adhésion bactérienne. De plus, les lipopolysaccharides (LPS) – lipides décorés de chaînes polysaccharidiques plus ou moins longues et caractéristiques des membranes externes des bactéries Gram négatif – ou bien les appendices, comme les pilis ou les flagelles, peuvent également contribuer à la fixation des cellules microbiennes à la surface.

Les pilis sont de fins filaments qui s'étendent hors de la cellule, essentiels pour l'interaction initiale avec les surfaces à coloniser, alors que les flagelles sont de longs filaments semi-rigides qui assurent la motilité des bactéries leur permettant d'atteindre ces surfaces³². Cette motilité bactérienne est essentielle à l'initiation de la formation de biofilms. Les flagelles peuvent également être impliqués dans la fixation des cellules aux surfaces, facilitant l'initiation de la formation de biofilm, ou encore dans le déplacement de bactéries au sein d'un biofilm en développement le long de la surface, facilitant la croissance et la propagation du biofilm³².

b. La formation de micro-colonies

Une fois les microorganismes adhérents à une surface, inerte ou biotique, et que cette fixation devient stable, un processus de multiplication et de division cellulaire, ainsi qu'un recrutement de bactéries planctoniques, permettent le développement de micro-colonies. Les bactéries perdent leur mobilité, notamment par la différenciation du flagelle³³ ou du pili IV³⁴ chez les bactéries Gram-négatif, et commencent à sécréter leur matrice. L'architecture tridimensionnelle des micro-colonies est indispensable à l'étape de sécrétion d'une MEC, nécessaire à leur coordination et à l'émergence de nouvelles fonctions, telles que la communication et la signalisation inter- et intracellulaire. Cette coordination favorise également les échanges de substrat, la distribution de produits métaboliques et l'excrétion des catabolites.

c. La synthèse d'une MEC

En règle générale, 5 à 35% du volume d'un biofilm sont occupés par les microorganismes. La MEC constitue le reste³⁵, ce qui témoigne de son rôle majeur dans la cohésion de la communauté bactérienne^{36,37}. La structure et la composition de cette matrice sont des éléments majeurs dans la régulation et la résistance des biofilms.

Dans sa version générique, la MEC est composée d'exopolysaccharides (EPS, entre 1 et 2%)³⁸, de protéines (> 2%)³⁹, d'acides nucléiques (<1%)⁴⁰, de lipides, d'ions et d'eau (97%), mais sa composition précise varie en fonction de l'espèce microbienne et des conditions de croissance. Chacun de ces composants participe à, et influe sur, l'architecture, la densité, la porosité et la stabilité mécanique de la MEC⁴¹. Néanmoins, les recherches sur la structure et la composition exacte de cette MEC sont difficiles en raison de leur complexité inhérente. Malgré ce défi, plusieurs analyses microscopiques et biochimiques ont été développées et appliquées pour annoter sa composition et déterminer les rôles fonctionnels de ses composants⁴².

La sécrétion d'une MEC par les bactéries leur assure une protection mécanique au sein du biofilm. Elle agit en premier lieu comme une barrière physique qui confère aux microorganismes une résistance accrue au système immunitaire⁴³, aux facteurs environnementaux, et aux antibiotiques⁴⁴ grâce au ralentissement de leur pénétration au sein du biofilm. Dans le cas de biofilms hétérogènes, constitués de plusieurs espèces microbiennes, la MEC « finale » sera la résultante de leurs multiples sécrétions, et présentera des caractéristiques physico-chimiques spécifiques voire uniques⁴⁵. Chez certaines espèces, des approches génétiques ont permis d'identifier des gènes à l'œuvre dans la sécrétion et la composition de la MEC de biofilm⁴⁶. Nous prenons l'exemple de *Pseudomonas aeruginosa*, bactérie Gram-négatif impliquée dans des infections chroniques ; l'exemple le plus connu étant la mucoviscidose, une maladie génétique qui favorise la colonisation microbienne dans les voies aériennes. Ce pathogène utilise trois EPS pour assembler ses biofilms : le Psl, le Pel et l'aginate⁴⁷.

- Le polysaccharide Psl intervient dans l'initiation et la maintenance des biofilms en promouvant les interactions intercellulaires^{48,49}. De plus, au stade de maturation des biofilms, il a été démontré que Psl s'accumule en surface pour permettre leur dispersion ultérieure^{50,51}.

- Le polysaccharide Pel est un composant essentiel dans la formation des biofilms associés à une surface solide; il joue vraisemblablement un rôle dans l'adhésion^{49,52}.
- L'alginate est l'EPS sécrété dans les biofilms de *P. aeruginosa* le plus étudié^{51,53} car il permet la distinction entre les biofilms mucoïdes ou non mucoïdes⁵⁴. En effet, isolée des poumons de patients atteints de mucoviscidose, *P. aeruginosa* subit souvent le passage à un phénotype mucoïde⁵⁵, résultant d'une surproduction d'alginate. Cette surproduction jouerait un rôle protecteur dans l'environnement sévère du poumon, renforçant ainsi la formation de biofilms⁵⁵.

Expérimentalement, les gènes présumés impliqués dans les biofilms peuvent être supprimés ou surexprimés, ce qui influencera la composition de la MEC résultante ainsi que les phénotypes associés. Ces derniers peuvent ensuite être testés par spectroscopie de masse^{56,57} et/ou par Résonance Magnétique Nucléaire (RMN)⁵⁸.

L'ADN extracellulaire est identifié comme un composant important pour le développement de biofilms chez plusieurs espèces^{40,59-61}. En effet, il a été montré que l'ajout de DNase, une endonucléase clivant non-spécifiquement l'ADN, au milieu de croissance des bactéries inhibe la formation de biofilms à des stades précoces. En revanche, l'ajout de l'endonucléase sur des biofilms matures ne les perturbe pas car ils sont protégés par la présence de la MEC⁴⁰. Les EPS contribuent quant à eux à la stabilité mécanique des biofilms, offrant une résistance à des forces de cisaillement considérables⁶². Plusieurs études ont montré que des mutants bactériens incapables de synthétiser des EPS sont incapables à former des biofilms, bien qu'ils puissent encore se fixer aux surfaces et former des micro-colonies^{63,64}. De plus, la cohésion d'un biofilm peut-être renforcée par la présence d'un réseau fibreux de nature amyloïde au sein de la matrice^{15,45,65}.

Globalement, la stabilité mécanique d'un biofilm est attribuée aux caractéristiques viscoélastiques de la MEC⁶⁶. Selon les espèces, les conditions environnementales et l'état de développement du biofilm, la nature de cette barrière biologique évolue drastiquement⁶⁷ et est temporellement corrélée aux prochaines étapes de maturation et de dispersion.

d. La maturation

Au sein d'un biofilm mature, le niveau d'expression protéique des bactéries est 50% plus faible que celui des mêmes bactéries à l'état planctonique⁶⁸. Certaines cellules du biofilm sont décrites comme étant en état de dormance métabolique, permettant aux biofilms d'être très résistants à leur environnement et notamment aux antibiotiques⁶⁹.

Le biofilm mature est donc constitué de bactéries très différenciées phénotypiquement et génétiquement, entre lesquelles une communication et une signalisation chimique particulière, plus connues sous le nom de « quorum sensing » (QS)⁷⁰, s'établissent au sein de la MEC sécrétée⁷¹⁻⁷³. Le QS (décrit ultérieurement) est primordiale aux bactéries pour assurer la maturation et la survie du biofilm^{70,74}. De plus, des composants de la MEC peuvent agir comme intermédiaire à d'autres biomolécules pour fournir des propriétés uniques qui supporteront la structure et la fonction de l'ensemble du biofilm^{75,76}.

e. La dispersion

L'étape de dispersion d'un biofilm permet aux bactéries de coloniser de nouvelles surfaces grâce à la ré-adoption d'un phénotype planctonique. Ce phénomène peut être induit par le vieillissement du biofilm, par certains facteurs environnementaux ou par des conditions de carences nutritives et/ou métaboliques.

Les communautés microbiennes formant des biofilms peuvent mettre en place plusieurs stratégies pour favoriser le processus de dispersion :

- Certaines bactéries produisent des enzymes saccharolytiques qui vont digérer la MEC et ainsi permettre la libération des microorganismes en surface, les laissant coloniser une nouvelle surface. Par exemple, *Escherichia coli* synthétise de la N-acétyl-héparosan lysase⁷⁷, *P. aeruginosa* et *Pseudomonas fluorescens* produisent de l'alginate lyase⁷²⁻⁷⁹, et *Streptococcus equi* libère de l'hyaluronidase⁸⁰.
- Certains microorganismes produisent un mélange d'acides aminés de série D et de fibres amyloïdes qui interagissent localement avec les EPS, entraînant leur effondrement⁶⁶.
- D'autres bactéries régulent positivement l'expression des protéines liées à la formation de flagelles, ce qui leur permettent de se déplacer vers un nouveau site à coloniser⁷⁶.

- Enfin, certains microorganismes s'extirpent du biofilm en digérant leur matrice, celle-ci restant une source d'énergie utile⁸³.

E. Comment communiquent-ils ?

Ce qui caractérise avant tout un biofilm c'est la capacité de communication intercellulaire accrue entre ses membres. Cette communication, le QS, est primordiale pour assurer la survie et la résistance des cellules du biofilms face au milieu extérieur, et joue un rôle déterminant dans divers processus tels que la différenciation et la maturation cellulaire⁸⁴⁻⁸⁶. Comme la détection du QS nécessite une densité de bactéries suffisante, aucun de ces signaux ne devrait participer aux étapes initiales de la formation, de l'attachement et de la prolifération de biofilms. Le QS repose sur quatre processus qui incluent la production de signaux intercellulaires inducteurs⁸⁴, la sécrétion de ces derniers, leur liaison à des récepteurs spécifiques, pour finir par l'induction de l'expression d'une série de gènes après activation desdits récepteurs⁸⁷. Ces signaux sont impliqués dans la communication intercellulaire et dans l'expression de nombreux facteurs de virulence sécrétés en réponse aux fluctuations des multiples signaux environnementaux. De plus, ils sont en charge de l'organisation spatiale des biofilms, du maintien de leur intégrité et de la synchronisation métabolique entre les différentes cellules de la communauté⁸⁸.

Par ailleurs, au sein d'un biofilm, le phénotype d'une cellule peut affecter significativement le mode de vie de ces bactéries voisines à travers la sécrétion de composés qui inhiberont ou favoriseront leur croissance cellulaire⁸⁹. Pour aller plus loin, il a même été montré qu'également entre deux biofilms séparés jusqu'à 1 000 longueurs de cellules (≈ 2 mm), une synchronisation métabolique existe (Figure 6. A), amenant les cellules à se nourrir en même temps et à la même fréquence⁹⁰ (Figure 6. B). En revanche, lorsque le taux de nutriments disponible diminue, les communautés modifient leurs oscillations pour les rendre complémentaires, ce qui conduit à une augmentation du taux de croissance au sein des deux biofilms. Les biofilms résolvent le conflit nutritionnel en passant d'oscillations en phase à des oscillations en antiphase, c'est à dire qu'une communauté se nourrit pendant que l'autre est en « pause » puis inversement⁹⁰ (Figure 6. B).

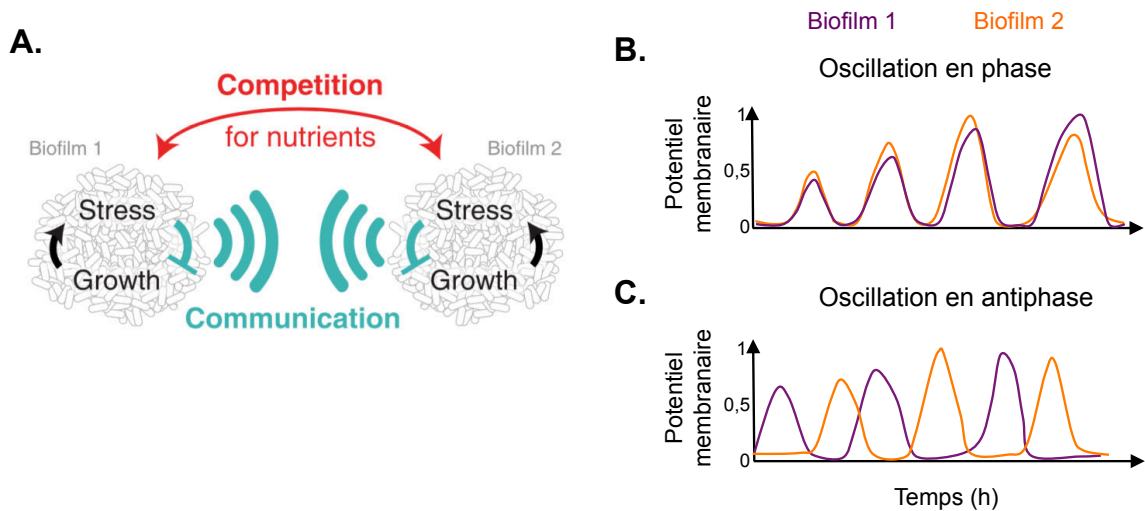


Figure 6. Les biofilms distants synchronisent leur dynamique de croissance. A. Les biofilms individuels subissent des oscillations métaboliques qui arrêtent périodiquement leur croissance. Les oscillations métaboliques sont facilitées par la communication électrique qui peut s'étendre au-delà d'un biofilm pour coupler deux biofilms distants (signaux cyan). De plus, deux biofilms peuvent être couplés par compétition pour les nutriments (flèches rouges). B. Le potentiel membranaire aux bords de deux biofilms – 1 (violet) et 2 (orange) – est synchronisé métaboliquement en phase. C. En condition de carence nutritionnelle, le potentiel membranaire des deux biofilms oscille en antiphase. Les figures sont extraites et modifiées de l'article de Liu et al⁹⁰.

F. Quels impacts ?

a. Les effets négatifs

Les biofilms provoquent de problèmes graves en productivité industrielle du fait des dégâts qu'ils provoquent sur les matériels (par exemple dans les conduites d'eau⁹¹ ou sur les échangeurs thermiques⁹²). Ils peuvent également poser de graves problèmes en santé humaine du fait, soit de la détérioration des dispositifs médicaux, soit d'infections nosocomiales (infections contractées à l'hôpital) (Figure 7).

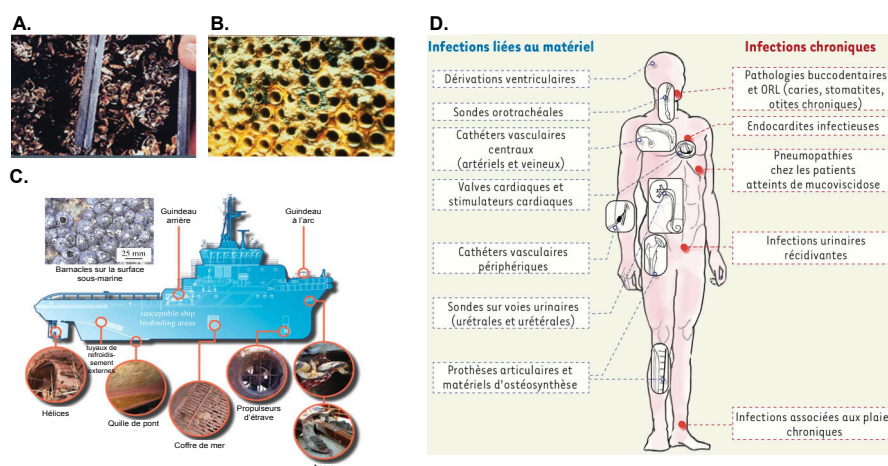


Figure 7. Les biofilms affectent profondément la productivité industrielle et la santé humaine.

A et B. Dans les industries, les biofilms entraînent l'encrassement des tuyaux. Les images proviennent de l'article de Hall-Stoodley et al¹⁷. C. Les navires représentent un « nid » à biofilms avec plusieurs zones susceptibles à l'encrassement biologique. La représentation schématique du navire est extraite de l'article de Bixler et Bhushan³⁰. D. Chez l'Homme, les biofilms sont associés à plusieurs infections, qu'elles soient liées au matériel (bleu) ou qu'elles soient chroniques (rouge). L'illustration est tirée de l'article de Lebeaux et Ghigo⁹³.

Des dizaines de milliards d'euros sont ainsi investis chaque année pour assurer la qualité de l'eau, éviter la corrosion des canalisations, maintenir l'efficacité des générateurs d'énergie et traiter les problèmes de santé. A l'hôpital, les biofilms apparaissent généralement sur ou à l'intérieur de prothèses et dispositifs médicaux tels que les cathéters veineux centraux, les valvules cardiaques mécaniques, les articulations prothétiques, les stimulateurs cardiaques ou encore les cathéters urinaires^{94,95}. Ils peuvent ainsi causer un grand nombre de maladies comme les caries dentaires, la péritonite, la mucoviscidose, l'otite, la prostatite ou encore des maladies de la peau. Selon l'Institut de Veille Sanitaire (InVS), ainsi que la Santé Publique France, environ 5% des patients hospitalisés présentent au moins une infection nosocomiale et plus de 16% sont traités par au minimum un antibiotique^{96,97}. Il faut savoir qu'à ce jour la France demeure l'un des pays les plus consommateurs d'antibiotiques en Europe, se plaçant au 3^{ème} rang derrière la Grèce et Chypre⁹⁸. Ces chiffres sont aussi contradictoires qu'alertants puisque l'antibiothérapie échoue très souvent dans l'éradication des biofilms⁹⁹. Par exemple, le taux de prévalence de la multi-résistance aux médicaments chez les uropathogènes bactériens est plus élevé chez les souches se socialisant en biofilms que chez celles restant planctoniques. La surveillance et le contrôle de biofilms dans les industries et dans les hôpitaux pourraient prévenir des pannes d'équipements, réduire les dégradations des installations, limiter les infections nosocomiales, et par conséquent diminuer les pertes économiques et humaines.

b. Les effets positifs

Durant la plus longue fraction de son existence, notre planète a abrité exclusivement des microbes. Aujourd'hui encore, les microorganismes dominent le monde du vivant en terme de nombre d'individus et de biomasse. Ainsi, malgré des conséquences parfois défavorables pour la vie et les activités humaines, les biofilms restent indispensables à notre survie, ainsi qu'à la plupart des écosystèmes nous environnant. Notre flore intestinale est un très bel exemple de biofilms multi-colonies dont nous tirons profit. Egalement, le biofilm microbien des vasières (habitat littoral, estuarien ou sous-marin constitué de matériaux sédimentés fin non sableux) est une source de nourriture naturel et directe pour les invertébrés ou quelques vertébrés supérieurs¹⁰⁰. Cependant, la vie et les actions humaines modifient cette activité microbienne à l'échelle mondiale et provoquent des changements importants, tels que des perturbations fortes des conditions physiques et chimiques dans les océans et à la surface des sols. Heureusement, les biofilms participent au recyclage des éléments vitaux pour la planète, à la détoxification des sols et des eaux souterraines d'une variété de polluants dangereux et d'éléments introduits dans l'environnement par l'activité humaine¹⁰¹, ainsi qu'à la (dé-) nitrification des eaux usées avec la mise en place en Europe du MBBR (Moving Bed Biofilm Reactor)¹⁰². Ils peuvent également être utilisés comme bio-indicateurs et marqueurs du degré de pollution spécifique à leur habitat¹⁰³.

c. Nécessité de trouver un équilibre

A ce jour, il est plus que nécessaire de définir et de maintenir un meilleur équilibre entre les nombreux effets bénéfiques et néfastes occasionnés par la présence des biofilms. Cet objectif réclame une compréhension plus approfondie du mécanisme de développement des biofilms, une connaissance fine de leur physiologie, ainsi qu'une capacité à maîtriser leur essor et à faire échouer leurs mécanismes de résistance.

d. Les thérapies anti-biofilms

Nous avons passé plusieurs lignes à décrire et à expliquer la résistance accrue des cellules bactériennes au sein des biofilms. Nous avons explicité en quoi cette résistance pouvait mettre à mal les activités et la santé humaines. Il est donc compréhensible qu'un large volet de la microbiologie et de la médecine soit voué à l'éradication de ces supra-structures bactériennes dans certaines conditions.

Plusieurs stratégies anti-biofilms sont en cours de développement, telles que:

- l'utilisation de molécules, peptides ou protéines ayant un effet antimicrobien^{104,105},
- l'inhibition du QS⁶⁷ afin d'éviter la maturation du biofilm¹⁰⁶,
- le ciblage de la MEC et notamment des EPS¹⁰⁷,
- l'inhibition de l'adhésion des bactéries à la surface^{108,109},
- le déclenchement de la dispersion du biofilm^{81,110}.

Cependant, ces méthodes restent défectueuses sur plusieurs lignées bactériennes différentes et en terme d'efficacité clinique.

Récemment, il a été montré que des protéines situées aux membranes externes des bactéries Gram négatif, les porines, peuvent être impliquées dans la formation de biofilms en favorisant l'interaction entre bactéries¹¹¹. Cette observation laisse espérer qu'un nouveau type de traitement anti-biofilm soit à porter, qui ciblerait l'interaction entre ces protéines membranaires pour faire échouer leur socialisation. Le prérequis est cependant de caractériser ces interactions afin de comprendre comment elles sont établies et comment elles pourraient être rompues.

3- Les porines

Les porines, découvertes en 1976, sont des pores qui permettent la diffusion de petites molécules hydrophiles (< 600 Da) à travers la membrane des bactéries sans les lier¹¹². Elles constituent les protéines membranaires emblématiques des bactéries Gram-négatif¹¹³.

A. Les bactéries Gram-négatif

Il est capable d'identifier les bactéries Gram-positif de celles Gram-négatif grâce à une méthode de coloration au violet de gentiane du fait qu'elles soient de compositions différentes¹¹⁴. En effet, les cellules Gram-positif sont constituées d'une seule membrane lipidique et possèdent une paroi riche en peptidoglycane (PG), alors que les bactéries Gram-négatif sont dotées d'une double membrane lipidique qui délimite un espace de transit et d'échange, le périplasme, qui contient une couche fine de PG^{115,116} (Figure 8. A). En pratique, l'utilisation du violet de gentiane, une molécule capable de traverser les parois et les membranes des bactéries pour se fixer dans leur cytoplasme, permet la coloration de toutes les cellules en violet. Le colorant est ensuite enlevé avec une solution d'éthanol et c'est à cette

étape que se distinguent les bactéries Gram-positif de celles Gram-négatif. Les cellules Gram positif apparaissent violettes du fait que leur paroi riche en PG empêche l'alcool d'emporter le violet de gentiane, qui restera dans le cytoplasme. Les cellules Gram-négatif se retrouvent quant à elles de couleur rose en raison de leur couche de PG fine qui ne retient que très peu le colorant.

a. Le périplasme

L'espace périplasmique intermembranaire représente entre 20 et 40% du volume de la cellule¹¹⁷. La fine couche de PG au sein du périplasme permet de former un réseau dense autour de la cellule, ce qui détermine sa forme et sa taille. De plus, en combinaison avec plusieurs protéines périplasmiques, la couche de PG est impliquée dans¹¹⁸:

- la synthèse des constituants de l'enveloppe, comme les LPS,
- la sécrétion de protéines et/ou de polysaccharides extracellulaires,
- la mise en place de flagelles et/ou des pilis,
- la nutrition par le transport de nutriments,
- la détoxification par la dégradation et/ou le transport sortant des toxiques,
- la signalisation par la perception et la transmission d'informations externes.

b. Les membranes interne et externe

La membrane interne est une simple bicouche de phospholipides, constituée de phosphatidyléthanolamine, de phosphatidylglycérol et de cardiolipine répartis de façon symétrique entre les feuillet cytoplasmique et périplasmique. La membrane externe est quant à elle asymétrique, composée d'un feuillet interne coté périplasmique – semblable aux feuillet de la membrane interne¹¹⁹ – et d'un feuillet externe principalement composé de LPS¹²⁰. Cette membrane est parsemée de protéines-canal dont la portion transmembranaire est exclusivement formée par des feuillet β ¹²¹. Ces dernières, principalement des porines, constituent l'essentiel porte d'influx pour les molécules provenant du milieu extérieur vers la bactérie^{122,123}.

c. Les LPS

Les LPS ont d'abord été mis en évidence pour leurs activités toxique et inflammatoire. Très brièvement, les récepteurs de reconnaissance cellulaires de type Toll (Toll-like receptors,

TLR en anglais) interviennent au cours des mécanismes d'immunité innée en reconnaissant des motifs moléculaires associés aux pathogènes¹²⁴⁻¹²⁶. Le LPS est une endotoxine se liant au récepteur TLR4 afin de promouvoir la libération de cytokines pro-inflammatoires, induisant des signes cliniques chez l'Homme¹²⁷. Nous savons aujourd'hui que le LPS joue plus qu'un rôle de toxine, étant la clé de voûte de l'intégrité structurale des bactéries Gram-négatif et représentant la première ligne de défense et de virulence des bactéries. Ils sont composés de 3 unités : un domaine hydrophobe appelé lipide A, un cœur hydrophile et un antigène O^{128,129} (Figure 8. B).

- Le lipide A est la portion extrêmement conservée du LPS¹³⁰ (Figure 8. C). Il s'agit d'un disaccharide phosphorylé de glucosamine décoré de multiples acides gras hydrophobes qui permet l'ancrage du LPS à la membrane bactérienne^{131,132}. Ce domaine lipidique A est responsable d'une grande partie de la toxicité des bactéries à Gram-négatif. En effet, les cellules bactériennes lysées par le système immunitaire libèrent des fragments de membrane contenant le lipide A dans la circulation ce qui provoque fièvre, diarrhée et éventuellement un choc endotoxique fatal^{127,133}.
- Le cœur hydrophile est un composant oligosaccharide très conservé, qui se lie directement au lipide A¹³⁴ et contribue à l'intégrité de la membrane¹³⁵.
- L'antigène O est une chaîne polysaccharidique peu conservée et spécifique d'une espèce à l'autre grâce à ces chaînes latérales¹²⁹. Lié au cœur hydrophobe, il constitue le domaine le plus externe de la molécule LPS, devenant par conséquent une cible pour la reconnaissance par les anticorps de l'hôte puisqu'exposé à la surface même de la bactérie. Le type de LPS est déterminé par la présence (« smooth ») ou l'absence (« rough ») de cet antigène O¹³⁶. Lors d'une infection bactérienne, le LPS change de structure et passe du type « rough » à « smooth », afin d'assurer une protection supplémentaire aux bactéries^{136,137}.

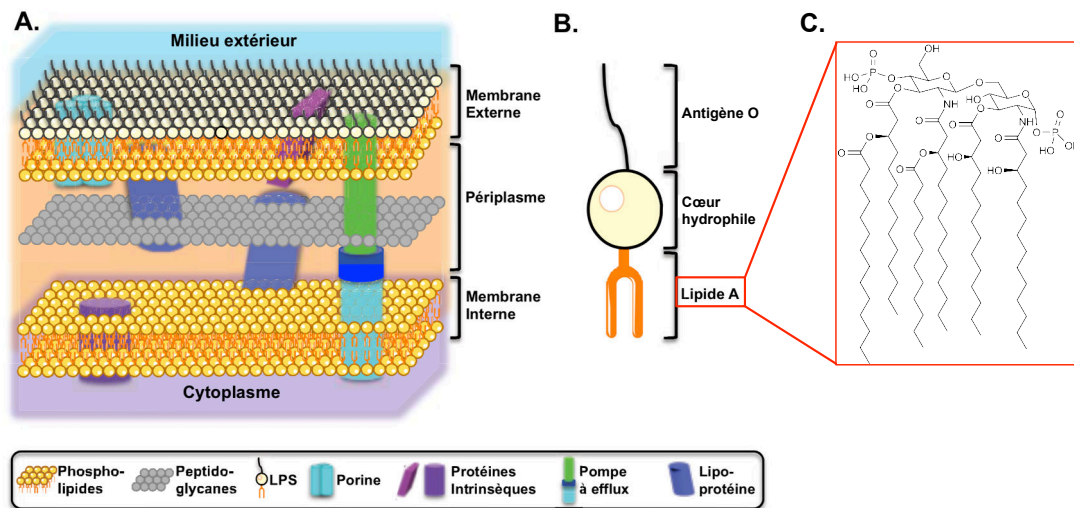


Figure 8. Schéma représentant la double membrane d'une bactérie Gram-négatif. A. La membrane interne est une simple bicouche de phospholipides alors que la membrane externe est composée d'un feuillet interne périplasmique et d'un feuillet externe. Ce dernier est essentiellement formé de LPS. Des protéines membranaires, telles que les porines, sont ancrées dans la double membrane externe. B. Une molécule de LPS est composée de 3 unités : un domaine hydrophobe appelé lipide A, un cœur hydrophile et un antigène O. C. Structure du lipide A d'*E. coli*¹³⁸. La figure a été reprise et modifiée de la thèse de Mariam El Khatib. [128,129](#)

B. Structure des porines

Les porines sont hautement abondantes aux membranes externes, 100 000 copies par bactérie, ce qui représente 50% de la masse membranaire et 70% du contenu protéique¹³⁹. L'étude structurale des porines a débuté dans les années 1980 grâce aux techniques de spectroscopie¹⁴⁰, de microscopie électronique^{141,142}, de RMN¹⁴³ et de cristallographie¹⁴⁴. Elles ont été parmi les premières protéines membranaires à être cristallisées¹⁴⁵, permettant la détermination des structures des porines OmpF¹¹², PhoE¹¹², LamB¹⁴⁶ et ScrY¹⁴⁷ d'*E. coli* à haute résolution (Figure 9).

Les porines sont des trimères de tonneaux β transmembranaires, composés de 16 feuillets β antiparallèles connectés par 8 tours courts périplasmiques et 8 longues boucles extracellulaires, et inclinés selon un angle de 30° à 60° par rapport à l'axe perpendiculaire à la membrane¹⁴⁰. Les boucles externes peuvent interagir avec divers composants du milieu extracellulaire, tels que les anticorps, les phages, les colicines ou encore les antibiotiques. Une boucle particulièrement longue, la boucle L3, se replie en hélice α à mi-hauteur du tonneau β , créant ainsi une zone de constriction qui contrôle le transit des solutés à travers la bactérie¹⁴⁸ (Figure 9). Les boucles L2 de chaque monomère s'intercalent pour former le trimère, stabilisé

à sa périphérie par des contacts entre les boucles L1 et L4 des monomères adjacents (Figure 10. A). Au sein de chaque monomère, une ceinture de résidus aromatiques assure la structuration secondaire des porines (Figure 10. B), et des résidus chargés au niveau des boucles extracellulaires sont impliqués dans l'interaction avec les LPS (Figure 10. C).

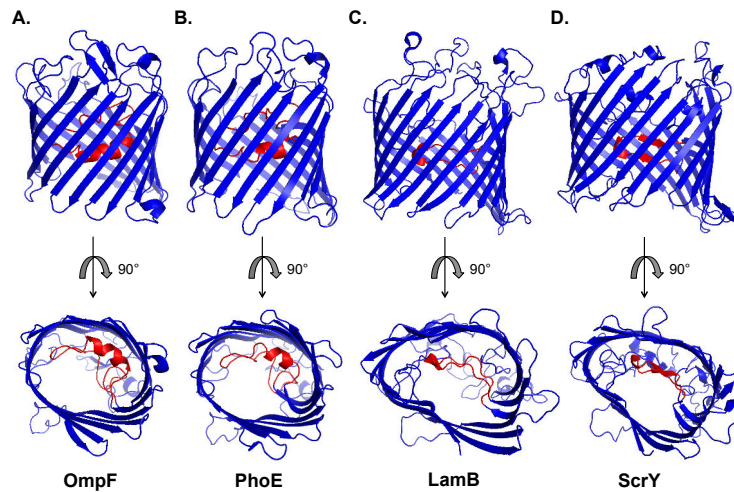


Figure 9. Comparaison de la structure monomérique de différentes porines d'*E. coli*. Vue de face et du côté périsplasmique du tonneau β (bleu) et de la boucle L3 (rouge) des porines OmpF (A. pdb : 2omf) et PhoE (B. pdb : 1pho), formées de 16 feuilletts β ; et de LamB (C. pdb : 1mal) et ScrY (D. pdb : 1a0s), constituées de 18 feuilletts β .

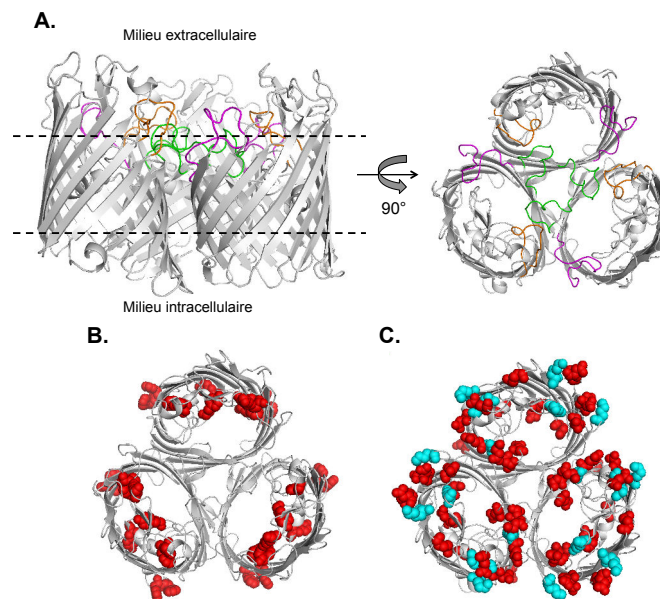


Figure 10. Structure du trimère d'OmpF présentant les principales caractéristiques communes aux porines. A. Vues de face et du côté périsplasmique du trimère d'OmpF montrant les boucles L1 (magenta), L2 (vert) et L4 (orange) impliquées dans les interactions entre monomères. B. Vue de la ceinture de résidus aromatiques (sphères rouges) au niveau des boucles extracellulaires et des tours périsplasmiques, assurant la structuration secondaire d'OmpF. C. Représentation de l'abondance des résidus chargés au niveau des boucles extracellulaires qui permettent l'interaction d'OmpF avec les LPS.

A ce jour, les porines sont classifiées en deux grands groupes¹⁴⁹ :

- i) les porines générales non spécifiques à 16 feuillets β ,
- ii) les porines spécifiques à 18 feuillets β .

Cependant, au vu de la grande diversité structurale des porines, cette classification est largement insuffisante. En effet, la porine Omp32, principale porine de *Delftia acidovorans*, est le premier exemple de porine à tonneau β à 16 brins dont la spécificité de substrat a été prouvée¹⁵⁰. La porine OmpG d'*E. coli*, qui facilite l'absorption de sucres dans les bactéries, forme un tonneau β de 14 brins β antiparallèles¹⁵¹. Egalement la porine Tsx d'*E. coli* forme un canal étroit de 12 brins β spécifiques des nucléosides¹⁵².

Des porines sont également retrouvées au sein de la membrane externe des mitochondries, renforçant l'hypothèse selon laquelle les eucaryotes ont été formés par encapsulation d'une bactérie Gram-négatif par une bactérie Gram-positif¹⁵³. Cependant, les porines de mitochondries présentent au contraire un nombre impair de brins β dans leur tonneau β .

C. Rôles des porines générales non spécifiques

Outre leurs propriétés structurales, les porines partagent plusieurs propriétés biochimiques et fonctionnelles communes. Elles sont impliquées dans un large spectre de rôles physiologiques et sont essentielles au bon fonctionnement et à la survie cellulaire.

a. Diffusion générale

Le rôle majeur des porines générales non spécifiques est d'assurer le passage actif ou passif de petits substrats, solutés et nutriments inférieurs à 600 Da à travers la membrane externe. A travers le tonneau β d'une porine, le trajet des anions diffère de celui des cations en fonction de ses charges internes^{154,155}. En fonction des conditions environnementales, les porines sont capables de faire évoluer leur sélectivité afin d'adapter la réponse bactérienne face aux stress extérieurs^{156,157}.

b. Activité immunologique

Les porines sont capables de contrecarrer l'activité immunologique eucaryote et procaryote en soutenant la pathogénicité et l'infection bactérienne. Quelques exemples sont exposés ci-dessous :

- La porine OprF de *P. fluorescens* facilite l'invasion cellulaire¹⁵⁸ en favorisant l'adhésion bactérienne aux surfaces biologiques^{158,159}.
- Les porines de *Neisseria gonorrhoeae* génèrent une activité pro-inflammatoire lorsqu'elles sont reconnues par les récepteurs TLR de l'hôte²⁹⁻³¹.
- Une porine particulière de *N. gonorrhoeae*, la porine PorB, soutient l'occupation microbienne en fusionnant les bactéries avec les membranes de l'hôte^{160,161}.

c. Signalisation transmembranaire

La signalisation médiée par un ligand à travers une membrane biologique se produit généralement lorsque le ligand se lie à un récepteur membranaire spécifique, le faisant changer de conformation ou d'oligomérisation¹⁶². Cependant, Housden et al. ont décrit un autre mécanisme de signalisation transmembranaire impliquant les porines OmpF et OmpC d'*E. coli*, par lesquelles des toxines enzymatiques (les colicines) sont transloquées pour délivrer des signaux épitopiques au périplasme bactérien¹⁶³.

d. Survie bactérienne

De part leurs propriétés diffusives variées, certaines porines se trouvent plus adaptées que d'autres pour la survie dans des conditions extrêmes. Non seulement le type, mais aussi le nombre de porines exprimées va varier selon l'environnement dans lequel se développe les bactéries. Entre autres, les porines OmpC et OmpF d'*E. coli* sont finement régulées en fonction du stress oxydatif et des fluctuations d'osmolarité et de pH¹³⁵, la porine PhoE est exprimée lorsque les bactéries d'*E. coli* sont en situation de carence en phosphate¹⁶⁴, et la porine MOMP du pathogène *Campylobacter jejuni* se retrouve surexprimée à haute température (42°C) ou à pH élevé (pH 8,5)¹⁶⁵. Ainsi, plus qu'une collection de pores, c'est comme un arsenal de transporteurs spécifiques qu'il faut considérer les porines.

e. Résistance aux antibiotiques

Afin de résister aux antibiotiques, les bactéries exploitent trois stratégies¹⁶⁹ :

- La modification de la cible de l'antibiotique, résultant d'une inaptitude de ce dernier à la reconnaître.
- La dégradation de l'antibiotique grâce à une machinerie enzymatique spécifique, permettant de réduire ou d'abroger son efficacité.
- La réduction de la perméabilité cellulaire aux antibiotiques grâce aux LPS, aux pompes à efflux et aux porines¹⁶⁶⁻¹⁶⁸. Ces trois acteurs agissent selon des mécanismes différents. Les LPS ont vocation à rigidifier la membrane ce qui réduit la diffusion passive ; les pompes à efflux permettent l'extrusion des antibiotiques du cytoplasme vers le périplasma et/ou le milieu extérieur ; et les porines réduisent l'influx d'antibiotiques par altération du profil membranaire – c'est à dire modification des porines et de leurs propriétés diffusives, ou réduction de leur expression.

A titre d'exemple, la première identification d'un isolat multi-résistant d'*Enterobacter aerogenes* en 1988 a permis d'établir les bases moléculaires du mécanisme de mutations spécifiques des porines. Le remplacement d'un résidu glycine par un aspartate dans la longue boucle L3, dans une séquence hautement conservée parmi les porines entérobactériennes¹⁷⁰, induit des modifications majeures de la fonction des pores, telles que la diminution de la conductance, l'augmentation de la sélectivité des cations et l'augmentation du potentiel de seuil de fermeture du canal – autrement dit le potentiel de membrane minimal auquel les porines commencent à se fermer. Ces modifications sont corrélées à une résistance élevée aux β -lactames¹⁷¹.

En 2004, des études ont démontré une régulation rapide de l'expression de la porine majoritaire d'*E. aerogenes* lorsque la bactérie était soumise à de l'imipénème. En effet, la prise de cet antibiotique s'est rapidement accompagnée de la disparition de la porine en charge de son influx dans la souche résistante aux β -lactamines. Lorsque le traitement fût arrêté, la protéine réapparue et la souche bactérienne redevint sensible¹⁷².

Plusieurs travaux réalisés sur *Klebsiella pneumoniae*, qui exprime deux porines principales OmpK35 et OmpK36, ont signalé l'altération des profils de ces dernières accentuant la résistance bactérienne face aux antibiotiques. En effet, la perte d'une des deux porines, accompagnée de la production de β -lactamase, cause une résistance élevée à la céphamycine, un antibiotique des β -lactamines¹⁷³. Après la perte de la porine restante, l'isolat clinique est

d'autant plus résistant aux antibiotiques¹⁷⁴. De manière surprenante, chez certains isolats cliniques dépourvus des deux porines majoritaires, les bactéries de *K. pneumoniae* se développent malgré tout grâce à l'expression à un niveau bas d'une troisième porine OmpK37, normalement au repos¹⁷⁵.

f. Fonction non diffusive des porines

Il s'avère que les porines jouent également un rôle essentiel à n'importe quelle étape de la formation de biofilms. Par exemple, les porines de *P. aeruginosa* participent à la formation de micro-colonies, étape préliminaire à l'établissement des biofilms. La porine OpdF est impliquée dans le transport de molécules de signalisation et dans l'adaptation bactérienne face au changement d'osmolarité au sein de la micro-colonie¹⁷⁶, tandis que la porine OprF assure le développement du biofilm en condition anaérobie¹⁷⁷. Par ailleurs, les études de Cattelan et al. en 2016 ont dévoilé que la porine OmpQ de *Bordetella bronchiseptica* est requise pour la formation d'un biofilm mature¹⁷⁸.

Nous comprenons vite que les porines sont primordiales au bon fonctionnement et à la survie des bactéries qui se développent en biofilms. C'est pourquoi, ces protéines membranaires représentent des cibles phares pour le développement de nouvelles stratégies thérapeutiques.

4- *Providencia stuartii*

A. Description

Notre organisme d'étude, *Providencia stuartii*, a été caractérisé pour la première fois par René Buttiaux en 1954¹⁷⁹. Il s'agit d'un agent pathogène opportuniste de la famille des *Enterobacteriaceae*¹⁸⁰. Ces derniers sont des bactéries Gram-négatif très ubiquitaires, c'est à dire qu'ils se retrouvent dans de nombreux écosystèmes, tels le sol, l'eau et surtout l'intestin (entéro-) de l'Homme et des animaux. La famille des *Enterobacteriaceae* est l'une des plus importantes familles bactériennes, autant du point de vue quantitatif – car elle comporte plus d'une quarantaine de genres (selon ITIS – Système d'information taxonomique intégré) – que du point de vue qualitatif.

La souche *P. stuartii*, du genre *Providencia*, est majoritairement retrouvée dans le tractus urinaire¹⁸, mais a également été isolée dans les reins¹⁸¹, l'endocarde¹⁸², le péricarde¹⁸³ et le

péritoine¹⁸⁴. Elle peut aussi se retrouver dans les selles, le sang, les crachats, les plaies et sur la peau. La présence d'une β -lactamase de type C (AmpC) dans son génome lui confère naturellement un phénotype de multi-résistance (MDR), contre des antibiotiques par exemple, tels que les tétracyclines, les pénicillines et les céphalosporines de 1^{ère} et 2^{ème} génération. Ce phénotype peut être aggravé par l'acquisition de β -lactamases à spectre étendu (BLSE) codées par un plasmide^{18,185,186}. Par exemple, des études de 2005 ont signalé que des isolats cliniques de *P. stuartii* provenant d'Algérie avaient acquis une β -lactamase du New Delhi (Inde)¹⁸⁷. Par ailleurs, les bactéries de *P. stuartii* présentent une propension forte à se développer en biofilm, accentuant plus encore leur résistance déjà élevée vis-à-vis de leur environnement et des antibiotiques.

B. Impact des biofilms de *P. stuartii*

P. stuartii est responsable d'environ 10% des infections des voies urinaires contractées à l'hôpital¹⁸⁸ (INU – Infections nosocomiales urinaires, qui comptent pour 25 à 40% de toutes les infections nosocomiales¹⁸⁹). *P. stuartii* infecte généralement des sujets immunodéprimés, tels que les résidents des unités de soins intensifs (ICU – Intensive care unit) et les patients sous cathétérisation longue^{84,190}. En pratique, l'implantation d'un cathéter dans le tractus urinaire d'une durée supérieure à 28 jours représente une niche des plus favorables à l'installation et à l'expansion de biofilms^{191,192}. En 2004, 62% des INU causées par des bactéries BLSE étaient des infections causées par *P. stuartii*¹⁸⁶, et en 2013, *P. stuartii* s'est retrouvé 3^{ème} en terme de prévalence dans les INU¹⁸⁸. Les antibiotiques administrés aux patients atteints d'une INU éradiquent les bactéries planctoniques mais ne présentent pas d'efficacité similaire vis-à-vis des bactéries formant des biofilms¹⁹². Grâce à leur capacité de socialisation en biofilms, les bactéries de *P. stuartii* sont en effet fortement résistantes aux traitements sous antibiotiques^{105,193}, même après retrait du cathéter¹⁹⁴. De plus, *P. stuartii* présente une activité uréase pouvant entraîner une alcalinisation de l'urine qui résultera en la cristallisation de sels autour du biofilm bactérien. Ce processus favorise l'incrustation et le blocage des cathéters, et sera responsable d'une inefficacité plus prononcée des antibiotiques contre les biofilms¹⁹⁵.

C. Les porines de *P. stuartii*

P. stuartii présente dans son génome des gènes codants pour deux porines générales non spécifiques, à savoir Omp-Pst1 et Omp-Pst2 (Figure 11).

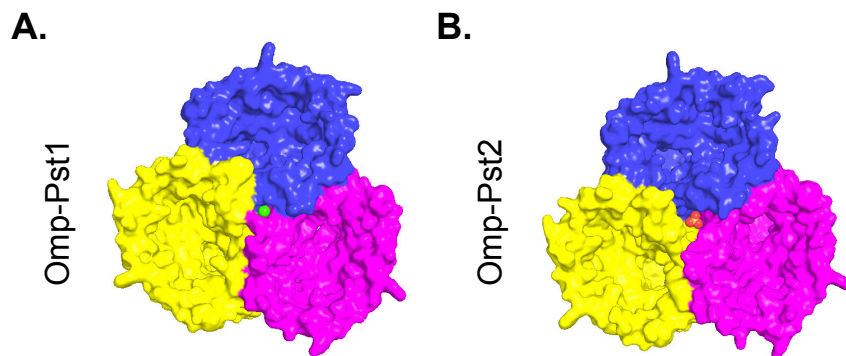


Figure 11. Omp-Pst1 et Omp-Pst2, les deux porines de *P. stuartii*. Vues latérale et du côté périplasmique du trimère d'Omp-Pst1 (A - pdb : 4d64) et d'Omp-Pst2 (B - pdb : 4d65)

En 2010, Tran et al. caractérisent Omp-Pst1 et Omp-Pst2¹⁹⁶ et révèlent que la porine Omp-Pst1 est exprimée environ 10 fois plus qu'Omp-Pst2 dans des conditions normales de croissance. Cette porine, faiblement anion-sélective, constitue donc la principale voie d'entrée des solutés hydrophiles à travers la membrane externe de *P. stuartii*^{111,196}. Omp-Pst2 est quant à elle une porine fortement cation-sélective qui assure la régulation du flux actif de cations vers le périplasma, ainsi que l'efflux du trop plein cationique du milieu périplasmique vers le milieu extérieur¹⁹⁶.

Des études d'électrophysiologie, qui consistent à étudier les courants ioniques à travers les porines, ont permis de comprendre la perméation de celles-ci au niveau moléculaire¹⁵⁶. A dessein, un courant électrique est mesuré dû au flux d'ions traversant une bicouche lipidique planaire, puis le potentiel transmembranaire nécessaire pour favoriser le mouvement des ions est déterminé. Les porines, spontanément insérées dans la bicouche lipidique, entraînent des sauts de courants dû au mouvement des ions à travers les canaux ouverts. En mesurant la taille de ces sauts, la conductance d'un canal est obtenue. Dans le cas des porines, une conductance trimérique est observée. La tension transmembranaire, plus connue sous le nom de « voltage gating », a été décrite comme provoquant une modulation rapide des porines¹⁹⁷. La sensibilité des porines au voltage est quantifiée par méthode d'électrophysiologie, en mesurant le potentiel de seuil de fermeture de canal. Lorsque ce potentiel est supérieur à la valeur seuil, d'environ 150 mV, les monomères de porines se ferment de manière typique et séquentielle¹⁵⁶. Contrairement à Omp-Pst1 et aux autres porines à diffusion générale, les canaux d'Omp-Pst2 affichent une forte sensibilité au voltage externe en se fermant dès 20 mV¹⁹⁸. Cette sensibilité est corrélée à la participation active de la porine à la régulation des flux cationiques à travers la membrane externe.

Une analyse d'interaction par électrophysiologie entre les porines et des molécules de β -lactames a prouvé l'implication des deux porines de *P. stuartii* dans le transport d'antibiotiques. En pratique, la souche BL21 (DE3) Δ Omp8 d'*E. coli*, déléetée de ses propres

porines de diffusion générales – c’est à dire OmpC, OmpF, OmpA et accessoirement LamB¹⁹⁹ – a été utilisée pour exprimer celles de *P. stuartii*, Omp-Pst1 et Omp-Pst2. L'expression de ces dernières augmente véritablement la sensibilité des cellules d'*E. coli* à la plupart des antibiotiques β -lactamines, ce qui démontre que le passage des β -lactames se réalise à travers les porines de *P. stuartii*. Des dosages de concentration minimale inhibitrice (CMI), calculant la plus faible concentration d’antibiotiques pour laquelle il n’y a pas de croissance visible de la souche bactérienne étudiée, ont suggéré une contribution significative de la porine majoritaire Omp-Pst1 à la sensibilité aux antibiotiques de la souche *E. coli* Δ Omp8¹⁹⁶. La régulation négative de l’expression des deux porines et/ou la modification de leurs séquences codantes ont été démontrées comme des causes participant à de nombreux cas de résistance aux antibiotiques²⁰⁰⁻²⁰². En guise d’exemple, *P. stuartii* est capable d’adapter le profil d’expression de ses deux porines, en particulier Omp-Pst1 en présence d’antibiotiques de type β -lactames, lui permettant de devenir résistante au fil des générations^{196,203}.

II - OBJECTIFS DE LA THESE

II - OBJECTIFS DE LA THESE

Mes travaux de thèse s'inscrivent dans la continuation directe des travaux de Mariam El Khatib, doctorante au laboratoire entre 2014 et 2017, qui a mis en évidence l'existence de communautés flottantes chez *P. stuartii* (El Khatib., Tran., Nasrallah., Lopes et al., 2017)²⁰⁴. Leur établissement précède celui des biofilms adhérents, ce qui suggère que ces derniers sont formés par la sédimentation des communautés flottantes (Figure 12). A mon arrivée au laboratoire, cet article était en révision et j'ai activement participé aux expériences nécessaires pour le valoriser et le publier.

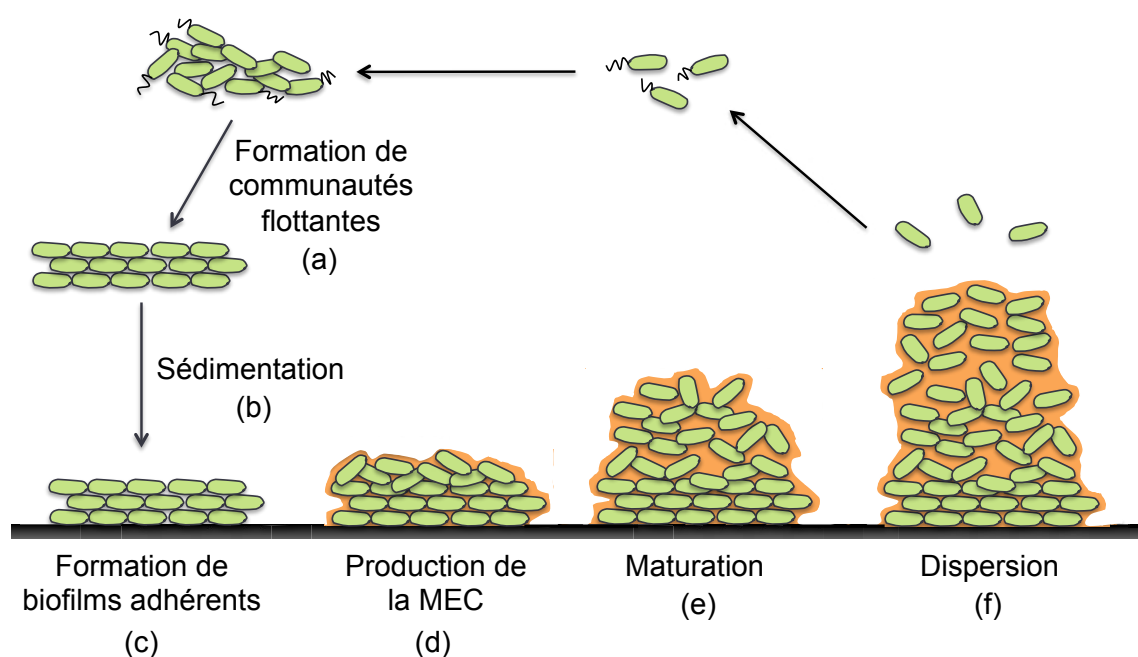


Figure 12. Représentation schématique des différentes étapes de développement de *P. stuartii* en communautés flottantes et en biofilms adhérents. (a) Les bactéries de *P. stuartii* en suspension se développent dans un premier temps en communautés flottantes, (b) avant de sédimenter à une surface et (c) de former des biofilms adhérents. Une fois ces derniers établis, (d) les bactéries sécrètent une MEC (e) leur permettant d'évoluer à un état de biofilm mature. (f) Le biofilm mature finira pas se disperser suite au détachement des bactéries le constituant.

Dans un second article auquel j'ai également participé activement, nous avons démontré le rôle majeur joué par les porines dans la socialisation de *P. stuartii*. Nous avons en effet montré qu'Omp-Pst1 et Omp-Pst2 ont la capacité de s'auto-associer grâce à leurs boucles extracellulaires, formant des dimères de trimères intercellulaires (DOTs) capables de riveter les cellules adjacentes (Figure 13) (El Khatib., Nasrallah., Lopes et al., 2018)¹¹¹. La mise en place de ces DOTs permet de supposer qu'ils jouent un rôle dans la communication cellulaire, dans la mesure où les canaux individuels des porines restent ouverts dans les

structures des DOTs, résolues par cristallographie aux rayons X. Ils pourraient également être à l'œuvre dans la résistance aux antibiotiques, étant entendu que la formation de DOTs réduit l'accès au périplasma via les porines. Ainsi les DOTs de porines pourraient constituer une nouvelle cible dans la lutte contre les biofilms de *P. stuartii* en particulier, et contre la socialisation bactérienne en général. Un prérequis serait cependant de comprendre comment sont affectés les DOTs par les conditions environnementales présentes dans le contexte pathophysiologique.

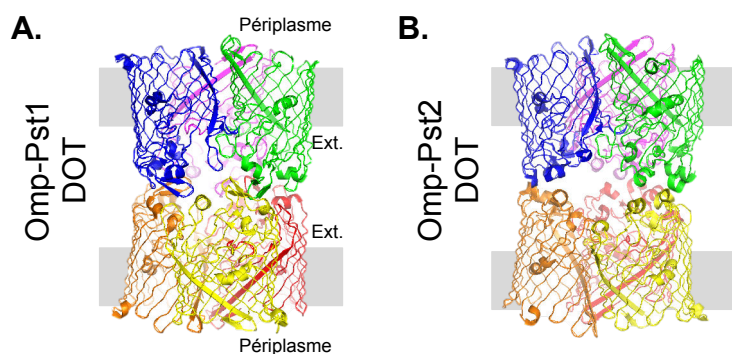


Figure 13. Les porines Omp-Pst1 et Omp-Pst2 de *P. stuartii* s'auto-associent en DOTs à travers leurs boucles extracellulaires. Vue latérale des DOT d'Omp-Pst1 (A) et d'Omp-Pst2 (B). Les positions présumées des membranes externes sont indiquées en gris.

Ainsi, les deux grands objectifs de cette thèse ont été de :

- 1) Comprendre l'effet sur la socialisation bactérienne des métabolites présents au niveau du site d'infection le plus courant pour *P. stuartii*, à savoir le tractus urinaire.
- 2) Tester la faisabilité d'inhibition de la socialisation bactérienne par ciblage direct des DOTs de porines.

Dans le premier article (*El Khatib., Tran., Nasrallah., Lopes et al., 2017*), nous avons étudiés la croissance et la formation des communautés flottantes et des biofilms adhérents de *P. stuartii* dans des conditions similaires à celles prévalant dans son habitat le plus courant chez l'Homme, les voies urinaires. Notre étude a démontré la capacité de *P. stuartii* à former des communautés flottantes et des biofilms adhérents dans diverses conditions hostiles, notamment en présence de fortes concentrations d'urée, de magnésium, de calcium et d'une variation forte de pH²⁰⁴. Pour aller plus loin, nous avons par la suite étudié d'autres métabolites présents dans l'urine, tels que l'ammonium, le bicarbonate et la créatinine. Nous avons étendue cette étude en caractérisant l'effet de toutes ces conditions environnementales sur la survie et la socialisation bactérienne, ainsi que sur l'expression des porines et leur propension s'auto-associer en DOTs (Figure 14) (*Lopes et al., 2019a – en soumission*).

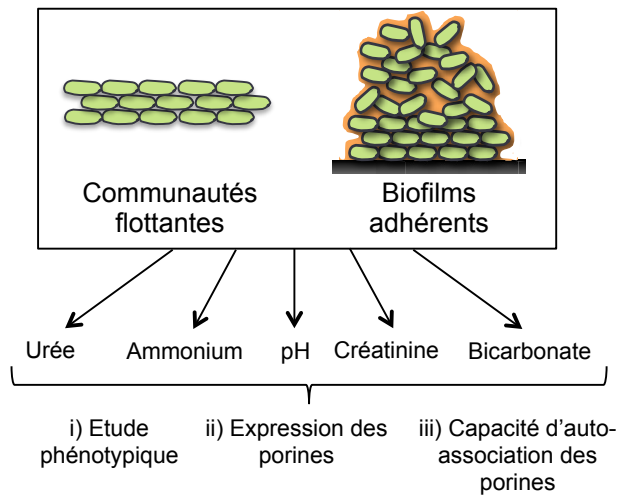


Figure 14. Illustration de la stratégie établie pour étudier les communautés flottantes et les biofilms adhérents, ainsi que les porines de *P. stuartii*, en présence d'urée, d'ammonium, de créatinine, de bicarbonate ou soumis à une variation de pH.

Nous avons introduit plus haut l'impact causé par *P. stuartii* sur la santé humaine du fait de sa forte résistance intrinsèque aux antibiotiques et de sa capacité à former des biofilms, qui rendront chroniques les infections contractées¹⁸⁸. Ainsi, plus que fondamentale, notre recherche a vocation à mettre en place des méthodes plus efficaces pour diagnostiquer et quantifier l'infection par des biofilms, ainsi qu'à développer des agents antimicrobiens plus spécifiques pour lutter contre la formation de biofilms. Une des stratégies possibles pour lutter contre les biofilms de *P. stuartii* serait de mettre à mal sa capacité à se structurer en communautés flottantes, puisque ce sont celles-ci qui, par sédimentation, donnent *in fine* naissance aux biofilms adhérents. L'examen des structures de DOTs formés par Omp-Pst1 et Omp-Pst2 révèle que leur formation procède d'une interaction homotypique de type steric zipper entre boucles extracellulaires – un type d'interaction jusqu'ici observé uniquement dans le cœur des fibres amyloïdes. Ces dernières sont de longues fibres rigides en feuillets β disposées perpendiculairement à l'axe de la fibre²⁰⁵, caractérisées par une grande robustesse et par une stabilité et insolubilité remarquables²⁰⁶. Les brins β opposés sont légèrement décalés les uns des autres, de sorte que leurs chaînes latérales s'interdigitent. Il existe huit classes théoriques de steric zipper, dictées par la directionnalité des brins β (parallèle ou anti-parallèle) et par la symétrie entre les feuillets β adjacentes²⁰⁷ (Figure 15).

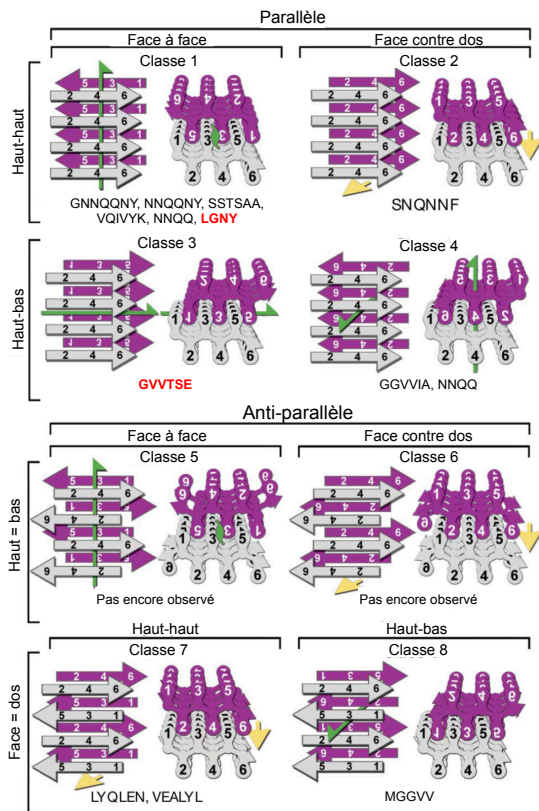


Figure 15. Les huit classes de steric zipper. Deux feuillettes β identiques peuvent être classées selon: i) l'orientation de leurs faces (soit «face à face» ou «face contre dos»), ii) l'orientation de leurs brins β (les deux feuillettes β ont le même bord du brins β , ou l'un est « en haut » et l'autre « en bas »), et iii) si les brins β à l'intérieur des feuillettes β sont parallèles ou antiparallèles. Les deux vues de côté (gauche) et de dessus (droite) montrent lequel des six résidus du segment pointe dans le steric zipper et lequel pointe vers l'extérieur. Les flèches vertes indiquent les axes de vis à deux brins β et les flèches jaunes indiquent la symétrie de translation. Au-dessous de chaque classe sont listés les segments de protéines qui appartiennent à celle-ci. Cette figure est adaptée de l'article de Sawaya et al.²⁰⁷

Chez l'Homme, les amyloïdes sont généralement liés au développement de maladies neurodégénératives, telles que les maladies d'Alzheimer et de Parkinson^{208,209}. Ils se forment lorsque des protéines précédemment bien repliées perdent leurs structures – et donc leurs fonctions – normales. Faute de système de dégradation adapté, celles-ci s'accumulent jusqu'à former des fibres cytotoxiques qui pourront s'assembler en plaques, marqueurs de certaines de ces maladies. Néanmoins, les amyloïdes peuvent également être fonctionnels, c'est à dire en charge d'une fonction attitrée ; par exemple, lors de la formation de pilis dans certains genres de bactéries, lors de la transmission de caractères épigénétiques chez les champignons, ainsi que dans la formation de biofilms bactériens^{65,210}.

Dans les structures des DOTs d'Omp-Pst1 et d'Omp-Pst2, des steric zippers sont à l'œuvre, associant des segments identiques face à face. Néanmoins, la classe de symétrie et les résidus impliqués diffèrent selon la porine considéré¹¹¹ :

- Chez Omp-Pst1, le steric zipper de chaque monomère est formé par les résidus 206-GVVTSE-211 de la boucle extracellulaire L5, appartenant à la classe de symétrie III (face à face, de haut en bas – Figure 15)²⁰⁷, avec une inclinaison de 15° entre les deux brins β se faisant face. Cette interface steric zipper est renforcée par une interaction électrostatique faible entre deux résidus, K28 et D213, des boucles extracellulaires L1 et L5, respectivement (Figure 16. A).

- Chez Omp-Pst2, les résidus 283-LGNY-286 des boucles extracellulaires L7 de chaque monomère en vis-à-vis interagissent via trois steric zippers non basculés, correspondant à la classe de symétrie I (face à face, en haut – Figure 15)²⁰⁷. Chaque interface est complétée par un réseau de liaisons hydrogènes liant les boucles extracellulaires L5, L7 et L8 (Figure 16. B).

Des expériences de mutagenèse dirigée ont été réalisées pour caractériser davantage l'auto-association d'Omp-Pst1 et d'Omp-Pst2, soit en ciblant le steric zipper, soit en modifiant la charge de l'interaction des DOTs. Les résultats ont montré que la principale force motrice derrière l'auto-association des deux porines est l'attraction électrostatique, tandis que l'interface steric zipper pourrait sous-tendre un mécanisme de verrouillage qui régule la formation de DOT¹¹¹

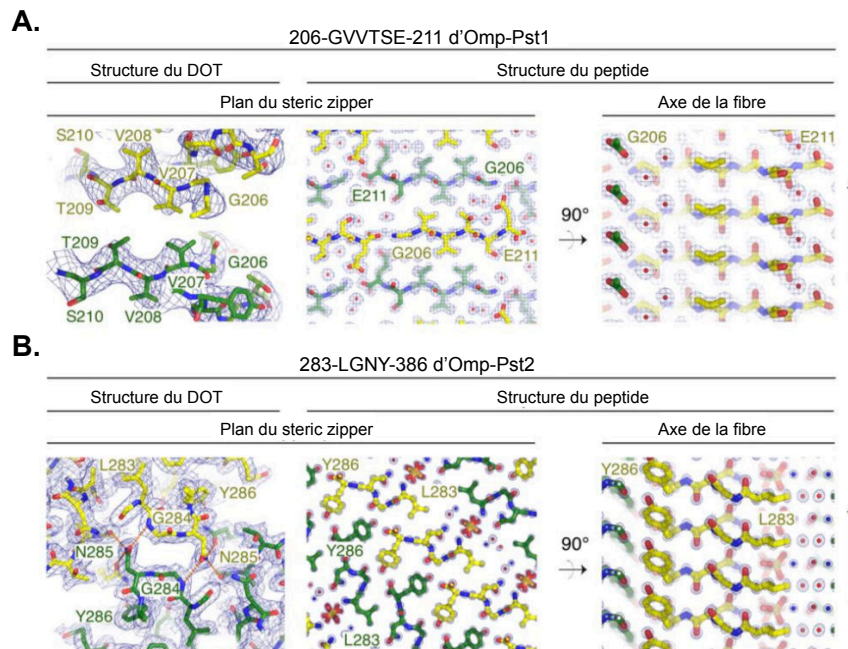


Figure 16. L'interface des DOTs d'Omp-Pst1 et d'Omp-Pst2 est médiée par des interfaces steric zipper différentes. Les résidus 206-GVVTSE-211 d'Omp-Pst1 (A) et 283-LGNY-286 d'Omp-Pst2 (B), impliqués dans l'établissement des DOTs d'Omp-Pst1 et d'Omp-Pst2 respectivement, forment des steric zippers (panels de gauche). Isolés de leur protéine mère, les peptides GVVTSE (pbd : 5n9i) et LGNY (pbd : 5n9h) forment des steric zippers (panels du milieu et de droite) qui appartiennent respectivement aux classes de symétrie III et I. Les panels du milieu montrent l'interface des steric zippers, tandis que les panels de droite révèlent une structure canonique en β croisée adoptée par les steric zippers GVVTSE et LGNY. Cette figure est reprise de l'article de El khatib et al.¹¹¹

Notre but étant d'inhiber les DOTs de porines afin d'empêcher la socialisation de *P. stuartii* en communautés flottantes et en biofilms adhérents, notre stratégie s'est orientée vers le design rationnel de peptides synthétisés suivant les caractéristiques d'interfaces électrostatiques et de steric zippers des DOTs de porines (*Lopes et al., 2019b – en préparation*).

III – Méthodologies

III – Méthodologies

Un des points forts de ce projet de thèse est sa pluridisciplinarité. Ainsi, une variété de techniques provenant de domaines biologiques différents a été utilisée, allant de la biologie moléculaire à la biologie cellulaire en passant par la cristallographie. Dans la partie suivante, le principe de chaque méthode utilisée au cours de cette thèse sera décrit. Par égard pour le lecteur et souci de concision, nous ne rentrerons pas dans le détail de chacune des méthodes mais présenterons l'information nécessaire et suffisante pour qu'il soit possible de comprendre pourquoi la méthode a été utilisée, quels résultats ont été obtenus et quelle information a pu être tirée de ces derniers.

1- Biologie moléculaire

A. PCR

La réaction en chaîne par polymérase, ou PCR (Polymerase Chain Reaction), est une méthode d'amplification *in vitro* de l'ADN²¹¹. Elle permet la duplication en grand nombre d'une séquence d'ADN ou d'ARN connue à partir d'une faible quantité d'acide nucléique et d'amorces spécifiques. Ces dernières sont des oligonucléotides de synthèse composés de 20 à 25 nucléotides qui sont complémentaires aux brins à amplifier. Initiant ainsi le processus de PCR par appariement spécifique, leur design est une étape déterminante. La formation d'un ADN double brin par complémentarité de l'amorce avec l'ADN simple brin est le point de départ pour l'activité enzymatique de l'ADN polymérase, capable de synthétiser de nouveaux brins d'ADN doubles brins dans le sens 3'-5'.

Le processus d'amplification se réalise grâce à des cycles successifs (35 à 50) de plusieurs étapes. La première est la dénaturation thermique de la double hélice d'ADN à 95°C (1), suivie de l'hybridation des amorces à une température adéquate (55-65°C) (2). La dernière étape est l'élongation des amorces à 72°C par l'ADN polymérase qui recrute les nucléotides complémentaires de la séquence matricielle dans un pool de dNTPs (3) (Figure 17). La réaction de PCR n'est possible que grâce à l'utilisation d'un ADN polymérase dit thermophile, c'est à dire stable à des températures élevées (~100°C). La polymérase thermostable la plus utilisée en PCR est la Taq polymérase, issue de la bactérie thermophile *Thermus aquaticus*, isolée pour la première fois en 1969^{212,213}. A la fin de tous les cycles, les produits d'amplification sont déposés sur un gel d'agarose et soumis à une électrophorèse. Le bromure d'éthidium (BEt), un agent s'intercalant entre les bases d'acides nucléiques, est

ajouté aux produits afin d'observer, sous UV courts (300 nm), l'apparition de bandes fluorescentes correspondant aux molécules d'ADN amplifiées.

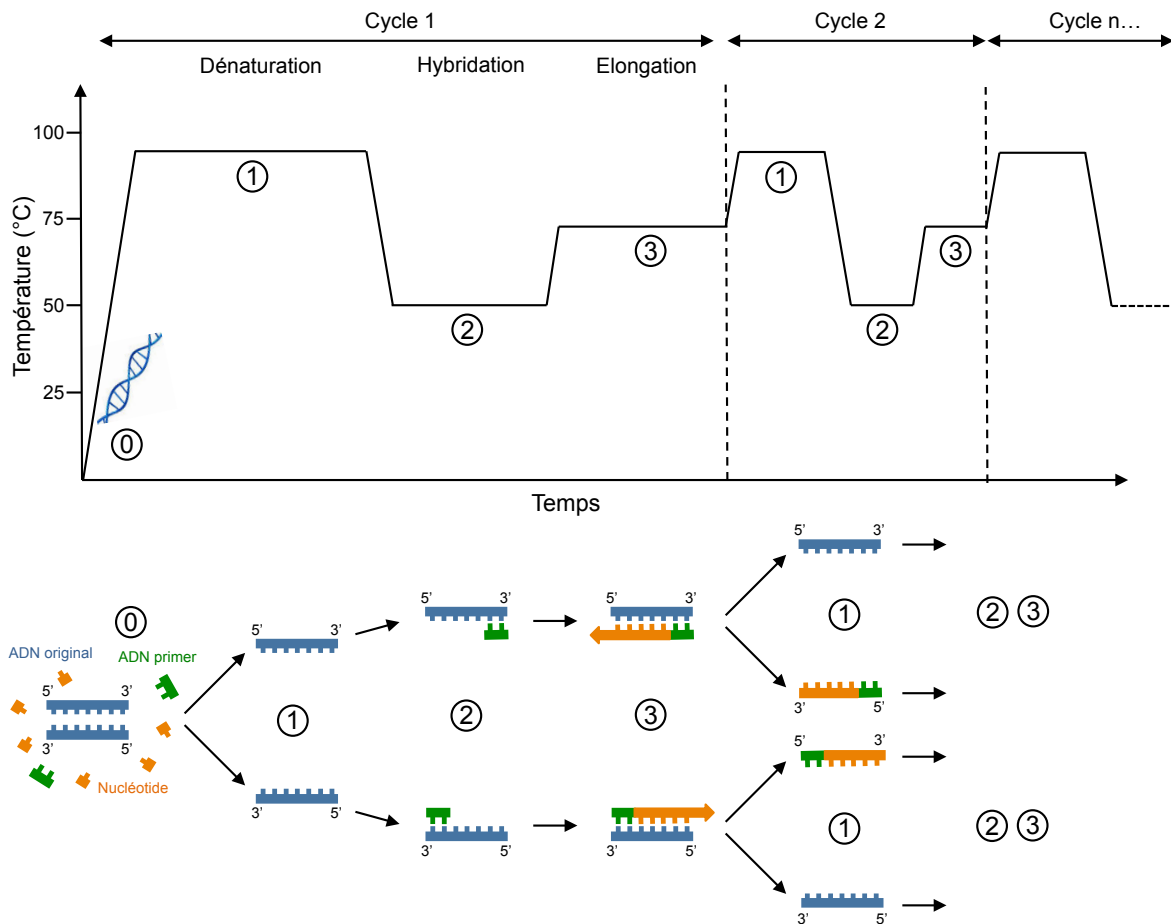


Figure 17. Les différentes étapes d'une PCR. Les étapes successives de dénaturation du double brin d'ADN (bleu), d'hybridation des amorces (vert) et d'élongation par recrutement des dNTPs (orange) grâce à l'activité de la polymérase, permettent l'amplification exponentielle d'ADN doubles brins.

B. RT-qPCR

Une méthode dérivée de la PCR est la RT-qPCR pour Reverse-Transcriptase quantitative PCR. Cette technique permet la réalisation d'une PCR quantitative à partir d'un échantillon d'ARN, et non pas d'ADN, comme matrice d'amplification^{214,215}. Ainsi, il sera possible de quantifier les ARN messagers correspondants à différents gènes.

La première étape est la rétro-transcription de l'ARN en ADN complémentaire (ADNc) grâce à l'enzyme transcriptase inverse. L'ADNc est ensuite utilisé pour la réaction de PCR quantitative, également appelée PCR en temps réel (Figure 18). Le nombre d'amplicon,

portion d'ADN définie par un couple d'amorces, mesuré au cours du processus d'amplification PCR est suivi en continu par mesure de fluorescence.

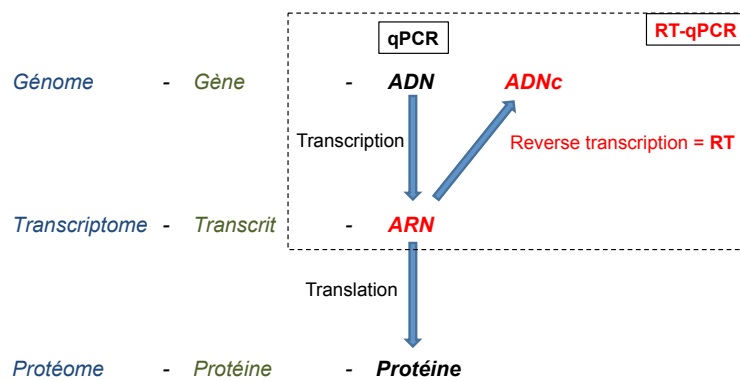


Figure 18. Schéma explicatif de la RT-qPCR. L'ADN génomique est transcrit en ARN. Ce dernier est retro-transcrit en ADN complémentaire (ADNc), qui devient l'ADN matricielle pour la réaction PCR.

Le principe est le suivant (Figure 19). Comme pour une réaction PCR conventionnelle, l'ADNc matricielle est dénaturé afin que les amorces spécifiques puissent s'hybrider au simple brin d'ADN. Durant l'étape d'élongation, une molécule fluorescente spécifique aux acides nucléiques double brin émet de la fluorescence, qui sera liée à la quantité d'ADN cible. Pour toutes nos expériences de RT-qPCR, nous utilisons le SYBR Green pour la détection d'ADN cible. Ce dernier est un composé organique aromatique fluorescent qui se lie au petit sillon de l'ADN et non entre les bases appariées ; ce n'est donc pas un agent intercalant. Le complexe ADN double brin/SYBR Green absorbe la lumière à une longueur d'onde $\lambda_{\text{max}} = 497 \text{ nm}$, et fluoresce à $\lambda_{\text{max}} = 520 \text{ nm}$. D'autres sondes fluorescentes existent également, comme la TaqMan (sonde d'hydrolyse) ou les couples de sondes d'hybridation double (FRET) plus spécifiques à une séquence d'ADN particulière, et sont donc idéaux pour les études à haut débit²¹⁶.

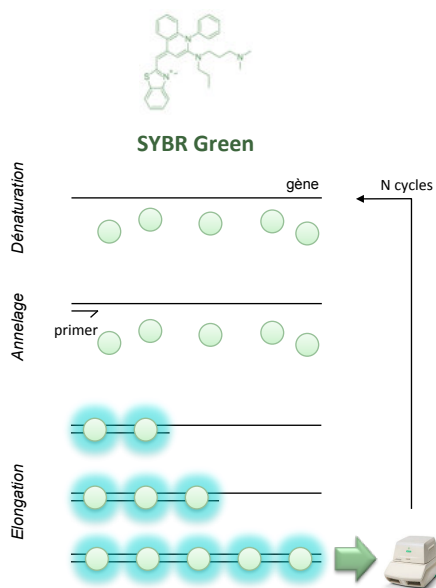


Figure 19. Schéma explicatif de la détection d'ADN cible par SYBR Green. Une fois l'ADNc dénaturé en simple brin, des amorces complémentaires s'hybrident. Au cours de l'élongation, des molécules SYBR Green fluorescentes se lient aux brins d'ADN double brins et génèrent de la fluorescence. La mesure de celle-ci est suivie en temps réel, permettant de quantifier les concentrations d'ADN cible. Le processus est exécuté durant n cycles jusqu'à saturation des composants de la réaction PCR.

Le profil d'une réaction de qPCR se décompose en trois parties (Figure 20. A):

- Une étape de « bruit de fond », durant laquelle la quantité de fragment amplifié est insuffisante pour générer un signal fluorescent supérieur au bruit de fond.
- Une étape de « phase exponentielle », où la quantité de fragment amplifié génère un signal fluorescent supérieur au seuil de détection. Le nombre de produits amplifiés double à chaque cycle (2^n).
- Une étape de « plateau », qui résulte du fait qu'au bout d'un certain temps les composants de la réaction deviennent limitants ; ainsi le signal mesuré n'est plus linéaire, n'étant plus proportionnel au nombre de produits amplifiés.

Le seuil de cycle (C_t) correspond à l'intersection entre la courbe d'amplification et la ligne de seuil²¹⁷, représentant la sortie du bruit de fond du signal quantifiant l'ADN double brin amplifié (début de la phase exponentielle). Le C_t représente une mesure relative de la concentration de l'ADN cible dans la réaction de PCR. Il est important de déterminer plusieurs C_t standards par dilution amplifiée en vue de quantifier l'amplification dans chacun de nos échantillons (Figure 20. B). Pour évaluer correctement l'efficacité d'une qPCR, un minimum de trois réplicats et de cinq dilutions de C_t standards sont nécessaires.

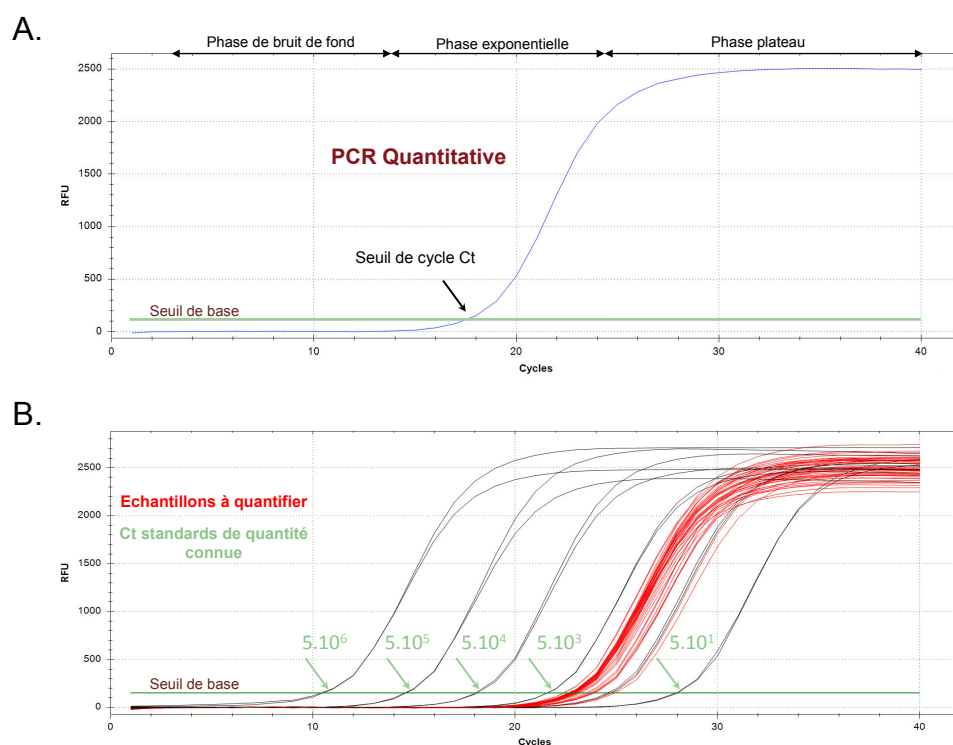


Figure 20. Profil d'une réaction de qPCR. A. La courbe résultante d'une réaction de PCR quantitative est divisée en trois parties : une phase de bruit de fond, une phase exponentielle et une phase plateau. Le seuil de cycle C_t correspond à l'intersection du seuil de base et la courbe d'amplification. B. Différents C_t standards de quantité connue (vert) sont nécessaires à la quantification des concentrations des ADN cibles (rouge).

Pour assurer une bonne qualité de nos résultats, les données expérimentales doivent être normalisées. En effet, la normalisation des données de RT-qPCR aide à garantir des résultats d'expression des gènes cibles de manière robustes, fiables et reproductibles, donnant ainsi une assurance sur les données, les interprétations et les conclusions de l'expérience^{218,219}. Si aucune normalisation n'est réalisée, alors la publication des données de qPCR est risquée et les conclusions potentiellement fausses²²⁰, ce qui a parfois entraîné la rétractation d'articles^{221,222}. Ce processus de normalisation permet de minimiser les effets de variabilité inhérente dans le nombre de copies d'ARN, de diversité des protocoles d'extraction (pouvant co-purifier des inhibiteurs), et d'efficacité de transcription inverse et de PCR²²³. Cependant, l'identification d'une référence valide pour la normalisation des données reste le problème le plus critique et aucune des solutions proposées dans la littérature n'est idéale.

Brièvement, cinq stratégies de normalisation ont été proposées, où chacune présente des avantages et des inconvénients :

- Une normalisation basée sur une quantité d'échantillon similaire ; cependant, il peut s'avérer difficile d'estimer la taille d'un échantillon composé de cellules car elles peuvent s'agglutiner ou présenter des morphologies différentes.
- Une normalisation utilisant de l'ADN génomique, qui ne nécessite donc pas d'étape de transcription inverse pour la détection par PCR en temps réel.
- Une normalisation à partir d'une molécule artificiellement incorporée dans l'échantillon : la molécule d'ARN « artificielle » peut être clonée et transcrite *in vitro* à partir d'une autre espèce ou bien générée par synthèse. La génération de ces standards a été proposée, mais tant qu'ils ne seront pas commercialement disponibles et que des recherches plus approfondies sur cette méthode ne seront pas effectuées, la normalisation artificielle de l'ARN restera un idéal théorique non validé²²⁴.
- Une normalisation par rapport à l'ARN total ; cette méthode présente l'inconvénient de ne pas contrôler les variations inhérentes à la transcription inverse ou aux réactions de PCR²²⁵.
- Une normalisation par des gènes de références internes : ces gènes contrôlent les variations du rendement d'extraction, du rendement de transcription inverse et de l'efficacité d'amplification, permettant une comparaison des concentrations d'ARNm entre les différents échantillons. Ils corrigent également les différences entre les quantités d'ADNc utilisées comme matrice²²⁶⁻²²⁸. En revanche, il est primordial que l'expression des gènes de références soit stable en fonction du temps et qu'elle ne soit pas affectée par les conditions expérimentales²²⁹. Cependant, ce type de normalisation est souvent réalisée en utilisant qu'un seul gène de référence non stable tel que celui

de la glycéraldéhyde-3-phosphate déshydrogénase (GADPH), de la β -actine, de la tubuline ou du 16S RNA²³⁰⁻²³³. Si le mauvais gène de référence est choisi, les résultats peuvent alors être altérés. Cette stratégie, simple et la plus répandue pour le contrôle interne des erreurs de RT-PCR en temps réel, s'est révélée inefficace au cours de cette thèse, du fait que l'expression des gènes de références internes testés était impactée par les conditions expérimentales ou le phénotype adopté chez notre espèce étudiée.

Dernière précaution, n'oublions pas que la méthode de RT-qPCR quantifie les niveaux d'ARNm à l'état d'équilibre et pas plus. La quantification précise de ces niveaux ne dit rien sur les niveaux de transcription protéique et sur la stabilité de l'ARNm. Il existe fréquemment un manque de concordance entre les données de concentration d'ARNm et de protéines^{227,234} car il se peut que l'ARNm ne soit pas rendu disponible aux ribosomes, qu'il soit dégradé ou en compétition avec d'autres ARNm non étudiés, ou également qu'il soit impacté par l'expérience réalisée, etc... En bref, il est important de vérifier au niveau protéomique une corrélation entre les variations d'expression des gènes et de production des protéines.

C. Clonage

On désigne par « clonage » le processus de réplication à l'identique d'une ou plusieurs molécules d'ADN. Ce terme peut avoir différentes significations et implications selon le but visé et la méthode utilisée :

- Le clonage thérapeutique permet la fabrication de tissus à partir de cellules souches²³⁵.
- Le clonage génomique permet la reproduction artificielle d'un être vivant²³⁶.
- Le clonage moléculaire donne lieu à la production et l'amplification d'un fragment d'ADN inséré dans un vecteur (ADN porteur) permettant sa réplication dans les organismes hôtes, procaryotes ou eucaryotes²³⁷.

Dans notre domaine de compétence, c'est à dire en biologie moléculaire et en biochimie, la technique la plus utilisée est de loin le clonage moléculaire. Dans notre projet, il a été utilisé pour insérer des fragments d'ADN correspondants à la séquence codante de nos protéines d'intérêt, les porines, dans des vecteurs d'expression pGOmp-pst1 et pGOmp-pst2 en vue de les sur-exprimer, de les purifier, de mesurer et caractériser leurs propriétés d'auto-association en DOTs, et de résoudre leurs structures pour révéler les séquences pouvant mener à la formation de rivets intercellulaires.

Selon le type de clonage, la taille de l'insert d'intérêt et du système d'expression envisagé (bactérie, levure, cellules d'insectes, végétales ou de mammifères), les vecteurs peuvent être des plasmides²³⁸, des phagémides²³⁹, des bactériophages²⁴⁰, des phages lambda²⁴¹, des cosmides²⁴² ou encore des BAC²⁴³/YAC²⁴⁴/HAC²⁴⁵ (Bacteria/Yeast/Human Artificial Chromosome). Dans notre cas, le vecteur hôte est plasmidique du fait que le fragment d'ADN que l'on souhaite insérer ne dépasse pas les 1 kb. Les plasmides sont des ADNs double-brins circulaires et ceux utilisés en laboratoire sont des plasmides d'expression comportant tous des propriétés communes, telles que (Figure 21):

- une origine de réplication (ori) indépendante de la réplication de l'hôte ;
- un gène de résistance à un antibiotique, afin de ne sélectionner que les clones positifs ayant incorporés le gène d'intérêt ;
- un site de clonage multiple (MCS), qui contient les sites spécifiques de plusieurs enzymes de restriction (ER) aidant à l'insertion du gène d'intérêt ;
- un promoteur d'expression, qui permet le contrôle de l'expression du gène d'intérêt par l'expérimentateur en ajoutant un inducteur d'expression. Certains plasmides, tels que les pETs que nous utilisons, sont des exceptions puisqu'ils ont des fuites d'expression même sans ajout d'inducteur. Dans notre cas, ce n'est cependant pas un problème mais un avantage puisque c'est la bactérie *E. coli* Δ Omp8 – déléetée de ses propres porines de diffusion générales¹⁹⁹ – qui active elle-même l'expression de nos porines du fait de l'avantage sélectif que ces dernières permettent de rétablir chez cette souche. A contrario, toute tentative de surexpression entraine automatiquement l'accumulation des porines sous la forme de corps d'inclusions. Celles-ci présentent toujours leur séquence signal d'adressage à la membrane externe mais ne peuvent être utilisées car mal repliées.
- le gène d'intérêt.

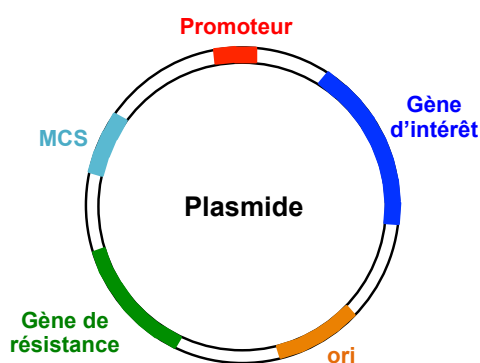


Figure 21. Schéma d'un plasmide double brin.

Un plasmide est constitué de son origine de réplication ori (orange), d'un gène de résistance (vert), d'un site de clonage multiple MCS (turquoise), d'un promoteur d'expression (rouge) et du gène d'intérêt (bleu).

Une fois le gène d'intérêt introduit dans le plasmide, il faut ensuite insérer le plasmide recombiné dans un organisme hôte. Le choix de ce dernier dépend majoritairement de la protéine d'intérêt et de son bon repliement, mais également du vecteur utilisé et de l'application que l'on souhaite réaliser. Dans notre cas, les hôtes compatibles avec les plasmides sont le plus généralement les bactéries, telles que *E. coli*, *Bacillus subtilis* ou *Streptomyces lividans*, mais aussi les levures avec *Saccharomyces cerevisiae*. Dans le cadre de nos expériences, nous avons utilisé deux souches bactériennes :

- *E. coli* DH5 α pour l'amplification des plasmides recombinants et,
- *E. coli* BL21 Δ Omp8 pour l'expression des porines d'intérêt.

La souche *E. coli* s'avère idéale du fait qu'elle appartient à la famille des *Enterobacteriaceae* comme *P. stuartii*. Le clone résultant est le transformant bactérien qui contient le plasmide d'intérêt, et tous les individus de la colonie bactérienne sont génétiquement identiques.

Il existe deux méthodes très utilisées permettant l'insertion d'un gène d'intérêt dans un plasmide, avant qu'il ne soit transformé dans des bactéries : la méthode de restriction/ligation (basée sur les ER) et l'assemblage de Gibson.

Les ER coupent le vecteur et l'insert à des sites spécifiques, générant deux fragments d'ADN linéaires à bouts complémentaires^{246,247} (Figure 22. A). Une fois purifiés, les deux fragments d'ADN sont liés par une ligase aboutissant en un plasmide recombinant circulaire. Il s'agit du processus de ligation. Cette méthode présente cependant deux limitations :

- Il faut vérifier la présence de sites de restriction uniques et convenables dans le plasmide et l'insert pour s'assurer de la spécificité et de la directionnalité de l'insertion d'une copie complète du gène dont on souhaite l'expression ;
- Le rendement de ligation est faible, ce qui se traduit par la nécessité d'utiliser des concentrations élevées en plasmide ($\approx 2 \mu\text{g}$) rendant chaque expérience coûteuse. De plus, les ER étant commerciales, il faudra fréquemment en recommander, ce qui va également augmenter les coûts.

La méthode alternative que nous avons utilisé est l'assemblage de Gibson²⁴⁸ qui ne nécessite pas de sites de restriction (Figure 22. B). Cette technique permet l'amplification du plasmide accepteur et de l'insert par une réaction de PCR classique grâce à l'utilisation d'amorces à bouts complémentaires. Un mix de trois enzymes est utilisé :

- une exonuléase, qui digère l'ADN en 5' et crée une extension simple brin coté 3', facilitant l'hybridation des deux fragments ;
- une polymérase, qui comble les lacunes de chaque fragment ;
- une ligase, qui lie les deux fragments.

Cette méthode présente ainsi l'avantage de ne pas recourir aux ER, mais d'autres enzymes sont utilisées. Malgré tout, la technique de l'assemblage de Gibson offre un meilleur rendement en ne nécessitant que 1 ng de plasmide.

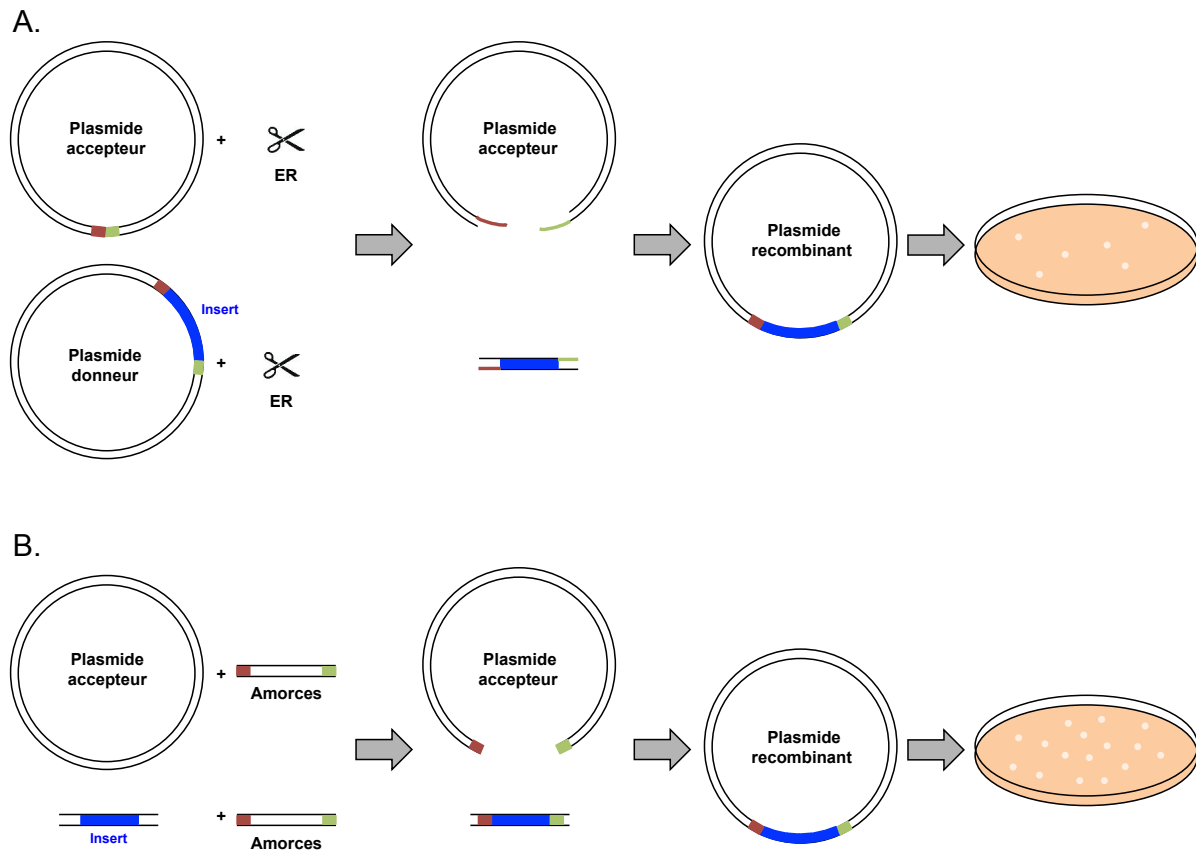


Figure 22. Schémas illustrant les différences entre le clonage par ER et par assemblage de Gibson. A. Le clonage par des enzymes de restriction (ER) nécessite des sites de restriction identiques (rouge et vert) au niveau du plasmide donneur avec l'insert (bleu) et du plasmide accepteur. Les sites permettront aux ER de cliver spécifiquement l'ADN en linéarisant le plasmide accepteur et en libérant le gène d'intérêt de son plasmide donneur. Le gène d'intérêt et le plasmide accepteur linéarisé sont ensuite purifiés du mélange par migration sur gel d'agarose et sont liés par une ligase. Le plasmide recombinant est utilisé pour transformer des bactéries DH5 α afin de sélectionner des colonies ayant intégrées celui-ci. B. Le clonage par assemblage de Gibson ne nécessite pas la présence de sites complémentaires. Ces sites sont générés par une réaction de PCR en utilisant deux couples d'amorces avec des sites complémentaires. Le produit PCR, purifié sur gel d'agarose, est assemblé via un mélange d'enzymes permettant l'obtention d'extrémités simples brins et la ligation de l'insert dans le plasmide accepteur. La transformation dans les bactéries DH5 α donne un meilleur rendement.

2- Biochimie des protéines membranaires

Les protéines membranaires sont impliquées dans des processus biologiques divers tels que le transport actif ou passif de molécules²⁴⁹, la réception ou transmission de signaux à travers la membrane²⁵⁰, le modelage et l'adhésion entre membranes²⁵¹, ou encore les activités enzymatiques²⁵². Constituant une fraction significative des gènes humains (environ un

tiers)²⁵³, les protéines membranaires sont les cibles de plus de la moitié des médicaments connus^{254,255}, quoiqu'une très large fraction de ces protéines reste à ce jour non identifiées ou non caractérisées^{256,257}. En effet, les protéines membranaires sont moins bien caractérisées que leurs homologues solubles à cause de leur nature hydrophobe, qui complique leur extraction, leur purification, et leur caractérisation structurale, dynamique et fonctionnelle²⁵⁸. L'utilisation de détergents de douceur appropriée est donc cruciale pour les extraire de leur membrane tout en maintenant leur structure intacte. Une fois solubilisé, le complexe protéine/détergent se manipule comme une protéine soluble, facilitant les prochaines étapes de purification.

A. Détergents

Un détergent est une molécule amphiphile composé de deux parties, une première dotée d'une tête polaire hydrophile ayant une affinité pour les phases aqueuses, et une seconde constituée d'une longue chaîne hydrocarbonée hydrophobe ayant une affinité pour les milieux hydrophobes²⁵⁹. En solution, les propriétés tensio-actives des détergents leur permettent une adsorption à l'interface liquide-air avec leur portion hydrophile face à la phase aqueuse et leur portion hydrophobe en contact avec l'air. Une fraction des molécules de détergents est solubilisée sous la forme de monomère, mais au delà d'une certaine concentration les monomères ne s'accumulent plus et c'est plutôt des agrégats, nommés micelles, qui commencent à se former. Dans une micelle, les chaînes hydrophobes sont en contact quand les têtes hydrophiles font face au solvant. La concentration à partir de laquelle les monomères de détergents commencent former des micelles est nommée Concentration Micellaire Critiques (CMC) (Figure 23). Chaque détergent a une CMC spécifique, aussi appelée douceur, et peut ainsi agir différemment sur la structure et la fonction des protéines membranaires. Différents paramètres physico-chimiques pourront affecter la CMC du détergent et moduler son interaction et son effet sur les protéines, notamment le pH, la force ionique, la température, et la nature tensio-actif dépendant de la taille de la chaîne hydrophobe et de la charge du groupement hydrophile.

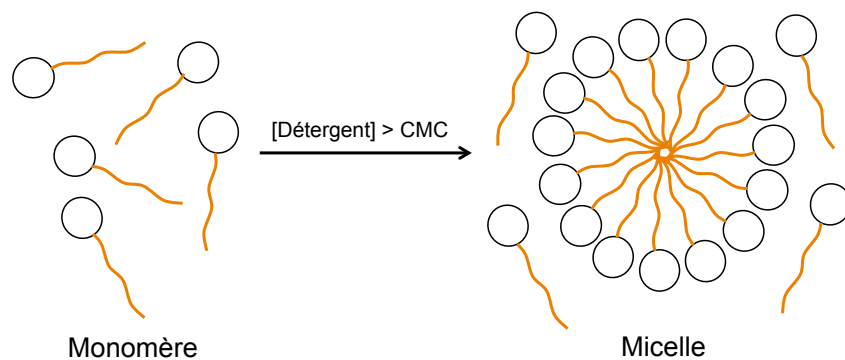


Figure 23. Représentation schématique de l'assemblage spontané de molécules de détergent monomériques en micelle, au dessus de la concentration micellaire critique (CMC).

En pratique, il sera primordial de minimiser la quantité de détergent utilisée au cours de la purification des protéines membranaires pour ne pas affecter leur stabilité, leur fonction, leur dynamique ou leur structure. Notamment, le choix du détergent est déterminant pour cristalliser une protéine membranaire et résoudre sa structure par cristallographie aux rayons X. Ce choix n'est pas moins important en RMN ou en cryo-microscopie électronique (cryo-ME), mais l'incidence n'est alors que sur la structure, et non pas sur la possibilité d'obtenir l'échantillon permettant de résoudre la structure.

Il existe trois méthodes pour éliminer, réduire ou échanger la nature du détergent²⁶⁰ :

- par adsorption des molécules de détergent en utilisant des biobeads (billes de polystyrènes hydrophobes) ;
- par dialyse contre un tampon sans détergent ;
- par lavage continu de la protéine accrochée à une colonne de chromatographie.

B. Liposomes et incorporation de protéines membranaires

Contrairement aux micelles, formées d'une monocouche hydrophobe, les liposomes sont des vésicules d'une ou plusieurs bicouches lipidiques mimant l'environnement d'une membrane biologique. Grâce à cette propriété, les applications basées sur l'utilisation de liposomes sont larges^{261,262}. L'une d'entre elles est la reconstitution des protéines membranaires, utilisée au cours de cette thèse, afin d'étudier leurs propriétés fonctionnelles. Pour ce faire, la première étape est la préparation des liposomes. Selon la méthode, le type de liposomes obtenu ainsi que leur taille pourront être différents. Il convient cependant, avant d'en parler, d'introduire la terminologie propre aux liposomes. On distingue les liposomes unilamellaires, formés d'une seule bicouche lipidique (UV : Unilamellar Vesicle), des liposomes multilamellaires qui en possèdent plusieurs (MLV : Multi-Lamellar Vesicle). Quand le diamètre du liposome est inférieur à 50 nm, on parle de SUV (Small Unilamellar Vesicle), s'il se tient entre 50 et 500

nm on parle de LUV, et enfin s'il est supérieur à 500 nm on les qualifie de GUV (Giant Unilamellar Vesicle). Pour toutes les expériences réalisées dans la thèse, nous avons préparé et utilisé des LUVs (Figure 24). Ils offrent un rayon de courbure suffisant pour l'insertion de toutes les protéines membranaires (contrairement aux SUVs) et ils sont aussi faciles à obtenir qu'à suivre de façon reproductible par différentes méthodes spectroscopiques ou d'imagerie (contrairement aux GUVs).

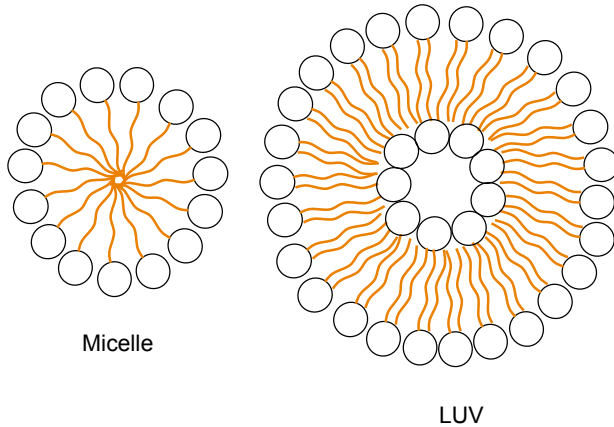


Figure 24. Représentation schématique d'une micelle (gauche) comparé à un liposome de type LUV (droite). Le liposome contient un cœur hydrophobe pouvant encapsuler des molécules. Les protéines membranaires, quant à elles, s'incorporent au niveau des bicouches lipidiques.

Pour la préparation des LUVs, la méthode d'hydratation des films lipidiques a été utilisée. En pratique, le chloroforme contenant les lipides est évaporé jusqu'à l'obtention d'une fine couche lipidique sur les parois du tube utilisé. Pour ce faire, un flux d'azote ou d'argon gazeux est utilisé afin d'éviter toute oxydation des doubles liaisons C=C des lipides²⁶³. Le film lipidique est ensuite hydraté et remis en suspension dans du tampon par vortex, permettant d'obtenir des MLVs avec une distribution de taille très large. Des cycles de congélation/décongélation sont appliqués à la solution, fragilisant les membranes lipidiques pour former des LUVs. *In fine*, nous obtenons des LUVs d'un diamètre d'environ 80 nm par extrusion à travers des membranes de polycarbonate (Figure 25).

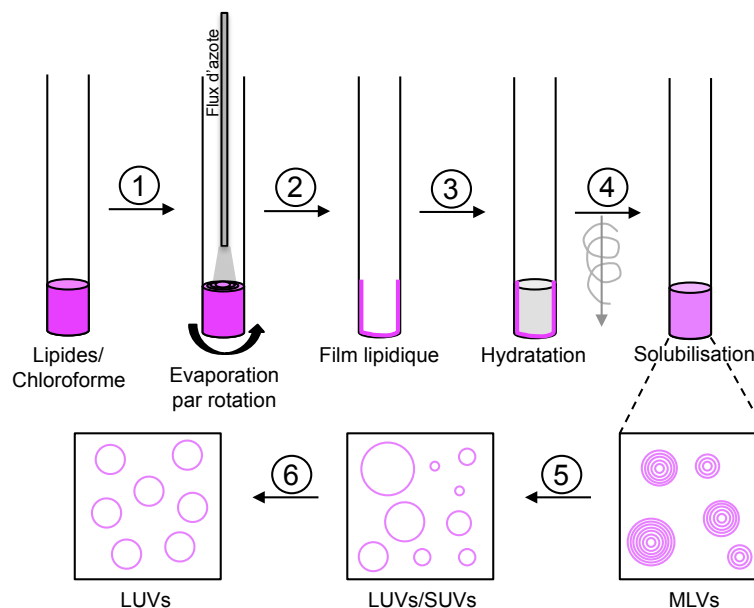


Figure 25. Schéma des différentes étapes de préparation des LUVs. La solution lipides/chloroforme est disposée dans un tube à essai en verre. (1) Le chloroforme, solubilisant les lipides, est évaporé sous flux d'azote gazeux. (2) L'évaporation par rotation du tube est primordiale pour obtenir une fine couche lipidique aux parois. (3) Cette dernière est réhydratée par ajout d'un tampon, (4) et les lipides sont solubilisés par vortex. Suite à cela, des liposomes MLVs de tailles variables sont formés. (5) Des cycles de congélation/décongélation sont soumis aux MLVs dans le but d'obtenir des liposomes de type LUVs et SUVs. (6) Une dernière étape d'extrusion permettra d'obtenir uniquement des LUVs de même taille. Par une méthode de diffusion dynamique de lumière (DLS), l'homogénéité de la solution finale obtenue est vérifiée.

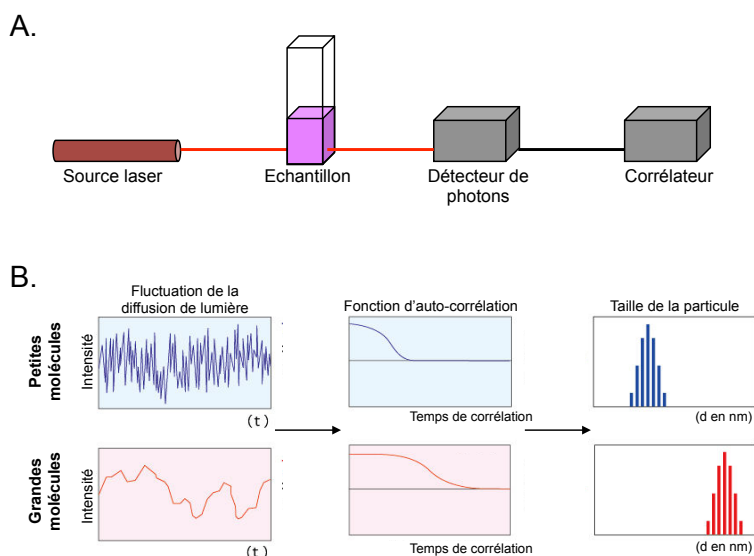
Les protéines membranaires peuvent être incorporées aux LUVs par différentes méthodes. La plus simple à mettre en œuvre est basée sur la dilution du détergent. Dans cette approche, les protéines sont directement ajoutées aux liposomes, entraînant une dilution du détergent en-dessous de sa CMC. Les micelles se dissocient alors en monomères de détergents et les protéines membranaires n'ont alors d'autre choix que de trouver refuge au sein de la bicouche lipidique des LUVs. Cependant, cette méthode ne permet pas de contrôler le taux d'insertion (précipitation de certaines protéines membranaires) et le sens d'incorporation des protéines dans la membrane des liposomes (généralement, insertion avec la face hydrophile la plus petite)^{264,265}. Si la dilution du détergent est trop brutale, les protéines auront tendance à précipiter. Pour s'affranchir de ces problèmes, des biobeads peuvent être utilisés, qui sont de petites billes de polystyrène absorbant le détergent. L'utilisation des biobeads va permettre de réduire plus doucement la concentration en détergent et donc favoriser la reconstitution des protéines dans les membranes des liposomes. Dans ce cas, le taux d'insertion productive, c'est à dire avec les boucles extracellulaires sur la surface externe des liposomes, est de 50% mais le taux de reconstitution est de 100 %.

C. Diffusion dynamique de lumière

La diffusion dynamique de lumière, généralement abrégée par l'acronyme DLS (Dynamic Light Scattering), est une méthode d'analyse spectroscopique parfaitement non invasive qui mesure le rayon hydrodynamique de nanoparticules en solution, entre 1 et 500 nm^{266,267}. Le principe repose sur la diffusion d'une lumière laser dans toutes les directions et à différentes intensités lorsque celle-ci rencontre les nanoparticules en suspension situées dans une cuvette. Les particules dans un liquide sont soumises au mouvement brownien (mouvement aléatoire d'une particule immergée dans un fluide) à cause de l'agitation thermique. La diffusion de la lumière dépend de ce paramètre, mais également de la taille et de la forme de la nanoparticule, de la température et de la viscosité du solvant. En effet, la vitesse de diffusion

diminue avec l'augmentation de la taille et de la viscosité alors qu'elle augmente avec une température croissante.

Les intensités de diffusion de la lumière mesurées sont analysées par différents composants de l'instrument utilisé pour la DLS²⁶⁸. Concrètement, la lumière diffusée par les nanoparticules en mouvement est collectée à un angle de diffusion θ connu (typiquement 90° par rapport au faisceau incident) grâce à un détecteur à photon de haute sensibilité, comme par exemple les photodiodes à avalanche ou les tubes photomultiplicateurs (PMT). Le détecteur convertit les fluctuations d'intensité diffusée en un signal électronique, qui sera ensuite traité numériquement par un corrélateur (Figure 26. A) afin de générer une fonction d'auto-corrélation en intensité (Figure 26. B). Pour finir, des algorithmes permettront de « fitter » cette fonction de corrélation afin d'en extraire de façon précise les distributions de taille (diamètre hydrodynamique), ainsi que l'indice de polydispersité des particules (Figure 26. B). Il est malgré tout nécessaire de connaître l'indice de réfraction de la solution ainsi que sa viscosité pour pouvoir interpréter les résultats de la mesure.



3- Imagerie cellulaire

L'imagerie cellulaire désigne l'ensemble des techniques rendant visible l'extérieur et/ou l'intérieur d'une cellule. C'est un outil indispensable au biologiste qui s'en servira pour

mettre en avant certains aspects du fonctionnement d'une cellule, dans le but de comprendre au mieux le monde du vivant.

Le principe de l'imagerie, commun à tous les types de microscopie, est basé sur l'interaction et la déviation de rayonnements de longueur d'onde variable d'une lumière incidente, tels que des photons, des électrons ou bien des ions, avec/par les particules de l'objet à imager. Les rayons émergents sont captés par un détecteur, pouvant être un film de carbone, un détecteur CCD (Charge Coupled Devices) ou encore des tubes photomultiplicateurs (PMT). Les premiers microscopes ont été développés dans les années 1600, commençant par la microscopie photonique par Galilée, Hook et van Leeuwenhoek, puis son développement s'est accéléré au XX^{ème} siècle par l'introduction de la microscopie de fluorescence (1908)²⁶⁹, de contraste de phase (1930)²⁷⁰, électronique (1931)²⁷¹, confocale (1953)²⁷², à rayons X (1983)²⁷³ ou encore à force atomique (1985)²⁷⁴. Nous décrirons ici les principes de la microscopie de fluorescence conventionnelle et de la microscopie électronique puisque seules ces deux méthodes ont été utilisées au cours de la thèse.

A. Microscopie de fluorescence conventionnelle

La microscopie de fluorescence est une technique de microscopie optique tirant profit du phénomène de fluorescence et parfois de phosphorescence²⁶⁹. Il s'agit d'une méthode d'imagerie non invasive déterminant la localisation cellulaire d'un compartiment, d'une organelle ou encore d'une protéine par marquage spécifique. Cependant, sa résolution spatiale est limitée à ≈ 250 nm du fait que l'image d'un point n'est en réalité pas un point mais une tâche de diffraction – plus connue sous le nom de disque d'Airy – dont la taille et la forme sont modulées par la fonction d'étalement du point PSF (Point Spread Function), spécifique à chaque lentille. Le disque d'Airy, décrit par Ernst Abbe en 1873²⁷⁵, est une lumière parasite associée au phénomène de diffraction. Autrement dit, deux points pourront être imagés seulement s'ils sont séparés d'une distance supérieure à la PSF (Figure 27). Cette distance minimale définit la résolution optimale pour la microscopie conventionnelle et obéit à la loi d'Abbe-Rayleigh :

$$d = \lambda / 2n \cdot \sin\phi$$

où « λ » définit la longueur d'onde d'excitation comprise entre 500 et 700 nm, « n » indique l'indice de réfraction et « ϕ » représente l'ouverture angulaire de l'objectif. Le produit $n \cdot \sin\phi$, de l'ordre de 1,4 pour la plupart des objectifs de microscopes modernes, définit l'ouverture numérique du microscope.

Etant donnée que la résolution maximale est d'environ 250 nm, des études de localisation et d'oligomérisation des protéines au sein d'une cellule ainsi que des études d'interactions avec d'autres partenaires cellulaires sont limitées.

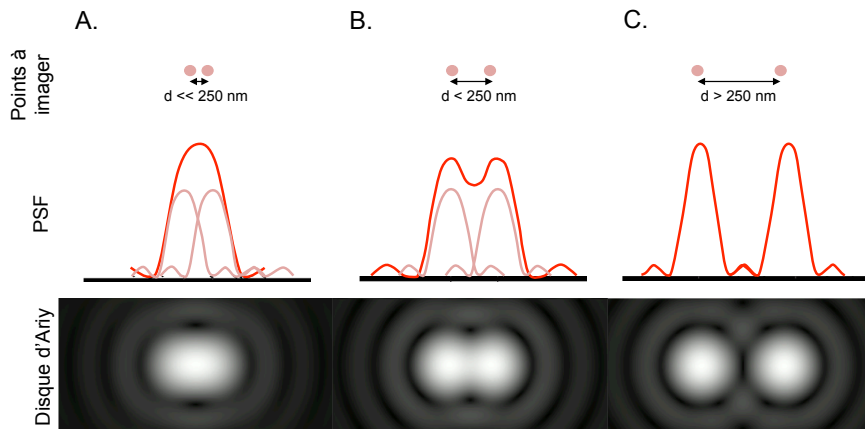


Figure 27. Illustration d'images de points à imager limitées ou non en résolution. A. Si la distance séparant deux points à imager est très inférieure à 250 nm, les PSF de chacun des points se chevauchent, n'imageant donc qu'un seul et unique point. B. Si la distance se rapproche de 250 nm, les deux points se distinguent légèrement. C. Une distance plus grande que 250 nm entre les deux points permet de les distinguer totalement.

La microscopie de fluorescence nécessite l'utilisation de molécules émettrices de lumière telles que les fluorochromes. Ils peuvent prendre la forme de :

- molécules conjuguées à des composés organiques fluorescents,
- colorants liés à des anticorps,
- marqueurs spécifiques,
- protéines fluorescentes²⁷⁶ (Figure 28).

Ces dernières sont des protéines structurées en tonneau β d'une trentaine de kilo-dalton environ. Au sein de ce tonneau, un chromophore est constitué via l'isomérisation d'un triplet d'acides aminés, souvent (X)-Y-G où X peut correspondre à n'importe quel résidu. Ces protéines fluorescentes ont un champ d'application large du fait de la vaste palette de couleurs disponibles couvrant tout le visible. Elles peuvent être utilisées comme étiquette pour permettre la localisation et le suivi de l'expression d'une protéine d'intérêt au sein de la cellule²⁷⁷.

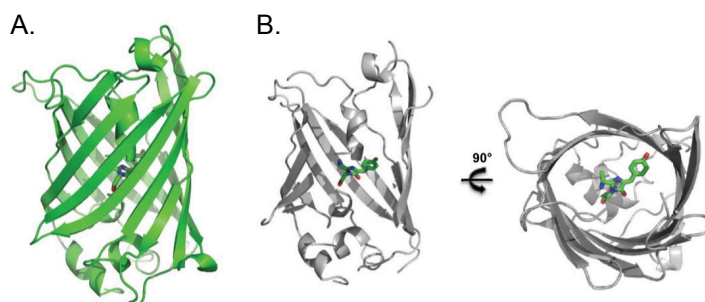


Figure 28. Structure générale des protéines fluorescentes. A. Vue de face d'une protéine fluorescente structurée en tonneau β . B. Vue de face et vue d'en haut du triplé d'acide aminé représentant le chromophore (vert) au sein du tonneau β (gris). Cette figure est reprise de la thèse de Mariam El Khatib.

Un fluorochrome est caractérisé par ses spectres d'absorption (λ_{abs}) et d'émission (λ_{em}), par son coefficient d'extinction molaire (ξ), qui informe sur sa capacité à absorber des photons à la longueur d'onde λ_{abs} , et par son rendement quantique (ϕ), qui révèle sa capacité à émettre des photons par fluorescence après absorption d'un photon. En suivant le diagramme d'énergie de Jablonski, le phénomène de fluorescence se produit en plusieurs étapes²⁷⁸ (Figure 29). Tout d'abord, le fluorochrome est dans son état d'énergie singulet basal S_0 . Il est ensuite porté à un état singulet excité S_1 ou S_2 par absorption d'un photon. Des relaxations vibrationnelles, sans émission de photons, peuvent survenir entre sous-états excités. Le fluorophore, étant dans un état peu stable, se désexcite en émettant un photon, soit par fluorescence, soit par phosphorescence, afin de retourner dans son état fondamental S_0 . L'émission par fluorescence est due à un phénomène de relaxation directe du niveau S_1 à S_0 sur l'échelle de la nanoseconde, tandis que l'émission par phosphorescence implique le passage inter-système du niveau S_1 vers un état triplet T_1 avant de revenir à l'état S_0 sur une échelle de temps plus grande, la milliseconde.

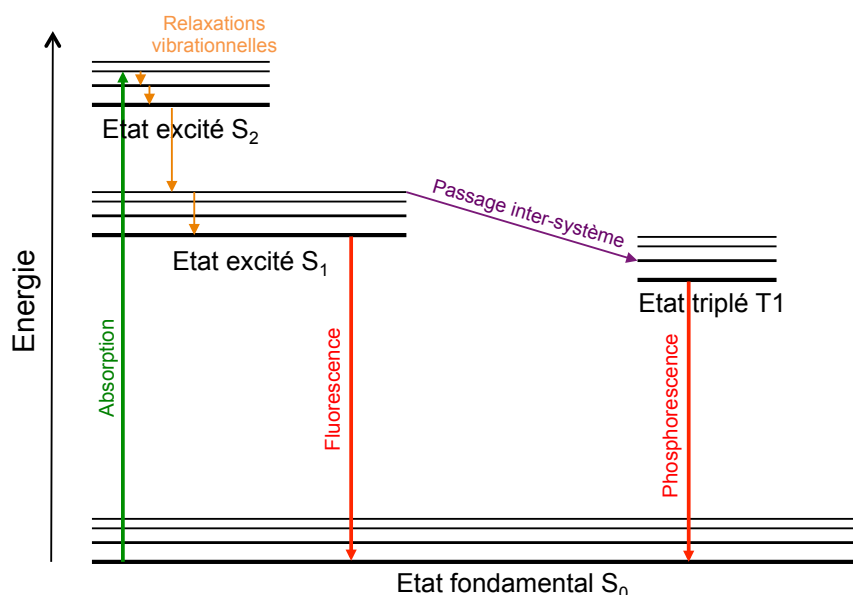


Figure 29. Simplification du diagramme d'énergie de Jablonski. L'absorption d'un photon (vert) entraîne le passage du fluorochrome de l'état fondamental S₀ à un état excité S₁ ou S₂. Des relaxations vibrationnelles (orange) et le passage inter-système vers l'état triplé T₁ (violet), sont accompagnés d'une perte d'énergie. Lors du retour du fluorochrome à son état fondamental S₀, l'émission de photons (rouge) se produit soit par fluorescence, soit par phosphorescence.

La microscopie de fluorescence est une technique optique parfaitement adaptée à l'étude d'ensemble de cellules vivantes. Il est possible d'observer leur phénotype et leur organisation au cours du temps, ainsi cette méthode est apparue idéale pour notre sujet, c'est à dire l'étude de biofilms bactériens.

B. Microscopie électronique

Une différence majeure entre la microscopie conventionnelle et la microscopie électronique (ME) est le type de rayonnement utilisé. Un faisceau d'électrons, et non de photons, est utilisé pour illuminer un échantillon permettant de créer une image très agrandie. En effet, les électrons ont l'avantage d'avoir (i) une faible longueur d'onde de 2,5 pm (comparé à 400 nm pour les photons) et (ii) une forte interaction avec la matière, ce qui leur procure un grand pouvoir résolutif avec des grossissements allant jusqu'à 5 millions de fois. Des lentilles électrostatiques et électromagnétiques sont utilisées en ME afin de contrôler la convergence du faisceau d'électrons sur l'échantillon. De plus, pour assurer que les électrons ne soient pas déviés, il est absolument nécessaire que le microscope soit sous-vide. Le Dr Ernst Ruska construisit le premier prototype de ME en 1931, ce qui lui valu le prix nobel de physique en 1986²⁷⁹.

Le champ d'application de la ME est très vaste, allant du domaine du vivant jusqu'à l'étude des matériaux. Ainsi, différents types de ME existent :

- à transmission (TEM : Transmission electron microscope)²⁸⁰,
- à balayage (SEM : Scanning electron microscope)²⁸¹²⁷⁹,
- à balayage en transmission (STEM : Scanning transmission electron microscope)²⁸²,
- par réflexion (REM : Reflection electron microscope)²⁸³.

On peut les différencier par leur source d'électrons, par leur mode d'acquisition, par l'intensité et le temps d'exposition, et par la préparation des échantillons, pouvant influencer la qualité de l'échantillon et de l'image. Le choix de ME va dépendre de l'application souhaitée mais également de la sensibilité de l'échantillon au faisceau d'électrons.

La préparation d'un échantillon peut être réalisée selon différentes méthodes :

- la coloration négative, technique rapide mais qui ne révèle qu'une « empreinte » de l'échantillon malgré un contraste élevé ;
- la cryo-ME, qui délivre une structure quasi-native de l'échantillon mais requiert une préparation relativement longue et difficile et génère des images à faible contraste, difficile à traiter pour les petites molécules monomériques ;
- l'ombrage, qui nécessite l'utilisation de métaux lourds adaptés pour l'imagerie des structures à mauvais contraste, offrant un très bel effet 3D. Néanmoins les particules métalliques présentent des risques d'agglomération et leur taille limite la résolution. Enfin, et quoique d'aspect 3D, l'image reste une projection sous une orientation unique.

Au cours de cette thèse, nous avons utilisé la ME pour visualiser les biofilms bactériens à plus forte résolution. La limite de cette technique est de ne pas pouvoir imager en temps réel les protéines d'intérêt provenant de bactéries vivantes. Il est effectivement nécessaire de fixer les bactéries avant de les observer, ce qui entraîne leur mort cellulaire. Malgré tout, la combinaison de la microscopie électronique et de microscopie de fluorescence conventionnelle est intéressante et complémentaire pour notre projet.

4- Cristallographie aux rayons X

La détermination de la structure d'une protéine permet une compréhension plus approfondie de son architecture, de sa fonction, de son ou ses interactions avec des ligands ou d'autres

macromolécules, ce qui aide au design rationnel de nouveaux inhibiteurs et/ou activateurs qui moduleront sa fonction. Il existe plusieurs méthodes permettant de déterminer la structure d'une protéine à résolution atomique, à savoir la cristallisation aux rayons X, la RMN et la cryo-ME (Figure 30).

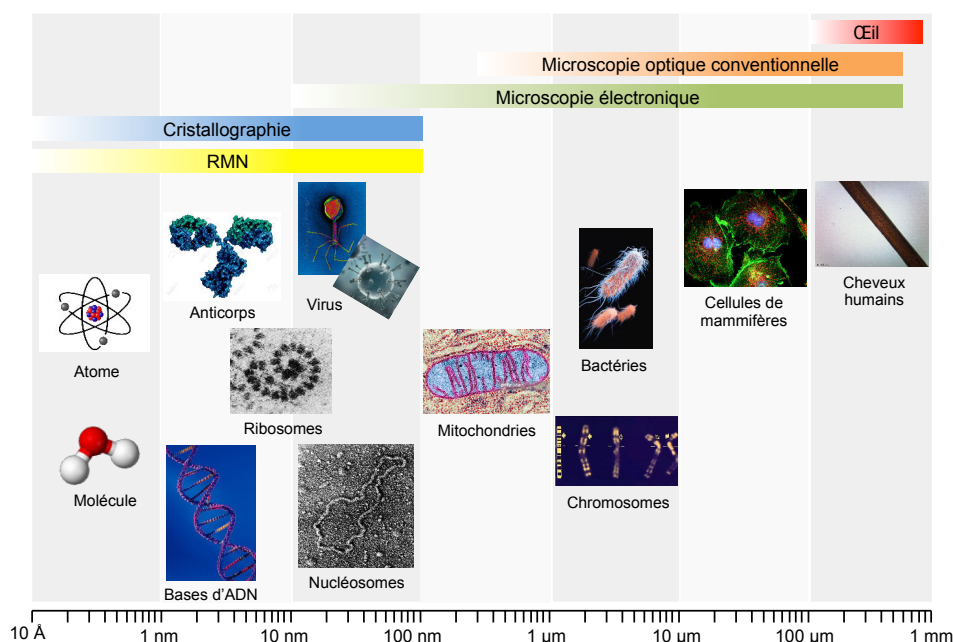


Figure 30. Echelle représentative des différentes tailles d'objets biologiques avec les techniques permettant de les observer et de les étudier.

Néanmoins, malgré des avancées de plus en plus majeures des techniques de RMN et de cryo-ME, la cristallographie aux rayons X reste à ce jour la technique de référence pour la détermination des structures protéiques à haute résolution (Figure 31).

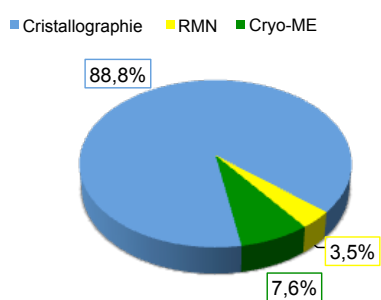


Figure 31. Proportion des structures protéiques publiées dans la PDB (Protein DataBase) en 2018, résolues par cristallographie aux rayons X (bleu), par cryo-ME (vert) ou par RMN (jaune).

L'utilisation des rayons X pour obtenir des informations à résolution atomique se justifie par leur longueur d'onde de taille similaire aux distances interatomiques. Cependant, du fait de la faible interaction des rayons X avec la matière, l'imagerie de particules uniques est très difficile en utilisant ces derniers (Coherent X-ray Imaging^{284,285}), réservée à de très gros objets généralement symétriques (virus ≥ 80 nm)²⁸⁶, mais jamais à résolution atomique. Ainsi, on aura recours à des cristaux composés de 10^{13} - 10^{14} copies de la protéine, qui diffuseront

suffisamment les rayons X pour qu'un signal puisse être enregistré. Ce sera dans ce cas la qualité du cristal qui déterminera la résolution de la structure obtenue. Plus il sera ordonné, plus la résolution de la diffraction sera élevée et plus grands seront les détails obtenus sur la structure de la protéine d'intérêt.

A. La cristallogénèse

Les protéines ont une tendance naturelle à s'auto-associer ; réussir à contrôler cette tendance peut permettre l'obtention de cristaux, lesquels seront utiles pour amplifier la diffusion des rayons X et permettre l'enregistrement d'un signal. Ainsi, la cristallographie aux rayons X nécessite une première étape de cristallisation de la macromolécule biologique d'intérêt. Cependant, la réalisation de cristaux de protéines à partir d'une solution soluble peut s'avérer compliquée. Il est primordial de trouver les conditions physico-chimiques adéquates qui assureront le passage de la protéine de l'état soluble à un état solide cristallin sans la faire précipiter. Le diagramme de phase illustre que la cristallisation varie majoritairement avec la concentration en protéine et en agent précipitant²⁸⁷ (Figure 32), quoiqu'elle soit également influencée par le pH, la quantité de sel non précipitant, la température et la pression. Le processus de cristallisation d'une protéine requière donc, en pratique, de passer d'un état de sous-saturation dans lequel les molécules sont solubles, dispersées mais stables, à un état de sursaturation où elles sont poussées à interagir avec elles-mêmes de la façon la plus ordonnée. A défaut, la protéine agrège et précipite ; ce qui est le résultat de la plupart des expériences de cristallisation.

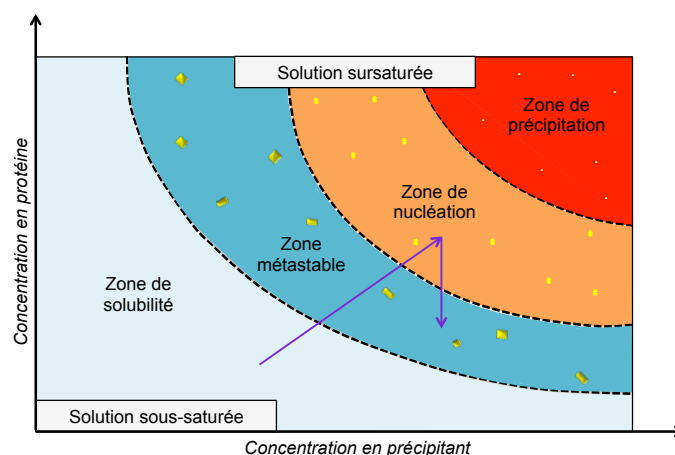


Figure 32. Schéma représentatif du diagramme de phase. La cristallisation d'une macromolécule biologique dépend principalement des concentrations en précipitant et en protéine. Premièrement, la solution protéique est soluble et stable (bleu clair). Avec le temps, les deux concentrations (protéine et précipitant) augmentent progressivement pour arriver en zone de sursaturation (flèche violette). La zone de nucléation (orange) est la zone où des microcristaux commencent à se former, puis la concentration protéique diminue jusqu'à atteindre la zone métastable (bleu), où des cristaux de plus grandes tailles croient (flèche violette). Si les protéines se retrouvent dans un état de déséquilibre trop

important, cela causera leur précipitation (rouge).

Dans les contacts cristallins, ce sont les contacts spécifiques entre résidus polaires par liaisons hydrogènes et par ponts salins qui sont le plus souvent à l'œuvre. Si une macromolécule peut parfois exploiter des interactions de van der Waals pour cristalliser, ces dernières, peu spécifiques, sont souvent limitantes pour l'obtention d'un cristal bien ordonné. Les protéines membranaires et amyloïdes, ayant tendance à principalement former ces contacts peu spécifiques, sont particulièrement difficiles à cristalliser.

Différentes méthodes de cristallisation existent comme le batch, la dialyse, la diffusion à l'interface et la diffusion de vapeur. Cette dernière, la plus répandue, a été utilisée pour la cristallisation de nos molécules d'intérêt durant la thèse. Le principe de cette méthode est d'arriver à un état de sursaturation dans une goutte de protéine par diffusion de vapeur à partir d'un réservoir. En pratique, on dépose une goutte – soit « assise », soit « suspendue » – constituée d'un ratio X:X (généralement 1:1) de protéine/agent précipitant faisant face à un réservoir qui contient le même agent précipitant, avant de fermer le tout hermétiquement. Avec le temps, les concentrations de la solution protéique et de cristallogénèse s'équilibrent du fait d'une évaporation lente de l'eau de la goutte vers le réservoir. Grâce à cette diffusion de vapeur, le mélange passe dans un état de sursaturation, favorisant la nucléation et potentiellement la croissance cristalline²⁸⁸ (Figure 33).

D'autres méthodes ont été développées pour pallier aux difficultés liées à la cristallisation des protéines membranaires. Elles sont basées sur l'utilisation de mélange lipide-détergent (bicelles)²⁸⁹ ou sur des phases lipidiques cubiques²⁹⁰, mimant au mieux l'environnement natif de la protéine. Les protéines membranaires, ainsi stabilisées, auront plus de chance de cristalliser.

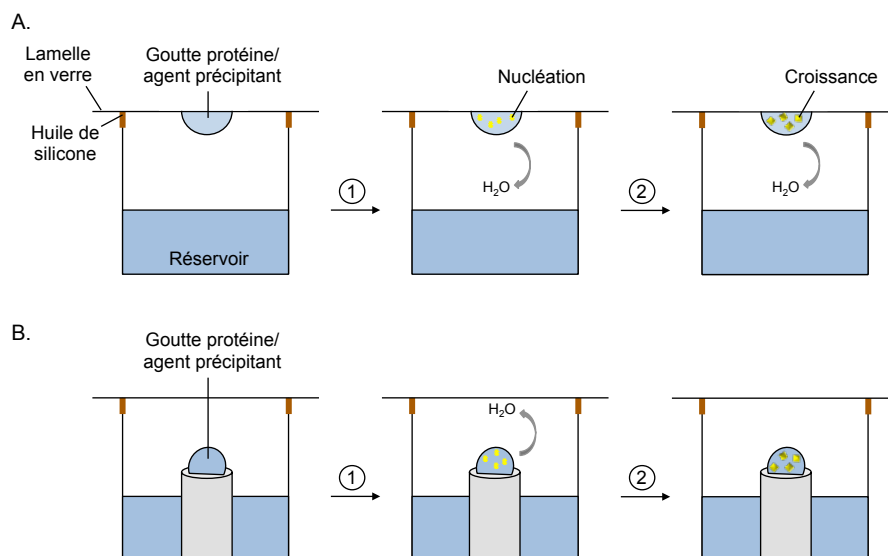


Figure 33. Schéma illustratif de la méthode de cristallogenèse par diffusion de vapeur. A. Une goutte du mélange protéine/agent précipitant (ratio X:X) est déposée sur une lame de verre. Celle-ci est retournée pour que la goutte se retrouve « suspendue » en face du réservoir contenant le même agent précipitant. B. La goutte peut également être « assise », c'est à dire déposée sur un support situé dans le puits contenant la solution réservoir. Le système est fermé hermétiquement grâce à une lamelle en verre posée au dessus du puits. Pour les deux techniques, la cristallogenèse par diffusion de vapeur se procède en deux temps : (1) l'évaporation de l'eau provenant de la goutte entraîne la nucléation protéique, qui amène ensuite (2) à la croissance de cristaux plus grands.

En pratique, pour trouver les conditions idéales de cristallogenèse, une première étape de criblage automatisé à l'aide d'un robot est réalisée. Une fois que des conditions initiales ont été identifiées, elles sont affinées manuellement en variant plusieurs paramètres comme la concentration protéique, l'agent précipitant, le sel, le pH et la température.

B. La diffraction

Un cristal est un empilement régulier, ordonné et périodique d'un motif en 2 ou 3 dimensions, et parce que l'interaction des rayons X avec la matière organique est extrêmement faible, ce réseau sert d'amplificateur du signal. L'unité de base d'un cristal, appelée maille, contient une ou plusieurs unités asymétriques permettant la reconstruction entière du cristal par des opérateurs de symétrie cristallographique.

Le phénomène de diffraction est le comportement des ondes des rayons X lorsqu'elles rencontrent un cristal. Le résultat de l'onde résultante correspond alors aux interférences des ondes diffractées par les différentes mailles du cristal. Le flux de photon X sera important ou au contraire très faible selon que ces interférences soient constructives ou destructives, respectivement (Figure 34). Ce phénomène a été découvert par Max von Laue puis longuement étudié par le père et le fils Bragg, ce qui leur valut le prix Nobel en 1914 et en 1915, respectivement. Les données collectées composent le diagramme de diffraction où les interférences des rayons diffusés sont renvoyées dans des directions spécifiques, déterminées par la longueur d'onde des rayons X et par les dimensions et l'orientation du réseau cristallin.

La loi de Bragg interprète le processus de diffraction en mesurant l'angle et l'amplitude de diffraction, ce qui renseigne sur les caractéristiques du cristal telles que :

- ses paramètres de maille,
- son groupe d'espace ; représentant l'ensemble des symétries de la structure cristalline,
- la composition et la structure du contenu de l'unité asymétrique.

Cette loi est exprimée selon la formule:

$$2.d.\sin\theta = n\lambda$$

avec « d » représentant l'espace entre deux plans réticulaires parallèles du réseau cristallin, « θ » l'angle de réflexion des rayons X sur ces plans et « λ » la longueur d'onde. Plus la distance entre les plans parallèles est petite, plus le signal sera diffusé à grand angle et contiendra une information structurale à haute résolution.

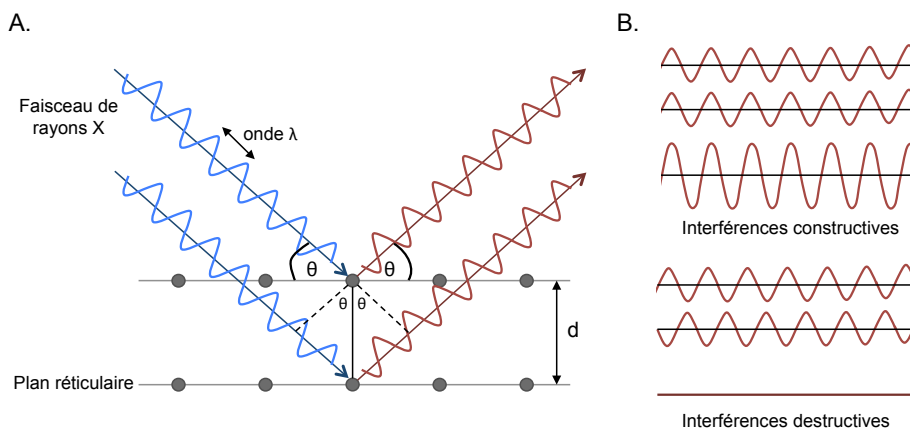


Figure 34. Illustration de la loi de Bragg. A. Schéma représentatif de la loi de Bragg et du concept de diffraction. B. Description des interférences constructives et destructives des ondes des rayons X diffusées par les composants d'un cristal.

Une fois le cristal protéique exposé aux rayons X, des tâches de diffraction correspondants aux faisceaux de rayonnements X réfléchis par les plans réticulaires du cristal sont enregistrées par un détecteur. Pour passer de l'espace de la diffraction (espace réciproque permettant l'interprétation du cliché de diffraction) à l'espace de la molécule (espace réel), la transformée de Fourier est utilisée selon la formule suivante :

$$\rho(x, y, z) = \frac{1}{V_m} \sum_{hkl} F(hkl) \exp[-2i\pi(hx + ky + lz)]$$

où « ρ » correspond à la densité électronique, « x,y,z » et « h,k,l » aux coordonnées respectives de l'espace réel et réciproque, « V » au volume de la maille, et « F » au facteur de structure défini par une amplitude et une phase. La transformée de Fourier pallie à l'absence de lentilles focalisant les rayons X mais réclame de connaître les phases des ondes diffusées par le cristal. Cependant, un problème majeur de la cristallographie aux rayons X est la perte de cette information au cours de la collecte. Pour solutionner ce « problème de phase », le phasage expérimental ou le remplacement moléculaire sont deux approches utilisées pour la récupération d'information. Une fois la phase retrouvée, une transformée de Fourier inverse est appliquée, permettant le calcul de la densité électronique de la maille. C'est à partir de celle-ci que la structure de la protéine d'intérêt sera construite et affinée.

C. La pratique

Pour enregistrer des données cristallographiques à haute résolution, une source de rayons X, qui soit idéalement intense et brillante, est nécessaire. A proximité de l'Institut de Biologie Structurale (IBS) se trouve l'European Synchrotron Radiation Facility (ESRF) de Grenoble générant des rayons X de très haute brillance avec une longueur d'onde comprise entre 0,5 et 2,5 Å. Durant la thèse, nous avons ainsi eu recours aux lignes de lumières du synchrotron pour collecter nos données sur nos cristaux d'intérêt.

L'ESRF est composé de trois éléments principaux (Figure 35) :

- un accélérateur linéaire, où les électrons sont accélérés sous l'action d'un champ électrique haute tension ;
- un booster, dans lequel les électrons provenant du précédent accélérateur sont de nouveau accélérés jusqu'à atteindre une vitesse proche de celle de la lumière, et ;
- un anneau de stockage, dans lequel les électrons accélérés sont injectés.

Les électrons émettent par la suite un faisceau de rayons X très fin, polarisé et très intense par l'application d'un champ magnétique perpendiculaire à leur trajectoire dans l'anneau.



Figure 35. Présentation des éléments constituant le synchrotron de Grenoble. Vue de haut de l'ESRF de Grenoble composé d'un accélérateur linéaire (jaune), d'un booster (rouge) et d'un anneau de stockage (vert).

Les cristaux de protéines, particulièrement membranaires, sont fragiles et sensibles aux dommages d'irradiations ce qui peut rendre les données de diffraction difficilement interprétables. Pour pallier à cela, il est conseillé et souhaitable de cryo-protéger les cristaux avant leur exposition aux rayons X, augmentant ainsi leur durée de vie dans le faisceau de rayons X d'environ 70 fois. Pour ce faire, les cristaux sont trempés dans une solution cryoprotectrice afin d'éviter la formation de glace, puis congelés immédiatement dans de l'azote à 100 K (liquide ou gazeux). Les données sont ensuite collectées dans ces mêmes conditions cryogéniques pour éviter tout endommagement du cristal au cours de la collecte. La détection des rayons X diffractés par le cristal passe par l'intermédiaire de détecteurs CCD ou à pixel, tel que Pilatus ou Eiger, qui fournissent un cliché de diffraction (Figure 36). Chaque tâche observée sur le détecteur correspond aux intersections entre le faisceau de rayon

X et les plans réticulaires du cristal. Pour une collecte de données complète, le cristal est soumis à une oscillation durant l'exposition aux rayons X, où chaque image enregistrée correspond à une oscillation entre 0,1 et 5° selon la taille de la maille et la symétrie interne du cristal.

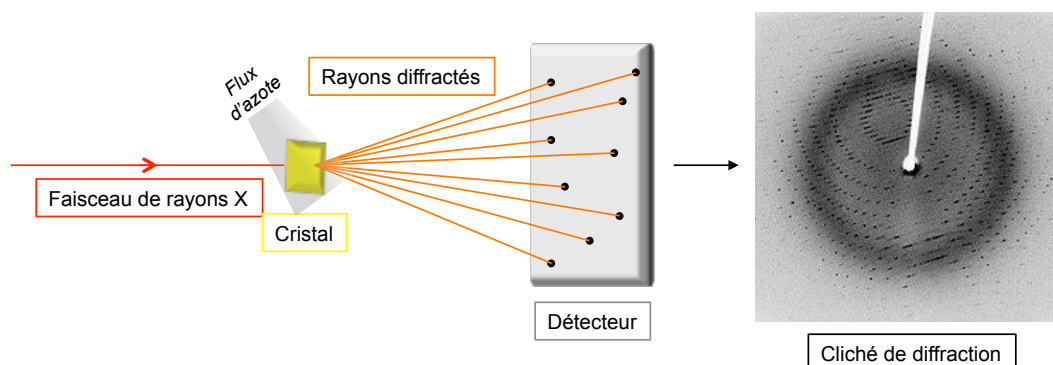


Figure 36. Schéma illustratif de la diffraction des rayons X à travers un cristal. Un cristal, placé sous un flux d'azote, est soumis à un faisceau de rayons X. Les rayons diffractés sont détectés par un détecteur qui fournit un cliché de diffraction.

La collecte de données doit également être optimisée à travers un ajustement du centrage du cristal, de la distance cristal-détecteur, de la transmission et du temps d'exposition du cristal aux rayons X.

D. Le traitement de données

A l'heure actuelle, le traitement de données cristallographiques est avant tout informatique et se décompose en plusieurs étapes²⁹¹ :

- i) l'indexation de l'ensemble des tâches collectées, qui détermine l'orientation et les paramètres de maille du cristal ;
- ii) l'intégration, qui mesure l'intensité des tâches de diffraction ;
- iii) la mise à l'échelle, qui met au même niveau d'intensité les différentes réflexions liées par la symétrie;
- iv) le phasage ;
- v) le calcul de la carte de densité électronique, par une application de la transformée de Fourier inverse sur les facteurs de structures ;
- vi) l'affinement de la structure, qui aboutit à la construction d'un modèle final.

En pratique, la résolution d'une structure requiert plusieurs itérations entre les points v) et vi), et peut souvent être mise en échec à l'étape iv).

La première étape d'indexation assigne à chaque réflexion un point du réseau réciproque d'indices h,k,l (indices de Miller) et propose les groupes d'espaces possibles avec une pénalité – écart entre position prédite et observée des différentes tâches de Bragg – pour chacun d'eux. Le choix se fera sur le groupe d'espace de plus faible pénalité et de plus haute symétrie.

La seconde étape, dite d'intégration, discerne les pixels à intégrer de ceux n'ayant enregistrés que du bruit, et pour chaque tâche, permet d'intégrer l'intensité diffractée. La qualité des données est en premier lieu évaluée sur le critère du rapport signal sur bruit, mais d'autres indicateurs statistiques permettent de déterminer la limite en résolution des données. Le facteur R_{merge} indique l'accord entre les intensités équivalentes par symétrie et leur moyenne²⁹². L'indicateur R_{pim} décrit également la précision des mesures mais de manière plus informatif que le R_{merge} car il tient compte de la redondance des données n ²⁹³. Le facteur R_{meas} est une version corrigée de la multiplicité (nombre de motifs par maille), rendant compte de manière fiable la cohérence des mesures individuelles²⁹⁴. Enfin, le coefficient de corrélation de Pearson (CC) est un paramètre permettant d'évaluer la précision des données ainsi que l'accord du modèle et des données sur une échelle commune. Le $CC_{1/2}$, correspondant à un demi-ensemble de données aléatoires, est calculé entre les intensités moyennes de chaque sous-ensemble grâce auquel le CC peut être estimé analytiquement²⁹⁵.

La troisième étape de mise à l'échelle génère une série de réflexions uniques qui seront nécessaires pour le calcul de la densité électronique.

La quatrième étape de phasage est plus complexe. En effet, une carte de densité électronique nécessite la connaissance de deux paramètres, l'amplitude et la phase des rayons diffractés ; hors, tandis que l'amplitude est proportionnelle à la racine carrée des intensités mesurées, l'information de la phase est perdue pendant la collecte de données²⁹⁶. Différentes méthodes existent pour phaser un jeu de données, telles que :

- le SAD (Single-wavelength anomalous dispersion)²⁹⁷,
- le MAD (Multi-wavelength anomalous diffraction)²⁹⁸,
- le SIR (Single isomorphous replacement)²⁹⁹,
- le MIR (Multi isomorphous replacement)²⁹⁹,
- le remplacement moléculaire³⁰⁰.

Les techniques de diffusion anormale et de remplacement isomorphe sont utilisées pour résoudre des structures de nouvelles protéines n'ayant pas d'homologues enregistrés dans la PDB, et nécessitent l'utilisation d'atomes généralement lourds. Quant au remplacement moléculaire, la stratégie est d'utiliser la structure d'une protéine déjà connue et homologue à plus de 20% à celle d'intérêt pour obtenir l'information de phase recherchée. Il s'agira ensuite

de trouver la matrice de rotation et les vecteurs de translation qui permettent de simuler au mieux le contenu de la maille étudiée.

Une fois l'information de phase obtenue, une carte de densité électronique peut être calculée dans laquelle le modèle initial de la protéine d'intérêt est construit. Les facteurs de structures calculés à partir du modèle initial (F_{calc}) ne sont que partiellement en accord avec ceux observés (F_{obs}), ainsi la dernière étape d'affinement du modèle atomique sert à faire converger le modèle de départ vers la structure inconnue. Pour cela, deux cartes de densité électroniques sont générées par transformée de Fourier à partir des amplitudes des facteurs de structures observés et calculés. La carte $2F_{\text{obs}}-F_{\text{calc}}$ génère une densité autour du modèle tandis que la carte de différence $F_{\text{obs}}-F_{\text{calc}}$ rend compte des différences entre le modèle et les données expérimentales. Sur cette dernière, des pics négatifs et positifs sont respectivement observés autour des atomes qui ne sont pas présents (ou pas à la place attendue) ou au contraire qui devraient être inclus. Le processus d'affinement doit aboutir à la construction du modèle final en limitant au maximum ce type de densités électroniques différentes, tout en maximisant la qualité de la géométrie du modèle et l'accord avec les données expérimentales. Dans la pratique, le processus d'affinement se réalise à travers plusieurs cycles de deux étapes :

- i) une étape d'optimisation du modèle par affinement dans l'espace réciproque ;
- ii) une étape de reconstruction manuelle, dans laquelle les atomes sont manuellement placés ou déplacés dans les cartes de densité électronique obtenues après l'étape précédente.

La qualité de l'affinement est évaluée par plusieurs indicateurs statistiques, dont des facteurs d'évaluation³⁰¹ tels que:

- le facteur R, qui permet de vérifier la qualité d'une structure. Il suit la convergence de l'affinement mais est biaisé par le modèle de départ ;
- le facteur R_{free} , qui est calculé à partir de réflexions non-utilisées (environ 5%) pour l'affinement – et donc n'est pas biaisé par le modèle de départ.

En effet, il est nécessaire d'éviter toute relation entre les réflexions utilisées lors de l'affinement et celles du jeu de données utilisé pour le calcul du R_{free} . La qualité du modèle est maximisée par la diminution conjointe de ces deux facteurs R ; dans le cas où le R_{free} augmente lorsque le facteur R diminue, on peut craindre le sur-affinement du modèle ou un placement faux dans la densité électronique, lors de la précédente étape de reconstruction manuelle. Ainsi le cristallographe est guidé vers la production du modèle le plus juste qui satisfait les données.

Pour valider le modèle final, d'autres critères d'évaluation seront à prendre en compte, comme :

- La complétude, qui correspond au nombre de réflexions mesurées par rapport au nombre de réflexions théoriques. Il est nécessaire que ce paramètre soit le plus élevé possible car les réflexions manquantes affectent la qualité de la carte de densité électronique après l'étape d'affinement. La valeur attendue de la complétude pour l'ensemble des données est comprise entre 95 et 100%.
- Le diagramme de Ramachandran, qui permet d'évaluer la qualité de la géométrie globale de la structure³⁰². Trois zones favorables sont définies en fonction des valeurs des angles de rotation des liaisons peptidiques (ϕ et ψ). Ces régions ont été établies en tenant compte des paramètres stéréochimiques³⁰³ et à partir des paramètres propres aux structures protéiques connues (zones régulièrement mises à jour). Les deux principales régions correspondent aux structures secondaires des protéines, la région des hélices α et celle des feuillets β . La troisième région, plus petite, correspond à une conformation en hélice gauche avec $\phi = 0$.
- Les déviations standard des liaisons covalentes (rmsd), qui évaluent les paramètres physico-chimiques de la molécule d'intérêt (longueurs et angles de liaisons, planarité...), et rendent compte de la qualité de la structure. Les valeurs ne doivent pas dépasser 0,02 Å et 2°, respectivement.
- Le facteur d'agitation thermique (facteur B), qui décrit la probabilité des déplacements thermiques d'un atome autour de sa position d'équilibre. Les facteurs B sont ajustés par rapport à ceux des atomes voisins constituant la protéine. Du fait que les atomes soient liés de manière covalente dans un cristal, ces déplacements sont particulièrement restreints selon certaines directions de l'espace.

IV – Matériels et méthodes

IV – Matériels et méthodes

1- Les souches bactériennes

En fonction de l'expérience à réaliser, différentes souches bactériennes sont utilisées:

- i) La souche DH5 α d'*E. coli* permet l'amplification des plasmides recombinants et la sélection des clones positifs après clonage ou assemblage de Gibson.
- ii) La souche BL21 DE3 d'*E. coli* est utilisée comme contrôle négatif au vu de son incapacité à former des biofilms adhérents.
- iii) La souche BL21 Δ Omp8 d'*E. coli*, dépourvue de ses principales porines ($\Delta lamB$, $\Delta ompF$, $\Delta ompA$, $\Delta ompC$)¹⁹⁹, est utilisé dans le but d'exprimer nos porines d'intérêt pour étudier leurs rôles dans la formation et la stabilité des communautés flottantes. Une cassette de résistance à la kanamycine a été intégrée dans la souche afin de pouvoir la sélectionner en utilisant 35 μ g/mL de kanamycine.
- iv) La souche ATCC 29914 de *P. stuartii*, fournie par l'Institut Pasteur (Paris), contribue à l'étude des biofilms et à leurs réponses aux stress extérieurs.
- v) La souche ATCC 29914 de *P. stuartii* Δ Omp-Pst2^{204,304} sert à étudier l'effet de l'absence de la seconde porine Omp-Pst2 sur la formation et la stabilité des communautés flottantes et des biofilms adhérents. Elle nous a été fournie par le Pr. Jean-Marie Pagès de l'Université de Marseille. Une cassette de résistance au chloramphénicol a été insérée à la souche mutée afin de la sélectionner par l'utilisation de 34 μ g/mL de chloramphénicol.

2- Biologie moléculaire

A. Les plasmides

Les plasmides utilisés sont des plasmides d'expression de type pET possédant un promoteur T7 pour permettre l'induction de l'expression de la protéine d'intérêt, soit en cas de carence en glucose³⁰⁵, soit grâce à l'ajout d'une molécule inductrice l'IPTG (Isopropyl β -D-1 thiogalactopyranose). Néanmoins, les plasmides pETs possèdent un niveau d'expression basal considérable même en absence d'induction³⁰⁶. Deux variants du plasmide d'expression pET3a, pGOmp-pst1 et pGOmp-pst2, fournis par le Pr. Mathias Winterhalter, sont utilisés pour exprimer les porines Omp-Pst1 et Omp-Pst2 de *P. stuartii*, respectivement. Les deux plasmides contiennent une cassette de résistance à l'ampicilline.

B. RT-qPCR

Les expressions relatives des deux porines de *P. stuartii* sont analysées et quantifiées par RT-qPCR au sein, soit des communautés flottantes, soit des biofilms adhérents, en présence d'urée à 500 mM, d'ammonium à 500 mM, de bicarbonate à 50 mM, et à différents pHs entre 5 et 9.

L'extraction d'ARN est la première étape à réaliser. En pratique, une colonie de *P. stuartii* ou de *P. stuartii*ΔOmp-Pst2 est mise en culture dans 30 mL de milieu LB puis incubée 1 h à 37°C sous 150 rpm d'agitation. Pour chaque souche et chaque condition testée, 3 puits (triplicats) d'une plaque 6-puits (CytoOne) sont remplis de 2 mL de la pré-culture. Pour étudier l'expression des porines à différentes phases de croissance, la plaque est incubée à 37°C sous 60 rpm d'agitation jusqu'à ce qu'une densité optique à 600 nm (DO_{600nm}) de 0.3, 0.5, 0.7, 0.9 ou 1.5 soit atteinte. Les communautés flottantes en suspension sont collectées par pipettage et brièvement centrifugées pour culoter les bactéries sans les endommager. Le culot est resuspendu, soit dans 2 mL de milieu LB frais contenant de l'urée, de l'ammonium ou du bicarbonate, soit dans 2 mL de LB à un pH spécifique, puis incubé à 37°C pendant 30 min sous 60 rpm d'agitation. En parallèle, les biofilms adhérents restés au fond des puits sont lavés avec du milieu LB avant d'être exposés à 2 mL de LB supplémenté de la condition désirée. La plaque est ensuite incubée 30 min à 37°C sous 60 rpm d'agitation. L'extraction d'ARN est effectuée via le kit RNeasy Mini (Qiagen) avec quelques modifications des premières étapes du protocole en fonction du phénotype étudié spécifiquement.

Pour les communautés flottantes, un des 2 mL de culture est enlevé puis remplacé par 1 mL de RNAProtect Cell Reagent (Qiagen). Après 5 min d'incubation, le mélange est centrifugé à 3 200 g pendant 10 min et le culot est resuspendu dans 110 µL de tampon TE (30 mM Tris-HCl, 1 mM EDTA, pH 8) contenant 15 mg/mL de lysozyme et 2 mg/mL de protéinase K (Qiagen), nécessaire pour lyser les cellules et extraire les acides nucléiques, puis incubé à température ambiante pendant 10 min.

Pour les biofilms adhérents, les 2 mL de LB sont ôtés des puits et 1 mL du mélange RNAProtect Cell Reagent:LB (ratio 1:1) est ajouté. Après 5 min d'incubation, le RNAProtect est enlevé et 410 µL de tampon TE contenant 15 mg/mL de lysozyme et 0,5 mg/mL de protéinase K sont ajoutés. Une fois les biofilms décrochés, en grattant manuellement le fond des puits, la solution bactérienne est incubée pendant 10 min à température ambiante.

L'extraction d'ARN total sur les communautés flottantes et les biofilms adhérents se poursuit en suivant les instructions du kit, et la quantité et la qualité des ARNs extraits pour les deux phénotypes bactériens sont évaluées au Nanodrop2000 (Figure 37).

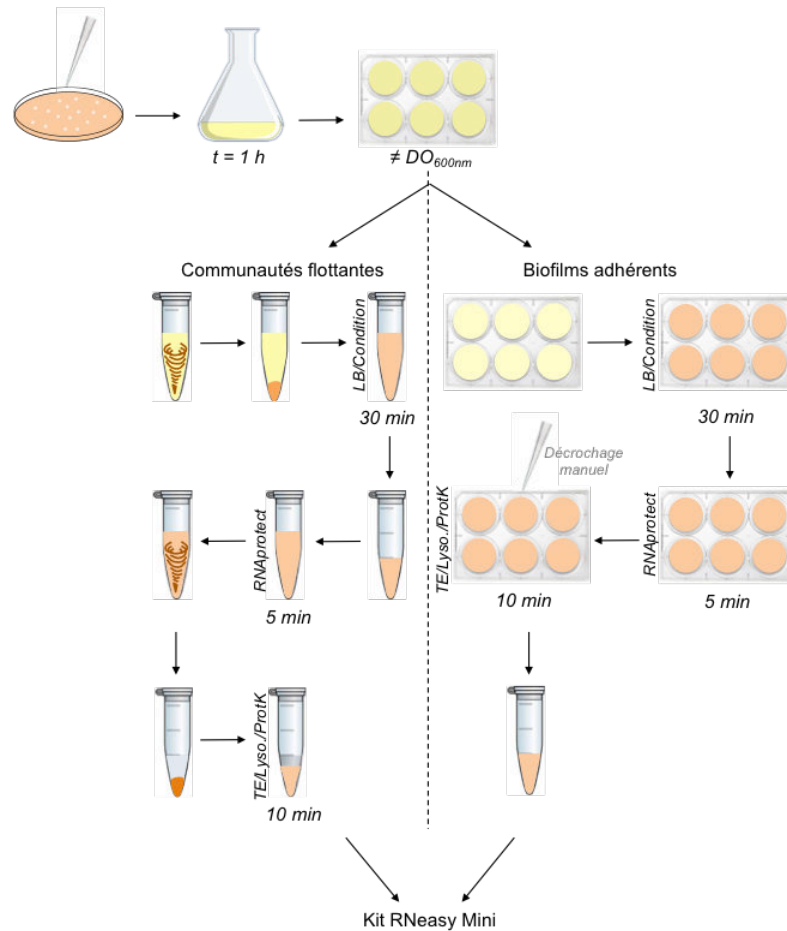


Figure 37. Représentation schématique des premières étapes du protocole d'extraction d'ARN total sur les communautés flottantes et biofilms adhérents. Une colonie est prélevée sur une boîte de pétri contenant du LB-agar et est inoculée dans du milieu LB pendant 1 h à 37°C sous agitation. La pré-culture est distribuée dans une plaque 6-puits et incubée à 37°C jusqu'à atteindre différentes DO_{600nm} correspondant à différentes phases du cycle de croissance de *P. stuartii*. Les communautés flottantes sont centrifugées et le culot est resuspendu dans du milieu LB supplémenté de la condition désirée pendant 30 min. Du RNAprotect est ajouté aux bactéries pendant 5 min qui sont ensuite centrifugées et resuspendues dans du tampon TE complété de lysozyme et de protéinase K. Pour les biofilms adhérents, les puits sont lavés et soumis à la condition désirée pendant 30 min. Le RNAprotect est ajouté pendant 5 min puis enlevé afin de décrocher manuellement les bactéries dans du tampon TE/lysozyme/protéinase K pendant 10 min. L'ARN est par la suite extrait grâce au kit RNeasy Mini.

Du fait de leur sensibilité notoire, les ARNs extraits des communautés flottantes et des biofilms adhérents sont immédiatement utilisés pour l'étape de réverse transcription. En pratique, 1 μ g de l'ARN total est retro-transcrit en ADNc en suivant les instructions du kit QuantiTect Reverse Transcription (Qiagen), puis stocké à -20°C jusqu'à son utilisation. L'ARN restant est conservé à -80°C.

Après avoir quantifié de manière absolue l'abondance des transcrits (1), le nombre exact de copies de l'ARNm correspondant à chaque porine est déterminé dans chacune des conditions testées (2). Ces deux étapes sont succinctement détaillées ci-après :

(1) Pour effectuer une quantification absolue des transcrits, des fragments d'ADN de séquence et de taille connues du génome de *P. stuartii* sont amplifiés et quantifiés pour être utilisés comme standards. A dessein, l'ADN génomique de *P. stuartii* est extrait en suivant les instructions du kit NucleoSpin Tissue (Macherey-Nagel). L'utilisation de la Q5 High-Fidelity DNA Polymerase (New England BioLabs) permet l'amplification d'un fragment de 954 pb et de 956 pb correspondant aux gènes d'*omp-pst1* et d'*omp-pst2*, respectivement, en utilisant les primers suivants :

	<i>omp-pst1</i>	<i>omp-pst2</i>
Primer n°1	OmpPst1_F3qs : 5'-GAAGATGGCGACGACTCACG-3'	OmpPst2_F4qs : 5'-ATTATTCGCGGCGGGTGTTAC-3'
Primer n°2	OmpPst1_R3qs : 5'-GTAAACCAGACCCAGACCCAGAAC-3'	OmpPst2_R4qs : 5'-CAGCGGCCATATTCTTGTTGA-3'

Le programme de PCR appliqué est le suivant :

- i) 5 min à 98°C,
- ii) 35 cycles de :
 - a. 30 sec à 98°C, pour la dénaturation de l'ADN,
 - b. 30 sec à 55°C, pour la fixation des primers sur l'ADN,
 - c. 2 min à 72°C, pour l'élongation des primers sur l'ADN,
- iii) 5 min à 72°C, assurant une dernière étape d'extension.

Une fois terminé, les amplicons de PCR sont visualisés sur un gel d'agarose à 1% supplémenté de SYBR Safe (ThermoFisher scientific), qui permet de vérifier la taille attendue. Pour chaque gène, la bande correspondante à l'amplicon est excisée du gel et purifiée en employant les instructions du kit NucleoSpin Gel and PCR Clean-up. La qualité et la quantité du gène purifié sont mesurées au Nanodrop2000. En se basant sur la composition, la longueur de la séquence et la concentration de chaque fragment de porines amplifié, le nombre de copies présent dans le standard est calculé et une courbe est établie en utilisant 8 concentrations de 5×10^1 à 5×10^8 copies de gène.

(2) Pour la quantification du nombre de copies de chaque porine dans chaque condition, deux fragments de 77 pb et de 82 pb des gènes d'*omp-pst1* et d'*omp-pst2*, respectivement, sont ciblés à l'aide des primers suivant :

	<i>omp-pst1</i>	<i>omp-pst2</i>
Primer n°1	OmpPst1_R1q : 5'-CGCATTTCGGTTATGTTGAT-3'	OmpPst2_R2q : 5'-CTTCGCTCTACAGTACCA-3'
Primer n°2	OmpPst1_F1q : 5'-CGCTTGACTTGTTGTTGT-3'	OmpPst2_F2q : 5'-GCCATCACCATTGTTATCTAA-3'

La réaction de qPCR est réalisée en présence de :

- i) 4 µL des échantillons dilués (10x) ou des standards,
- ii) 0,6 µL de chaque primer à 10 µM finale,
- iii) 7 µL de SsoAdvanced Universal SYBR Green Supermix (Bio-Rad),
- iv) qsp 15 µL avec de l'eau RNase-free.

La réaction est permise par un système CFX Connect Real-Time PCR Detection (Bio-Rad), qui réalise des cycles de plusieurs rampes de température dont une étape initiale (i) à 95°C pendant 3 min, suivi de 39 cycles (ii) à 95°C pendant 10 sec (dénaturation) et (iii) à 60°C pendant 45 sec (fixation et élongation des primers, respectivement). Le nombre de copies transcrits d'*omp-pst1* et *omp-pst2* est ensuite calculé à partir des courbes standards pour *P. stuartii* ATCC 29914 et *P. stuartii*ΔOmp-Pst2 avec le logiciel Bio-Rad CFX Manager v3.1 (Bio-Rad).

Afin de normaliser les résultats d'expression des porines, nous avons voulu suivre la méthode d'analyse décrite par Danilo et al.³⁰⁷, qui rapporte une liste de gènes de référence pouvant être considérés invariants dans les études de RT-qPCR chez plusieurs espèces bactériennes et les propose comme utiles pour la normalisation des mesures d'expression. Nous avons ainsi sélectionné et mesuré l'expression des gènes des gyrases A et B, de *secA* et du 16S RNA. Cependant, nous avons pu découvrir que l'expression de chacun de ces gènes varie (au moins chez *P. stuartii*) dans les conditions expérimentales/environnementales testées, prohibant leur utilisation comme gènes de références et nous forçant à plutôt normaliser nos données en fonction du nombre de copies d'ARN totaux. En effet, il a été suggéré par Johnson et al., que cette méthode de normalisation est préférable lorsqu'aucun gène de référence interne ne peut être validé chez l'espèce testée³⁰⁸, ce qui est notre cas. Néanmoins, cette normalisation nécessite une quantification précise de la teneur en ARN dans chaque échantillon.

3- Etude de la croissance et de la socialisation bactérienne

A. Transformation bactérienne

Comme évoqué plus haut, nous avons utilisé le choc thermique comme méthode de transformation bactérienne, qu'il s'agisse des bactéries DH5 α ou BL21 Δ Omp8, où le prérequis est de rendre ces bactéries compétentes. A dessein, les bactéries non-compétentes sont étalées sur des boîtes LB-agar et incubées à 37°C sur la nuit. Le lendemain, une colonie est inoculée dans 5 mL de LB pour une nuit supplémentaire à 37°C sous 150 rpm d'agitation. Une culture de 100 mL de LB est ensuiteensemencée à partir de 1 mL prélevé de la pré-culture, et incubée à 37°C sous agitation jusqu'à atteindre une DO_{600nm} d'environ 0,4. La culture est alors centrifugée à 4 000 rpm pendant 15 min à 4°C et le culot bactérien est resuspendu dans 30 mL de tampon RF1 glacé (Tableau ci-après). Après une incubation de 15 min dans la glace, la solution est centrifugée une nouvelle fois à 4 000 rpm pendant 15 min à 4°C et ce dernier culot est resuspendu dans 8 mL de tampon RF2 glacé (Tableau). Après une nouvelle incubation de 15 min sur glace, les bactéries ainsi rendues compétentes sont aliquotées (50 μ L) puis conservées à -80°C.

	Tampon RF1	Tampon RF2
Composition pour 1 L de volume final	- 30 g CH ₃ COOK à pH 5,8 - 12 g RbCl - 9,9 g MnCl ₂ .4H ₂ O - 1,5 g CaCl ₂ .2H ₂ O - 150 g glycérol	- 10 mM MOPS à pH 6,8 - 1,2 g RbCl - 11 g CaCl ₂ .2H ₂ O - 150 g glycérol

C'est seulement après avoir rendu les bactéries compétentes que peut être envisagé une transformation par choc thermique. En pratique, 1 à 5 μ L du plasmide d'intérêt est ajouté à un aliquot de bactéries compétentes. Le mélange subit ensuite une suite d'incubation de:

- i) 30 min dans la glace, durant lesquelles l'ADN plasmidique s'accroche aux bactéries,
- ii) 45 sec à 42°C, durant lesquelles les membranes bactériennes sont fragilisées, et
- iii) 2 min dans la glace, au cours desquelles l'entrée du plasmide dans la bactérie a effectivement lieu.

Une fois le choc thermique réalisé, les bactéries sont immédiatement incubées dans 500 μ L de milieu riche SOC (Super Optimal Broth - ThermoFischer) pendant environ 1 h à 37°C sous agitation, les aidant ainsi à récupérer et à débiter leur croissance. Pour ne sélectionner que les bactéries ayant intégrées le plasmide d'intérêt, les cellules microbiennes sont étalées sur des

milieux de culture supplémentés de l'antibiotique nécessaire à la sélection des clones positifs puis incubées sur la nuit à 37°C sous 150 rpm d'agitation.

B. Etude des effets environnementaux, ou de l'addition de peptides et d'acides aminés, sur la formation de communautés flottantes et de biofilms adhérents par *P. stuartii*

La croissance bactérienne présente quatre phases : une phase de latence, une phase exponentielle, une phase stationnaire et une phase de déclin. Chez *P. stuartii*, la phase exponentielle est associée à la formation de communautés flottantes, puis en phase stationnaire ces dernières sédimentent, formant ainsi des biofilms adhérents. Comparée aux bactéries planctoniques isolées, cette socialisation repousse la phase de déclin bactérienne assurant une survie plus importante à *P. stuartii*.

Au cours de cette thèse, la croissance des bactéries *E. coli* BL21, *E. coli* BL21ΔOmp8 (transformées par pGOmp-pst1 ou pGOmp-pst2), *P. stuartii* et *P. stuartii*ΔOmp-Pst2 a été suivie et comparée dans les différentes conditions testées. Pour ce faire, les bactéries sont préalablement étalées sur un milieu LB-agar, supplémenté ou non de l'antibiotique approprié, puis incubées à 37°C sur la nuit. Une colonie de chaque lignée est inoculée dans 5 mL de LB, soit standard (10 g/L de bacto-tryptone, 5 g/L d'extrait de levure et 10 g/L de NaCl à pH 7), soit tamponné à un pH spécifique, pendant 1 h à 37°C sous agitation. Les bactéries en phase de latence sont distribuées dans des plaques 96-puits. Spécifiquement, entre 120 et 150 µL/puits sont déposés en présence de 15 µL de solutions à (i) 10X d'urée (entre 0 et 1M), d'ammonium (entre 0 et 1M), de bicarbonate (entre 0 et 100 mM), de créatinine (entre 0 et 100 mM), ou (ii) d'acides aminés tels que l'arginine (entre 0 et 82,5 mM) et le glutamate (entre 0 et 21,22 mM) ; ou encore (iii) de peptides, seuls ou en combinaison, à des concentrations initiales comprises entre 0 et 50 mM. Les courbes de croissance des différentes souches dans chaque condition sont suivies en temps réel grâce au lecteur de plaque Synergy™ H4 (Biotek™), dans lequel les plaques multipuits sont incubées à 37°C sous agitation (100 rpm). Toutes les 10 minutes, la DO_{600nm} de chaque puits est enregistrée. Le lendemain, la plaque est récupérée et les bactéries en suspension sont retirées puis marquées spécifiquement afin d'être observées au microscope d'épifluorescence (méthode décrite ultérieurement). Le fond des puits est lavé trois fois au PBS (Phosphate Buffered Saline) pour enlever le maximum de bactéries planctoniques restées en suspension, puis incubé dans 150 µL de PrestoBlue® (ThermoFischer scientific) pendant 30 min à température ambiante. La

fluorescence du PrestoBlue[®], un marqueur de viabilité cellulaire quantifiant les biofilms adhérents, est mesurée à une longueur d'onde d'émission (λ_{em}) de 590 nm après excitation à 560 nm (λ_{ex}). Ils sont ensuite marqués une seconde fois spécifiquement, cette fois ci pour une observation par microscopie d'épifluorescence (Figure 38. A).

C. Etude des effets environnementaux ou de l'ajout d'acides aminés sur les communautés flottantes et biofilms adhérents de *P. stuartii* déjà développées

L'effet des facteurs environnementaux et des acides aminés est également étudié sur les bactéries de *P. stuartii* déjà socialisées en communautés flottantes et en biofilms adhérents, telles qu'en fin de phase stationnaire. A dessein, une colonie est mise en culture dans 5 mL de LB standard à 37°C pendant 1 h. Celle-ci est ensuite distribuée dans une plaque multipuits (150 μ L/puits) et incubée dans un lecteur de plaque SynergyTM H4 à 37°C sous agitation (100 rpm). Pendant 24 h, la DO_{600nm} est mesurée toutes les 10 min, et le lendemain les bactéries en suspension dans les puits sont centrifugées et le culot est resuspendu dans 450 μ L de solution à 1X d'urée (entre 0 et 1M), d'ammonium (entre 0 et 1M), de bicarbonate (entre 0 et 100 mM), de créatinine (entre 0 et 100 mM), d'arginine (entre 0 et 82,5 mM) ou de glutamate (entre 0 et 21,22 mM), pendant 1 h. Les bactéries adhérentes au fond des puits sont lavées trois fois au PBS avant d'être exposées aux mêmes conditions par l'ajout de 150 μ L par puits de milieu plus ou moins modifié, et d'être incubées pendant la même durée de temps. Comme dans la section précédente, les biofilms adhérents vivants sont quantifiés par l'utilisation du PrestoBlue[®] (Figure 38. B).

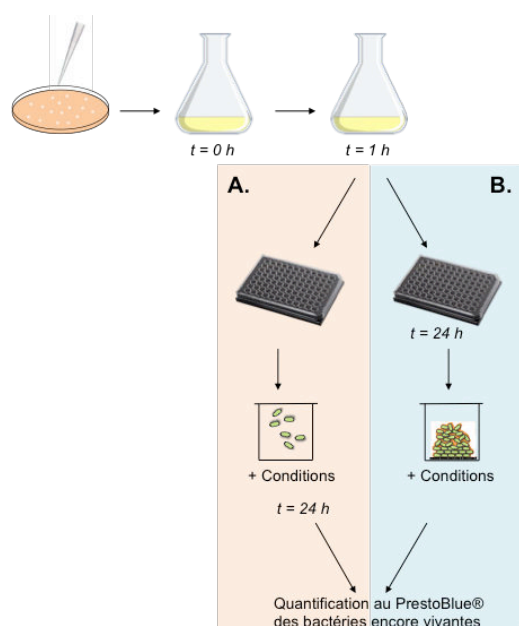


Figure 38. Protocoles d'étude des communautés flottantes et biofilms adhérents en conditions de stress environnementaux. (A) Les différentes conditions sont appliquées directement sur les bactéries encore isolées au début de leur croissance et les courbes de croissance sont suivies pendant 24 h dans un lecteur de plaque. (B) Une fois les communautés flottantes et les biofilms adhérents établis par *P. stuartii* (24 h plus tard), les facteurs de stress sont ajoutés sur les bactéries. Dans les deux cas, les bactéries adhérentes et vivantes au fond des puits sont quantifiées par l'utilisation du PrestoBlue[®].

4- Imagerie des bactéries

A. Microscopie d'épifluorescence

Pour observer les bactéries flottantes et adhérentes, les cellules sont marquées spécifiquement, soit au niveau de leur ADN grâce à 5 μM de Syto[®] 9 Green, soit au niveau de leurs membranes grâce à 20 μM de FM 1-43X (ThermoFischer scientific). La combinaison de Hoechst 33258 (5 $\mu\text{g}/\text{mL}$ - Sigma) et de propidium iodide (20 μM - Sigma) pour marquer l'ADN permet de distinguer les cellules vivantes des mortes ; le premier les marque toutes tandis que le second ne marque que les mortes. Après une incubation de 30 min dans le noir à température ambiante, 7 μL des bactéries flottantes marquées sont étalées sur des lames GelZan, préparées selon le protocole décrit par De Jong et al. en 2011³⁰⁹. En bref, 8 g/L de GelZan[™] sont dissous dans du milieu LB et 300 μL de ce mélange sont déposés sur une lame de verre. Afin d'avoir une observation plus claire et plus facile au microscope, une épaisseur minimale de milieu GelZan est requise, ce qui est assurée par l'utilisation d'un cadre déposé sur la lamelle (Figure 39). La lame est conservée 45 min à 4°C pour que le LB-GelZan polymérise, puis 45 min à température ambiante pour éviter tout choc thermique aux cellules. Les bactéries sont ensuite déposées sur ce milieu LB-GelZan solidifié, puis sandwichées grâce à une lamelle en verre avant d'être imagées avec l'objectif 100X du microscope d'épifluorescence IX81 inversé d'Olympus, de la plateforme « M4D » de l'IBS. Les bactéries adhérentes marquées sont imagées directement au fond des puits, préalablement lavés au PBS, avec l'objectif 20X.

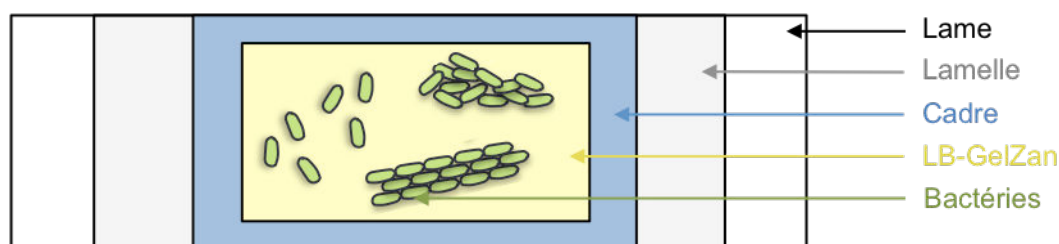


Figure 39. Illustration d'une lame GelZan. Sur une lame en verre (noir), un cadre adhésif (bleu) est collé et 300 μL de LB-GelZan (jaune) sont disposés. Une lamelle en verre (gris) est posée par dessus et le système est conservé à 4°C pendant 45 min puis à température ambiante pour 45 min supplémentaires. La lamelle est ensuite ôtée et les bactéries marquées (vert) sont déposées sur le LB-GelZan polymérisé et à bonne température. Une nouvelle lamelle est déposée par dessus pour fermer le système.

B. Microscopie électronique

En vue d'imager les communautés flottantes de *P. stuartii* à plus haute résolution, nous avons eu recours à la microscopie électronique à transmission. Le microscope Tecnai 12 LaB6 120 kV de la plateforme « EM » de l'IBS, équipé d'une caméra CCD Gatan Orius 1000, fût utilisé à dessein en collaboration avec Daphna Fenel et Dr. Guy Schohen.

Pour pallier à l'absence de contraste des échantillons biologiques, nous avons eu recours à la coloration négative. En effet, du fait de leur faible teneur en atomes lourds, les échantillons biologiques ont un pouvoir diffusant très limité. La coloration négative consiste en une incubation de l'échantillon dans une solution d'atomes lourds, qui vont plus ou moins spécifiquement marquer les protéines/ADN/ARN, suivie de plusieurs lavages pour retirer les atomes lourds non fixés. Nous pouvons alors observer une empreinte de l'échantillon naturel par microscopie électronique à température ambiante avec une résolution maximale d'environ $18 - 20 \text{ \AA}^{310}$. En pratique, une colonie est inoculée dans 5 mL de milieu LB standard pendant 1 h à 37°C sous agitation (150 rpm), puis distribuée dans une plaque multi-puits (150 μL /puits) sur la nuit. Le lendemain, les 150 μL de bactéries sont fixées pendant 2 h avec un mélange de 2% de para-formaldéhyde (PFA) et 0,2% de glutaraldéhyde dilué dans du tampon cacodylate (0,1 M à pH 7,2). Dix microlitres des bactéries fixées sont déposées sur une grille de microscopie électronique en cuivre recouverte d'un film carbone, puis laissées à sédimenter pendant 30 min ou 2 h. La grille est ensuite lavée trois fois, soit au PBS, soit à l'eau distillé avant d'être colorée avec 30 μL d'acétate d'uranyle (AcUr), de sodium silico tungstate (SST) ou d'acide phosphotungstique (PTA). L'excès de solution est absorbé par un papier filtre et la grille est séchée à l'air avant d'être imagée en microscopie électronique (Figure 40).

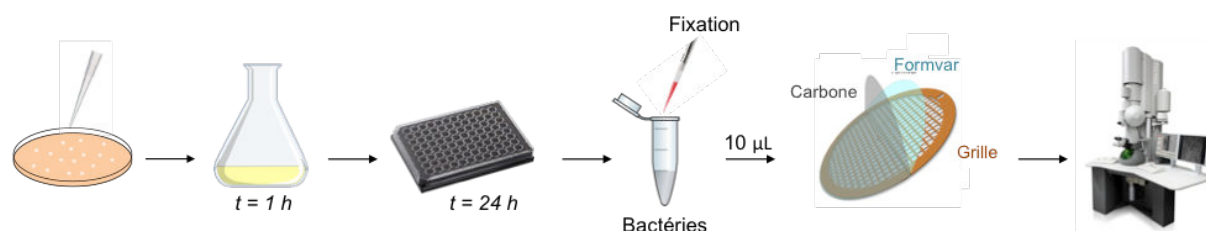


Figure 40. Illustration du protocole de préparation d'échantillon bactérien par coloration négative sur une grille de microscopie électronique. Une colonie est inoculée dans du milieu LB pendant 1 h avant d'être distribuée dans une plaque multi-puits. Les bactéries sont fixées puis déposées sur une grille de microscopie électronique où elles seront colorées pour être imagées au microscope électronique.

5- Etudes *in vivo* des porines de *P. stuartii*

A. Etude des effets environnementaux sur les porines

Une colonie de *P. stuartii* ou de *P. stuartii* Δ Omp-Pst2 est inoculée dans 5 mL de LB tamponné à un pH spécifique (entre 5 et 9) ou à pH 7 mais en présence d'urée (de 150 à 1000 mM), d'ammonium (de 150 à 1000 mM), ou de bicarbonate (de 10 à 100 mM). Les cultures, en triplicats, sont incubées à 37°C sur la nuit sous 150 rpm d'agitation. Le lendemain, 20 μ L de bactéries en suspension dans chaque condition sont centrifugées 30 sec à 11 000 g, afin de les culoter sans endommagements. Les culots sont resuspendus dans 20 μ L d'un mélange H₂O/DDT/bleu de dénaturation (bromophénol/ β -mercaptoéthanol/SDS/Glycérol concentré au 4X), incubés 5 min à 95°C puis chargés dans les puits d'un gel SDS-PAGE (sodium dodecyl sulfate polyacrylamide gel electrophoresis) à 12% de polyacrylamide recouvert du tampon d'électrophorèse (50 mM Tris-HCl pH 8,5 ; 200 mM glycine ; 0,1% SDS). Les bandes protéiques sont révélées par coloration à l'Instant Blue[®] (Sigma) après leurs migrations sous l'application d'un courant de 140 V pendant environ 1 h 30.

B. Observation des porines

Nous avons tenté d'observer les DOTs de porines directement sur gel SDS-PAGE en utilisant la méthode du « cross-link » (ou de réticulation). Pour ce faire, deux agents réticulant ont été utilisés, le DTSSP (3,3'-dithiobis(sulfosuccinimidylpropionate)) et le DMP (dimethyl pimelimidate) (ThermoFischer scientific). Les protéines ont généralement plusieurs amines primaires dans la chaîne latérale des résidus de lysine ; celle-ci et l'extrémité N-terminale de chaque polypeptide sont des cibles possibles pour les réactifs de réticulation sulfo-NHS-ester, tel que le DTSSP. Le DMP est quant à lui un agent de réticulation perméable à la membrane qui contient un groupe imidoester. Ce groupe fonctionnel est l'un des groupes d'acylation les plus spécifiques disponibles pour la modification des amines primaires. Il est important de noter qu'il ne modifie en aucun cas la charge globale de la protéine, conservant ainsi la conformation et l'activité native de la protéine.

En pratique, une colonie de *P. stuartii*, *E. coli* BL21 Δ Omp8-pGOmp-pst1 ou *E. coli* BL21 Δ Omp8-pGOmp-pst2 est inoculée dans 25 mL de milieu LB à 37°C sous agitation sur la nuit. Le lendemain, la culture est centrifugée à 4 500 g pendant 30 min et le culot est resuspendu pendant 30 min supplémentaires dans du tampon phosphate (20 mM à pH 7,4)

complété en MgSO_4 (1 mM), d'un quart de pastille anti-protéase, de quelques grains de DNaseI et, soit du DMP, soit du DTSSP (5 mM). Le processus de réticulation est arrêté après différents temps par l'ajout de 1 M de tampon Tris à pH 7, puis les cellules sont cassées au microfluidizer à 14 000 Psi (6x) et centrifugées à 18 000 g à 4°C pendant 45 min. Le surnageant contenant la fraction cytoplasmique est enlevé avant de resuspendre le culot dans 20 mL de tampon phosphate additionné d'OPOE à 0,3% pendant 2 h sous agitation à température ambiante, afin de solubiliser les membranes internes. Après une ultra-centrifugation à 35 000 g pendant 45 min à 4°C, les protéines de membrane interne ainsi solubilisées se retrouvent dans le surnageant qui est sacrifié et le culot correspondant aux membranes externes est suspendu dans 20 mL de tampon phosphate avec 3% d'OPOE sur la nuit à 4°C, avec à dessein de désormais solubiliser les membranes externes. Après une nouvelle ultra-centrifugation à 35 000 g pendant 45 min à 4°C, les protéines de membrane externe ainsi solubilisées se retrouvent à leur tour dans le surnageant, duquel trois aliquots de 15 μL sont prélevés auxquels 5 μL de bleu de dénaturation (4X) sont ajoutés. Dix des 20 μL totaux sont dénaturés à 95°C pendant 5 min. Les fractions dénaturées et non dénaturées sont déposées sur deux gels SDS-PAGE à 12% et un troisième à 6% de polyacrylamide, recouvert de tampon d'électrophorèse. Après une migration d'une heure sous 180 V, les bandes protéiques sont révélées soit par coloration basique à l'Instant Blue[®], soit par coloration au nitrate d'argent.

Pour la coloration au nitrate d'argent, nous suivons les instructions du kit Silver Stain Plus (BioRad). Il s'agit d'une excellente technique de détection de protéines séparées par électrophorèse sur gel SDS-PAGE, en raison de son efficacité à détecter jusqu'à quelques dixième de nanogrammes, typiquement entre 0,2 et 0,6 ng par bande, c'est à dire 100 fois plus sensible qu'une coloration à l'Instant Blue[®]. Les protéines d'intérêt sont détectées grâce à la réduction sélective des ions argent en argent métallique insoluble à des sites spécifiques, à proximité des molécules de protéine³¹¹. Le processus de coloration consiste successivement en la fixation de protéines, la sensibilisation, le lavage, l'imprégnation à l'argent et enfin le développement de l'image. En fonction de la quantité d'argent incorporée dans les bandes de protéines, une couleur de gel différente est produite.

6- Biochimie des protéines membranaires

A. Purification des protéines membranaires

Au cours de cette thèse, nous avons besoin de protéines pures pour vérifier différentes hypothèses sur la fonction et la structure des porines de *P. stuartii*. La purification de ces protéines se réalise en quatre étapes :

- i) l'expression protéique dans les bactéries,
- ii) l'extraction des membranes,
- iii) la purification sur colonne échangeuse d'anions avec délipidation et échange de détergent, et
- iv) la purification sur chromatographie d'exclusion stérique.

Les tampons nécessaires pour ces différentes étapes sont répertoriés dans le tableau suivant :

	Tampons		
Extraction membranaire	(1) - 20 mM de tampon phosphate à pH 7,4 - Pastille anti-protéase cOmplete™ (Roche) - DNase (quelques milligrammes -Sigma)	(2) - 20 mM de tampon phosphate à pH 7,4 - 0,3% du détergent OPOE (n-Octyl-polyoxyéthylène)	(3) - 20 mM de tampon phosphate à pH 7,4 - 3% du détergent OPOE
	Purification	(4) - 0,1 M MES à pH 6,5 - 25 mM NaCl - 0,12% LDAO (N,N-dimethyldodecylamine N-oxide)	(5) - 0,1 M MES à pH 6,5 - 25 mM NaCl - 2% LDAO

a. Expression et extraction

Les plasmides pGomp-pst1 ou pGomp-pst2 sont transformés dans les bactéries BL21ΔOmp8 par choc thermique. Les bactéries transformées sont étalées sur des boîtes LB-agar supplémentés en ampicilline et en kanamycine à des concentrations finales de 100 et 25 μL/mL, respectivement. Une colonie transformée est inoculée dans 25 mL de LB, contenant les mêmes concentrations des deux antibiotiques, puis incubée à 37°C sous agitation à 150 rpm sur la nuit. Le lendemain, 1 L de LB estensemencé à partir de la pré-culture. Etant donné que les plasmides d'intérêt pET utilisés confèrent aux bactéries BL21ΔOmp8 la capacité de les exprimer par elles-mêmes, l'expression des porines n'est pas induite ici. Une induction engendrerait en effet une surexpression nocive pour la bactérie, présumément du fait d'un mauvais repliement de nos protéines qui résulte en leur adressage dans des corps d'inclusion.

Une fois la DO_{600nm} proche de 1.5, la culture est interrompue et les bactéries sont culotées à 4 500 rpm pendant 30 min à 4°C. Le culot bactérien est resuspendu dans 20 mL de tampon (1) (Voir tableau ci-dessus). Les cellules sont ensuite lysées par plusieurs passages (entre 6 et 8) au microfluidizer à 14 000 Psi. Une nouvelle centrifugation de 45 min à 18 000 rpm à 4°C est réalisée pour séparer les protéines cytoplasmiques solubles (surnageant) des membranes internes et externes (culot). Les membranes sont resuspendues dans 20 mL de tampon contenant 0,3% OPOE (2) pendant 2 h à température ambiante. Cette concentration en OPOE permet de solubiliser les membranes internes qui se retrouveront dans le surnageant à la suite d'une centrifugation à 35 000 rpm pendant 45 min à 4°C. Le culot résultant, constitué uniquement des membranes externes, est alors soumis à 3 cycles successifs de solubilisation dans 20 mL de tampon contenant 3% OPOE (3) pendant 2 h à température ambiante, suivi d'une centrifugation de 35 000 rpm pendant 45 min à 4°C. A cette concentration d'OPOE, les protéines de la membrane externe se retrouvent progressivement solubilisées dans le surnageant. La qualité d'extraction des porines est contrôlée en réalisant un gel SDS-PAGE. Brièvement, 2 μ L du mélange bleu de dénaturation (4X) sont ajoutés à 10 μ L de la solution protéique et incubés 5 min à 95°C pour dénaturer les protéines. L'échantillon est chargé sur un gel SDS-PAGE à 12% de polyacrylamide, lui-même submergé dans un tampon d'électrophorèse, puis un courant de 180 V est appliqué pendant environ 1h. Après migration, les bandes sont révélées par coloration à l'Instant Blue® (Figure 43).

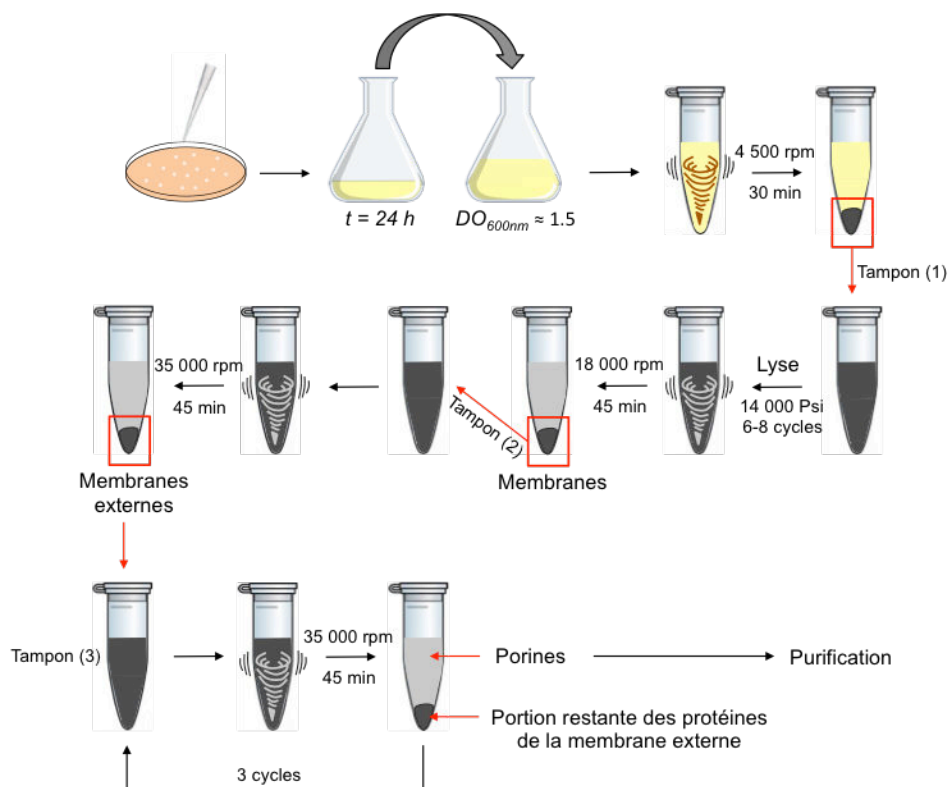


Figure 41. Représentation schématique illustrant le protocole d'expression et d'extraction de protéines membranaires. Une colonie est inoculée dans du milieu LB pendant une nuit. La pré-culture est transférée dans une culture de 1 L où les bactéries se multiplient jusqu'à une DO_{600nm} d'environ 1,5. Les cellules centrifugées sont lysées puis à nouveau centrifugées. Le culot est resuspendu avec 0,3% OPOE, solubilisant les protéines des membranes internes. Après centrifugation, le culot est resuspendu avec 3% OPOE pour solubiliser les protéines des membranes externes, récupérées par une nouvelle centrifugation. Après 3 cycles successifs de cette dernière étape, les porines sont solubilisées en présence de détergent dans le surnageant.

b. Purification des porines de *P. stuartii* par chromatographie échangeuse d'ion et d'exclusion stérique

Le surnageant contenant les porines solubilisées est chargé sur une colonne échangeuse d'anions HiTrap HQ de 5 mL (GE healthcare), préalablement équilibrée avec 3 volumes de tampon d'équilibration contenant 3% OPOE (3). Une fois les protéines fixées, l'OPOE est échangé contre un autre détergent, le LDAO, par lavage de la colonne avec un tampon de substitution (4). Cette étape est cruciale pour une cristallisation efficace des porines. Afin d'améliorer l'homogénéité de la préparation protéique, il est nécessaire d'éliminer les lipides attachés aux porines. Pour ce faire, une étape de délipidation est réalisée en passant le tampon (5) riche en détergent pendant 4 h à un débit faible de 0,2 mL/min. Pour finir, la colonne est équilibrée avec le tampon de substitution (4) et la porine est éluée grâce à un gradient de NaCl (aux alentours de 350 mM). La qualité de l'élution est vérifiée sur gel SDS-PAGE et les fractions contenant la porine d'intérêt sont concentrées grâce à un concentrateur Amicon Ultra 100 kDa (Merck Millipore). La concentration protéique finale est ajustée à 7 mg/mL avec une concentration finale en NaCl de 150 mM.

Une dernière étape de purification par chromatographie d'exclusion stérique est réalisée. La protéine concentrée est injectée sur une colonne Superdex 200 10/300 GL (GE healthcare) puis éluée avec du tampon (6). Après élution, la pureté des fractions est évaluée sur gel SDS-PAGE, et celles contenant la porine pure sont poolées puis concentrées jusqu'à 7 mg/mL. La porine purifiée est stockée à 4°C jusqu'à son utilisation en DLS et en cristallogénèse.

B. Etude *in vitro* des capacités d'auto-association des porines de *P. stuartii* par DLS

Pour étudier la capacité d'auto-association de nos porines une fois purifiées, il est essentiel qu'elles soient dans un environnement mimant celui d'une membrane biologique. Ainsi, nos porines ont été insérées dans des liposomes d'une seule bicouche lipidiques, les LUVs, avant d'être étudiées.

a. La formation des liposomes

Les LUVs sont préparés selon la méthode d'hydratation des films lipidiques de la manière suivante. Un mélange lipidique composé de 10 mg de EggPC (L- α -phosphatidylcholine) et de 0,1 mg de Rhod PE (1,2-dioleoyl-sn-glycero-3-phosphoethanolamine-N-(lissamine rhodamine B sulfonyle)) (Avanti Polar Lipids) est soumis à un flux d'azote gazeux afin d'évaporer le maximum de chloroforme. Le film lipidique obtenu est gardé sous-vide pendant la nuit avant d'être réhydraté le lendemain avec 2 mL de tampon phosphate (20 mM, à un pH spécifique entre 5 et 9) supplémenté de 150 mM de NaCl. A ce stade, des MLVs de tailles hétérogènes sont obtenus. Des LUVs sont ensuite formés par dix cycles successifs de congélation/décongélation dans de l'azote liquide puis dans un bain-marie à 40°C, respectivement. Ces derniers sont dilués dans le même tampon phosphate pour obtenir une concentration finale de 1,25 mg/mL, et des aliquots de 500 μ L sont conservés à -80°C. Une dernière étape de calibration de la taille des liposomes est réalisée en extrudant 30 fois un aliquot de la solution stock à travers une membrane de polycarbonate et de deux filtres de 100 nm dans un mini-extruder (Avanti Polar Lipids) (Figure 44). Les LUVs obtenus sont stables pendant environ une semaine à 4°C.

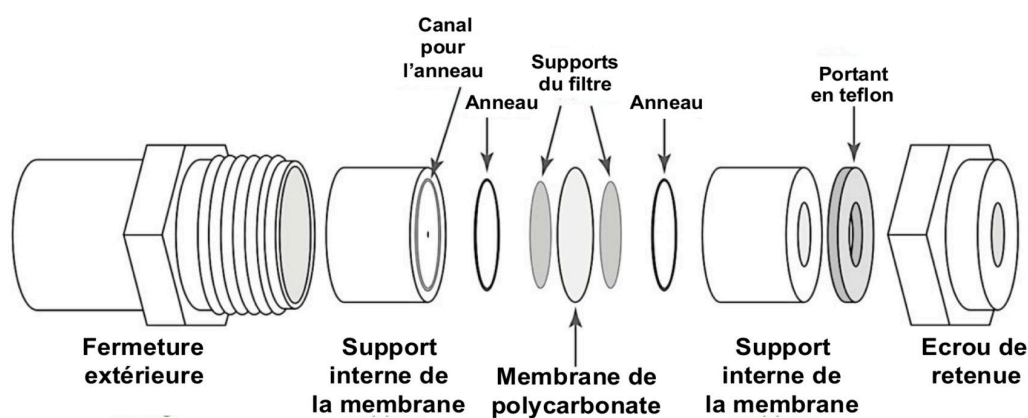


Figure 42. Présentation schématique du mini-extruder et de ses composants. La figure est adaptée du site d'Avanti Polar Lipids.

b. La DLS

La technique de la diffusion dynamique de lumière (DLS), implantée sur la plateforme « PAOL » de l'IBS, est utilisée pour :

- i) vérifier la taille des LUVs préalablement préparés ;

- ii) étudier l'effet des conditions environnementales rencontrées dans le tractus urinaire, telles que l'urée, l'ammonium, le bicarbonate, la créatinine et une variation de pH, sur les propriétés d'auto-association des porines;
- iii) analyser les conséquences sur les propriétés d'auto-association des porines de la présence de peptides synthétisés et d'acides aminés polaires.

Pour mesurer la taille des LUVs, 50 μ L de la solution sont placés dans une cuvette et l'analyse spectroscopique indique un rayon hydrodynamique (Rh). Après avoir vérifié la taille des liposomes, d'environ 80 nm, les porines sont ajoutées pour former des protéoliposomes en solution. Si le Rh est supérieur à 500 nm, il est jugé que les LUVs agrègent.

Pour étudier les effets environnementaux sur la capacité d'auto-association des porines, 30 μ L de LUVs sont mélangés à 10 μ L de protéines à différentes concentrations finales (de 0,27 à 1,07 μ M), puis 10 μ L de la solution à 5X d'urée (entre 0 et 1M), d'ammonium (entre 0 et 1M), de bicarbonate (entre 0 et 100 mM) ou de créatinine (entre 0 et 100 mM) sont additionnés. L'étude du pH est réalisée avec des liposomes préalablement préparés au pH souhaité. Pour chaque stress environnemental, le détergent présent dans le mélange porines/LUVs/condition est absorbé par des biobeads sur la nuit et le Rh est mesuré le lendemain. Dans ces conditions, 50% de porines sont reconstitués de façon productive c'est à dire avec leurs boucles extracellulaires présentées à l'extérieur du liposome, permettant la formation de DOTs entre deux porines.

Pour analyser l'impact d'acides aminés et de peptides sur les DOTs de porines, le même principe que précédemment est effectué. Brièvement, un mélange de 30 μ L de LUVs, 10 μ L de porines aux différentes concentrations et 10 μ L de la solution à 5X de peptides (entre 0 et 50 mM), d'arginine (entre 0 et 82,5 mM) ou de glutamate (entre 0 et 21,22 mM) est soumis aux biobeads et le Rh est mesuré après 24 h.

c. Visualisation des protéoliposomes

Nous avons la possibilité d'observer au microscope d'épifluorescence les protéoliposomes soumis aux différentes conditions grâce à la présence de lipides fluorescents Rhod PE dans la composition des liposomes. Pour ce faire, 7 μ L des échantillons mesurés par DLS sont sandwichés entre une lame et une lamelle en verre, puis imagés au microscope IX81 inversé d'Olympus à l'aide de l'objectif 100X. Pour obtenir des images de meilleure résolution, nous avons également eu recours à la microscopie électronique. Dix microlitres des échantillons de

DLS sont déposés sur une grille de microscopie électronique puis incubés pendant 3 min. Celle-ci est colorée avec 50 μ L d'AcUr ou de PTA pendant 2 min et l'excès de solution est absorbé par un papier filtre. La grille est ensuite séchée à l'air puis observée sur le microscope Tecnai 12 LaB6.

C. Cristallographie aux rayons X

Nous avons eu recours à la cristallisation aux rayons X pour caractériser la structure de nos porines et de certains de nos peptides. La structure de la porine Omp-Pst2 ainsi que celle du peptide RQNNIKT ont été résolues. Nous décrivons ci dessous les différentes étapes ayant permis l'obtention de ces structures.

a. La cristallisation

La diffusion de vapeur, en goutte suspendue et en goutte assise, a été la méthode utilisée pour la cristallisation d'Omp-Pst2 et du peptide RQNNIKT, respectivement. Dans les deux cas, un criblage au robot sur la plateforme de cristallisation à haut débit du laboratoire HTX (ESRF) a été réalisé. Les conditions permettant l'obtention de cristaux ont ensuite été optimisées par criblage manuel en variant principalement les concentrations en sel et en agent précipitant. Les cristaux d'Omp-Pst2 apparaissent sous 21 jours à 4°C dans les conditions suivantes : 28% PEG 400, 0,2 M MgCl₂ et 0,1 M HEPES à pH 7,5. Ceux du peptide RQNNIKT poussent en une journée à 20°C en présence de 55% PEG 200, 0,2 M NaCl et 0,1 M Na₃PO₄. Les cristaux obtenus sont ensuite pêchés, cryoprotégés et collectés sous flux d'azote gazeux au synchrotron (ESRF).

b. La collecte et le traitement de données

Les données cristallographiques collectées sur les cristaux d'Omp-Pst2 et du peptide RQNNIKT ont été mesurées sur les lignes de lumière ID30a1 et ID29, respectivement.

La ligne ID30a1 a une énergie non modulable (12,65 keV) et délivre un faisceau maximum de 100 x 65 μ m². Elle permet de travailler sur des cristaux de 10 à 100 μ m grâce à des ouvertures de dimensions variables, et est équipée d'un détecteur Pilatus3 2M offrant une caractérisation et une collecte de données entièrement automatisées. Un seul cristal d'Omp-

Pst2 a diffracté jusqu'à 3,2 Å et les données de diffraction ont été collectées avec une oscillation de 1° par image (180).

La ligne ID29 a une énergie modulable (6-20 keV) et délivre un faisceau maximum de 40 x 30 µm². Elle permet également de travailler sur des cristaux entre 10 et 100 µm grâce aux ouvertures, et est équipée d'un détecteur Pilatus 6M fournissant une écriture très rapide des clichés de diffraction. Les cristaux peptidiques sont montés délicatement sur un micro capillaire en verre avant d'être soumis à un flux d'azote gazeux. Les cristaux ont diffractés à une résolution comprise entre 1,3 et 2,5 Å et 40 images ont été collectées avec une oscillation de 5° par image.

Les données collectées pour Omp-Pst2 et le peptide RQNNIKT sont indexées puis intégrées grâce au logiciel XDS, et mises à l'échelle par XSCALE³¹². Les facteurs de structures sont ensuite générés par XDSCONV et les données sous format « .mtz » sont obtenues. La première structure d'Omp-Pst2, résolue avant mon arrivée au laboratoire, et une chaîne de 7 acides aminés alanines ont servi de modèles de départ pour phaser la nouvelle structure d'Omp-Pst2 et celle de RQNNIKT, respectivement, par remplacement moléculaire via PHASER³¹³. A l'aide du logiciel COOT, la porine et le peptide sont reconstruits puis affinés dans l'espace réel afin d'obtenir des structures interprétables et de bonne qualité pour les résolutions considérées³¹⁴. L'affinement de ces structures dans l'espace réciproque est réalisé par les programmes REFMAC³¹⁵ et PHENIX³¹⁶.

V – Résultats

Article n°1 – *Providencia stuartii* form biofilms and floating communities of cells that display high resistance to environmental insults

Résumé

Les biofilms sont des communautés microbiennes enrobées d'une matrice extracellulaire et adhérentes à une surface, qui sont impliqués dans la majorité des infections chroniques. *Providencia stuartii* est une bactérie pathogène Gram-négatif responsable de fréquentes infections urinaires chroniques nosocomiales dû à sa forte capacité à former des biofilms. Dans ce premier article, nous avons étudié la capacité des bactéries de *P. stuartii* à croître et à se socialiser dans les conditions pathophysiologiques du tractus urinaire – son site d'infection le plus courant chez l'Homme. Dans un premier temps, nous avons mis en avant la capacité de *P. stuartii* à se socialiser en communautés flottantes avant de sédimenter à une surface et adopter un phénotype de biofilms adhérents. Dans un second temps, notre étude a démontré que la socialisation en biofilms adhérents assurait aux bactéries de *P. stuartii* une résistance élevée aux diverses conditions hostiles des voies urinaires, telles que l'urée, le calcium, le magnésium et une variation soudaine de pH. Etant donné que les porines constituent la porte d'entrée principale de petits solutés hydrophiles à travers la membrane externe des bactéries Gram-négatif, nous nous sommes intéressés aux potentiels rôles des porines de *P. stuartii* dans cette forte résistance. Nos résultats ont suggéré qu'Omp-Pst2, une des deux porines de *P. stuartii*, joue un rôle important dans les premières phases de croissance et est impliquée dans la résistance aux fortes concentrations d'urée et à une large variation de pH.

***Providencia stuartii* form biofilms and floating communities of cells that display high resistance to environmental insults.**

Authors: Mariam El Khatib¹, Que-Tien Tran², Chady Nasrallah^{1,#a}, Julie Lopes¹, Jean-Michel Bolla³, Michel Vivaudou¹, Jean-Marie Pagès³, Jacques-Philippe Colletier^{1*}

Affiliations:

¹ Institut de Biologie Structurale, Université Grenoble Alpes – Commissariat à l'Énergie Atomique – Centre National de la Recherche Scientifique, Grenoble, France

² School of Biophysics, Jacobs University of Bremen, Bremen, Germany

³ Équipe Transporteurs Membranaires, Chimiorésistance et Drug-Design, Université Aix-Marseille – Institut de Recherche Biomédicale des Armées, Marseille, France

^{#a} Present address: Department of Neuroscience, Institut de Génomique Fonctionnelle, Montpellier, France

* Corresponding author:

Email: colletier@ibs.fr

Abstract

Biofilms are organized communities of bacterial cells that are responsible for the majority of human chronic bacterial infections. *Providencia stuartii* is a Gram-negative biofilm-forming bacterium involved in high incidence of urinary tract infections in catheterized patients. Yet, the structuration of these biofilms, and their resistance to environmental insults remain poorly understood. Here, we report on planktonic cell growth and biofilm formation by *P. stuartii*, in conditions that mimic its most common pathophysiological habitat in humans, *i.e.* the urinary tract. We observed that, in the planktonic state, *P. stuartii* forms floating communities of cells, prior to attachment to a surface and subsequent adoption of the biofilm phenotype. *P. stuartii* planktonic and biofilm cells are remarkably resistant to calcium, magnesium and to high concentrations of urea, and show the ability to grow over a wide range of pHs. Experiments conducted on a *P. stuartii* strain knocked-out for the Omp-Pst2 porin sheds light on the role it plays in the early stages of growth, as well as in the adaptation to high concentration of urea and to varying pH.

Introduction

Bacteria are known to live as organized community of cells termed biofilms. In humans, these supra-cellular structures are responsible for the majority of chronic bacterial infections^{1,2}. Prominent examples of biofilm-related infections include catheter-associated infections, the leading cause of secondary nosocomial bacteremia (20%)³, and cystic fibrosis⁴, a genetic disorder that favours the colonisation of aerial tissues by *P. aeruginosa*. The chronic nature of biofilm-related infections originates from their increased resistance to the immune system and antibiotherapy. The current model for biofilm formation includes five different stages⁵, viz. i/ the initial attachment of cells on a biotic or abiotic surface; ii/ the formation of a monolayer of cells; iii/ the migration of cells into a multi-layered colony; iv/ the synthesis of an extracellular matrix around the cells; and v/ the maturation of the biofilm into a characteristic 3D ensemble, composed of cells flapping in a self-produced polymeric matrix⁵. A sixth stage would be the release and dispersion of biofilm cells to colonize other niches. Depending on species, the biofilm polymeric matrix may be composed of extracellular polysaccharides¹, amyloid fibers⁶ and DNA⁷. The versatile and adaptable nature of the matrix allows bacteria to attach on, and thus colonize, a range of disparate (biotic or abiotic) surfaces. It also affects antibiotic efficiency through a variety of mechanisms, including reduced diffusion of drugs within the biofilm, masking or alteration of drug targets by the biofilm environment, or the adoption by some cells of a dormant – and therefore less drug-susceptible – phenotype^{8,9}.

Providencia stuartii is an opportunistic biofilm-forming pathogen from the *Enterobacteriaceae* family¹⁰ that is ubiquitous in the environment¹¹. A recent study reported an incidence rate of 4 per 100,000 hospital admissions, suggesting a low rate of prevalence in the general population¹¹. *P. stuartii* is yet responsible for ≈ 9% of urinary tract infections, in patients undergoing long-term catheterization¹¹⁻¹⁵. These patients are often nursing home (NH) or intensive care unit (ICU) residents; hence this contingent is bound to increase with aging of the population. The in-hospital mortality rate of *P. stuartii* infections is around 30%¹¹, in part

due to its high intrinsic multidrug resistance (MDR) phenotype conferred by the presence of an inducible chromosomal AmpC¹⁶. This MDR phenotype can be further exaggerated in clinical isolates, a majority of which were shown to feature plasmid-encoded extended-spectrum β -lactamases (ESBLs)¹⁷. More recently, clinical isolates presenting carbapenemase activities were isolated in Afghanistan¹⁸ and Portugal¹⁹. *P. stuartii* is adept at biofilm dispersion, explaining that infections sometimes migrate from the urinary tract to other organs, causing endocarditis²⁰, pericarditis²¹, peritonitis²² or meningitis²³. These facts, together with the now established ability of *P. stuartii* to disseminate amidst patients in hospital settings^{24,25}, explain the growing concern among health professionals¹¹. As yet, however, studies remain scarce on *P. stuartii* and on the nature and resistance of its biofilms to environmental cues²⁶⁻²⁸. More investigations are needed to characterize how *P. stuartii* biofilms form, and what their specifics are in terms of extracellular matrix composition, cell sub-types and behaviour, and mechanisms of adherence-to and detachment-from surfaces or other cells. Such information is crucial to eventually prevent or manage chronic infections by *P. stuartii*, and the high toll they take on NH and ICU residents^{11,29}.

In urine, the metabolite urea is found at a concentration of 150 mM, at which it displays a strong anti-microbial effect. Thus, bacteria that colonize the urinary tract must find means to evade this stress. One of these is to feature (or acquire) a urease activity, that will hydrolyze urea into two ammoniums and an carbonate³⁰. Calcium and magnesium are generally found at normal serum concentration (2 and 2.5 mM) but may reach higher concentrations in pathological conditions, e.g. in patients presenting bladder stones whose formation correlates with a 2-fold increase in the calcium-concentration/osmolarity ratio of urine^{31,32}. The pH of urine is usually acidic but may vary from 6 to 8 depending on diet or pre-conditions. For example, infection by *P. mirabilis* is known to raise urine pH above 8, due to its strong urease activity that degrades urea into carbon monoxide and ammonia²⁹. Some clinical isolates of *P. stuartii* feature a plasmid-encoded urease activity, but this activity is generally too weak to induce alkalinisation of urine³³. Therefore alternative mechanisms,

which allow *P. stuartii* cells to evade detrimental effects of urea, must exist. One of these is co-infection with species that have a strong urease activity such as *P. mirabilis*, whose presence was shown to increase *P. stuartii* colonization and bacteremia incidence³⁴. Another efficient mechanism could be the limited diffusion of urea across the extracellular matrix of *P. stuartii* biofilms, which would result in reducing the effective concentration of urea in cells, thence preserving these. Access to the periplasm is mainly controlled by general-diffusion porins, which are water-filled channels sprinkling the outer-membrane thence allowing passive diffusion of nutrients and ions into the periplasm. Porins are the most abundantly expressed outer-membrane (OM) proteins (up to 100,000 copies/cell), with a single porin often accounting for up to 70% of the OM proteinaceous content³⁵. Current interest in porins mostly stems from their involvement in antibiotic uptake³⁶ and in the emergence of antibiotic resistance³⁷. But as the first door opened toward the exterior, they also play a number of additional roles in bacterial survival, homeostasis and pathogenesis, adhesion to surfaces and host cells³⁸, and sometimes penetration into these³⁹. Porins are therefore good candidates for playing a role in limiting excessive urea accumulation in the periplasm.

The genome of *P. stuartii* features two porins, Omp-Pst1 and Omp-Pst2⁴⁰. When grown in rich medium (*per se*, Luria-Bertani or LB), *P. stuartii* predominantly expresses Omp-Pst1, and it was proposed that Omp-Pst1 is the major porin of the bacterium⁴⁰. Electrophysiology measurements revealed that Omp-Pst2 is highly cation-selective and prone to voltage-gating (critical voltage $V_c = 20-90$ mV), whereas Omp-Pst1 channel gates normally ($V_c > 199$ mV), is mildly anion selective and comparatively more permissive to β -lactam antibiotics^{40,41}. MD simulations suggested that Omp-Pst2 atypical voltage-gating behaviour is asymmetric and triggered by the influx of cations from the extracellular to the periplasmic side of the porin. Efflux of cations, on the other hand, would be facilitated, suggesting a potential role for this porin in the regulation of charge distribution across the OM⁴².

Here, we report on *P. stuartii* growth and biofilm formation under environmental conditions that mimic its most common habitat in humans, *i.e.* the urinary tract. We used the methodology of Mishra *et al.*⁴³ to characterize the effect of pH, urea, calcium and magnesium on biofilm genesis, attachment and consolidation. We found that *P. stuartii* growth is independent on pH in the viability range (pH 6 to 9), yet biofilm genesis and attachment onto the surface are favoured at pH \geq 8. We observed that *P. stuartii* biofilms survive in high concentrations of urea (up to 500 mM), calcium and magnesium (up to 50 mM), and that these environmental stresses trigger the consolidation of *P. stuartii* biofilms. Magnesium and calcium both inhibit the attachment of new cells onto surfaces in a dose-dependent manner, but magnesium activates biofilm genesis. Epifluorescence micrographs were taken at various stages of growth, of cells both in the planktonic (floating cells) and in the biofilm state (adherent cells). Most unexpectedly, we observed that planktonic *P. stuartii* cells exhibit a highly social behaviour, whereby cell-to-cell contact occurs prior to attachment of cells onto the surface, resulting in floating communities of cells that precede – and later coexist – with surface-attached biofilms. This observation suggested cell-to-cell contact as the primary mechanism by which *P. stuartii* cells form a community, and prompted us to examine whether or not porins – as the main proteinaceous component of the outer membrane – are involved. A knock-out strain for Omp-Pst2, *P. stuartii* $\Delta P2$, was obtained (*P. stuartii* ATCC 29914 $\Delta ompPst2::Cm$) that formed more biofilms (+70%) but displayed retarded growth, higher sensitivity to urea and cations, and a clear dependence of the lag-time on pH. Results suggest that Omp-Pst2 is an important actor in the early stages of *P. stuartii* growth and in adaptation to alkalinity.

Results

- *P. stuartii* form floating communities of cells prior to adherent biofilm

In order to characterize *P. stuartii* growth and its ability to form biofilms, we compared it to one of the most common *E. coli* strains used in laboratories, BL21 DE3. This *E. coli* strain is known not to form biofilms⁴⁶ and was therefore used as a negative control. When cultivated in LB medium, both *P. stuartii* and *E. coli* show a typical growth curve that can be divided into three phases: (1) a lag phase, (2) an exponential phase, and (3) a stationary phase (Figure 1A). *E. coli* and *P. stuartii* have similar lag phase duration and the same growth rate in the beginning of the exponential phase (Figure 1B). After five hours, however, *E. coli* cells decline whereas *P. stuartii* cells continue to exhibit a positive rate of growth.

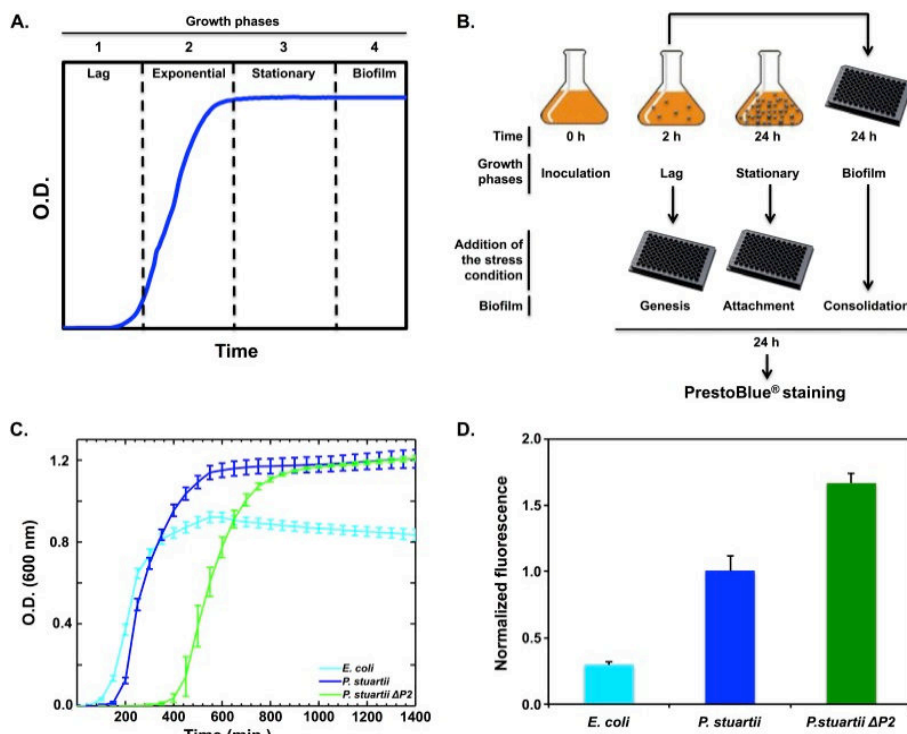


Figure 1. Planktonic bacterial growth and biofilm formation. (A) Bacterial growth can be divided into 4 main phases: (1) the lag phase, (2) the exponential phase, (3) the stationary phase and (4) the biofilm establishment phase. (B) Growth curves of *E. coli* BL21, *P. stuartii* and *P. stuartii* ΔP2. (C) Experimental protocol designed to challenge the effect of various environmental stresses on the different stages of biofilm formation (genesis, attachment, consolidation) by *P. stuartii*. (D) Biofilm quantification after 24h of growth in 96-well plates, as revealed by of adherent cells using PrestoBlue. Data are normalized with respect to measurements performed on *P. stuartii*.

Micrographic examination of attached *P. stuartii* cells reveals that no biofilm forms before the stationary phase (Figures 2A-C), in agreement with the idea that bacteria form biofilms when faced with an environmental stress. After five hours of growth, the well is covered with a large biofilm, presumably as a result of starvation (Figure 2D). Examination of planktonic cells at the exponential and stationary phases reveals that floating communities of cells form by cell-to-cell contact in solution (Figures 2E-G and S1 Movie), prior to the attachment of cells on the surface (Figures 2A-C) – that is, prior to the formation of canonical biofilms. After five hours of growth, these floating communities of cells are multi-layered and coexist with surface-attached biofilms (Figures 2D-H).

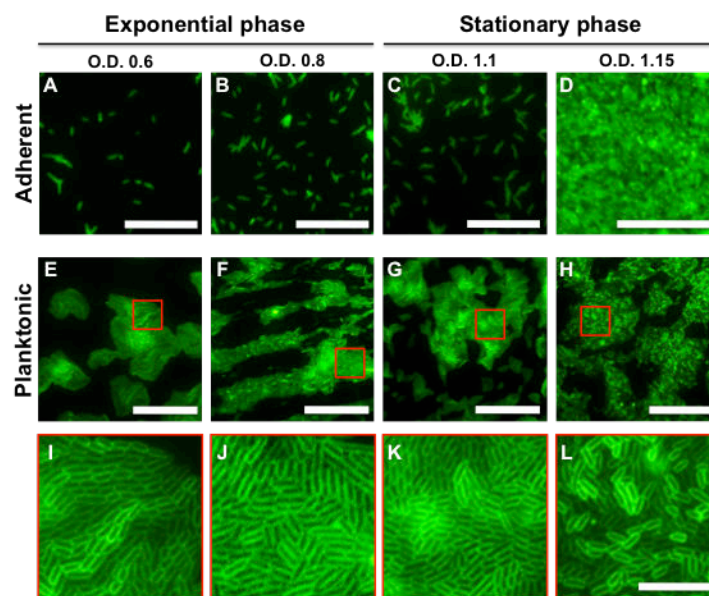


Figure 2. *P. stuartii* form floating communities of planktonic-cells prior to adherent biofilms. (A-D) Micrographs of bacteria that remain bound to the well surface, after discard of planktonic cells by PBS washes. (E-H) Micrographs of planktonic bacteria. Cells were pipetted from the LB medium, spread on LB-Gelzan and imaged immediately. (I-L) Close-up views of the red-delineated regions in panels E-H showing close contact between the membrane of adjacent cells. Bacterial membranes were stained using FM1-43X. Scale bars: 50 μ m (A-H) and 10 μ m (I-L)

The viable adherent biomass formed by *P. stuartii* was 3-fold greater than that formed by *E. coli* (Figure 1C), with virtually all cells being alive in *P. stuartii* biofilms (Figure 3A). In contrast, *E. coli* adherent biomass amounted to only few dispersed cells, roughly the half of which were dead (Figure 3A). Phenotypic differences between *P. stuartii* and *E. coli* cells were also clear at the planktonic level, where the dispersion of *E. coli* cells contrasted with the highly gregarious behaviour of *P. stuartii* floating communities (Figure 3B).

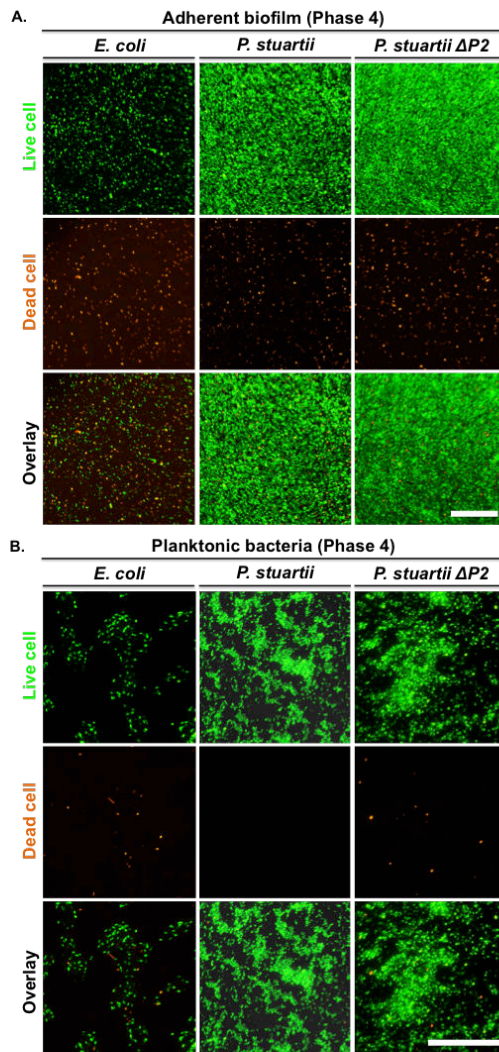


Figure 3. *P. stuartii* is adept at forming large biofilms mainly composed of living cells. (A) Micrographs of bacteria adherent to the wells surface after discard of planktonic cells by PBS washes. (B) Micrographs of planktonic bacteria. Cells were pipetted from the LB medium, spreaded on LB-Gelzan and imaged immediately. Live and dead cells were stained with SYTO9 Green and propidium iodide, respectively. Scale bars are 100 and 50 μm in panel (A) and (B), respectively.

We examined whether Omp-Pst2 could play a role in biofilm formation by repeating these experiments on the *P. stuartii* ATCC 29914 $\Delta\text{ompPst2}::\text{Cm}$ strain (*P. stuartii* $\Delta P2$). The growth rate of *P. stuartii* $\Delta P2$ in the exponential and stationary phases was identical to that of the wild-type strain, showing a rapid adaptation to Omp-Pst2 depletion (Figure 1B). However, cells devoid of Omp-Pst2 displayed retarded growth (+ 60% increase in lag time; Figure 1B) and a 70% increase in biofilm formation (Figure 1C). *P. stuartii* $\Delta P2$ biofilms were comparatively denser, but the lack of Omp-Pst2 did not perturb the microscopic appearance of *P. stuartii* cells – in either planktonic (Figure 3A) or biofilm (Figure 3B) states. Increased biofilm formation by *P. stuartii* $\Delta P2$ could underlie a pathway undertaken by this K.O. strain to overcome the stress induced by the lack of Omp-Pst2 in the early stages of growth.

- *P. stuartii* is resistant to urea and forms biofilm over a large range of pH

Inasmuch as urea is the principal component of urine, we set to determine the effect of this metabolite on *P. stuartii* planktonic cell growth as well as on biofilm genesis, attachment and consolidation. We used to this end the methodology recently introduced by Mishra *et al.*⁴³. Briefly, cells were submitted to increasing urea concentration at various phases of their growth (lag, stationary and biofilm phases), grown overnight (ON) under this environmental pressure, and the viable biofilm mass was then quantified using Presto Blue (Figure 1D). We found that *P. stuartii* planktonic cells sustain normal growth up to 500 mM urea but display an 85% decrease in growth at 1 M urea (Figure 4A). Exposure of cells to urea in the lag and stationary phases reveals that biofilm genesis and attachment to surfaces are unaffected by concentrations of urea up to 200 and 500 mM, respectively (Figure 4B and Supplementary S1). Exposure to urea furthermore consolidates pre-formed *P. stuartii* biofilms, in the viability range (0-500 mM) (Figure 4B and Supplementary S2). Clearly, ATCC 29914 is a urease-positive *P. stuartii* strain, sustaining urea concentrations \geq 4-fold higher than that encountered in its human habitat (150 mM). The urease activity of *P. stuartii* is cytoplasmic and produces 2 ammoniums and 1 carbonate per hydrolysed molecule of urea³⁰.

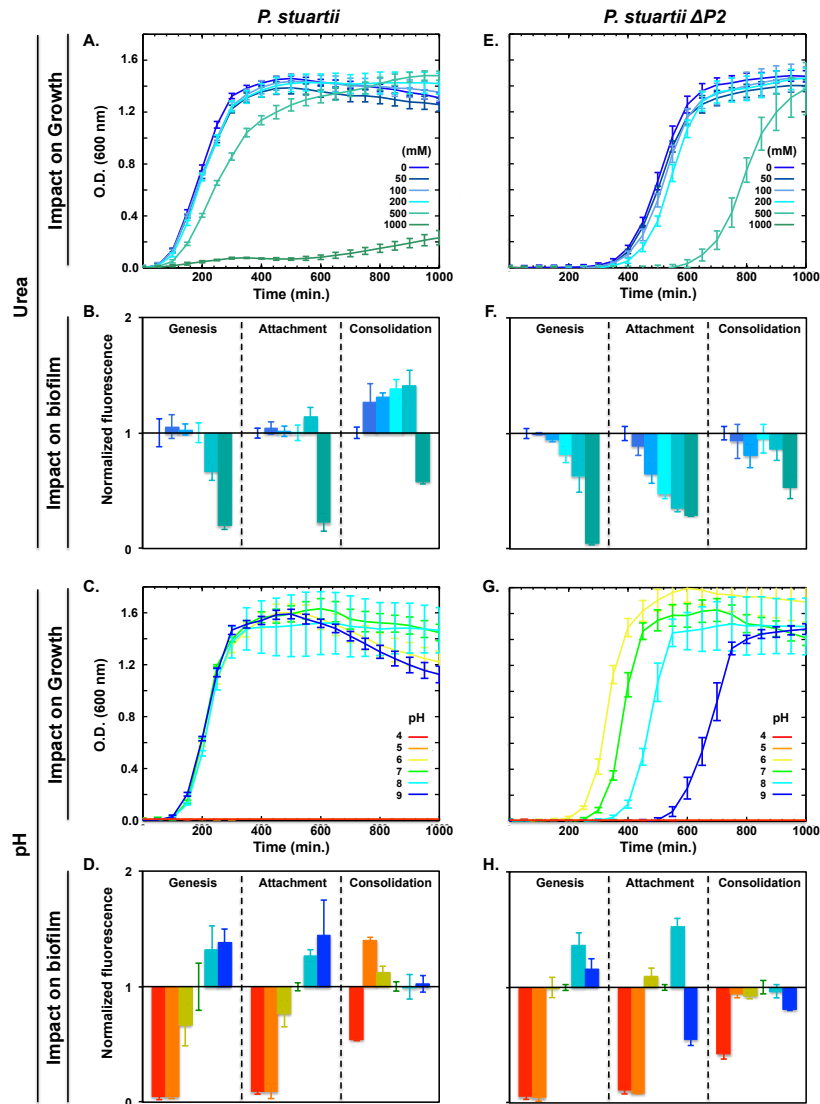


Figure 4. Resistance of *P. stuartii* and *P. stuartii* $\Delta P2$ cells to high concentrations of urea and to pH variations. Effect of urea (A and E) and pH (C and G) on bacterial growth, as judged from the O.D. of cultures at 600 nm. The impact on biofilm genesis, attachment and consolidation was evaluated by adding urea (B and F) or changing the pH (D and H) during the lag, stationary and preformed biofilm phases, respectively. Biofilm formation was quantified 24 h later, by PrestoBlue staining. Fluorescence values were normalized with respect to the control wells containing no urea and buffered at pH7.

We then investigated how *P. stuartii* responds to changes in pH. Using the approach summarized above – and further detailed in the Methods section – we found that *P. stuartii* is unable to grow at pH 4 and 5, but viable between pH 6 and 9 (Figure 4C). Within this range, neither planktonic cells (Figure 4C) nor cells from preformed biofilms are affected by pH variations, although alkalinity favours biofilm genesis and attachment of cells onto the surface (Figure 4D and Supplementary S1). While partially destroyed at pH 4, preformed *P. stuartii* biofilms consolidate at pH 5 (Figure 4D and Supplementary S2) underlining their resistance to extreme environmental conditions.

- Omp-Pst2 is involved in urea uptake and in the regulation of pH in the periplasm.

We examined the impact of urea on planktonic growth and biofilm formation by the Δ Omp-Pst2 strain of *P. stuartii*. *P. stuartii* Δ P2 showed normal growth in urea up to 200 mM, but an increased lag time at 500 mM. At 1 M, the strain could not grow, suggesting that Omp-Pst2 participates in alleviating urea toxicity in parental cells (Figure 4E). The fitness loss induced by lack of Omp-Pst2 was also visible at the biofilm level, with biofilm genesis, attachment and consolidation all being negatively impacted by urea in a dose-dependent manner (Figure 4F and Supplementary S1-S2).

We also investigated the sensitivity of *P. stuartii* Δ P2 to variations in pH. At the planktonic level, we observed a clear dependency on pH of the lag time of *P. stuartii* Δ P2 growth. The K.O. strain remains unable to grow at pH 4 and 5, but displays a faster and more productive planktonic growth at pH 6 than at pH 9 (Figure 4G). In strong contrast, the growth of the parental strain is equally favoured from pH 6 to 9 (Figure 4C). At the biofilm level, *P. stuartii* Δ P2 cells show reduced biofilm genesis and attachment to the surface at pH 9, resulting in a shift of the optimal pH for biofilm formation from pH 9 to 8 (Figure 4H and Supplementary S1). Absence of Omp-Pst2 also lowers biofilm consolidation at pH5, as compared to the parental strain (Figures 4D, H and Supplementary S2). Altogether, these results indicate a role for Omp-Pst2 in the regulation of periplasmic pH.

- *P. stuartii* biofilms benefit from the presence of Ca^{2+} and Mg^{2+}

Calcium and magnesium are the most abundant divalent-cations in the urine. Therefore, their effect on the growth and fitness of *P. stuartii* cells was investigated, at the planktonic and biofilm levels. Upon addition of 50 mM of calcium and magnesium into the growth medium, *P. stuartii* growth level increased by 17 and 25% respectively (Figures 5A, C). Addition of calcium had an inhibitory effect on biofilm genesis as well and on cell attachment onto the surface, but triggered the consolidation of preformed-biofilms (Figure 5B) and a drastic

reorganisation of their supracellular structure. Micrographs indeed reveal that *P. stuartii* biofilms change shape, forming compact assemblies of tightly aggregated cells (Supplementary S2), upon exposure to high calcium concentration. Magnesium also inhibited cell attachment to surfaces, but was beneficial to biofilm genesis and consolidation (Figure 5D) and did not affect the shape of pre-formed biofilms, even at the highest concentrations tested.

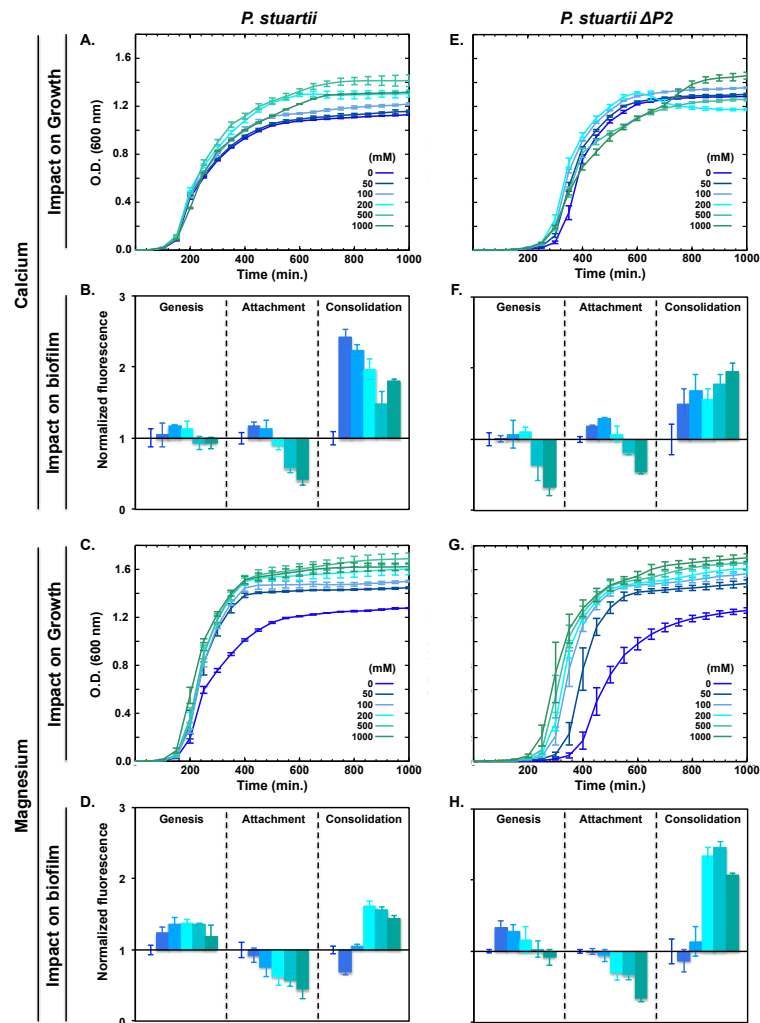


Figure 5. Resistance of *P. stuartii* and *P. stuartii* $\Delta P2$ cells to high concentrations of calcium and magnesium. Effect of calcium (A and E) and magnesium (C and G) on bacterial growth, as judged from the O.D. of cultures at 600 nm. The impact on biofilm genesis, attachment and consolidation was evaluated by adding calcium (B and F) or magnesium (D and H) during the lag, stationary and preformed biofilm phases, respectively. Biofilm formation was quantified 24 h later, by PrestoBlue staining. Fluorescence values were normalized with respect to the control wells buffered at pH7 and devoid of calcium and magnesium.

Deletion of *Omp-Pst2* reproduced or enhanced the impact of the two divalent cations on *P. stuartii* $\Delta P2$ cells, planktonic and biofilm alike. The beneficial effect of calcium on planktonic growth was preserved, and likewise for its inhibitory effect on biofilm genesis and cell

attachment onto the surface (Figures 5B, F). Pre-formed biofilms of *P. stuartii* $\Delta P2$ also displayed more sensitivity to high calcium concentrations, as exposed by the observation of more compact cell-assemblies characterized by a higher mortality level (Supplementary S2), in epifluorescence micrographs. The beneficial effect of magnesium on planktonic growth was also preserved in *P. stuartii* $\Delta P2$ cells, while that on biofilm consolidation was further potentiated (Figure 5H).

Discussion

P. stuartii is a biofilm-forming pathogen (Figure 1B), mainly involved in urinary tract infections in elderly patients^{11,15}. It is occasionally implicated in others types of infections⁴⁷, including endocarditis²⁰, pericarditis²¹, peritonitis²² and meningitis²³. Notwithstanding that the prevalence of infections is increasing alarmingly, knowledge regarding the species and its biofilms remains scarce.

Here, we aimed at studying *P. stuartii* growth and biofilm formation in conditions that mimic its most common habitat in humans, *i.e.* the urinary tract. Our study demonstrated the ability of the microbe to form biofilms in a variety of insulting conditions. Furthermore, it shed light on the highly gregarious behaviour of *P. stuartii* planktonic cells, which associate from the early stages of growth through cell-to-cell contact, forming floating community of cells prior to formation of canonical – per say, adherent – biofilms (Figure 2 and Supplementary S1 Movie). Cell-to-cell contact in the planktonic state could provide a means to maximize cell density, inter-communication and resistance to environmental cues, before formation of the mature biofilm. We observed that the floating communities of cells could attach altogether to surfaces, allowing biofilms to start from a critical mass.

Planktonic and biofilm cells of *P. stuartii* adapt well to changes in pH, in the pH 6 to 9 range. Alkaline pH furthermore activates *P. stuartii* biofilm genesis and attachment to surfaces

(Figure 4A-D). This fitness suggests the existence of periplasmic pH regulators, which would support the swift adaptation of *P. stuartii* to pH variation. *P. stuartii* $\Delta P2$, plagued by delayed growth, displays a clear dependence of the lag time on pH, suggesting that Omp-Pst2 contributes to the ability of the parental strain to immediately grow regardless of pH (Figures 4C, G). Thus Omp-Pst2 could play a role in regulating/buffering periplasmic pH, thereby supporting the adaptation of wild-type *P. stuartii* to changes in environmental pH. In the absence of this presumed regulator, *P. stuartii* $\Delta P2$ cells would take longer to adapt to increasing pH, hence explaining their retarded growth (+300 min at pH 9, compared to pH 7, Figure 4G).

The urease activity of *P. stuartii* ATCC 29914 was uncovered by its ability to grow normally in mediums containing up to 500 mM urea. The species furthermore survives (15%) in 1 M urea (Figure 4A) demonstrating that it would be able to grow in the urinary tract. *P. stuartii* $\Delta P2$ is nevertheless more sensitive to urea, displaying an increased lag time at 500 mM urea (+ 250 min) and showing no growth at 1M urea (Figure 4E). Accordingly, biofilm genesis, attachment and consolidation by this strain are affected by urea in a dose-dependent manner (Figure 4F). This mechanism of toxicity is not detectable in the parental strain. It appears unlikely that Omp-Pst2 absence would effect in increasing urea concentration in the periplasm. Rather, Omp-Pst2 is involved in a process downstream of the penetration of urea into cells, such as efflux of urea or of its hydrolytic products. We see at least three possible explanations for the reduced resistance to urea of the *P. stuartii* $\Delta P2$ strain. (i) Omp-Pst2 could contribute to the efflux of urea from the periplasm, hence reducing the actual periplasmic (and thus cytoplasmic) concentration of urea. Given the large excess present in the surrounding growth medium, it nevertheless appears unlikely that this efflux activity would significantly affect the periplasmic concentration in urea. (ii) Omp-Pst2 could facilitate the influx of anions neutralizing the periplasmic ammonium generated by urea degradation – but again, given the strong cation-selectivity of Omp-Pst2, however, this hypothesis also appears unlikely. (iii) Omp-Pst2 could be involved in the direct efflux of periplasmic

ammonium and in limiting its re-penetration into the periplasm; this is the only hypothesis that fits the prior knowledge on Omp-Pst2. Indeed, MD simulations have suggested that Omp-Pst2 could be involved in the facilitated transport of cations from the periplasm to the extracellular side of the OM⁴². They furthermore highlighted that Omp-Pst2 channel would respond by gating to a massive transit of cations from the external medium to the periplasm⁴². Thus, we favour the hypothesis that Omp-Pst2 alleviates the toxic effects of urea on *P. stuartii* cells by mitigating the toxic accumulation of ammonium in their periplasm. Of note, rough calculations indicate that accumulation of 10 μ M ammonium would raise the periplasmic pH from 7 to 9. Thus, the delayed growth displayed by *P. stuartii* $\Delta P2$ cells in the presence of 500 mM urea could result from increased periplasmic pH, due to reduced efflux of ammonium. More generally, Omp-Pst2 could act on periplasmic pH by regulating the cationic content of the periplasm ; this hypothesis will have to be confirmed by electrophysiology.

Elevated calcium and magnesium consolidate preformed *P. stuartii* biofilms, activate planktonic cell growth (Figures 5A, C), and reduce cell attachment onto surfaces (Figures 5B, D). Calcium at 50 mM induces changes in the macroscopic appearance of biofilms, leading to their compaction (Supplementary S2), whereas magnesium slightly activates their genesis. These effects are further exaggerated in *P. stuartii* $\Delta P2$ (Figures 5F, H), again supporting that the absence of Omp-Pst2 could lead to accumulation of cations in the periplasm, aggravating the effect of these on cellular metabolism.

Altogether, our results suggest that *P. stuartii* exploits sociability as a means to foster cellular growth and resist to environmental stress, before formation of a canonical – per say, surface-attached – biofilm. Our work also points out that Omp-Pst2 plays a crucial role in the early stages of *P. stuartii* growth (Figure 1A). Data show that Omp-Pst2 is involved in pH regulation (Figure 4G) and could be in charge of ammonium clearance/neutralization from/in the periplasm, a hypothesis supported by electrophysiology data⁴⁰ and more recently molecular dynamics simulations on the porin⁴². Our data add to the growing body of evidence

that suggests an implication of OM components in biofilm formation and regulation^{48,49}. Further studies are needed to understand how *P. stuartii* cells are riveted to one another in floating communities of planktonic cells, and how this phenotype influences the ability of the species to form biofilms.

Materials and methods

Strains and materials

Escherichia coli BL21 DE3 strain was used as a negative control strain and the wild type *Providencia stuartii* ATCC 29914 strain was obtained from the Pasteur Institute (Paris, France). All fluorescent dyes were from Thermo Fischer Scientific. Unless specified otherwise, chemicals were from Sigma-Aldrich. Polystyrene-bottom 96-well plates were from Greiner.

Generation of the omp-pst2 knock out strain, P. stuartii ΔP2

The disruption of the *omp-Pst2* gene in *P. stuartii* ATCC 29914 was carried out by adapting the protocol described by Datsenko and Wanner⁴⁴, based on the use of phage lambda Red recombinase⁴⁴. The PCR primers were OmpPst2_XbaI 5'- GTG TCT AGA CAC TTA GTT AGT AAA TGG C -3' (forward) and OmpPst2_BamHI 5'- GTT GGA TCC GGA TAA TTG CGT ATG ATG G -3' (reverse). The *ompPst2* PCR amplicon was cloned into pGem-T-Easy vector and the construct was transferred by electroporation into *E. coli* DH5α for plasmid maintenance and amplification. The plasmid was digested with HindIII enzyme and the subsequent protruding ends were filled in by Klenow enzyme. The construct was then ligated to chloramphenicol-resistance (Cm) cassette making *omp-Pst2::Cm* knockout construct. pCAM-MSV suicide vector for *Enterobacteriaceae* was then used to bring the *omp-Pst2::Cm* into *E. coli* S17-1λpir. Biparental mating with *P. stuartii* was then carried out by homology conjugation. Selection of *P. stuartii* ATCC 29914 *omp-Pst2::Cm* mutants was performed in the presence of chloramphenicol at 33 μg/mL concentration. The resulting genetic

modification of *P. stuartii* ATCC 29914 *omp-Pst2::Cm* was finally confirmed by both colony PCR and sequencing, using primers flanking the *omp-Pst2* gene in the *P. stuartii* genome.

Bacterial growth studies

E. coli and *P. stuartii* bacteria were grown in Luria-Bertani (LB) growth medium without antibiotics. LB medium was supplemented with 33 µg/ml chloramphenicol for the growth of the *P. stuartii* $\Delta P2$ bacteria. Control experiments showed that chloramphenicol at this concentration has no effect on cell-growth and biofilm formation by *P. stuartii*- $\Delta P2$ (data not shown). For each experiment, a single bacterial colony was inoculated in standard LB or pH-specific LB medium for 2 h, yielding cells in their lag phase. These were then distributed into a 96-wells plates supplemented with 0 – 1 M urea, 0 – 50 mM Ca^{2+} or 0 – 50 mM Mg^{2+} , and incubated at 37°C and under 100 rpm agitation overnight, to form biofilms. Bacterial growth was monitored in terms of absorbance at 600 nm for 24 h (10 minutes interval between time points) using a Biotek Synergy H4 microplate reader (Winooski, VT, USA)

Environmental stresses impact on biofilm genesis and attachment onto surface

For each experiment, a single bacterial colony was used to inoculate 25 mL of standard LB medium (37°C). A large flask was used, that was maintained under constant shaking at 200 rpm on the rotatory platform, thence preventing bacterial attachment onto the surface and subsequent formation of adherent biofilms. After 2 hours, aliquots of this culture (cells in the lag phase) were transferred in a 96-well plate (see below), serving to study the effect of environmental stresses on biofilm genesis. After 24 h, another set of aliquots was transferred in the 96-well plate, with view to study the effect of environmental stresses on the attachment of cells onto the well surfaces (see below). Cells were confronted with environmental insults after transfer into the 96-well plate. Briefly, above-mentioned aliquots were distributed into wells containing 150 µL LB medium buffered at increasing pH (4 to 9) or supplemented with increasing concentrations of urea (0 – 1 M), Ca^{2+} or Mg^{2+} (0 – 0.05 M). Cells were then

incubated at 37°C under constant shaking at 100 rpm. Biofilms were revealed after 24-hours incubation in the 96-well plate.

Environmental stresses impact on established biofilms

For each experiment, a single bacterial colony was used to inoculate 25 mL of standard LB medium (37°C). A large flask was used, that was maintained under constant shaking at 200 rpm on the rotatory platform, thence preventing bacterial attachment onto the surface and subsequent formation of adherent biofilms. After 2 hours, aliquots of this culture (cells in the lag phase) were transferred in a 96-well plate and incubated for 24 hours at 37°C under constant shaking at 100 rpm, resulting in the formation of biofilms at the bottom of the wells. The medium was then removed to discard planktonic bacteria and replaced by fresh LB medium buffered at increasing pH (4 to 9) or supplemented with urea (0 – 1 M), Ca²⁺ or Mg²⁺ (0 – 0.05 M). The plate was then incubated at 37°C and 100 rpm overnight. Biofilms were revealed after an additional 24-hours incubation in this plate.

Imaging

Epifluorescence micrographs were taken on an IX81 Olympus inverted microscope; samples were magnified through 20 or 60X objectives (Plan APON60XO, Olympus). SYTO[®] 9 Green fluorescent nucleic acid stain and propidium iodide solution were used at 5 and 20 µM concentration to stain live and dead cells respectively. Bacterial membranes were stained by the fluorescent dye FM1-43FX at 5 µg/mL. Bacterial biofilms were grown in a 96-wells plates as described above. For the imaging of planktonic bacteria, 10 µL of the culture were spread on LB-Gelzan[™] cover slides prepared as previously described ⁴⁵ and imaged directly afterwards. For biofilm imaging, wells were washed twice with phosphate-buffered saline (PBS) to remove all planktonic bacteria; the remaining adherent bacteria forming the biofilm were then imaged.

Biofilm quantification

Well plates incubated overnight were washed extensively with PBS to remove all planktonic bacteria. Adherent biofilms were then stained with PrestoBlue[®] cell viability reagent. For each plate, fluorescence emission was measured at 590 nm, upon excitation at 560 nm. All experiments were performed at least in triplicate and biofilm formation was quantified with respect to *P. stuartii* cells grown in the absence of environmental stresses.

Acknowledgments

We are indebted to Martin Weik for continuous support and fruitful discussions. We are grateful to Jean-Philippe Kleman and Françoise Lacroix for their technical support and advices during epifluorescence microscopy experiments. We thank Alexandre Dos Santos Martins and Coline Burnet-Merlin for technical support. This work used the platforms of the Grenoble Instruct Center (ISBG: UMS 3518 CNRS-CEA-UGA-EMBL) within the Grenoble Partnership for Structural Biology (PSB).

References

1. Costerton, J. W., Stewart, P. S. & Greenberg, E. P. Bacterial biofilms: a common cause of persistent infections. *Science* **284**, 1318–1322 (1999).
2. Hall-Stoodley, L. & Stoodley, P. Evolving concepts in biofilm infections. *Cell. Microbiol.* **11**, 1034–1043 (2009).
3. Gould, C. V. *et al.* Guideline for prevention of catheter-associated urinary tract infections 2009. *Infect. Control Hosp. Epidemiol.* **31**, 319–326 (2010).
4. Chapman, C. M. C., Gibson, G. R. & Rowland, I. Effects of single- and multi-strain probiotics on biofilm formation and in vitro adhesion to bladder cells by urinary tract pathogens. *Anaerobe* **27**, 71–76 (2014).
5. Branda, S. S., Vik, S., Friedman, L. & Kolter, R. Biofilms: the matrix revisited. *Trends Microbiol.* **13**, 20–26 (2005).
6. Chapman, M. R. *et al.* Role of *Escherichia coli* curli operons in directing amyloid fiber formation. *Science* **295**, 851–855 (2002).
7. Whitchurch, C. B., Tolker-Nielsen, T., Ragas, P. C. & Mattick, J. S. Extracellular DNA required for bacterial biofilm formation. *Science* **295**, 1487–1487 (2002).
8. Stewart, P. S. & William Costerton, J. Antibiotic resistance of bacteria in biofilms. *The Lancet* **358**, 135–138 (2001).
9. Lebeaux, D., Ghigo, J.-M. & Beloin, C. Biofilm-related infections: bridging the gap between clinical management and fundamental aspects of recalcitrance toward antibiotics. *Microbiol. Mol. Biol. Rev. MMBR* **78**, 510–543 (2014).

10. Manos, J. & Belas, R. The Genera *Proteus*, *Providencia*, and *Morganella*. in *The Prokaryotes* (eds. Dworkin, M., Falkow, S., Rosenberg, E., Schleifer, K.-H. & Stackebrandt, E.) 245–269 (Springer New York, 2006).
11. Wie, S.-H. Clinical significance of *Providencia* bacteremia or bacteriuria. *Korean J. Intern. Med.* **30**, 167–169 (2015).
12. McHale, P. J., Walker, F., Scully, B., English, L. & Keane, C. T. *Providencia stuartii* infections: a review of 117 cases over an eight year period. *J. Hosp. Infect.* **2**, 155–165 (1981).
13. Warren, J. W. *Providencia stuartii*: A Common Cause of Antibiotic-Resistant Bacteriuria in Patients with Long-Term Indwelling Catheters. *Rev. Infect. Dis.* **8**, 61–67 (1986).
14. Stickler, D. J. Bacterial biofilms in patients with indwelling urinary catheters. *Nat. Clin. Pract. Urol.* **5**, 598–608 (2008).
15. De Vecchi, E. *et al.* Aetiology and antibiotic resistance patterns of urinary tract infections in the elderly: a 6-month study. *J. Med. Microbiol.* **62**, 859–863 (2013).
16. Aubert, D., Naas, T., Lartigue, M.-F. & Nordmann, P. Novel Genetic Structure Associated with an Extended-Spectrum β -Lactamase blaVEB Gene in a *Providencia stuartii* Clinical Isolate from Algeria. *Antimicrob. Agents Chemother.* **49**, 3590–3592 (2005).
17. Tumbarello, M. *et al.* ESBL-producing multidrug-resistant *Providencia stuartii* infections in a university hospital. *J. Antimicrob. Chemother.* **53**, 277–282 (2004).
18. Mc Gann, P. *et al.* Complete Sequence of a Novel 178-Kilobase Plasmid Carrying blaNDM-1 in a *Providencia stuartii* Strain Isolated in Afghanistan. *Antimicrob. Agents Chemother.* **56**, 1673–1679 (2012).
19. Manageiro, V. *et al.* Draft Genome Sequence of the First NDM-1-Producing *Providencia stuartii* Strain Isolated in Portugal. *Genome Announc.* **3**, (2015).
20. Krake, P. R. & Tandon, N. Infective endocarditis due to *Providencia stuartii*. *South. Med. J.* **97**, 1022–1023 (2004).
21. Simon, C. *et al.* Images in cardiovascular medicine. Bacterial pericarditis due to *Providencia stuartii*: an atypical case of relapsing pericarditis. *Circulation* **122**, e401-403 (2010).
22. Unverdi, S. *et al.* Peritonitis due to *Providencia stuartii*. *Perit. Dial. Int. J. Int. Soc. Perit. Dial.* **31**, 216–217 (2011).
23. Sipahi, O. R. *et al.* Meningitis due to *Providencia stuartii*. *J. Clin. Microbiol.* **48**, 4667–4668 (2010).

24. Bret, L. & Di Martino, P. Effect of Ceftazidime, Amikacin and Ciprofloxacin on Biofilm Formation by Some Enterobacterial Clinical Isolates. *Chemotherapy* **50**, 255–259 (2004).
25. Lahlaoui, H. *et al.* Nosocomial dissemination of extended-spectrum β -lactamase VEB-1a-producing *Providencia stuartii* isolates in a Tunisian hospital. *Eur. J. Clin. Microbiol. Infect. Dis.* **30**, 1267–1270 (2011).
26. Sturgill, G., Toutain, C. M., Komperda, J., O'Toole, G. A. & Rather, P. N. Role of CysE in Production of an Extracellular Signaling Molecule in *Providencia stuartii* and *Escherichia coli*: Loss of *cysE* Enhances Biofilm Formation in *Escherichia coli*. *J. Bacteriol.* **186**, 7610–7617 (2004).
27. Kateete, D. P. *et al.* Rhomboids of Mycobacteria: Characterization Using an *aarA* Mutant of *Providencia stuartii* and Gene Deletion in *Mycobacterium smegmatis*. *PLoS ONE* **7**, e45741 (2012).
28. Ostrowska, K., Kamysz, W., Dawgul, M. & Różalski, A. Synthetic amphibian peptides and short amino-acids derivatives against planktonic cells and mature biofilm of *Providencia stuartii* clinical strains. *Pol. J. Microbiol. Pol. Tow. Mikrobiol. Pol. Soc. Microbiol.* **63**, 423–431 (2014).
29. Stickler, D. J. Clinical complications of urinary catheters caused by crystalline biofilms: something needs to be done. *J. Intern. Med.* **276**, 120–129 (2014).
30. MOBLEY, H. L., CHIPPENDALE, G. R., TENNEY, J. H. & WARREN, J. W. Adherence to uroepithelial cells of *Providencia stuartii* isolated from the catheterized urinary tract. *Microbiology* **132**, 2863–2872 (1986).
31. Isaacson, L. C. Urinary composition in calcific nephrolithiasis. *Invest. Urol.* **6**, 356–363 (1969).
32. Raman, A. & Sreenevasan, G. A. Urinary Osmolarity and Excretion of Sodium, Calcium and Magnesium in Patients with Renal Calculi. *Br. J. Urol.* **44**, 537–540 (1972).
33. Broomfield, R. J., Morgan, S. D., Khan, A. & Stickler, D. J. Crystalline bacterial biofilm formation on urinary catheters by urease-producing urinary tract pathogens: a simple method of control. *J. Med. Microbiol.* **58**, 1367–1375 (2009).
34. Armbruster, C. E., Smith, S. N., Yep, A. & Mobley, H. L. T. Increased Incidence of Urolithiasis and Bacteremia During *Proteus mirabilis* and *Providencia stuartii* Coinfection Due to Synergistic Induction of Urease Activity. *J. Infect. Dis.* **209**, 1524–1532 (2014).
35. Zeth, K. & Thein, M. Porins in prokaryotes and eukaryotes: common themes and variations. *Biochem. J.* **431**, 13–22 (2010).

36. Pagès, J.-M., James, C. E. & Winterhalter, M. The porin and the permeating antibiotic: a selective diffusion barrier in Gram-negative bacteria. *Nat. Rev. Microbiol.* **6**, 893–903 (2008).
37. Delcour, A. H. Outer membrane permeability and antibiotic resistance. *Biochim. Biophys. Acta BBA - Proteins Proteomics* **1794**, 808–816 (2009).
38. Hemery, G., Chevalier, S., Bellon-Fontaine, M.-N., Haras, D. & Orange, N. Growth temperature and OprF porin affect cell surface physicochemical properties and adhesive capacities of *Pseudomonas fluorescens* MF37. *J. Ind. Microbiol. Biotechnol.* **34**, 49–54 (2006).
39. Galdiero, S. *et al.* Microbe-host interactions: structure and role of Gram-negative bacterial porins. *Curr. Protein Pept. Sci.* **13**, 843–854 (2012).
40. Tran, Q.-T. *et al.* Implication of Porins in β -Lactam Resistance of *Providencia stuartii*. *J. Biol. Chem.* **285**, 32273–32281 (2010).
41. Bajaj, H. *et al.* Antibiotic Uptake through Membrane Channels: Role of *Providencia stuartii* OmpPst1 Porin in Carbapenem Resistance. *Biochemistry (Mosc.)* **51**, 10244–10249 (2012).
42. Song, W. *et al.* Understanding Voltage Gating of *Providencia stuartii* Porins at Atomic Level. *PLOS Comput Biol* **11**, e1004255 (2015).
43. Mishra, B., Golla, R. M., Lau, K., Lushnikova, T. & Wang, G. Anti-Staphylococcal Biofilm Effects of Human Cathelicidin Peptides. *ACS Med. Chem. Lett.* (2015). doi:10.1021/acsmchemlett.5b00433
44. Datsenko, K. A. & Wanner, B. L. One-step inactivation of chromosomal genes in *Escherichia coli* K-12 using PCR products. *Proc. Natl. Acad. Sci.* **97**, 6640–6645 (2000).
45. de Jong, I. G., Beilharz, K., Kuipers, O. P. & Veening, J.-W. Live Cell Imaging of *Bacillus subtilis* and *Streptococcus pneumoniae* using Automated Time-lapse Microscopy. *J. Vis. Exp.* (2011). doi:10.3791/3145
46. Zalewska-Piatek, B. M., Wilkanowicz, S. I., Piatek, R. J. & Kur, J. W. Biofilm formation as a virulence determinant of uropathogenic *Escherichia coli* Dr+ strains. *Pol. J. Microbiol. Pol. Tow. Mikrobiol. Pol. Soc. Microbiol.* **58**, 223–229 (2009).
47. Frey, K. G. *et al.* Full-Genome Assembly of Reference Strain *Providencia stuartii* ATCC 33672. *Genome Announc.* **2**, e01082-14 (2014).

48. Gaddy, J. A., Tomaras, A. P. & Actis, L. A. The *Acinetobacter baumannii* 19606 OmpA Protein Plays a Role in Biofilm Formation on Abiotic Surfaces and in the Interaction of This Pathogen with Eukaryotic Cells. *Infect. Immun.* **77**, 3150–3160 (2009).
49. Phillips, N. J. *et al.* Proteomic Analysis of *Neisseria gonorrhoeae* Biofilms Shows Shift to Anaerobic Respiration and Changes in Nutrient Transport and Outermembrane Proteins. *PLOS ONE* **7**, e38303 (2012).

Supplementary Information

***Providencia stuartii* form biofilms and floating communities of cells that display high resistance to environmental insults.**

Authors: Mariam El Khatib¹, Que-Tien Tran², Chady Nasrallah^{1,#a}, Julie Lopes¹, Jean-Michel Bolla³, Michel Vivaudou¹, Jean-Marie Pagès³, Jacques-Philippe Colletier^{1*}

Affiliations:

¹ Institut de Biologie Structurale, Université Grenoble Alpes – Commissariat à l'Énergie Atomique – Centre National de la Recherche Scientifique, Grenoble, France

² School of Biophysics, Jacobs University of Bremen, Bremen, Germany

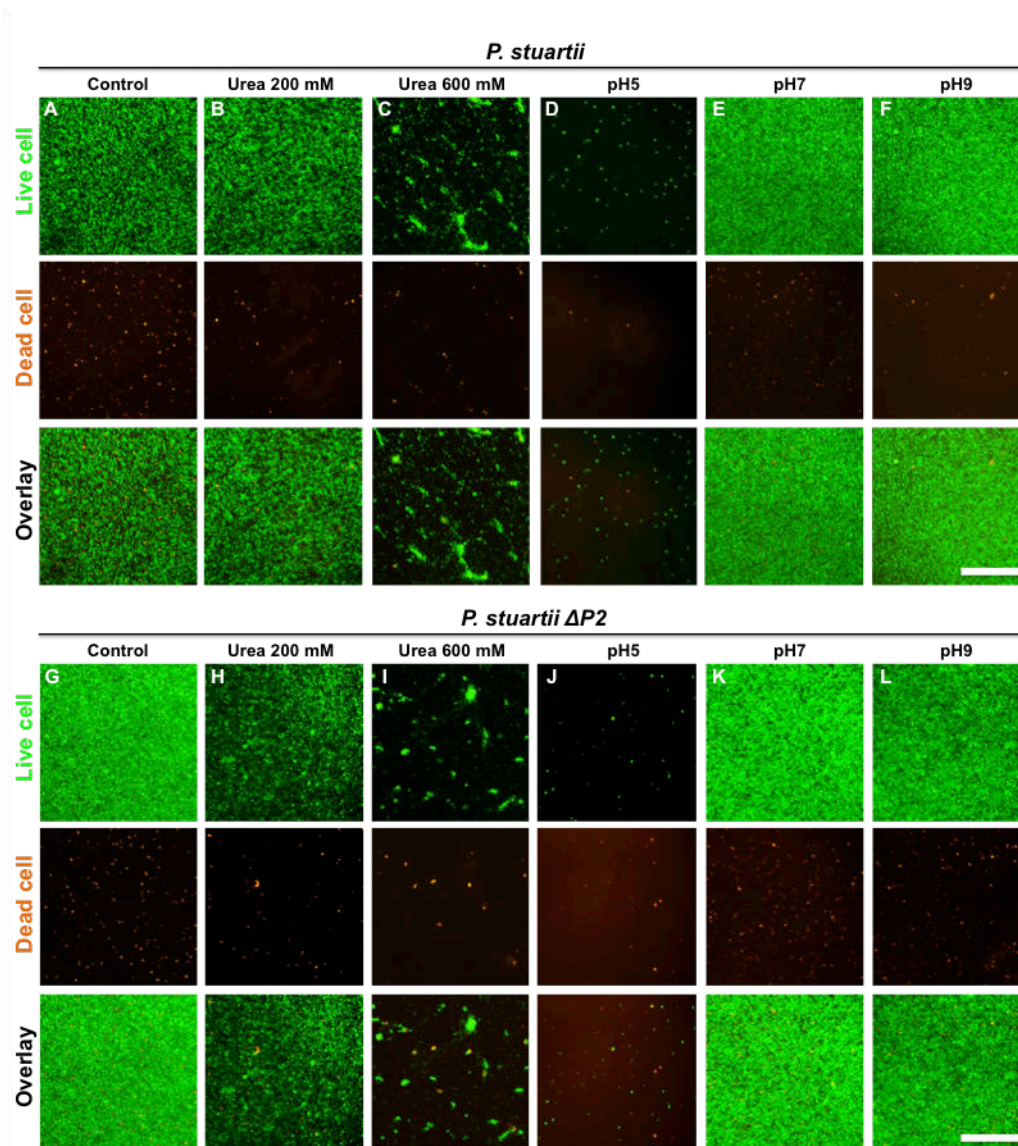
³ Équipe Transporteurs Membranaires, Chimiorésistance et Drug-Design, Université Aix-Marseille – Institut de Recherche Biomédicale des Armées, Marseille, France

^{#a} Present address: Department of Neuroscience, Institut de Génomique Fonctionnelle, Montpellier, France

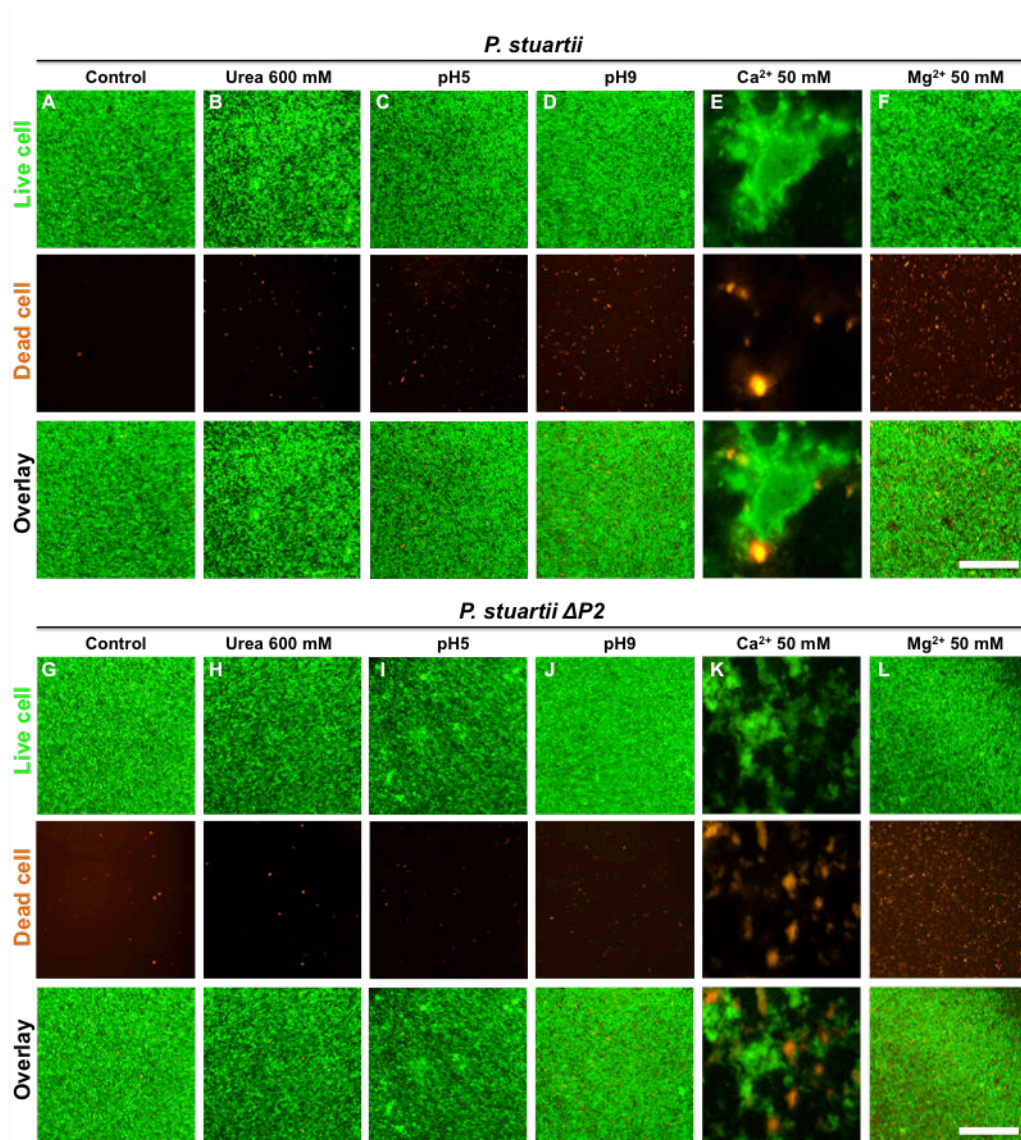
* Corresponding author:

Email: colletier@ibs.fr

S1 Movie. *P. stuartii* forms floating communities of cells. Bacteria were grown to an O.D. of 0.5 at 600 nm and imaged by conventional microscopy without washing. The movie shows a Z-scan acquisition of the whole well (bottom-to-top). Planktonic cells assemble into a floating community, wherein cells appear to be attached to one another and are presumably in close contact.



Supplementary S1. Impact of urea and pH impact on biofilm genesis. Effect of urea (B-C and H-I) and pH (D-F and J-L) on the genesis of *P. stuartii* (A-F) and *P. stuartii* $\Delta P2$ (G-L) biofilms. Cells were subjected to environmental stresses for 24 h and bacteria adherent to the well surface were imaged after discard of planktonic cells by PBS washes. Live and dead cells were stained with SYTO9 Green and propidium iodide, respectively. Scale bar : 100 μ m.



Supplementary S2. Impact of urea, pH and divalent cations on consolidation of pre-formed biofilms. Effect of urea (B, H), calcium (E, K), magnesium (F, L) and pH (C- D, I-J) on the consolidation of *P. stuartii* (A-F) and *P. stuartii* ΔP2 (G-L) biofilms. Cells were subjected to environmental stresses for 24 h and bacteria adherent to the well surface were imaged after discard of planktonic cells by PBS washes. Live and dead cells were stained with SYTO9 Green and propidium iodide, respectively. Scale bar : 100 μm.

Article n°2 – Porin self-association enables cell-to-cell contact in *Providencia stuartii* floating communities of cells

Article n°2 – Résumé

Le précédent article démontre l'importance des porines dans la résistance des bactéries de *P. stuartii* à diverses conditions hostiles du tractus urinaire. Dans ce deuxième article, nous cherchons à connaître le rôle exact de ces porines dans la physiologie de *P. stuartii*. Pour ce faire, nous avons résolu les structures atomiques des deux porines de *P. stuartii* et avons découvert qu'elles ont la capacité de s'auto-associer en face à face à travers leurs boucles extracellulaires formant un dimère de trimère (DOT). Par la suite, nous avons étudié les capacités d'auto-association des porines après reconstitution dans des bicouches lipidiques, ainsi que l'effet de leur expression ectopique dans des bactéries dépourvues de porines sur le phénotype. Nos résultats suggèrent un rôle des DOTs de porines dans le contact étroit entre bactéries adjacentes conduisant à la formation des communautés flottantes. De plus, nous avons déterminé la nature des interactions porine-porine à partir des données cristallographiques et par mutagenèse dirigée. Il s'avère que l'auto-association des porines est médiée par une attraction électrostatique ainsi que par des interactions de type « steric zipper » hautement spécifiques.

Porin self-association enables cell-to-cell contact in *Providencia stuartii* floating communities of cells.

Authors: Mariam El-Khatib^{a,1}, Chady Nasrallah^{a,1,2}, Julie Lopes^a, Que-Tien Tran^b, Guillaume Tetreau^a, Hind Basbous^a, Daphna Fenel^a, Benoit Gallet^a, Mathilde Lethier^a, Jean-Michel Bolla^c, Jean-Marie Pagès^c, Michel Vivaudou^{a,d}, Martin Weik^a, Mathias Winterhalter^b and Jacques-Philippe Colletier^{a,3}.

Affiliations:

^a Institut de Biologie Structurale (IBS), Univ. Grenoble Alpes, CNRS, CEA, IBS, 38000 Grenoble, France

^b Jacobs University, Life Sciences & Chemistry, 28759 Bremen, Germany

^c UMR_MD1, Aix-Marseille Univ, IRBA, Marseille, F-13385 Marseille, France

^d Laboratories of Excellence, Ion Channel Science and Therapeutics, Nice, France

¹ These authors contributed equally.

² Present address: *Institut de Génomique Fonctionnelle, UMR 5203, F-34094 Montpellier, France*

³ To whom correspondence should be addressed. Email: colletier@ibs.fr

Abstract

The Gram-negative pathogen *Providencia stuartii* forms floating communities within which adjacent cells are in apparent contact, prior to depositing as canonical surface-attached biofilms. Because porins are the most abundant proteins in the outer-membrane of Gram-negative bacteria, we hypothesized that they could be involved in cell-to-cell contact and undertook a structure-function relationship study on the two porins of *P. stuartii*, Omp-Pst1 and Omp-Pst2. Our crystal structures reveal that these porins can self-associate through their extracellular loops, forming dimer of trimers (DOTs) that could enable cell-to-cell contact within floating communities. Support for this hypothesis was obtained by studying the porin-dependent aggregation of liposomes and model cells. The observation that facing channels are open in the two porin structures suggest that DOTs could not only promote cell-to-cell contact, but also contribute to inter-cellular communication.

Keywords: biofilms, porins, steric zipper, intercellular communication, cell adhesion, bacterial socialization

Introduction

Providencia stuartii is an opportunistic pathogen from the *Enterobacteriaceae* family¹ that is involved in increasingly frequent infections in burn victims and patients undergoing long-term catheterization²⁻⁵. Treatment of infections by *P. stuartii* is complicated by its intrinsically strong resistance to a wide range of antibiotics^{4,6-8} and by its ability to form biofilms. The latter may attach and grow both on indwelling catheters^{3,9,10} and uroepithelial cells¹¹. Recently, we reported the microscopic characterization of *P. stuartii* plankton and biofilms, and the unexpected finding that this species forms floating communities of cells in solution, prior to its deposition as a surface-attached biofilm¹². Within floating communities, cells are in apparent contact and presumably stick to one another *via* protein-protein interactions¹². Inasmuch as the general diffusion porins are the most abundant proteins in the outer-membrane (OM) of Gram-negative bacteria, with a major porin often accounting for up to 70% of the OM protein content (up to 10^5 copies per cell)¹³, we set to verify whether *P. stuartii* porins could partake in the formation of floating communities.

Porins are water-filled channels spanning the OM of Gram-negative bacteria¹⁴ and they constitute the principal entry route for hydrophilic nutrients, ions and antibiotics into the periplasm. They are generally assembled as trimers, within which each monomer displays a conserved β -stranded architecture that delineates a hydrophilic channel. Substrate-specific porins are barrels of 18 β -strands, while porins governed by general diffusion (referred to as porins throughout the manuscript) feature 16 β -strands. In both cases, sifting properties are determined by the amino-acid distribution at their constriction zone, contributed by the folding of extracellular loop L3 into the channel lumen. The genome of *P. stuartii* encodes two porins, Omp-Pst1 and Omp-Pst2. Uptake of β -lactams (cephalosporins and carbapenems, in particular), quinolones and fluoroquinolones is mainly due to their passive diffusion through Omp-Pst1^{6,7}. Omp-Pst1 is essential to *P. stuartii* survival, while Omp-Pst2 promotes rapid growth, possibly through regulation of the cationic content of the periplasm¹².

To obtain insights into how Omp-Pst1 and Omp-Pst2 could be linked to the pathogenicity of *P. stuartii*, we first determined their three-dimensional structures. These reveal the molecular basis for the distinct ion selectivity of Omp-Pst1 and Omp-Pst2, while that of a complex with maltose suggests an involvement of Omp-Pst1 in carbohydrate harvesting and uptake. Analysis of crystal packing interactions led to the discovery of a new oligomeric assembly, common to both porins, and formed by the face-to-face association of two porins trimers, through their extracellular loops. These dimers of trimers (DOTs) assemble through steric zipper interactions between homo-specific segments. Incorporation of either of the porins into liposomes results in proteoliposome aggregation, while their ectopic expression in a porin-devoid *E. coli* strain induces a shift from the state of isolated plankton, to that of floating communities. Thus, our results support the hypothesis that porins contribute to cell-to-cell contact in floating communities of *P. stuartii*¹². We propose that DOTs are the biological assemblies at the basis of cell-to-cell contact property and that they could provide a means of direct communication between cells.

Results

- Structures of Omp-Pst1 and of its complex with maltose

The structure of native Omp-Pst1 was solved in two space groups, C2 (type-A; 3.2 Å resolution) and P2₁2₁2₁ (type-B; 2.7 Å resolution) (Supplementary Information Appendix, Table S1). In both crystal forms, the asymmetric unit contains a single trimer. In type-A crystals, dimerization of trimers along the crystallographic 2-fold results in dimer of trimers (DOT), assembled through steric zipper interactions between homologous segments in facing extracellular loops (Figure 1A). In type-B crystals, contact is also observed between extracellular loops, but does not involve self-matching interactions. In both types of crystals, no contact is observed between intracellular turns, and complementary contact is established between transmembrane regions. The trimeric structures of Omp-Pst1 in type-A and type-B crystals are similar, superimposing with an rmsd of 0.356 Å over 1056 residues. While extracellular loops of Omp-Pst1 are mostly folded as α -helices, in each monomer, extracellular loop L5 contributes a β -hairpin that is positioned over the channel's extracellular vestibule and complicates access to the pore (Supplementary Information Appendix, Figure S1A). In type-A crystals, the L5 β -hairpins are additionally involved in the crystal-packing interactions that underlie DOT assembly, at the unit cell level (Figures 1A, B).

Compared to the canonical porins OmpF, OmpC and PhoE from *E. coli*, Omp-Pst1 displays a similar pattern of charge distribution. In particular, Omp-Pst1 channel is positively charged (+5e in Omp-Pst1, vs. +3e, +3e and +6e in OmpF, OmpC and PhoE, respectively) (Figure. 1I and Supplementary Information Appendix, Figure S2A), with a net charge of +1e at the constriction zone (0e, -2e and 0e in OmpF, OmpC and PhoE, respectively) (Figure 1K, L and Supplementary Information Appendix, Figure S2B). The electrostatic potential profile calculated along the channel of Omp-Pst1 indicates mild anion selectivity (Figure. 1L), in line with electrophysiology measurements and with MD simulations based on this structure¹⁵. Nevertheless, the Omp-Pst1 channel features more charged residues than *E. coli* porins (48,

35 and 20 % more charged residues than OmpF, OmpC and PhoE, respectively), suggesting higher translocation selectivity. The extracellular vestibule of Omp-Pst1 is negatively charged (Figures 1I, L).

In an attempt to determine whether or not Omp-Pst1 is involved in translocation of uncharged nutrients into the periplasm, a structure of a complex with maltose was obtained, by soaking type-B crystals in a mother liquor solution containing 100 mM maltose. The structure of the complex indicates electron density for three maltose molecules, one per monomer with identical binding site. Residues from extracellular loops L1 (K31, E33), L3 (Q121), L6 (R251, G253), L7 (L300) and L8 (G337, N339) form a groove above the constriction zone within which each maltose establishes six to eight H-bonds (depending on the monomer), burying ca. 70% of its accessible surface (Supplementary Information Appendix, Figure S1B). The presence of a tight binding-site at the channel entrance could underlie a role for Omp-Pst1 in the facilitated translocation of carbohydrates. Ensemble refinement of the maltose-bound Omp-Pst1 structure reveals increased dynamics in L3 residue D117, positioned below the maltose binding site and above the channel constriction zone (Supplementary Information Appendix, Figure S1B). Hence D117 could participate in the translocation of maltose, from its binding site in the extracellular vestibule to the periplasmic side. Moreover, in all Omp-Pst1 structures, a Ca^{2+} ion could be modelled at the interfacial cavity between the three monomers of the trimer, stabilized by cation- π interaction with the side chain of Trp62 from each monomer (Supplementary Information Appendix, Figure S3A, B). Interestingly, this central cavity is opened to the intracellular side, but closed at the extracellular side by symmetrical interactions between Asn75 side chains from the three monomers. Substitution of the Ca^{2+} by exposure of porin to high Zn^{2+} concentrations leads to a dissociation of the trimer, suggesting that this channel-buried ion binding-site could be involved in the regulation of Omp-Pst1 oligomerization (Supplementary Information Appendix, Figure S3C).

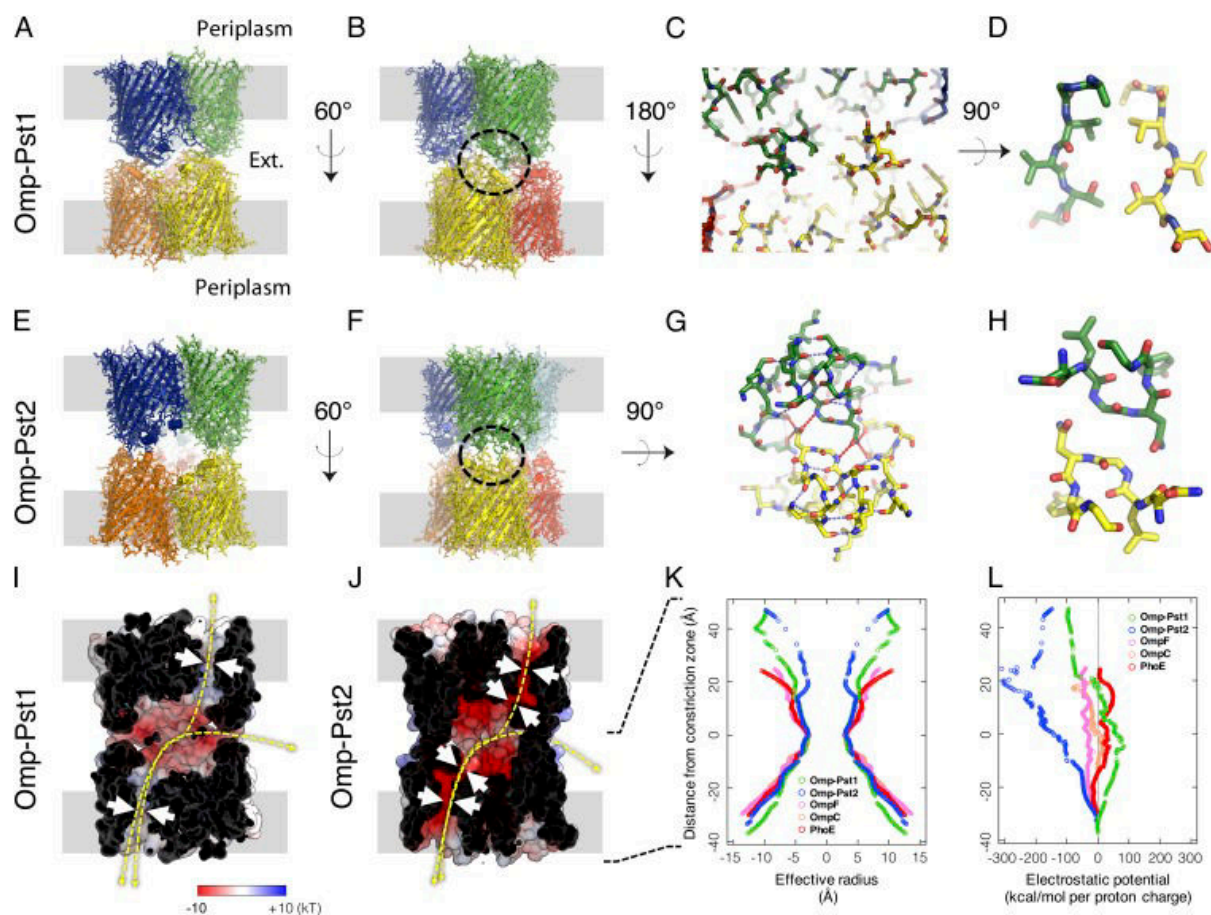


Figure 1: Omp-Pst1 and Omp-Pst2 form dimers of trimers (DOTs). (A) Lateral view of the Omp-Pst1 DOT. The presumed positions of outer-membranes (OMs) are shown in grey. (B) Same view after 60° vertical rotation. (C) Interaction region (circled in panel b) between facing monomers. (D) Enlarged view of the center of panel C showing a symmetry-class III steric zipper that is buried in the core of the DOT structure. (E, F, G, H) Equivalent views of the Omp-Pst2 DOT. Main differences are the ellipsoidal fenestrations evident in panel E, and the presence of a symmetry-class I steric zipper in panel H. (I) The dimerization interface of the Omp-Pst1 DOT, viewed as in panel B, delineates a large negatively charged cavity. The electrostatic potential is mapped on the solvent-accessible surface. (J) Equivalent representation of Omp-Pst2. In panels (I) and (J), white arrows indicate constrictions along the porin channels, whereas yellow arrows indicate possible translocation pathways across porin DOTs – viz. between the periplasm of two adjacent cells, along porin channels, or between the periplasmic space of each cell and the external medium, through fenestrations of the DOTs. (K) Effective radii measured along Omp-Pst1 (green), Omp-Pst2 (blue) and *E. coli* porins channels using a 1-Å positively-charged rolling probe (equivalent to a proton). The y-axis indicates vertical position along the channels from periplasmic (positive y values) to extracellular (negative y values) ends, with reference to the central constriction zone (z=0) contributed by L3. Channels of Omp-Pst1, Omp-Pst2 and *E. coli* porins all display similar radii at their central constriction zone, but Omp-Pst2 channel features an additional constriction zone in its extracellular vestibule. (L) Equivalent plots of electrostatic potentials associated with the translocation of a proton, indicating that Omp-Pst1 is mildly anion-selective, while Omp-Pst2 is strongly cation-selective. The energy profile of Omp-Pst2 further suggests a facilitated transport of cations from the periplasm to the external medium.

- Structure of Omp-Pst2

The structure of Omp-Pst2 was solved in the $P2_1$ space group, at 2.2 Å resolution (Supplementary Information Appendix, Table S1). A DOT is observed in the asymmetric unit, formed by the face-to-face, self-matching interaction of two trimers through their extracellular loops (Figures 1E, F). Hence, Omp-Pst2 and type-A Omp-Pst1 crystals reveal a similar

biological assembly (Figures 1A, B, E, F). The extracellular loops of Omp-Pst2 are mostly folded as α -helices (Supplementary Information Appendix, Figure S1C), thus contributing an additional constriction zone at the entrance of the channel, which could affect the diffusion of large solutes across Omp-Pst2 (Figures 1J, K). As compared to *E. coli* OmpF, OmpC and PhoE, the Omp-Pst2 channel features a similar amount of charged residues (20 % more charged residues than OmpF, and 8 and 4 % less than OmpC and PhoE, respectively), but has a characteristic pronounced acidic nature (Supplementary Information Appendix, Figure S2C). The net charge of Omp-Pst2 channel is indeed -4e at the constriction zone, suggesting a strong cation selectivity (Supplementary Information Appendix, Figure S2D) which has been verified by electrophysiology measurements¹⁵. Calculations of the electrostatic potential along the Omp-Pst2 channel furthermore suggest a facilitated transport of cations from the intracellular to the extracellular side of the porin (Figures 1J, L), in line with recent MD simulations based on the structure¹⁵. We note that as in Omp-Pst1 crystals, no contact is observed between intracellular turns of Omp-Pst2, and a cavity is apparent at the center of the trimeric complex. This cavity is open at its intracellular end, but insulated from the extracellular bulk by symmetrical interactions between Asn72 (equivalent to Omp-Pst1 Asn75) side chains from the three monomers. At the top of this cavity, a SO_4^{2-} was modelled which appears to be stabilized by anion- π interaction with the side chain of Trp59 from each monomer (Supplementary Information Appendix, Figure S3E, F). Similar to Omp-Pst1, exposure of Omp-Pst2 to high Zn^{2+} concentrations leads to a dissociation of the trimer, suggesting a critical role for this central ion binding site in the regulation of Omp-Pst2 oligomerization (Supplementary Information Appendix, Figure S3C, D). Furthermore, it shows that the central channel of Omp-Pst2 can accommodate both positively-charged and negatively-charged divalent ions.

-
- Omp-Pst1 and Omp-Pst2 form DOTs assembled through steric zipper interactions.

In Omp-Pst2 and in type-A Omp-Pst1 crystals, packing is supported by the face-to-face interaction of two trimers *via* their extracellular loops, yielding DOTs (Figures 1A, B, E, F). In both DOTs, the dimerization interface delineates a large negatively charged cavity (volumes of 30,610 and 37,959 Å³ for Omp-Pst1 and Omp-Pst2, respectively) (Figures 1I, J). The cavity of Omp-Pst2 is accessible from the bulk *via* three ellipsoidal fenestrations of 17 × 29 Å (Figures 1E, F, J), while that of Omp-Pst1 is shielded from the bulk and presumably only accessible to waters (Figures 1A, B, I). The buried surface areas per facing trimers are 921 Å² for Omp-Pst1 and 1215 Å² for Omp-Pst2 DOTs, *i.e.*, values above the threshold of 856 Å² that has been proposed to discriminate between artificial and biological dimers in crystal structures¹⁶. In comparison, the buried surface area per facing trimers is 350 Å² in type-B Omp-Pst1 crystals. The surface complementary between facing trimers of the DOT is 0.40 for Omp-Pst1 and 0.64 for Omp-Pst2. The latter value is close to that displayed by antibody-antigen complexes, *viz.* 0.65¹⁷.

The DOTs formed by Omp-Pst1 and Omp-Pst2 are singular in that they appear to be supported by steric zipper interactions – a structural motif that has to date been observed only in prions and amyloid fibers. Steric zippers form from the tight interdigitation of side chains emanating from equivalent residues in short self-matching sequences (4-11 residues); they are by nature highly self-selective. In amyloid and prion assemblies, steric zippers associate β-sheets into highly-ordered fibers^{18,19}, but the steric zipper interfaces that formed between facing monomers of Omp-Pst1 and Omp-Pst2 trimers are single-layered. Thus perhaps, neither Omp-Pst1 nor Omp-Pst2 would, if monomeric, be able to dimerize face-to-face through these motifs.

The steric zipper interfaces differ in the two porins. In Omp-Pst1, the three single-layered steric zipper interfaces are contributed by residues 206-GVVTSE-211 from extracellular loop L5 and would belong to the symmetry class III of steric zippers (face-to-face; up-down)¹⁸ (Figures 1C, D), with a 15° tilt between the two facing β-strands. This interface is only

reinforced by weak electrostatic interaction (distance between non-hydrogen atoms $\geq 3.5\text{\AA}$) between K28 and D213 from facing extracellular loops L1 and L5, respectively (Supplementary Information Appendix, Figure S4A). The formation of Omp-Pst1 DOT thus appears fully governed by extracellular loop L5. In Omp-Pst2, residues 282-NLGNYG-287 from facing extracellular loops L7 interact *via* three single-layered non-tilted steric zippers that would correspond to the symmetry class I of steric zippers¹⁸ (face-to-face, up-up) (Figures 1G, H). Each steric zipper interface, centred around residues G284 and N285, is complemented by a network of H-bonds, which fastens extracellular loops L5, L7 and L8 from facing monomers (Figure 1G and Supplementary Information Appendix, Figure S5A). Of note, Omp-Pst1 features a 290-NLGNGY-295 sequence in its extracellular loop L7, similar to the 282-NLGNYG-287 sequence of Omp-Pst2. However, the L5 β -hairpin protrusion that contributes the 206-GVVTSE-211 steric zipper interface renders L7 inaccessible in Omp-Pst1 (Supplementary Information Appendix, Figure S1A). Nonetheless N293, equivalent to Omp-Pst2 N285, plays an important role in Omp-Pst1 DOT formation, contributing two H-bonds to Y216, at the base of the L5 β -hairpin, which stabilize the latter and therefore the steric zipper interface (Supplementary Information Appendix, Figure S4A).

To evaluate the steric zipper propensity of Omp-Pst1 and Omp-Pst2 segments involved in their dimerization into DOTs, we crystallized the corresponding peptides. For each, we chose the smallest fragment hypothetically involved in the interaction, *i.e.* 206-GVVTSE-211 from Omp-Pst1, and 283-LGNY-286 from Omp-Pst2. Both peptides produced urchin-like microcrystals, from which their structures were solved at 1.7 and 1.0 \AA resolution, respectively (Figure 2A, B and Supplementary Information Appendix, Table S1). The two peptides display canonical cross- β structures, characterized by the in-register stacking of strands into sheets, and by the mating of these sheets *via* a steric zipper, perpendicular to the fiber axis. Thus, both 206-GVVTSE-211 and 283-LGNY-286 have a high propensity to form steric zippers (Figure 2) in isolation of their respective parent proteins. The 3-D profile method²⁰ also identified these segments as highly prone to form steric zippers, with scores of -26.2 and -

22.1 kcal/mol, respectively (Supplementary Information Appendix, Figure S6). They accordingly form fibrils *in vitro* (Supplementary Information Appendix, Figure S6A, B).

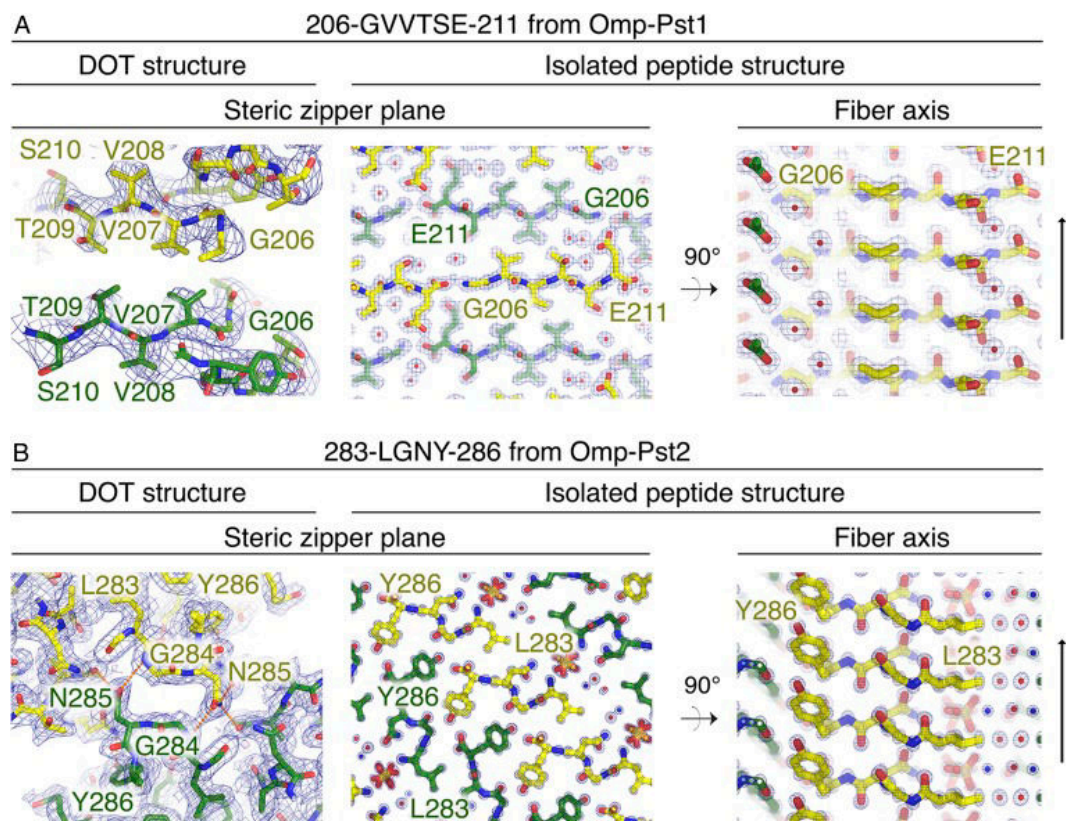


Figure 2: The segments involved in the formation of the Omp-Pst1 and Omp-Pst2 DOTs also form steric zippers in isolation from their parent protein. (A, B) Both 206-GVVTSE-211 from Omp-Pst1 (A) and 283-LGNY-286 from Omp-Pst2 (B) form single-layered steric zippers in the DOT structures of Omp-Pst1 and Omp-Pst2, respectively (left panels). The 206-GVVTSE-211 and 283-LGNY-286 steric zippers would belong to symmetry classes III and I, respectively. In isolation, the GVVTSE and LGNY peptides also form steric zippers (middle and right panels), as revealed by their crystal structures solved at 1.7 and 1.0 Å resolution, respectively. The middle panels show the steric zipper interfaces. The right panels show a view of 90° apart which reveal that both GVVTSE and LGNY adopt a canonical cross-β structure, whereby the steric zipper repeats itself every 4.8 Å through hydrogen bonding along a fiber axis. In the peptide structures, GVVTSE and LGNY form steric zippers that belong to symmetry classes I and III, respectively. In all panels, the corresponding refined 2mF_o-DF_c electron density map is contoured at 1σ.

- Omp-Pst1 and Omp-Pst2 self-interact *in vitro*

We investigated whether Omp-Pst1 and Omp-Pst2 can have adhesion properties *in vitro*. If so, incorporation of either porin into liposomes should lead to proteoliposome aggregation – a process we monitored by dynamic light scattering (DLS). We first examined phosphatidylcholine (PC) liposomes, whose surfaces are neutral at physiological pH. We used the direct-dilution method to incorporate porins into liposomes, enabling real-time monitoring of the process. Using centrifugation on sucrose gradient²¹, we confirmed insertion

of Omp-Pst1 and Omp-Pst2 into preformed liposomes, and observed that this process is favoured at acidic pH (Supplementary Information Appendix, Figure S7). We then used DLS to monitor the average hydrodynamic radius of the proteoliposome aggregates which form upon incorporation of Omp-Pst1 or Omp-Pst2 at increasing concentrations, into preformed liposomes (60 nm starting radius). We found that insertion of either porin into liposomes results in a fast (~30-45s) and porin-concentration dependent aggregation of proteoliposomes (Figure 3 and Supplementary Information Appendix, Figure S8A). In contrast, incorporation of *E. coli* OmpF into PC liposomes by the same method had comparatively no effect on their average size distribution (Supplementary Information Appendix, Figure S8A). The proteoliposome aggregation induced by Omp-Pst1 and Omp-Pst2 is visible in the pH 4-8 range, though reduced (smaller liposomes aggregates) at pH 7 and 8 – either due to a suboptimal incorporation of porins into liposomes at these pHs or to a reduced self-affinity (Supplementary Information Appendix, Figure S7). To increase the stringency of further measurements, we nonetheless worked at pH 7, which avoided the formation of proteoliposomes aggregates too large (> 1 μ m) and too polydisperse (> 50%) to be resolved by our DLS instrument.

We ascertained the presence of Omp-Pst1 and Omp-Pst2 in proteoliposome aggregates by labeling lipids and porins specifically, and then examining porin-induced proteoliposome aggregation using epifluorescence microscopy (Supplementary Information Appendix, Figure S8B). Omp-Pst1 and Omp-Pst2 were specifically labeled by engineering of a cysteine (Omp-Pst1-K221C and Omp-Pst2-K211C) at the C-terminal extremity of their L5 loop (Supplementary Information Appendix, Figures S4B and S5B, respectively) followed by derivatisation of the resulting mutants with a maleimide-coupled green fluorophore (Alexa488). Fluorescent liposomes were prepared by introduction of a red fluorescent lipid (rhodamine derivative) in the bilayer composition. Both Omp-Pst1-K221C and Omp-Pst2-K211C retained the ability to induce proteoliposome aggregation in DLS experiments (Supplementary Information Appendix, Figure S8A). Furthermore, in epifluorescence

micrographs, we observed a co-localization of the fluorescence signals arising from the lipids and the porins. The observation that the Omp-Pst1-K221C mutant can still self-associate indicates that the interface revealed by type-B crystals is not relevant for proteoliposome aggregation, as the H-bond between K221(NZ) and N293(O) is central to this interface (Supplementary Information Appendix, Figure S4). Aggregates of proteoliposomes formed at 2 μ M porin concentration were examined by transmission electron microscopy, revealing stacks of lipid bilayers (Supplementary Information Appendix, Figure S9). Those aggregates display periodic order, further exemplifying the strong tendency of Omp-Pst1 and Omp-Pst2 porin to self-associate, both laterally and axially.

Additional DLS data were collected on liposomes composed of palmitoyl-oleyl phosphatidylcholine (POPC) and phosphatidylserine (POPS), in presence and absence of rough and smooth lipopolysaccharides (LPS). Data were collected at pH 7, at two liposome concentrations (0.125 and 1.25 mg/ml, corresponding to ~2 and ~20 nM of 60 nm liposomes in Supplementary Information Appendix, Figures S10 and S11, respectively) and two LPS-to-phospholipid mass ratios (1:10 and 1:100), before and after the removal of the detergent using biobeads.

The data show that *P. stuartii* porins self-association is hindered by electrostatic repulsion between (overall negatively charged) POPS liposomes. Omp-Pst2 self-association is inhibited in the presence of rough and smooth LPS (Supplementary Information Appendix, Figures. S10C, D and S11C-F), additional to those already co-purified with the protein (Supplementary Information Appendix, Figure S12A, B). Omp-Pst1 self-association is not affected by inclusion of rough LPS (which lack O-antigen but possess shorter core oligosaccharides and lipid A) in (overall neutral) POPC liposome bilayers, even at LPS-to-phospholipid mass ratio of 1:10 (Supplementary Information Appendix, Figures S10C, D and S11C, D), whereas it is reduced by the inclusion of smooth LPS (which possess O-antigen, complete core oligosaccharides and the lipid A) at a LPS-to-phospholipid mass ratio of 1:100

(Supplementary Information Appendix, Figure S10I, J) and suppressed at 1:10 (Supplementary Information Appendix, Figure S11E, F).

The data also show that detergent does not promote proteoliposome aggregation. First, removal of detergent hardly affects the size of proteoliposome aggregates when phospholipid-only liposomes are used (Supplementary Information Appendix, Figure S10A, B, E, F). Second, the detergent, at concentrations much higher than used in our study, reduces the size of liposomes (Supplementary Information Appendix, Figure S13A and Supplementary Methods), whereas incorporation of porins augments it. Additionally, smaller proteoliposomes aggregates are observed when higher concentrations of liposomes are used (Supplementary Information Appendix, Figures S10 and S11 show data at 0.125 and 1.25 mg/ml, corresponding to ~2 and ~20 nM of 60 nm radius liposomes), supporting the hypothesis that proteoliposome aggregation depends on the number of porins inserted per liposome (Supplementary Information Appendix, Figures S10 and S11).

We also investigated the effect of high concentrations of salt and chaotropes (urea, NH_4Cl , NaCl , NaSCN). Efforts to investigate the effects of CaCl_2 , MgCl_2 and ZnCl_2 were thwarted by the aggregating effect of these ions on liposomes. We found that Omp-Pst1-induced aggregation of phospholipid-only liposomes is reduced, albeit to different extents, in the presence of urea, NH_4Cl , NaCl and NaSCN . In contrast, Omp-Pst2-induced aggregation of such liposomes is prevented by urea, promoted by NH_4Cl and NaCl , and unaffected by NaSCN . The presence of LPS changes these patterns, restoring self-association for Omp-Pst1 in the presence of NaCl , although still inhibiting Omp-Pst2 self-association. We note that biobeads and LPS are incompatible, as LPS strongly interact with both biobeads and porins, resulting in the extraction of the latter from liposome bilayers (Supplementary Information Appendix, Figures S10C, D, I, J and S14). Finally, we used DLS to measure the dissociation constants for LDAO-solubilized Omp-Pst1 and Omp-Pst2 DOTs (Supplementary Information Appendix, Figure S13B and Supplementary Methods). Fitting of these data suggests dissociation constants of 0.6 and 0.4 μM for Omp-Pst1 and Omp-Pst2 at pH 7.

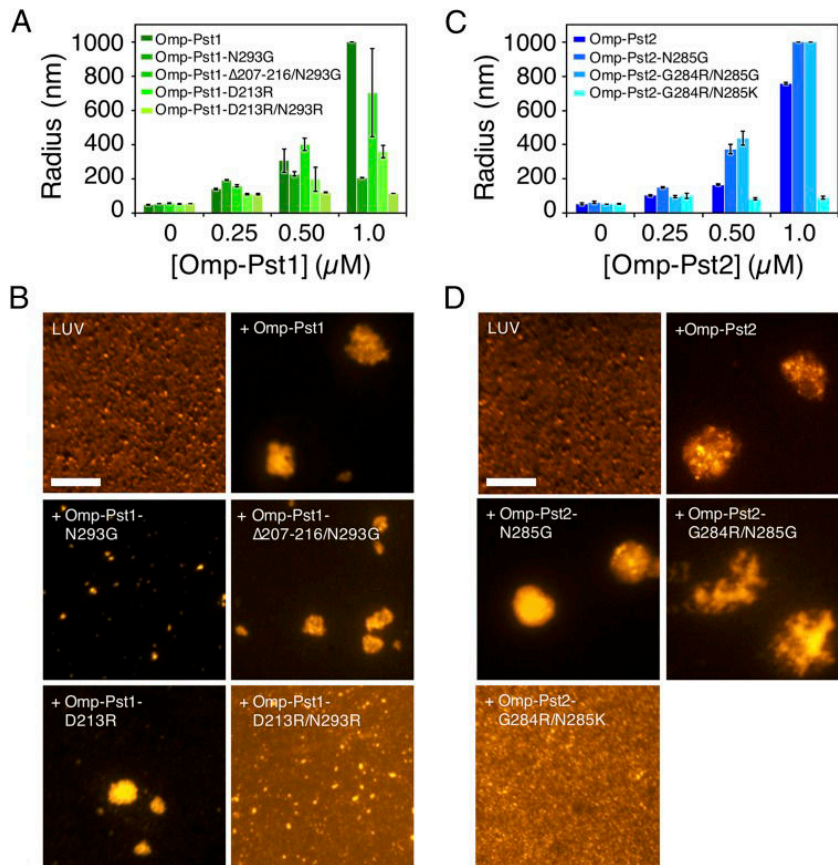


Figure 3: Altering charge distribution at the DOT interface reduces aggregation properties of Omp-Pst1 and Omp-Pst2 *in vitro*. (A) Dynamic light scattering was used to measure the hydrodynamic radii of proteoliposomes formed 24 h after the addition of increasing concentrations of Omp-Pst1 and its specified mutants (A; colored in shades of green) to a monodispersed 60 nm liposome solution. (B) Proteoliposomes formed at 1 μM porin were spread onto an agarose-coated cover slide for epifluorescence imaging. LUVs were labeled using rhodamine-derivatized lipids. Scale bars are 20 μm (60X magnification). (C, D) Same as panels A and B for Omp-Pst2.

- Self-association of Omp-Pst1 and Omp-Pst2 is driven by electrostatic interactions

We used site-directed mutagenesis to further characterize self-association of Omp-Pst1 and Omp-Pst2 in liposomes. First, we targeted the steric zipper interface observed in Omp-Pst1 DOTs (Supplementary Information Appendix, Figure S4), either by introduction of point mutations in L5 and L7 (Omp-Pst1-D213R, Omp-Pst1-N293G, and Omp-Pst1-D213R/N293R) or by deletion of the full L5 β-hairpin that support this interface (Omp-Pst1-Δ207-216/N293G) (Supplementary Information Appendix, Figure S4D). The charge-altering mutations D213R (Supplementary Information Appendix, Figure S4E) and D213R/N293R (Supplementary Information Appendix, Figure S4F), respectively reduced and suppressed the ability of Omp-Pst1 to induce proteoliposome aggregation (Figure 3A, B). The L7 mutant

Omp-Pst1-N293G (Supplementary Information Appendix, Figure S4C), designed to destabilize extracellular loop L5 – and inhibit steric zipper formation – through suppression of the strong H-bond (2.4 Å) between N293(OD1) and Tyr216(N), was unable to promote proteoliposome aggregation (Figure 3A, B and Supplementary Information Appendix, Figure S4). The inability of Omp-Pst1-N293G to induce proteoliposome aggregation was yet fully reversed by deletion of the entire L5 β -hairpin, *viz.* Omp-Pst1- Δ 207-216/N293G (Supplementary Information Appendix, Figure S4D). Hence, the self-association properties of Omp-Pst1 are impacted by electrostatic repulsion or destabilization of the steric zipper interface, but not by the complete suppression of the L5 β -hairpin (Figure 3A, B). Likewise, two Omp-Pst2 mutants aimed at disrupting the 282-NLGNYG-287 steric zipper interface, *viz.* Omp-Pst2 N285G and Omp-Pst2-G284R/N285G (Supplementary Information Appendix, Figure S5C, D), showed increased ability to induce proteoliposome aggregation (Figure. 3C, D). Again, only the Omp-Pst2-G284R/N285K mutant with two positive charges added side-by-side (Supplementary Information Appendix, Figure S5E), displayed a reduced ability to induce proteoliposome aggregation – reminiscent of Omp-Pst1-D213R/N293R. Hence, the main driving force behind Omp-Pst1 and Omp-Pst2 self-association appears to be electrostatic attraction, while single-layered steric zipper interaction between facing monomers could underlie a slotting mechanism that regulates DOT formation. In that case, Omp-Pst1- Δ 207-216/N293G should form DOTs that solely assemble through electrostatic interactions, since both steric zipper interfaces available at the surface of Omp-Pst1 will be disrupted in that mutant.

To verify this hypothesis, we crystallized Omp-Pst1- Δ 207-216/N293G and solved its structure at 3.2 Å resolution (Supplementary Information Appendix, Figure S15 and Table S1). Reminiscent of type-A Omp-Pst1 crystals, those of Omp-Pst1- Δ 207-216/N293G belong to the C2 space group, and reveal the presence of a DOT at the unit cell level (Supplementary Information Appendix, Figure S4A, B). The buried surface area per facing trimer is 1,126 Å² and the dimerization interface delineates a large negatively charged cavity characterized by

a volume of 24,540 Å³ (Supplementary Information Appendix, Figure S15C). As proposed, electrostatic interactions between extracellular loops are at the basis of this DOT, which is not supported by steric zipper interactions and wherein facing channels do not join at their extracellular ends – another difference with the DOTs formed by wild-type Omp-Pst1 and Omp-Pst2. Rather, one monomer from each trimer plugs into the centre of the facing trimer and establishes contact with the three facing monomers through extracellular loops L7 (to L4 in a first monomer), L8 (to L6 and L8 in a second monomer) and L5 (to L5 in the third monomer). The two first interaction zones are polar, featuring H-bonds between respectively Asp296(OD2) and Met168(N), and the NZ atom K334 and the main chain carbonyl oxygen of Asp254 (Supplementary Information Appendix, Figure S15D). The unnatural Omp-Pst1-Δ207-216/N293G DOT is nevertheless characterized by a more accessible central cavity, showing reduced surface complementarity between facing trimers (0.37) and featuring six large ellipsoidal fenestrations (up to 7 x 20 Å) (Supplementary Information Appendix, Figure S15).

- Omp-Pst1 and Omp-Pst2 support cell-to-cell contact in *P. stuartii* floating communities

P. stuartii is highly social, forming floating communities of cells prior to depositing as surface-attached biofilms¹². We thus asked whether a correlation would exist between expression of *P. stuartii* porins and the formation of such floating communities. Omp-Pst1 is the major porin of *P. stuartii* (Supplementary Information Appendix, Figure S12C) and essential to its survival, hence a knock-out strategy was unsuited to challenge our hypothesis¹². Rather, we opted for an ectopic expression strategy, using as a surrogate for *P. stuartii* a strain of *E. coli* BL21 deleted of its major porins OmpF, OmpC, OmpA and LamB, *i.e.*, *E. coli* ΔOmp8²² (see Supplementary Methods). Like BL21, the ΔOmp8 strain does not form detectable floating or surface-attached biofilms (Supplementary Information Appendix, Figure S16). However, this strain displays reduced growth and fitness, and a longer lag-phase (Supplementary Information Appendix, Figure S17A). Ectopic expression of either Omp-Pst1 or Omp-Pst2 in

Δ Omp8 cells restores normal growth and reduces the lag phase (Supplementary Information Appendix, Figure S17A). Furthermore, it confers to *E. coli* Δ Omp8 cells the ability to form floating communities similar to those formed by *P. stuartii* (Figures 4-5 and Supplementary Information Appendix, Figure S16). Formation of these is independent of that of surface-attached biofilms, which recombinant Δ Omp8 strains remain unable to form (Supplementary Information Appendix, Figure S16).

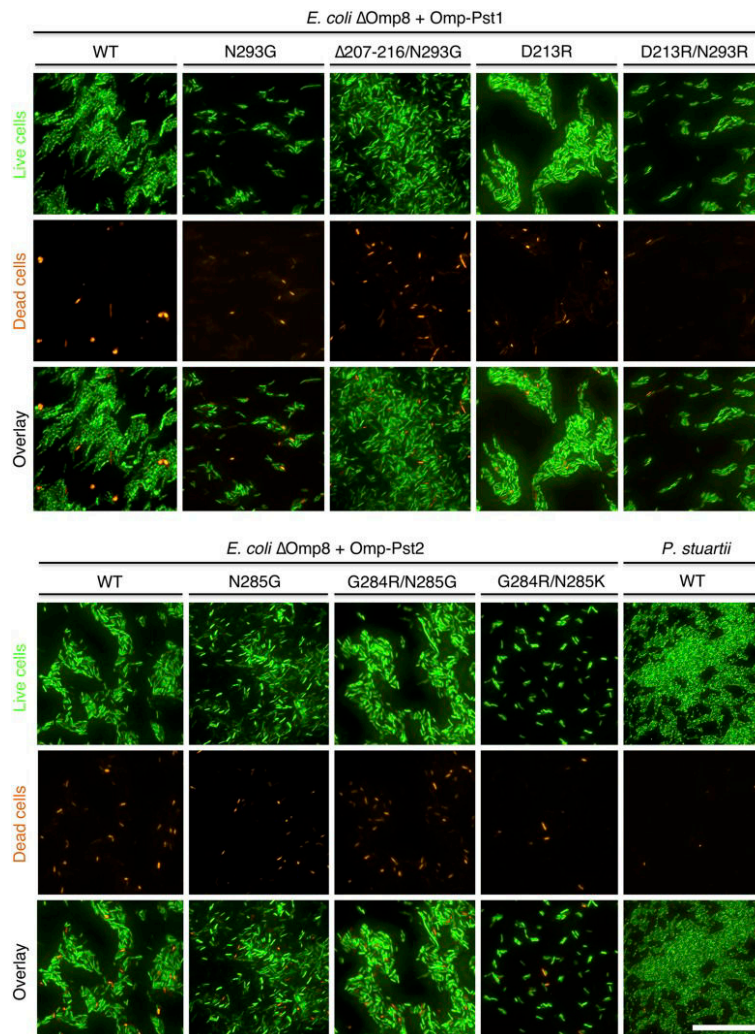


Figure 4: Omp-Pst1 and Omp-Pst2 mutations affect the formation of floating communities of cells by transformed *E. coli* Δ Omp8 cells. Bacterial strains were grown for 24h in 96-well plates. Subsequently, live and dead cells were stained with SYTO9 Green and propidium iodide, respectively. Planktonic cells were harvested by direct pipetting from the LB medium, spread on LB-Gelzan® and imaged immediately afterwards. For comparison, the floating communities natively formed by *P. stuartii* cells are also shown. The scale bar is 50 μ m for all panels (60X magnification).

We then set to verify whether mutants unable to induce aggregation of proteoliposomes would also fail at forming floating communities. Δ Omp8 cells expressing mutated versions of Omp-Pst1 (D213R, N293G, D213R/N293R, Δ 207-216/N293G) or Omp-Pst2 (N285G, G284R/N285G, G284R/N285K) display similar growth and lag phases as cells expressing wild-type Omp-Pst1 and Omp-Pst2, demonstrating that the mutants are well-expressed and folded, and that their diffusive properties are not affected (Supplementary Information Appendix, Figure S17B, C). Strikingly, however, Δ Omp8 cells expressing porin mutants that are able to induce aggregation of proteoliposomes *in vitro* form floating communities, whereas those expressing mutants unable to self-associate *in vitro*, do not (Figures 3 and 4). Thus, our data show that the expression of self-associating *P. stuartii* porins is sufficient to enable formation of communities of cells by a non biofilm-forming *E. coli* strain (Figure 4 and Supplementary Information Appendix, Figure S16). We therefore propose that this mechanism is at play in the formation of *P. stuartii* floating communities (Figure 5), wherein cell-to-cell contacts are observed. As the formation of floating communities precedes that of surface-attached biofilms¹² (Figure 5 and Supplementary Information Appendix, Figure S18), porins could also be involved in the cell-to-cell contacts observed within the core of surface-attached biofilms (Supplementary Information Appendix, Figure S19).

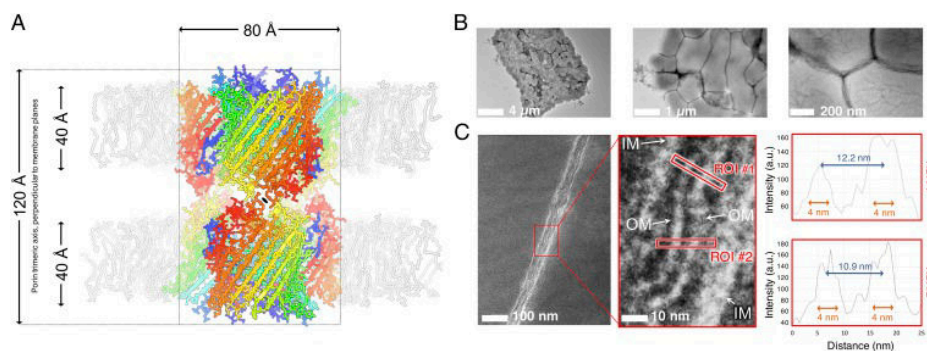


Figure 5: The distance between adjacent cells in *P. stuartii* floating communities is compatible with the formation of a porin DOT. (A) Lateral and longitudinal extent of a porin DOT. The Omp-Pst2 DOT is shown as sticks and ribbons, colored sequence-wise, from cold (N-ter) to hot (C-ter) colour. A phospholipid bilayer was reconstituted around each trimer in the DOT at the presumed positions of outer membranes (OMs); phospholipids are depicted as grey sticks. (B, C) Negatively-stained transmission electron micrographs of *P. stuartii* floating communities. (B) *P. stuartii* floating communities can incorporate hundreds of closely-connected cells. Empty spaces with cellular debris are sometimes observed within floating communities, suggesting that cellular death could play a role in the regulation of cell-to-cell contacts of these floating communities. (C) A close contact is observed between the OMs of adjacent cells in floating communities (left panel). In the close-up view (middle panel), OMs are ~10 nm apart – a distance that would allow a DOT to form between two OMs. The right panel shows integrated intensity plots for the two regions of interest (ROIs) highlighted by red squares in the middle panel.

Discussion

The crystallographic structures of Omp-Pst1 and Omp-Pst2 reveal that, within crystals, these porins are able to form DOTs through self-matching interaction of homologous segments in their extracellular loops (Figures 1 and 2). Using liposome-based assays, we found that Omp-Pst1 and Omp-Pst2 display self-association properties *in vitro* (Figure 3), while by means of ectopic expression in Δ Omp8, a porin-devoid strain of *E. coli*, we showed that the sole expression of Omp-Pst1 or Omp-Pst2 endows these model cells with the capability to form floating communities (Figure 4). Thus, our data suggest that the self-association of porins from adjacent cells can sustain cell-to-cell contact between these. Based on buried surface area statistics, the DOTs revealed by type-A crystals of Omp-Pst1 and by crystals of Omp-Pst2 and Omp-Pst1- Δ 207-216/N293G are compatible with the adhesive properties of these porins, but the side-by-side DOTs observed in type-B crystals of Omp-Pst1 are not. We thus propose that the DOT structures are the biological assemblies that contribute to rivet cells one to another in *P. stuartii* floating communities (Figure 5) – possibly in parallel with other adhesion mechanisms. Our observation that DOT formation is impaired by smooth LPS suggests that DOTs may be specific to ‘rough’ colonies.

Floating communities of cells associated through DOTs could provide a scaffold for biofilm genesis, allowing the building of a critical biomass prior to deposition onto a surface and secretion of an extracellular matrix. In line with this hypothesis, cells within the core layers of *P. stuartii* surface-attached biofilms (Supplementary Information Appendix, Figure S19A, B) display the same phenotype as those in floating communities – that is, a close contact is observed between their OMs (Figures 4 and 5, and Supplementary Information Appendix, Figure S19A, B). Hence, Omp-Pst1 and Omp-Pst2 DOTs could be targeted to inhibit socialization of *P. stuartii* in its early stages, *i.e.*, before formation of a canonical biofilm,

when only cell-to-cell contact is at play. We showed that a simple disruption or removal of the steric zipper interface does not suppress the self-associating properties of the porins, but that self-association can be abolished *in vitro* and *in vivo* through destabilization of the steric zipper interface or by electrostatic repulsion (Figures 3 and 4). In yeast, steric zippers promote the selection of strains based on self-templating prions, and in amyloid diseases¹⁹, the enrichment of specific fiber polymorphs which differ in toxicity and shape. In *P. stuartii* porins, steric zippers could serve to avoid interspecies DOT formation, thus restricting contact to cells of the same strain only.

Within crystallographic DOTs, facing channels are opened, suggesting that they could provide *in vivo* an effective conduit for the exchange of signaling solutes or nutrients by passive diffusion (Figure 1) – irrespectively of whether or not they are at the origin of the cell-to-cell contact phenotype. It is known that within biofilms, cells exchange chemical information through a mechanism termed *quorum sensing* (QS), which orchestrates the phenotypic adaptation undergone by bacteria as they morph from the planktonic isolated state to the multicellular biofilm state²³. QS is also involved in the adaptation of biofilm cells to local environmental changes²³, in metabolic co-dependence²⁴ and time-sharing processes²⁵, and in the release of cells from the biofilm²³. As yet, however, it had remained unclear how soluble QS effectors could mediate intercellular communication in the first stages of biofilm formation, *i.e.*, when the cell density is low and no surrounding matrix is present. The DOT structures hint at a direct intercellular communication mechanism, which would be effective regardless of the cell density or the diffusion volume. Such a mechanism would be well adapted to enable cell crosstalk in the floating communities that form prior to attachment on a surface.

The crystallographic structures show that Omp-Pst1 forms more hermetic DOTs (virtually no fenestrations) than Omp-Pst2, suggesting that intercellular solute translocation would be more efficient across Omp-Pst1 DOTs (Figure 1B, F). Also, the presence of an additional constriction zone in Omp-Pst2 channel would limit large solute exchange across Omp-Pst2

DOTs (Figure 1J, K). Hence, Omp-Pst1 DOTs are better candidates than Omp-Pst2 DOTs for the exchange of signaling solutes²³ and nutrients^{24,25} between *P. stuartii* cells. The structure of maltose-bound Omp-Pst1 is particularly interesting in this context, because it reveals not only that this porin could be involved in the harvesting of maltose (and other di-glycosides) at the surface of the OM (Supplementary Information Appendix, Figure S1B), but also that the binding site for maltose is not affected by the oligomerization into a DOT. Hence, Omp-Pst1 DOTs could permit equilibration of di-glycoside concentrations between adjacent cells. In contrast, the protrusion contributed by the longer L6 loop of Omp-Pst2 would prevent the binding of a solute at this locus. Furthermore Omp-Pst2 is highly cation-selective and the electrostatic potential developed along its channel is suggestive of a facilitated transport of cations from the periplasm to the bulk (Figure 1L). MD simulations have revealed the propensity of Omp-Pst2 to become nonconductive when cations translocate towards the periplasm, while recent experimental work highlighted the essential role it plays in the resistance to high urea concentrations and the regulation of the cationic content of the periplasm¹². In pathophysiological conditions where *P. stuartii* cells encounter high urea concentrations²⁻⁵, Omp-Pst2 could facilitate the export of the ammonium that accumulates in the periplasm due to *P. stuartii* urease activity¹². Omp-Pst2 DOTs would therefore function as check valves, allowing adjacent cells to expel cationic waste through fenestrations at the dimerization interface, while not re-absorbing it. The observation that Omp-Pst2 self-association is promoted by high concentrations of ammonium chloride is in favour of this hypothesis.

In conclusion, our results suggest a previously uncharacterized role for porins, *i.e.*, to form primitive junctions between *P. stuartii* cells. These junctions could foster the formation of floating communities (Figures. 4 and 5) and support intercellular communications. Porin DOTs could thus represent new targets for diagnosis, disruption and eradication of *P. stuartii* biofilms and associated chronic infections. It remains unclear if biofilm-forming species other than *P. stuartii* also form floating communities prior to surface-attached biofilms, and if so,

whether or not porin DOTs could support the formation of these floating communities. Examination of porin structures deposited in the wwPDB, and of their crystal packing interactions, reveals that many crystallize as DOTs associated through their extracellular loops. Thus, some porins may need to be reexamined for their putative propensity to self-associate, in light of the DOTs they form in crystals (2j4u, 2xe1, 2xe2, 2xe5, 2y0h, 3poq, 3pou, 3pox, 3t0s, 3t24, 3wi4, 3wi5, 4aui, 4frt, 4fso, 4gey, 4gf4). Further work will be needed to examine the occurrence of porin DOTs in other Gram-negative biofilm-forming bacteria – and the extent to which these DOTs are supported by steric zipper interactions.

Methods

A full description of methods is given in Supplementary Information. Briefly, *E. coli* strain BL21 (DE3) Δ omp8 (Δ lamB ompF::Tn5 Δ ompA Δ ompC) was used to generate recombinant strains. Expression of Omp-Pst1 and Omp-Pst2 in *P. stuartii* and *E. coli* Δ Omp8 strains was monitored using RT-qPCR. Crystallization conditions were screened using standard crystallization screens and improved manually. Porin crystals were grown by the sitting drop method and peptide crystals by the hanging drop method. X-ray data were collected at ESRF beamlines ID14-EH4, ID23-EH2 and ID30B, processed and scaled using standard software, and phased either by molecular replacement with homology models or by direct methods. Large unilamellar liposomes were produced by the standard film hydration method; their average hydrodynamic radius was determined using dynamic light scattering and epifluorescence imaging was performed using an inverted microscope. Floating and surface attached biofilms of *E. coli* and *P. stuartii* were prepared and imaged by epifluorescence microscopy as described¹². Electron micrographs of *P. stuartii* floating communities were obtained by sedimentation (30 min) of fixated planktonic cells, followed by negative staining with phosphotungstic acid (Figure 5) or sodium silicotungstic acid (Supplementary Information Appendix, Figure S19).

Acknowledgments

We warmly thank E. Kandiah, D. Cascio, M.R. Sawaya and J. Zaccari for critically reading the manuscript. We thank C. Breyton and D. Levy for suggesting on-column delipidation of porins and sucrose gradient experiments, respectively. We thank A. Martel, A. Flayhan, A. Laganowsky, A. Davin-Regli, E. Moiseeva, M. Zhao and T. Vernet for stimulating discussions. We are indebted to I. Snigireva for scanning electron micrographs and to J.-P. Kleman and F. Lacroix for their technical support and advices during epifluorescence microscopy experiments. This work used the platforms of the Grenoble Instruct Center (ISBG: UMS 3518 CNRS-CEA-UJF-EMBL) with support from FRISBI (ANR-10-INSB-05-02) and GRAL (ANR-10-LABX-49-01) within the Grenoble Partnership for Structural Biology (PSB). The electron microscopy facility is supported by the Rhône-Alpes Region, the Fondation Recherche Medicale (FRM), the Fonds Européen de Développement Régional (FEDER), the CNRS, the CEA, the University of Grenoble, EMBL, and the GIS-Infrastructures en Biologie, Santé et Agronomie (IBISA). We are grateful to the ESRF for beam-time under long-term projects MX722, MX1464 and MX1583 (IBS BAG). We acknowledge financial support by CEA, CNRS, Université Grenoble Alpes, ANR (Grant Nr. ANR-15-CE18-0005-02 to J.-P.C), GRAL (Grant Nr. C7H-LXG11A20-COLLETIER to J.-P.C), Laboratory of Excellence “Ion Channel Science and Therapeutics” (LabEX ICST, ANR-11-LABX-0015-01 to M.V.), the Aix-Marseille University and the Service de Santé des Armées (to J.-M.P.). M.E.K. is supported by a joint CEA-GRAL doctoral fellowship (Grant Nr. C7H-LXG11A20-DYNAMOP).

Author Contributions and Information

M.E.K., C.N. and J.P.C. designed research. M.E.K, C.N., J.L., G.T., H.B. and M.L. prepared samples and performed biophysical experiments; M.E.K., C.N., J.L., G.T., M.We., M.V. and J-P.C. analysed the data; M.E.K., J.L., B.G., D.F., and G.S. performed microscopy; Q-T.T.,

G.T., J.-M.B. J.-M.P., M.We., M.Wi. and M.V. contributed new materials; M.V. and J-P.C wrote the manuscript with inputs from M.E.K., C.N., J.L., G.T., J.-M.P., M.We. and M.Wi.

File deposition information

Atomic coordinates and structure factors have been deposited in the Protein Data Bank under the following accession codes: Omp-Pst1 type-A (4d64), Omp-Pst1 type-B (5nxr), maltose complex with Omp-Pst1 type-B (5nxu), Omp-Pst2 (4d65), 283-LGNY-286 (5n9i) and 206-GVVTSE-211 (5n9h), and Omp-Pst1- Δ 207-216-N293G (5nxn).

List of supplementary materials

The SI Appendix contains Supplementary Figures S1-19, Supplementary Table S1 and Supplementary Material and Methods.

References

1. Manos, J. & Belas, R. The Genera *Proteus*, *Providencia*, and *Morganella*. in *Prokaryotes* **3.3.12**, 245–269 (2006).
2. McHale, P. J., Walker, F., Scully, B., English, L. & Keane, C. T. *Providencia stuartii* infections: a review of 117 cases over an eight year period. *J. Hosp. Infect.* **2**, 155–165 (1981).
3. Stickler, D. J. Bacterial biofilms in patients with indwelling urinary catheters. *Nat. Clin. Pract. Urol.* **5**, 598–608 (2008).
4. Warren, J. W. *Providencia stuartii*: a common cause of antibiotic-resistant bacteriuria in patients with long-term indwelling catheters. *Rev. Infect. Dis.* **8**, 61–67 (1986).
5. Warren, J. W. The catheter and urinary tract infection. *Med. Clin. North Am.* **75**, 481–493 (1991).
6. Tran, Q.-T. *et al.* Implication of Porins in β -Lactam Resistance of *Providencia stuartii*. *J. Biol. Chem.* **285**, 32273–32281 (2010).

-
7. Bajaj, H. *et al.* Antibiotic Uptake through Membrane Channels: Role of *Providencia stuartii* OmpPst1 Porin in Carbapenem Resistance. *Biochemistry (Mosc.)* **51**, 10244–10249 (2012).
 8. STOCK, I. & WIEDEMANN, B. Natural antibiotic susceptibility of *Providencia stuartii*, *P. rettgeri*, *P. alcalifaciens* and *P. rustigianii* strains. *J. Med. Microbiol.* **47**, 629–642 (1998).
 9. Broomfield, R. J., Morgan, S. D., Khan, A. & Stickler, D. J. Crystalline bacterial biofilm formation on urinary catheters by urease-producing urinary tract pathogens: a simple method of control. *J. Med. Microbiol.* **58**, 1367–1375 (2009).
 10. Hollick, G. E. *et al.* Characterization of endemic *Providencia stuartii* isolates from patients with urinary devices. *Eur. J. Clin. Microbiol.* **3**, 521–525 (1984).
 11. Mobley, H. L., Chippendale, G. R., Tenney, J. H. & Warren, J. W. Adherence to uroepithelial cells of *Providencia stuartii* isolated from the catheterized urinary tract. *J. Gen. Microbiol.* **132**, 2863–2872 (1986).
 12. Khatib, M. E. *et al.* *Providencia stuartii* form biofilms and floating communities of cells that display high resistance to environmental insults. *PLOS ONE* **12**, e0174213 (2017).
 13. Zeth, K. & Thein, M. Porins in prokaryotes and eukaryotes: common themes and variations. *Biochem. J.* **431**, 13–22 (2010).
 14. Nikaido, H. Molecular basis of bacterial outer membrane permeability revisited. *Microbiol. Mol. Biol. Rev. MMBR* **67**, 593–656 (2003).
 15. Song, W. *et al.* Understanding Voltage Gating of *Providencia stuartii* Porins at Atomic Level. *PLoS Comput Biol* **11**, e1004255 (2015).
 16. Ponstingl, H., Henrick, K. & Thornton, J. M. Discriminating between homodimeric and monomeric proteins in the crystalline state. *Proteins* **41**, 47–57 (2000).
 17. Lawrence, M. C. & Colman, P. M. Shape complementarity at protein/protein interfaces. *J. Mol. Biol.* **234**, 946–950 (1993).
 18. Sawaya, M. R. *et al.* Atomic structures of amyloid cross-beta spines reveal varied steric zippers. *Nature* **447**, 453–457 (2007).
 19. Eisenberg, D. & Jucker, M. The amyloid state of proteins in human diseases. *Cell* **148**, 1188–1203 (2012).
 20. Goldschmidt, L., Teng, P. K., Riek, R. & Eisenberg, D. Identifying the amyloids, proteins capable of forming amyloid-like fibrils. *Proc. Natl. Acad. Sci. U. S. A.* **107**, 3487–3492 (2010).

-
21. Lévy, D., Gulik, A., Bluzat, A. & Rigaud, J. L. Reconstitution of the sarcoplasmic reticulum Ca(2+)-ATPase: mechanisms of membrane protein insertion into liposomes during reconstitution procedures involving the use of detergents. *Biochim. Biophys. Acta* **1107**, 283–298 (1992).
 22. Prilipov, A., Phale, P. S., Van Gelder, P., Rosenbusch, J. P. & Koebnik, R. Coupling site-directed mutagenesis with high-level expression: large scale production of mutant porins from *E. coli*. *FEMS Microbiol. Lett.* **163**, 65–72 (1998).
 23. Davies, D. Understanding biofilm resistance to antibacterial agents. *Nat. Rev. Drug Discov.* **2**, 114–122 (2003).
 24. Liu, J. *et al.* Metabolic co-dependence gives rise to collective oscillations within biofilms. *Nature* **523**, 550–554 (2015).
 25. Liu, J. *et al.* Coupling between distant biofilms and emergence of nutrient time-sharing. *Science* **356**, 638–642 (2017).

Supplementary Information Appendix

Porin self-association enables cell-to-cell contact in *Providencia stuartii* floating communities of cells.

Authors: Mariam El-Khatib^{a,1}, Chady Nasrallah^{a,1,2}, Julie Lopes^a, Que-Tien Tran^b, Guillaume Tetreau^a, Hind Basbous^a, Daphna Fenel^a, Benoit Gallet^a, Mathilde Lethier^a, Jean-Michel Bolla^c, Jean-Marie Pagès^c, Michel Vivaudou^{a,d}, Martin Weik^a, Mathias Winterhalter^b and Jacques-Philippe Colletier^{a,3}.

Affiliations:

^a *Institut de Biologie Structurale (IBS), Univ. Grenoble Alpes, CNRS, CEA, IBS, 38000 Grenoble, France*

^b *Jacobs University, Life Sciences & Chemistry, 28759 Bremen, Germany*

^c *UMR_MD1, Aix-Marseille Univ, IRBA, Marseille, F-13385 Marseille, France*

^d *Laboratories of Excellence, Ion Channel Science and Therapeutics, Nice, France*

¹ These authors contributed equally.

² Present address: *Institut de Génomique Fonctionnelle, UMR 5203, F-34094 Montpellier, France*

³ To whom correspondence should be addressed. Email: colletier@ibs.fr

This PDF file contains:

- Materials and Methods
- Supplementary Figures S1-19
- Supplementary Table S1
- Supplementary Material and Methods

Materials and Methods

Chemicals

The *Providencia stuartii* ATCC 29914 strain was obtained from the Pasteur Institute in Paris (France). *Escherichia coli* DH5 α was used for cloning and *E. coli* BL21 (DE3) $\Delta omp8$ ($\Delta lamB ompF::Tn5 \Delta ompA \Delta ompC$) was used for porins expression¹. Lipids were from Avanti Polar Lipids Co. (Albaster, AL, USA) and detergents were from Affymetrix (UK). Smooth and rough lipopolysaccharides (LPS) from *E. coli* strain O111:B4 and Rc mutant, respectively, were from Sigma-Aldrich. Synthetic peptides (LGNY; GVVTSSE) were from CSBio Co (CA, USA). Alexa Fluor® 488 C5 Maleimide, FM1-43X, SYTO9 Green® and Hoechst 33342 were from Thermo Scientific, USA. Other chemicals were from Sigma-Aldrich. Polystyrene bottom plates used for epifluorescence imaging (96-well plates) were from Greiner.

Cloning of Omp-Pst1, Omp-Pst2 and mutants thereof.

Genomic DNA purification kit (QIAGEN, Valencia, CA) was used to isolate chromosomal DNA of *P. stuartii* ATCC 29914. *Omp-pst1* (1125 bp) and *omp-pst2* (1098 bp) genes were amplified by PCR with the following primers: Forward Pst1-XbaI (5'-GTGTCTAGATGTCCGAATAACACCAATG-3'); Reverse Pst1-BamHI (5'-GTTGGATCCCAGATTTCACTGTTGTCTG-3'); Forward Pst2-XbaI (5'-GTGTCTGACACTTAGTTAGTAAATGGC-3'); Reverse Pst2-BamHI (5'-GTTGGATCCGGATAATTGCGTATGATGG-3'). Restriction sites are underlined. 30 cycles of PCR (45 sec. at 94 °C, 30 sec. at 55 °C, and 1 min. at 72 °C) were performed. PCR products were treated with XbaI and BamHI restriction enzymes overnight and ligated into XbaI-BamHI-digested pGOmpF¹ to yield the expression plasmids pGOmpPst1 and pGOmpPst2.

Genesis of porins mutants

Single and double mutants of Omp-Pst1 and Omp-Pst2 (Omp-Pst1-N293G, Omp-Pst1-D213R, Omp-Pst1-D213R/N293R, Omp-Pst1-K221C, Omp-Pst2-N285G, Omp-Pst2-G284R/N285G, Omp-Pst2-G284R/N285K and Omp-Pst2-K211C) were obtained by site-

directed mutagenesis using pGOmp-Pst1 and pGOmp-Pst2 as templates. Briefly, overlapping primers of 30 base pairs containing the desired mutation were designed and used to generate the mutated DNA by PCR. Plasmids were then purified using QIAquick PCR purification kit and the template plasmids were digested using DpnI enzyme. The Gibson assembly technique² was used to generate the L5-loop deletion mutant (Omp-Pst1- Δ 207-216/N293G) using pGOmp-Pst1 N293G as a template. Overlapping primers were designed to amplify the DNA from either sides of the desired deletion sequence. The resulting DNA was then purified after migration on agarose gel using QIAquick Gel extraction kit and ligated using the Gibson assembly mix[®]. The different generated plasmids were transformed into *E. coli DH5 α* cells by heat shock and positive clones were identified by ampicillin selection. Sequences of all mutants were verified by DNA sequencing.

Expression of Omp-Pst1, Omp-Pst2, and mutants thereof

We used heat-shock to transform 1 μ L of plasmids pGOmp-Pst1 or pGOmp-Pst2 (100 ng/ μ L; ampicillin-resistant) into 40 μ L of *E. coli Δ omp8* competent cells (kanamycin-resistant; optical density at 600 nm \sim 0.7)^{1,3}. Cells were then recovered in 500 μ L of SOC medium and incubated for 1 hour at 37 °C. 20 μ L of cell suspension was then transferred onto agar plates and incubated overnight at 37 °C. A colony was introduced in 25 mL of LB media and incubated overnight, yielding a pre-culture that was further diluted into 1 L of LB media culture. During both pre-culture and culture, selection of transformed strains was achieved through the addition of ampicillin and kanamycin at final concentrations of 100 μ g/mL and 25 μ g/mL, respectively. After the optical density of cultures at 600 nm (OD_{600nm}) reached a value of 1, cells were harvested by centrifugation at 4,000 rpm for 20 min. It is noteworthy that the presence of a strong T7-phage promoter on the pGOmp-Pst1 and pGOmp-Pst2 plasmids allows sufficient porin expression without induction by IPTG. The addition of IPTG in fact results in the over-expression of porins as inclusion bodies, thus complicating purification.

Extraction and solubilization of Omp-Pst1, Omp-Pst2 and mutants thereof.

Extraction and solubilization of porins were performed as previously described⁴ with minor modifications. In brief, 5 g of cells were suspended in 20 mM phosphate buffer at pH 7.4, supplemented with DNase (final concentration: 0.15 mU/L) in the presence of 1 mM MgSO₄, and an anti-proteases cocktail (Roche®). Cells were disrupted using a micro-fluidizer at 1,400 Psi (4-5 passes). Non-disrupted cell debris were pelleted and discarded by centrifugation at 6,000 rpm for 15 min. Membranes were collected by subjecting the supernatant to centrifugation at 35,000 rpm for 20 min. Inner-membrane constituents were solubilized by a 1-hour incubation at 20 °C under mild shaking (225 rpm) in buffer complemented with 0.3% octyl-polyoxyethylene (Octyl-POE). A 20 min centrifugation at 35,000 rpm was then performed and the resulting pellet was resuspended and incubated for 1 hour at 20 °C under mild shaking (225 rpm) in buffer complemented with 3% octyl-POE. Outer-membrane proteins were isolated from membrane debris by centrifugation at 35,000 rpm for 20 min. The last solubilization step was performed three times to maximize outer membrane protein recovery. Supernatants containing the solubilized porins were stored at 4°C.

Purification of Omp-Pst1, Omp-Pst2 and mutants thereof.

The purification procedures for Omp-Pst1, Omp-Pst2 and mutants thereof were identical. Briefly, solubilized porins were loaded onto an anionic-exchange column (Hitrap HQ, 5 mL) and subjected to detergent exchange by flushing the column with 0.1 M MES buffer at pH 6.5 complemented with lauryldimethylamine N-oxide (LDAO) at 0.12 % (*i.e.*, ~5.2 times the critical micellar concentration (CMC) in water) and 25 mM NaCl. Elimination of most LPS was achieved by washing the column with 0.1 M MES pH 6.5 buffer complemented with LDAO at 2 % (*i.e.*, ~87 times the CMC in water). After 4 hours of slow washing (0.2 mL/min), the column was re-equilibrated with 0.1 M MES buffer at pH 6.5 complemented with LDAO at 0.12% and 25 mM NaCl. The protein was then eluted by the application of a NaCl gradient. Fractions containing the pure protein were pooled together and concentrated to 7 mg/mL on a 50 kDa cutoff AMICON ultra-filtration unit. NaCl concentration was then adjusted to 150

mM. Protein solutions were stored at 4 °C. Protein purity was estimated to be ca. 95%, based on Coomassie blue and silver-staining SDS-PAGE gels. For both Omp-Pst1 and Omp-Pst2, 5-6 mg of purified protein were obtained per litre of culture. On-column delipidation was crucial to obtain crystal-grade porins. These yet still contained LPS, as revealed by SDS-PAGE gels of purified porins (Figure S12A, B).

Porin labeling

Mutation of conserved K221/K211 (at the base of the L5 loop) into a cysteine enabled Omp-Pst1/Omp-Pst2 labeling with the fluorescent dye maleimide. Indeed, in neither porin is this conserved lysine involved in the structuration of DOTs (Figures S4 and S5). Briefly, the MES buffer of purified Omp-Pst1-K221C and Omp-Pst2-K211C was exchanged for a HEPES buffer containing DTT as a reducing agent (20 mM HEPES pH 7; 150 mM NaCl; 0.12% LDAO; 10 mM DTT) in three steps of dialysis. The DTT was then removed by dialysis and the porins were incubated with 20 fold molar excess of Alexa Fluor® 488 C5 maleimide for 2 h at room temperature. The reaction was then stopped by the addition of 10 mM DTT. Free dye and unreacted DTT were removed by gel filtration. Labeled porins were concentrated to 1 µM and incorporated into large unilamellar liposomes (LUVs) (see details in the next section).

Liposome preparation

LUVs were produced by the standard film-hydration method. In brief, fluorescent liposome mixtures were generated by the addition of 0.02% lissamine-rhodamine-sn-glycero-3-phosphoethanolamine to L- α -phosphatidylcholine (egg PC), palmitoyl-oleyl PC (POPC), palmitoyl-oleyl phosphatidylserine (POPS) or mixtures of these with smooth and rough LPS. The lipids were dried under N₂ flow to obtain a thin lipid film and residual chloroform was eliminated by overnight vacuum. The lipid film was then rehydrated with buffer and vortexed, yielding multilamellar vesicles. The vesicles were freeze-thawed (100 K – 310 K) 20 times to obtain LUVs. Extrusion was then performed to calibrate LUVs with a narrow size distribution (mini-extruder with polycarbonate filters; Avanti Polar Lipids). For the DLS experiments, we

used lipid concentration of 0.125 or 1.25 mg/mL, and a 100 nm filter for extrusion, generating liposomes of ~60 nm radius (see details in the next section). To obtain mixed phospholipid-LPS liposomes, the lipids were dried under N₂ flow until a thin lipid film was obtained, which was then rehydrated by 20 µL of LPS dissolved in 150 mM HEPES pH 7, 150 mM NaCl, 0.12% LDAO. The lipid mixture was then partially dried under N₂ flow and residual chloroform and water were eliminated by overnight vacuum. From there, LPS-containing liposomes were prepared as phospholipid-only liposomes, *i.e.* by re-solubilisation of the lipid film, freeze-thaw of multilamellar vesicles, and extrusion.

Determination of optimal pH to insert porins into LUVs

We used centrifugation on sucrose gradient to examine the proteoliposome aggregates formed by incorporation of 0.01, 0.05, 0.1 and 1 µM Omp-Pst1 and Omp-Pst2 into preformed ~60 nm radius POPC liposomes (lipid concentration: 0.125 mg/mL) at pH 4 and 8. After incorporation of porins, Triton X-100 detergent was added at 0.02% to permeabilize liposomes and 8-anilino-1-naphtalenesulfonic acid (ANS; λ_{ex} 388 nm; λ_{em} 470 nm) was added at 4 µM to reveal porins. The mixture was deposited on a 5-30% sucrose gradient (deposited in decreasing steps of 5%) and centrifuged overnight at 25,000 rpm (TLS 55, Beckman) and at 4 °C, allowing the separation of liposomes, proteoliposomes and porins (Figure S7A-F). To estimate the relative distributions of porins that incorporate in liposomes or precipitate, corresponding layers of the sucrose gradient were isolated, heated 5 min at 90 °C and then subjected to SDS PAGE (12%). These experiments show that the insertion of *P. stuartii* porins into liposomes is favoured at acidic pH (Figure S7G). In sucrose gradient and DLS experiments, we used concentrations of 0.125-1.25 mg/mL lipid, corresponding to ~2-20 nM of 60 nm radius liposomes.

Dynamic Light Scattering

We used dynamic light scattering (DLS, DynaPro Nanostar instrument from Wyatt Technology) to monitor the hydrodynamic radii of liposomes before and after the incorporation of porins (Omp-Pst1, Omp-Pst2, mutants thereof, and *E. coli* OmpF as a

control) into their bilayer, at concentrations ranging from 0.01 to 8 μM . For DLS experiments, we used LUVs (prepared as described above) that had been extruded through a 100 nm polycarbonate filter, yielding an effective starting hydrodynamic radius of ~ 60 nm. Experiments aiming at determining the optimal pH for porin insertion (see next section) and DOT formation, respectively, were performed in phosphate buffer (125 mM). Other experiments on liposomes were performed in 150 mM HEPES buffer pH 7, 150 mM NaCl. Porin insertion into LUVs was achieved by a direct approach, where dilution of detergent-solubilized porins at a final concentration below the CMC of the detergent results in either their insertion into LUV bilayers, or their precipitation (see previous section). With this method, the orientation of the incorporated protein in the bilayer depends on the relative size of hydrophilic segments harboured on its two sides. In the case of porins, extracellular loops are large and well folded, whereas intracellular turns are short (4-6 amino-acids). Thus, porins are most likely oriented in LUVs in the natural way, *i.e.* with their intracellular turns facing the lumen of the LUV, and the extracellular loops facing the outside⁵. In DLS experiments, measured hydrodynamic radii started increasing immediately after the incorporation of Omp-Pst1 and Omp-Pst2 into LUVs, but continued to evolve overnight; results reported herein are following 24 h of incubation at 4 $^{\circ}\text{C}$, and with or without further detergent removal by addition of biobeads (24 h, 4 $^{\circ}\text{C}$). Insertion of *E. coli* OmpF into LUVs yielded comparatively smaller proteoliposome aggregates. In the various liposome experiments, the final LDAO concentrations were 0.004-0.02 % and 0.0026-0.02 % for Omp-Pst1 and Omp-Pst2, respectively, corresponding to concentrations 17 fold lower (experiments at 0.125 mg/mL lipid) to one time (experiments at 1.25 mg/mL lipid) the detergent CMC (0.023 %). Controls established that in absence of porins, LUVs remain unaffected in size up to a concentration of 0.04 % LDAO (*i.e.* ~ 2 times the CMC), after what they degrade leading to a decrease in the measured hydrodynamic radii – not an increase (Figure S13A).

We further verified that the observed proteoliposome aggregation was not an effect of the detergent, by both performing control experiments in the presence of the same amount of detergent (liposomes without porins), and by measuring hydrodynamic radii before and after addition of biobeads (Figure S10). In the latter case, porins and liposomes were mixed and incubated at pH 7 (higher stringency) for 24 h before a first DLS measure was taken, after what biobeads were added and another DLS measure was taken 24 h later. We obtained similar results for Omp-Pst1, Omp-Pst2 and OmpF before and after detergent removal, demonstrating that porin-induced proteoliposome aggregation does not depend on the detergent. Additionally, smaller proteoliposome aggregates form when higher concentrations of liposomes are used (Figures S10 and S11 show data at 0.125 and 1.25 mg/mL lipid, corresponding to ~2 and ~20 nM of 60 nm radius liposomes), supporting the hypothesis that proteoliposome aggregation depends on the number of porins inserted per liposome. Furthermore, we found that at concentration two to hundreds of times higher than used in our study, the detergent effects in reducing the size of liposomes (Figure S13A), when to the contrary, porin incorporation triggers proteoliposome aggregation (Figures 3, S8, S10 and S11). Hence, data support that the observed proteoliposomes aggregation does not result from, nor depend on, the presence of the detergent.

We then tested the influence of substituting the phosphatidylcholine head-group (POPC) by a phosphatidylserine (POPS) (Figure S11). We found that the strong electrostatic repulsion between negatively-charged POPS liposomes inhibits self-association, requiring porin concentrations as high as 2 μ M for a modest proteoliposome aggregation to become visible (as assessed by a doubling of the hydrodynamic radius). Omp-Pst1 and Omp-Pst2 co-purify with their own LPS, as revealed by SDS-PAGE gels (Figure S12). We investigated the effect of adding more rough or smooth LPS to the bilayer composition; rough and smooth LPS both possess core oligosaccharides and lipid A, but only smooth LPS feature O-antigens. We examined POPC-LPS and POPS-LPS liposomes produced at LPS-to-phospholipid mass ratio of 1:10 (Figure S10C, D) and 1:100 (Figure S11C-F), at respectively 1.25 and 0.125

mg/mL total lipid concentration. Hence, the LPS-to-porin ratio was comparable in both experiments. Rough LPS had no effect on Omp-Pst1 self-association (Figures. S10C-F and S11C, D), whereas an inhibitory effect was observed for smooth LPS (Figures. S10I, J and S11E, F). This effect was subtle at added LPS-to-phospholipid mass ratio of 1:100 (Figure. S11E, F), but total at a ratio of 1:10 (Figure. S10I, J). In the case of Omp-Pst2, both rough and smooth LPS displayed an inhibitory effect on porin self-association (Figure. S10C-J and S11A, C, E). By analogy to POPS liposomes (Figure. S11B, D, F), we propose that smooth LPS exert their inhibitory effect on Omp-Pst1 and Omp-Pst2 self-association through electrostatic repulsion between their negatively-charged O-antigens.

We introduced earlier that the most common habitat of *P. stuartii* in humans is the urinary tract. Hence, we also sought to determine whether high concentrations of urine components such as urea, NH₄Cl and NaCl, are compatible with the self-association of Omp-Pst1 and Omp-Pst2. As a reference chaotrope, we used sodium thiocyanate (NaSCN). None of these compounds affect the trimeric structure of Omp-Pst1 and Omp-Pst2 (Figure. S3B). All DLS experiments were performed at pH 7, using porin and effector concentrations of 1 μM and 1 M, respectively. We found that all four effectors inhibit Omp-Pst1 self-association at such high concentrations, yet each to a different extent: urea is the least efficient at disrupting Omp-Pst1 self-association, whereas NaSCN and ammonium chloride are equally efficient (Figure. S10E-J). By contrast, Omp-Pst2 self-association is challenged by urea, but NH₄Cl promotes it. No significant effect on Omp-Pst2 self-association is observed upon addition of NaCl and NaSCN (Figure. S10E-J). The presence of LPS changes these patterns for Omp-Pst1, restoring self-association in the presence of NaCl, although still inhibiting Omp-Pst2 self-association.

DLS was also used to measure dissociation constants for Omp-Pst1 and Omp-Pst2 DOTs. Hydrodynamic radii of solubilized porins were measured in triplicate, in the 0.01-8 μM concentration range. Observed values spanned from $\sim 3.9 \pm 0.3$ to 6.3 ± 0.5 nm for both Omp-Pst1 and Omp-Pst2, significantly exceeding predicted radii of gyration of 3.0 and 4.3 for

nude (no LDAO molecules) trimers and DOTs, respectively. The measured hydrodynamic radius of isolated LDAO micelles was 3.07 ± 0.8 nm in a 0.12% solution buffered at pH 7 by 150 mM HEPES and containing 150 mM NaCl. Hence, LDAO solubilized porin trimers and LDAO micelles commensurate in hydrodynamic radii in our buffered solution, and the apparition of Omp-Pst1 and Omp-Pst2 species with hydrodynamic radii of $\sim 6.3 \pm 0.71$ nm and 5.95 ± 0.49 nm, respectively, can be ascribed to the apparition of DOTs. Fitting of the DLS data suggests dissociation constants of 0.6 and 0.4 μ M for Omp-Pst1 and Omp-Pst2 at pH 7, respectively (Figure. S13B).

Crystallization

Screening of crystallization conditions was performed at the HTX-Lab of the PSB (IBS, ESRF, ILL, EMBL) using a Cartesian PixSys 4200 crystallization robot (Genomic Solutions, U.K.) and commercial screens from Hampton and Qiagen. Screening was carried out at the nL scale using the hanging-drop vapour-diffusion method. Several conditions yielded poorly or non-diffracting crystals. Manual screening around these conditions was thus performed using the sitting-drop vapour-diffusion method, yielding diffraction-grade crystals after a few days to a few weeks. The protein (or peptide) to mother liquor ratio was 1:1. Mother liquor solutions were: i/ 14% PEG6000 MME, 0.1 M MES pH 6.5, 0.1 M $MgCl_2$ for Omp-Pst1 (both types of crystals); ii/ 8% PEG 6000, 0.1 M TRIS pH 8, 1 M lithium chloride for Omp-Pst2; iii/ 25% PEG 600, 0.2 M NaCl, 0.1 M MES pH 6.5 for Omp-Pst1- Δ 207-216/N293G; iv/ 3.2 M ammonium sulfate, 0.1 M sodium citrate pH 4 for 283-LGNY-286; v/ 2.5 M ammonium sulfate, 0.1 M sodium citrate pH 4 for 206-GVVTSE-211. Omp-Pst1, Omp-Pst2 and Omp-Pst1- Δ 207-216/N293G were crystallized at 4 °C at a concentration of 7 mg/mL, while 283-LGNY-286 and 206-GVVTSE-211 crystallized at 20 °C at a concentration of 8 mg/mL. The micro-needle crystals formed by 283-LGNY-286 diffracted reproducibly between 0.8 and 1.5 Å, while those of 206-GVVTSE-211 diffracted between 1.5 and 2 Å. Crystals of porins were however very soft in nature and only 2-5 % of crystals diffracted to a resolution better than

3.5 Å. The complex with maltose was obtained by soaking crystals for 24 h in a mother liquor solution complemented with maltose at 100 mM.

X-ray data collection and processing

Crystals of Omp-Pst1, Omp-Pst1- Δ 207-216/N293G and Omp-Pst2 were soaked for 30 sec. in mother liquor solutions containing 18% of glycerol, mounted in a cryo-loop and flash-cooled in a nitrogen stream at 100 K. X-ray Data were collected at the European Synchrotron Radiation Facility (ESRF) on beamLines ID14-EH4 (Omp-Pst1 type-A and Omp-Pst2), ID23-EH1 (Omp-Pst1 native type-B crystal), ID29 (Omp-Pst1 type-B crystal soaked with maltose) and ID30-B (Omp-Pst1- Δ 207-216/N293G). Micro-crystalline needles of 283-LGNY-286 and 206-GVVTSE-211 were mounted on pulled glass-capillaries and directly flashcooled in the nitrogen gas stream at 100 K, without cryo-protection. Microcrystallographic data were collected on ESRF beamLine ID23-EH2 using a transmission of 100% and a beamsize of $5 \times 7 \mu\text{m}^2$ ($\lambda=0.87 \text{ \AA}$). All data were processed, merged and scaled using XDS/XSCALE and amplitude factors were generated using XDSCONV⁶.

Structure determination and refinement

Omp-Pst1, Omp-Pst1- Δ 207-216/N293G and Omp-Pst2 X-ray data were phased by molecular replacement using PHASER⁷. For Omp-Pst1 type-A, a homology model based on the X-ray structure of OmpF (PDB access code: 1OPF) was used as the search model. For Omp-Pst2, a homology model based on the X-ray structure of Omp-Pst1 was used as the search model. Homology modelling was performed using MODELLER⁸. After reconstruction of Omp-Pst1 structure from type A crystals, we used this structure to phase data from Omp-Pst1 type-B and Omp-Pst1- Δ 207-216/N293G crystals. For Omp-Pst1- Δ 207-216/N293G, phasing by molecular replacement required using as a search model the structure of Omp-Pst1 devoid of the L5 β -hairpin. The asymmetric unit of Omp-Pst2 features a dimer of trimers (DOT), within which trimers are related by non-crystallographic symmetry. The asymmetric units of type-A Omp-Pst1 and Omp-Pst1- Δ 207-216/N293G feature a trimer, and the DOT is formed by crystallographic symmetry. The asymmetric unit of type-B Omp-Pst1 crystals features a

trimer, which establishes side-by-side contact with symmetry related trimers. In all three structures, all residues are visible in the electron density maps.

The structure of 206-GVVTSE-211 was solved by molecular replacement with PHASER, using the corresponding segment from the Omp-Pst1 structure as a starting model. The structure of 283-LGNY-286 could not be solved by molecular replacement owing to the low contrast originating from the low solvent content (<15%) and the failure to find an appropriate model; 283-LGNY-286 is indeed the first symmetry class-III steric zipper to be characterized in the amyloid state. The sub-atomic resolution of the 283-LGNY-286 data nevertheless allowed phasing by direct methods, using SHELXD and SHELXL⁹.

For all structures, diffraction data from 20 Å to the highest resolution limits were used for refinement and maps were calculated using all data between 15 Å and the highest resolution limits. Graphic operations, modelling and model building were performed with COOT¹⁰. Energy minimization and individual B-factor refinement followed each stage of manual rebuilding. Refinement and map calculations were performed using PHENIX¹¹ or REFMAC¹². Specific to the structure of 206-GVVTSE-211, we had to perform refinement in the presence of multiple twin operators, which only REFMAC could allow. Ensemble refinement was performed using *phenix.ensemble_refinement*¹³. Polder omit maps were calculated using *phenix.polder*¹⁴. Figures were generated using PyMOL (The PyMOL Molecular Graphics System, Version 1.8 Schrödinger, LLC). For electrostatic surface potential calculation, PDB2PQR and PROPKA were used to assign hydrogens at pH 7.4 (AMBER force field)¹⁵, APBS was used to solve the non-linear Poisson-Boltzmann equation and surface representations were produced in PyMOL using the APBS plug-in written by Dr. Michael Lerner (<http://pymolwiki.org/index.php/User:Mglerner>). Channel topographies, effective radii and electrostatic potentials associated to the translocation of a proton were calculated using HOLE¹⁶ and the protonated structures produced by PDB2PQR. For calculations on OmpF, OmpC and PhoE, we used structures deposited in the wwPDB under accession codes 1opf, 2j1n and 2por, respectively. The propensity to form steric zippers of Omp-Pst1 and Omp-

Pst2 hexapeptide segments were predicted using the ZipperDB (<http://services.mbi.ucla.edu/zipperdb/>)^{17,18} and mapped onto the ribbon diagrams of Omp-Pst1 and Omp-Pst2 using a python script kindly provided by Dr. Arthur Laganowsky. Details on data collection and refinement statistics are given in Table S1.

Bacterial growth studies.

P. stuartii and *E. coli*ΔOmp8 transformants were grown in LB growth medium. For each experiment, a single bacterial colony was inoculated in standard LB medium for 2 h, allowing to start with cells in their lag phase. Bacteria were then distributed into a 96-well plates and incubated at 37 °C under 100 rpm shaking overnight to grow (and potentially form biofilms) on the well-surface. Bacterial growth was monitored in terms of absorbance at 600 nm for 24 h (10 minutes interval between time points) using a Biotek Synergy H4 microplate reader (Winooski, VT, USA).

Total RNA extraction & qRT-PCR.

We used the same protocol to monitor the relative expressions of Omp-Pst1 and Omp-Pst2 in *P. stuartii* ATCC 29914 and *E. coli* ΔOmp8 expressing Omp-Pst1 or Omp-Pst2. Briefly, one colony was added to 10 mL of LB medium and incubated at 37 °C for 1 h under 150 rpm agitation. For each strain, three wells (triplicates) of a 6-well plate (CytoOne) were filled with 2 mL from the LB pre-culture. Plates were incubated overnight at 37 °C under 50 rpm agitation. The culture was then collected, briefly centrifuged to pellet the bacteria without damaging them, and the pellet was then re-suspended in 1 mL of fresh LB medium and incubated at 37 °C for 1 h under 50 rpm agitation. One mL of RNeasy Protect Cell Reagent (Qiagen) was directly added to the culture and the mix underwent vigorous mixing. After 5 min. incubation, the mixture was centrifuged at 5,000 g for 10 min. before the pellet was re-suspended in 110 μL of TE buffer (Tris-HCl 30 mM, EDTA 1mM, pH 8.0) containing 15 mg/mL of lysozyme and 6 mAU of Proteinase K (Qiagen) and incubated at RT for 10 min. Total RNA was then extracted by using the RNeasy Mini Kit (Qiagen) following manufacturer's instructions with minor modifications; specifically, β-mercaptoethanol (1%

final) was added to RLT[®] buffer to maximize RNA recovery and the elution was performed in 40 µL of RNase-free water (two rounds of elution with 20 µL) after 5 min. incubation at 4 °C before centrifugation. Quantity and quality of RNA was assessed using a Nanodrop2000 (Thermo Fisher Scientific). RNA was immediately used for reverse transcription and the remaining RNA was stored at -80 °C. For each triplicate from each strain, 1 µg of total RNA was retro-transcribed into cDNA by using the QuantiTect Reverse Transcription Kit (Qiagen) following manufacturer's instructions. cDNA was stored at -20 °C until use.

Expression of *omp-pst1* and *omp-pst2* was quantified by qRT-PCR. *P. stuartii* genomic DNA was extracted using NucleoSpin Tissue kit (Macherey-Nagel) following manufacturer's instructions and it was used for porin genes amplification for the standard curve. A 954 bp fragment of *omp-pst1* gene was amplified using the primers OmpPst1_F3qs (5'-GAAGATGGCGACGACTCACG-3') and OmpPst1_R3qs (5'-GTAAACCAGACCCAGACCCAGAAC-3') and a 956 bp fragment of *omp-pst2* gene was amplified using the primers OmpPst2_F4qs (5'-ATTATTCGCGGCGGGTGTAC-3') and OmpPst2_R4qs (5'-CAGCGCCATATTCTTGTGA-3'). Q5 High-Fidelity DNA Polymerase (New England BioLabs) was used for its low error rate. The PCR program consisted in an initial step at 98 °C for 5 min., then 35 cycles of 98 °C for 30 sec. (denaturation), 55 °C for 30 sec. (primers annealing) and 72 °C for 2 min. (elongation) and ended by a final extension step at 72 °C for 5 min. PCR amplicons were visualized on a 1.2% agarose gel using SYBR Safe (Thermo Fisher Scientific). For each gene, the band corresponding to the amplicon was excised from the gel and purified using NucleoSpin Gel and PCR Clean-up kit (Macherey-Nagel) following manufacturer's instructions. Quality and quantity were measured using a Nanodrop2000 (Thermo Fisher Scientific). Based on the sequence composition and length of each porin fragment amplified, the number of copies present in the standard was calculated and the standard curve was established using seven concentrations from 5.0×10^1 to 5.0×10^7 gene copies.

For the quantitative PCR, a 77 bp fragment of *omp-pst1* gene was amplified using the primers OmpPst1_F1q (5'-CGCATTCGGTTATGTTGAT-3') and OmpPst1_R1q (5'-CGCTTGACTTGTTGTTGT-3') and a 82 bp fragment of *omp-pst2* gene was amplified using the primers OmpPst2_F2q (5'-CTTCGCTCTACAGTACCA-3') and OmpPst2_R2s (5'-GCCATCACCATTGTTATCTAA-3'). The reaction consisted in 4 μ L of tenfold-diluted samples or of the standards, 0.6 μ L of each primer (final concentration of 10 μ M each), 7 μ L of SoAdvanced Universal SYBR Green Supermix (Bio-Rad) and RNase-free water for a final reaction volume of 15 μ L in each well. For each biological triplicate of each strain, two technical replicates were done. qPCR was run on a CFX Connect Real-Time PCR Detection System (Bio-Rad). The qPCR program consisted in an initial step at 95 °C for 3 min., then 39 cycles of 95 °C for 10 sec. (denaturation) and 60 °C (*omp-pst1*) or 59 °C (*omp-pst2*) for 45 sec. (primers annealing & elongation). A melt curve analysis was performed to assess the specificity of the amplification. The number of transcript copies of *omp-pst1* and *omp-pst2* was calculated using the standard curves for *P. stuartii* ATCC 29914, *E. coli* Δ Omp8 + Omp-Pst1 and *E. coli* Δ Omp8 + Omp-Pst2 by using Bio-Rad CFX Manager v.3.1 (Bio-Rad). The standard curves were of high quality for both *omp-pst1* (Efficacy = 96.7%; R^2 = 0.999; Slope = -3.403; y-intercept = 36.187) and *omp-pst2* (Efficacy = 103.5%; R^2 = 0.994; Slope = -3.241; y-intercept = 35.397).

Epifluorescence microscopy

Epifluorescence microscopy experiments were performed on an IX81 Olympus inverted microscope; samples were magnified through a 60X objective (Plan APON60XO, Olympus). LUVs containing the fluorescent lipid lissamine-rhodamine-sn-glycero-3-phosphoethanolamine (excitation: 557 nm; emission: 571 nm) were prepared as described above. Experiments were conducted following the introduction of 5 μ L LUV solutions onto microscopic cover-slides coated with 2% agarose dehydrated film. Porin-mediated proteo-LUV aggregation was imaged after the incubation of LUV with the different porins at 1 μ M for 24 h.

Experiments on bacteria were performed using the same microscope. DNA was labeled using the cell-permeant dye Hoechst 33342 (361 nm excitation; 486 nm emission) at 5 µg/mL, membranes were labeled using FM 1-43X dye at 4 µg/mL (479 nm excitation; emission: 598 nm emission), living bacteria were labeled using Syto® 9 Green (485 nm excitation; 498 nm emission) at 5 µM, and dead bacteria were labeled with propidium iodide at 20 µM (533 nm excitation; 617 nm emission). Fluorescence images sequentially recorded on the blue and green channels, or on the green and red channels, were used for overlays. For biofilm imaging, a single fresh bacterial colony was inoculated in 5 mL of LB media and incubated 2 h at 37 °C, before distribution of cells into 96-well plates for a further overnight growth at 37 °C. 10 µL of the planktonic bacteria were collected and spread in the interstice between LB-Gelzan solid media (LB-Lennox solidified with 8 g/L Gelzan™) and a glass cover-slide¹⁹ and imaged immediately afterwards. The wells were then extensively washed by PBS, allowing the removal of all floating bacteria and to image cells tightly attached to the well surface – *i.e.* biofilm core cells²⁰.

Electron microscopy

Transmission electron microscopy (TEM) was performed to visualize the ultrastructure of proteoliposome aggregates formed at 2 µM porin during DLS experiments (see DLS section). Experiments were performed at pH 7. Samples were negatively stained using the mica floatation technique. Briefly, 4 µL of the proteoliposome mixture were adsorbed on the clean side of a carbon film on a mica sheet (carbon/mica interface). After 30 seconds, negative staining was performed with 2% (w/v) uranyl acetate (pH 4.5).

TEM was also used to image *P. stuartii* floating communities of cells (Figure 5B). *P. stuartii* cells were grown overnight to an optical density > 1 at 600 nm (OD^{600nm}), fixated by addition of paraformaldehyde and glutaraldehyde at 2 and 0.2 % final concentration, respectively, and then 10 µL of fixated cells were deposited on an electron microscopy grid. After allowing sedimentation for 30 min, the grid was rinsed three times with water without blotting. Negative staining of the sample was then performed with phosphotungstic acid (30 s. before

blotting of excess volume). We used a slightly different protocol to obtain the high resolution electron micrograph shown in Fig. 5C. Briefly, *P. stuartii* cells were grown overnight to an optical density of > 1 at 600 nm (OD^{600nm}), diluted to an OD^{600nm} of 0.1. Twenty microliters of diluted cells were deposited on LB-agar media, incubated for 1 h at 37 °C, before adding an electron microscopy grid atop of them, in contact with the liquid medium. Plates were incubated for 3 h at 37 °C. EM grids were then removed gently, washed 6 times with a drop of sterile water and subjected to negative staining with 2% (w/v) sodium silicotungstate.

Images were taken under low-dose conditions with a CM12 and Tecnai 12 LaB6 electron microscope working at 120 kV and with nominal magnifications of 11000, 23000 X and 49000X using an Orius TM SC1000 CCD camera from Gatan. Calibrated Fourier transforms of the images were performed with the software ImageJ (<http://rsb.info.nih.gov/ij/>).

References:

1. Prilipov, A., Phale, P. S., Van Gelder, P., Rosenbusch, J. P. & Koebnik, R. Coupling site-directed mutagenesis with high-level expression: large scale production of mutant porins from *E. coli*. *FEMS Microbiol. Lett.* **163**, 65–72 (1998).
2. Gibson, D. G. *et al.* Enzymatic assembly of DNA molecules up to several hundred kilobases. *Nat. Methods* **6**, 343–345 (2009).
3. Tran, Q.-T. *et al.* Implication of Porins in β -Lactam Resistance of *Providencia stuartii*. *J. Biol. Chem.* **285**, 32273–32281 (2010).
4. Garavito, R. M. & Rosenbusch, J. P. Isolation and crystallization of bacterial porin. *Methods Enzymol.* **125**, 309–328 (1986).
5. Zgurskaya, H. I. & Nikaido, H. Bypassing the periplasm: reconstitution of the AcrAB multidrug efflux pump of *Escherichia coli*. *Proc. Natl. Acad. Sci. U. S. A.* **96**, 7190–7195 (1999).
6. Kabsch, W. Automatic processing of rotation diffraction data from crystals of initially unknown symmetry and cell constants. *J. Appl. Crystallogr.* **26**, 795–800 (1993).

-
7. McCoy, A. J. *et al.* Phaser crystallographic software. *J. Appl. Crystallogr.* **40**, 658–674 (2007).
 8. Sali, A., Potterton, L., Yuan, F., van Vlijmen, H. & Karplus, M. Evaluation of comparative protein modeling by MODELLER. *Proteins* **23**, 318–326 (1995).
 9. Sheldrick, G. M. Experimental phasing with SHELXC/D/E: combining chain tracing with density modification. *Acta Crystallogr. D Biol. Crystallogr.* **66**, 479–485 (2010).
 10. Emsley, P. & Cowtan, K. Coot: model-building tools for molecular graphics. *Acta Crystallogr. D Biol. Crystallogr.* **60**, 2126–2132 (2004).
 11. Adams, P. D. *et al.* PHENIX: a comprehensive Python-based system for macromolecular structure solution. *Acta Crystallogr. D Biol. Crystallogr.* **66**, 213–221 (2010).
 12. Murshudov, G. N. *et al.* REFMAC5 for the refinement of macromolecular crystal structures. *Acta Crystallogr. D Biol. Crystallogr.* **67**, 355–367 (2011).
 13. Burnley, B. T., Afonine, P. V., Adams, P. D. & Gros, P. Modelling dynamics in protein crystal structures by ensemble refinement. *eLife* **1**, e00311 (2012).
 14. Liebschner, D. *et al.* Polder maps: improving OMIT maps by excluding bulk solvent. *Acta Crystallogr. Sect. Struct. Biol.* **73**, 148–157 (2017).
 15. Unni, S. *et al.* Web servers and services for electrostatics calculations with APBS and PDB2PQR. *J. Comput. Chem.* **32**, 1488–1491 (2011).
 16. Smart, O. S., Neduvellil, J. G., Wang, X., Wallace, B. A. & Sansom, M. S. HOLE: a program for the analysis of the pore dimensions of ion channel structural models. *J. Mol. Graph.* **14**, 354–360, 376 (1996).
 17. Goldschmidt, L., Teng, P. K., Riek, R. & Eisenberg, D. Identifying the amyloids, proteins capable of forming amyloid-like fibrils. *Proc. Natl. Acad. Sci. U. S. A.* **107**, 3487–3492 (2010).
 18. Thompson, M. J. *et al.* The 3D profile method for identifying fibril-forming segments of proteins. *Proc. Natl. Acad. Sci. U. S. A.* **103**, 4074–4078 (2006).

19. de Jong, I. G., Beilharz, K., Kuipers, O. P. & Veening, J.-W. Live Cell Imaging of *Bacillus subtilis* and *Streptococcus pneumoniae* using Automated Time-lapse Microscopy. *J. Vis. Exp. JoVE* (2011). doi:10.3791/3145
20. Khatib, M. E. *et al.* *Providencia stuartii* form biofilms and floating communities of cells that display high resistance to environmental insults. *PLOS ONE* **12**, e0174213 (2017).

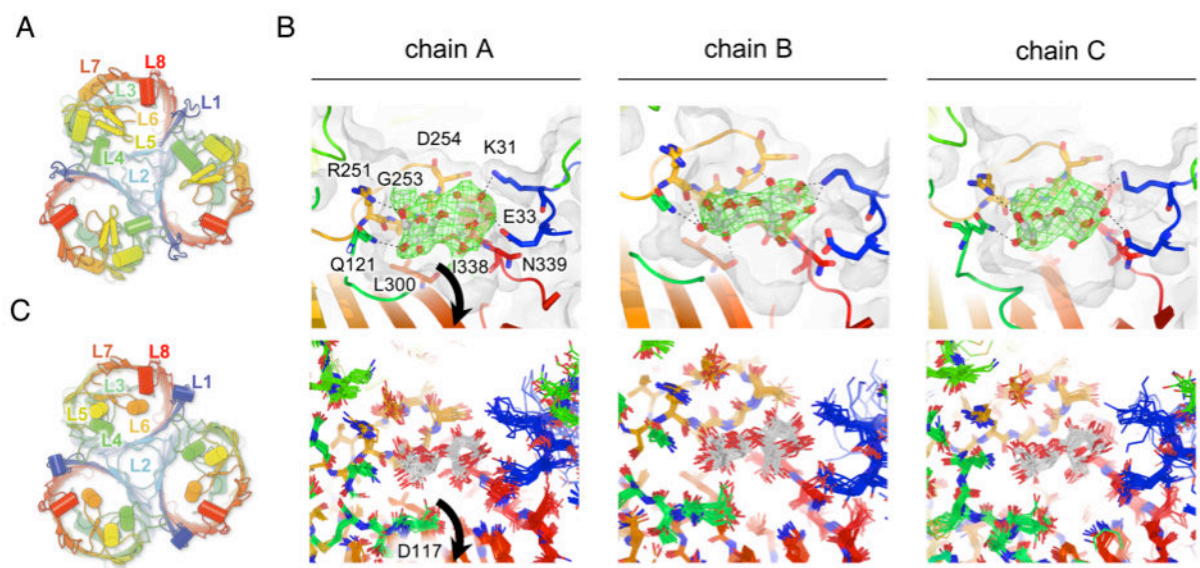


Figure S1 | Location of the maltose binding site of Omp-Pst1 and extracellular topology of the Omp-Pst1 and Omp-Pst2 trimers. (A) Ribbon diagram of Omp-Pst1 coloured sequence-wise, from cold (N-ter) to hot (C-ter) colours. Extracellular loops L1 to L8 are labeled. As in all general-diffusion porins, L2 cements subunits into a trimer, whereas L3 folds into the channel lumen contributing a constriction zone at mid-height. In Omp-Pst1, extracellular loops are mostly folded as α -helices. Nevertheless, L5 folds as a β -hairpin, which is involved in the DOT formation. (B) Residues from extracellular loops L1 and L6-L8 contribute a binding site for maltose, in the extracellular vestibule. The upper panels show, for each monomer in the asymmetric unit trimer, the refined position of maltose (balls and sticks) and residues that contribute to the binding site (sticks). A polder omit map for maltose atoms is shown, contoured at $+3\sigma$. H-bonds (2.5-3.2 Å distance) between maltose molecules and Omp-Pst1 residues are highlighted as black dashes. The lower panel shows a modelisation of maltose dynamics at its binding position, obtained by means of ensemble refinement. Maltose appears stable at its binding position. In all panels, the arrow indicates the way down the channel, towards the constriction zone and the periplasmic side. L3 residue D117, positioned at the interface between the maltose binding site and the constriction zone, displays increased structural dynamics in the complex structure. (C) Equivalent to panel A for Omp-Pst2. Apart from L2 and L7, respectively involved in trimer and DOT formation, all extracellular loops are folded as α -helices.

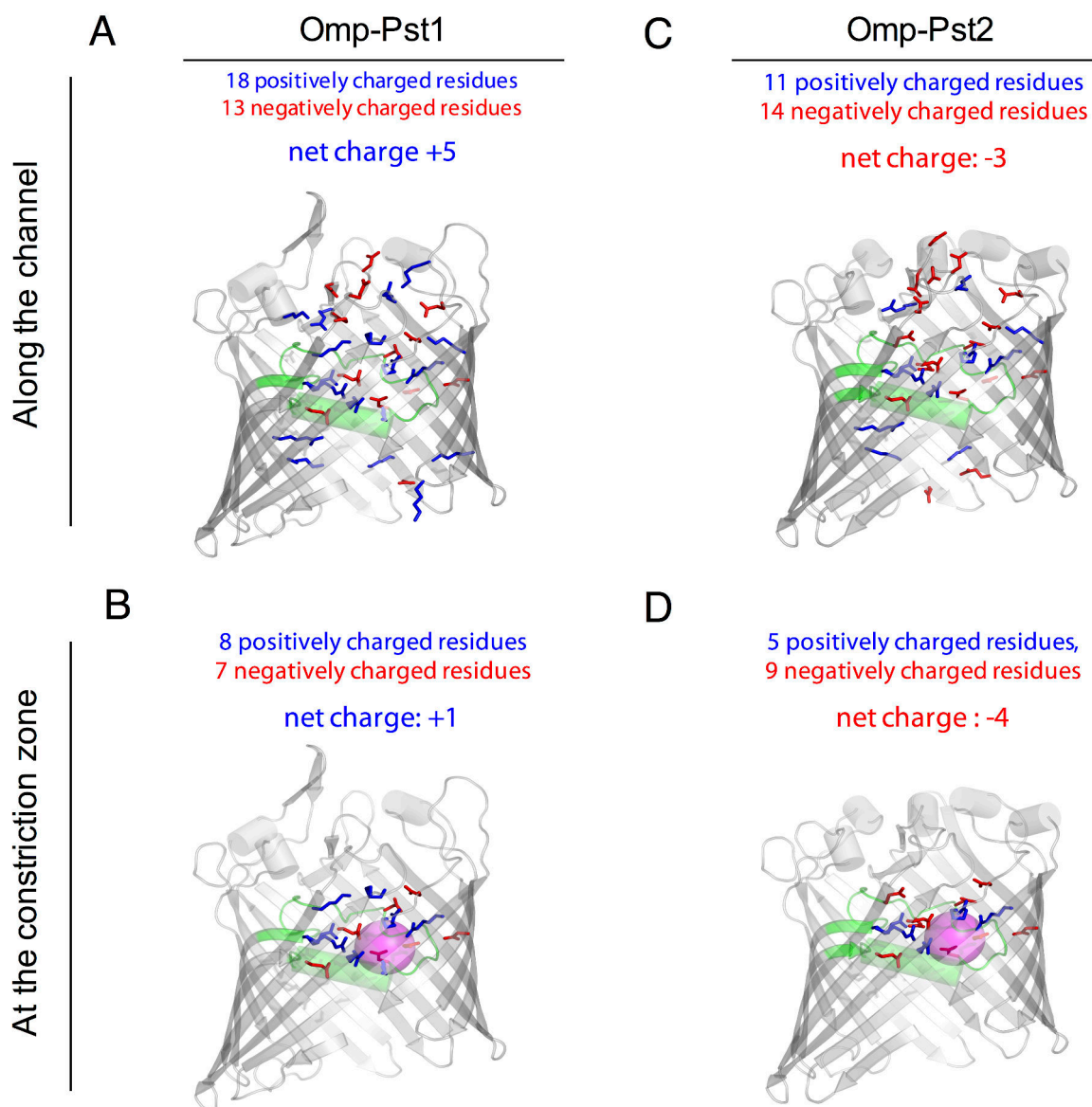


Figure S2 | Distribution of charged residues along Omp-Pst1 and Omp-Pst2 channels. (A, C) Distribution of charged amino-acids along the channel of Omp-Pst1 (A) and Omp-Pst2 (C). (B, D) Distribution of charged amino-acids within a 5 Å radius of the constriction zone of Omp-Pst1 (B) and Omp-Pst2 (D). The magenta sphere is centred at, and has the radius of, the constriction zone in Omp-Pst1 (B) and Omp-Pst2 (D), respectively.

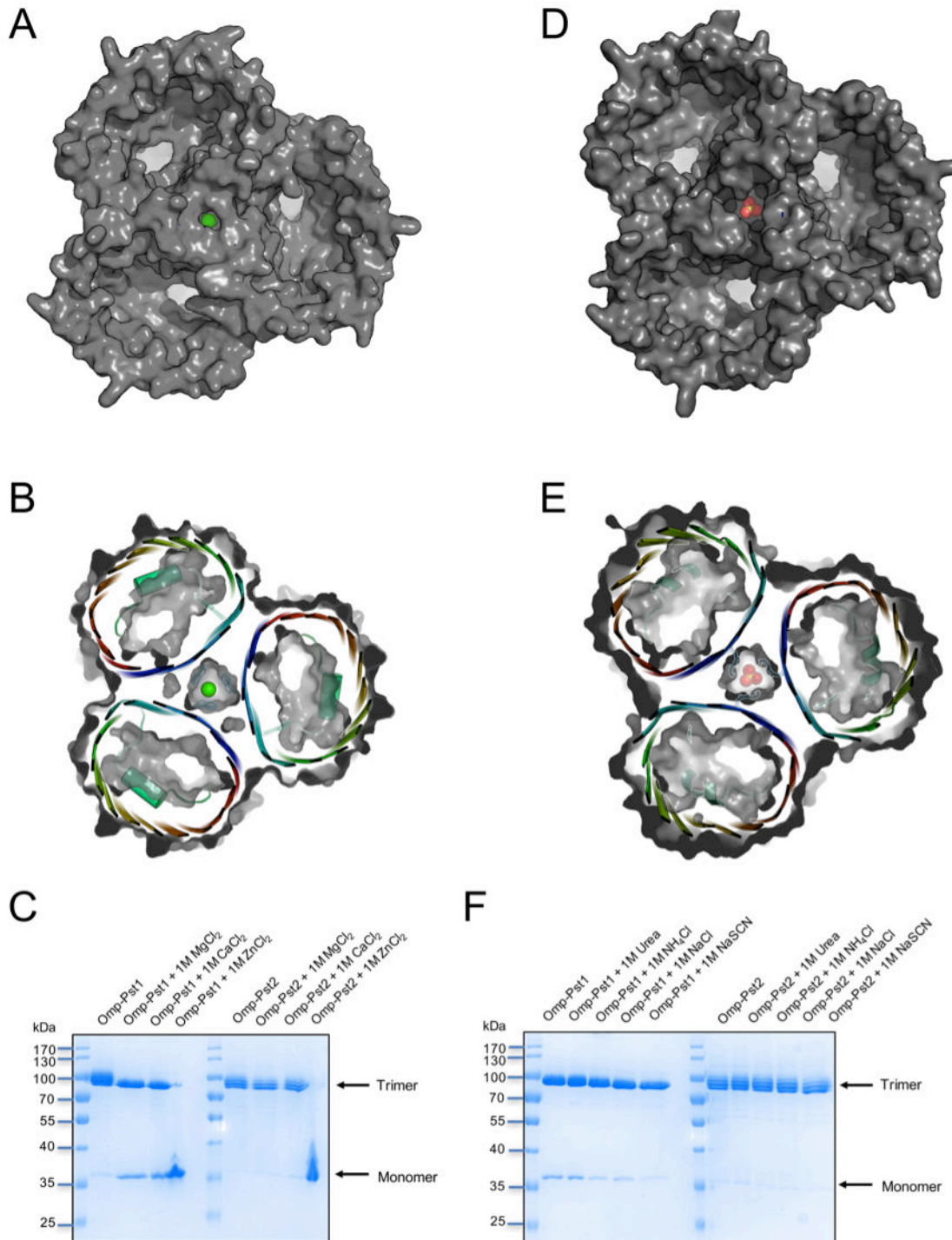


Figure S3 | Omp-Pst1 and Omp-Pst2 trimers feature a fourth central channel. (A, B, D, E) In both Omp-Pst1 and Omp-Pst2, an ion is observed in the interfacial cavity between the three monomers in a trimer. These ions (Ca^{2+} in Omp-Pst1; SO_4^{2-} in Omp-Pst2) are shown as spheres, overlaid on the molecular surface of Omp-Pst1 (A, B) and Omp-Pst2 (D, E). The central cavities are opened to the intracellular side (B, E), but closed at the other side (A, D). (C, F) Commassie-blue stained SDS-PAGE gels of non-denaturated (no heating to 95°C) purified Omp-Pst1 and Omp-Pst2 in the absence and presence of divalent cations (C), salts and chaotropes (F). The gels show that in non-denaturing conditions, Omp-Pst1 and Omp-Pst2 trimers remain intact, even in the presence of chaotropes such as urea and NaSCN. Only Zn^{2+} affects the oligomeric state of the two porins, presumably by substitution of the divalent ion present in their interfacial cavities.

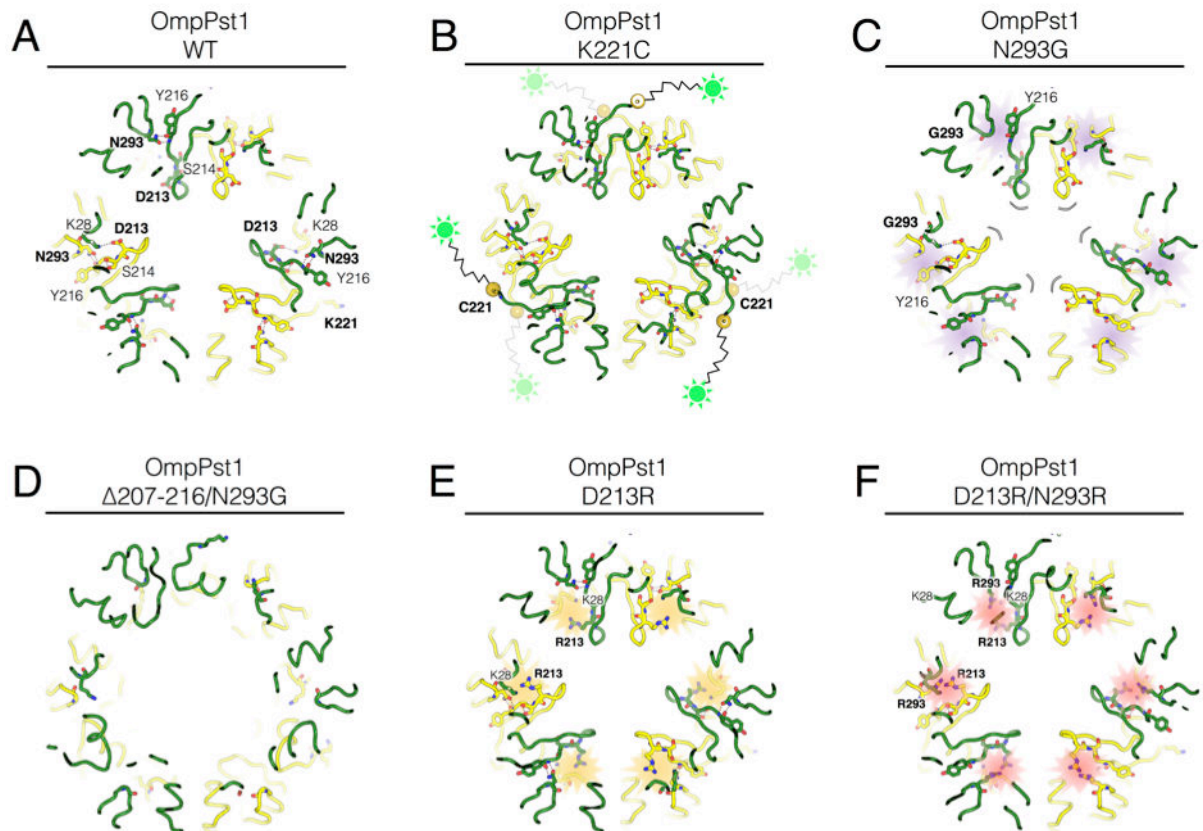


Figure S4 | Contacts in the Omp-Pst1 DOT and mutation strategy. (A) The Omp-Pst1 DOT is mainly stabilized by steric zipper interaction between L5 loops. Only H-bonds (red dashes) between the side chains of K28 and D213 from facing monomers complement the interface. In each monomer, the L5 loop folds as a β -hairpin, stabilized by two H-bonds between Y216 main chain and N293 side chain atoms. D213 is found at the tip of the L5 β -hairpin. K221, at its C-terminal end, shows non-involvement in the DOT formation. (B) Omp-Pst1 was specifically labeled with a maleimide coupled fluorophore after engineering a cysteine at the position 221 (Omp-Pst1-K221C). (C) Mutation of N293 into a glycine (Omp-Pst1-N293G) is expected to result in unfolding of the L5 β -hairpin, due to the loss of the two H-bonds contributed by N293 side chain, which anchored L5 at the surface of the protein. (D) Deletion of the full L5 β -hairpin (OmpPst1- Δ 207-216/N293G) is expected to result in reduced Omp-Pst1 self-association, if steric zipper formation is the driving force for this process. Otherwise, another driving force is at play and the steric zipper interface only contributes to specificity. (E) Mutation of D213 into an arginine (OmpPst1-D213R) is expected to induce electrostatic repulsion between the two facing trimers, owing to the close distance to K28. (F) The additional mutation of N293 into an arginine (OmpPst1-D213R/N293R) should completely abolish the DOT formation.

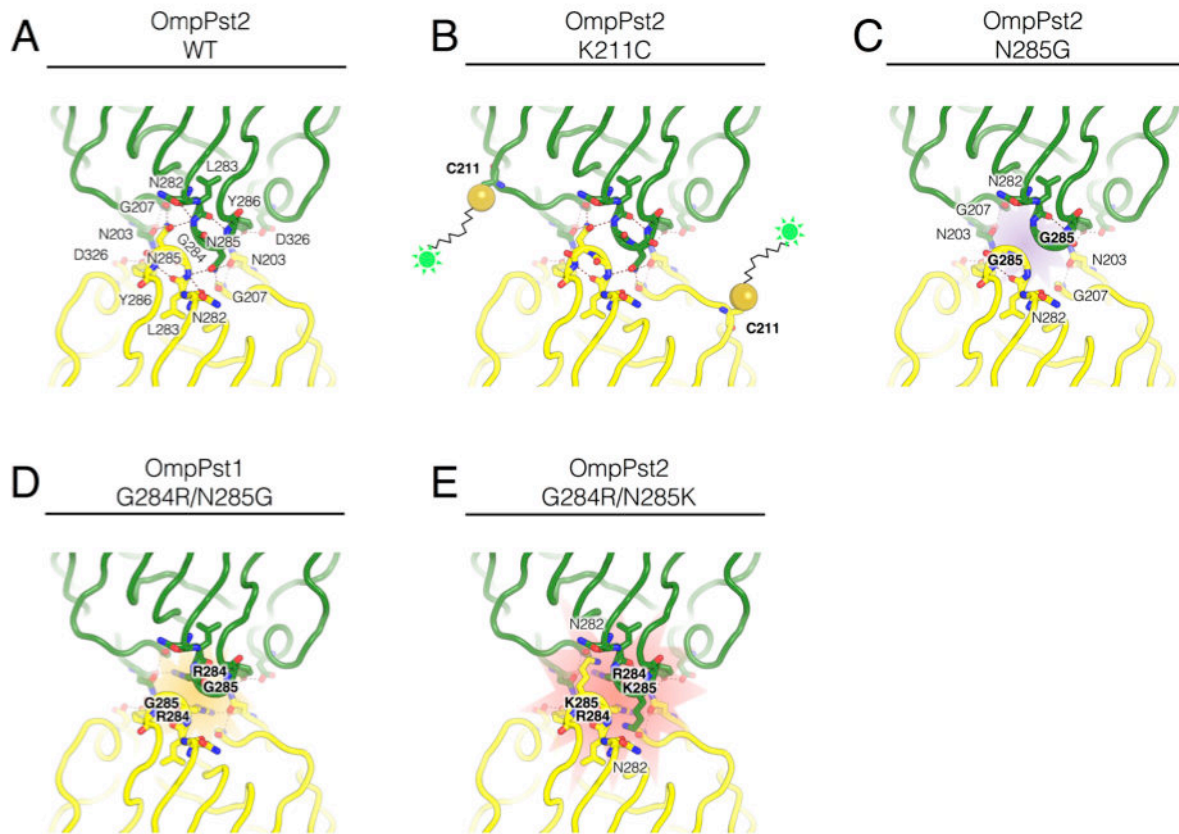


Figure S5 | Contacts in the Omp-Pst2 DOT and mutation strategy. (A) The Omp-Pst2 DOT is stabilized by multiple H-bonds emanating from the steric zipper interface, centred around L7 residue G284. (B) K211, at the C-terminal end of Omp-Pst2 L5 loop, is not involved in the DOT formation. Omp-Pst2 was specifically labeled with a maleimide coupled fluorophore after engineering a cysteine at the position 211 (Omp-Pst2-K211C). (C) Mutation of N285 into a glycine is expected to result in reduced Omp-Pst2 self-association, due to the loss of stabilizing H-bonds between the two facing trimers. (D) Mutation of G284 into an arginine (OmpPst2-G284R) is expected to further disrupt the steric zipper interface, and to induce electrostatic repulsion between the two facing trimers, owing to the close distance between G284 side chains. (E) The additional mutation of N285 into a lysine (OmpPst2-G284R/N285K) should completely abolish the DOT formation, due to increased electrostatic repulsion.

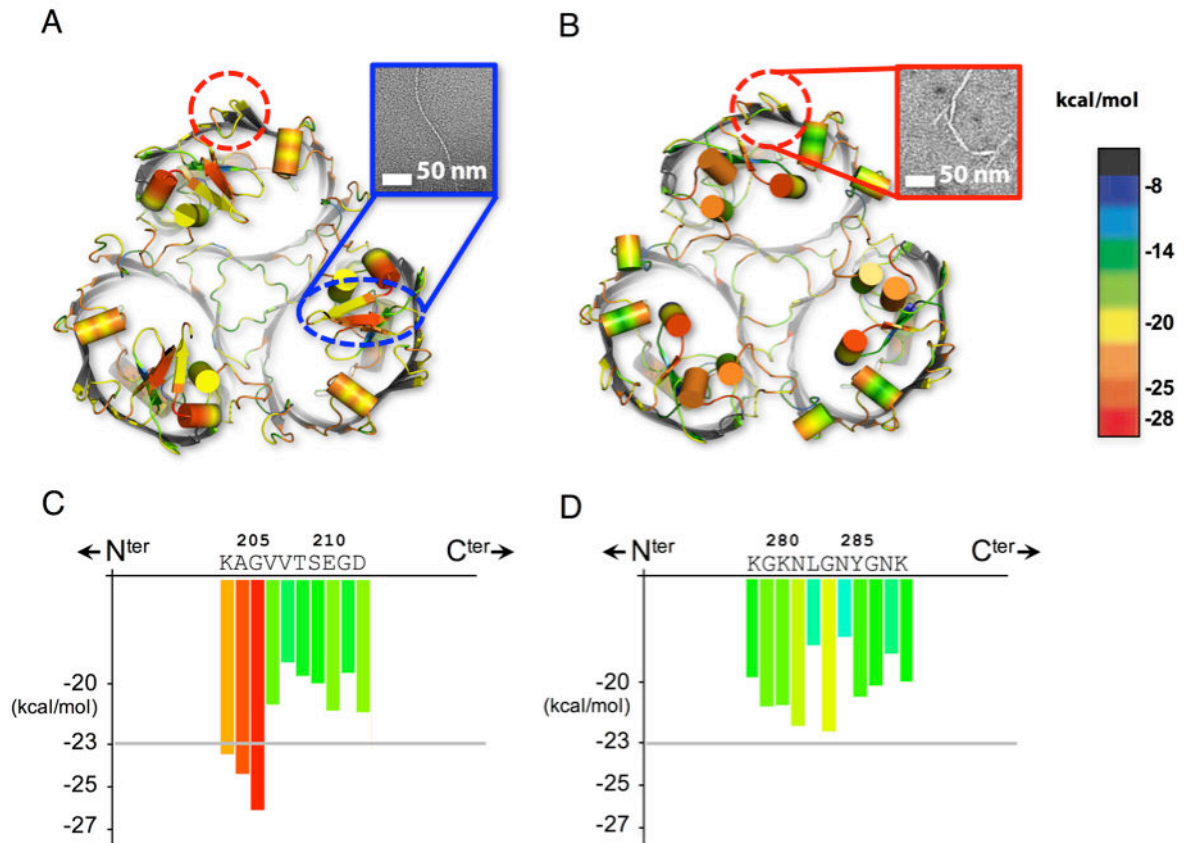


Figure S6 | Extracellular loops L5 from Omp-Pst1 and L7 from Omp-Pst2 display high propensity to form steric zippers. (A, B) Ribbon diagrams of Omp-Pst1 (A) and Omp-Pst2 (B) coloured by propensity of hexapeptidic segments to form steric zippers, with red being the highest and blue the lowest propensity. Most high-propensity segments are found in the membrane-embedded β -barrel and in α -helices contributed by extracellular loops. Both the extracellular loop L5 (blue oval in (A)) and the extracellular loops L7 of Omp-Pst1 and Omp-Pst2 (red circle in (A, B)) are exposed in a β -sheet compatible geometry. Inserts show that both fragments 206-GVVTSE-211 isolated from Omp-Pst1 L5 (A) and 282-NLGNYG-287 from Omp-Pst2 L7 (B) form thin amyloid fibrils at pH 7. (C, D) 3D-profile scores for Omp-Pst1 L5 and Omp-Pst2 L7. Hexapeptidic segments with an energy below -23 kcal/mol are predicted as highly prone to form steric zippers.

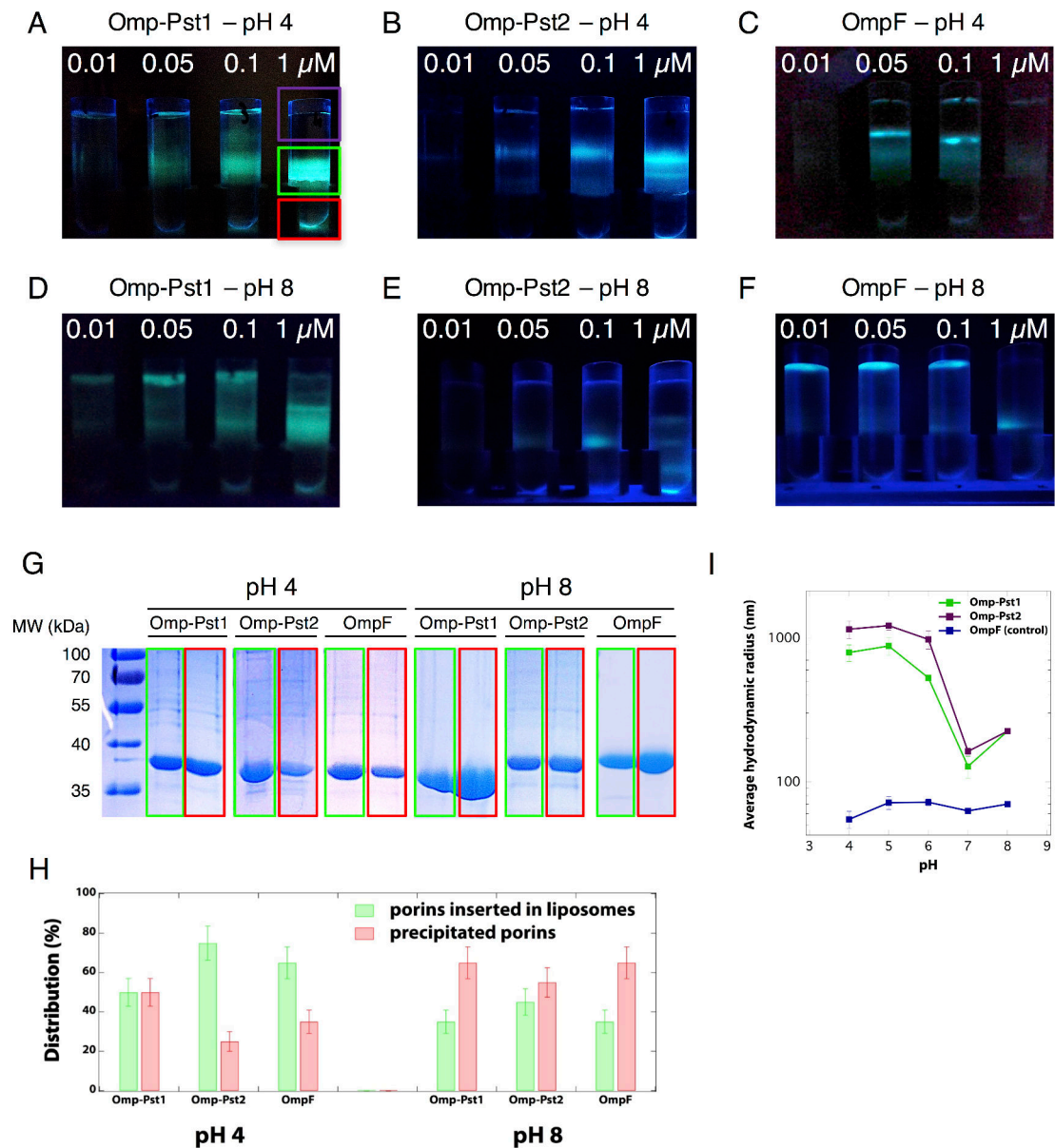


Figure S7 | Porin incorporation into liposomes is slightly favoured at acidic pH. (A-F) Pre-formed 60 nm liposomes were incubated 30 min at pH 4 (A-C) or pH 8 (D-F) with increasing concentrations (0, 0.01, 0.1 and 1 μ M; from left to right) of Omp-Pst1 (A, D), Omp-Pst2 (B, E) or *E. coli* OmpF (C, F control). The protein-specific fluorescent probe 8-anilino-1-naphthalene-sulfonic acid was then added to the mixtures, which were centrifuged on a sucrose gradient to separate liposomes (upper fraction; purple rectangle in (A)), proteoliposomes (middle fraction; green rectangle in (A)) and precipitated porins (lower fraction; red rectangle in (A)). (G) Proteoliposomes aggregates (green rectangles) and precipitated porins (red rectangles) were isolated, denatured by heating to 95 $^{\circ}$ C for 5 min and migrated on an SDS-page gel for quantification. Molecular weight markers are shown on the left. The ~39 kDa band corresponds to porin monomers. Gels reveal that a large fraction of porins precipitate (red lining) upon incorporation in pre-formed liposomes by direct dilution. Nevertheless, at acidic pH, insertion (green lining) is favoured over precipitation. (H) Estimated fractions of Omp-Pst1, Omp-Pst2 and OmpF that insert into liposomes at pH 4 and pH 8, when the initial porin concentration is 1 μ M. This estimation is based on the relative intensity of the ~39kDa band on the various SDS-PAGE gels shown in (G). (I) Sub-optimal incorporation of porins into liposomes at pH \geq 7 could be at the origin of their reduced self-association properties at pH 7-8.

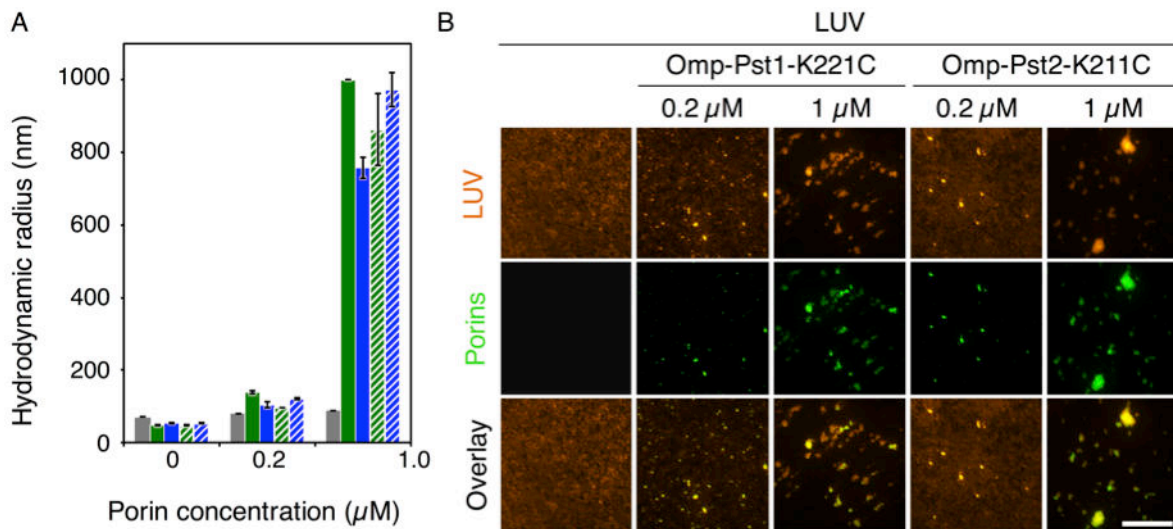


Fig. S8 | Omp-Pst1 and Omp-Pst2 display self-adhesion properties *in vitro*. (A) Dynamic light scattering was used to measure the hydrodynamic radii of proteoliposomes formed 24 h following addition, to a monodispersed solution of 60 nm liposomes, of OmpF (grey), Omp-Pst1 (plain green), Omp-Pst1-K221C (hatched green), Omp-Pst2 (plain blue) or Omp-Pst2-K211C (hatched blue). (B) Epifluorescence microscopy reveals that porins are concentrated in the proteoliposome aggregates. LUVs were labeled using rhodamine-coupled lipids. Omp-Pst1-K221C and Omp-Pst2-K211C were labeled by Alexa 488 using a maleimide conjugate. Proteoliposomes were spread on an agarose-coated cover slide, and imaged immediately. Scale bars are 40 μm (60X magnification). The fluorescence signals arising from porins and liposomes colocalize, asserting porins are present in the proteoliposome aggregates.

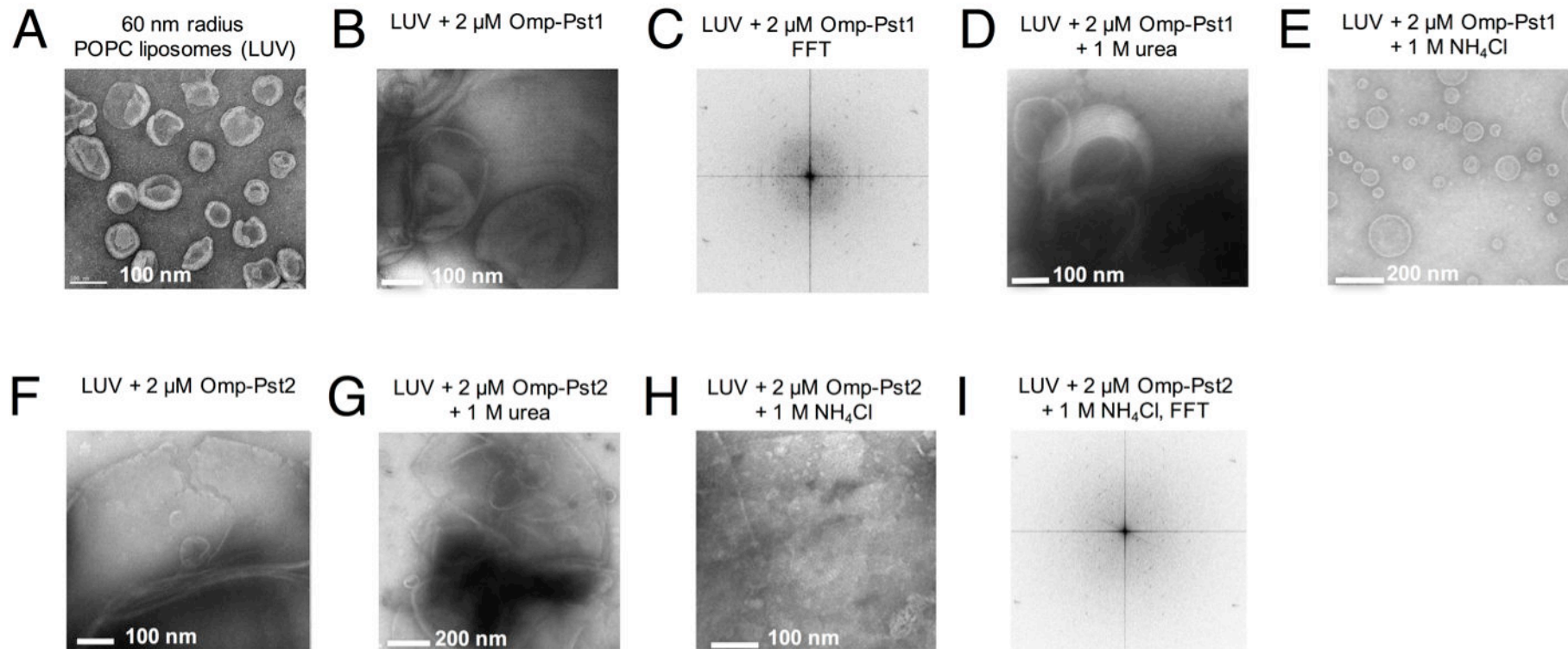


Figure S9 | Transmission electron microscopy reveals the highly ordered nature of Omp-Pst1 and Omp-Pst2 proteoliposome aggregates. (A) Pre-formed 60 nm POPC liposomes. (B, D, E) Proteoliposome aggregates obtained following incorporation of 2 μM Omp-Pst1 into pre-formed 60 nm POPC liposomes in absence (B) or presence of urea (D) and NH_4Cl (E). (F, G, H) Proteoliposome aggregates obtained following incorporation of 2 μM Omp-Pst2 into pre-formed 60 nm POPC liposomes in absence (F) or presence of urea (G) and NH_4Cl (H). (A-I) Stacks of lipid bilayers are apparent in proteoliposomes aggregates. (C, I) Fourier transforms of the images shown in (B) and (H) reveals periodic order in the proteoliposomes aggregates formed by Omp-Pst1 and Omp-Pst2, in various conditions.

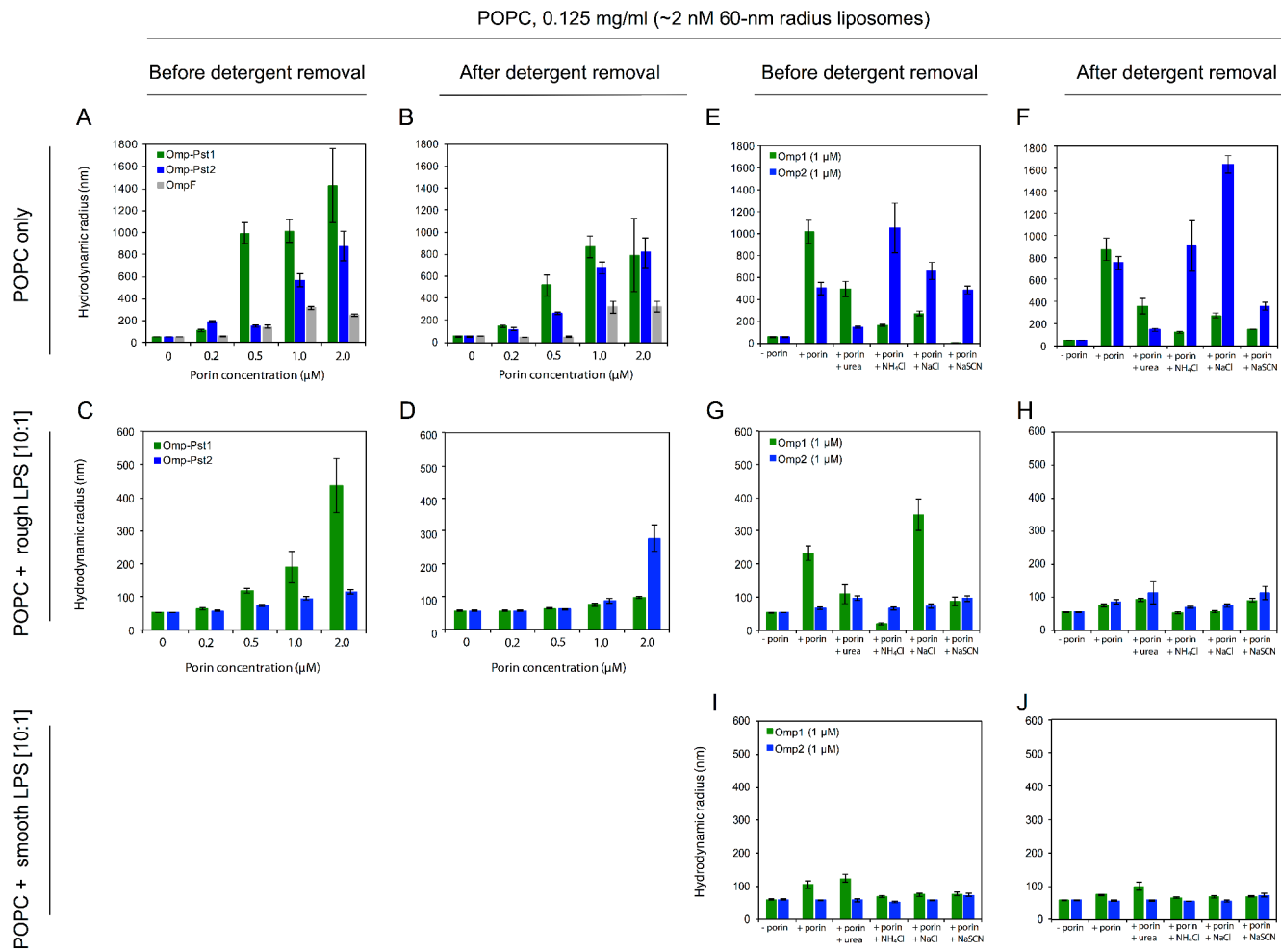


Figure S10 | Porin induced proteoliposomes aggregation is not affected by detergent removal, but is sensitive to high concentration of salt and chaotropes. (A) Average hydrodynamic radii of proteoliposomes obtained by incorporation of Omp-Pst1 and Omp-Pst2 at different concentrations, in preformed 60 nm POPC liposomes. DLS measurements were performed 24 h after addition of porins to the liposome solutions. (B) Biobeads were then added to proteoliposome aggregates and DLS measurements were performed 24 h later. (C-D) Same as panels A and B, but using preformed 60 nm POPC liposomes containing rough lipopolysaccharides (LPS) at a LPS-to-phospholipid mass ratio of 1:10. (E-J) Effect of salts and chaotropes on porin induced proteoliposome aggregation. Porin and effector concentrations were 1 μM and 1 M, respectively. Experiments were conducted on liposomes composed of POPC only (E, F) or containing rough (G, H) or smooth (I, J) LPS at a LPS-to-phospholipid mass ratio of 1:10. (E, G, I) Results of DLS measurements 24 h after addition of porin and effectors to the liposome solution. (F, H, J) Biobeads were then added to proteoliposome aggregates and DLS measurements were performed 24 h later. In all experiments, the liposome concentration was ~2 nM.

Phospholipids (PL), 1.25 mg/ml (~20 nM 60-nm radius liposomes)

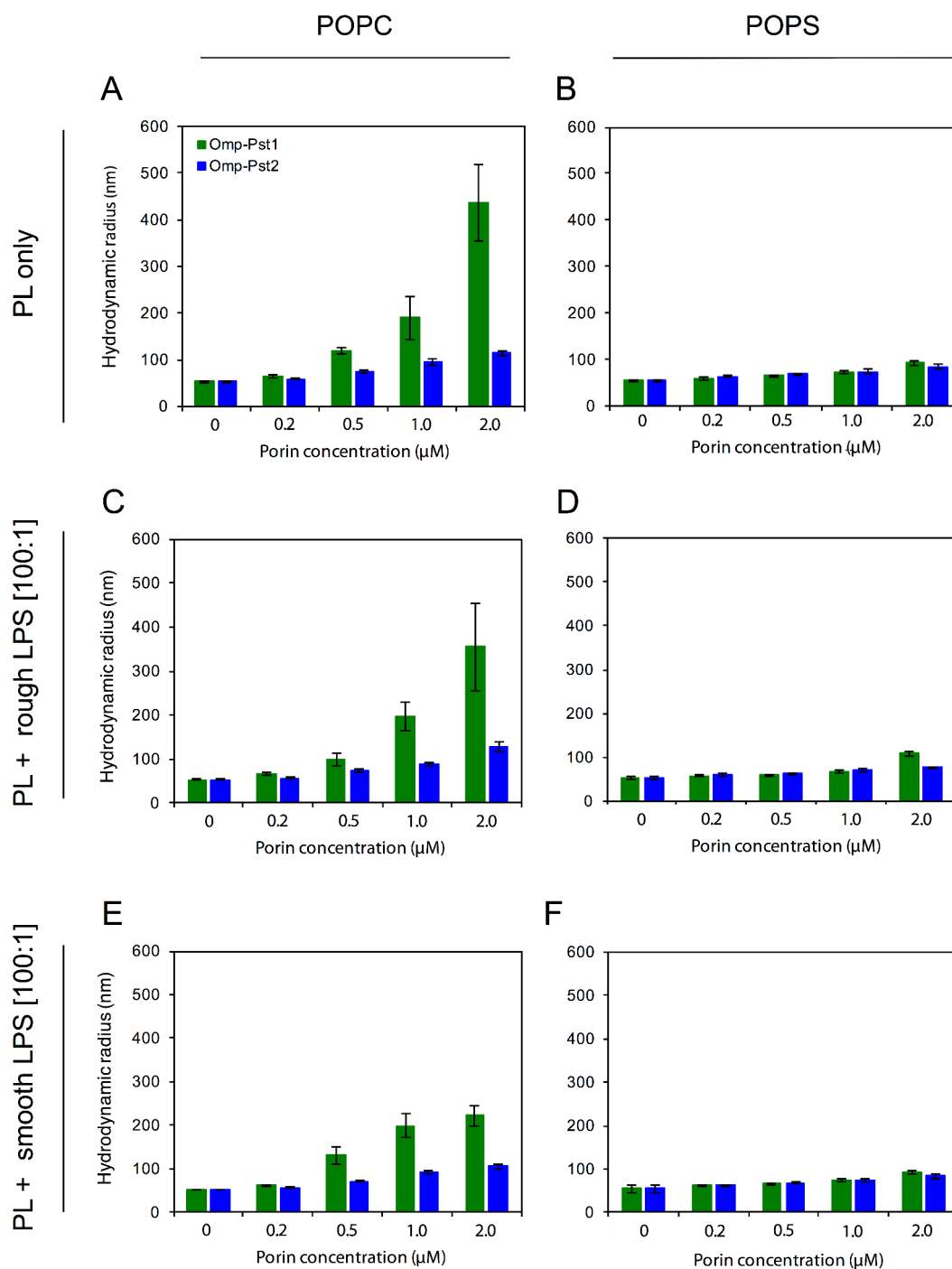


Figure S11 | Porin induced proteoliposomes aggregation is unaffected by rough LPS but inhibited by POPS and smooth LPS. (A-B) Average hydrodynamic radii of proteoliposomes obtained by incorporation of Omp-Pst1 and Omp-Pst2 at different concentrations, into preformed 60 nm POPC (A) or POPS (B) liposomes. The liposome concentration was ~20 nM in all experiments. (C-D) Same as panels A and B, but using preformed 60 nm POPC (C) or POPS (D) liposomes containing rough LPS at a LPS-to-phospholipid mass ratio of 1:100. (E-F) Same as panels A and B, but using preformed 60 nm POPC (E) or POPS (F) liposomes containing smooth LPS at a LPS-to-phospholipid mass ratio of 1:100.

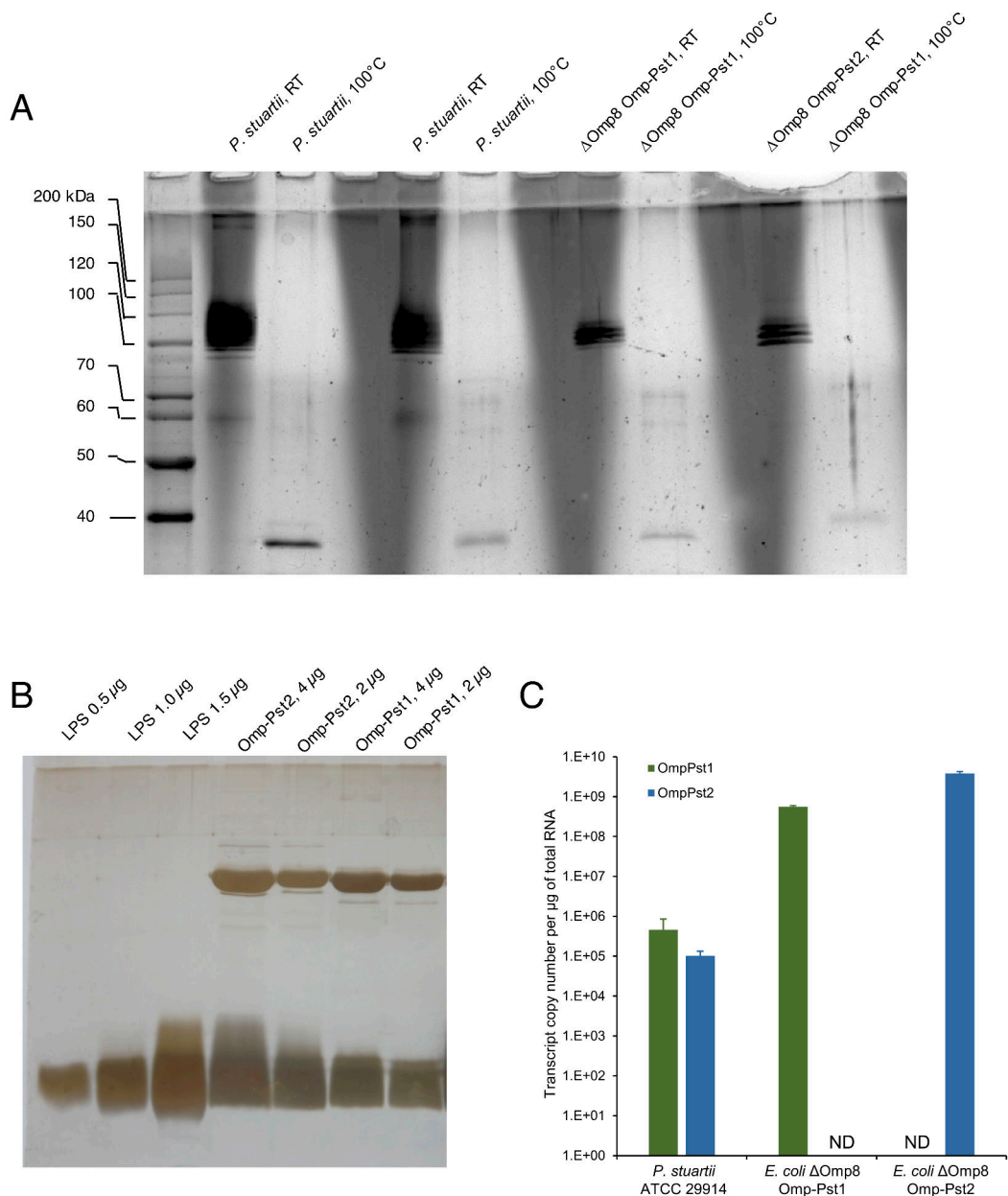


Figure S12 | Omp-Pst1 and Omp-Pst2 are expressed at similar level and co-purify with LPS in *P. stuartii* and recombinant Δ Omp8 strains. (A) Silver-stained SDS-PAGE gels of outer-membrane extracts of *P. stuartii* and recombinant Δ Omp8 cells expressing Omp-Pst1 or Omp-Pst2. The first lane shows molecular weight markers, and subsequent lanes show alternations of unboiled and boiled outer-membrane extracts of *P. stuartii* (2 successive extractions), Δ Omp8-Omp-Pst1 and Δ Omp8-Omp-Pst2. Boiled samples show denatured porin monomers, when unboiled samples reveal trimers apparently complexed with different numbers of LPS molecules (up to 10 in *P. stuartii* outer-membrane extracts, and 1 – 4 in Δ Omp8 cells). **(B)** Support to the hypothesis that *P. stuartii* porins co-purify with LPS was obtained by running boiled purified LPS, Omp-Pst1 and Omp-Pst2 on a silver-stained SDS-PAGE gel. The gel suggests that Omp-Pst1 and Omp-Pst2 both co-purify with LPS, at a LPS-to-porin mass ratio of 1:2. **(C)** qRT-PCR was used to quantify the expression of porins in the *P. stuartii* ATCC 29914 and in recombinant *E. coli* Δ Omp8 strains. *P. stuartii* ATCC 29914 expresses both Omp-Pst1 (green) and Omp-Pst2 (blue). *E. coli* Δ Omp8 + Omp-Pst1 only expresses Omp-Pst1 at high level (green) but not Omp-Pst2 (ND = not detected) while *E. coli* Δ Omp8 + Omp-Pst2 only expresses Omp-Pst2 at high level (blue) but not Omp-Pst1 (ND). Values are indicated as mean \pm standard deviation (N = 3).

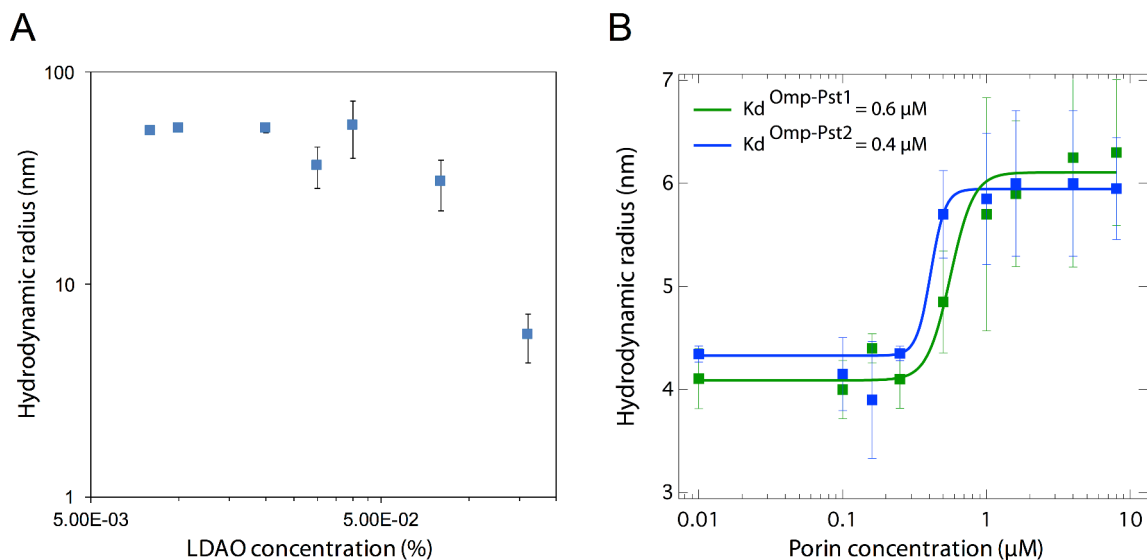


Figure S13 | The detergent lauryldimethylamine N-oxide (LDAO) leads to a decrease of liposome radius at concentration ~2 times higher than the CMC, and does not prevent determination of dissociation constants for *P. stuartii* DOTs. (A) Effect of increasing concentration of LDAO on the hydrodynamic radius of liposomes. A sharp decrease occurs above 0.04 % LDAO, showing that LDAO effects on liposomes by dissolving them – not aggregating them. (B) Measured hydrodynamic radii of LDAO-solubilized Omp-Pst1 and Omp-Pst2 at various concentrations between 0.01 and 8 μM. Predicted radii of gyration for nude (no LDAO molecules) trimers and DOTs are 3.0 and 4.3 nm, respectively, while the measured hydrodynamic radius of isolated LDAO micelles is 3.07 ± 0.8 nm in a 0.12% buffered solution. Hence, LDAO solubilized porin trimers and LDAO micelles commensurate in hydrodynamic radii in our buffered solutions, and the appearance of Omp-Pst1 and Omp-Pst2 species with hydrodynamic radii of $\sim 6.3 \pm 0.71$ nm and 5.95 ± 0.49 nm, respectively, can be ascribed to the appearance of DOTs. Fitting of the data suggests dissociation constants of 0.6 and 0.4 μM for Omp-Pst1 and Omp-Pst2, respectively.

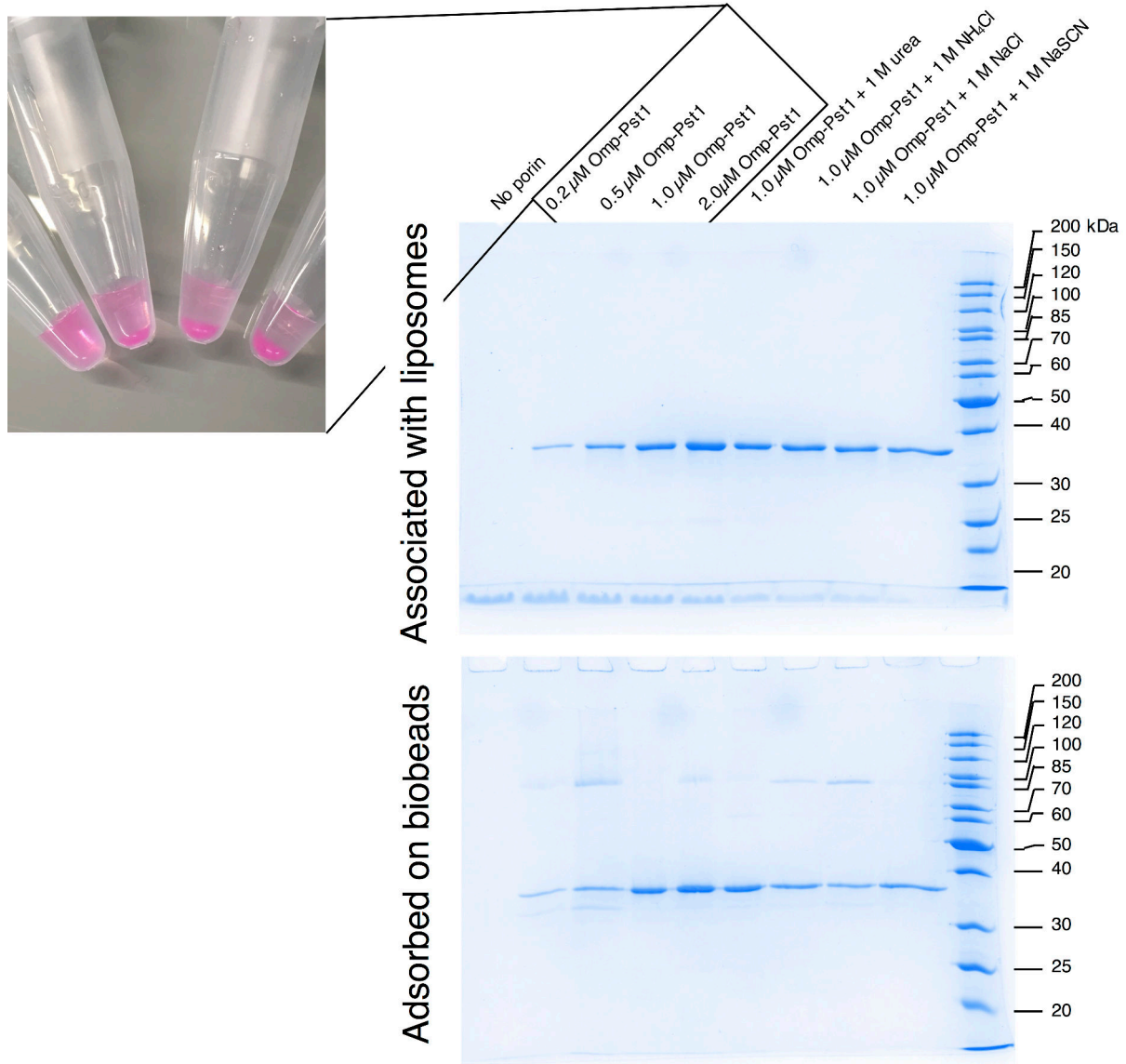


Figure S14 | Biobeads can extract LPS-Omp-Pst1 complexes from POPC bilayers. Omp-Pst1 was incorporated, at various concentrations and in presence of various effectors, in preformed 60 nm POPC liposomes featuring rough LPS at a LPS-to-phospholipid mass ratio of 1:10, and the fluorescent lipid lissamine-rhodamine-sn-glycero-3-phosphoethanolamine (0.02 %). The inset shows a picture of the proteoliposomes aggregates formed at 0, 0.5, 1 and 2 μM Omp-Pst1, before addition of biobeads. The liposomes aggregates were then incubated with biobeads for 24 h, after what proteoliposomes were separated from the biobeads, and SDS-PAGE gels were run from boiled separated proteoliposomes aggregates (upper gel) and from the boiling of equivalent volumes of commassie blue in the presence of separated biobeads. The gels reveal that only half of Omp-Pst1 remains associated with liposomes (upper gel). The other half adsorbs on the biobeads (lower gel), resulting in a reduction of the average hydrodynamic radius of proteoliposomes aggregates (Fig. S10C, D). As this effect was not observed in the absence of LPS, we propose that LPS, rather than porins, interact with the biobeads, and that porins are in turn co-purified with the LPS.

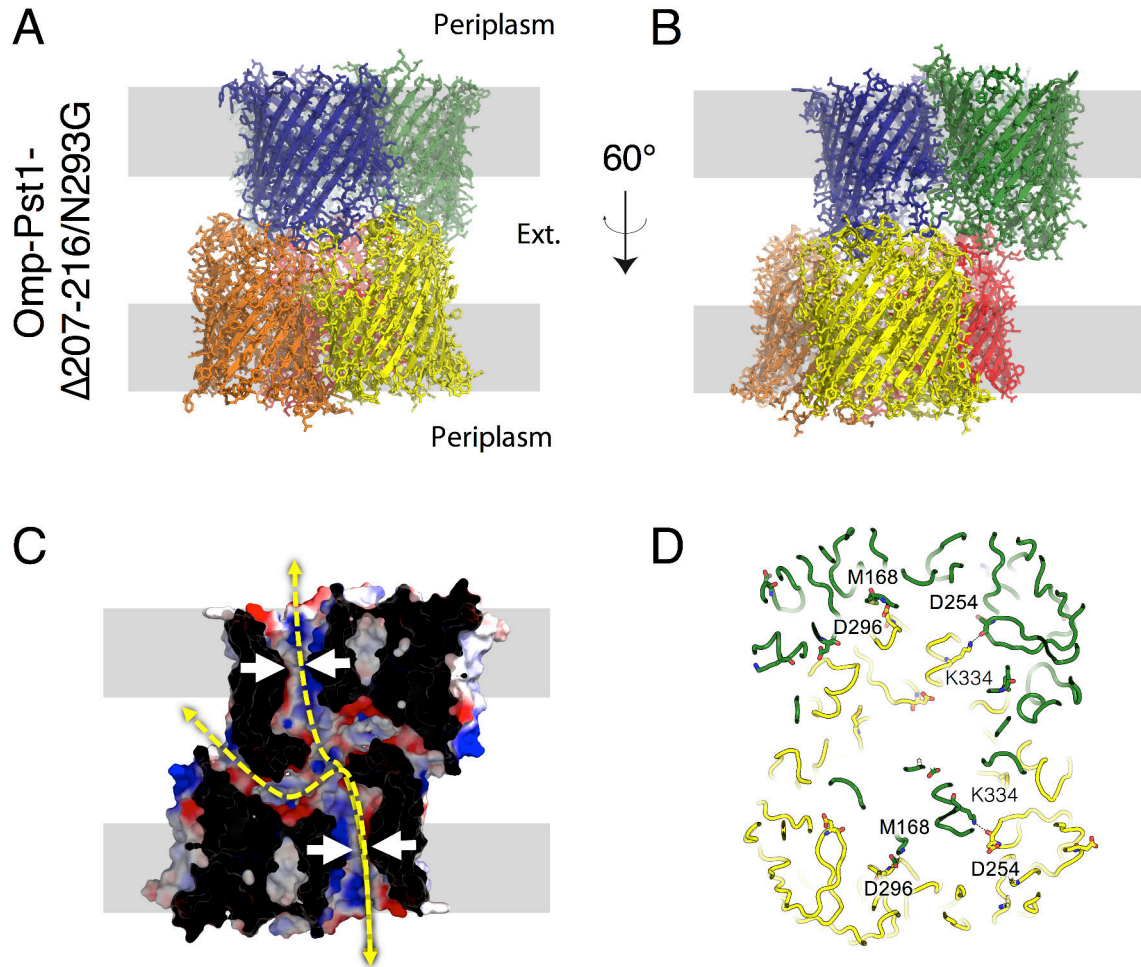


Figure S15 | Omp-Pst1- Δ 207-216/N293G also forms a crystallographic dimer of trimers (DOTs). (A, B) Lateral views of the Omp-Pst1- Δ 207-216/N293G DOT in the same orientations as in panels (A) and (B) of Fig. 1, respectively. The presumed positions of outer-membranes (OMs) are shown in grey. (C, D) The interacting region between facing monomers in the Omp-Pst1- Δ 207-216/N293G DOT does not involve a steric zipper. (C) The dimerization interface delineates a large cavity, which is less negatively charged than that of Omp-Pst1 due to suppression of the highly acidic β -hairpin contributed by L5 in Omp-Pst1- Δ 207-216/N293G. The Omp-Pst1- Δ 207-216/N293G DOT is also characterized by a reduced surface complementarity. The electrostatic potential of Omp-Pst1- Δ 207-216/N293G is mapped on its solvent accessible surface. The orientation is the same as in (B). (D) The Omp-Pst1- Δ 207-216/N293G DOT is locked-in by electrostatic interactions (M168(N) vs. D296(OD2), D254(O) vs. K334(NZ)) between the central monomer and the two facing non-central monomers in facing trimers.

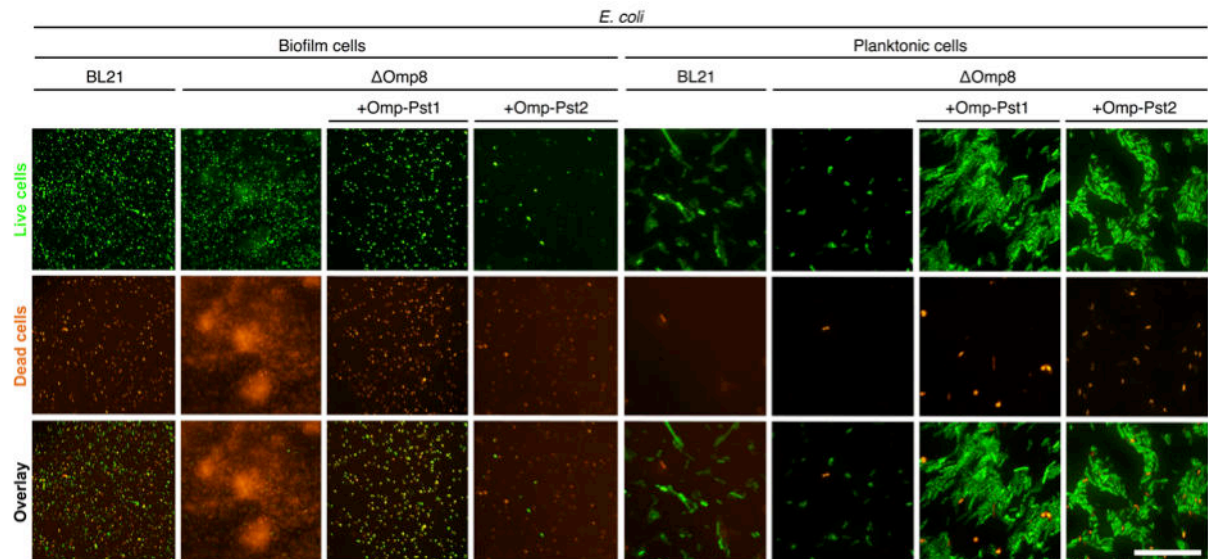


Figure S16 | Ectopic expression of Omp-Pst1 and Omp-Pst2 enables cell-to-cell contact in *E. coli* Δ Omp8. Bacterial strains were grown for 24 h in 96-well plates. Subsequently, live and dead cells were stained with SYTO9 Green and propidium iodide, respectively. Planktonic cells were harvested by direct pipetting from the LB medium, spread on LB-Gelzan and imaged immediately afterwards. Biofilm cells attached to the well surface were imaged after intensive PBS washes. Scale bars are 100 μ m for biofilm cells (20X magnification) and 50 μ m for planktonic cells (60X magnification).

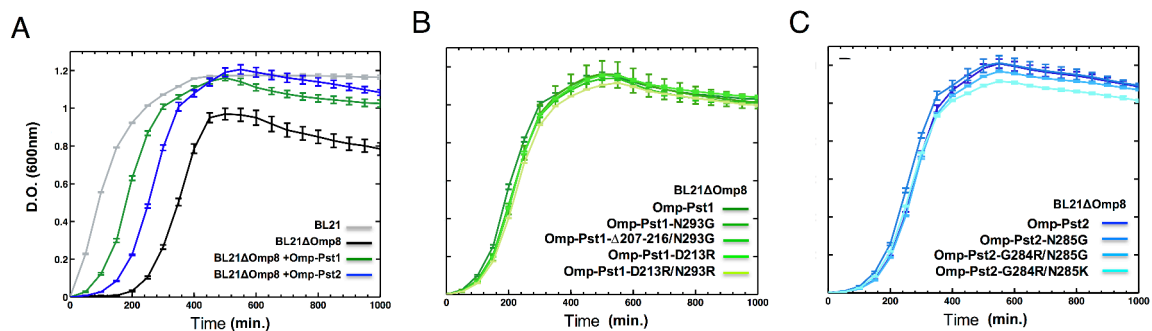


Figure S17 | Expressions of Omp-Pst1 and Omp-Pst2 restore normal growth of *E. coli* Δ Omp8 cells. (A) The *E. coli* strain Δ Omp8 (black) is a BL21 strain (grey) deleted of its major porins (OmpF, OmpC, OmpA and LamB), and it comparatively displays a reduced growth and a longer lag phase. Ectopic expression of Omp-Pst1 or Omp-Pst2 in *E. coli* Δ Omp8 restores normal growth and reduces the lag phase. Expression of Omp-Pst1 appears more profitable to Δ Omp8 cells than that of Omp-Pst2, in terms of rapidity of growth. (B, C) *E. coli* Δ Omp8 cells expressing mutants of Omp-Pst1 (B) and Omp-Pst2 (C) appear as fit as those expressing wild-type Omp-Pst1 and Omp-Pst2, respectively. The diffusive properties of the porins are thus presumably unaffected in these mutants.

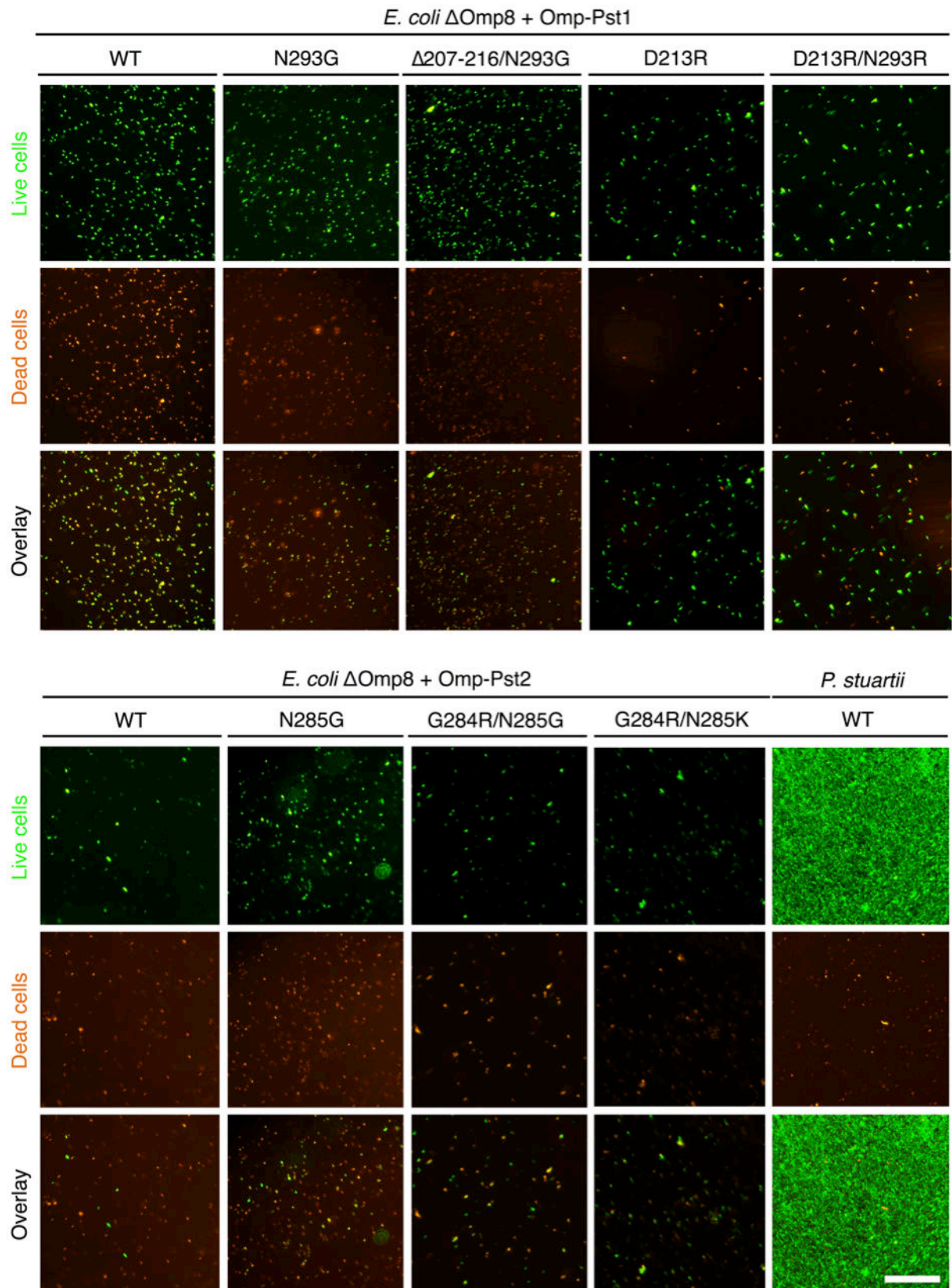


Figure S18 | *E. coli* expressing Omp-Pst1 and Omp-Pst2 mutants do not form adherent biofilms. Bacterial strains were grown for 24 h in 96-well plates. Subsequently, live and dead cells were stained with SYTO9 Green and propidium iodide, respectively. Biofilm cells attached to the well surface were imaged after intensive PBS washes. For comparison purposes, the biofilms formed by *P. stuartii* are shown. The scale bar is 100 μ m (20X magnification).

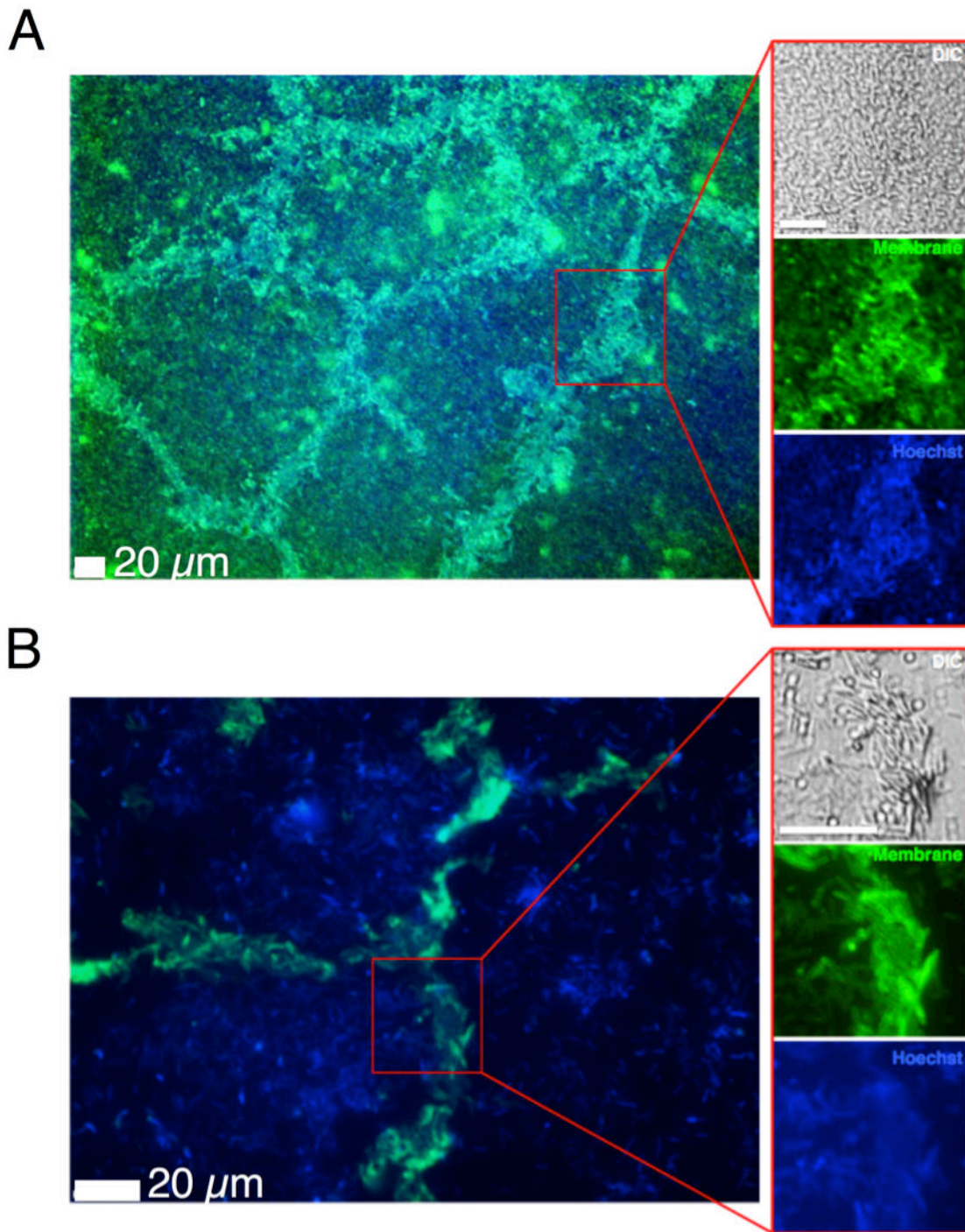


Figure S19 | *P. stuartii* cells are in close contact in the core layers of surface-attached biofilms. (A, B) *P. stuartii* cells were grown for 24 h in LB medium in 96-well plate. Well surfaces were imaged before (A) and after (B) extensive PBS washing, allowing observation of the core layers of the biofilm attached on the well surface (B). FM1-43X and Hoechst 33342 were used to stain the bacterial membrane and cytosol (DNA), respectively.

	Omp-Pst1 (type A) ^a	Omp-Pst1 (type B) ^a	Omp-Pst1- Maltose (type B) ^a	Omp-Pst2 ^a	²⁰⁶ GTVTSE ² 11 from Omp- Pst1 ^a	²⁸³ LGNY ²⁸ 6 from Omp- Pst2 ^a	Omp-Pst1- Δ207- 216/N293 G ^a
Data collection							
Space group	C 2	P 2 ₁ 2 ₁ 2 ₁	P 2 ₁ 2 ₁ 2 ₁	P 2 ₁	P1	P1	C 2
Cell dimensions							
a, b, c (Å)	151.52, 142.02, 113.32	108.11, 129.14, 160.05	104.20, 127.12, 150.72	143.26, 135.51, 151.71	4.81, 16.95, 45.50	4.78, 11.55, 47.04	126.32, 158.98, 101.33
α, β, γ (°)	90.0, 131.0, 90.0	90.0, 90.0, 90.0	90.0, 90.0, 90.0	90.0, 114.6, 90.0	90.0, 90.0, 90.0	90.0, 90.0, 90.0	90.0, 124.6, 90.0
Resolution (Å) [*]	50.0 – 3.20 (3.28 – 3.20)	50 – 2.70 (2.75 – 2.70)	50.0 – 3.0 (3.05 – 3.00)	45.7 – 2.2 (2.26 – 2.2)	50 – 1.91 (1.98 – 1.91)	47.04 – 1.00 (1.03 – 1.00)	48.76 – 3.11 (3.21 – 3.11)
R _{sym} or R _{merge} (%) [*]	11.2 (57.7)	8.1 (74.8)	11.4 (134.0)	5.2 (54.0)	12.0 (18.8)	4.3 (17.3)	20.2 (168.1)
CC ^{1/2} (%) [*]	99.0 (66.3)	99.9 (82.4)	99.7 (54.5)	99.9 (73.7)	99.1 (97.3)	99.8 (94.3)	99.8 (60.5)
I / σI [*]	10.98 1.97	23.48 (2.02)	10.20 (0.98)	19.43 (2.0)	4.90(3.24)	15.21 (4.93)	8.56 (1.51)
Completeness (%)	90.5 (93.2)	80.6 (73.1)	99.2 (100.0)	93.9 (73.7)	96.7 (100.0)	89.6 (89.0)	96.7 (79.2)
Redundancy [*]	2.68 (2.66)	4.35 (4.14)	5.00 (5.34)	3.01 (2.57)	2.20 (2.20)	2.17 (2.15)	6.78 (6.10)
Refinement							
PDB accession code	4d64	5nxr	5nxu	4d65	5n9i	5n9h	5nxn
Resolution (Å)	36.25 – 3.2	38.80 – 2.70	39.15 – 3.00	45.7 – 2.2	22.72 – 1.91	47.04 – 1.00	86.99 – 3.11
No. reflections	27279	59296	38580	249377	1076	4934	25757
R _{work} / R _{free}	20.75/26.1 1	24.10/28.4 8	21.15/25.3 8	16.83/19.6 8	14.74/20.59	8.11/9.5 9	24.62/26.8 0
No. atoms							
Protein	8298	8375	8312	16377	164	244	8133
Ligand/ion	1	1122	344	2487	n/a	20	1
Water	160	833	535	3115	18	8	520
B-factors ^Δ							
Protein	76.40	69.70	61.49	35.53	12.70	2.66	98.63
Ligands and ions	83.79	110.47	112.52	84.79	n/a	3.29	79.05
Water	57.24	66.31	83.20	57.63	12.41	16.58	86.69
R.m.s. deviations							
Bond lengths (Å)	0.006	0.012	0.008	0.007	0.019	0.013	0.018
Bond angles (°)	1.007	2.048	1.738	1.432	2.122	1.929	1.869
Table S1 Data collection and refinement statistics:							
^a Structure was solved from single crystal; [*] Values in parentheses are for highest-resolution shell; ^Δ These values include TLS contributions when applicable							

**Article n°3 – Socialization of *Providencia stuartii*
enables resistance to environmental insults**

Article n°3 – Résumé

Les deux premiers articles ont montrés que les bactéries de *P. stuartii* se socialisent en communautés flottantes puis en biofilms adhérents par sédimentation et synthèse d'une matrice extracellulaire. Les deux porines de *P. stuartii*, Omp-Pst1 et Omp-Pst2, supportent la socialisation des bactéries en communautés flottantes grâce à leur capacité à s'auto-associer en DOTs à travers leurs boucles extracellulaires. Dans ce troisième article, nous avons étudié l'effet des conditions pathophysiologiques du tractus urinaire – principal site d'infection de *P. stuartii* – telles que de fortes concentrations d'urée, d'ammonium, de bicarbonate, de créatinine et d'une variation de pH, sur l'expression des porines, leurs propriétés d'auto-association, ainsi que sur la formation et la survie des communautés flottantes et des biofilms adhérents. Nos résultats montrent que la socialisation garantit une résistance plus élevée des bactéries aux environnements hostiles, qui semble être assurée par différents mécanismes selon le type de communauté bactérienne établi. En effet, au sein des communautés flottantes, *P. stuartii* a tendance à sous-exprimer sa porine Omp-Pst1, qui se révèle être la principale porte d'entrée de l'urée, de l'ammonium et du bicarbonate, afin de limiter leur pénétration dans la cellule. En revanche, la présence de la matrice extracellulaire enrobant les biofilms adhérents semble être suffisante pour protéger efficacement les bactéries. La porine Omp-Pst2 est quant à elle impliquée dans la résistance élevée des bactéries aux facteurs environnementaux et assure un échafaudage alternatif lorsque Omp-Pst1 est sous-exprimée.

Socialization of *Providencia stuartii* enables resistance to environmental insults.

Authors:

Julie Lopes¹, Guillaume Tetreau¹, Kevin Pounot¹, Mariam El Khatib¹, Jacques-Philippe Colletier¹

Affiliations:

¹ Univ. Grenoble Alpes – CEA – CNRS, Institut de Biologie Structurale (IBS), Grenoble, France

Correspondence: colletier@ibs.fr

Abstract

Providencia stuartii is a Gram-negative pathogen responsible for urinary tract infections and characterized by a stringent antibiotic-resistance phenotype. *P. stuartii* is able to form floating communities of cells (FCCs), in addition and prior to surface-attached biofilms (SABs). The two porins of *P. stuartii*, Omp-Pst1 and Omp-Pst2, support the formation of FCCs by enabling cell-to-cell contact through self-matching interaction between their extracellular loops, forming intercellular dimers of trimers (DOTs) that rivet cell one onto another. In pathophysiological conditions, *P. stuartii* cells are principally exposed to high concentrations of urea, ammonia, bicarbonate, creatinine and to large variations of pH, raising questions as to how these environmental cues may affect formation of SABs and FCCs, and whether these modes of socialization protect cells against them. Here, we investigated in the presence of increasing concentrations of urea, ammonia, bicarbonate, creatinine and at varying pHs, bacterial growth, porin expression and self-association properties, and FCC and SAB formation and persistence. Our results show that Omp-Pst1 is the main gateway supporting urea, bicarbonate and ammonia uptake into the periplasm while Omp-Pst2 is involved in resistance of *P. stuartii* to these cues. Our data also demonstrate that FCCs are, alike SABs, communities of cells endowed with increased fitness and resistance.

Keywords: *Providencia stuartii*; floating communities of cells; surface-attached biofilms; porins; urinary tract infections

Introduction

Bacterial biofilms are multicellular communities embedded into a self-produced extracellular matrix (ECM) that allows their attachment onto a variety of surfaces^{1,2}. The formation of surface-attached biofilms (SABs) enables bacteria to endure environmental insults and to survive in ecological niches otherwise hostile for their planktonic counterparts^{1,3-5}. This explains that SABs are found in numerous and contrasting environments, ranging from glacial surfaces to ships and cooling systems to the surface of all earth oceans^{6,7}. Most worryingly, SABs can also niche into human tissues or on prosthetic implants, thereby posing a direct threat to human health. Indeed, SAB-engulfed bacteria exhibit an increased tolerance to antimicrobials agents and to the immune system, making them difficult to eradicate once settled⁸. Accordingly, SABs – and bacterial socialization in general – are involved in most chronic bacterial infections^{1,9,10}.

Providencia stuartii is a Gram-negative biofilm-forming opportunistic-pathogen from the *Enterobacteriaceae* family, and it is responsible for ~10% of hospital-acquired urinary tract infections. The bacterium is not epidemic, and generally infects immunocompromised individuals such as intensive care unit (ICU) residents and patients under long-term catheterization¹¹⁻¹⁵. It is yet highly endemic due to its ability to form biofilms and its strong intrinsic multidrug resistance (MDR) phenotype. The latter is mostly due to the presence of an inducible chromosomally-encoded AmpC, a β -lactamase specifically targeting most penicillins and several cephalosporin antibiotics¹⁶. The MDR phenotype can be further aggravated by horizontal transfer of plasmid-encoded extended-spectrum β -lactamases (ESBLs) and metallo- β -lactamases yielding strains capable of resisting to most β -lactam and carbapenem antibiotics, and therefore leaving only few alternatives for antibiotic treatment¹⁷⁻²⁰.

SAB formation has been extensively studied in biofilm-forming human pathogens such as *Bacillus subtilis*, *Pseudomonas aeruginosa* and *Staphylococcus aureus*²¹, allowing to derive a four-step model. Briefly, planktonic [isolated] bacteria first adhere to a surface forming a

monolayer of cells, which further develop into a multi-layer colony upon bacterial division and migration. The multilayered colony then matures by synthesizing its ECM. Upon exhaustion of nutritional resources, the biofilm will release planktonic cells enabling colonization of other niches²¹. Recently, we showed that *P. stuartii* exploits an additional means of socialization before adhesion of cells onto surfaces, whereby self-matching interactions between the extracellular loops of outer membrane (OM) embedded general-diffusion porins enables formation of floating communities of tightly packed cells (FCCs). Formation of FCCs precedes that of SABs, suggesting that the latter are formed from sedimentation of the former^{22,23}.

Porins are water-filled channels present in the OM of Gram-negative bacteria. Their main function is to ensure influx of hydrophilic solutes and ions into the periplasm. Among these, general-diffusion porins (hereafter referred to as porins), which only discriminate solutes on the basis of size and charge, are the most abundantly expressed with up to 100,000 copies per cell^{24–26}. Down-regulation of porins can be associated with antibiotic resistance in Gram-negative bacteria, effectively reducing the uptake of hydrophilic antibiotics, e.g. β -lactams. Notably, a lack of expression of general-diffusion porins was observed in antibiotic-resistance clinical isolates of *Klebsiella pneumoniae* and *P. aeruginosa*^{25,27–29}. In *P. stuartii* ATCC 29914 (thereafter referred to as *P. stuartii*), two porins are expressed, Omp-Pst1 and Omp-Pst2. Both play a major structural role in *P. stuartii* socialization, enabling the scaffolding of FCCs through formation of intercellular dimers of OM-embedded trimers (DOTs) acting as rivets between adjacent cells^{30,31}. Omp-Pst1 is ~10 times more expressed than Omp-Pst2 under normal growth conditions, constituting the principal entry route of cations and hydrophilic solutes into the periplasm^{23,32} but also the principal DOT provider. While present at lower concentration, Omp-Pst2 presents a higher propensity to form DOTs (dissociation constant of 0.4 μ M compared to 0.6 μ M for Omp-Pst1²³) and it plays a role during the early stages of *P. stuartii* growth, as well as in the adaptation of the bacterium to high concentrations of urea and varying pH²². A *P. stuartii* strain

knocked-out for Omp-Pst2 could be obtained, but not one for Omp-Pst1, suggesting that only Omp-Pst1 is essential.

The principal pathophysiological habitat of *P. stuartii* in humans is the urinary tract and accordingly, the bacterium can survive in urine. Urea is the main catabolite present in urine (170 mM), followed by ammonia (25 mM), bicarbonate (25 mM), creatinine (7 mM), magnesium (2.5 mM) and calcium (2 mM)^{33,34}. The pH of urine is generally slightly acidic, but it can vary from 6 to 8 depending on the dietary habits of patients and/or their genetic background^{34,35}. It was shown that the presence of urea and ions (Ca^{2+} and Mg^{2+}) at concentrations similar to those found in the urinary tract does not impact the survival of *P. stuartii*²², nor does variation of pH across the pH 6 to pH 9 range. It remains unclear, however, how these environmental cues affect the formation of FCCs and SABs, and if socialization into these two types of communities endow *P. stuartii* cells with higher resistance to the cues. Thus is the question we sought to provide an answer to in the present article.

To this end, we used a combination of epifluorescence microscopy, dynamic light scattering (DLS), and transcriptomic and proteomic approaches, allowing to investigate the impact of different concentrations of urea, ammonia, bicarbonate, and creatinine on the structuration, fitness [capacity to grow] and porin content of *P. stuartii* FCCs and SABs. We also investigated the impact of sudden variations of pH, such as those that occur along the day of even healthy individuals. Aware of the role of *P. stuartii* porins in the scaffolding and genesis of FCCs and SABs, we paralleled these phenotypic investigations with both *in vivo* monitoring of Omp-Pst1 and Omp-Pst2 expression and *in vitro* measurements of their ability to self-associate into DOTs. Our results show the role played by Omp-Pst1 and Omp-Pst2 in the uptake of and resistance to harmful solutes, respectively, and establish that FCC formation is a socialization mechanism that increases the tolerance of cells to a variety of chemical aggressions. Thus, atop of providing new insights into the formation and resistance of *P. stuartii* communities in their pathophysiological

environment, our results suggest that future treatments against the bacterium should be tested on FCCs and SABs in conditions mimicking the urinary tract, as both supracellular structures are able to form and survive in this habitat.

Results

We used reverse transcription quantitative PCR (RT-qPCR) to monitor the expression of the genes encoding the two porins of *P. stuartii* ATCC29914, *omp-pst1* and *omp-pst2*, at different stages of growth and in both FCCs (Figure 1.a) and SABs (Figure 1.b). FCCs develop after 4 hours of growth and sediment about 3 hours later (7h) to form SABs. Regardless of the stage of growth or of the mode of socialization, we found that Omp-Pst1 is 10-15 fold more expressed than Omp-Pst2, in line with previous results²³ and with the proposition that Omp-Pst1 is the major porin in *P. stuartii*^{22,32}. In both phenotypes, a comparable level of expression was observed at all stages, i.e. from 4h to 15h and 7h to 15h of growth for FCCs and SABs, respectively.

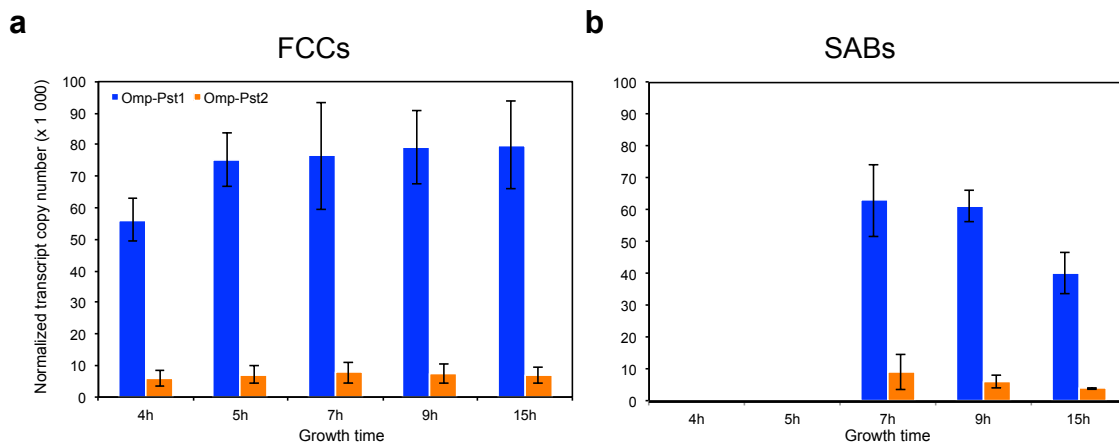


Figure 1. *omp-pst1* gene is more expressed than *omp-pst2* in *P. stuartii* floating cell communities (FCCs) and surface-attached biofilms (SABs). The expression of *omp-pst1* (blue) and *omp-pst2* (orange) porins is analyzed by RT-qPCR method, at different stages of growth, in both FCCs (panel a) and SABs (b). Normalized mRNA expression values are indicated as the mean of three biological replicates for each condition. Error = SD.

- *P. stuartii* cells are highly resistant to urea

The fitness and survival of *P. stuartii* cells in the presence of increasing concentrations of urea were assessed by optical density (OD) measurements and epifluorescence microscopy (Supplementary Figure S1). No effect was observed on bacterial growth and socialization at concentrations up to 150 mM urea. At 500 mM urea, the reach of the exponential phase was delayed by 5 hours, yet neither the formation of FCCs nor SABs was affected. At 1,000 mM urea, no bacterial growth was observed, indicating that the mechanism enabling adaptation to high urea concentration become inefficient above 500 mM.

Porins being the main gateway for hydrophilic solutes into Gram-negative cells, we examined whether exposure to increasing urea concentrations affects their expressions. At the proteomic level, *i.e.* as assessed from the intensity of bands on SDS-PAGE gels of OM extracts (see Methods), we found that urea concentrations up to 150 mM have no effect on porin abundance, while a 500 mM concentration results in a significant overall decrease of 33% in the abundance of porins in the OM (Supplementary Figure S2 and Table S1). We therefore chose this concentration to further investigate the effect of urea on porin gene transcription in growing FCCs and SABs by RT-qPCR (Supplementary Figure S2). We found that in the early stages of growth (*i.e.* ~4 hours after inoculation in medium containing 500 mM urea), *i.e.* when only FCCs are present, the presence of 500 mM urea results in a significant 4-fold overexpression of Omp-Pst2. In contrast, the expression of Omp-Pst1 remains unchanged (Figure 2.a and Supplementary Table S2). In SABs, which form from the sedimentation of FCCs and become visible only after ~7 hours of growth, neither the expression of Omp-Pst1 nor of Omp-Pst2 is significantly affected by the presence of urea (Figure 2.b and Supplementary Table S2).

To characterize the effect of urea on already socialized *P. stuartii* cells, FCCs and SABs were grown in the absence of urea, and then exposed to increasing concentrations of the catabolite.

The ability of socialized bacteria to resume growth was monitored by OD measurements, and FCCs and SABs were examined by epifluorescence microscopy for possible morphological changes, after 1-, 4- and 7-hours of treatment (Supplementary Figure S3). Cells were not affected by exposure to 150 mM urea but lag times of 2 and 2.5 hours were observed in the presence of 500 and 1,000 mM of urea, respectively. Regardless, socialization in itself was not affected by urea, with FCCs and SABs maintaining their organization and morphology even at concentrations as high as 1,000 mM. This observation suggested that once formed, FCCs and SABs can endure urea concentrations higher than in their early stage of growth.

To shed further light on the possible role of Omp-Pst2 in the adaptation to high urea concentration, we repeated our experiments on a strain of *P. stuartii* knocked-out for this porin (called hereafter *P. stuartii*ΔOmp-Pst2), i.e. expressing only Omp-Pst1 as a general diffusion porin. This strain retains the ability of the parental wild-type (WT) strain to socialize into FCCs and SABs but is characterized by a 6-hours lag-time in normal (laboratory) growth conditions²². Absence of Omp-Pst2 resulted in a lag time of ~10 hours in presence of 150 mM urea, again indicating an important role for this porin in the early stages of growth (Supplementary Figure S4). The capacity of cells to form FCCs and SABs, however, was not impacted, nor was their capacity to endure the presence of urea at up to 500 mM concentration (Supplementary Figure S4). At this concentration, the expression of Omp-Pst1 is 3-fold down-regulated within developing FCCs and SABs (Figure 2.c and d, respectively, and Supplementary Table S2). Thus, Omp-Pst2 could play a role in the resistance of *P. stuartii* communities to high urea concentrations – a role that could be diffusive (efflux or reduced influx of urea) or structural (promotion of DOT formation). To address the latter possibility, i.e. determine whether urea influences the formation of DOT by Omp-Pst1 and Omp-Pst2, we reconstituted these in liposomes and assayed the porin-induced proteoliposome aggregation, characteristic of DOT formation²³, at increasing concentrations of urea by using dynamic light scattering (DLS)

(Supplementary Figure S5 and Table S3). We found that urea does not affect the self-association into DOTs of *P. stuartii* porins, which is consistent with the fact that urea does not impact FCC formation.

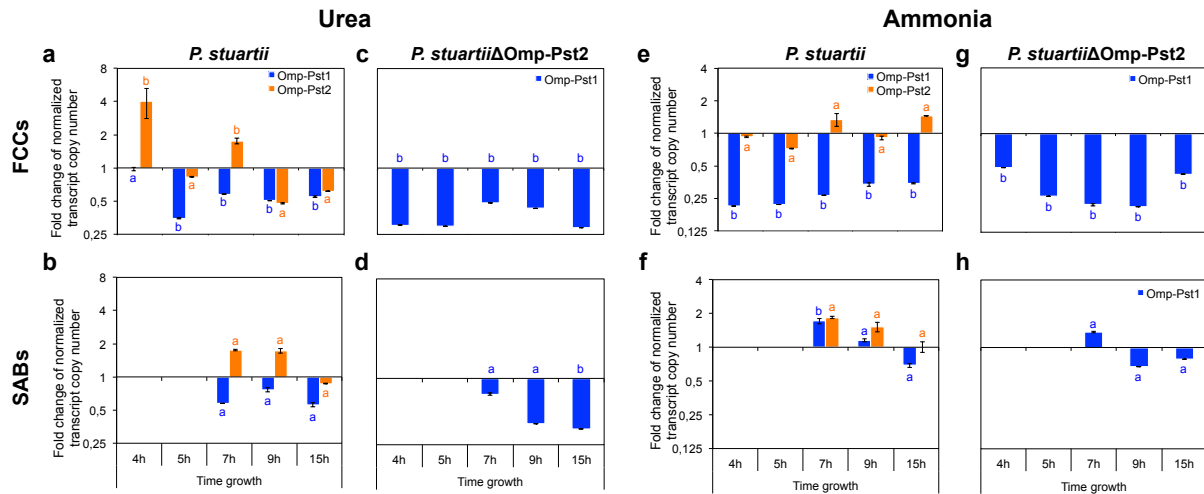


Figure 2. The expression of Omp-Pst1 is down-regulated in FCCs to protect *P. stuartii* bacteria against urea and ammonia conditions. The expression of Omp-Pst1 (blue) and Omp-Pst2 (orange) of *P. stuartii* wild-type or *P. stuartii*ΔOmp-Pst2 was measured by RT-qPCR in FCCs and SABS, upon exposure to 500 mM of urea concentration (panels a, b and c, d, respectively) and to 500 mM ammonia concentration (e, f and g, h). For each growth time point, data were represented as the ratio of the normalized transcript copy number in the exposed bacteria divided by the one in unexposed bacteria. Each measurement was performed in triplicates. Error = SD. Different letters above the bars indicate significant differences ($p < 0.05$; ANOVA followed by post-hoc Tukey HSD test) and statistics data are available in the Supplementary Table S2.

- Resistance of *P. stuartii* to high concentration of ammonia involves Omp-Pst2

We investigated the effect of high concentrations of ammonia on *P. stuartii* fitness, survival, socialization, and porin expression and self-association using the same approaches described above for urea. At the growth level, the presence of ammonia at 500 and 1,000 mM concentrations resulted in lag times of 45 min and 6.4 hours, respectively, with no effect seen at 150 mM (Supplementary Figure S1). The increased lag times were paralleled by significant decreases in the abundance of porins in the OM, viz. - 20 and - 50% at 500 and 1,000 mM ammonia, respectively (Supplementary Figure S2 and Table S1). Transcriptomic studies revealed that only expression of Omp-Pst1 is affected, with a significant 4-fold reduction in expression observed at 500 mM ammonia in developing FCCs (Figure 2.e and Supplementary

Table S2). Contrastingly, Omp-Pst1 expression is 2-fold increased in developing SABs exposed to the same concentration of ammonia (Figure 2.f and Supplementary Table S2). Within both type of communities, the expression of Omp-Pst2 remains steady (Figure 2.e and f). Thus, the regulation of Omp-Pst1 expression in the presence of ammonia is different in SABs and FCCs, possibly underlying differences in the access of this solute to the periplasm in the two types of communities. Indeed, an extracellular matrix (ECM) is present around SABs cells which could protect them against the adverse effects of ammonia. As this matrix is not visible and therefore presumably absent in FCCs, reduction of Omp-Pst1 expression could there serve the purpose of reducing penetration of the harmful solute into the periplasm. The observation that the expression of Omp-Pst2 is not down-regulated suggested that it does not partake in ammonia influx. This hypothesis is supported by experiments performed on the *P. stuartii*ΔOmp-Pst2 strain which confirm that a significant down-regulation of Omp-Pst1 expression (~ 2-4 fold) is required for FCCs to survive at high ammonia concentration (Figure 2.g and Supplementary Table S2). These experiments furthermore suggested that expression of Omp-Pst2 is beneficial to *P. stuartii* survival and fitness in the presence of ammonia; indeed, deletion of Omp-Pst2 resulted in an inability to grow at 1,000 mM concentration (Supplementary Figure S4).

Socialization was challenged by high concentrations of ammonia, with a complete inability to form SABs at 1,000 mM ammonia. Exposure of preformed FCCs to high concentrations of ammonia (≥ 500 mM) result in their breaking into smaller communities of living cells, whereas preformed SABs are disrupted at 1,000 mM ammonia with only dead cells remaining attached onto the surface (Figure 3.a and b). This result evidence that for an ECM to efficiently protect cells against ammonia, it needs to be produced in the presence of ammonia. It also demonstrates that formation of FCCs can be a more fit socialization mechanism for *P. stuartii* than SABs, e.g. in the presence of ammonia. The observation that socialization is not affected by the deletion of Omp-Pst2 supports the hypothesis that Omp-Pst2 does not partake in the

influx of ammonia into the periplasm (Supplementary Figure S4). It also exemplifies that in the presence of ammonia, Omp-Pst1 is the main porin supporting cell-to-cell contact by DOT formation in the FCCs.

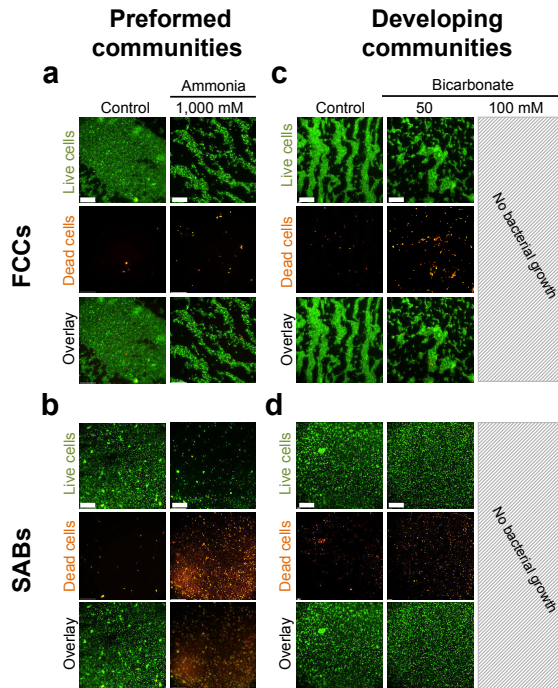


Figure 3. Preformed SABs of *P. stuartii* are challenged by ammonia, while the development of FCCs and SABs is challenged by bicarbonate. The resistance of preformed FCCs and SABs in presence of 1,000 mM ammonia concentration (panels a and b, respectively) and the capacity of bacteria to form FCCs and SABs in presence of increasing concentrations of bicarbonate (c, d) was visualized by epifluorescence microscopy. Concentrations at which bacteria were unable to grow were represented as a grey-hatched rectangle. All bacteria were shown in green (Syto 9 green labelling, upper line) while dead cells were in red (propidium iodide labelling, middle line). A merged image was shown on the bottom line of each panel.

We asked whether the formation of smaller FCCs in the presence of high ammonia concentrations only parallels the observed reduction in porin expression or is associated with a reduced propensity of porins to self-associate. We used DLS to monitor DOT formation by each of the two porins at increasing concentrations of ammonia. We found that ammonia significantly inhibits DOT formation by Omp-Pst1, but not that by Omp-Pst2 (Figure 4.a and Supplementary Table S3). Indeed, the proteoliposome aggregation driven by 1 μ M Omp-Pst1 can be fully reversed by concentration as low as 150 mM ammonia, whereas that of Omp-Pst2 was not affected by ammonia concentration up to 1,000 mM. Thus, the formation of smaller FCCs stems both from the reduced number of Omp-Pst1 present in their OMs and from the inhibition of DOT formation Omp-Pst1 at high ammonia concentration.

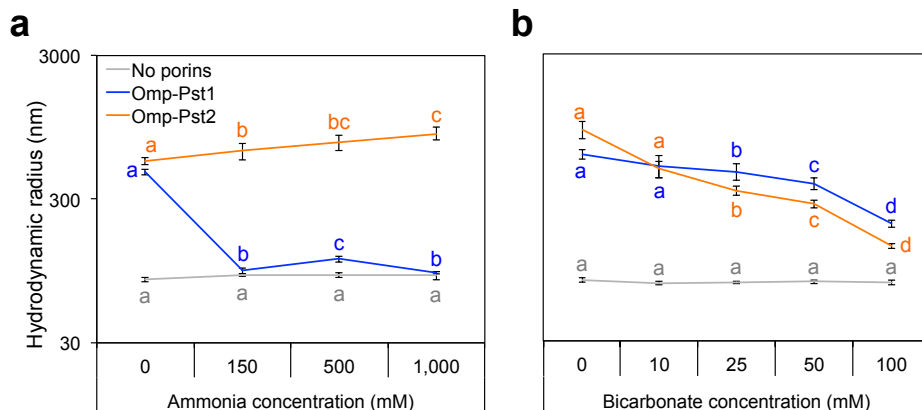


Figure 4. The propensity to self-associate of Omp-Pst1 only is challenged by the presence of ammonia, while the DOTs of the two porins Omp-Pst1 and Omp-Pst2 are inhibited by bicarbonate. The hydrodynamic radius of proteoliposomes was observed by DLS, 24 hours after the addition of Omp-Pst1 (blue) or Omp-Pst2 (orange) into LUV suspension, in presence of increasing concentrations of ammonia (a) or bicarbonate (b). As a control, the hydrodynamic radius of LUVs without porin insertion, in the same conditions, was measured (grey). Different letters above each point indicate significant differences ($p < 0.05$; ANOVA followed by post-hoc Tukey HSD test) and statistics data are available in Supplementary Table S3.

- *P. stuartii* is highly sensitive to bicarbonate but unaffected by creatinine

After urea and ammonia, bicarbonate and creatinine are the two most abundant metabolites present in the urine. Performing the same investigations as described above for urea and ammonia, we found that, up to 100 mM, i.e. a concentration 14-time higher than encountered in the urinary tract (7 mM), creatinine has no effect on *P. stuartii* fitness, survival, socialization (Supplementary Figure S1 and S4) and porin self-association (Supplementary Figure S5).

P. stuartii cells are, however, very sensitive to changes in bicarbonate concentration, displaying all signs of normal growth at 50 mM (Supplementary Figure S1), but a complete inability to develop FCCs and SABs at 100 mM (Figure 3.c and d, respectively). Moreover, a decrease in size of the FCCs is observed when the bicarbonate concentration is increased (up to 50 mM), coherent with the significant inhibition of Omp-Pst1 and Omp-Pst2 self-association into DOTs (Figure 4.b and Supplementary Table S3). However, full inhibition of DOT formation was not attained, even at 100 mM bicarbonate, supporting that the complete inhibition of *P. stuartii* socialization is not only due to the inhibition of porins.

By RT-qPCR, we found that Omp-Pst1 undergoes a 2-fold down-regulation in expression just post-exposure to bicarbonate at 50 mM concentration, but along with time the expression of Omp-Pst1 is restored and even augmented in SABs. Contrastingly, the expression of Omp-Pst2 is slightly augmented in FCCs (Supplementary Figure S2 and Supplementary Table S3) and deletion of Omp-Pst2 renders cells even more sensitive to bicarbonate, with growth being observed up to 25 mM bicarbonate only (Supplementary Figure S4). Thus, Omp-Pst2 is necessary for *P. stuartii* cells to survive in the presence of bicarbonate. The expressions of both porins did not vary significantly on SABs, again supporting that the presence of an ECM around SAB cells ensures resistance to bicarbonate without necessity of porin regulation.

We then verified the effect of bicarbonate on already established communities of *P. stuartii* cells. Preformed FCCs and SABs were able to resume growth without delay at concentration up to 100 mM bicarbonate (Supplementary Figure S3). These results again illustrate that socialization profits *P. stuartii* survival. They also raise questions as to which mechanism(s) Omp-Pst2 may exploit to protect cells against the adverse effects of bicarbonate.

- Variation of pH hardly affects *P. stuartii* socialization and fitness

We last investigated the effect of pH variation. As reported earlier, *P. stuartii* can grow and socialize into FCCs and SABs within the pH 6 to pH 9 range²². Within FCCs, however, growth at extreme pHs is poised with increased lag times (5, 1 and 2 hours lag time at pH 5, 8 and pH 9, respectively) (Supplementary Figure S1) and characterized by a 20% reduction in the abundance of porins in the OM at pH 9 (Supplementary Figure S2 and Table S1). Transcriptomic studies indicate that this decrease can be fully accounted for by Omp-Pst1, whose expression is down-regulated by 2.6-fold in FCCs at pH 9, while that of Omp-Pst2 remains steady. Within SABs, the situation is different and dependent on pH, with a 2.1-fold overexpression at pH 5 but at 1.6-fold reduced expression at pH 9 (Supplementary Figure S2

and Table S2). The expression of the two porins did not vary significantly along the time within both phenotypes (Supplementary Table S2). No further insights could be obtained on the effect of pH on porin expression due to lack of a clear pattern sustained along time.

Experiments performed on the *P. stuartii*ΔOmp-Pst2 strain suggest that Omp-Pst2 plays a role in the adaptation of cells to variations of pH. Firstly, lag times before growth are increased at pH 5 and pH 9 (6 and 7 hours lag time, respectively) and, to a lesser extent, at pH 8 (~3 hours lag time), in the absence of Omp-Pst2 (Supplementary Figure S4). Secondly, a significant increase is observed in the amount of Omp-Pst1 present within OMs at pH 8 and 9 (Supplementary Figure S2 and Table S1), suggesting that to survive at these pHs *P. stuartii* could compensate the absence of Omp-Pst2 by increasing the amount of Omp-Pst1 in OMs. Unfortunately, we cannot draw a parallel with transcriptomic results due to highly variations and non-significant changes of Omp-Pst1 expression within FCCs and SABs over the time. We note that while variations of pH do not affect the propensity of Omp-Pst2 to self-associate into DOTs, that of Omp-Pst1 decreases by 2.1 and 2.3 times at pH 8 and pH 9, respectively (Supplementary Figure S5 and Table S3). Again, this could underlie a means by which *P. stuartii* compensates the absence of one porin by overexpression of the other.

Discussion

Providencia stuartii is a pathogen causing chronic urinary tract infections that can result in the death of victims^{11,15}. *P. stuartii* is of all *Enterobacteriaceae*, the one that intrinsically most resistant to antibiotics, likely due to its ability to socialize into floating communities of cells (FCCs) and surface-attached biofilms (SABs)²³. FCCs are supported by self-matching interaction between residues in the extracellular loops of porins and are at the origin of SABs, which they form by sedimentation²³ and subsequent secretion of an extracellular matrix (ECM).

In this study, we examined the impact of a variety of environmental cues on the fitness, survival and socialization of *P. stuartii*, as well as on the expression of its porins and their propensity to self-associate into DOTs. Experiments were hence performed on both types of multicellular communities (FCCs and SABs), and on both developing and established communities. The effect of four metabolites present at high concentration in the urinary tract was investigated, viz. urea (up to 170 mM), ammonia (25 mM), bicarbonate (25 mM) and creatinine (7 mM); we also verified the effect of sudden pH variations. Overall, we found that *P. stuartii* is highly resistant to these cues, requiring 2-40 times higher concentrations than those encountered in the urinary tract to display a phenotype change.

Socialization into FCCs and SABs was observed in presence of all tested environmental cues at all concentrations tested, with the exception of bicarbonate at 100 mM. Given that this concentration is 4-times that observed for bicarbonate in the urinary tract, our results are indicative of the bacterium likely being present in a socialized state (FCCs and SABs) during urinary tract infections. Overall, we found that socialization increases the fitness of *P. stuartii* by raising tolerated concentrations by at least 2-fold, irrespective of the tested cue. For example, bicarbonate was the most harmful to *P. stuartii* cells, with no growth observed at a concentration as low as 50 mM, but preformed FCCs and SABs could survive up to 100 mM concentration. Likewise, urea was the second most toxic metabolite we tested, with no growth observed at 1,000 mM concentration and, in this case also, preformed FCCs and SABs could sustain whereas developing FCCs could not. In the case of ammonia, which is less toxic to *P. stuartii* cells with growth being observed up to 1,000 mM concentration, the increased fitness of socialized cells was visible in the lag times before growth, these being 45 min and 6.4 hours at 500 and 1,000 mM, respectively, in developing FCCs, but decreasing to 1.5 hours at 1,000 mM in preformed FCCs. Thus FCCs represent a socialization mode which, alike SABs, benefits cells by allowing them to endure higher concentrations of harmful solutes.

Experiments performed on the *P. stuartii*ΔOmp-Pst2 strain showed that DOTs of Omp-Pst1 were sufficient to scaffold FCCs, and thereby SABs, as one would expect given the relative abundance of Omp-Pst1 and Omp-Pst2 in *P. stuartii* OM. They also demonstrated that the presence of Omp-Pst2 was beneficial to *P. stuartii* fitness, enabling survival at 2-times higher ammonia and bicarbonate concentrations (1,000 & 500 mM ammonia and 50 & 25 mM bicarbonate for *P. stuartii* WT & *P. stuartii*ΔOmp-Pst2, respectively), and reducing lag-time before growth at high concentrations of urea and ammonia (5 & 9 hours at 500 mM urea and 6.5 hours & no growth at 1,000 mM ammonia for WT & *P. stuartii*ΔOmp-Pst2, respectively). At the present time, we can only speculate as to how Omp-Pst2 promotes resistance against high urea, ammonia and bicarbonate concentrations since, alike its role in the early stage of growth, it could either be diffusive, i.e. a result of the peculiar positively-charged amino-acid distribution along the channel of Omp-Pst2^{32,36,37}, or structural, i.e. stemming from the ability of this porin to form intercellular dimers or trimers (DOTs) that can rivet adjacent cells one onto another forming FCCs²³. We conjecture that it is unlikely that influx of urea, ammonia or bicarbonate occur across Omp-Pst2, whose electrostatic potential favors efflux of cations and gates the channel in case of a massive cation influx³⁶. Rather, our data suggested that it is Omp-Pst1 which serves as the entry route for these solutes into cells, with a ~2-4 fold reduced expression in FCCs and SABs formed in presence of 500 mM urea and ammonia and of 50 mM bicarbonate – and this, regardless of whether Omp-Pst2 is expressed (*P. stuartii* WT) or not (*P. stuartii*ΔOmp-Pst2). Hence, if any, the diffusive role of Omp-Pst2 in resistance to high ammonia concentrations would be to facilitate the efflux of positively charged ammonia from the periplasm³⁶, following urea catalysis by the cytoplasmic urease of *P. stuartii* or degradation by self-hydrolysis. The role of Omp-Pst2 could alternatively be to provide a substitute scaffold to promote FCC establishment by DOT formation when expression of Omp-Pst1 needs to be repressed. In line with this hypothesis, Omp-Pst2 propensity to self-associate into DOTs is higher than that of Omp-Pst1²³ and is promoted by increasing ammonia concentrations. Together with the fact that

DOT formation by Omp-Pst1 and Omp-Pst2 are unaffected by urea, this compensation mechanism would explain why cells exposed to 500 mM urea are still able to form FCCs despite a 33% reduced abundance of porin in their OM. Close-up views of these FCCs indeed show the characteristic tight packing and “standing” orientation of cells – almost orthogonal to that observed in micro-colonies (Supplementary Figure S6) – confirming that even at high urea concentration (and therefore low cell density), the structural integrity of FCCs is preserved. To the contrary, FCCs formed at 500 mM ammonia showed defects, with cells losing their “standing” orientation (Supplementary Figure S6). This could stem from the combination of the 50% reduction in porin abundance in the OM, accounted entirely by Omp-Pst1 (no change in Omp-Pst2 expression in the *P. stuartii* WT strain and same expression profile for Omp-Pst1 in the *P. stuartii*ΔOmp-Pst2 strain), and from the marked inhibition of its self-association into DOTs by ammonia. Again, Omp-Pst2 could compensate – whose self-association into DOTs is promoted by increasing ammonia concentrations – but not up to 1,000 mM concentration where planktonic cells are observed instead of FCCs. Loss of the ability to scaffold FCCs and/or to efflux ammonia would then explain why deletion of Omp-Pst2 result in an increased sensitivity to ammonia. By extension, bicarbonate influx likely occurs through Omp-Pst1 – whose channel is mildly anion selective – considering the immediate down-regulation undergone by this porin when the bacterium is put in presence of the solute. The increase in Omp-Pst2 expression was yet observed only after 15 hours, suggesting that it does not come into play to rescue FCC scaffolding by providing an alternative DOT architecture. In line with this premise, bicarbonate displayed an inhibitory effect on DOT formation by both porins, likely explaining the disruption of FCCs into planktonic cells.

We explained earlier that FCCs are at the origin of SABs, which they form by sedimentation. SABs are characterized by an ECM, but it is unknown whether such a structure exists around FCCs, or in other words whether synthesis of the ECM debuts or not at the FCC stage. In the

present work, we have tried to specifically label the ECM of *P. stuartii* using three common markers (viz. Wheat Germ Agglutinin (WGA) lectin, Concanavaline A lectin and FilmTracer™ SYPRO™ Ruby Biofilm Matrix Strain (ThermoFischer)), none of which succeeded in revealing the ECM of *P. stuartii* SABs; hence the question as to whether or not FCCs also feature an ECM remains open. Data collected in the presence of 500 mM ammonia, however, showed a 3-fold reduction in Omp-Pst1 expression in developing FCCs, whereas a 2-fold increase in the expression of the two porins was observed in developing SABs. This difference could underlie the fact that in the latter an ECM is present that protects cells against the adverse effects of ammonia, eliminating the need to down-regulate porin expression. Our results yet evidence that the ECM may only be able to do so in the case it has been synthesized in the presence of ammonia; indeed SABs preformed in normal growth conditions are eradicated by exposure to 1,000 mM ammonia. We note that preformed FCCs can sustain this concentration, demonstrating that in the presence of ammonia at least they represent a more fit socialization mechanism than SABs.

In conclusion, our results provided new insights into the formation and resistance of socialized *P. stuartii* in conditions that mimic its pathophysiological habitat. *P. stuartii* is most often isolated from patients undergoing long-term catheterization^{11,15}, and the severity of infections results not only from the intrinsic antibiotic resistance of the bacterium, but also from its socialization into FCCs and SABs²², which display higher resistance to environmental cues (this work), antibiotics and the immune system^{38,39}. Our data indicate that future treatments against *P. stuartii* should be evaluated on FCCs and SABs, and in conditions mimicking the urinary tract, for them to be efficient and potentially eradicate infections in the clinical context.

Methods

Strains

The *Providencia stuartii* ATCC 29914 strain was obtained from the Pasteur Institute (Paris, France). A disruption of the *omp-pst2* gene in *P. stuartii* ATCC 29914 (chloramphenicol-resistant)²² was performed to study the importance of Omp-Pst2 porin for adaptation to pathophysiological conditions. The *Escherichia coli* BL21 DE3 Δ Omp8 strain^{32,40} – deleted of its principal porins OmpF, LamB, OmpA and OmpC – was used for the expression of *P. stuartii* porins for their purification prior to analyze their self-association capacity in DOTs by Dynamic Light Scattering (see detailed method below).

All chemicals were from Sigma-Aldrich, unless specified otherwise.

Production of porins from P. stuartii in E. coli

One μ L of plasmid pGOmp-Pst1 or pGOmp-Pst2 was transformed into 50 μ L of *E. coli* Δ Omp8 competent kanamycin-resistant cells by the heat-shock method^{32,41}. Cells were recovered in 500 μ L of SOC medium for 1 hour at 37°C. 20 μ L of cell suspension was then transferred onto agar plates containing 100 and 25 ng. μ L⁻¹ ampicillin and kanamycin respectively, and incubated overnight at 37°C. A colony was introduced in 25 mL of Luria Bertani (LB) medium overnight, yielding a pre-culture that was further inoculated into 1 L of LB culture, selected by the addition of ampicillin and kanamycin at final concentrations of 100 μ g/mL and 25 μ g/mL, respectively. pGOmp-Pst1 and pGOmp-Pst2 plasmids contain a strong T7-phage promoter allowing sufficient porin expression without induction by IPTG. After the optical density of cultures at 600 nm reached a value of 1, cells were harvested by centrifugation at 4,500 rpm for 30 min and the pellets were immediately used for porins extraction.

Porin extraction and solubilization

Pellet cells were resuspended in 20 mM phosphate buffer pH 7.4, supplemented with DNase (few mg), 1 mM MgSO₄ and an anti-protease cocktail (Complete, Roche). The cells were disrupted using a micro-fluidizer (Constant system LTD, UK) at 14,000 Psi. Membranes were separated from cytoplasm by centrifugation at 4,500 rpm for 45 min. The pellet containing the membranes was resuspended in 20 mM phosphate buffer pH 7.4 with 0,3% n-octyl-polyoxyethylene (OPOE) detergent (Affymetrix, UK) and incubated at 20°C for 2 h under agitation to separate inner (IM) from outer membranes (OM). A 45-min ultracentrifugation at 35,000 rpm (Optima XE, Beckman Coulter) was then performed. The supernatant containing the OM was collected and the resulting pellet containing the IM and some remaining OM was resuspended and incubated at 20°C for 2 h in 20 mM phosphate buffer pH 7.4 with 3% OPOE. The last solubilization step was performed three times to maximize OM protein recovery. The supernatants containing the solubilized porins from the OM were stored at 4°C until purification.

Porin purification

Solubilized porins were loaded onto an anionic-exchange column (Hitrap HQ, 5 mL, GE Healthcare Life Science, France) and subjected to detergent exchange with 0.1 M MES buffer pH 6.5 complemented with 0.1% lauryldimethylamine-oxide (LDAO) detergent (Affymetrix, UK) and 25 mM NaCl. The elimination of most lipopolysaccharides (LPS) was achieved by washing the column with 0.1 M MES pH 6.5 buffer complemented with 2% LDAO. After 4 h of slow washing (0.2 mL.min⁻¹), the column was re-equilibrated with 0.1 M MES buffer pH 6.5 complemented with 0.1% LDAO and 25 mM NaCl. Proteins were then eluted by using of a NaCl gradient (0 to 1M). The fractions containing the pure protein were analyzed on SDS-PAGE to verify their purity. Those containing pure porin were pooled together and concentrated to 7 mg.mL⁻¹ on a 100-kDa cutoff Amicon (Sigma-Aldrich, France) ultra-filtration unit. Purified porins

were stored at 4°C until use.

Liposome preparation

Large unilamellar liposomes (LUVs) were produced by standard film-hydration method⁴². Briefly, the liposome mixture was generated by adding 0.02% lissamine-rhodamine-sn-glycero-3-phosphoethanolamine (Rhod PE, Avanti Polar, Lipids Co., USA) to 4% L- α -phosphatidylcholine (egg PC, Avanti Polar, Lipids Co., USA) suspended in a chloroform solution. The lipids were dried under N₂-flow to obtain a thin lipid film. Residual chloroform was eliminated by overnight vacuum. The lipid film was rehydrated with phosphate buffer (125 mM, pH 7.4) and vortexed continuously during 5 min to produce multilamellar vesicles. The vesicles were freeze-thawed (100K-310K) ten times to obtain LUVs. To finish, an extrusion with a 100-nm filter was performed to calibrate LUVs toward 70-nm diameter (mini-extruder with polycarbonate filters, Avanti Polar Lipids).

Dynamic Light Scattering (DLS)

The hydrodynamic radius of LUVs was calculated after the incorporation of porins into their bilayer by using the DLS method (DynaPro Nanostar from Wyatt Technology). To this end, liposomes (0.125 mg.mL⁻¹) and porins (ranged from 0.033 to 1.07 μ M) were mixed and incubated at pH 7.4. To avoid a sudden decrease of detergent concentration in solution leading to a porin aggregation, we used biobeads (hydrophobic polystyrene) to decrease slightly the detergent below the critical micellar concentration (CMC). In the lipid bilayer, porins are oriented in natural way meaning oriented mostly with their intracellular turns facing the lumen of the LUVs and their extracellular loops facing the outside⁴³. The incorporation of porins into liposomes generates the increase of hydrodynamic radius of liposomes continuing during 24 h at 4°C. The DLS measurement was then taken.

The most common habitat of *P. stuartii* in humans is the urinary tract. The aim of DLS study is to

determine whether high concentrations of urea, ammonia (from 100 to 1,000 mM), bicarbonate, creatinine (from 10 to 100 mM) or pH variation (between 5 and 9) are compatible with the self-association of Omp-Pst1 and Omp-Pst2. For that purpose, stress conditions were applied before the incorporation of porins into LUVs. After 24 h incubation, biobeads were added and the hydrodynamic radii of proteoliposomes were determined another 24 h later.

Transcriptomic study

P. stuartii forms FCCs and SABs. Within both phenotypes, we aimed at monitoring the relative expression of Omp-Pst1 and Omp-Pst2 in *P. stuartii* ATCC 29914 and *P. stuartii*ΔOmp-Pst2 mutant when exposed to different concentrations of urea, ammonia and various pH.

Total RNA extraction

One colony was added to 30 mL of LB liquid medium and incubated at 37°C for 1 h under 150 rpm agitation. For each strain and each condition tested, three wells (triplicates) of a 6-well plate (CytoOne) were filled with 2 mL from the LB pre-culture. Plates were incubated at 37°C under 60 rpm agitation up to different OD at 600nm: 0.3, 0.5, 0.7, 0.9 or 1.5 to investigate porin expression at different growth phases. FCC in suspension were collected and briefly centrifuged to pellet the bacteria without damaging them. The pellet was resuspended in either 2 mL of fresh LB containing urea, ammonia (500 mM), bicarbonate (50 mM), or in 2 mL of LB medium pH-specific (between 5 and 9), and incubated at 37°C for 30 min under 60 rpm agitation. Concomitantly, adherent biofilms were washed with LB then 2 mL of fresh LB containing the stress conditions described above were added. The plate was incubated at 37°C for 30 min under 60 rpm agitation. The RNA extraction was performed using RNeasy Mini Kit (Qiagen) with some adjustments for the two different phenotypes in the primary steps. For FCCs, 1 mL of the 2-mL culture was removed and replaced by 1 mL of RNAlater Cell Reagent (Qiagen). After 5 min of incubation, the mixture was centrifuged at 3,200 g for 10 min and the pellet was

resuspended in 110 µL of TE buffer (Tris-HCl 30 mM, EDTA 1 mM, pH 8.0) containing 15 mg/mL of lysozyme and 2 mg/mL of proteinase K (Qiagen), and incubated at RT for 10 min. For SABs, the 2 mL of LB medium were removed from well and 1 mL of RNAprotect Cell Reagent: LB (1: 1) was added. After 5 min incubation, the RNAprotect was removed and 410 uL of TE buffer containing 15 mg/mL of lysozyme and 0.5 mg/mL of proteinase K were added. The adherent biofilm was disrupted manually by scratching the well bottom and the solution was incubated at RT for 10 min. Total RNA from both phenotypes was extracted following manufacturer's instructions. For both, quantity and quality of RNAs were assessed using a Nanodrop2000 (Thermo Fisher Scientific).

Reverse transcription quantitative PCR (RT-qPCR)

RNA extracted from FCCs and SABs were immediately used for reverse transcription. One µg of total RNA was retro-transcribed into complementary DNA (cDNA) by using the QuantiTect Reverse Transcription Kit (Qiagen) following manufacturer's instructions. cDNA was stored at -20°C until use and the remaining RNA were stored at -80°C.

The expressions of *omp-pst1* and *omp-pst2* were quantified by RT-qPCR. To perform an absolute quantification of transcript abundance of each porin in each condition tested, DNA fragments of known size and sequence were amplified and quantified from the genome of *P. stuartii* to be used as standards. To do so, *P. stuartii* genomic DNA was extracted using NucleoSpin Tissue kit (Macherey-Nagel) following manufacturer's instructions. A 954 bp fragment of *omp-pst1* gene was amplified using the primers OmpPst1_F3qs (5'-GAAGATGGCGACGACTCACG-3') and OmpPst1_R3qs (5'-GTAAACCAGACCCAGACCCAGAAC-3'), and a 956 bp fragment of *omp-pst2* gene was amplified using the primers OmpPst2_F4qs (5'-ATTATTCGCGGCGGGTGTAC-3') and OmpPst2_R4qs (5'-CAGCGGCCATATTCTTGTTGA-3') using the Q5 High-Fidelity DNA

Polymerase (New England BioLabs). The PCR program consisted in an initial step at 98°C for 5 min, then 35 cycles of 98°C for 30 sec (denaturation), 55°C for 30 sec (primers annealing) and 72°C for 2 min (elongation), ended by a final extension step at 72°C for 5 min. PCR amplicons were visualized on a 1 % agarose gel using SYBR Safe (Thermo Fisher Scientific). For each gene, the band corresponding to the amplicon was excised from the gel and purified using NucleoSpin Gel and PCR Clean-up kit (Macherey-Nagel) following manufacturer's instructions. Quality and quantity were measured using a Nanodrop2000 (Thermo Fisher Scientific). Based on the sequence composition and length of each porin fragment amplified, the number of copies present in the standard was calculated and the standard curve was established using eight concentrations from 5.0×10^1 to 5.0×10^8 gene copies.

For the quantification of the copy number of each porin in each condition, a 77 bp fragment of *omp-pst1* gene was targeted using the primers OmpPst1_F1q (5'-CGCATTCGGTTATGTTGAT-3') and OmpPst1_R1q (5'-CGCTTGACTTGTTGTTGT-3'), and a 82 bp fragment of *omp-pst2* gene using the primers OmpPst2_F2q (5'-CTTCGCTCTACAGTACCA-3') and OmpPst2_R2q (5'-GCCATCACCATTGTTATCTAA-3'). The reaction consisted of 4 μ L of ten fold-diluted samples or of the standards, 0.6 μ L of each primer (final concentration of 10 μ M each), 7 μ L of SsoAdvanced Universal SYBR Green Supermix (Bio-Rad) and RNase-free water for a final reaction volume of 15 μ L in each well. For each biological triplicate of each strain, two technical replicates were done. qPCR was run on a CFX Connect Real-Time PCR Detection System (Bio-Rad), and the qPCR program consisted in an initial step at 95°C for 3 min, then 39 cycles of 95°C for 10 sec (denaturation) and 60°C for 45 sec (primers annealing & elongation). A melt curve analysis was performed to assess the specificity of the amplification. The number of transcript copies of *omp-pst1* and *omp-pst2* was calculated using the standard curves for *P. stuartii* ATCC 29914 and *P. stuartii* Δ *Omp-Pst2* by using Bio-Rad CFX Manager v.3.1 (Bio-Rad). Gene expression data was normalized using the total RNA content for each condition, which is

the preferable normalization method when no housekeeping gene has been validated in the tested species, which is our case in *P. stuartii*⁴⁴.

Proteomic study

The abundance of porin proteins was quantified for *P. stuartii* ATCC 29914 and *P. stuartii*ΔOmp-Pst2 mutant under different conditions. One colony of each strain was inoculated in LB medium supplemented with 0, 100, 500 or 1,000 mM of urea, ammonia or with 0, 10, 25, 50 or 100 mM of bicarbonate, creatinine, or in pH-specific LB medium overnight. Ten microliters of bacteria from each condition was centrifuged for 30 s at 11,000 g, the pellet was resuspended in solution containing loading buffer 4X and 166 mM DDT, and heated to 95°C for 5 min. Cells denatured were then migrated on a SDS-PAGE gel for 90 min at 140 V. For porin quantification, the intensity of the corresponding band (between 35 and 40 kDa) was quantified and normalized by the total intensity of the profile using ImageJ software (v1.50i).

Bacterial growth studies

First, we intended to understand the impact of the conditions from the human urinary tract on *P. stuartii* survival and ability to form FCCs and SABs. We exposed *P. stuartii* to environmental cues such as urea, ammonia, bicarbonate, creatinine and pH variation. To this end, one colony of *P. stuartii* or *P. stuartii*ΔOmp-Pst2 (selected with 33 µg/mL of chloramphenicol) was inoculated in LB medium supplemented with 0, 100, 500 or 1,000 mM of urea, ammonia or with 0, 10, 25, 50 or 100 bicarbonate, creatinine, or in pH-specific LB medium for 1 h. Then, 150 µL of bacteria were disposed into a 96-well plate (Greiner) and incubated at 37°C under 100 rpm shaking overnight to promote biofilm formation on the well bottom and FCCs in suspension. The bacterial growth was monitored by absorbance at 600 nm for 24 h (10 min interval between time points) using a Biotek Synergy H4 microplate reader (Winooski, VT, USA). Secondly, we investigated the effect of urea, ammonia, bicarbonate, creatinine and pH variation on FCCs and

SABs already established. We inoculated one colony of both *P. stuartii* strains in LB medium for 1 h. One hundred and fifty microliters of bacteria were then disposed into a 96-well plate and incubated overnight at 37°C under 100 rpm. The day after, FCCs and SABs were exposed to 0, 100, 500 or 1,000 mM of urea, ammonia, or to 0, 10, 25, 50 or 100 bicarbonate, creatinine LB medium for 1 h, and the growth recovery was monitored over the day in terms of absorbance at 600 nm for 24h (10 minutes interval between time points) using a Biotek Synergy H4 microplate reader (Winooski, VT, USA).

Imaging

To observe FCCs and SABs, 7 µL of the planktonic bacteria were deposit between LB-Gelzan solid media (LB-Lennox solidified with 8 g/L Gelzan™) and a glass cover-slide, and imaged immediately afterwards⁴⁵. The wells were then washed with PBS three times to remove all floating bacteria and to image cells tightly attached to the well surface (= canonical biofilm). Bacteria were observed using an IX81 Olympus inverted microscope and samples were magnified thanks to a 100X objective (Plan APON100X, Olympus). The membranes were labeled using FM1-43X dye at 5 µg.ml⁻¹ (479 nm excitation; emission: 598 nm emission), all bacteria (live and dead) were labeled using Syto® 9 Green at 5 µM (485 nm excitation; 498 nm emission) and only dead bacteria were labeled by propidium iodide solution at 20 µM (533 nm excitation; 617 nm emission). All fluorescent dyes were purchased from Thermo Scientific, USA.

Statistical analysis

The *statsmodels* Python package was used for all analysis in this study⁴⁶. We used the 'Generalized Linear Model' module. As we are dealing with positive, and continuous response variables, we chose the Gamma family, using an inverse law as link function. All factors and their correlation were included for a first fit, then insignificant correlations were removed until the most parsimonious model, containing all significant variables, was found – in less than 10

iterations on average, indicating a good convergence. The two porins were treated as independent throughout the process. Then, TukeyHSD test was used to perform post-hoc analyses on the most significant factors.

Acknowledgements

We thank Martin Weik for continuous support, and Jean-Philippe Kleman, Françoise Lacroix, Aline Leroy and Anne-Marie Villard for their technical support during epifluorescence microscopy (V-M4D platform), DLS and RT-qPCR (RoBioMol platform) experiments. Financial support by the Agence Nationale de la Recherche (ANR-15-CE18-0005 ClickBiofilm) and the GRAL labex (C7H-LXG11A20-DYNAMOP) is acknowledged, as well as support from the CEA, the CNRS and the Université Grenoble Alpes. This work used the platforms of the Grenoble Instruct Center (ISBG: UMS 3518 CNRS-CEA-UJF-EMBL) with support from FRISBI (ANR-10-INSB-05-02) and GRAL (ANR-10-LABX-49-01) within the Grenoble Partnership for Structural Biology (PSB).

Conflict of interests

The authors declare no conflict of interest.

Author Contributions

J.L, G.T, M.E.K and J-P.C designed research and analyzed the data; J.L prepared samples and performed all experiments; G.T participated to RT-qPCR experiments; K.P. performed the statistical analyses of the data; M.E.K contributed preliminary data; J.L, G.T. and J.P.C. wrote the manuscript with input of all authors.

References

1. Costerton, J. W. Bacterial Biofilms: A Common Cause of Persistent Infections. *Science* **284**, 1318–1322 (1999).
2. Donlan, R. M. & Costerton, J. W. Biofilms: survival mechanisms of clinically relevant microorganisms. *Clin. Microbiol. Rev.* **15**, 167–193 (2002).

3. Das, T., Sehar, S. & Manefield, M. The roles of extracellular DNA in the structural integrity of extracellular polymeric substance and bacterial biofilm development: The roles of eDNA in the bacterial biofilm development. *Environ. Microbiol. Rep.* **5**, 778–786 (2013).
4. Okshevsky, M., Regina, V. R. & Meyer, R. L. Extracellular DNA as a target for biofilm control. *Curr. Opin. Biotechnol.* **33**, 73–80 (2015).
5. de la Fuente-Núñez, C., Reffuveille, F., Fernández, L. & Hancock, R. E. Bacterial biofilm development as a multicellular adaptation: antibiotic resistance and new therapeutic strategies. *Curr. Opin. Microbiol.* **16**, 580–589 (2013).
6. Thomas, D. N. & Dieckmann, G. S. Antarctic Sea ice--a habitat for extremophiles. *Science* **295**, 641–644 (2002).
7. Xu, Y., Miao, L., Li, X.-C., Xiao, X. & Qian, P.-Y. Antibacterial and antilarval activity of deep-sea bacteria from sediments of the West Pacific Ocean. *Biofouling* **23**, 131–137 (2007).
8. Stickler, D. J. Bacterial biofilms in patients with indwelling urinary catheters. *Nat. Clin. Pract. Urol.* **5**, 598–608 (2008).
9. Hall-Stoodley, L. & Stoodley, P. Evolving concepts in biofilm infections. *Cell. Microbiol.* **11**, 1034–1043 (2009).
10. Lebeaux, D. & Ghigo, J.-M. Infections associées aux biofilms: Quelles perspectives thérapeutiques issues de la recherche fondamentale ? *médecine/sciences* **28**, 727–739 (2012).
11. Wie, S.-H. Clinical significance of *Providencia* bacteremia or bacteriuria. *Korean J. Intern. Med.* **30**, 167 (2015).
12. McHale, P. J., Walker, F., Scully, B., English, L. & Keane, C. T. *Providencia stuartii* infections: a review of 117 cases over an eight year period. *J. Hosp. Infect.* **2**, 155–165 (1981).
13. Gould, C. V. *et al.* Guideline for prevention of catheter-associated urinary tract infections 2009. *Infect. Control Hosp. Epidemiol.* **31**, 319–326 (2010).
14. Chapman, C. M. C., Gibson, G. R. & Rowland, I. Effects of single- and multi-strain probiotics on biofilm formation and in vitro adhesion to bladder cells by urinary tract pathogens. *Anaerobe* **27**, 71–76 (2014).
15. De Vecchi, E. *et al.* Aetiology and antibiotic resistance patterns of urinary tract infections in the elderly: a 6-month study. *J. Med. Microbiol.* **62**, 859–863 (2013).
16. Jacoby, G. A. AmpC beta-lactamases. *Clin. Microbiol. Rev.* **22**, 161–182, Table of Contents (2009).

17. Nicolle, L. E. Resistant pathogens in urinary tract infections. *J. Am. Geriatr. Soc.* **50**, S230-235 (2002).
18. Warren, J. W. *Providencia stuartii*: a common cause of antibiotic-resistant bacteriuria in patients with long-term indwelling catheters. *Rev. Infect. Dis.* **8**, 61–67 (1986).
19. Tumbarello, M. ESBL-producing multidrug-resistant *Providencia stuartii* infections in a university hospital. *J. Antimicrob. Chemother.* **53**, 277–282 (2004).
20. Aubert, D., Naas, T., Lartigue, M.-F. & Nordmann, P. Novel genetic structure associated with an extended-spectrum beta-lactamase bla_{VEB} gene in a *Providencia stuartii* clinical isolate from Algeria. *Antimicrob. Agents Chemother.* **49**, 3590–3592 (2005).
21. Vlamakis, H., Chai, Y., Beauregard, P., Losick, R. & Kolter, R. Sticking together: building a biofilm the *Bacillus subtilis* way. *Nat. Rev. Microbiol.* **11**, 157–168 (2013).
22. El Khatib, M. *et al.* *Providencia stuartii* form biofilms and floating communities of cells that display high resistance to environmental insults. *PLOS ONE* **12**, e0174213 (2017).
23. El-Khatib, M. *et al.* Porin self-association enables cell-to-cell contact in *Providencia stuartii* floating communities. *Proc. Natl. Acad. Sci.* **115**, E2220–E2228 (2018).
24. Stevens, J. C., Jones, N. B. & Fay, D. F. Apparatus for uniaxial testing of soft human tissues in vitro. *Med. Biol. Eng. Comput.* **16**, 226–228 (1978).
25. Pagès, J.-M., James, C. E. & Winterhalter, M. The porin and the permeating antibiotic: a selective diffusion barrier in Gram-negative bacteria. *Nat. Rev. Microbiol.* **6**, 893–903 (2008).
26. Zeth, K. & Thein, M. Porins in prokaryotes and eukaryotes: common themes and variations. *Biochem. J.* **431**, 13–22 (2010).
27. Delcour, A. H. Outer membrane permeability and antibiotic resistance. *Biochim. Biophys. Acta BBA - Proteins Proteomics* **1794**, 808–816 (2009).
28. Pagès, J.-M. Porines bactériennes et sensibilité aux antibiotiques. *médecine/sciences* **20**, 346–351 (2004).
29. Nikaido, H. Prevention of drug access to bacterial targets: permeability barriers and active efflux. *Science* **264**, 382–388 (1994).
30. Ficarra, F. A. *et al.* *Xanthomonas citri* ssp. *citri* requires the outer membrane porin OprB for maximal virulence and biofilm formation: *Xanthomonas citri* requires OprB for virulence. *Mol. Plant Pathol.* **18**, 720–733 (2017).

31. Yantorno, O. *et al.* Outer membrane protein OmpQ of *Bordetella bronchiseptica* is required for mature biofilm formation. *Microbiology* **162**, 351–363 (2016).
32. Tran, Q.-T. *et al.* Implication of Porins in β -Lactam Resistance of *Providencia stuartii*. *J. Biol. Chem.* **285**, 32273–32281 (2010).
33. Bajaj, H. *et al.* Antibiotic Uptake through Membrane Channels: Role of *Providencia stuartii* OmpPst1 Porin in Carbapenem Resistance. *Biochemistry (Mosc.)* **51**, 10244–10249 (2012).
34. Song, W. *et al.* Understanding Voltage Gating of *Providencia stuartii* Porins at Atomic Level. *PLOS Comput. Biol.* **11**, e1004255 (2015).
35. Brooks, T. & Keevil, C. W. A simple artificial urine for the growth of urinary pathogens. *Lett. Appl. Microbiol.* **24**, 203–206 (1997).
36. Raman, A. & Sreenevasan, G. A. Urinary osmolarity and excretion of sodium, calcium and magnesium in patients with renal calculi. *Br. J. Urol.* **44**, 537–540 (1972).
37. Isaacson, L. C. Urinary composition in calcific nephrolithiasis. *Invest. Urol.* **6**, 356–363 (1969).
38. Leid, J. G. *et al.* The exopolysaccharide alginate protects *Pseudomonas aeruginosa* biofilm bacteria from IFN-gamma-mediated macrophage killing. *J. Immunol. Baltim. Md 1950* **175**, 7512–7518 (2005).
39. Khoury, A. E., Lam, K., Ellis, B. & Costerton, J. W. Prevention and control of bacterial infections associated with medical devices. *ASAIO J. Am. Soc. Artif. Intern. Organs 1992* **38**, M174-178 (1992).
40. Prilipov, A., Phale, P. S., Gelder, P., Rosenbusch, J. P. & Koebnik, R. Coupling site-directed mutagenesis with high-level expression: large scale production of mutant porins from *E. coli*. *FEMS Microbiol. Lett.* **163**, 65–72 (1998).
41. Prilipov, A., Phale, P. S., Van Gelder, P., Rosenbusch, J. P. & Koebnik, R. Coupling site-directed mutagenesis with high-level expression: large scale production of mutant porins from *E. coli*. *FEMS Microbiol. Lett.* **163**, 65–72 (1998).
42. Dijkstra, J., Ryan, J. L. & Szoka, F. C. A procedure for the efficient incorporation of wild-type lipopolysaccharide into liposomes for use in immunological studies. *J. Immunol. Methods* **114**, 197–205 (1988).
43. Zgurskaya, H. I. & Nikaido, H. Bypassing the periplasm: reconstitution of the AcrAB

multidrug efflux pump of Escherichia coli. *Proc. Natl. Acad. Sci. U. S. A.* **96**, 7190–7195 (1999).

44. Kruij, J., Karapetyan, N. V., Terekhova, I. V. & Rögner, M. In vitro oligomerization of a membrane protein complex. liposome-based reconstitution of trimeric photosystem I from isolated monomers. *J. Biol. Chem.* **274**, 18181–18188 (1999).

45. Johnson, G., Nour, A. A., Nolan, T., Huggett, J. & Bustin, S. Minimum information necessary for quantitative real-time PCR experiments. *Methods Mol. Biol. Clifton NJ* **1160**, 5–17 (2014).

46. de Jong, I. G., Beilharz, K., Kuipers, O. P. & Veening, J.-W. Live Cell Imaging of Bacillus subtilis and Streptococcus pneumoniae using Automated Time-lapse Microscopy. *J. Vis. Exp.* (2011). doi:10.3791/3145

47. Seabold, S. & Perktold, J. Statsmodels: Econometric and Statistical Modeling with Python. 5 (2010).

Supplementary Information

Socialization of *Providencia stuartii* enables resistance to environmental insults.

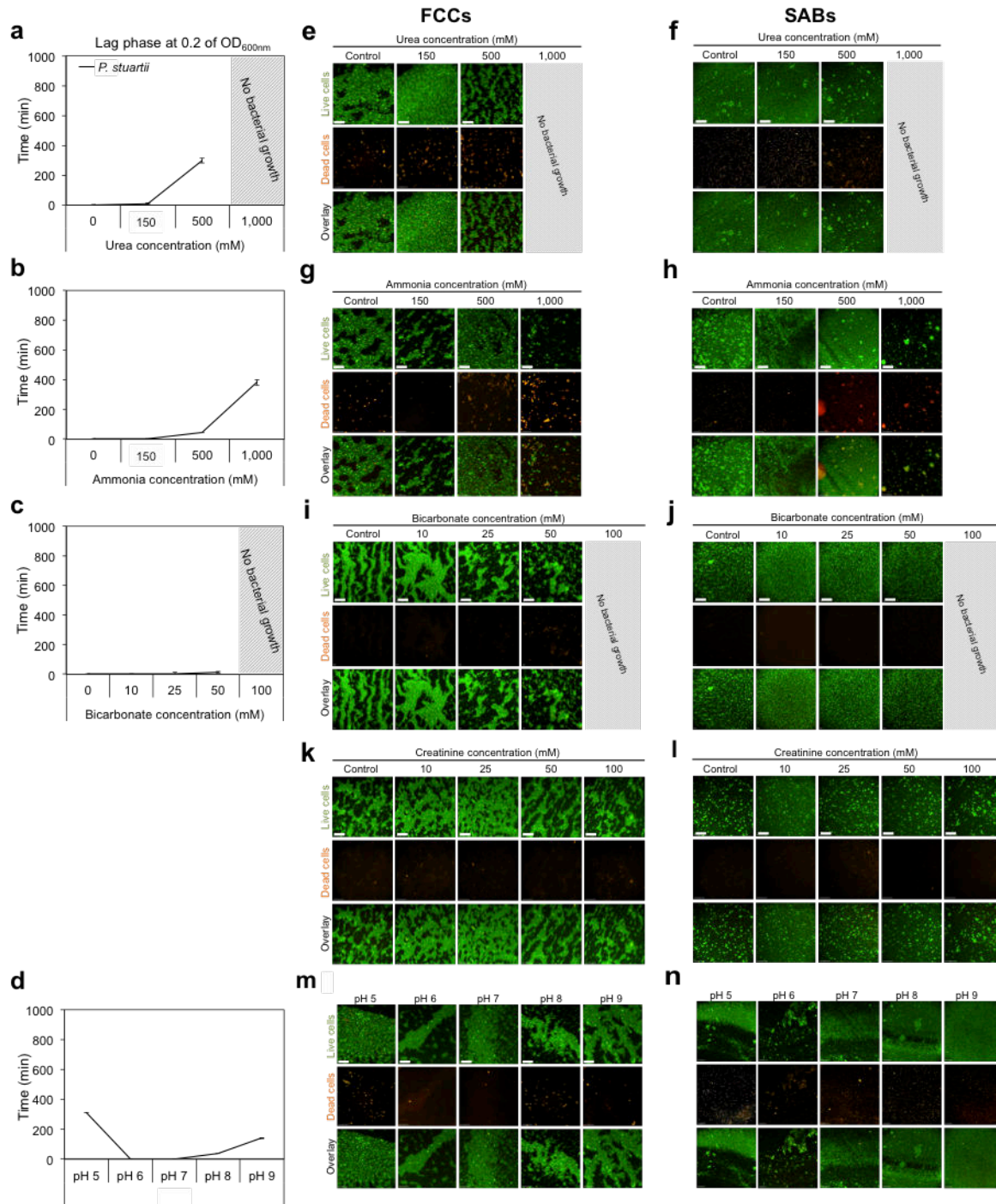
Authors:

Julie Lopes¹, Guillaume Tetreau¹, Kevin Pounot¹, Mariam El Khatib¹, Jacques-Philippe Colletier¹

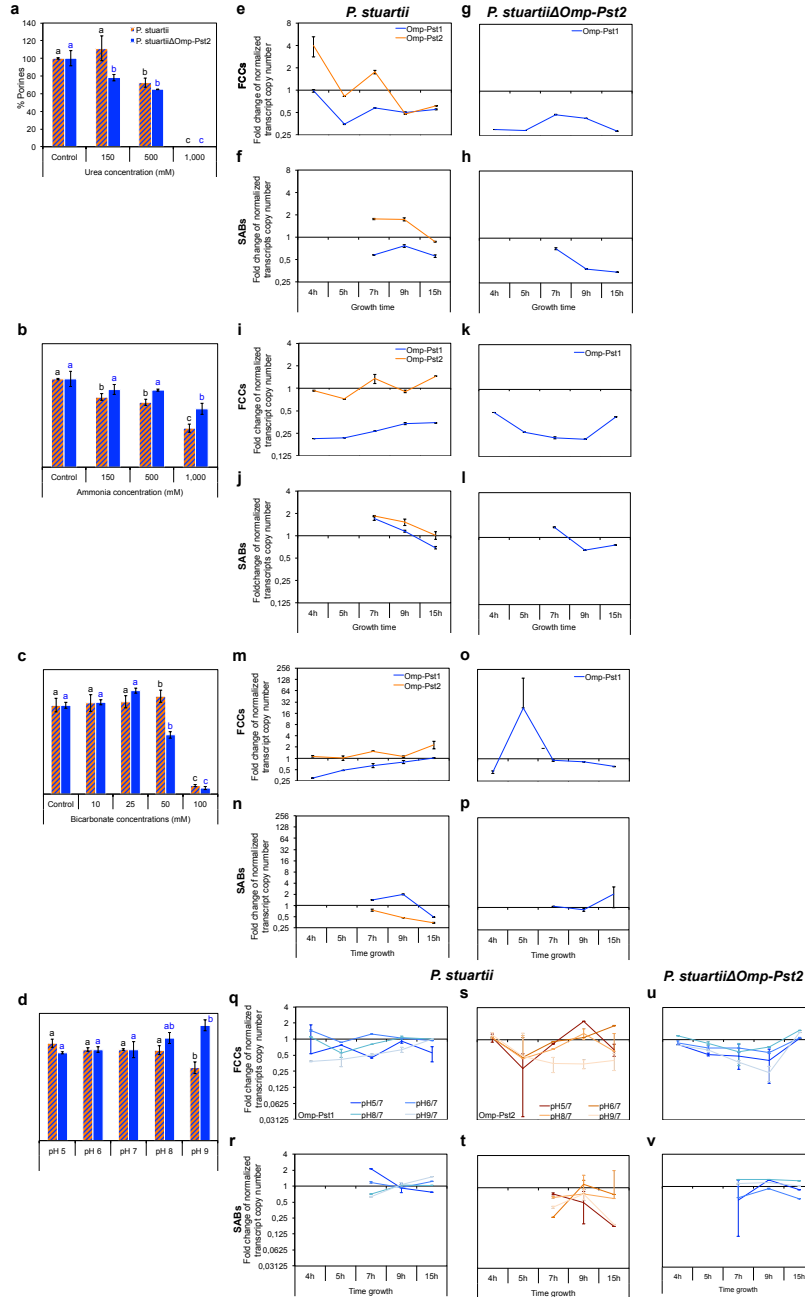
Affiliations:

¹ Univ. Grenoble Alpes – CEA – CNRS, Institut de Biologie Structurale (IBS), Grenoble, France

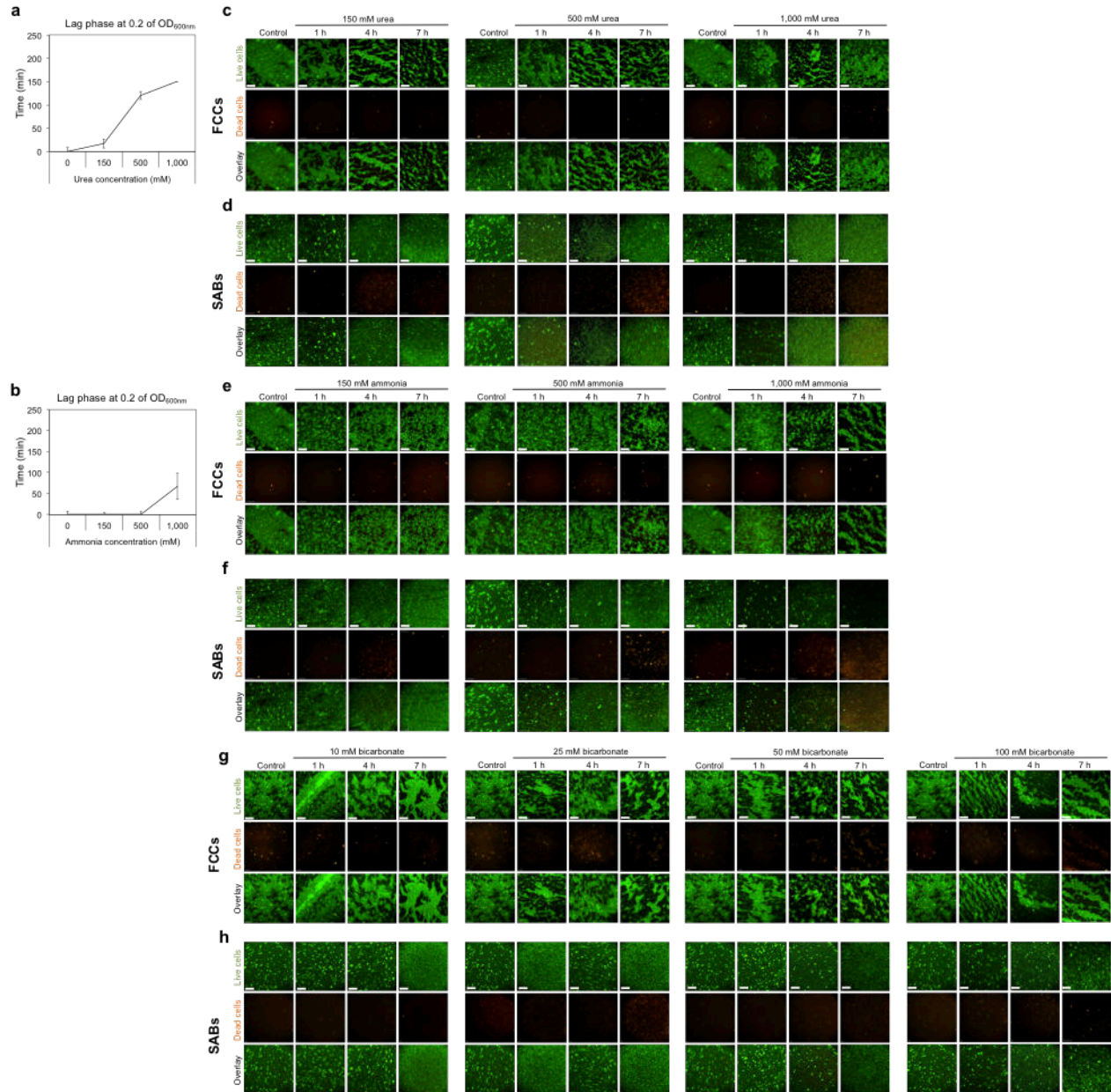
Correspondence: colletier@ibs.fr



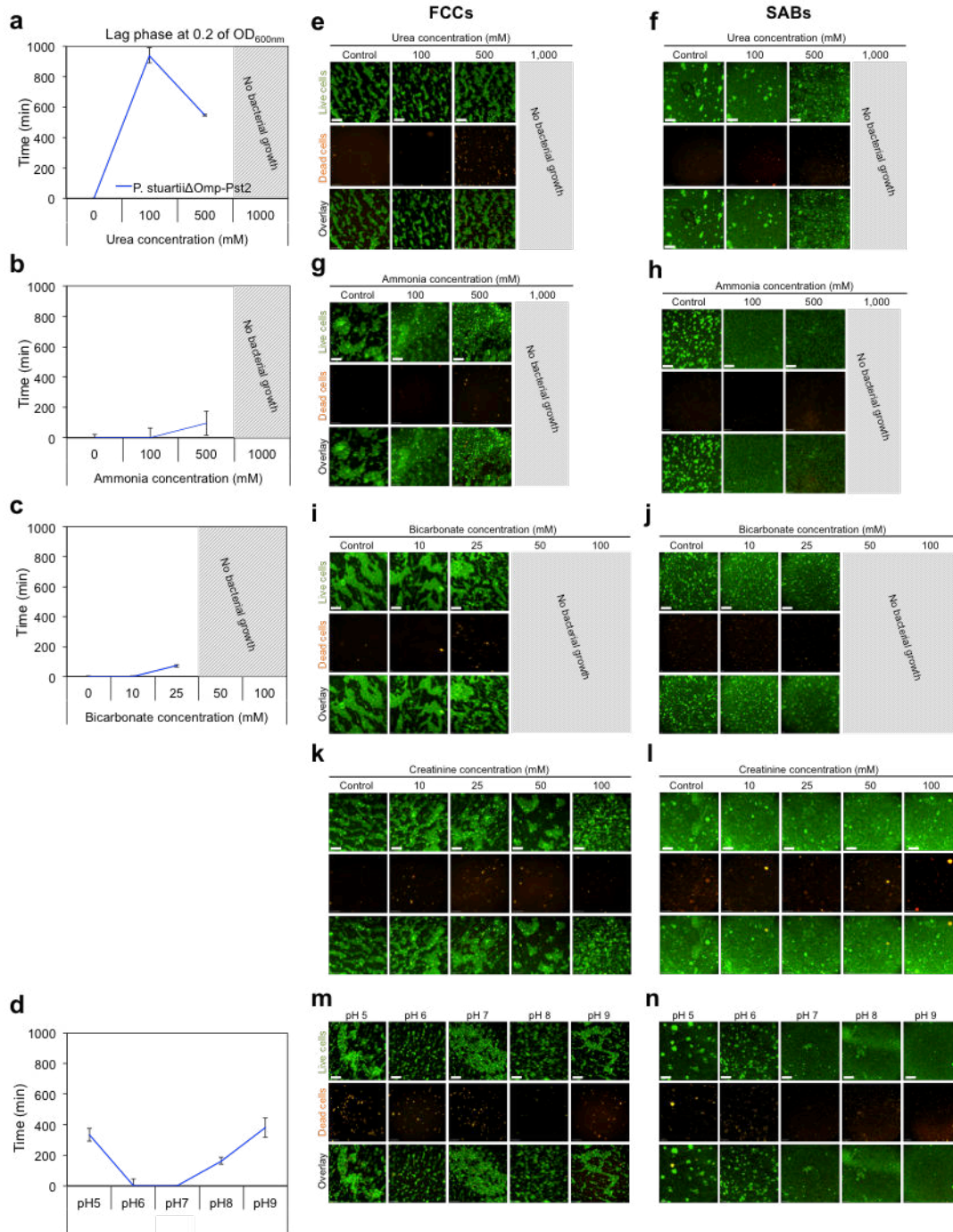
Supplementary Figure S1. *P. stuartii* is highly resistant to conditions that mimic its pathophysiological environment. Impact of environmental stress on *P. stuartii* growth was quantified as the delay in the time required to reach an OD_{600nm} of 0.2 in bacteria exposed to different concentrations of urea (panel a), ammonia (b), bicarbonate (c) or different pHs (d) compared to unexposed bacteria. Each measurement was performed in triplicates and was represented as the mean ± SD. Concentrations at which bacteria were unable to grow were represented as a grey-hatched rectangle. The capacity of bacteria to form FCCs and SABs in presence of urea (panels e and f, respectively), ammonia (g, h), bicarbonate (i, j), creatinine (k, l) and different pHs (m, n) was visualized by epifluorescence microscopy. All bacteria were shown in green (Syto 9 green labelling, upper line in all panels) while dead cells were in red (propidium iodide labelling, middle line). A merged image was shown for each condition on the bottom line of each panel. Concentrations at which bacteria were unable to grow were represented as a grey-hatched rectangle. The scale bars are 50 μm and 200 μm for FCCs and SABs, respectively.



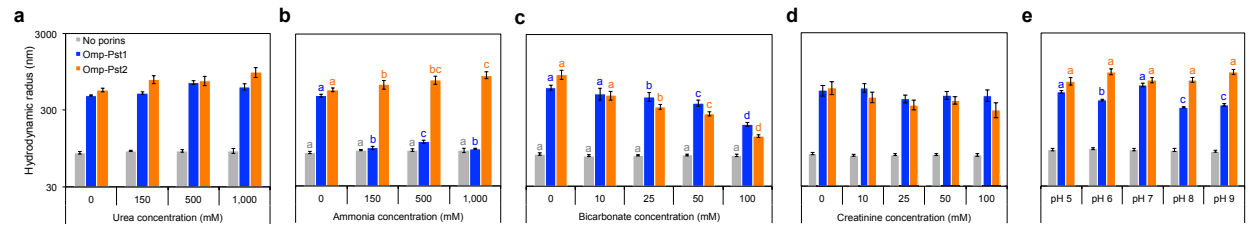
Supplementary Figure S2. *P. stuartii* adapts the expression of its two porins and the porin abundance in outer membrane (OM) to survive at hostile environments. The porin abundance in the OM of *P. stuartii* wild-type (hatched blue and orange) or *P. stuartii*ΔOmp-Pst2 (blue) bacteria, exposed to increasing concentrations of urea (panel a), ammonia (b), bicarbonate (c) and to various pH (d) was evaluated on SDS-PAGE gels. ImageJ software was used to normalize the bands corresponding to porins from bacteria exposed to environmental conditions with porin bands from unexposed bacteria. Different letters above the bars indicate significant differences (p < 0.05; ANOVA followed by post-hoc Tukey HSD test) and statistics data are available in the Supplementary Table S1. In parallel, the expression of Omp-Pst1 (blue) and Omp-Pst2 (orange) of *P. stuartii* wild-type or *P. stuartii*ΔOmp-Pst2 was measured by RT-qPCR in FCCs and SABs, upon exposure to 500 mM of urea (panels e, f and g, h, respectively), to 500 mM ammonia (i, j and k, l), to 50 mM bicarbonate (m, n and o, p), or to pH variation (q, r, s, t and u, v). For each growth time point, data were represented as the ratio of the normalized transcript copy number in the exposed bacteria divided by the one in unexposed bacteria. Each measurement was performed in triplicates. Error = SD and statistics data are available in Supplementary Table S2.



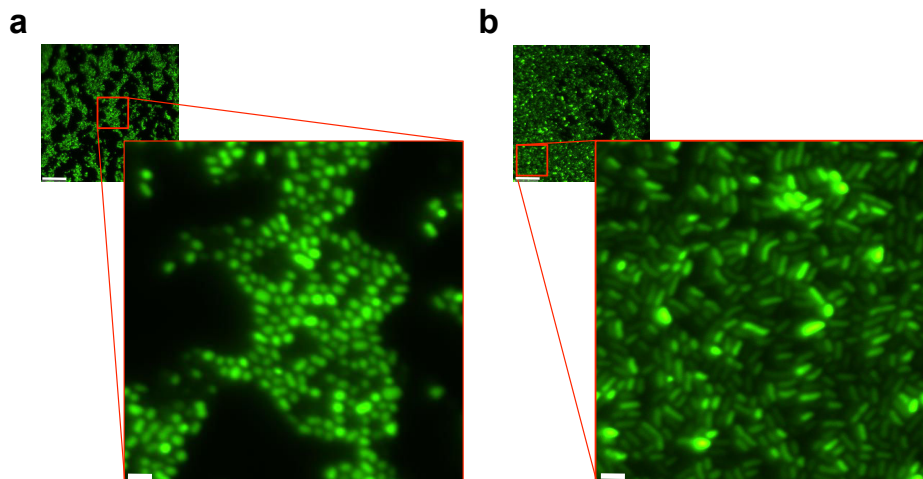
Supplementary Figure S3. Socialization offers greater resistance to conditions mimicking its pathophysiological environment. Impact of environmental stress on *P. stuartii* growth was quantified as the delay in the time required to reach an OD_{600nm} of 0.2 in bacteria already developed in FCCs and SABs, exposed to different concentrations of urea (panel a) and ammonia (b) compared to unexposed bacteria. Each measurement was performed in triplicates and was represented as the mean \pm SD. The resistance of preformed FCCs and SABs in presence of increasing concentrations of urea (panels c and d, respectively), ammonia (e, f), and bicarbonate (g, h) was visualized by epifluorescence microscopy. All bacteria were shown in green (Syto 9 green labelling, upper line in all panels) while dead cells were in red (propidium iodide labelling, middle line). A merged image was shown for each condition on the bottom line of each panel. The scale bars are 50 μ m and 200 μ m for FCCs and SABs, respectively.



Supplementary Figure S4. Omp-Pst2 porin is beneficial for resistance of *P. stuartii* to its physiopathological environment. Impact of environmental stress on *P. stuartii*ΔOmp-Pst2 bacterial growth was quantified as the delay in the time required to reach an OD_{600nm} of 0.2 in cells exposed to different concentrations of urea (panel a), ammonia (b), bicarbonate (c) or to different pHs (d) compared to unexposed ones. Each measurement was performed in triplicates and was represented as the mean ± SD. Concentrations at which bacteria were unable to grow were represented as a grey-hatched rectangle. The capacity of bacteria to form FCCs and SABs in presence of urea (panels e and f, respectively), ammonia (g, h), bicarbonate (i, j), creatinine (k, l) and at different pHs (m, n) was visualized by epifluorescence microscopy. All bacteria were shown in green (Syto 9 green labelling, upper line in all panels) while dead cells were in red (propidium iodide labelling, middle line). A merged image was shown for each condition on the bottom line of each panel. Concentrations at which bacteria were unable to grow were represented as a grey-hatched rectangle. The scale bars are 50 μm and 200 μm for FCCs and SABs, respectively.



Supplementary Figure S5. The porin propensity to self-associate into DOTs is differently challenged by environmental cues. The hydrodynamic radius of proteoliposomes was observed by DLS, 24 hours after the addition of Omp-Pst1 (blue) or Omp-Pst2 (orange) into LUV suspension, in presence of increasing concentrations of (a) urea, (b) ammonia, (c) bicarbonate, (d) creatinine and (e) at different pHs. As a control, the hydrodynamic radius of LUVs without porin insertion, in the same conditions, was measured (grey). Different letters above the bars indicate significant differences ($p < 0.05$; ANOVA followed by post-hoc Tukey HSD test) and statistics data are available in Supplementary Table S3.



Supplementary Figure S6. *P. stuartii* bacteria socialize with a different orientation in FCCs according to environmental conditions. Close-up views of FCCs developed in the presence of urea (a) and ammonia (b), showed "standing" and "seated" orientations of cells, respectively. Images were visualized by epifluorescence microscopy, whereby bacteria were shown in green (Syto 9 green labelling). The scale bars of small and large images are 50 μm and 5 μm for FCCs and SABs, respectively.

GLM –SDS-PAGE Gels

All statistic parameters – *P. stuartii*:

Generalized Linear Model Regression Results

```

=====
Dep. Variable:          Y      No. Observations:          39
Model:                 GLM    Df Residuals:              35
Model Family:         Gamma  Df Model:                  3
Link Function:        inverse_power  Scale:                    0.20020
Method:               IRLS   Log-Likelihood:           inf
Date:                 Thu, 14 Feb 2019  Deviance:                 212.99
Time:                 16:59:38     Pearson chi2:             7.01
No. Iterations:       8      Covariance Type:         nonrobust
=====

```

	coef	std err	z	P> z	[0.025	0.975]
Intercept	0.4455	0.395	1.129	0.259	-0.328	1.219
Urea	4.854e-05	1.21e-05	4.011	0.000	2.48e-05	7.23e-05
Ammonium	1.704e-05	6.75e-06	2.524	0.012	3.81e-06	3.03e-05
Urea:Ammonium	8.351e-16	7.63e-16	1.094	0.274	-6.61e-16	2.33e-15
pH	0.0362	0.057	0.638	0.523	-0.075	0.147
Urea:pH	0.0003	8.47e-05	4.011	0.000	0.000	0.001
Ammonium:pH	0.0001	4.73e-05	2.524	0.012	2.67e-05	0.000
Urea:Ammonium:pH	0	0	nan	nan	0	0

Bicarbonate – *P. stuartii*:

Generalized Linear Model Regression Results

```

=====
Dep. Variable:          Y      No. Observations:          15
Model:                 GLM    Df Residuals:              13
Model Family:         Gamma  Df Model:                  1
Link Function:        inverse_power  Scale:                    0.29338
Method:               IRLS   Log-Likelihood:          -136.43
Date:                 Mon, 20 May 2019  Deviance:                 5.1540
Time:                 09:29:53     Pearson chi2:             3.81
No. Iterations:       7      Covariance Type:         nonrobust
=====

```

	coef	std err	z	P> z	[0.025	0.975]
Intercept	0.0001	3.41e-05	4.046	0.000	7.11e-05	0.000
Concentration	3.294e-06	1.26e-06	2.606	0.009	8.17e-07	5.77e-06

All statistic parameters – *P. stuartii*ΔOmp-Pst2:

Generalized Linear Model Regression Results

```

=====
Dep. Variable:          Values  No. Observations:          39
Model:                 GLM    Df Residuals:              35
Model Family:         Gamma  Df Model:                  3
Link Function:        inverse_power  Scale:                    0.19051
Method:               IRLS   Log-Likelihood:           inf
Date:                 Mon, 20 May 2019  Deviance:                 212.67
Time:                 09:37:42     Pearson chi2:             6.67
No. Iterations:       8      Covariance Type:         nonrobust
=====

```

	coef	std err	z	P> z	[0.025	0.975]
Intercept	1.2797	0.498	2.572	0.010	0.305	2.255
Urea	0.0041	0.001	4.534	0.000	0.002	0.006
Ammonia	0.0005	0.000	1.670	0.095	-9.18e-05	0.001
pH	-0.0586	0.069	-0.855	0.392	-0.193	0.076

Bicarbonate – *P. stuartii*ΔOmp-Pst2:

Generalized Linear Model Regression Results

```

=====
Dep. Variable:          Y      No. Observations:          15
Model:                 GLM    Df Residuals:              13
Model Family:         Gamma  Df Model:                  1
Link Function:        inverse_power  Scale:                    0.31456
Method:               IRLS   Log-Likelihood:          -133.53
Date:                 Mon, 20 May 2019  Deviance:                 7.3202
Time:                 09:30:46     Pearson chi2:             4.09
No. Iterations:       7      Covariance Type:         nonrobust
=====

```


	coef	std err	z	P> z	[0.025	0.975]
Intercept	0.0001	3.93e-05	3.569	0.000	6.33e-05	0.000
Concentration	7.247e-06	2.08e-06	3.491	0.000	3.18e-06	1.13e-05

2-2 comparison (Tukey) – *P. stuartii*

Urea condition:

Multiple Comparison of Means - Tukey HSD, FWER=0.05

group1	group2	meandiff	lower	upper	reject
0	150	0.1542	-0.1792	0.4876	False
0	500	-0.3759	-0.7093	-0.0425	True
0	1000	-1.3651	-1.6985	-1.0317	True
150	500	-0.5301	-0.8635	-0.1966	True
150	1000	-1.5193	-1.8527	-1.1858	True
500	1000	-0.9892	-1.3226	-0.6558	True

Ammonia condition:

Multiple Comparison of Means - Tukey HSD, FWER=0.05

group1	group2	meandiff	lower	upper	reject
0	150	-0.2778	-0.4343	-0.1212	True
0	500	-0.3618	-0.5183	-0.2052	True
0	1000	-0.7592	-0.9157	-0.6026	True
150	500	-0.084	-0.2405	0.0726	False
150	1000	-0.4814	-0.6379	-0.3248	True
500	1000	-0.3974	-0.5539	-0.2408	True

Bicarbonate condition:

Multiple Comparison of Means - Tukey HSD, FWER=0.05

group1	group2	meandiff	lower	upper	reject
0	10	975.8383	211.0188	1740.6579	True
0	25	756.3667	-8.4529	1521.1862	False
0	50	780.3097	15.4901	1545.1292	True
0	100	-4409.2103	-5174.0299	-3644.3908	True
10	25	-219.4717	-984.2912	545.3479	False
10	50	-195.5287	-960.3482	569.2909	False
10	100	-5385.0487	-6149.8682	-4620.2291	True
25	50	23.943	-740.8765	788.7625	False
25	100	-5165.577	-5930.3965	-4400.7575	True
50	100	-5189.52	-5954.3395	-4424.7005	True

pH condition:

Multiple Comparison of Means - Tukey HSD, FWER=0.05

group1	group2	meandiff	lower	upper	reject
5	6	-0.0942	-0.2838	0.0954	False
5	7	-0.0976	-0.2871	0.092	False
5	8	-0.1051	-0.2947	0.0844	False
5	9	-0.3684	-0.558	-0.1788	True
6	7	-0.0034	-0.1929	0.1862	False
6	8	-0.0109	-0.2005	0.1786	False
6	9	-0.2742	-0.4638	-0.0846	True
7	8	-0.0076	-0.1972	0.182	False
7	9	-0.2708	-0.4604	-0.0813	True
8	9	-0.2632	-0.4528	-0.0737	True

2-2 comparison (Tukey) – *P. stuartii*ΔOmp-Pst2

Urea condition:

Multiple Comparison of Means - Tukey HSD,FWER=0.05

```

=====
group1 group2 meandiff lower upper reject
-----
 0      150  -0.2351 -0.4253 -0.045 True
 0      500  -0.3753 -0.5654 -0.1851 True
 0     1000  -1.0683 -1.2585 -0.8782 True
150     500  -0.1401 -0.373  0.0928 False
150    1000  -0.8332 -1.0661 -0.6003 True
500    1000  -0.6931 -0.926  -0.4602 True
    
```

Ammonia condition:

Multiple Comparison of Means - Tukey HSD,FWER=0.05

```

=====
group1 group2 meandiff lower upper reject
-----
 0      150  -0.1283 -0.3409  0.0842 False
 0      500  -0.135  -0.3475  0.0775 False
 0     1000  -0.3613 -0.5738 -0.1487 True
150     500  -0.0066 -0.2669  0.2536 False
150    1000  -0.2329 -0.4932  0.0274 False
500    1000  -0.2263 -0.4865  0.034  False
    
```

Bicarbonate condition:

Multiple Comparison of Means - Tukey HSD,FWER=0.05

```

=====
group1 group2 meandiff lower upper reject
-----
 0      10   346.731  -289.3837  982.8457 False
 0      25   154.9093 -481.2053  791.024  False
 0      50  -2002.9833 -2639.098 -1366.8687 True
 0     100  -4633.1367 -5269.2513 -3997.022  True
10     25  -191.8217 -827.9363  444.293  False
10     50  -2349.7143 -2985.829 -1713.5997 True
10    100  -4979.8677 -5615.9823 -4343.753  True
25     50  -2157.8927 -2794.0073 -1521.778  True
25    100  -4788.046  -5424.1607 -4151.9313 True
50    100  -2630.1533 -3266.268  -1994.0387 True
    
```

pH condition:

Multiple Comparison of Means - Tukey HSD,FWER=0.05

```

=====
group1 group2 meandiff lower upper reject
-----
 5      6    0.0374 -0.2237  0.2985 False
 5      7    0.0388 -0.1744  0.252  False
 5      8    0.1749 -0.0862  0.436  False
 5      9    0.3246  0.0635  0.5857  True
 6      7    0.0014 -0.2118  0.2146 False
 6      8    0.1375 -0.1236  0.3986 False
 6      9    0.2872  0.0261  0.5483  True
 7      8    0.1361 -0.0771  0.3493 False
 7      9    0.2858  0.0726  0.499  True
 8      9    0.1497 -0.1114  0.4108 False
    
```

Supplementary Table S1 – Statistical analysis from SDS-PAGE gels experiments on porin abundance in OMs. All experiments were conducted for at least three biologically independent replicates. Technical replicates were averaged to produce replicate means that were subsequently used for analysis. Mean values were compared within and between groups using one-way ANOVA followed by Tukey's post hoc for two-two comparisons. Differences were considered statistically significant if $p < 0.05$ (True).

GLM – RTqPCR – *P. stuartii*

Parameter correlations: Urea - Omp-Pst1

Generalized Linear Model Regression Results

```

=====
Dep. Variable:          Y      No. Observations:          88
Model:                 GLM    Df Residuals:              80
Model Family:         Gamma  Df Model:                  7
Link Function:        inverse_power  Scale:                    0.22000
Method:               IRLS   Log-Likelihood:           -1032.9
Date:                 Tue, 21 May 2019  Deviance:                 19.302
Time:                 15:24:28   Pearson chi2:             17.6
No. Iterations:       7        Covariance Type:         nonrobust
=====

```

	coef	std err	z	P> z	[0.025	0.975]
Intercept	1.976e-05	4.34e-06	4.553	0.000	1.13e-05	2.83e-05
C(Phenotype) [T.Floating]	-5.015e-06	4.73e-06	-1.060	0.289	-1.43e-05	4.26e-06
Time	-5.654e-07	3.72e-07	-1.518	0.129	-1.3e-06	1.64e-07
C(Phenotype) [T.Floating]:Time	1.242e-07	4.13e-07	0.301	0.763	-6.85e-07	9.33e-07
Urea	-8.492e-09	3.04e-08	-0.279	0.780	-6.81e-08	5.11e-08
C(Phenotype) [T.Floating]:Urea	1.565e-08	3.27e-08	0.478	0.632	-4.85e-08	7.98e-08
Time:Urea	3.323e-09	3.17e-09	1.049	0.294	-2.89e-09	9.53e-09
C(Phenotype) [T.Floating]:Time:Urea	-1.773e-09	3.47e-09	-0.511	0.609	-8.57e-09	5.03e-09

Parameter correlations: Urea - Omp-Pst2

Generalized Linear Model Regression Results

```

=====
Dep. Variable:          Y      No. Observations:          88
Model:                 GLM    Df Residuals:              80
Model Family:         Gamma  Df Model:                  7
Link Function:        inverse_power  Scale:                    0.78223
Method:               IRLS   Log-Likelihood:           -881.32
Date:                 Tue, 21 May 2019  Deviance:                 56.367
Time:                 15:25:17   Pearson chi2:             62.6
No. Iterations:       8        Covariance Type:         nonrobust
=====

```

	coef	std err	z	P> z	[0.025	0.975]
Intercept	0.0001	4.72e-05	2.651	0.008	3.26e-05	0.000
C(Phenotype) [T.Floating]	8.957e-05	7.12e-05	1.257	0.209	-5e-05	0.000
Time	-4.41e-06	3.91e-06	-1.127	0.260	-1.21e-05	3.26e-06
C(Phenotype) [T.Floating]:Time	-1.412e-06	6.45e-06	-0.219	0.827	-1.4e-05	1.12e-05
Urea	-1.312e-07	1.32e-07	-0.995	0.320	-3.9e-07	1.27e-07
C(Phenotype) [T.Floating]:Urea	-9.149e-08	2.12e-07	-0.431	0.666	-5.08e-07	3.25e-07
Time:Urea	6.08e-09	1.15e-08	0.530	0.596	-1.64e-08	2.86e-08
C(Phenotype) [T.Floating]:Time:Urea	1.064e-08	2.18e-08	0.488	0.625	-3.21e-08	5.33e-08

Parameter correlations: Ammonia - Omp-Pst1

Generalized Linear Model Regression Results

```

=====
Dep. Variable:          Y      No. Observations:          89
Model:                 GLM    Df Residuals:              81
Model Family:         Gamma  Df Model:                  7
Link Function:        inverse_power  Scale:                    0.18900
Method:               IRLS   Log-Likelihood:           -1039.4
Date:                 Tue, 21 May 2019  Deviance:                 15.403
Time:                 15:26:44   Pearson chi2:             15.3
No. Iterations:       7        Covariance Type:         nonrobust
=====

```

	coef	std err	z	P> z	[0.025	0.975]
Intercept	1.976e-05	4.02e-06	4.913	0.000	1.19e-05	2.76e-05
C(Phenotype) [T.Floating]	-5.015e-06	4.39e-06	-1.143	0.253	-1.36e-05	3.58e-06
Time	-5.654e-07	3.45e-07	-1.638	0.101	-1.24e-06	1.11e-07
C(Phenotype) [T.Floating]:Time	1.242e-07	3.82e-07	0.325	0.745	-6.25e-07	8.74e-07
Ammonium	-2.697e-08	1.19e-08	-2.259	0.024	-5.04e-08	-3.57e-09
C(Phenotype) [T.Floating]:Ammonium	8.771e-08	2.01e-08	4.364	0.000	4.83e-08	1.27e-07
Time:Ammonium	1.78e-09	1.11e-09	1.601	0.109	-3.99e-10	3.96e-09
C(Phenotype) [T.Floating]:Time:Ammonium	-4.559e-09	1.8e-09	-2.530	0.011	-8.09e-09	-1.03e-09

Parameter correlations: Ammonia - Omp-Pst2

Generalized Linear Model Regression Results

```

=====
Dep. Variable:          Y      No. Observations:          89
Model:                 GLM    Df Residuals:              81
Model Family:         Gamma  Df Model:                  7
Link Function:        inverse_power  Scale:                    0.74485
Method:               IRLS   Log-Likelihood:           -869.64
Date:                 Tue, 21 May 2019  Deviance:                 51.910
Time:                 15:27:33   Pearson chi2:             60.3
No. Iterations:      8      Covariance Type:         nonrobust
=====

```

	coef	std err	z	P> z	[0.025	0.975]
Intercept	0.0001	4.61e-05	2.717	0.007	3.49e-05	0.000
C(Phenotype) [T.Floating]	8.957e-05	6.95e-05	1.289	0.198	-4.67e-05	0.000
Time	-4.41e-06	3.82e-06	-1.155	0.248	-1.19e-05	3.07e-06
C(Phenotype) [T.Floating]:Time	-1.412e-06	6.29e-06	-0.225	0.822	-1.37e-05	1.09e-05
Ammonium	1.805e-07	2.8e-07	0.644	0.520	-3.69e-07	7.3e-07
C(Phenotype) [T.Floating]:Ammonium	4.068e-07	4.24e-07	0.961	0.337	-4.23e-07	1.24e-06
Time:Ammonium	-5.772e-09	2.3e-08	-0.251	0.802	-5.08e-08	3.93e-08
C(Phenotype) [T.Floating]:Time:Ammonium	-3.723e-08	3.37e-08	-1.106	0.269	-1.03e-07	2.87e-08

Parameter correlations: Bicarbonate - Omp-Pst1

Generalized Linear Model Regression Results

```

=====
Dep. Variable:          Values  No. Observations:          48
Model:                 GLM    Df Residuals:              40
Model Family:         Gamma  Df Model:                  7
Link Function:        inverse_power  Scale:                    0.28273516624
Method:               IRLS   Log-Likelihood:           -618.86
Date:                 Fri, 05 Jul 2019  Deviance:                 12.855
Time:                 13:51:13   Pearson chi2:             11.3
No. Iterations:      8
=====

```

	coef	std err	z	P> z	[95.0% Conf. Int.]
Intercept	1.779e-05	4.1e-06	4.341	0.000	9.76e-06 2.58e-05
C(Phenotypes) [T.Floating]	-1.118e-05	4.31e-06	-2.591	0.010	-1.96e-05 -2.72e-06
Time	-1.128e-06	2.75e-07	-4.098	0.000	-1.67e-06 -5.88e-07
C(Phenotypes) [T.Floating]:Time	8.29e-07	2.97e-07	2.791	0.005	2.47e-07 1.41e-06
Cconditions	-1.554e-08	9.83e-09	-1.581	0.114	-3.48e-08 3.73e-09
C(Phenotypes) [T.Floating]:Cconditions	3.568e-08	1.16e-08	3.063	0.002	1.29e-08 5.85e-08
Time:Cconditions	1.162e-09	6.73e-10	1.728	0.084	-1.56e-10 2.48e-09
C(Phenotypes) [T.Floating]:Time:Cconditions	-2.541e-09	8.11e-10	-3.133	0.002	-4.13e-09 -9.51e-10

Parameter correlations: Bicarbonate - Omp-Pst2

Generalized Linear Model Regression Results

```

=====
Dep. Variable:          Values  No. Observations:          48
Model:                 GLM    Df Residuals:              40
Model Family:         Gamma  Df Model:                  7
Link Function:        inverse_power  Scale:                    0.350373625544
Method:               IRLS   Log-Likelihood:           -516.90
Date:                 Fri, 05 Jul 2019  Deviance:                 15.804
Time:                 14:02:51   Pearson chi2:             14.0
No. Iterations:      7
=====

```

	coef	std err	z	P> z	[95.0% Conf. Int.]
Intercept	2.502e-05	2.08e-05	1.204	0.229	-1.57e-05 6.58e-05
C(Phenotypes) [T.Floating]	-3.345e-05	2.65e-05	-1.262	0.207	-8.54e-05 1.85e-05
Time	7.925e-07	2.01e-06	0.394	0.694	-3.15e-06 4.74e-06
C(Phenotypes) [T.Floating]:Time	7.57e-06	3.53e-06	2.143	0.032	6.48e-07 1.45e-05
Cconditions	-8.522e-08	9.79e-08	-0.870	0.384	-2.77e-07 1.07e-07
C(Phenotypes) [T.Floating]:Cconditions	1.389e-07	1.06e-07	1.312	0.190	-6.87e-08 3.46e-07
Time:Cconditions	1.602e-08	1.1e-08	1.452	0.146	-5.6e-09 3.76e-08
C(Phenotypes) [T.Floating]:Time:Cconditions	-2.859e-08	1.29e-08	-2.221	0.026	-5.38e-08 -3.36e-09

Parameter correlations: pH - Omp-Pst1

Generalized Linear Model Regression Results

```

=====
Dep. Variable:          Y      No. Observations:          156
Model:                 GLM    Df Residuals:              148
Model Family:         Gamma  Df Model:                  7

```

Link Function:	inverse_power	Scale:	0.29369
Method:	IRLS	Log-Likelihood:	-1843.2
Date:	Tue, 21 May 2019	Deviance:	47.729
Time:	15:29:23	Pearson chi2:	43.5
No. Iterations:	7	Covariance Type:	nonrobust

	coef	std err	z	P> z	[0.025	0.975]
Intercept	-3.249e-05	2.38e-05	-1.365	0.172	-7.91e-05	1.42e-05
C(Phenotype) [T.Floating]	3.936e-05	2.59e-05	1.522	0.128	-1.13e-05	9.01e-05
Time	3.894e-06	2.45e-06	1.593	0.111	-8.98e-07	8.69e-06
C(Phenotype) [T.Floating]:Time	-3.441e-06	2.61e-06	-1.317	0.188	-8.56e-06	1.68e-06
pH	7.667e-06	3.44e-06	2.227	0.026	9.2e-07	1.44e-05
C(Phenotype) [T.Floating]:pH	-5.688e-06	3.74e-06	-1.523	0.128	-1.3e-05	1.63e-06
Time:pH	-6.133e-07	3.43e-07	-1.786	0.074	-1.29e-06	5.97e-08
C(Phenotype) [T.Floating]:Time:pH	4.35e-07	3.67e-07	1.186	0.236	-2.84e-07	1.15e-06

Parameter correlations: pH - Omp-Pst2

Generalized Linear Model Regression Results			
Dep. Variable:	Y	No. Observations:	155
Model:	GLM	Df Residuals:	147
Model Family:	Gamma	Df Model:	7
Link Function:	inverse_power	Scale:	0.90306
Method:	IRLS	Log-Likelihood:	-1510.8
Date:	Tue, 21 May 2019	Deviance:	112.64
Time:	15:28:36	Pearson chi2:	133.
No. Iterations:	8	Covariance Type:	nonrobust

	coef	std err	z	P> z	[0.025	0.975]
Intercept	6.154e-05	0.000	0.222	0.825	-0.000	0.001
C(Phenotype) [T.Floating]	0.0002	0.000	0.511	0.609	-0.001	0.001
Time	2.285e-06	2.74e-05	0.083	0.934	-5.14e-05	5.6e-05
C(Phenotype) [T.Floating]:Time	-2.104e-05	3.64e-05	-0.578	0.563	-9.23e-05	5.03e-05
pH	1.1e-05	3.96e-05	0.278	0.781	-6.65e-05	8.85e-05
C(Phenotype) [T.Floating]:pH	-1.724e-05	5.17e-05	-0.334	0.739	-0.000	8.4e-05
Time:pH	-7.931e-07	3.88e-06	-0.204	0.838	-8.4e-06	6.82e-06
C(Phenotype) [T.Floating]:Time:pH	3.284e-06	5.26e-06	0.624	0.532	-7.02e-06	1.36e-05

GLM – RTqPCR – *P. stuartii*ΔOmp-Pst2

Parameter correlations: Urea

Generalized Linear Model Regression Results			
Dep. Variable:	Y	No. Observations:	96
Model:	GLM	Df Residuals:	88
Model Family:	Gamma	Df Model:	7
Link Function:	inverse_power	Scale:	0.20053
Method:	IRLS	Log-Likelihood:	-1144.3
Date:	Tue, 21 May 2019	Deviance:	19.798
Time:	16:17:17	Pearson chi2:	17.6
No. Iterations:	8	Covariance Type:	nonrobust

	coef	std err	z	P> z	[0.025	0.975]
Intercept	5.906e-06	2.35e-06	2.509	0.012	1.29e-06	1.05e-05
C(Phenotype) [T.Floating]	1.85e-06	2.72e-06	0.681	0.496	-3.48e-06	7.18e-06
Time	2.43e-07	2.34e-07	1.038	0.299	-2.16e-07	7.02e-07
C(Phenotype) [T.Floating]:Time	-7.038e-08	2.84e-07	-0.248	0.804	-6.26e-07	4.86e-07
Urea	-5.05e-08	2.39e-08	-2.115	0.034	-9.73e-08	-3.7e-09
C(Phenotype) [T.Floating]:Urea	6.131e-08	2.77e-08	2.215	0.027	7.06e-09	1.16e-07
Time:Urea	8.384e-09	2.96e-09	2.835	0.005	2.59e-09	1.42e-08
C(Phenotype) [T.Floating]:Time:Urea	-5.163e-09	3.54e-09	-1.459	0.144	-1.21e-08	1.77e-09

Parameter correlations: Ammonia

Generalized Linear Model Regression Results			
Dep. Variable:	Y	No. Observations:	96
Model:	GLM	Df Residuals:	88
Model Family:	Gamma	Df Model:	7

Link Function:	inverse_power	Scale:	0.15986
Method:	IRLS	Log-Likelihood:	-1145.4
Date:	Tue, 21 May 2019	Deviance:	15.809
Time:	16:18:11	Pearson chi2:	14.1
No. Iterations:	7	Covariance Type:	nonrobust

	coef	std err	z	P> z	[0.025	0.975]
Intercept	5.906e-06	2.1e-06	2.810	0.005	1.79e-06	1e-05
C(Phenotype)[T.Floating]	1.85e-06	2.43e-06	0.763	0.446	-2.91e-06	6.61e-06
Time	2.43e-07	2.09e-07	1.162	0.245	-1.67e-07	6.53e-07
C(Phenotype)[T.Floating]:Time	-7.038e-08	2.53e-07	-0.278	0.781	-5.67e-07	4.26e-07
Ammonium	-7.175e-09	7.82e-09	-0.918	0.359	-2.25e-08	8.14e-09
C(Phenotype)[T.Floating]:Ammonium	5.693e-08	1.47e-08	3.863	0.000	2.8e-08	8.58e-08
Time:Ammonium	5.944e-10	8.13e-10	0.731	0.465	-9.98e-10	2.19e-09
C(Phenotype)[T.Floating]:Time:Ammonium	-2.649e-09	1.48e-09	-1.785	0.074	-5.56e-09	2.59e-10

Parameter correlations: Bicarbonate

Generalized Linear Model Regression Results

Dep. Variable:	Values	No. Observations:	48
Model:	GLM	Df Residuals:	40
Model Family:	Gamma	Df Model:	7
Link Function:	inverse_power	Scale:	1.13895772977
Method:	IRLS	Log-Likelihood:	-612.73
Date:	Fri, 05 Jul 2019	Deviance:	30.400
Time:	15:15:31	Pearson chi2:	45.6
No. Iterations:	9		

	coef	std err	z	P> z	[95.0% Conf. Int.]
Intercept	3.441e-05	1.61e-05	2.135	0.033	2.83e-06 6.6e-05
C(Phenotypes)[T.Floating]	-2.833e-06	1.91e-05	-0.148	0.882	-4.03e-05 3.46e-05
Time	-2.157e-06	1.09e-06	-1.988	0.047	-4.28e-06 -3e-08
C(Phenotypes)[T.Floating]:Time	1.842e-07	1.29e-06	0.143	0.886	-2.34e-06 2.71e-06
Cconditions	8.339e-09	4.73e-08	0.176	0.860	-8.43e-08 1.01e-07
C(Phenotypes)[T.Floating]:Cconditions	-5.474e-08	5.21e-08	-1.051	0.293	-1.57e-07 4.74e-08
Time:Cconditions	-7.075e-10	3.17e-09	-0.223	0.823	-6.92e-09 5.51e-09
C(Phenotypes)[T.Floating]:Time:Cconditions	4.06e-09	3.53e-09	1.149	0.250	-2.86e-09 1.1e-08

Parameter correlations: pH

Generalized Linear Model Regression Results

Dep. Variable:	Y	No. Observations:	168
Model:	GLM	Df Residuals:	160
Model Family:	Gamma	Df Model:	7
Link Function:	inverse_power	Scale:	0.21959
Method:	IRLS	Log-Likelihood:	-2016.9
Date:	Tue, 21 May 2019	Deviance:	34.902
Time:	16:19:02	Pearson chi2:	35.1
No. Iterations:	7	Covariance Type:	nonrobust

	coef	std err	z	P> z	[0.025	0.975]
Intercept	1.953e-05	1.05e-05	1.856	0.063	-1.1e-06	4.02e-05
C(Phenotype)[T.Floating]	-9.239e-06	1.27e-05	-0.725	0.468	-3.42e-05	1.57e-05
Time	-2.693e-07	1.01e-06	-0.266	0.790	-2.25e-06	1.71e-06
C(Phenotype)[T.Floating]:Time	5.56e-07	1.27e-06	0.436	0.663	-1.94e-06	3.05e-06
pH	-1.726e-06	1.41e-06	-1.222	0.222	-4.49e-06	1.04e-06
C(Phenotype)[T.Floating]:pH	2.052e-06	1.73e-06	1.183	0.237	-1.35e-06	5.45e-06
Time:pH	6.412e-08	1.37e-07	0.469	0.639	-2.04e-07	3.32e-07
C(Phenotype)[T.Floating]:Time:pH	-1.241e-07	1.74e-07	-0.712	0.476	-4.66e-07	2.17e-07

2-2 comparison (Tukey) - Urea condition – P. stuartii

Omp-Pst1 porin – FCCs

Multiple Comparison of Means - Tukey HSD, FWER=0.05

group1	group2	meandiff	lower	upper	reject	
4h	0	500	16574.1498	-30452.3034	63600.6031	False
5h	0	500	-38902.0202	-69962.3523	-7841.6881	True
7h	0	500	-71189.8961	-123737.1743	-18642.618	True
9h	0	500	-63057.0912	-127634.1388	1519.9565	True
15h	0	500	-63286.2712	-114749.5456	-11822.9968	True

Omp-Pst2 porin – FCCs						
Multiple Comparison of Means - Tukey HSD,FWER=0.05						
=====						
group1	group2	meandiff	lower	upper	reject	

4h	0	500	6261.4946	1996.197	10526.7923	True
5h	0	500	-2134.6555	-12996.94	8727.629	False
7h	0	500	7521.8879	1598.1456	13445.6302	True
9h	0	500	-657.2522	-10717.0073	9402.5029	False
15h	0	500	-539.4299	-9813.6084	8734.7485	False
2-2 comparison (Tukey) - Urea condition – P. stuartii – According Time						
Omp-Pst1 porin – FCCs						
Multiple Comparison of Means - Tukey HSD,FWER=0.05						
=====						
group1	group2	meandiff	lower	upper	reject	

4	5	-69510.7473	-90915.2466	-48106.248	True	
4	7	-30288.1114	-51692.6107	-8883.6121	True	
4	9	-47009.2685	-68413.7677	-25604.7692	True	
4	15	-35263.6879	-56668.1872	-13859.1886	True	
5	7	39222.6359	17818.1367	60627.1352	True	
5	9	22501.4789	1096.9796	43905.9781	True	
5	15	34247.0594	12842.5601	55651.5587	True	
7	9	-16721.1571	-38125.6564	4683.3422	False	
7	15	-4975.5765	-26380.0758	16428.9228	False	
9	15	11745.5806	-9658.9187	33150.0798	False	
2-2 comparison (Tukey) – Ammonia condition – P. stuartii						
Omp-Pst1 porin – FCCs						
Multiple Comparison of Means - Tukey HSD,FWER=0.05						
=====						
group1	group2	meandiff	lower	upper	reject	

4H	0	500	-48214.2397	-94654.66	-1773.8194	True
5H	0	500	-35184.7269	-66101.6521	-4267.8018	True
7H	0	500	-80993.2267	-134113.1314	-27873.3221	True
9H	0	500	-54354.4792	-118532.4498	9823.4914	True
15H	0	500	-63325.4663	-115029.2888	-11621.6438	True
Omp-Pst1 porin – SABs						
Multiple Comparison of Means - Tukey HSD,FWER=0.05						
=====						
group1	group2	meandiff	lower	upper	reject	

7H	0	500	51763.2687	13226.7333	90299.804	True
9H	0	500	44588.3453	-2241.4323	91418.123	False
15H	0	500	122.8988	-69268.6729	69514.4706	False
2-2 comparison (Tukey) – Bicarbonate condition – P. stuartii						
Omp-Pst1 porin – FCCs						
Multiple Comparison of Means - Tukey HSD,FWER=0.05						
=====						
group1	group2	meandiff	lower	upper	reject	

4h	0	50	-252343.4867	-407839.5819	-96847.3915	True
5h	0	50	-54122.7379	-107260.2379	-985.2379	True
7h	0	50	-53049.4907	-161346.8928	55247.9113	False
9h	0	50	-37971.1624	-256101.1496	180158.8249	False
15h	0	50	5929.5254	-256043.3444	267902.3952	False
Omp-Pst2 porin – FCCs						
Multiple Comparison of Means - Tukey HSD,FWER=0.05						
=====						
group1	group2	meandiff	lower	upper	reject	

4h	0	50	6895.8395	-59887.8827	73679.5616	False
5h	0	50	345.2546	-17834.8625	18525.3718	False

7h	0	50	11245.2606	-8163.8192	30654.3404	False
9h	0	50	877.444	-9994.3841	11749.2721	False
15h	0	50	16834.8001	595.501	33074.0991	True

2-2 comparison (Tukey) – pH condition – *P. stuartii*

Omp-Pst1 porin – FCCs

4h:

Multiple Comparison of Means - Tukey HSD,FWER=0.05

group1	group2	meandiff	lower	upper	reject
5	6	30203.4498	-33493.5242	93900.4238	False
5	7	49864.7744	-2949.9663	102679.5152	False
5	8	18929.9289	-44767.0451	82626.9029	False
5	9	-5065.2398	-68762.2138	58631.7342	False
6	7	19661.3246	-33153.4161	72476.0654	False
6	8	-11273.5209	-74970.4949	52423.4531	False
6	9	-35268.6896	-98965.6636	28428.2843	False
7	8	-30934.8455	-83749.5863	21879.8952	False
7	9	-54930.0143	-107744.755	-2115.2735	True
8	9	-23995.1687	-87692.1427	39701.8052	False

5h:

Multiple Comparison of Means - Tukey HSD,FWER=0.05

group1	group2	meandiff	lower	upper	reject
5	6	4324.7478	-35825.5557	44475.0512	False
5	7	19422.9899	-13867.883	52713.8628	False
5	8	-9858.4211	-50008.7245	30291.8823	False
5	9	-15480.8529	-55631.1564	24669.4505	False
6	7	15098.2422	-18192.6308	48389.1151	False
6	8	-14183.1688	-54333.4722	25967.1346	False
6	9	-19805.6007	-59955.9041	20344.7027	False
7	8	-29281.411	-62572.2839	4009.4619	False
7	9	-34903.8429	-68194.7158	-1612.9699	True
8	9	-5622.4319	-45772.7353	34527.8716	False

7h:

Multiple Comparison of Means - Tukey HSD,FWER=0.05

group1	group2	meandiff	lower	upper	reject
5	6	83222.8583	9312.0111	157133.7054	True
5	7	77210.3097	15926.6727	138493.9467	True
5	8	37275.7864	-36635.0608	111186.6335	False
5	9	6370.9945	-67539.8527	80281.8416	False
6	7	-6012.5486	-67296.1855	55271.0884	False
6	8	-45947.0719	-119857.919	27963.7752	False
6	9	-76851.8638	-150762.7109	-2941.0167	True
7	8	-39934.5233	-101218.1603	21349.1136	False
7	9	-70839.3152	-132122.9522	-9555.6783	True
8	9	-30904.7919	-104815.639	43006.0552	False

Omp-Pst1 porin – SABs

7h:

Multiple Comparison of Means - Tukey HSD,FWER=0.05

group1	group2	meandiff	lower	upper	reject
5	6	-26759.8469	-78909.5474	25389.8536	False
5	7	-33941.5292	-76521.5814	8638.5229	False
5	8	-66739.4717	-118889.1722	-14589.7711	True
5	9	-70736.6287	-122886.3292	-18586.9282	True
6	7	-7181.6824	-49761.7345	35398.3698	False
6	8	-39979.6248	-92129.3253	12170.0757	False
6	9	-43976.7818	-96126.4823	8172.9187	False

7	8	-32797.9424	-75377.9946	9782.1098	False
7	9	-36795.0995	-79375.1516	5784.9527	False
8	9	-3997.157	-56146.8576	48152.5435	False

2-2 comparison (Tukey) - Urea condition – *P. stuartii*ΔOmp-Pst2

Omp-Pst1 porin – FCCs

Multiple Comparison of Means - Tukey HSD,FWER=0.05

group1	group2	meandiff	lower	upper	reject	
4h	0	500	-48814.8603	-79244.6239	-18385.0967	True
5h	0	500	-79571.3733	-112223.3454	-46919.4013	True
7h	0	500	-84041.5601	-146780.2218	-21302.8985	True
9h	0	500	-80294.8613	-120605.1033	-39984.6194	True
15h	0	500	-66788.6326	-124584.7873	-8992.4779	True

Omp-Pst1 porin – SABs

Multiple Comparison of Means - Tukey HSD,FWER=0.05

group1	group2	meandiff	lower	upper	reject	
7h	0	500	-51532.3838	-131390.0291	28325.2614	False
9h	0	500	-67561.3871	-143722.56	8599.7859	False
15h	0	500	-85432.9544	-138213.5268	-32652.382	True

2-2 comparison (Tukey) – Ammonia condition – *P. stuartii*ΔOmp-Pst2

Omp-Pst1 porin – FCC

Multiple Comparison of Means - Tukey HSD,FWER=0.05

group1	group2	meandiff	lower	upper	reject	
4h	0	500	-40754.5817	-70288.9453	-11220.2181	True
5h	0	500	-79073.6582	-112314.5001	-45832.8162	True
7h	0	500	-104908.034	-169132.0224	-40684.0456	True
9h	0	500	-108527.7472	-148262.142	-68793.3525	True
15h	0	500	-21559.4458	-79543.416	36424.5245	True

2-2 comparison (Tukey) – pH condition – *P. stuartii*ΔOmp-Pst2

Omp-Pst1 porin – FCC

5h:

Multiple Comparison of Means - Tukey HSD,FWER=0.05

group1	group2	meandiff	lower	upper	reject
5	6	17463.0878	-29975.2601	64901.4357	False
5	7	61544.038	22810.7891	100277.2868	True
5	8	31719.0228	-15719.3251	79157.3706	False
5	9	11726.8916	-35711.4563	59165.2394	False
6	7	44080.9502	5347.7013	82814.199	True
6	8	14255.935	-33182.4129	61694.2828	False
6	9	-5736.1962	-53174.5441	41702.1516	False
7	8	-29825.0152	-68558.2641	8908.2336	False
7	9	-49817.1464	-88550.3953	-11083.8976	True
8	9	-19992.1312	-67430.4791	27446.2167	False

7h:

Multiple Comparison of Means - Tukey HSD,FWER=0.05

group1	group2	meandiff	lower	upper	reject
5	6	25669.2245	-61218.4629	112556.9119	False
5	7	82700.2695	11756.7698	153643.7692	True
5	8	12770.8041	-74116.8833	99658.4916	False

5	9	-14547.9893	-101435.6767	72339.6981	False
6	7	57031.045	-13912.4547	127974.5447	False
6	8	-12898.4204	-99786.1078	73989.267	False
6	9	-40217.2138	-127104.9013	46670.4736	False
7	8	-69929.4654	-140872.9651	1014.0343	False
7	9	-97248.2588	-168191.7585	-26304.7591	True
8	9	-27318.7935	-114206.4809	59568.894	False

9h:

Multiple Comparison of Means - Tukey HSD,FWER=0.05

group1	group2	meandiff	lower	upper	reject
5	6	21948.695	-38626.9602	82524.3501	False
5	7	84516.5196	35056.7043	133976.3349	True
5	8	43319.6633	-17255.9918	103895.3184	False
5	9	-22639.6063	-83215.2615	37936.0488	False
6	7	62567.8246	13108.0093	112027.6399	True
6	8	21370.9683	-39204.6868	81946.6235	False
6	9	-44588.3013	-105163.9564	15987.3538	False
7	8	-41196.8563	-90656.6716	8262.959	False
7	9	-107156.1259	-156615.9412	-57696.3107	True
8	9	-65959.2696	-126534.9248	-5383.6145	True

Supplementary Table S2 – Statistical analysis from RT-qPCR experiments on porin expression into FCCs and SABs. All experiments were conducted for at least three biologically independent replicates. Technical replicates were averaged to produce replicate means that were subsequently used for analysis. Mean values were compared within and between groups using one-way ANOVA followed by Tukey's post hoc for two-two comparisons. Differences were considered statistically significant if $p < 0.05$ (True).

GLM - DLS

Omp-Pst1 porin – All statistic parameters:

Generalized Linear Model Regression Results

```

=====
Dep. Variable:          Y      No. Observations:      389
Model:                GLM      Df Residuals:          381
Model Family:         Gamma    Df Model:              7
Link Function:        inverse_power  Scale:                0.097908
Method:              IRLS      Log-Likelihood:       -1972.8
Date:                Mon, 18 Mar 2019  Deviance:             33.696
Time:                14:17:24    Pearson chi2:         37.3
No. Iterations:      7          Covariance Type:      nonrobust
=====

```

	coef	std err	z	P> z	[0.025	0.975]
Intercept	0.0137	0.002	8.950	0.000	0.011	0.017
Cporin	-0.0130	0.002	-7.730	0.000	-0.016	-0.010
Urea	2.3e-07	6.93e-07	0.332	0.740	-1.13e-06	1.59e-06
Cporin:Urea	7.344e-07	8.34e-07	0.881	0.378	-9e-07	2.37e-06
Ammonium	3.751e-06	9.29e-07	4.036	0.000	1.93e-06	5.57e-06
Cporin:Ammonium	4.42e-06	1.36e-06	3.246	0.001	1.75e-06	7.09e-06
pH	-0.0007	0.000	-3.151	0.002	-0.001	-0.000
Cporin:pH	0.0012	0.000	5.136	0.000	0.001	0.002

Omp-Pst2 porin – All statistic parameters:

Generalized Linear Model Regression Results

```

=====
Dep. Variable:          Y      No. Observations:      386
Model:                GLM      Df Residuals:          378
Model Family:         Gamma    Df Model:              7
Link Function:        inverse_power  Scale:                0.36485
Method:              IRLS      Log-Likelihood:       -2501.6
Date:                Mon, 18 Mar 2019  Deviance:             123.99
Time:                14:19:20    Pearson chi2:         138.
No. Iterations:      8          Covariance Type:      nonrobust
=====

```

	coef	std err	z	P> z	[0.025	0.975]
Intercept	0.0066	0.001	4.551	0.000	0.004	0.010
Cporin	-0.0046	0.001	-3.105	0.002	-0.008	-0.002
Urea	4.958e-07	6.87e-07	0.722	0.470	-8.51e-07	1.84e-06
Cporin:Urea	-6.935e-07	6.79e-07	-1.022	0.307	-2.02e-06	6.36e-07
Ammonium	1.284e-05	1.92e-06	6.681	0.000	9.07e-06	1.66e-05
Cporin:Ammonium	-1.208e-05	1.82e-06	-6.651	0.000	-1.56e-05	-8.52e-06
pH	-0.0003	0.000	-1.475	0.140	-0.001	9.77e-05
Cporin:pH	0.0002	0.000	1.107	0.268	-0.000	0.001

Omp-Pst1 porin – Bicarbonate – All statistic parameters:

Generalized Linear Model Regression Results

```

=====
Dep. Variable:          Y      No. Observations:      96
Model:                GLM      Df Residuals:          92
Model Family:         Gamma    Df Model:              3
Link Function:        inverse_power  Scale:                0.0066722
Method:              IRLS      Log-Likelihood:       -380.86
Date:                Sat, 20 Apr 2019  Deviance:             0.62057
Time:                11:22:54    Pearson chi2:         0.614
No. Iterations:      7          Covariance Type:      nonrobust
=====

```

	coef	std err	z	P> z	[0.025	0.975]
Intercept	0.0129	0.000	60.130	0.000	0.012	0.013
Bicarbonate	2.458e-06	4.09e-06	0.601	0.548	-5.56e-06	1.05e-05
Concentration	-0.0109	0.000	-50.047	0.000	-0.011	-0.010
Bicarbonate:Concentration	1.985e-05	4.23e-06	4.691	0.000	1.16e-05	2.81e-05

Omp-Pst1 porin – Bicarbonate:

Generalized Linear Model Regression Results

```

=====
Dep. Variable:                Y      No. Observations:                96
Model:                        GLM      Df Residuals:                    94
Model Family:                  Gamma   Df Model:                        1
Link Function:                  inverse_power  Scale:                            0.49076
Method:                          IRLS   Log-Likelihood:                   -601.92
Date:                            Sat, 20 Apr 2019  Deviance:                          56.351
Time:                            11:23:18    Pearson chi2:                       46.1
No. Iterations:                  7      Covariance Type:                  nonrobust
=====

```

	coef	std err	z	P> z	[0.025	0.975]
Intercept	0.0037	0.000	8.701	0.000	0.003	0.005
Bicarbonate	2.78e-05	1.06e-05	2.634	0.008	7.11e-06	4.85e-05

Omp-Pst2 porin – Bicarbonate – All statistic parameters:

```

=====
Generalized Linear Model Regression Results
=====
Dep. Variable:                Y      No. Observations:                50
Model:                        GLM      Df Residuals:                    48
Model Family:                  Gamma   Df Model:                        1
Link Function:                  inverse_power  Scale:                            0.016299
Method:                          IRLS   Log-Likelihood:                   -246.36
Date:                            Sat, 20 Apr 2019  Deviance:                          0.76802
Time:                            11:34:22    Pearson chi2:                       0.782
No. Iterations:                  18     Covariance Type:                  nonrobust
=====

```

	coef	std err	z	P> z	[0.025	0.975]
Intercept	0.0013	3.89e-05	33.427	0.000	0.001	0.001
Bicarbonate	1.703e-05	1.17e-06	14.569	0.000	1.47e-05	1.93e-05
Concentration	0.0013	3.89e-05	33.427	0.000	0.001	0.001
Bicarbonate:Concentration	1.703e-05	1.17e-06	14.569	0.000	1.47e-05	1.93e-05

Omp-Pst2 porin – Bicarbonate:

```

=====
Generalized Linear Model Regression Results
=====
Dep. Variable:                Y      No. Observations:                50
Model:                        GLM      Df Residuals:                    48
Model Family:                  Gamma   Df Model:                        1
Link Function:                  inverse_power  Scale:                            0.016299
Method:                          IRLS   Log-Likelihood:                   -246.36
Date:                            Sat, 20 Apr 2019  Deviance:                          0.76802
Time:                            11:35:15    Pearson chi2:                       0.782
No. Iterations:                  6      Covariance Type:                  nonrobust
=====

```

	coef	std err	z	P> z	[0.025	0.975]
Intercept	0.0026	7.79e-05	33.427	0.000	0.002	0.003
Bicarbonate	3.405e-05	2.34e-06	14.569	0.000	2.95e-05	3.86e-05

2-2 comparison (Tukey) – Ammonia condition

Omp-Pst1 porin

Multiple Comparison of Means - Tukey HSD,FWER=0.05

```

=====
group1 group2 meandiff lower upper reject
=====
0 100 -226.57 -347.8389 -105.3011 True
0 500 -207.49 -328.7589 -86.2211 True
0 1000 -230.26 -351.5289 -108.9911 True
100 500 19.08 -120.9493 159.1093 False
100 1000 -3.69 -143.7193 136.3393 False
500 1000 -22.77 -162.7993 117.2593 False
=====

```

Omp-Pst2 porin

Multiple Comparison of Means - Tukey HSD,FWER=0.05

```

=====
group1 group2 meandiff lower upper reject
=====

```

0	100	98.33	2.99	193.67	True
0	500	193.62	98.28	288.96	True
0	1000	308.39	205.411	411.369	True
100	500	95.29	-14.7991	205.3791	False
100	1000	210.06	93.2928	326.8272	True
500	1000	114.77	-1.9972	231.5372	False

2-2 comparison (Tukey) – Bicarbonate condition

Omp-Pst1 porin

Multiple Comparison of Means - Tukey HSD, FWER=0.05

group1	group2	meandiff	lower	upper	reject
0	10	-57.92	-125.4145	9.5745	False
0	25	-71.63	-126.739	-16.521	True
0	50	-185.4	-240.509	-130.291	True
0	100	-260.72	-315.829	-205.611	True
10	25	-13.71	-81.2045	53.7845	False
10	50	-127.48	-194.9745	-59.9855	True
10	100	-202.8	-270.2945	-135.3055	True
25	50	-113.77	-168.879	-58.661	True
25	100	-189.09	-244.199	-133.981	True
50	100	-75.32	-130.429	-20.211	True

Omp-Pst2 porin

Multiple Comparison of Means - Tukey HSD, FWER=0.05

group1	group2	meandiff	lower	upper	reject
0	10	-116.89	-151.1648	-82.6152	True
0	25	-139.98	-174.2548	-105.7052	True
0	50	-221.96	-256.2348	-187.6852	True
0	100	-242.87	-277.1448	-208.5952	True
10	25	-23.09	-57.3648	11.1848	False
10	50	-105.07	-139.3448	-70.7952	True
10	100	-125.98	-160.2548	-91.7052	True
25	50	-81.98	-116.2548	-47.7052	True
25	100	-102.89	-137.1648	-68.6152	True
50	100	-20.91	-55.1848	13.3648	True

2-2 comparison (Tukey) – pH condition

Omp-Pst1 porin

Multiple Comparison of Means - Tukey HSD, FWER=0.05

group1	group2	meandiff	lower	upper	reject
5	6	-110.6	-137.2876	-83.9124	True
5	7	14.73	-11.9576	41.4176	False
5	8	-192.42	-219.1076	-165.7324	True
5	9	-165.36	-192.0476	-138.6724	True
6	7	125.33	98.6424	152.0176	True
6	8	-81.82	-108.5076	-55.1324	True
6	9	-54.76	-81.4476	-28.0724	True
7	8	-207.15	-233.8376	-180.4624	True
7	9	-180.09	-206.7776	-153.4024	True
8	9	27.06	0.3724	53.7476	True

Supplementary Table S3 – Statistical analysis from DLS experiments on porin propensity to self-associate in DOTs. All experiments were conducted for at least three biologically independent replicates. Technical replicates were averaged to produce replicate means that were subsequently used for analysis. Mean values were compared within and between groups using one-way ANOVA followed by Tukey's post hoc for two-to-two comparisons. Differences were considered statistically significant if $p < 0.05$ (True).

Article n°4 – Targeting bacterial porins : a possible alternative strategy for disrupting biofilms to combat infections from the human pathogen *Providencia stuartii*

Article n°4 – Résumé

Dans l'article précédent, nous avons montré que la socialisation en communautés flottantes et en biofilms adhérents assurait aux bactéries de *P. stuartii* une résistance forte aux environnements hostiles, leur permettant de survivre dans le tractus urinaire. Cette résistance élevée pourrait expliquer que jusqu'à présent aucun traitement ne s'est révélé efficace pour éradiquer spécifiquement les infections urinaires chroniques causées par *P. stuartii*. Dans ce quatrième article, nous proposons une stratégie thérapeutique potentielle qui vise à inhiber la socialisation bactérienne en communautés flottantes dans le but d'empêcher la formation des biofilms adhérents. Etant donné que les DOTs de porines sont impliqués dans le rivetage des cellules au sein des communautés flottantes, nous avons designé des peptides bio-inspirés dans le but d'inhiber l'auto-association des porines en DOTs. Nos résultats ont révélés que certains peptides, couplés à un fragment de coumarine, étaient prometteurs pour identifier, contrôler et/ou contrecarrer les infections par *P. stuartii*.

**Targeting bacterial porins: a possible alternative strategy for
disrupting biofilms to combat infections from the human pathogen
*Providencia stuartii***

Authors:

Julie Lopes¹, Guillaume Tétreau¹, Pierrick Bruyat², Amandine Paoli¹, Mariam ElKhatib¹, Ludovic Jean², Pierre-Yves Renard², Jacques-Philippe Colletier¹

Affiliations:

¹ Univ. Grenoble Alpes – CEA – CNRS, Institut de Biologie Structurale (IBS), Grenoble, France

² Normandie Univ, UNIROUEN, INSA Rouen, CNRS, COBRA (UMR 6014), 76000 Rouen, France

Correspondence: JPC, jacques-philippe.colletier@ibs.fr

PYR, pierre-yves.renard@univ-rouen.fr

Abstract

Providencia stuartii is a highly social Gram-negative pathogen characterized by its ability to form floating communities of cells (FCCs) in addition and prior to surface-attached biofilms (SABs). The socialization ability of *P. stuartii* explains, together with its chromosomal AmpC and possible plasmid acquired resistance genes, that it displays a stringent antibiotic-resistance. To date, however, treatments to specifically eradicate chronic urinary tract infections caused by *P. stuartii* are lacking. Also lacking are diagnostic tools, which would allow to detect and counteract *P. stuartii* in the early stages of infection, when it is worst vulnerable to attack. Here, we report on the design and characterization of peptides intended to counteract SAB formation by inhibition of socialization into FCCs. Our data suggest that synthetic peptides, combined with a coumarin molecule, can be used to identify, control and/or counteract *P. stuartii* biofilms infections. We furthermore show that these peptides could be used in combination with last generation antibiotics to ensure that these are used at their maximum potential.

Keywords: *Providencia stuartii*; porins; floating communities of cells; surface-attached biofilms; steric zipper; bio-inspired peptides; antibiotics

Introduction

Antibiotic resistance is now recognised as one of the most pressing public health issues of the 21st century^{1,2}. Three strategies are exploited by microbes to resist to antibiotics³: i) modification of antibiotic targets – by mutation and/or modification of their expression, ii) antibiotic inactivation – by degradation and/or compartmentalization, and iii) decrease of antibiotic concentration at the site of action – by decreasing influx and/or increasing efflux. The latter strategy relies on a modification of membrane permeability through modified expression of porins and efflux pumps, respectively. In addition, some bacteria are capable of socialization into biofilms, conferring them an extra-edge against the immune system and antibiotherapy⁴. Biofilms are defined as multicellular, structured and metastable bacterial communities, adherent to surfaces and surrounded by an extracellular matrix (ECM)^{4,5}. The ECM is composed of extracellular polymeric substances (EPS), polysaccharides, proteins, extracellular DNA and amyloid-like protein fibers, which all play roles in the attachment, virulence and structural integrity of biofilms^{6,7}. The ability of the matrix to protect bacterial cells from the immune system and antibiotics, together with the non-established differentiation of cells within biofilms, explain that these structures are involved in the most majority of chronic bacterial infections^{4,8,9}. Indeed, it has been estimated that biofilm cells are on the overall a 1,000 times less sensitive to antibiotics than their planktonic counterparts¹⁰. New therapeutic strategies, directly aimed at dissociating biofilms, are therefore needed.

Providencia stuartii is a Gram-negative biofilm-forming opportunistic-pathogen from the *Enterobacteriaceae* family, responsible for 10% of hospital-acquired urinary tract infections^{11–15}. Victims are often immunocompromised individuals, such as the elderly, residents of intensive care unit (ICU), or long-term catheterization patients¹⁶. The chronicity of *P. stuartii* infections can be partly explained by its intrinsic multidrug resistance (MDR) phenotype, resulting from the presence of a chromosomal AmpC in its genome, complemented or not by plasmid acquired

ESBLs¹⁷⁻²⁰. It also stems from the ability of this bacterium to form biofilms. Compared to the current biofilm model, in which planktonic bacteria first adhere to a surface to form a monolayer of cells²¹, *P. stuartii* exploits an additional means of socialization, forming floating communities of cells (FCCs), prior to sedimentation, adhesion onto surfaces and ECM secretion to yielding surface-attached biofilms (SABs)²². FCCs are supported by intercellular self-matching interaction between porins from adjacent cells.

General-diffusion porins (thereafter referred to as porins) are the most abundant proteins expressed in the outer membrane (OM) of Gram-negative bacteria with up to 100,000 copies per cell, representing 70% of the OM proteinaceous content^{23,24}. Porins control the access of nutrients, ions and antibiotics to the bacterial periplasm and as such, they are vital for the bacterium. Each porin monomer folds in a 16-stranded β -barrel, with comparatively long extracellular loops and short intracellular turns. The long L3 loop folds into the β -barrel, contributing a constriction zone that sieves molecules reaching the periplasm. These may be antibiotics and accordingly, down-regulation or mutations of porins have been associated to an accentuation of the antibiotic resistance character²⁵⁻²⁷. *P. stuartii* ATCC 29914 (thereafter referred to as *P. stuartii*) expresses two porins, Omp-Pst1 and Omp-Pst2, both in the form of functional trimers. Omp-Pst1 is 10 times more expressed than Omp-Pst2 and constitutes the principal entry of ions, nutrients and hydrophilic solutes into cells²⁸⁻³⁰. The Omp-Pst2 porin was proposed to be involved in the regulation of the cation flux in the periplasm^{28,31}. The two porins of *P. stuartii* are unusual in that they display the ability to self-associate into intercellular dimers of trimers (DOTs), thereby enabling cell-to-cell contact and promoting the formation of FCCs²⁹. The main driving force behind DOT formation is electrostatic attraction, but we have shown that the DOT structure is locked-in by steric zipper-like interactions between facing extracellular loops²⁹. These interactions motifs could be LARKS³² rather than canonical steric zippers, which would explain the reversibility of cell-to-cell contact upon ECM secretion. It was indeed shown that

LARKS can dissociate upon heating and mixing³². Regardless, we have proposed that the presence of these motifs in the extracellular loops of porins could underlie the means by which cell-to-cell contact is restricted to cells of the same clonal origin.

Because FCCs form prior and are at the origin of SABs, they appear as valuable targets in the treatment of *P. stuartii* infections, offering a means to counterfeit the bacterium when it is still vulnerable to attack. In the present work, we explored the relevance of this strategy by synthesizing and testing the biological activity of peptides designed with aim to disrupt the DOT interface. The peptides retained the aggregation properties at play in the parent proteins, causing inactivity and prompting us to graft a coumarin moiety with view to monitor their interaction with *P. stuartii* cells by epifluorescence microscopy. Our results show that these peptides are able to i) co-aggregate with porins, ii) co-precipitate cells, and iii) in the best scenario, kill those. Additionally, we tested the effect of these peptides in combination with antibiotics used in hospital setting to combat *P. stuartii* infections. Surprisingly, we observed that our peptides potentialize the effect of some antibiotics, but can, in others cases, increase resistance against these. Our work thus validates the approach of targeting FCCs to avoid SABs, but shows how complex the targeting of socialized cells can be, reinforcing the case that novel anti-biofilm therapies, notably against *P. stuartii*, must be developed and tested in combination with antibiotics as their combined effect may be synergic.

Results

1. Antibiotic resistance of *P. stuartii* cells

Our goal being to determine whether or not peptides targeting FCCs could ameliorate the treatments of *P. stuartii* infections, we first set to verify how these supracellular structures and the SABs, which they form by sedimentation, are influenced by antibiotic treatments. We focused on three antibiotics, viz. cefepime and meropenem, which are both used in the treatment of *P. stuartii* infections, and tetracycline, against which it known to display resistance. The minimum inhibitory concentrations (MICs), i.e. the lowest concentration preventing detectable growth of bacterium, were determined to be 0.05 µg/mL, 0.18 µg/mL and 80 µg/mL for cefepim, meropenem and tetracycline, respectively (Supplementary Figure S1).

We then examined the formation of FCCs and SABs (Supplementary Figure S2) and the overall growth of *P. stuartii* (Supplementary Figures S1 and S3), at three concentrations below or up to the MIC values. We found that cefepim being the most efficient against *P. stuartii*, affecting cell appearance and self-association into FCCs at concentration as low as 0.0075 µg/mL and abolishing formation of SABs at 0.05 µg/mL. Specifically, we observed elongated cells, suggesting that cell division is arrested at concentration well below the MIC. We note that alike cells in FCCs, those present in SABs formed in presence of cefepim display an elongated appearance and that no SABs is formed when FCCs are absent. This again supports the hypothesis that SABs form from the sedimentation of FCCs. Meropenem was slightly less efficient than cefepim, but also abolished formation of FCCs and SABs at concentration as low as 0.05 µg/mL. No effect on cell shape was visible in the concentration range we tested, but again a clear correspondence was visible between the absence of FCCs and that of SABs. Tetracycline was however completely inefficient at inhibiting FCC and SAB formation by *P. stuartii*, even at concentrations as high as 40 µg/mL, in line with the known resistance of the

bacterium to this antibiotic. If anything, tetracycline promoted the formation of SABs, perhaps by accelerating the sedimentation of FCCs and/or increasing the attachment of SABs. Irrespectively, our results are in agreement with the known sensitivity of *P. stuartii* to the three tested antibiotics and evidence that SAB formation is always associated with the presence of FCCs.

2. Targeting porin DOTs to avoid FCC and SAB formation

Results presented above, as well as prior data (El khatib et al. 2017²² and Lopes et al. 2019, in submission) support the notion that *P. stuartii* SABs form from the sedimentation of FCCs. If true, molecules capable of inhibiting the formation of FCCs should allow to avoid SAB formation. We showed earlier that *P. stuartii* FCCs are scaffolded through self-matching interaction between the extracellular loops of their porins, yielding intercellular dimers or trimers (DOTs) that act as rivets between cell membranes. In previous work, we showed that the introduction of positive charges at the DOT interface, resulting in electrostatic repulsion between facing porins, can challenge DOT formation *in vitro* – in experiment where liposome aggregation is monitored post-reconstitution of porins – and *in vivo*, when mutated porins are recombinantly expressed in model *E. coli* cells devoid of their own porins^{29,33}. Here, we hypothesized that positively charged amino acids would bind to the highly negatively charged cavities delineated by facing Omp-Pst1 and Omp-Pst2 trimers, reducing the electrostatic attraction between these and thereby challenging their respective DOT interfaces. Indeed, we found that arginine can abrogate DOT formation *in vitro*, following reconstitution in liposomes and as assessed by DLS (Figure 1. a and Supplementary Table S1). We observed a stronger reduction of Omp-Pst2 self-association into DOTs, in line with its higher negative charge²⁹. Arginine also abrogated the formation of FCCs and SABs *in vivo* (Figure 1. b and c, respectively). To the contrary, glutamate only caused slight inhibition of DOT formation *in vitro* and no effect at all on FCC and SAB formation *in vivo* (Supplementary Figure S4). These experiments demonstrate a direct link between the formation

of *P. stuartii* FCCs and the self-association of its porins. Most interestingly, the formation of SABs was completely abolished when FCCs did not form, establishing that the former form from the latter, and that the strategy of targeting FCCs to counterfeit SAB formation by *P. stuartii* is valid.

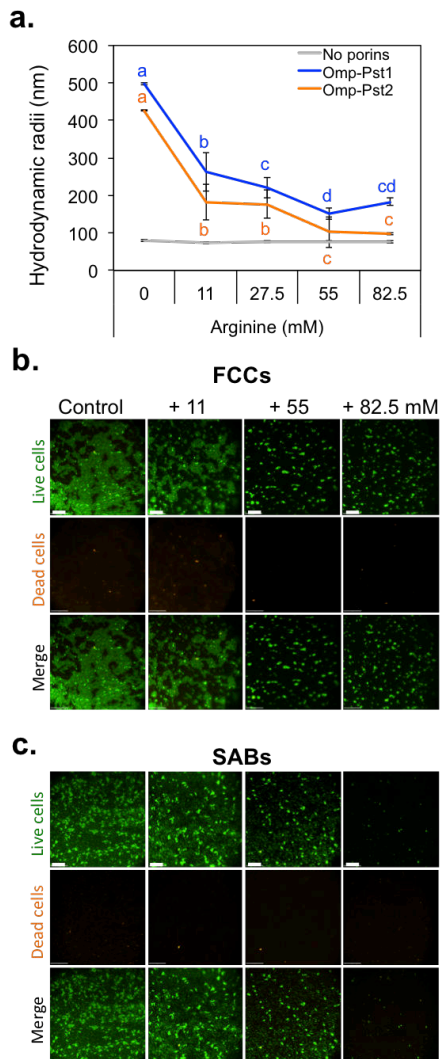


Figure 1. Arginine abolishes FCC and SAB formation by inhibiting the porin ability to self-associate in DOTs.

(a) The hydrodynamic radius of proteoliposomes was observed by DLS, 24 hours after the addition of Omp-Pst1 (blue) or Omp-Pst2 (orange) into LUV suspension, in presence of increasing concentrations of arginine. As control, the hydrodynamic radius of LUVs without porin insertion, in the same conditions, was measured (grey). Different letters above each point indicate significant differences ($p < 0.05$; ANOVA followed by post-hoc Tukey HSD test) and statistics data are available in Supplementary Table S1. The capacity of bacteria to form FCCs (b) and SABs (c) in presence of increasing concentration of arginine was visualized by epifluorescence microscopy. All bacteria were shown in green (Syto 9 green labelling, upper line in all panels) while dead cells were in red (propidium iodide labelling, middle line). A merged image was shown for each condition on the bottom line of each panel. The scale bars are 50 μm and 200 μm for FCCs and SABs, respectively.

3. Target the locking interface

Data presented thus far show that challenging the electrostatic attraction between *P. stuartii* porins can reduce the ability of the bacterium to socialize into FCCs, and thereafter in SABs. We further sought to verify whether binding at the steric zipper-like interface between porins in the

DOTs could challenge FCC formation. To this end, we synthesized peptides and peptidomimetic molecules, as described in Bruyat et al³⁴. The structures of these molecules are shown in Supplementary Table S2, and hereafter referred to as compound n°1 to n°10.

In a first attempt, we directly used peptides of sequence identical to the steric zipper segment in Omp-Pst1 (AGVVTSE) and Omp-Pst2 (LGNY). As to the latter, a new crystal form was obtained for Omp-Pst2, which revealed the structure of yet another DOT associated by a new steric zipper-like interface, contributed by facing 200-SQNNIKT-206 segments in extracellular loop L5 (Supplementary Figure S5 and Table S3). This segment was assayed by computation of rosetta as steric zipper-prone profile, confirming the propensity of this loop segment to form steric zippers, and by crystallization yielding of tiny urchin-like nanocrystals typical of steric zipper segments, yet but too small to enable structure determination by synchrotron methods. Introduction of an arginine in place of the serine residue enabled the growth of bigger microcrystals from which the structure could be determined (Supplementary Figure S5 and Table S3). It was that of a steric zipper, indicating that even introduction of the arginine residue did not abolish the proneness of this segment to self-associate by such interactions. Hence, we also included in our tests the SQNNIKT (n°3) and RQNNIKT (n°6) segments. Their effect, as well as of AGVVTSE (n°1) and LGNY (n°2) peptides, was assayed at 1 mM, on bacterial survival and socialization *in vivo* (Supplementary Figure S3 and S6, respectively) and on porin self-association *in vitro* (Supplementary Figure S7 and Table S4), using the same methods described above for arginine and glutamate (and in the Method section). Another feature of this DOT structure was that Omp-Pst2 trimers also associated by their intracellular turns, with the N-terminal extremity of each porin being swapped at the turn-to-turn interface.

None of the peptides were able to challenge the formation of FCCs and SABs, indicating that they fail to interact at the site of action they were intended to. Indeed, DOT formation *in vitro* was also not affected by the addition of peptide, for neither of the two porins. In the contrary, the

peptide n°6 potentiates the propensity of Omp-Pst2 *in vitro*. We then considered using a combination of the peptides n°1, n°2 and n°3. We found that the peptide-mix had no effect on FCCs, however a toxic effect was exerted on SAB cells, which were basically all dead. Because the three peptides could be crystallized as steric zippers, we hypothesized that they could self-associate in solution, which would explain their unavailability for their intended site of binding at the DOT interface of either porin.

We therefore attempted to reduce the self-association properties of the peptides by introduction of an arginine or a lysine or both in the peptide sequence. We also tested whether introduction of kink in the sequence by use of a triazole (-tr-) moiety in place of a peptidic bond would reduce the propensity to self-associate of the sequence. To track the fate of peptides in our microscopy experiments, we developed versions of these grafted with a 7-diethylaminocoumarine (thereafter referred to as coumarine) moiety. The latter has in itself no effect on FCC and SAB formation (Supplementary Figure S3 and S6), nor does it interfere with porin self-association (Supplementary Figure S7). We found that addition of an arginine of the extremity of LGNY does not improve the desired activities of the peptides. Indeed LGNYR (n°4) has no effect on DOT formation and does not affect FCC and SAB formation (Supplementary Figure S7 and S6, respectively). Replacement of the peptidic bond by a triazole in L-tr-NYR (n°5) slightly improved the inhibition of DOT formation by Omp-Pst1, but not by Omp-Pst2 (Figure 2. a and Supplementary Table S4). Addition of the otherwise soluble and innocuous coumarine moiety to the peptides n°4 and n°5 scaffold resulted in an increase proneness of the two molecules to co-aggregate in the presence of lipidic vesicles (Figure 2. a and Supplementary Table S4). LGNY-cou (n°7) and L-tr-NYRK(tr-cou) (n°8) also displayed the unexpected property to co-precipitate with FCCs, killing cells within in these (Figure 2. b). Accordingly, SAB cells are inexistent or dead, respectively (Figure 2. c). These properties were not present in the parent coumarin nor LGNY and L-tr-NYR moieties, but were elicited upon combination of these. In some respect, this

result illustrated the importance of serendipity. It must be noted that the LGNY (n°2) and L-tr-NYR (n°5) displayed a similar behaviour in all assays except DOT formation by Omp-Pst1 *in vitro*; also, upon addition of the coumarin moiety, by two resulting peptidomimetic molecules (n°7 and n°8) display similar properties (Supplementary Figure S6 and S7). This result shows that usage of a triazole as a replacement for a peptidic bond is a valid strategy. Further addition of the second or third positively charged residue (n°9 and n°10 peptides) abolished the self-aggregation properties of the coumarine-derived peptides, and improved their inhibition of DOT formation by Omp-Pst2 (Figure 2. a and Supplementary Table S4), and losing their toxic effect against FCC cells while their binding (Figure 2. b). No binding of the peptide was observed on SABs cells, suggesting that their binding site on porin is made unavailable by the extracellular matrix (ECM) (Figure 2. c). As to cell binding and potential toxic activities of the four coumarine-derived peptides (n°7, 8, 9 and 10), it must be noted that peptides n°7 and n°8 would be used for *P. stuartii* diagnoses, but this will need to be more deeply investigated in future work.

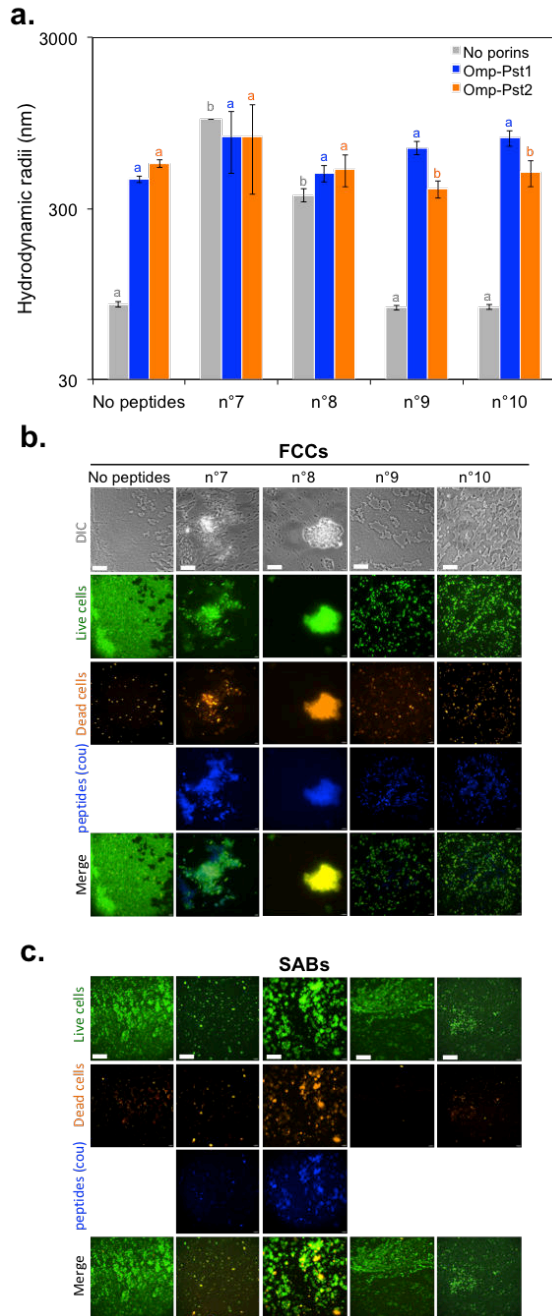


Figure 2. Peptidomimetic molecules inhibit or accentuate porin self-association, and also impact the socialization of *P. stuartii* in FCCs and SABs. (a) The hydrodynamic radius of proteoliposomes was observed by DLS, 24 hours after the addition of Omp-Pst1 (blue) or Omp-Pst2 (orange) into LUV suspension, in presence of peptidomimetic molecules (n°7, 8, 9 and 10). As a control, the hydrodynamic radius of LUVs without porin insertion, in the same conditions, was measured (grey). Different letters above the bars indicate significant differences ($p < 0.05$; ANOVA followed by post-hoc Tukey HSD test) and statistics data are available in Supplementary Table S4. The capacity of bacteria to form FCCs and SABs (panels b and c, respectively) in presence of peptidomimetic molecules (n°7, 8, 9 and 10) was visualized by epifluorescence microscopy. FCCs were observed in DIC (grey, upper line in all FCC panels), and all bacteria were shown in green (Syto 9 green labeling, second line in all panels) while dead cells were in red (propidium iodide labelling, third line). The coumarine-derived synthetic peptides were observed in blue (coumarine-fluorescence). A merged image was shown for each condition on the bottom line of each panel. The scale bars are 50 μm and 200 μm for FCCs and SABs, respectively.

Molecules aimed at disrupting biofilms are envisaged as complementary elements in the clinical toolbox to fight chronic bacterial infections, rather than as antibiotics themselves. Hence, we sought to verify whether the desired activities of the antibiotics, but also of the peptides and peptidomimetic molecules, were preserved, augmented or reduced when these were administrated together.

In the presence of cefepime at concentration lower than the MIC value (0.0130 µg/mL), the L-tr-NYRK(tr-cou) (n°8) preserved the ability to co-precipitate FCC cells, but not the LGNY-cou (n°7) and RL-tr-NYRK(tr-cou) (n°9), underlining that lower activity – here even less visible because in a context where fewer cells are present that can be aggregated and co-precipitated. Surprisingly, in the presence of cefepime, the RKL-tr-NYRK(tr-cou) peptide (n°10) also co-precipitate with cells. (Figure 3. a and Supplementary Figure S8). At the SAB level, there are more dead cells in the presence of peptides n°8 and n10 (Figure 3. b). In the case of peptide n°8, the fluorescence of the molecule was co-localized with that of the cells, again indicating co-precipitation. Hence, these cells are highly aggregated FCC debris. In the case of peptide n°10, the observation of more SABs cells could underlie an activation by the peptide of cell division and of the establishment of biofilms, although because of the toxic effect of both the antibiotic and the peptide, the cells are eventually die. The same effect was seen for this last peptide at the higher 0.05 µg/mL concentration of cefepime (Figure 3. c and d). Again, we could not observe binding of the peptide n°10 at the SAB level, suggesting they cannot access on binding site on porins in the SABs. For the peptide n°8, we observed no cells at the SAB level but patches of dead cells co-localized with the peptide, consistent with the hypothesis of the sedimentation of FCCs. We note that at 0.05 µg/mL concentration of cefepime, the presence of the coumarine became beneficial to growth in the form of FCCs with patches of dead FCC cells observed in conditions where cells without coumarine did not grow (Figure 3. c).

The peptides and peptidomimetic molecules had a very different effect on cells treated with meropenem. At 0.05 µg/mL concentration, where no cells growth is observed in the absence of the compound, we observed a beneficial effect of LGNY (n°2), L-tr-NYR (n°5) and coumarine on FCC formation (Figure 3. e and f). Somehow, the peptides or the dye appear to favour survival, possibly by offering an amyloid matrix for cells to develop on in the case of the peptides, or by effectively binding in the channel of their porins that block influx of the antibiotic. L-tr-NYRK(tr-

cou) (n°8), and a lower extent LGNY-cou (n°7), retained the ability to co-precipitate and kill cells, which resulted in the patches of dead FCC cells sedimenting and being observed at the SAB level (Figure 3. e and f). The RL-tr-NYRK(tr-cou) peptide (n°9) was surprisingly co-precipitate with *P. stuartii* cells as if it activated cell division at the FCC and SAB level, although all cells were eventually killed by the antibiotic or the peptide (Figure 3. e and f). The RKL-tr-NYRK(tr-cou) (n°10) peptide did not display an activating effect on FCC cells and was not found to bind at the SAB level; however it activated deposition of dead cells into SABs, as observed in the presence of cefepime already (Figure 3. e and f). The same set of observations was made at the higher 0.1 µg/mL concentration of meropenem (Supplementary Figure S8). Indeed, a beneficial effect was observed of peptides n°2 and n°5 on FCC formation. The peptide n°8 retained the ability to co-precipitate dead cells. The peptide n°9 activated the division of FCC cells and their settlement into SABs, but the cells did not survive due to the combined action of the peptide and the antibiotic. A co-localization of dead SAB and FCC cells with the peptide n°9 was yet clearly visible. Last, the peptide n°10 peptide did not influence the formation or survival of FCCs, but it induced an increased deposition into SABs. As the lower meropenem concentration, no co-localization was seen between the SAB cells and the peptide, but all biofilm cells were dead.

Tetracycline was seen to foster the development of FCCs and SABs at 40 µg/mL (Supplementary Figure S2 and S3). Addition of coumarin was able not only to revert this effect but also kill cells, with almost no SABs nor FCCs formed (Figure 3. g and h). LGNY (n°2) and L-tr-NYR (n°5) were able to reduce the formation of ultra large FCCs but had no effect on SAB formation (Supplementary Figure S8 and S3). The L-tr-NYRK(tr-cou) (n°8) peptide retained its ability to co-precipitate and kill cells at the FCC level, resulting in sedimented patches of aggregated dead cells being visible at the SAB level (Figure 3. g and h). The RL-tr-NYRK(tr-cou) (n°9) also co-localized with and killed cells at the FCC and SAB levels, again evidencing that this peptide, as the parent L-tr-NYRK(tr-cou), is able to target and kill cell both at FCC and SAB

levels (Figure 3. g and h). The reduced self-aggregation properties of the peptide n°9, together with its ability to target DOT formation by Omp-Pst2, and kill and label cells at SAB at FCC levels, make it a promising lead compound for the development of inhibitors of *P. stuartii* infections in combination with the tetracycline. The peptide n°8 again appears promising as a diagnosis tool against *P. stuartii*.

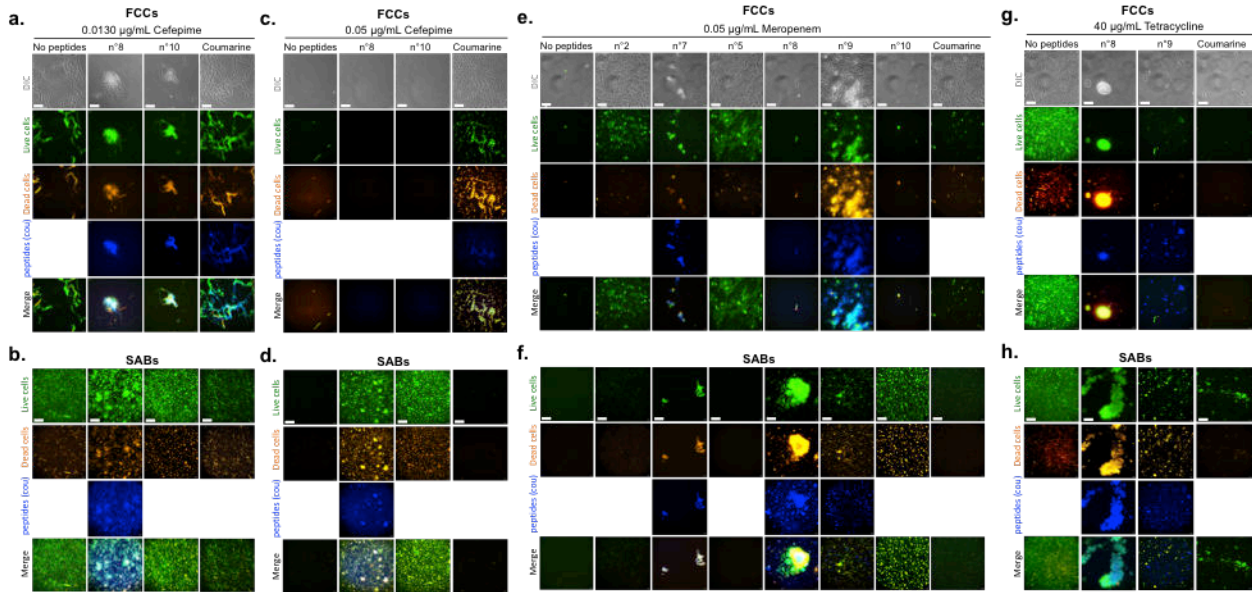


Figure 3. Synthetic peptides and peptidomimetic molecules improve or decrease bacterial resistance to meropenem or tetracycline antibiotics, respectively. The capacity of bacteria to form FCCs and SABs in presence of increasing concentrations of cefepime (panels a and b for 0.0130 µg/mL, and c and d for 0.05 µg/mL, respectively), meropenem (e, f) and tetracycline (g, h), in presence of synthetic peptide (n°2) or peptidomimetic molecules (n°5, 7, 8, 9 and 10), was visualized by epifluorescence microscopy. FCCs were observed in DIC (grey, upper line in all FCC panels), and all bacteria were shown in green (Syto 9 green labeling, second line in all panels) while dead cells were in red (propidium iodide labelling, third line). The coumarine-derived synthetic peptides were observed in blue (coumarine-fluorescence). A merged image was shown for each condition on the bottom line of each panel. The scale bars are 50 µm and 200 µm for FCCs and SABs, respectively.

Discussion

Providencia stuartii is a biofilm-forming pathogen involved in increasingly frequent chronic urinary tract infections acquired on the hospital^{11,14}. The mortality of these infections is high, between 6 and 33% depending on reports and on the strain that was isolated in the outbreak, and directly stems from the stringent antibiotic resistance phenotype of the bacterium known to possess a chromosomal AmpC but capable of acquiring further resistance genes by horizontal transfer³⁵. The resistance of the bacterium to antibiotics is also a result of its propensity to socialize, first into floating communities of cells (FCCs) and later, into surface-attached biofilms (SABs) by sedimentation²². We have shown that the porins of *P. stuartii*, Omp-Pst1 and Omp-Pst2, are involved in the scaffolding of FCCs through self-matching interaction between their extracellular loops, resulting in the formation of intercellular dimers of trimers (DOTs) that maintain adjacent cells riveted one the other in the FCCs²⁹. In previous work, we identified the segment 205-AGVVTSE-211 from Omp-Pst1 and 283-LGNY-286 from Omp-Pst2 is responsible for the locking of the DOT interface. In the present study, a new crystal form was obtained for Omp-Pst2, which revealed yet another segment capable of yielding on Omp-Pst2 DOT. Peptides corresponding to these sequences were synthesized but they did not allow to reduce FCC (and thereby SAB) formation, presumably because their own self-association by steric zipper (or LARKS) rendered them unavailable for binding at the intended site at the DOT interface of either porins. Only in the case where the three peptides were co-administrated we observed an effect on SAB cell viability, but the FCCs were left untouched. In contrast, the use of arginine to fix negative charges at the surface of porins and thereby avoid formation of DOTs was successful, with a clear dose dependant disruption of FCCs and consequently, no formation of SABs. These results offer a direct link between the self-association of porins into DOTs, FCC and SAB formation, thereby validating our strategy to target DOTs to deceive FCC and SAB formation by *P. stuartii*. To reduce the self-association properties of our LGNY peptide, we introduced an

arginine residue in the sequence, but also attempted to introduce a kink in the structure by introduction of a triazole in place of the first peptidic bond. While introduction of the charge in LGNY (LGNYR) had no effect that introduced in combination with the triazole linker (L-tr-NYR) resulted in improved inhibition of DOT formation by Omp-Pst1 *in vitro*. FCC and SAB formation were however not affected unless tetracycline were present. On the contrary, in the presence of meropenem, the two peptides fostered the development of SABs and FCCs.

In an attempt to track the fate of our peptides after addition to growing cell cultures, we decided to introduce a 7-diethylaminocoumarine moiety at the C-terminal extremity of LGNY and L-tr-NYR. Surprisingly, addition of the coumarine moiety endowed the peptides with the capacity to co-precipitate and kill cells at the SAB and FCC levels. In the case of L-tr-NYRK(tr-cou), which displays superior toxicity and cell aggregation properties, we suspect that SABs do not form *per se*, but rather aggregated FCCs sediment, explaining the co-localization of the fluorescence of the peptide with that of bacterial cells. In the SABs – where their binding site on porins is presumably unavailable – as well as in the FCCs – where no extracellular matrix (ECM) is present and porin should be accessible, the two peptides LGNY-cou and L-tr-NYRK(tr-cou) preserved their toxicity and cell aggregation properties in the presence of antibiotics, suggesting that they do not interfere with the mode of action exploited by the latter to kill cells. However, the two peptides displayed a strong propensity to self-aggregate in the presence of liposomes, yielding aggregates of size similar to that of the liposomes aggregates formed upon reconstitution of porins into liposomes. To reduce the propensity to self-associate of L-tr-NYRK(tr-cou), we either added an arginine and/or a lysine at its N-terminal end. Both peptides lost the ability to self-associate into aggregates larger than 60 nm, and were able to bind Omp-Pst2, inhibiting DOT formation by the latter. The two porins retained the ability to target *P. stuartii* FCC cells and kill them, but did not co-localize with SAB cells nor killed them. These toxic and FCC binding properties of the RL-tr-NYRK(tr-cou) peptide were however superior to those of the

RKL-tr-NYRK(tr-cou) peptide. In the case of RKL-tr-NYRK(tr-cou), we observe an activation of the disposition of cells into biofilms in the presence of antibiotics, but the cells die due to the toxic effect of both the antibiotics (meropenem and cefepime) and/or the peptide.

Thus, our work not only validates the strategy of targeting *P. stuartii* porins DOTs to challenge FCC formation and thereby avoid formation of SABs, but also put forwards two peptidomimetic molecules as potential lead compounds for the development of diagnostic (L-tr-NYRK(tr-cou)) and therapeutic (RL-tr-NYRK(tr-cou)) tools against *P. stuartii* infections. Further studies will be required to ameliorate the activity of these compounds and notably improve their affinity for their binding site on porins. It is also tantalizing to evaluate the activity of the compound on other biofilm-forming bacteria, to verify whether they could represent a clan of molecule active against different species. Indeed, bacterial biofilm are generally composed by different strains, requiring that molecules display a large spectrum to be active in the biological context.

Methods

Peptide Synthesis

General Information:

All reagents and solvents were obtained from commercial suppliers (Sigma-Aldrich, Acros, Alfa Aesar, Iris Biotech GmbH) unless otherwise stated. ^1H and ^{13}C NMR spectra were recorded at 298 K on a Bruker DPX 300 (300 MHz) spectrometer and aF AVIII HD 400 Bruker (400 MHz) spectrometer (Bruker, Wissembourg, France). Analytic HPLC (Thermo Hypersil GOLD C18 column, 5 μm , 2.1 mm \times 100 mm) was performed with CH_3CN and 0.1% aq. TFA as eluents [100% aq. TFA (5 min), then linear gradient from 0% to 100% (45 min) CH_3CN] at a flow rate of 0.25 mL/min. UV/vis detection was achieved with the “Max Plot” (i.e., chromatogram at

absorbance maximum for each compound) mode (220–700 nm). Purification steps by semipreparative HPLC were performed using Interchim puriFlash C18-HP (15 μ m, 120 g) with CH₃CN and 0.1% aq. TFA as eluents [0% CH₃CN (5 min), followed by a linear gradient from 0% to 40% (80 min) CH₃CN] at a flow rate of 34.0 mL/min. UV/vis detection was achieved with a UV diode array detector (200–600 nm). HRMS were obtained using the electrospray ionization (ESI) technique and a time of-flight (TOF) analyzer. Manual peptide synthesis was performed on a CEM Discover Bio microwave peptide synthesizer, with a 20 mL fritted glass reactor. Microwave reactions were performed under open-air conditions and were controlled with a fiber optic temperature probe.

Synthesis of building blocks:

Modified amino acids were synthesized as previously described in the literature^{36,37}. 3-carboxy-7-diethylaminocoumarin was synthesized in accordance with the protocol developed by Creaven et al³⁸.

General Procedure for SPPS:

Solid phase synthesis was performed using either Rink amide polystyrene resin (200 mg, 0.8 mmol/g) or ChemMatrix resin (rink amide linker and preloaded Arg(Pbf)-HMPB linker, 200 mg, 0.4–0.6 mmol/g). The resin was inserted in a fritted glass and washed 3 times with DCM (5 mL) and DMF (5 mL). Two equiv of Fmoc protected amino-acids, activated with 2 equiv of HBTU/HOBt and 4 equiv of DIPEA in degassed DMF (6 mL), were added to the resin after 5 min of preactivation. Coupling reactions were performed under microwave irradiation at 75 °C (25 W) in 5 min (twice). Modified coupling was used for Fmoc- Arg(Pbf)-OH, using COMU instead of HBTU/HOBt, 1 min of preactivation, and 10 min of reaction at 50 °C (25 W). The resin was then washed with DMF (5 \times 5 mL) and completion of the reaction was checked by using TNBS test. The Fmoc protecting group was released using a 20% solution of piperidine in DMF (5 mL), at

75 °C (50 W) in 3 min (twice). For N-terminal deprotection of Asp residues, a 5% piperazine solution in DMF (5 mL) was used, at 50 °C (50 W) in 3 min. The resin was washed with DMF (5 × 5 mL). These steps were repeated until completion of the peptide. When completed, a solution of TFA/TIS/H₂O (95:2.5:2.5 v/v/v) was added to the resin, which was stirred during 3 h at room temperature. After filtration, the filtrate was evaporated and the product was precipitated and washed several times with diethyl ether. After purification by reverse phase column chromatography (0.1% TFA in H₂O/acetonitrile), peptides were identified using ¹H NMR, HRMS, and HPLC analysis. Peptidotriazole compounds were obtained by solid phase copper(I)-catalyzed azide-alkyne cycloadditions (CuAAC), using the recent conditions developed in our laboratory³⁴

Strains

The *Providencia stuartii* ATCC 29914 strain was obtained from the Pasteur Institute (Paris, France). *P. stuartii*'s porins were expressed into a *E. coli* BL21 DE3 Δ *Omp8* strain, deleted of these principal porins (Δ *ompF*, Δ *lamB*, Δ *ompA*, Δ *OmpC*)^{28,39}, in order to purify them and analyze their self-association capacity in DOTs by Dynamic Light Scattering (see detailed method below).

Production of porins from P. stuartii in E. coli

One microliter of plasmid pGOmp-Pst1 or pGOmp-Pst2 was transformed into 50 μ L of *E. coli* Δ *Omp8* competent kanamycin-resistant cells by heat-shock method^{28,33}. Cells were recovered in 500 μ L of SOC (Super Optimal Broth) medium for 1 h at 37°C, and then 20 μ L was transferred onto agar plates (100 and 25 ng. μ L⁻¹ ampicillin and kanamycin respectively). Plates were incubated at 37°C overnight to select only the bacterial colonies containing porin plasmids. A colony was inoculated in 25 mL of LB medium overnight. The pre-culture was introduced into 1 L of LB culture, selected by the addition of 100 μ g/mL ampicillin and 25 μ g/mL kanamycin. Porin

expression was sufficient without induction by IPTG because of the presence of a strong T7-phage promoter in pGOMP-Pst1 and pGOMP-Pst2 plasmids. Bacteria grew until reached an optical density value at 600 nm of 1. Cells were then harvested by centrifugation at 4,500 rpm for 30 min, where the pellets were immediately used for porin extraction.

Porin extraction and solubilisation

Pellet cells were re-suspended in phosphate buffer (20 mM pH 7.4), supplemented with DNase (few mg), $MgSO_4$ (1 mM) and an anti-protease cocktail cOmplete (from Roche). The cells were then disrupted using a micro-fluidizer at 14,000 Psi (Constant system LTD, UK). A centrifugation at 4,500 rpm for 45 min separated membranes from cytoplasm. The pellet, containing the both membranes, was resuspended in phosphate buffer (20 mM pH 7.4) with 0.3% n-Octyl-polyoxyethylene (OPOE) detergent (Affymetrix, UK) and incubated for 2 h at 20°C under agitation. To separate inner (IM) from outer membranes (OM), a 45-min ultracentrifugation at 35,000 rpm (Optima XE, Beckman Coulter) was performed. The OM from the supernatant was collected and the resulting pellet, containing the IM and some remaining OM, was resuspended and incubated at 20°C for 2 h in phosphate buffer (20 mM pH 7.4) with 3% OPOE. To maximize OM protein recovery, the last solubilisation step was performed three times. The supernatants containing the solubilized porins from the OM were stored at 4°C until purification.

Porin purification

Solubilized porins were loaded onto an anionic-exchange column (Hitrap HQ, 5 mL, GE Healthcare Life Science, France). A detergent exchange was applied with 0.1 M MES buffer pH 6.5 complemented with 0.1% lauryldimethylamine-oxide (LDAO) detergent (Affymetrix, UK) and 25 mM NaCl. The most lipopolysaccharides (LPS) was eliminated by washing the column with MES buffer (0.1 M pH 6.5) complemented with 2 % LDAO, for 4h of slow washing ($0.2 \text{ mL} \cdot \text{min}^{-1}$). The column was then re-equilibrated with MES buffer (0.1 M pH 6.5) complemented with 0.1%

LDAO and 25 mM NaCl. A NaCl gradient (0 to 1 M) was applied to elute proteins from column. To verify the purity, the fractions containing the protein were analysed on SDS-PAGE. Those containing pure porin were pooled together and concentrated to 7 mg.mL⁻¹ on a 100-kDa cutoff Amicon ultra-filtration unit (Sigma-Aldrich, France). Purified porins were stored at 4°C until use.

Omp-Pst2 crystallization

Crystallization conditions screening was performed at the HTX-Lab of the ESRF using a Cartesian PixSys 420 crystallization robot (Genomic Solutions, U.K). Screening was performed at the nano-litre scale using sitting-drop vapour-diffusion method. Some poorly or non-diffracting crystals were obtained under certain conditions. Around these conditions, manual screening was performed using the sitting and hanging-drop vapour-diffusion method, producing diffracting crystals after a few days. The Omp-Pst2 porin to mother buffer ratio was 1:1. The solution of mother buffer was 32% PEG 400, 0.2 M MgCl₂, 0.1 M HEPES pH 7.5. Omp-Pst2 was crystallized at a concentration of 7 mg/mL at 4°C. Only few crystals diffracted to a resolution of 3.2 Å.

X-ray data collection and processing

Crystals of Omp-Pst2 were soaked in mother buffer solutions containing 18% of glycerol for a few seconds, before to be mounted in a cryo-loop and flash-cooled in a nitrogen stream at 100 K. X-ray data were collected at the European Synchrotron Radiation Facility (ESRF) on beamline ID30A-1 and were processed, merged and scaled using XDS/XSCALE^{40,41}. The amplitude factors were generated using XDSCONV⁴².

Liposome preparation

Large Unilamellar Vesicles (LUVs) were produced by standard film-hydration method⁴³. Briefly, a mixture of liposomes was generated by adding 0.02% lissamine-rhodamine-sn-glycero-3-

phosphoethanolamine (Rhod PE, Avanti Polar, Lipids Co., USA) to 4% L- α -phosphatidylcholine (egg PC, Avanti Polar, Lipids Co., USA). Both were suspended in a chloroform solution, which were evaporated under N₂-flow to obtain a thin lipid film. The residual chloroform was then eliminated by overnight vacuum. The lipid film was rehydrated with 125 mM of phosphate buffer at pH 7.4 and vortexed during 5 min continuously to obtain multilamellar vesicles (MLVs). These were freeze-thawed (100K-310K) for 10 times and LUVs were obtained. To finish, an extrusion was performed with a 100-nm filter to calibrate LUVs toward 70-nm diameter (mini-extruder with polycarbonate filters, Avanti Polar Lipids).

Dynamic Light Scattering

The hydrodynamic radius of LUVs was calculated after the incorporation of porins into their bilayer by using the DLS method (DynaPro Nanostar from Wyatt Technology). To this end, liposomes (0.125 mg.mL⁻¹) and porins (ranged from 0.033 to 1.07 μ M) were mixed and incubated at pH 7.4. To avoid a sudden decrease of detergent concentration in solution leading to a porin aggregation, we used biobeads (hydrophobic polystyrene) to decrease slightly the detergent below the critical micellar concentration (CMC). In the lipid bilayer, porins are oriented in natural way meaning oriented mostly with their intracellular turns facing the lumen of the LUVs and their extracellular loops facing the outside⁴⁴. The incorporation of porins into liposomes generates the increase of hydrodynamic radius of liposomes continuing during 24 h at 4°C. The DLS measurement was then taken.

P. stuartii form FCCs and SABs, causing chronic infections in human urinary tract. The DLS study will determine whether some synthetic peptides and peptidomimetic molecules might inhibit the self-association of Omp-Pst1 and Omp-Pst2. To this end, peptides were applied before the incorporation of porins into LUVs, and the hydrodynamic radii of proteoliposomes were measured after 24 h at 4°C.

Bacterial growth studies

Calculation of antibiotic MICs (Minimal Inhibitory Concentrations)

Different concentrations of antibiotics were tested on bacteria to determine the one for which *P. stuartii* stop to growth; it will be this concentration that will determine the MIC. To achieve this, one colony of *P. stuartii* was inoculated in LB medium for 1 h, and then 100 μL of bacteria, supplemented with 100 μL of antibiotics (from 0 to 0,1 $\mu\text{g}/\text{mL}$ for cefepim; from 0 to 0,36 $\mu\text{g}/\text{mL}$ for meropenem; from 0 to 160 $\mu\text{g}/\text{mL}$ for tetracycline), were disposed into a 96-well plate (Greiner) and incubated at 37°C under 100 rpm shaking overnight. The bacterial growth was monitored by absorbance at 600 nm for 24h (10 min interval between time points) using a Biotek Synergy H4 microplate reader (Winooski, VT, USA).

In the presence of synthetic peptides and peptidomimetic molecules

To understand the survival of *P. stuartii* and potentially inhibit its ability to form FCC and SAB, we study the impact of synthetic peptides and peptidomimetic molecules on bacteria. To this end, one colony of *P. stuartii* was inoculated in LB medium for 1 h, and then 135 μL of bacteria, supplemented with 15 μL of peptides from 0 to 5 mM, were disposed into a 96-well plate (Greiner) and incubated at 37°C under 100 rpm shaking overnight. The bacterial growth was monitored by absorbance at 600 nm for 24 h (10 min interval between time points) using a Biotek Synergy H4 microplate reader (Winooski, VT, USA).

Combination of peptides and antibiotics

To evaluate a synergic effect of antibiotics and peptides on bacterial growth, one colony of *P. stuartii* was inoculated in LB medium for 1 h, and then 100 μL of bacteria, with 100 μL of antibiotics (from 0 to 0,1 $\mu\text{g}/\text{mL}$ for cefepim; from 0 to 0,2 $\mu\text{g}/\text{mL}$ for meropenem; from 0 to 80 $\mu\text{g}/\text{mL}$ for tetracycline), supplemented by 20 μL of peptides from 0 to 5 mM were disposed into a

96-well plate (Greiner) and incubated at 37°C under 100 rpm shaking overnight. The bacterial growth was monitored by absorbance at 600 nm for 24 h (10 min interval between time points) using a Biotek Synergy H4 microplate reader (Winooski, VT, USA).

Imaging

The observation of FCCs was realized by deposit 7 μL of the planktonic bacteria between LB-Gelzan solid media (LB-Lennox solidified with 8 g/L GelzanTM) and a glass cover-slide, which will image immediately afterwards⁴⁵. The remaining floating bacteria were removed by washing wells with PBS three times, and then SABs were imaged. Both FCCs and SABs were observed using an IX81 Olympus inverted microscope with a 100X objective magnification (Plan APON100X, Olympus). The membranes, the living and the dead bacteria were labelled using FM1-43X dye at 5 $\mu\text{g}\cdot\text{ml}^{-1}$ (479 nm excitation; emission: 598 nm emission), Syto® 9 Green at 5 μM (485 nm excitation; 498 nm emission) and propidium iodide at 20 μM (533 nm excitation; 617 nm emission), respectively. All fluorescent dyes were from Thermo Scientific (USA).

Statistical analysis

The *statsmodels* Python package was used for all analysis in this study⁴⁶. We used the 'Generalized Linear Model' module. As we are dealing with positive, and continuous response variables, we chose the Gamma family, using an inverse law as link function. All factors and their correlation were included for a first fit, then insignificant correlations were removed until the most parsimonious model, containing all significant variables, was found – in less than 10 iterations on average, indicating a good convergence. The two porins were treated as independent throughout the process. Then, TukeyHSD test was used to perform post-hoc analyses on the most significant factors.

Conflict of interests

The authors declare no conflict of interest.

Author Contributions

J.L, M.E.K J-P.C, P.B, P-Y.R, L.J

References

1. Landecker, H. Antibiotic Resistance and the Biology of History. *Body Soc.* **22**, 19–52 (2016).
2. Aslam, B. *et al.* Antibiotic resistance: a rundown of a global crisis. *Infect. Drug Resist.* **11**, 1645–1658 (2018).
3. Munita, J. M. & Arias, C. A. Mechanisms of Antibiotic Resistance. *Microbiol. Spectr.* **4**, (2016).
4. Costerton, J. W. Bacterial Biofilms: A Common Cause of Persistent Infections. *Science* **284**, 1318–1322 (1999).
5. Donlan, R. M. & Costerton, J. W. Biofilms: survival mechanisms of clinically relevant microorganisms. *Clin. Microbiol. Rev.* **15**, 167–193 (2002).
6. Flemming, H.-C., Neu, T. R. & Wozniak, D. J. The EPS matrix: the ‘house of biofilm cells’. *J. Bacteriol.* **189**, 7945–7947 (2007).
7. Xiao, Y. *et al.* Extracellular polymeric substances are transient media for microbial extracellular electron transfer. *Sci. Adv.* **3**, e1700623 (2017).
8. Lebeaux, D. & Ghigo, J.-M. Infections associées aux biofilms: Quelles perspectives thérapeutiques issues de la recherche fondamentale ? *médecine/sciences* **28**, 727–739 (2012).
9. Hall-Stoodley, L. & Stoodley, P. Evolving concepts in biofilm infections. *Cell. Microbiol.* **11**, 1034–1043 (2009).
10. Olson, M. E., Ceri, H., Morck, D. W., Buret, A. G. & Read, R. R. Biofilm bacteria: formation and comparative susceptibility to antibiotics. *Can. J. Vet. Res. Rev. Can. Rech. Veterinaire* **66**, 86–92 (2002).
11. Wie, S.-H. Clinical significance of *Providencia* bacteremia or bacteriuria. *Korean J. Intern. Med.* **30**, 167 (2015).

12. McHale, P. J., Walker, F., Scully, B., English, L. & Keane, C. T. *Providencia stuartii* infections: a review of 117 cases over an eight year period. *J. Hosp. Infect.* **2**, 155–165 (1981).
13. Gould, C. V. *et al.* Guideline for prevention of catheter-associated urinary tract infections 2009. *Infect. Control Hosp. Epidemiol.* **31**, 319–326 (2010).
14. De Vecchi, E. *et al.* Aetiology and antibiotic resistance patterns of urinary tract infections in the elderly: a 6-month study. *J. Med. Microbiol.* **62**, 859–863 (2013).
15. Chapman, C. M. C., Gibson, G. R. & Rowland, I. Effects of single- and multi-strain probiotics on biofilm formation and in vitro adhesion to bladder cells by urinary tract pathogens. *Anaerobe* **27**, 71–76 (2014).
16. O’Hara, C. M., Brenner, F. W. & Miller, J. M. Classification, identification, and clinical significance of *Proteus*, *Providencia*, and *Morganella*. *Clin. Microbiol. Rev.* **13**, 534–546 (2000).
17. Nicolle, L. E. Resistant pathogens in urinary tract infections. *J. Am. Geriatr. Soc.* **50**, S230–235 (2002).
18. Warren, J. W. *Providencia stuartii*: a common cause of antibiotic-resistant bacteriuria in patients with long-term indwelling catheters. *Rev. Infect. Dis.* **8**, 61–67 (1986).
19. Tumbarello, M. ESBL-producing multidrug-resistant *Providencia stuartii* infections in a university hospital. *J. Antimicrob. Chemother.* **53**, 277–282 (2004).
20. Aubert, D., Naas, T., Lartigue, M.-F. & Nordmann, P. Novel genetic structure associated with an extended-spectrum beta-lactamase blaVEB gene in a *Providencia stuartii* clinical isolate from Algeria. *Antimicrob. Agents Chemother.* **49**, 3590–3592 (2005).
21. Vlamakis, H., Chai, Y., Beauregard, P., Losick, R. & Kolter, R. Sticking together: building a biofilm the *Bacillus subtilis* way. *Nat. Rev. Microbiol.* **11**, 157–168 (2013).
22. El Khatib, M. *et al.* *Providencia stuartii* form biofilms and floating communities of cells that display high resistance to environmental insults. *PLOS ONE* **12**, e0174213 (2017).
23. Pagès, J.-M., James, C. E. & Winterhalter, M. The porin and the permeating antibiotic: a selective diffusion barrier in Gram-negative bacteria. *Nat. Rev. Microbiol.* **6**, 893–903 (2008).
24. Zeth, K. & Thein, M. Porins in prokaryotes and eukaryotes: common themes and variations. *Biochem. J.* **431**, 13–22 (2010).
25. Delcour, A. H. Outer membrane permeability and antibiotic resistance. *Biochim. Biophys. Acta BBA - Proteins Proteomics* **1794**, 808–816 (2009).

26. Pagès, J.-M. Porines bactériennes et sensibilité aux antibiotiques. *médecine/sciences* **20**, 346–351 (2004).
27. Nikaido, H. Prevention of drug access to bacterial targets: permeability barriers and active efflux. *Science* **264**, 382–388 (1994).
28. Tran, Q.-T. *et al.* Implication of Porins in β -Lactam Resistance of *Providencia stuartii*. *J. Biol. Chem.* **285**, 32273–32281 (2010).
29. El-Khatib, M. *et al.* Porin self-association enables cell-to-cell contact in *Providencia stuartii* floating communities. *Proc. Natl. Acad. Sci.* **115**, E2220–E2228 (2018).
30. Bajaj, H. *et al.* Antibiotic Uptake through Membrane Channels: Role of *Providencia stuartii* OmpPst1 Porin in Carbapenem Resistance. *Biochemistry (Mosc.)* **51**, 10244–10249 (2012).
31. Song, W. *et al.* Understanding Voltage Gating of *Providencia stuartii* Porins at Atomic Level. *PLOS Comput. Biol.* **11**, e1004255 (2015).
32. Hughes, M. P. *et al.* Atomic structures of low-complexity protein segments reveal kinked β sheets that assemble networks. *Science* **359**, 698–701 (2018).
33. Prilipov, A., Phale, P. S., Van Gelder, P., Rosenbusch, J. P. & Koebnik, R. Coupling site-directed mutagenesis with high-level expression: large scale production of mutant porins from *E. coli*. *FEMS Microbiol. Lett.* **163**, 65–72 (1998).
34. Bruyat, P., Gautier, A., Jean, L. & Renard, P.-Y. Use of an Air-Stable Cu(I)-NHC Catalyst for the Synthesis of Peptidotriazoles. *J. Org. Chem.* **83**, 13515–13522 (2018).
35. McGann, P. *et al.* Complete sequence of a novel 178-kilobase plasmid carrying bla(NDM-1) in a *Providencia stuartii* strain isolated in Afghanistan. *Antimicrob. Agents Chemother.* **56**, 1673–1679 (2012).
36. Mondal, S. & Fan, E. Mild and Efficient Synthesis of Fmoc-Protected Amino Azides from Fmoc-Protected Amino Alcohols. *ChemInform* **37**, (2006).
37. Galibert, M., Renaudet, O., Dumy, P. & Boturyn, D. Access to biomolecular assemblies through one-pot triple orthogonal chemoselective ligations. *Angew. Chem. Int. Ed Engl.* **50**, 1901–1904 (2011).
38. Creaven, B. S. *et al.* Synthesis, characterization and antimicrobial activity of a series of substituted coumarin-3-carboxylatosilver(I) complexes. *Inorganica Chim. Acta* **359**, 3976–3984 (2006).

39. Prilipov, A., Phale, P. S., Gelder, P., Rosenbusch, J. P. & Koebnik, R. Coupling site-directed mutagenesis with high-level expression: large scale production of mutant porins from *E. coli*. *FEMS Microbiol. Lett.* **163**, 65–72 (1998).
40. Kabsch, W. Integration, scaling, space-group assignment and post-refinement. *Acta Crystallogr. D Biol. Crystallogr.* **66**, 133–144 (2010).
41. Kabsch, W. XDS. *Acta Crystallogr. D Biol. Crystallogr.* **66**, 125–132 (2010).
42. Kabsch, W. Automatic processing of rotation diffraction data from crystals of initially unknown symmetry and cell constants. *J. Appl. Crystallogr.* **26**, 795–800 (1993).
43. Dijkstra, J., Ryan, J. L. & Szoka, F. C. A procedure for the efficient incorporation of wild-type lipopolysaccharide into liposomes for use in immunological studies. *J. Immunol. Methods* **114**, 197–205 (1988).
44. Zgurskaya, H. I. & Nikaido, H. Bypassing the periplasm: reconstitution of the AcrAB multidrug efflux pump of *Escherichia coli*. *Proc. Natl. Acad. Sci. U. S. A.* **96**, 7190–7195 (1999).
45. de Jong, I. G., Beilharz, K., Kuipers, O. P. & Veening, J.-W. Live Cell Imaging of *Bacillus subtilis* and *Streptococcus pneumoniae* using Automated Time-lapse Microscopy. *J. Vis. Exp.* (2011). doi:10.3791/3145
46. Seabold, S. & Perktold, J. Statsmodels: Econometric and Statistical Modeling with Python. 5 (2010).

Supplementary Information

Targeting bacterial porins: a possible alternative strategy for disrupting biofilms to combat infections from the human pathogen

Providencia stuartii

Authors:

Julie Lopes¹, Guillaume Tétreau¹, Amandine Paoli¹, Pierrick Bruyat², Mariam El Khatib¹, Ludovic Jean², Pierre-Yves Renard², Jacques-Philippe Colletier¹

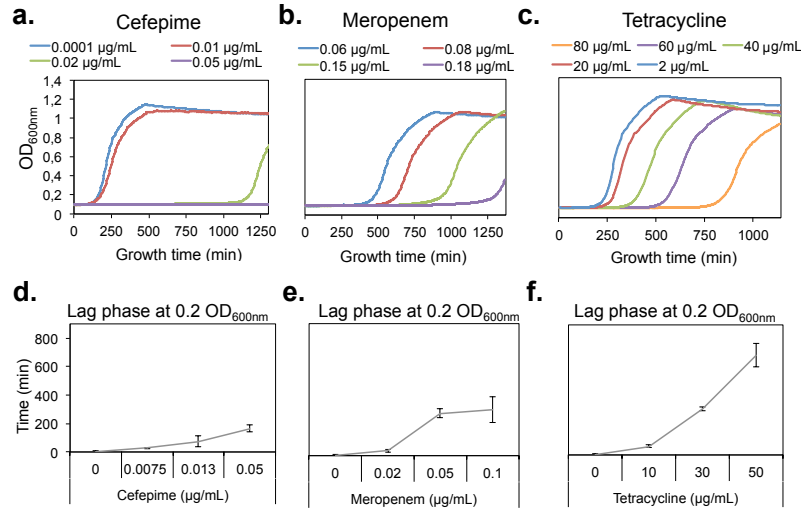
Affiliations:

¹ Univ. Grenoble Alpes – CEA – CNRS, Institut de Biologie Structurale (IBS), Grenoble, France

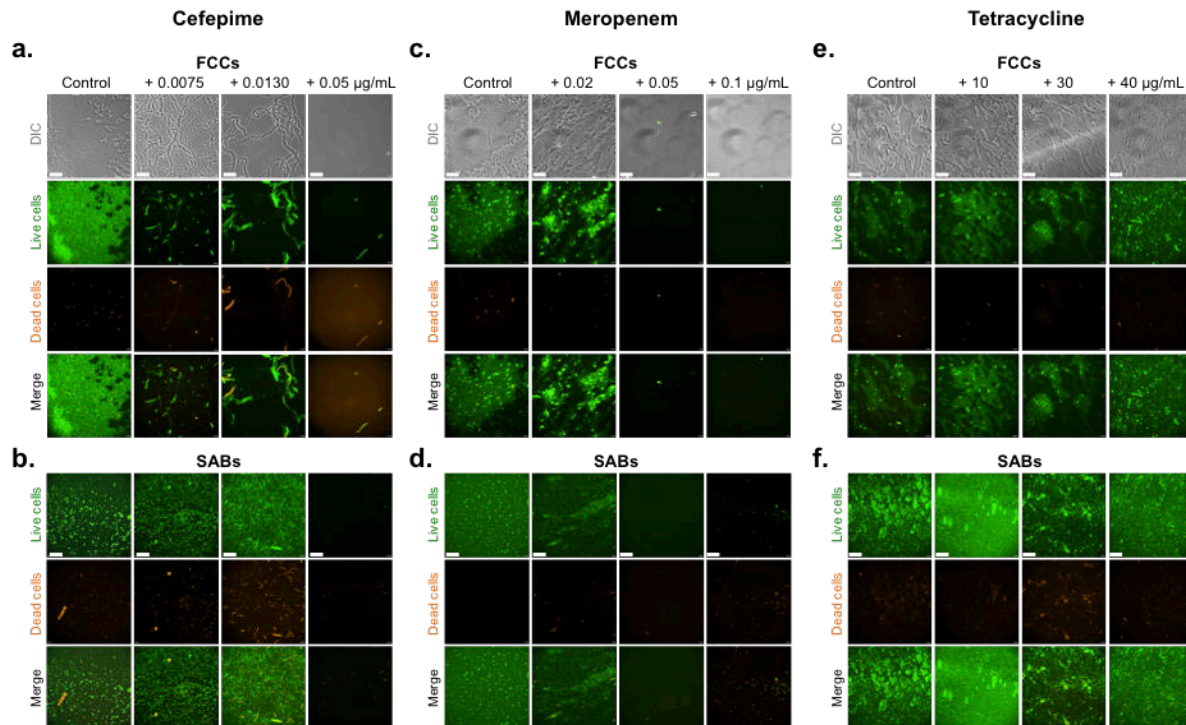
² Normandie Univ, UNIROUEN, INSA Rouen, CNRS, COBRA (UMR 6014), 76000 Rouen, France

Correspondence: JPC, jacques-philippe.colletier@ibs.fr

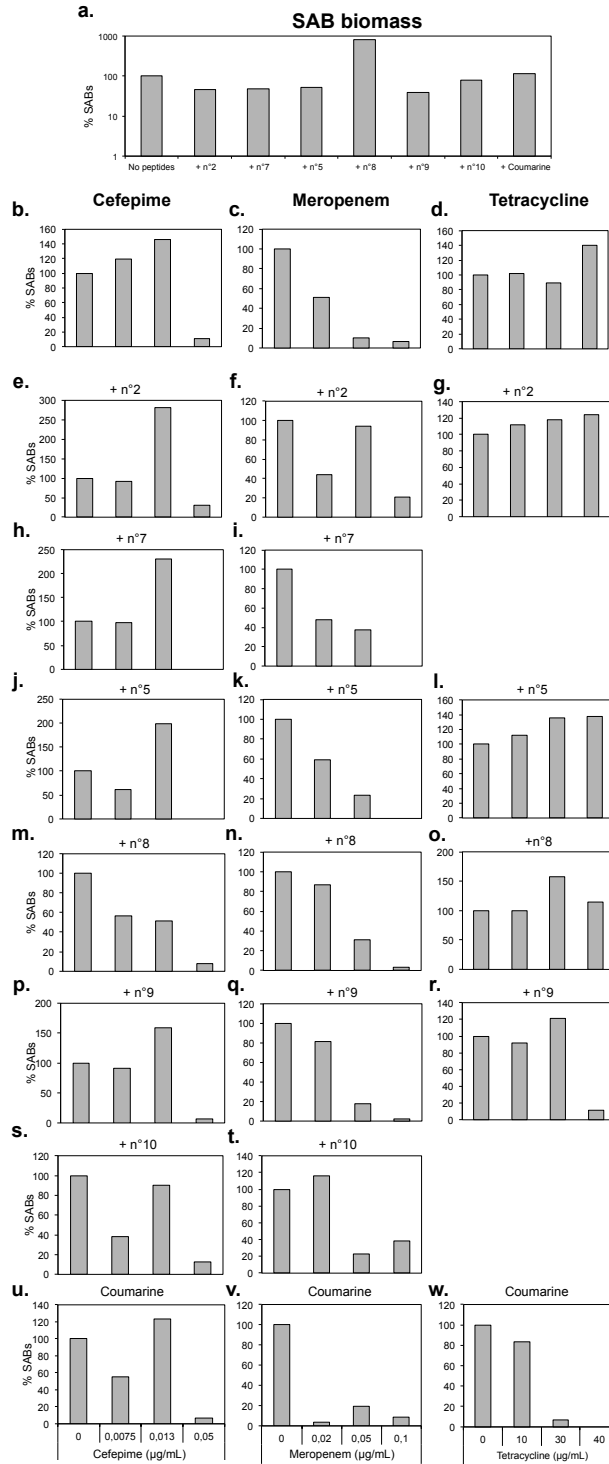
PYR, pierre-yves.renard@univ-rouen.fr



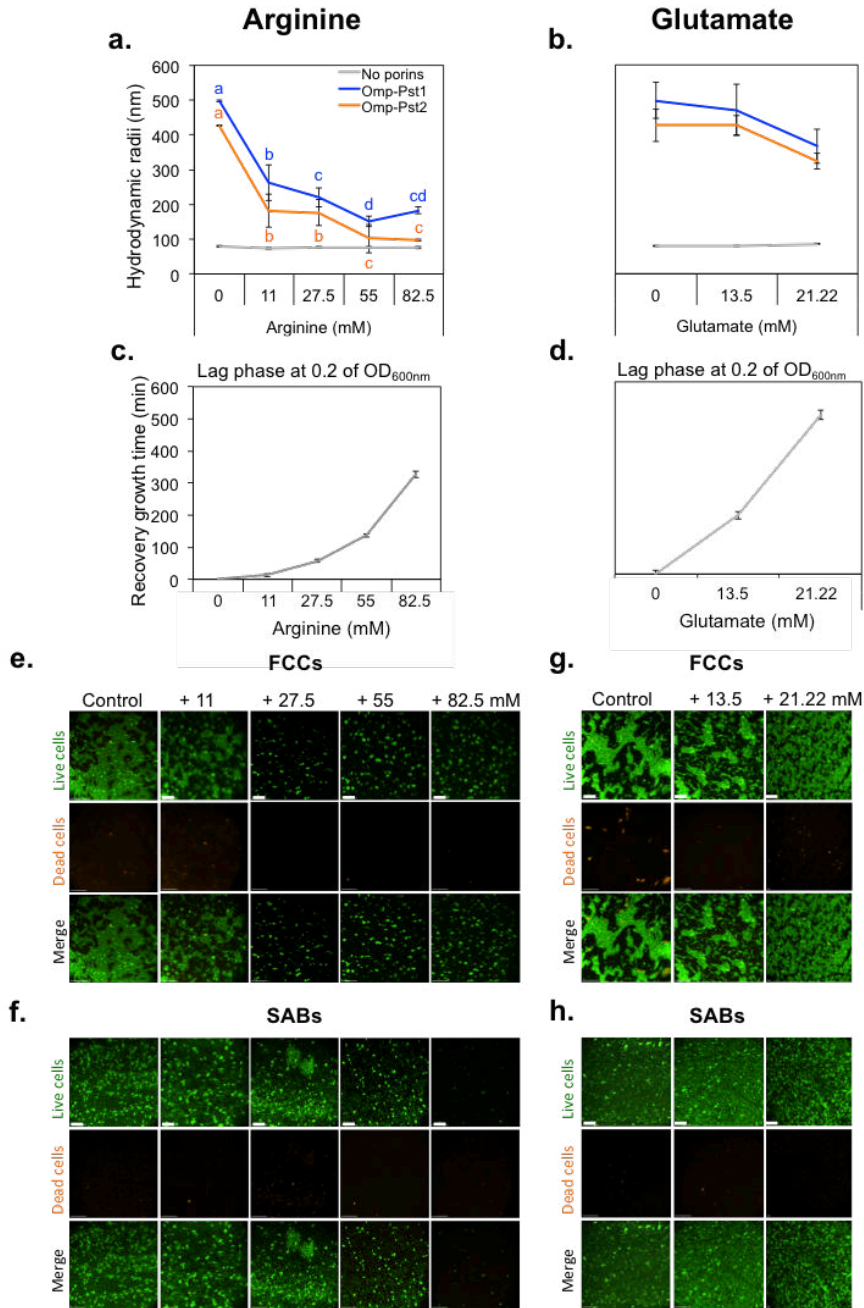
Supplementary Figure S1. *P. stuartii* is sensitive to cefepime and meropenem antibiotics, contrary to tetracycline for which it is resistant. The MIC (Minimal Inhibitory Concentration) of cefepime (a), meropenem (b) and tetracycline (c) was determined on *P. stuartii* by applying increasing concentrations of antibiotics on cells at the early stages of growth. Bacterial growth was followed in real time by OD_{600nm} measurement, and the concentration at which bacteria were unable to grow corresponding to the MIC. Impact of cefepime (d), meropenem (e) or tetracycline (f) on *P. stuartii* bacterial growth was quantified as the delay in the time required to reach an OD_{600nm} of 0.2 in cells exposed to three concentrations below of up to the MIC values, compared to unexposed ones. Each measurement was performed in triplicates and was represented as the mean ± SD.



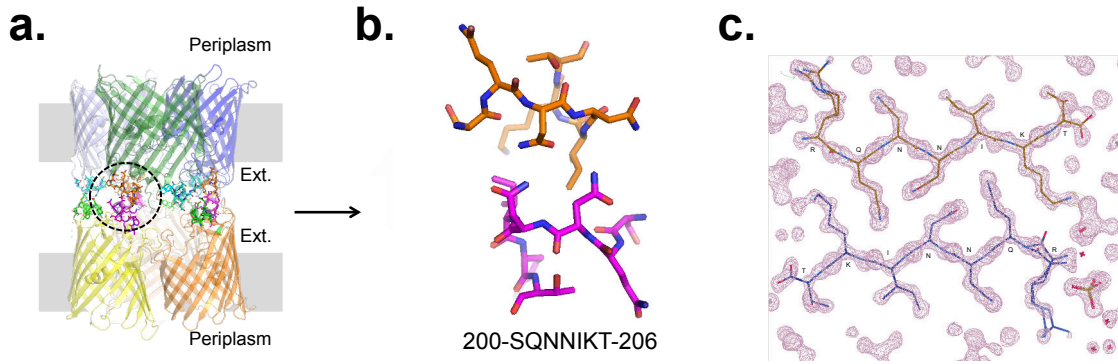
Supplementary Figure S2. Cefepime and meropenem antibiotics are efficient to kill *P. stuartii* cells, contrary to tetracycline, which promotes its capacity to socialize into FCCs and SABs. The capacity of bacteria to form FCCs and SABs in presence of increasing concentrations of cefepime (panels a and b, respectively), meropenem (c, d) and tetracycline (e, f) was visualized by epifluorescence microscopy. All bacteria were shown in green (Syto 9 green labelling, upper line in all panels) while dead cells were in red (propidium iodide labelling, middle line). A merged image was shown for each condition on the bottom line of each panel. The scale bars are 50 µm and 200 µm for FCCs and SABs, respectively.



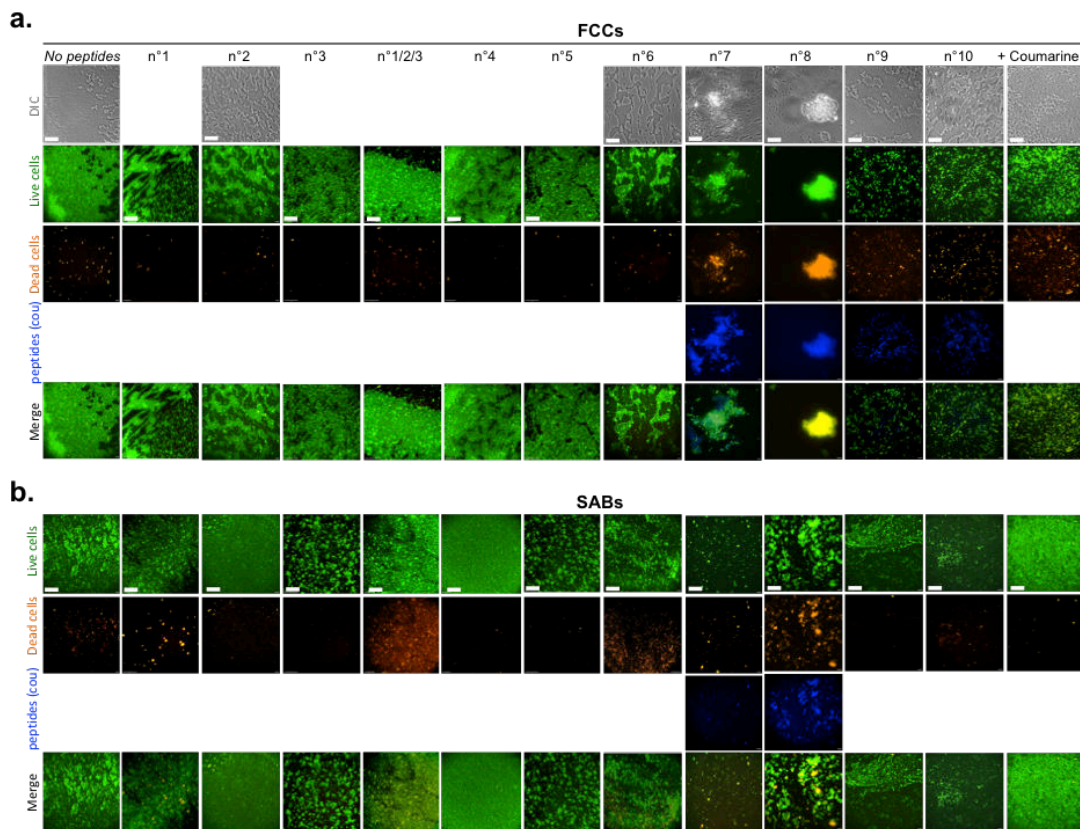
Supplementary Figure S3. The viability of SABs at the surface varies according to applied synthetic peptides and peptidomimetic molecules, combined or not with cefepime, meropenem or tetracycline. The biomass of SABs in presence of synthetic peptides (n°1, 2, 3 and 4), peptidomimetic molecules (n°5, 6, 7, 8, 9 and 10) and coumarin (panel a), or in presence of increasing concentrations of cefepime (b), meropenem (c) and tetracycline (d), was evaluated by the addition of Presto Blue, a cell viability reagent, which measure the rate of live cells within SABs. Peptides and antibiotics were then combined (panels e, h, j, m, p, s and u for cefepime; panels f, i, k, n, q, t and v for meropenem; panels g, l, o, r and w for tetracycline) and SAB biomass was determined using the same approach. The percentage of SABs was calculated according to the condition without peptides (a) or antibiotics (others panels).



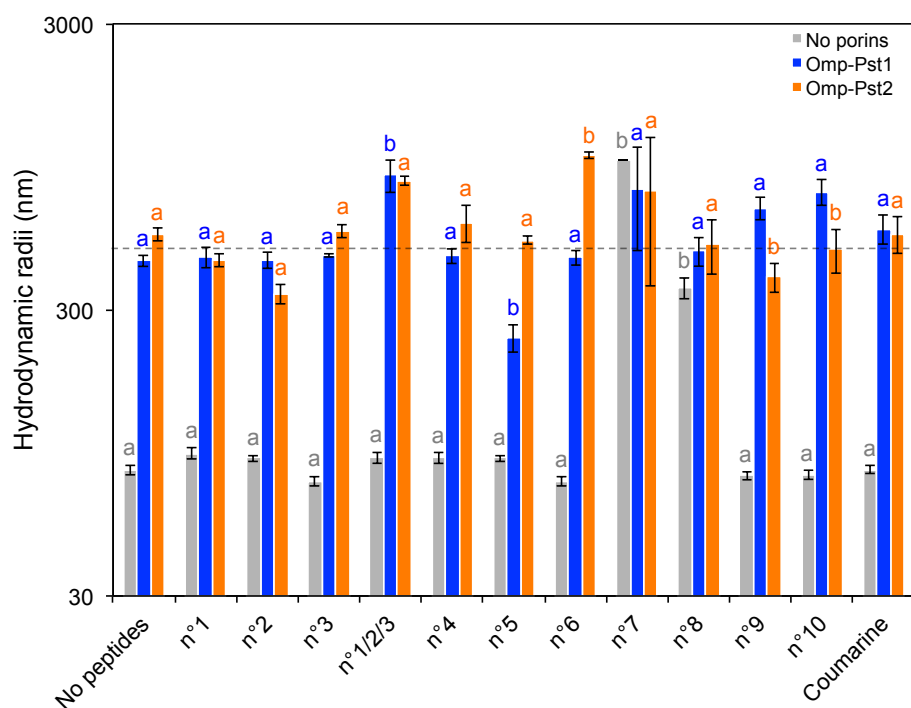
Supplementary Figure S4. Arginine and glutamate, positively and negatively charged amino acids, impact differently DOT, FCC and SAB formation of *P. stuartii*. The hydrodynamic radius of proteoliposomes was observed by DLS, 24 hours after the addition of Omp-Pst1 (blue) or Omp-Pst2 (orange) into LUV suspension, in presence of increasing concentrations of arginine (panel a) and glutamate (b) residue. As a control, the hydrodynamic radius of LUVs without porin insertion, in the same conditions, was measured (grey). Different letters above each point indicate significant differences ($p < 0.05$; ANOVA followed by post-hoc Tukey HSD test) and statistics data are available in Supplementary Table S1. Impact of charged amino acids on *P. stuartii* bacterial growth was quantified as the delay in the time required to reach an OD_{600nm} of 0.2 in cells exposed to different concentrations of arginine (panel c) and glutamate (d) compared to unexposed ones. Each measurement was performed in triplicates and was represented as the mean \pm SD. The capacity of bacteria to form FCCs and SABs in presence of arginine (panels e and f, respectively) and glutamate (g, h) was visualized by epifluorescence microscopy. All bacteria were shown in green (Syto 9 green labelling, upper line in all panels) while dead cells were in red (propidium iodide labelling, middle line). A merged image was shown for each condition on the bottom line of each panel. The scale bars are 50 μ m and 200 μ m for FCCs and SABs, respectively.



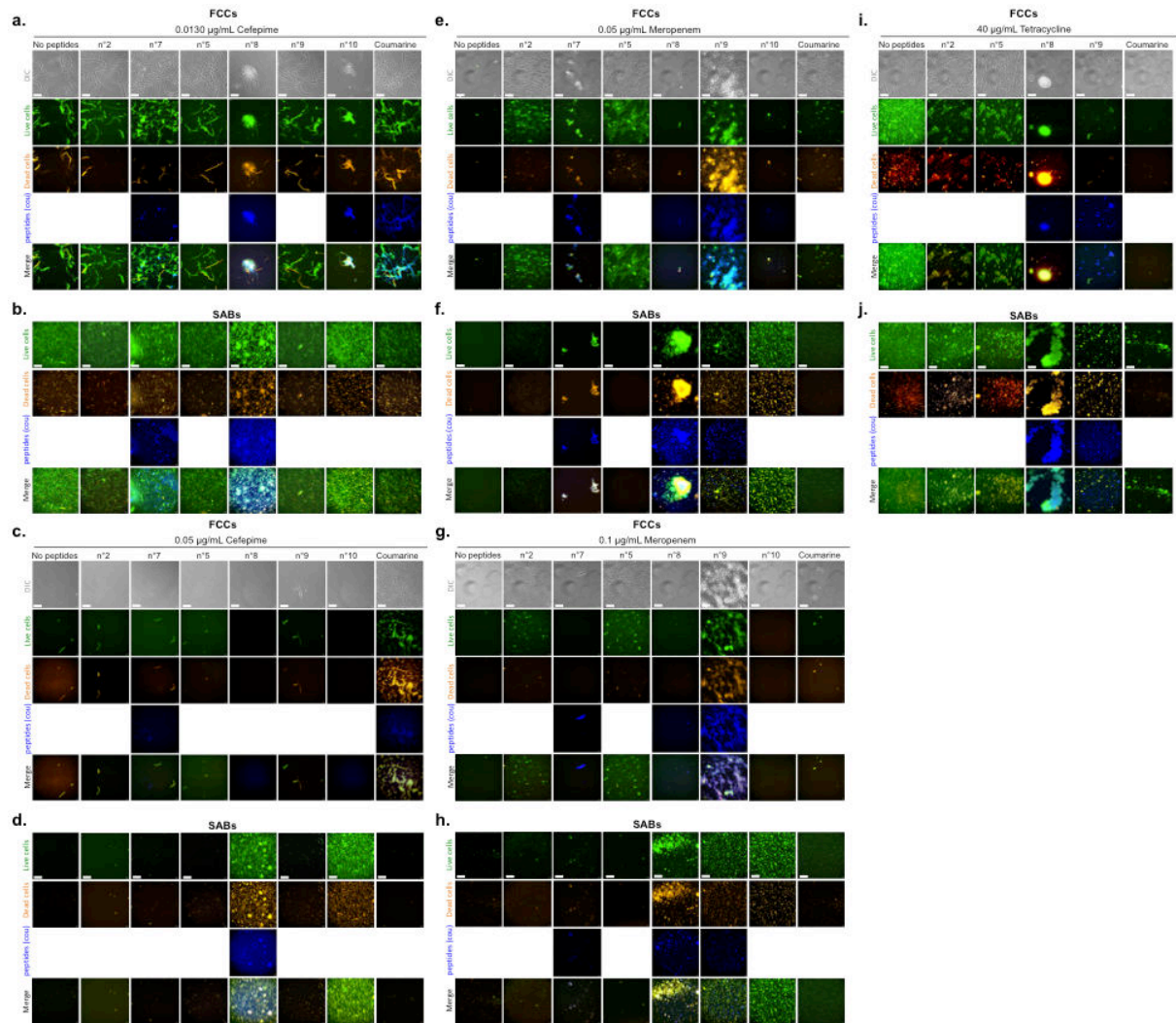
Supplementary Figure S5. Omp-Pst2 self-associates by another steric zipper-like interface. (a) Lateral view of the second DOT structure of Omp-Pst2 associating by a new steric zipper interface, contributed by facing 200-SQNNIKT-206 segments in extracellular loop L5 (magenta/orange residues circled-dashed). The presumed positions of the OM are indicated in grey. (b) Enlarged view of the symmetry-class I steric zipper interaction region, 200-SQNNIKT-206 (circled area in a), in the core of the DOT structure. (c) RQNNIKT motif, a variant of SQNNIKT segment, solved at 1.5 Å, forms a single-layered steric zipper to symmetric class I, suggesting that 200-SQNNIKT-206 is able to form steric zipper in isolation of Omp-Pst2 porin. Characteristics of Omp-Pst2 DOT structure and RQNNIKT peptide are in Supplementary Table S3



Supplementary Figure S6. FCC and SAB formation are differently affected by the presence of synthetic peptides and peptidomimetic molecules. The capacity of bacteria to form FCCs and SABs in presence of synthetic peptides (n°1, 2, 3 and 4), peptidomimetic molecules (n°5, 6, 7, 8, 9 and 10) and coumarine was visualized by epifluorescence microscopy. FCCs were observed in DIC (grey, upper line in all FCC panels), and all bacteria were shown in green (Syto 9 green labeling, second line in all panels) while dead cells were in red (propidium iodide labelling, third line). The coumarine-derived synthetic peptides were observed in blue (coumarine-fluorescence). A merged image was shown for each condition on the bottom line of each panel. The scale bars are 50 µm and 200 µm for FCCs and SABs, respectively.



Supplementary Figure S7. The capacity of *P. stuartii* porins to self-associate in DOTs is differently affected by the presence of synthetic peptides and peptidomimetic molecules. The hydrodynamic radius of proteoliposomes was observed by DLS, 24 hours after the addition of Omp-Pst1 (blue), Omp-Pst2 (orange) into LUV suspension, in presence of synthetic peptides (n°1, 2, 3 and 4), peptidomimetic molecules (n°5, 6, 7, 8, 9 and 10) and coumarine. As a control, the hydrodynamic radius of LUVs without porin insertion, in the same conditions, was measured (grey). Different letters above the bars indicate significant differences ($p < 0.05$; ANOVA followed by post-hoc Tukey HSD test) and statistics data are available in Supplementary Table S4.



Supplementary Figure S8. Effect of synthetic peptides and peptidomimetic molecules on *P. stuartii* socialization in combination with cefepime, meropenem and tetracycline. The capacity of bacteria to form FCCs and SABs in presence of increasing concentrations of cefepime (panels a and b, and c and d, respectively), meropenem (e, f and g, h) and tetracycline (i, j), in presence of synthetic peptides (n°1, 2, 3 and 4), peptidomimetic molecules (n°5, 6, 7, 8, 9 and 10) and coumarine, was visualized by epifluorescence microscopy. FCCs were observed in DIC (grey, upper line in all FCC panels), and all bacteria were shown in green (Syto 9 green labeling, second line in all panels) while dead cells were in red (propidium iodide labelling, third line). The coumarine-derived synthetic peptides were observed in blue (coumarine-fluorescence). A merged image was shown for each condition on the bottom line of each panel. The scale bars are 50 µm and 200 µm for FCCs and SABs, respectively.

GLM - Arginine condition

Omp-Pst1 porin – All statistic parameters:

```

=====
Generalized Linear Model Regression Results
=====
Dep. Variable:                Y      No. Observations:                97
Model:                        GLM    Df Residuals:                    93
Model Family:                  Gamma  Df Model:                        3
Link Function:                  inverse_power  Scale:                          0.025358
Method:                        IRLS   Log-Likelihood:                  -430.32
Date:                          Sat, 20 Apr 2019  Deviance:                        2.2338
Time:                          16:24:22   Pearson chi2:                    2.36
No. Iterations:                7     Covariance Type:                nonrobust
=====

```

	coef	std err	z	P> z	[0.025	0.975]
Intercept	0.0130	0.000	28.774	0.000	0.012	0.014
Arginine	1.953e-06	9.79e-06	0.200	0.842	-1.72e-05	2.11e-05
Concentration	-0.0106	0.000	-22.891	0.000	-0.011	-0.010
Arginine:Concentration	5.845e-05	1.06e-05	5.526	0.000	3.77e-05	7.92e-05

Omp-Pst1 porin – Statistic parameters: Arginine

```

=====
Generalized Linear Model Regression Results
=====
Dep. Variable:                Y      No. Observations:                97
Model:                        GLM    Df Residuals:                    95
Model Family:                  Gamma  Df Model:                        1
Link Function:                  inverse_power  Scale:                          0.34223
Method:                        IRLS   Log-Likelihood:                  -567.39
Date:                          Sat, 20 Apr 2019  Deviance:                        35.829
Time:                          16:24:52   Pearson chi2:                    32.5
No. Iterations:                7     Covariance Type:                nonrobust
=====

```

	coef	std err	z	P> z	[0.025	0.975]
Intercept	0.0041	0.000	9.615	0.000	0.003	0.005
Arginine	7.139e-05	1.46e-05	4.886	0.000	4.28e-05	0.000

Omp-Pst2 porin – All statistic parameters:

```

=====
Generalized Linear Model Regression Results
=====
Dep. Variable:                Y      No. Observations:                50
Model:                        GLM    Df Residuals:                    48
Model Family:                  Gamma  Df Model:                        1
Link Function:                  inverse_power  Scale:                          0.055827
Method:                        IRLS   Log-Likelihood:                  -256.90
Date:                          Sat, 20 Apr 2019  Deviance:                        3.0385
Time:                          16:29:07   Pearson chi2:                    2.44
No. Iterations:                100   Covariance Type:                nonrobust
=====

```

	coef	std err	z	P> z	[0.025	0.975]
Intercept	0.0014	8.82e-05	15.500	0.000	0.001	0.002
Arginine	5.628e-05	4.08e-06	13.799	0.000	4.83e-05	6.43e-05
Concentration	0.0014	8.82e-05	15.500	0.000	0.001	0.002
Arginine:Concentration	5.628e-05	4.08e-06	13.799	0.000	4.83e-05	6.43e-05

Omp-Pst2 porin – Statistic parameters: Arginine

```

=====
Generalized Linear Model Regression Results
=====
Dep. Variable:                Y      No. Observations:                50
Model:                        GLM    Df Residuals:                    48
Model Family:                  Gamma  Df Model:                        1
Link Function:                  inverse_power  Scale:                          0.050820
Method:                        IRLS   Log-Likelihood:                  -257.21
Date:                          Sat, 20 Apr 2019  Deviance:                        3.0385
Time:                          16:28:39   Pearson chi2:                    2.44
No. Iterations:                7     Covariance Type:                nonrobust
=====

```

	coef	std err	z	P> z	[0.025	0.975]
Intercept	0.0027	0.000	16.246	0.000	0.002	0.003
Arginine	0.0001	7.78e-06	14.462	0.000	9.73e-05	0.000

2-2 comparison (Tukey) – Arginine condition

Omp-Pst1 porin

Multiple Comparison of Means - Tukey HSD,FWER=0.05

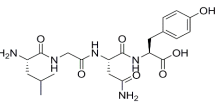
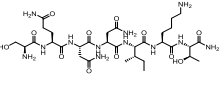
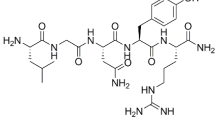
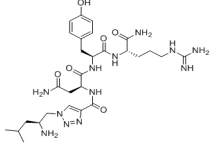
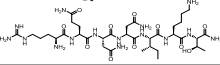
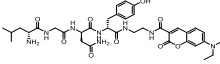
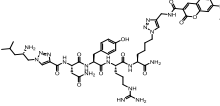
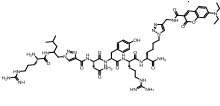
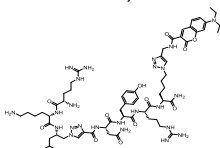
group1	group2	meandiff	lower	upper	reject
0.0	11.0	-236.078	-274.4106	-197.7454	True
0.0	27.5	-277.13	-315.4626	-238.7974	True
0.0	55.0	-347.0	-385.3326	-308.6674	True
0.0	82.5	-314.98	-357.2205	-272.7395	True
11.0	27.5	-41.052	-79.3846	-2.7194	True
11.0	55.0	-110.922	-149.2546	-72.5894	True
11.0	82.5	-78.902	-121.1425	-36.6615	True
27.5	55.0	-69.87	-108.2026	-31.5374	True
27.5	82.5	-37.85	-80.0905	4.3905	False
55.0	82.5	32.02	-10.2205	74.2605	False

Omp-Pst2 porin

Multiple Comparison of Means - Tukey HSD,FWER=0.05

group1	group2	meandiff	lower	upper	reject
0.0	11.0	-245.19	-289.1919	-201.1881	True
0.0	27.5	-249.84	-293.8419	-205.8381	True
0.0	55.0	-324.95	-368.9519	-280.9481	True
0.0	82.5	-329.01	-373.0119	-285.0081	True
11.0	27.5	-4.65	-48.6519	39.3519	False
11.0	55.0	-79.76	-123.7619	-35.7581	True
11.0	82.5	-83.82	-127.8219	-39.8181	True
27.5	55.0	-75.11	-119.1119	-31.1081	True
27.5	82.5	-79.17	-123.1719	-35.1681	True
55.0	82.5	-4.06	-48.0619	39.9419	False

Supplementary Table S1 – Statistics analysis from DLS experiments in arginine condition. All experiments were conducted for at least three biologically independent replicates. Technical replicates were averaged to produce replicate means that were subsequently used for analysis. Mean values were compared within and between groups using one-way ANOVA followed by Tukey’s post hoc for two-two comparisons. Differences were considered statistically significant (True) if $p < 0.05$.

N° Peptide	Molecule	Formula	Molar mass (g/mol)	Solubility	Aspect
1	AGVVTSE	$C_{27}H_{47}N_7O_{12}$	661,7	Water, DMSO	White solid
2	LGNY 	$C_{21}H_{31}N_5O_7$	465,51	Water, MeOH, DMSO	White solid
3	SQNNIKT 	$C_{32}H_{58}N_{12}O_{12}$	802,89	Water, DMSO	White solid
4	LGNYR 	$C_{27}H_{44}N_{10}O_7$	620,71	Water, MeOH, DMSO	White solid
5	L-tr-NYR 	$C_{28}H_{44}N_{12}O_6$	644,74	Water, MeOH, DMSO	White solid
6	RQNNIKT 	$C_{35}H_{65}N_{15}O_{11}$	872	Water, DMSO	White solid
7	LGNY-cou 	$C_{32}H_{50}N_8O_9$	750,85	DMSO	Yellow solid
8	L-tr-NYRK(tr-cou) 	$C_{51}H_{72}N_{18}O_{10}$	1097,25	DMSO	Yellow solid
9	RL-tr-NYRK(tr-cou) 	$C_{57}H_{84}N_{22}O_{11}$	1253,44	Water, DMSO	Yellow solid
10	RKL-tr-NYRK(tr-cou) 	$C_{63}H_{96}N_{24}O_{12}$	1381,62	Water, DMSO	Yellow solid

Supplementary Table 2. Synthetic peptides (n°1, 2, 3 and 4) and peptidomimetic molecules tested and their characteristics

	Omp-Pst2	RQNNIKT
Wavelength (Å...)		
Resolution range (Å...)	40.45 - 3.2 (3.107 - 3.0)	26.05 - 1.3 (1.347 - 1.3)
Space group	R 3 2 :H	P 1
Unit cell	150.92 150.92 206.05 90 90 120	4.89 20.02 26.06 91.48 89.97 90
Total reflections		
Unique reflections	17925 (1781)	1566 (139à)
Multiplicity		
Completeness (%)	97.91 (99.33)	64.50 (62.61)
Mean I/sigma(I)		
Wilson B-factor	109.23	6.52
R-merge		
R-meas		
CC1/2		
CC*		
Reflections used for R-free		
R-work	0.2860 (0.5296)	0.1904 (0.2624)
R-free	0.3227 (0.4999)	0.2097 (0.3380)
CC(work)		
CC(free)		
Number of non-hydrogen atoms	5270	153
macromolecules	5270	133
ligands		15
water	0	5
Protein residues	669	14
RMS(bonds)	0.001	0.11
RMS(angles)	0.41	2.36
Ramachandran favored (%)	92	1e+02
Ramachandran allowed (%)		
Ramachandran outliers (%)	0	0
Clashscore	3.83	3.38
Average B-factor	100.10	8.90
macromolecules	100.10	7.60
ligands		18.5
solvent		16.4
Supplementary Table S3. Data collection and refinement of the new Omp-Pst2 DOT and the peptide RQNNIKT		

DLS – Peptides – Statistics

GLM – n°1 & 2 peptides

All statistic parameters:

Generalized Linear Model Regression Results

```

=====
Dep. Variable:          Y      No. Observations:          51
Model:                 GLM      Df Residuals:              45
Model Family:         Gamma      Df Model:                  5
Link Function:        inverse_power      Scale:                    0.019136
Method:               IRLS      Log-Likelihood:           -262.18
Date:                 Mon, 20 May 2019      Deviance:                 0.83987
Time:                 11:09:06      Pearson chi2:             0.861
No. Iterations:       8      Covariance Type:         nonrobust
=====

```

	coef	std err	z	P> z	[0.025	0.975]
Intercept	0.0121	0.001	22.860	0.000	0.011	0.013
C(Porins) [T.P2]	-0.0001	6.16e-05	-1.757	0.079	-0.000	1.25e-05
C(Cporins) [T.1]	-0.0103	0.001	-19.139	0.000	-0.011	-0.009
C(LGNY_AGVVTSE) [T.1]	-0.0017	0.001	-2.434	0.015	-0.003	-0.000
C(Porins) [T.P2]:C(Cporins) [T.1]	-0.0001	6.16e-05	-1.757	0.079	-0.000	1.25e-05
C(Porins) [T.P2]:C(LGNY_AGVVTSE) [T.1]	8.286e-05	7.22e-05	1.148	0.251	-5.86e-05	0.000
C(Cporins) [T.1]:C(LGNY_AGVVTSE) [T.1]	0.0009	0.001	1.240	0.215	-0.001	0.002
C(Porins) [T.P2]:C(Cporins) [T.1]:C(LGNY_AGVVTSE) [T.1]	8.286e-05	7.22e-05	1.148	0.251	-5.86e-05	0.000

Statistic parameters: Omp-Pst1 porin

Generalized Linear Model Regression Results

```

=====
Dep. Variable:          Y      No. Observations:          40
Model:                 GLM      Df Residuals:              36
Model Family:         Gamma      Df Model:                  3
Link Function:        inverse_power      Scale:                    0.012213
Method:               IRLS      Log-Likelihood:           -187.89
Date:                 Mon, 20 May 2019      Deviance:                 0.43865
Time:                 11:10:35      Pearson chi2:             0.440
No. Iterations:       8      Covariance Type:         nonrobust
=====

```

	coef	std err	z	P> z	[0.025	0.975]
Intercept	0.0121	0.000	28.614	0.000	0.011	0.013
C(Cporins) [T.1]	-0.0103	0.000	-23.957	0.000	-0.011	-0.009
C(LGNY_AGVVTSE) [T.1]	-0.0017	0.001	-3.047	0.002	-0.003	-0.001
C(Cporins) [T.1]:C(LGNY_AGVVTSE) [T.1]	0.0009	0.001	1.552	0.121	-0.000	0.002

Statistic parameters: Omp-Pst2 porin

Generalized Linear Model Regression Results

```

=====
Dep. Variable:          Y      No. Observations:          11
Model:                 GLM      Df Residuals:              9
Model Family:         Gamma      Df Model:                  1
Link Function:        inverse_power      Scale:                    0.046826
Method:               IRLS      Log-Likelihood:           -70.532
Date:                 Mon, 20 May 2019      Deviance:                 0.40123
Time:                 11:11:14      Pearson chi2:             0.421
No. Iterations:       6      Covariance Type:         nonrobust
=====

```

	coef	std err	z	P> z	[0.025	0.975]
Intercept	0.0016	0.000	11.320	0.000	0.001	0.002
C(LGNY_AGVVTSE) [T.1]	-0.0007	0.000	-3.830	0.000	-0.001	-0.000

2-2 comparison (Tukey) – n°1 & 2 peptides

Omp-Pst1 porin

Multiple Comparison of Means - Tukey HSD, FWER=0.05

```

=====
group1 group2 meandiff lower upper reject
=====
0 1 434.23 318.4729 549.9871 True
=====

```


Omp-Pst2 porin

Multiple Comparison of Means - Tukey HSD,FWER=0.05

```

=====
group1 group2 meandiff lower upper reject
-----
  0      1    413.5733 141.6825 685.4641 True
=====

```

GLM – n°3 peptide

Omp-Pst1 porin – All statistic parameters:

Generalized Linear Model Regression Results

```

=====
Dep. Variable:          Y      No. Observations:          60
Model:                  GLM      Df Residuals:                56
Model Family:           Gamma    Df Model:                    3
Link Function:          inverse_power  Scale:                      0.022102
Method:                  IRLS     Log-Likelihood:             -317.41
Date:                   Sat, 20 Apr 2019  Deviance:                   1.1738
Time:                   11:51:18    Pearson chi2:                1.24
No. Iterations:         9      Covariance Type:            nonrobust
=====

```

	coef	std err	z	P> z	[0.025	0.975]
Intercept	0.0138	0.001	21.271	0.000	0.013	0.015
SQNNIKT	-0.0001	0.000	-0.620	0.536	-0.000	0.000
Concentration	-0.0114	0.001	-17.554	0.000	-0.013	-0.010
SQNNIKT:Concentration	-0.0003	0.000	-1.434	0.152	-0.001	9.49e-05

Omp-Pst1 porin – All statistic parameters: SQNNIKT

Generalized Linear Model Regression Results

```

=====
Dep. Variable:          Y      No. Observations:          60
Model:                  GLM      Df Residuals:                58
Model Family:           Gamma    Df Model:                    1
Link Function:          inverse_power  Scale:                      0.47999
Method:                  IRLS     Log-Likelihood:             -445.98
Date:                   Sat, 20 Apr 2019  Deviance:                   58.081
Time:                   11:52:26    Pearson chi2:                27.8
No. Iterations:         8      Covariance Type:            nonrobust
=====

```

	coef	std err	z	P> z	[0.025	0.975]
Intercept	0.0029	0.000	8.437	0.000	0.002	0.004
SQNNIKT	-0.0004	7.74e-05	-5.257	0.000	-0.001	-0.000

Omp-Pst2 porin – All statistic parameters:

Generalized Linear Model Regression Results

```

=====
Dep. Variable:          Y      No. Observations:          36
Model:                  GLM      Df Residuals:                34
Model Family:           Gamma    Df Model:                    1
Link Function:          inverse_power  Scale:                      0.067622
Method:                  IRLS     Log-Likelihood:             -260.37
Date:                   Sat, 20 Apr 2019  Deviance:                   2.1930
Time:                   11:58:02    Pearson chi2:                2.30
No. Iterations:         7      Covariance Type:            nonrobust
=====

```

	coef	std err	z	P> z	[0.025	0.975]
Intercept	0.0005	2.75e-05	18.635	0.000	0.000	0.001
SQNNIKT	-7.057e-05	6.95e-06	-10.158	0.000	-8.42e-05	-5.7e-05
Concentration	0.0005	2.75e-05	18.635	0.000	0.000	0.001
SQNNIKT:Concentration	-7.057e-05	6.95e-06	-10.158	0.000	-8.42e-05	-5.7e-05

Omp-Pst2 porin – All statistic parameters: SQNNIKT

Generalized Linear Model Regression Results

```

Dep. Variable:          Y      No. Observations:          36
Model:                  GLM      Df Residuals:              34
Model Family:           Gamma   Df Model:                  1
Link Function:          inverse_power  Scale:                    0.067622
Method:                 IRLS    Log-Likelihood:           -260.37
Date:                   Sat, 20 Apr 2019  Deviance:                 2.1930
Time:                   11:58:33   Pearson chi2:             2.30
No. Iterations:         7      Covariance Type:         nonrobust

```

```

=====
              coef      std err          z      P>|z|      [0.025      0.975]
-----+-----+-----+-----+-----+-----
Intercept    0.0010      5.5e-05     18.635     0.000     0.001     0.001
SQNNIKT     -0.0001      1.39e-05    -10.158     0.000    -0.000    -0.000
=====

```

2-2 comparison (Tukey) – SQNNIKT peptide

Omp-Pst1 porin

Multiple Comparison of Means - Tukey HSD,FWER=0.05

```

=====
group1 group2 meandiff  lower  upper  reject
-----+-----+-----+-----+-----
0.0    1.0    16.16   -355.8009  388.1209  False
0.0    2.5    277.18   -94.7809  649.1409  False
0.0    5.0    1565.42  1193.4591 1937.3809  True
1.0    2.5    261.02  -110.9409  632.9809  False
1.0    5.0    1549.26  1177.2991 1921.2209  True
2.5    5.0    1288.24   916.2791 1660.2009  True

```

Omp-Pst2 porin

Multiple Comparison of Means - Tukey HSD,FWER=0.05

```

=====
group1 group2 meandiff  lower  upper  reject
-----+-----+-----+-----+-----
0.0    1.0    202.43  -421.1162  825.9762  False
0.0    2.5    212.62  -410.9262  836.1662  False
0.0    5.0    2278.0733 1558.0642 2998.0825  True
1.0    2.5    10.19   -613.3562  633.7362  False
1.0    5.0    2075.6433 1355.6342 2795.6525  True
2.5    5.0    2065.4533 1345.4442 2785.4625  True

```

GLM – n°1 & 2 & 3 peptides

All statistic parameters:

Generalized Linear Model Regression Results

```

=====
Dep. Variable:          Y      No. Observations:          49
Model:                  GLM      Df Residuals:              43
Model Family:           Gamma   Df Model:                  5
Link Function:          inverse_power  Scale:                    0.021419
Method:                 IRLS    Log-Likelihood:           -247.61
Date:                   Mon, 20 May 2019  Deviance:                 0.89565
Time:                   10:27:01   Pearson chi2:             0.921
No. Iterations:         8      Covariance Type:         nonrobust

```

```

=====
              coef      std err          z      P>|z|      [0.025      0.975]
-----+-----+-----+-----+-----
Intercept    0.0121      0.001     21.607     0.000     0.011     0.013
C(Porins) [T.P2]  0.0001      8.1e-05     1.394     0.163    -4.59e-05     0.000
C(Cporins) [T.1] -0.0101      0.001    -17.785     0.000    -0.011    -0.009
C(L_A_S_D) [T.1] -0.0011      0.001    -1.471     0.141    -0.003     0.000
C(Porins) [T.P2]:C(Cporins) [T.1]  0.0001      8.1e-05     1.394     0.163    -4.59e-05     0.000
C(Porins) [T.P2]:C(L/A/S) [T.1] -0.0001     9.77e-05    -1.088     0.277    -0.000     8.52e-05
C(Cporins) [T.1]:C(L/A/S) [T.1]  0.0002      0.001     0.313     0.754    -0.001     0.002
C(Porins) [T.P2]:C(Cporins) [T.1]:C(L/A/S) [T.1] -0.0001     9.77e-05    -1.088     0.277    -0.000     8.52e-05
=====

```

Statistic parameters: Omp-Pst1 porin

Generalized Linear Model Regression Results

```

Dep. Variable:          Y      No. Observations:          33
Model:                  GLM      Df Residuals:              29
Model Family:           Gamma   Df Model:                  3
Link Function:          inverse_power  Scale:                    0.0095464
Method:                 IRLS    Log-Likelihood:           -140.11
Date:                   Mon, 20 May 2019  Deviance:                  0.28337
Time:                   10:27:26  Pearson chi2:              0.277
No. Iterations:         8      Covariance Type:          nonrobust
=====
                    coef      std err          z      P>|z|      [0.025      0.975]
-----+-----
Intercept              0.0121      0.000      32.365      0.000      0.011      0.013
C(Cporins) [T.1]       -0.0101      0.000     -26.641      0.000     -0.011     -0.009
C(L_A_S_D) [T.1]       -0.0011      0.001     -2.204      0.028     -0.002     -0.000
C(Cporins) [T.1]:C(A/L/S) [T.1]  0.0002      0.001      0.468      0.639     -0.001      0.001
=====

```

Statistic parameters: Omp-Pst2 porin

Generalized Linear Model Regression Results

```

=====
Dep. Variable:          Y      No. Observations:          16
Model:                  GLM      Df Residuals:              14
Model Family:           Gamma   Df Model:                  1
Link Function:          inverse_power  Scale:                    0.046013
Method:                 IRLS    Log-Likelihood:           -100.87
Date:                   Mon, 20 May 2019  Deviance:                  0.61229
Time:                   10:28:13  Pearson chi2:              0.644
No. Iterations:         6      Covariance Type:          nonrobust
=====
                    coef      std err          z      P>|z|      [0.025      0.975]
-----+-----
Intercept              0.0022      0.000     11.419      0.000      0.002      0.003
C(A/L/S) [T.1]         -0.0011      0.000     -5.164      0.000     -0.001     -0.001
=====

```

2-2 comparison (Tukey) – n°1 & 2 & 3 peptides

Omp-Pst1 porin

Multiple Comparison of Means - Tukey HSD, FWER=0.05

```

=====
group1 group2 meandiff lower upper reject
-----
0      1      385.5567 262.1757 508.9377 True
=====

```

Omp-Pst2 porin

Multiple Comparison of Means - Tukey HSD, FWER=0.05

```

=====
group1 group2 meandiff lower upper reject
-----
0      1      425.9567 259.8935 592.0198 True
=====

```

GLM – n°4 peptide

All statistic parameters:

Generalized Linear Model Regression Results

```

=====
Dep. Variable:          Y      No. Observations:          98
Model:                  GLM      Df Residuals:              88
Model Family:           Gamma   Df Model:                  9
Link Function:          inverse_power  Scale:                    0.014883
Method:                 IRLS    Log-Likelihood:           -511.78
Date:                   Mon, 20 May 2019  Deviance:                  1.2579
Time:                   11:16:33  Pearson chi2:              1.31
No. Iterations:         8      Covariance Type:          nonrobust
=====
                    coef      std err          z      P>|z|      [0.025      0.975]
-----+-----
Intercept              0.0110      0.000     25.921      0.000      0.010      0.012
C(Porins) [T.P2]       -0.0010      6.58e-05  -14.844      0.000     -0.001     -0.001
C(Cporins) [T.1]       -0.0078      0.000     -17.684      0.000     -0.009     -0.007
C(LGNYR) [T.1.0]       -1.022e-17  0.001     -1.71e-14  1.000     -0.001      0.001
C(LGNYR) [T.2.5]       -0.0001      8.29e-05  -1.762      0.078     -0.000      1.64e-05
C(LGNYR) [T.5.0]       -0.0008      7.03e-05  -11.311      0.000     -0.001     -0.001
C(Porins) [T.P2]:C(Cporins) [T.1] -0.0010      6.58e-05  -14.844      0.000     -0.001     -0.001
C(Porins) [T.P2]:C(LGNYR) [T.1.0] -0.0001      9.4e-05  -1.206      0.228     -0.000      7.09e-05
=====

```

C(Porins) [T. P2] :C(LGNYR) [T. 2. 5]	6. 77e-05	8. 87e-05	0. 763	0. 445	-0. 000	0. 000
C(Porins) [T. P2] :C(LGNYR) [T. 5. 0]	0. 0007	7. 73e-05	9. 632	0. 000	0. 001	0. 001
C(Cporins) [T. 1] :C(LGNYR) [T. 1. 0]	0. 0001	0. 001	0. 184	0. 854	-0. 001	0. 001
C(Cporins) [T. 1] :C(LGNYR) [T. 2. 5]	-0. 0001	8. 29e-05	-1. 762	0. 078	-0. 000	1. 64e-05
C(Cporins) [T. 1] :C(LGNYR) [T. 5. 0]	-0. 0008	7. 03e-05	-11. 311	0. 000	-0. 001	-0. 001
C(Porins) [T. P2] :C(Cporins) [T. 1] :C(LGNYR) [T. 1. 0]	-0. 0001	9. 4e-05	-1. 206	0. 228	-0. 000	7. 09e-05
C(Porins) [T. P2] :C(Cporins) [T. 1] :C(LGNYR) [T. 2. 5]	6. 77e-05	8. 87e-05	0. 763	0. 445	-0. 000	0. 000
C(Porins) [T. P2] :C(Cporins) [T. 1] :C(LGNYR) [T. 5. 0]	0. 0007	7. 73e-05	9. 632	0. 000	0. 001	0. 001

Statistic parameters: Omp-Pst1 porin

Generalized Linear Model Regression Results

Dep. Variable:	Y	No. Observations:	58
Model:	GLM	Df Residuals:	52
Model Family:	Gamma	Df Model:	5
Link Function:	inverse_power	Scale:	0. 012142
Method:	IRLS	Log-Likelihood:	-264. 33
Date:	Mon, 20 May 2019	Deviance:	0. 59000
Time:	11:19:06	Pearson chi2:	0. 631
No. Iterations:	7	Covariance Type:	nonrobust

	coef	std err	z	P> z	[0. 025	0. 975]
Intercept	0. 0110	0. 000	28. 698	0. 000	0. 010	0. 012
C(Cporins) [T. 1]	-0. 0078	0. 000	-19. 578	0. 000	-0. 009	-0. 007
C(LGNYR) [T. 1. 0]	6. 073e-18	0. 001	1. 12e-14	1. 000	-0. 001	0. 001
C(LGNYR) [T. 2. 5]	-0. 0001	7. 49e-05	-1. 951	0. 051	-0. 000	7. 02e-07
C(LGNYR) [T. 5. 0]	-0. 0008	6. 35e-05	-12. 523	0. 000	-0. 001	-0. 001
C(Cporins) [T. 1] :C(LGNYR) [T. 1. 0]	0. 0001	0. 001	0. 203	0. 839	-0. 001	0. 001
C(Cporins) [T. 1] :C(LGNYR) [T. 2. 5]	-0. 0001	7. 49e-05	-1. 951	0. 051	-0. 000	7. 02e-07
C(Cporins) [T. 1] :C(LGNYR) [T. 5. 0]	-0. 0008	6. 35e-05	-12. 523	0. 000	-0. 001	-0. 001

Statistic parameters: Omp-Pst2 porin

Generalized Linear Model Regression Results

Dep. Variable:	Y	No. Observations:	40
Model:	GLM	Df Residuals:	36
Model Family:	Gamma	Df Model:	3
Link Function:	inverse_power	Scale:	0. 018842
Method:	IRLS	Log-Likelihood:	-246. 03
Date:	Mon, 20 May 2019	Deviance:	0. 66789
Time:	11:19:50	Pearson chi2:	0. 678
No. Iterations:	6	Covariance Type:	nonrobust

	coef	std err	z	P> z	[0. 025	0. 975]
Intercept	0. 0012	5. 33e-05	23. 037	0. 000	0. 001	0. 001
C(LGNYR) [T. 1. 0]	-0. 0001	7. 21e-05	-1. 555	0. 120	-0. 000	2. 92e-05
C(LGNYR) [T. 2. 5]	-0. 0002	7. 08e-05	-2. 215	0. 027	-0. 000	-1. 8e-05
C(LGNYR) [T. 5. 0]	-0. 0001	7. 24e-05	-1. 397	0. 162	-0. 000	4. 08e-05

2-2 comparison (Tukey) – n°4 peptide

Omp-Pst1 porin

Multiple Comparison of Means - Tukey HSD, FWER=0.05

group1	group2	meandiff	lower	upper	reject
0. 0	1. 0	-10. 93	-72. 8589	50. 9989	False
0. 0	2. 5	31. 77	-30. 1589	93. 6989	False
0. 0	5. 0	314. 1625	248. 477	379. 848	True
1. 0	2. 5	42. 7	-19. 2289	104. 6289	False
1. 0	5. 0	325. 0925	259. 407	390. 778	True
2. 5	5. 0	282. 3925	216. 707	348. 078	True

GLM – n°6 peptide

Omp-Pst1 porin – All statistic parameters:

Generalized Linear Model Regression Results

```

=====
Dep. Variable:          Y      No. Observations:      70
Model:                 GLM    Df Residuals:          66
Model Family:         Gamma  Df Model:              3
Link Function:        inverse_power  Scale:                 0.14020
Method:              IRLS    Log-Likelihood:       -422.92
Date:                Sat, 20 Apr 2019  Deviance:             8.8133
Time:                16:12:06  Pearson chi2:         9.25
No. Iterations:      9      Covariance Type:      nonrobust
=====

```

	coef	std err	z	P> z	[0.025	0.975]
Intercept	0.0138	0.001	10.775	0.000	0.011	0.016
RQNNIKT	-0.0001	0.000	-0.281	0.779	-0.001	0.001
Concentration	-0.0123	0.001	-9.520	0.000	-0.015	-0.010
RQNNIKT:Concentration	-4.75e-05	0.000	-0.111	0.911	-0.001	0.001

Omp-Pst1 porin – Statistic parameters: RQNNIKT

Generalized Linear Model Regression Results

```

=====
Dep. Variable:          Y      No. Observations:      70
Model:                 GLM    Df Residuals:          68
Model Family:         Gamma  Df Model:              1
Link Function:        inverse_power  Scale:                 0.92390
Method:              IRLS    Log-Likelihood:       -509.16
Date:                Sat, 20 Apr 2019  Deviance:             87.265
Time:                16:12:39  Pearson chi2:         62.8
No. Iterations:      8      Covariance Type:      nonrobust
=====

```

	coef	std err	z	P> z	[0.025	0.975]
Intercept	0.0025	0.000	6.534	0.000	0.002	0.003
RQNNIKT	-0.0002	9.81e-05	-2.541	0.011	-0.000	-5.7e-05

Omp-Pst2 porin – All statistic parameters:

Generalized Linear Model Regression Results

```

=====
Dep. Variable:          Y      No. Observations:      28
Model:                 GLM    Df Residuals:          26
Model Family:         Gamma  Df Model:              1
Link Function:        inverse_power  Scale:                 0.15194
Method:              IRLS    Log-Likelihood:       -219.45
Date:                Sat, 20 Apr 2019  Deviance:             3.9657
Time:                16:17:45  Pearson chi2:         3.95
No. Iterations:      21     Covariance Type:      nonrobust
=====

```

	coef	std err	z	P> z	[0.025	0.975]
Intercept	0.0004	3.89e-05	9.285	0.000	0.000	0.000
RQNNIKT	-2.679e-05	1.01e-05	-2.656	0.008	-4.66e-05	-7.02e-06
Concentration	0.0004	3.89e-05	9.285	0.000	0.000	0.000
RQNNIKT:Concentration	-2.679e-05	1.01e-05	-2.656	0.008	-4.66e-05	-7.02e-06

Omp-Pst2 porin – Statistic parameters: RQNNIKT

Generalized Linear Model Regression Results

```

=====
Dep. Variable:          Y      No. Observations:      28
Model:                 GLM    Df Residuals:          26
Model Family:         Gamma  Df Model:              1
Link Function:        inverse_power  Scale:                 0.15194
Method:              IRLS    Log-Likelihood:       -219.45
Date:                Sat, 20 Apr 2019  Deviance:             3.9657
Time:                16:17:13  Pearson chi2:         3.95
No. Iterations:      6      Covariance Type:      nonrobust
=====

```

	coef	std err	z	P> z	[0.025	0.975]
Intercept	0.0007	7.78e-05	9.285	0.000	0.001	0.001
RQNNIKT	-5.357e-05	2.02e-05	-2.656	0.008	-9.31e-05	-1.4e-05

2-2 comparison (Tukey) – n°6 peptide

Omp-Pst1 porin

Multiple Comparison of Means - Tukey HSD,FWER=0.05

group1	group2	meandiff	lower	upper	reject
0.0	1.0	778.27	539.2239	1017.3161	True
0.0	2.5	8.23	-230.8161	247.2761	False
0.0	5.0	1049.72	810.6739	1288.7661	True
1.0	2.5	-770.04	-1009.0861	-530.9939	True
1.0	5.0	271.45	32.4039	510.4961	True
2.5	5.0	1041.49	802.4439	1280.5361	True

Omp-Pst2 porin

Multiple Comparison of Means - Tukey HSD,FWER=0.05

group1	group2	meandiff	lower	upper	reject
0.0	1.0	1476.39	414.8606	2537.9194	True
0.0	2.5	1478.0614	979.279	1976.8438	True
0.0	5.0	876.5	423.8624	1329.1376	True
1.0	2.5	1.6714	-1080.3395	1083.6823	False
1.0	5.0	-599.89	-1661.4194	461.6394	False
2.5	5.0	-601.5614	-1100.3438	-102.779	True

GLM – n°5 peptide

Omp-Pst1 porin – All statistic parameters:

Generalized Linear Model Regression Results

Dep. Variable:	Y	No. Observations:	70
Model:	GLM	Df Residuals:	66
Model Family:	Gamma	Df Model:	3
Link Function:	inverse_power	Scale:	0.11788
Method:	IRLS	Log-Likelihood:	-440.49
Date:	Sat, 20 Apr 2019	Deviance:	8.1584
Time:	16:43:52	Pearson chi2:	7.78
No. Iterations:	9	Covariance Type:	nonrobust

	coef	std err	z	P> z	[0.025	0.975]
Intercept	0.0110	0.001	11.745	0.000	0.009	0.013
LtrNYR	-8.196e-05	0.000	-0.263	0.793	-0.001	0.001
Concentration	-0.0103	0.001	-10.987	0.000	-0.012	-0.008
LtrNYR:Concentration	0.0001	0.000	0.476	0.634	-0.000	0.001

Omp-Pst1 porin – Statistic parameters: L-tr-NYR peptide

Generalized Linear Model Regression Results

Dep. Variable:	Y	No. Observations:	70
Model:	GLM	Df Residuals:	68
Model Family:	Gamma	Df Model:	1
Link Function:	inverse_power	Scale:	0.91356
Method:	IRLS	Log-Likelihood:	-532.96
Date:	Sat, 20 Apr 2019	Deviance:	92.983
Time:	16:44:31	Pearson chi2:	62.1
No. Iterations:	7	Covariance Type:	nonrobust

	coef	std err	z	P> z	[0.025	0.975]
Intercept	0.0012	0.000	5.891	0.000	0.001	0.002
LtrNYR	7.365e-05	8.2e-05	0.898	0.369	-8.71e-05	0.000

Omp-Pst2 porin – All statistic parameters:

Generalized Linear Model Regression Results

Dep. Variable:	Y	No. Observations:	40
----------------	---	-------------------	----

```

Model: GLM Df Residuals: 38
Model Family: Gamma Df Model: 1
Link Function: inverse_power Scale: 0.30395
Method: IRLS Log-Likelihood: -346.87
Date: Sat, 20 Apr 2019 Deviance: 17.483
Time: 16:47:39 Pearson chi2: 11.5
No. Iterations: 57 Covariance Type: nonrobust

```

	coef	std err	z	P> z	[0.025	0.975]
Intercept	0.0002	2.23e-05	7.006	0.000	0.000	0.000
LtrNYR	2.262e-05	1.02e-05	2.209	0.027	2.55e-06	4.27e-05
Concentration	0.0002	2.23e-05	7.006	0.000	0.000	0.000
LtrNYR:Concentration	2.262e-05	1.02e-05	2.209	0.027	2.55e-06	4.27e-05

Omp-Pst2 porin – Statistic parameters: L-tr-NYR peptide

Generalized Linear Model Regression Results

```

Dep. Variable: Y No. Observations: 40
Model: GLM Df Residuals: 38
Model Family: Gamma Df Model: 1
Link Function: inverse_power Scale: 0.30395
Method: IRLS Log-Likelihood: -346.87
Date: Sat, 20 Apr 2019 Deviance: 17.483
Time: 16:47:04 Pearson chi2: 11.5
No. Iterations: 7 Covariance Type: nonrobust

```

	coef	std err	z	P> z	[0.025	0.975]
Intercept	0.0003	4.47e-05	7.006	0.000	0.000	0.000
LtrNYR	4.525e-05	2.05e-05	2.209	0.027	5.1e-06	8.54e-05

2-2 comparison (Tukey) – n°5 peptide

Omp-Pst2 porin

Multiple Comparison of Means - Tukey HSD,FWER=0.05

group1	group2	meandiff	lower	upper	reject
0.0	1.0	-4056.48	-5096.9738	-3015.9862	True
0.0	2.5	-1975.61	-3016.1038	-935.1162	True
0.0	5.0	-2622.73	-3663.2238	-1582.2362	True
1.0	2.5	2080.87	1040.3762	3121.3638	True
1.0	5.0	1433.75	393.2562	2474.2438	True
2.5	5.0	-647.12	-1687.6138	393.3738	True

GLM – n°7 peptide

Omp-Pst1 porin – All statistic parameters:

Generalized Linear Model Regression Results

```

Dep. Variable: Y No. Observations: 49
Model: GLM Df Residuals: 45
Model Family: Gamma Df Model: 3
Link Function: inverse_power Scale: 0.033481
Method: IRLS Log-Likelihood: -299.94
Date: Sat, 20 Apr 2019 Deviance: 1.5598
Time: 16:53:46 Pearson chi2: 1.51
No. Iterations: 10 Covariance Type: nonrobust

```

	coef	std err	z	P> z	[0.025	0.975]
Intercept	0.0140	0.001	24.419	0.000	0.013	0.015
LGNYSOU	-0.0028	0.000	-24.228	0.000	-0.003	-0.003
Concentration	-0.0135	0.001	-23.489	0.000	-0.015	-0.012
LGNYSOU:Concentration	0.0027	0.000	23.711	0.000	0.002	0.003

Omp-Pst1 porin – Statistic parameters: LGNY-cou peptide

Generalized Linear Model Regression Results

```

Dep. Variable: Y No. Observations: 49

```

```

Model: GLM Df Residuals: 47
Model Family: Gamma Df Model: 1
Link Function: inverse_power Scale: 0.80313
Method: IRLS Log-Likelihood: -406.26
Date: Sat, 20 Apr 2019 Deviance: 78.202
Time: 16:55:16 Pearson chi2: 37.7
No. Iterations: 9 Covariance Type: nonrobust
=====
coef std err z P>|z| [0.025 0.975]
-----
Intercept 0.0011 0.000 7.005 0.000 0.001 0.001
LGNYCOU -0.0002 3.47e-05 -5.225 0.000 -0.000 -0.000
=====

```

Omp-Pst2 porin – All statistic parameters:

```

Generalized Linear Model Regression Results
=====
Dep. Variable: Y No. Observations: 31
Model: GLM Df Residuals: 29
Model Family: Gamma Df Model: 1
Link Function: inverse_power Scale: 0.11512
Method: IRLS Log-Likelihood: -225.21
Date: Sat, 20 Apr 2019 Deviance: 3.2764
Time: 16:58:38 Pearson chi2: 3.34
No. Iterations: 7 Covariance Type: nonrobust
=====
coef std err z P>|z| [0.025 0.975]
-----
Intercept 0.0006 4.21e-05 13.227 0.000 0.000 0.001
LGNYCOU -7.406e-05 1.61e-05 -4.612 0.000 -0.000 -4.26e-05
Concentration 0.0006 4.21e-05 13.227 0.000 0.000 0.001
LGNYCOU:Concentration -7.406e-05 1.61e-05 -4.612 0.000 -0.000 -4.26e-05
=====

```

Omp-Pst2 porin – Statistic parameters: LGNY-cou peptide

```

Generalized Linear Model Regression Results
=====
Dep. Variable: Y No. Observations: 31
Model: GLM Df Residuals: 29
Model Family: Gamma Df Model: 1
Link Function: inverse_power Scale: 0.11512
Method: IRLS Log-Likelihood: -225.21
Date: Sat, 20 Apr 2019 Deviance: 3.2764
Time: 16:58:04 Pearson chi2: 3.34
No. Iterations: 7 Covariance Type: nonrobust
=====
coef std err z P>|z| [0.025 0.975]
-----
Intercept 0.0011 8.42e-05 13.227 0.000 0.001 0.001
LGNYCOU -0.0001 3.21e-05 -4.612 0.000 -0.000 -8.52e-05
=====

```

2-2 comparison (Tukey) – n^o7 peptide

No porins

Multiple Comparison of Means - Tukey HSD,FWER=0.05

```

=====
group1 group2 meandiff lower upper reject
-----
0.0 1.0 0.0 -2.5849 2.5849 False
0.0 5.0 9920.62 9914.5579 9926.6821 True
1.0 5.0 9920.62 9914.5579 9926.6821 True

```

Omp-Pst1 porin

Multiple Comparison of Means - Tukey HSD,FWER=0.05

```

=====
group1 group2 meandiff lower upper reject
-----
0.0 1.0 942.795 180.2145 1705.3755 True
0.0 2.5 1159.385 396.8045 1921.9655 True
0.0 5.0 2378.675 1467.2169 3290.1331 True
1.0 2.5 216.59 -359.8667 793.0467 False
1.0 5.0 1435.88 673.2995 2198.4605 True
2.5 5.0 1219.29 456.7095 1981.8705 True

```


Omp-Pst2 porin

Multiple Comparison of Means - Tukey HSD, FWER=0.05

group1	group2	meandiff	lower	upper	reject
0.0	1.0	436.68	7.8502	865.5098	True
0.0	2.5	678.45	249.6202	1107.2798	True
0.0	5.0	1256.96	251.2649	2262.6551	True
1.0	2.5	241.77	-187.0598	670.5998	False
1.0	5.0	820.28	-185.4151	1825.9751	False
2.5	5.0	578.51	-427.1851	1584.2051	False

GLM – n°8 peptide

Omp-Pst1 porin – All statistic parameters:

Generalized Linear Model Regression Results

Dep. Variable:	Y	No. Observations:	39
Model:	GLM	Df Residuals:	35
Model Family:	Gamma	Df Model:	3
Link Function:	inverse_power	Scale:	0.017429
Method:	IRLS	Log-Likelihood:	-184.36
Date:	Sat, 20 Apr 2019	Deviance:	0.61404
Time:	17:01:30	Pearson chi2:	0.610
No. Iterations:	9	Covariance Type:	nonrobust

	coef	std err	z	P> z	[0.025	0.975]
Intercept	0.0135	0.000	32.607	0.000	0.013	0.014
LtrNYRKtrCOU	-0.0018	9.18e-05	-20.009	0.000	-0.002	-0.002
Concentration	-0.0129	0.000	-31.040	0.000	-0.014	-0.012
LtrNYRKtrCOU:Concentration	0.0018	9.23e-05	19.169	0.000	0.002	0.002

Omp-Pst1 porin – Statistic parameters: L-tr-NYRK(tr-cou) peptide

Generalized Linear Model Regression Results

Dep. Variable:	Y	No. Observations:	39
Model:	GLM	Df Residuals:	37
Model Family:	Gamma	Df Model:	1
Link Function:	inverse_power	Scale:	2.4201
Method:	IRLS	Log-Likelihood:	-285.17
Date:	Sat, 20 Apr 2019	Deviance:	73.679
Time:	17:01:51	Pearson chi2:	89.5
No. Iterations:	8	Covariance Type:	nonrobust

	coef	std err	z	P> z	[0.025	0.975]
Intercept	0.0019	0.001	3.052	0.002	0.001	0.003
LtrNYRKtrCOU	-3.818e-05	0.000	-0.183	0.855	-0.000	0.000

Omp-Pst2 porin – All statistic parameters:

Generalized Linear Model Regression Results

Dep. Variable:	Y	No. Observations:	20
Model:	GLM	Df Residuals:	18
Model Family:	Gamma	Df Model:	1
Link Function:	inverse_power	Scale:	0.060592
Method:	IRLS	Log-Likelihood:	-135.93
Date:	Sat, 20 Apr 2019	Deviance:	1.1500
Time:	17:04:53	Pearson chi2:	1.09
No. Iterations:	7	Covariance Type:	nonrobust

	coef	std err	z	P> z	[0.025	0.975]
Intercept	0.0007	4.24e-05	15.553	0.000	0.001	0.001
LtrNYRKtrCOU	-8.817e-05	1.45e-05	-6.100	0.000	-0.000	-5.98e-05
Concentration	0.0007	4.24e-05	15.553	0.000	0.001	0.001
LtrNYRKtrCOU:Concentration	-8.817e-05	1.45e-05	-6.100	0.000	-0.000	-5.98e-05

Omp-Pst2 porin – Statistic parameters: L-tr-NYRK(tr-cou) peptide

Generalized Linear Model Regression Results

```

=====
Dep. Variable:          Y      No. Observations:          20
Model:                 GLM    Df Residuals:              18
Model Family:         Gamma  Df Model:                  1
Link Function:        inverse_power  Scale:                    0.060592
Method:               IRLS   Log-Likelihood:           -135.93
Date:                 Sat, 20 Apr 2019  Deviance:                 1.1500
Time:                 17:04:10  Pearson chi2:             1.09
No. Iterations:       7      Covariance Type:         nonrobust
=====

```

	coef	std err	z	P> z	[0.025	0.975]
Intercept	0.0013	8.49e-05	15.553	0.000	0.001	0.001
LtrNYRKtrCOU	-0.0002	2.89e-05	-6.100	0.000	-0.000	-0.000

2-2 comparison (Tukey) – n°8 peptide

No porins

Multiple Comparison of Means - Tukey HSD,FWER=0.05

```

=====
group1 group2 meandiff lower upper reject
-----
0.0 1.0 0.0 -6.0345 6.0345 False
0.0 5.0 154.44 148.4055 160.4745 True
1.0 5.0 154.44 148.4055 160.4745 True
=====

```

Omp-Pst1 porin

Multiple Comparison of Means - Tukey HSD,FWER=0.05

```

=====
group1 group2 meandiff lower upper reject
-----
0.0 1.0 521.5083 -388.0665 1431.0832 False
0.0 2.5 1793.275 461.7938 3124.7562 True
0.0 5.0 1561.875 230.3938 2893.3562 True
1.0 2.5 1271.7667 -103.3812 2646.9146 False
1.0 5.0 1040.3667 -334.7812 2415.5146 False
2.5 5.0 -231.4 -1915.6053 1452.8053 False
=====

```

Omp-Pst2 porin

Multiple Comparison of Means - Tukey HSD,FWER=0.05

```

=====
group1 group2 meandiff lower upper reject
-----
0.0 1.0 55.9933 -374.206 486.1926 False
0.0 2.5 503.7267 166.2506 841.2028 True
0.0 5.0 1256.96 571.5428 1942.3772 True
1.0 2.5 447.7333 -14.3749 909.8415 False
1.0 5.0 1200.9667 446.3472 1955.5862 True
2.5 5.0 753.2333 47.3514 1459.1153 True
=====

```

GLM – n°9 peptide

Omp-Pst1 porin – All statistic parameters:

Generalized Linear Model Regression Results

```

=====
Dep. Variable:          Y      No. Observations:          34
Model:                 GLM    Df Residuals:              30
Model Family:         Gamma  Df Model:                  3
Link Function:        inverse_power  Scale:                    0.0080476
Method:               IRLS   Log-Likelihood:           -142.24
Date:                 Sat, 20 Apr 2019  Deviance:                 0.23918
Time:                 17:13:39  Pearson chi2:             0.241
No. Iterations:       8      Covariance Type:         nonrobust
=====

```

	coef	std err	z	P> z	[0.025	0.975]
--	------	---------	---	------	--------	--------

Intercept	0.0127	0.000	35.251	0.000	0.012	0.013
RLtrNYRKtrCOU	-8.039e-06	0.001	-0.016	0.987	-0.001	0.001
Concentration	-0.0110	0.000	-30.041	0.000	-0.012	-0.010
RLtrNYRKtrCOU:Concentration	-0.0002	0.001	-0.331	0.740	-0.001	0.001

Omp-Pst1 porin – Statistic parameters: RL-tr-NYRK(tr-cou) peptide

Generalized Linear Model Regression Results

```

=====
Dep. Variable:          Y      No. Observations:          34
Model:                 GLM      Df Residuals:              32
Model Family:          Gamma    Df Model:                  1
Link Function:         inverse_power  Scale:                    0.90296
Method:                IRLS     Log-Likelihood:           -228.71
Date:                  Sat, 20 Apr 2019  Deviance:                 33.604
Time:                  17:14:05    Pearson chi2:             28.9
No. Iterations:        7      Covariance Type:          nonrobust
=====

```

	coef	std err	z	P> z	[0.025	0.975]
Intercept	0.0044	0.001	3.938	0.000	0.002	0.007
RLtrNYRKtrCOU	-0.0017	0.001	-1.389	0.165	-0.004	0.001

Omp-Pst2 porin – All statistic parameters:

Generalized Linear Model Regression Results

```

=====
Dep. Variable:          Y      No. Observations:          10
Model:                 GLM      Df Residuals:              8
Model Family:          Gamma    Df Model:                  1
Link Function:         inverse_power  Scale:                    0.028121
Method:                IRLS     Log-Likelihood:           -57.250
Date:                  Sat, 20 Apr 2019  Deviance:                 0.22476
Time:                  17:18:10    Pearson chi2:             0.225
No. Iterations:        25     Covariance Type:          nonrobust
=====

```

	coef	std err	z	P> z	[0.025	0.975]
Intercept	0.0008	6.03e-05	13.334	0.000	0.001	0.001
RLtrNYRKtrCOU	0.0005	0.000	4.192	0.000	0.000	0.001
Concentration	0.0008	6.03e-05	13.334	0.000	0.001	0.001
RLtrNYRKtrCOU:Concentration	0.0005	0.000	4.192	0.000	0.000	0.001

Omp-Pst2 porin – Statistic parameters: RL-tr-NYRK(tr-cou) peptide

Generalized Linear Model Regression Results

```

=====
Dep. Variable:          Y      No. Observations:          10
Model:                 GLM      Df Residuals:              8
Model Family:          Gamma    Df Model:                  1
Link Function:         inverse_power  Scale:                    0.028121
Method:                IRLS     Log-Likelihood:           -57.250
Date:                  Sat, 20 Apr 2019  Deviance:                 0.22476
Time:                  17:17:42    Pearson chi2:             0.225
No. Iterations:        6      Covariance Type:          nonrobust
=====

```

	coef	std err	z	P> z	[0.025	0.975]
Intercept	0.0016	0.000	13.334	0.000	0.001	0.002
RLtrNYRKtrCOU	0.0009	0.000	4.192	0.000	0.001	0.001

2-2 comparison (Tukey) – n°9 peptide

Omp-Pst2 porin

Multiple Comparison of Means - Tukey HSD, FWER=0.05

```

=====
group1 group2 meandiff  lower  upper  reject
-----
0      1      -231.0  -368.6685 -93.3315 True

```

GLM – n°10 peptide

Omp-Pst1 porin – All statistic parameters:

Generalized Linear Model Regression Results

```

=====
Dep. Variable:          Y      No. Observations:          28
Model:                 GLM    Df Residuals:              24
Model Family:         Gamma  Df Model:                  3
Link Function:        inverse_power  Scale:                    0.0087782
Method:               IRLS   Log-Likelihood:           -111.15
Date:                 Sat, 20 Apr 2019  Deviance:                  0.21267
Time:                 17:20:40   Pearson chi2:              0.211
No. Iterations:       8      Covariance Type:          nonrobust
=====

```

	coef	std err	z	P> z	[0.025	0.975]
Intercept	0.0127	0.000	33.752	0.000	0.012	0.013
RKLtrNYRKtrCOU	-0.0001	0.001	-0.229	0.819	-0.001	0.001
Concentration	-0.0110	0.000	-28.764	0.000	-0.012	-0.010
RKLtrNYRKtrCOU:Concentration	-0.0002	0.001	-0.444	0.657	-0.001	0.001

Omp-Pst1 porin – Statistic parameters: RKL-tr-NYRK(tr-cou) peptide

Generalized Linear Model Regression Results

```

=====
Dep. Variable:          Y      No. Observations:          28
Model:                 GLM    Df Residuals:              26
Model Family:         Gamma  Df Model:                  1
Link Function:        inverse_power  Scale:                    1.3189
Method:               IRLS   Log-Likelihood:           -183.77
Date:                 Sat, 20 Apr 2019  Deviance:                  30.679
Time:                 17:21:04   Pearson chi2:              34.3
No. Iterations:       8      Covariance Type:          nonrobust
=====

```

	coef	std err	z	P> z	[0.025	0.975]
Intercept	0.0044	0.001	3.258	0.001	0.002	0.007
RKLtrNYRKtrCOU	-0.0008	0.002	-0.442	0.659	-0.004	0.003

Omp-Pst2 porin – All statistic parameters:

Generalized Linear Model Regression Results

```

=====
Dep. Variable:          Y      No. Observations:          15
Model:                 GLM    Df Residuals:              13
Model Family:         Gamma  Df Model:                  1
Link Function:        inverse_power  Scale:                    0.035812
Method:               IRLS   Log-Likelihood:           -88.790
Date:                 Sat, 20 Apr 2019  Deviance:                  0.43491
Time:                 17:24:03   Pearson chi2:              0.466
No. Iterations:       10     Covariance Type:          nonrobust
=====

```

	coef	std err	z	P> z	[0.025	0.975]
Intercept	0.0008	6.8e-05	11.816	0.000	0.001	0.001
RKLtrNYRKtrCOU	0.0002	9.15e-05	2.402	0.016	4.04e-05	0.000
Concentration	0.0008	6.8e-05	11.816	0.000	0.001	0.001
RKLtrNYRKtrCOU:Concentration	0.0002	9.15e-05	2.402	0.016	4.04e-05	0.000

Omp-Pst2 porin – Statistic parameters: RKL-tr-NYRK(tr-cou) peptide

Generalized Linear Model Regression Results

```

=====
Dep. Variable:          Y      No. Observations:          15
Model:                 GLM    Df Residuals:              13
Model Family:         Gamma  Df Model:                  1
Link Function:        inverse_power  Scale:                    0.035812
Method:               IRLS   Log-Likelihood:           -88.790
Date:                 Sat, 20 Apr 2019  Deviance:                  0.43491
Time:                 17:23:37   Pearson chi2:              0.466
No. Iterations:       6      Covariance Type:          nonrobust
=====

```

	coef	std err	z	P> z	[0.025	0.975]
--	------	---------	---	------	--------	--------

Intercept	0.0016	0.000	11.816	0.000	0.001	0.002
RKLtrNYRKtrCOU	0.0004	0.000	2.402	0.016	8.09e-05	0.001

2-2 comparison (Tukey) – n°10 peptide

Omp-Pst2 porin

Multiple Comparison of Means - Tukey HSD,FWER=0.05

group1	group2	meandiff	lower	upper	reject
0	1	-133.61	-253.9482	-13.2718	True

Supplementary Table S4 – Statistics analysis from DLS experiments on synthetic peptides and peptidomimetic molecules. All experiments were conducted for at least three biologically independent replicates. Technical replicates were averaged to produce replicate means that were subsequently used for analysis. Mean values were compared within and between groups using one-way ANOVA followed by Tukey’s post hoc for two-two comparisons. Differences were considered statistically significant (True) if $p < 0.05$.

VI – Conclusions et perspectives

VI - Conclusions et perspectives

Les biofilms bactériens sont des communautés multicellulaires adhérentes à une surface (ou une interface) et enrobées d'une matrice extracellulaire (MEC) qui sont cruciaux pour le maintien de la plupart des écosystèmes de notre planète¹³. Ils représentent par ailleurs une menace, aussi bien en productivité industrielle qu'en santé humaine³¹⁷. Du fait de leur résistance très élevée aux antibiotiques, les biofilms sont extrêmement difficiles à éradiquer¹⁸. *Providencia stuartii*, organisme d'étude de cette thèse, est un pathogène Gram-négatif impliqué dans des infections endémiques souvent mortelles chez les personnes âgées. Cette souche, décrite comme étant la plus résistante de son genre au sein des *Enterobacteriaceae*, est connue pour sa capacité à former des biofilms dans le tractus urinaire humain. Elle est ainsi responsable d'environ 10% des infections nosocomiales urinaires (INU) chroniques¹⁸⁸, face auxquelles les antibiotiques sont inefficaces³¹⁸. En raison d'une faible compréhension du mécanisme de développement et de résistance des biofilms de *P. stuartii*, l'avancement de nouvelles thérapies pour lutter, prévenir et/ou éradiquer ces infections est compromis.

Les porines, protéines emblématiques et prépondérantes de la membrane externe des bactéries Gram-négatif, assurent la régulation de la perméabilité membranaire en contrôlant le flux de nutriments et de métabolites hydrophiles vers le périplasma, indispensable à la croissance bactérienne et à sa survie¹⁵³. À travers ces trimères de tonneaux β transmembranaires, les antibiotiques peuvent également circuler, menaçant d'extinction la bactérie. Les porines peuvent également participer à la résistance aux antibiotiques en réduisant, voire en empêchant, la diffusion des antibiotiques à travers la membrane externe^{167,319,320}. *P. stuartii* exprime deux porines présentes dans son génome, Omp-Pst1 et Omp-Pst2. La porine majoritaire Omp-Pst1, légèrement anion-sélective, est en grande partie responsable de l'entrée des antibiotiques de type β -lactames au sein de *P. stuartii*¹⁹⁶. La seconde porine Omp-Pst2, fortement cation-sélective, est impliquée dans l'efflux du trop plein cationique du milieu périplasmique vers le milieu extérieur¹⁹⁶. De plus, nos travaux ont révélé que les porines jouent un rôle essentiel dans la formation des biofilms chez *P. stuartii*^{177,178,321,322}. Ainsi, nous avons montré que *P. stuartii* forme des communautés flottantes, état de socialisation préliminaire à l'adhésion des cellules aux surfaces pour former les biofilms adhérents (*El Khatib., Nasrallah., Tran., Lopes., et al. 2017*²⁰⁴) qui s'établiront par sécrétion d'une MEC. Les structures des deux porines de *P. stuartii*, résolues par les Drs. Chady Nasrallah et Jacques-Philippe Colletier, ont révélées une organisation en dimère des trimères de porines associés en face à face par leur boucles extracellulaires (Dimer of Trimers – DOTs)¹¹¹. Cette

capacité d'auto-association des porines contribue au contact étroit des membranes entre cellules adjacentes au sein du biofilm, et pourrait participer à une communication cellulaire précoce en favorisant la formation des communautés flottantes (*El Khatib., Nasrallah., Lopes., et al. 2018*¹¹¹).

Les DOTs de porines interagissent à travers des motifs de type steric zipper qui associent deux-à-deux les monomères se faisant face dans le DOT. Récemment, nous avons suggéré que ces motifs pourraient en réalité être des LARKS (Low-complexity aromatic-rich kinked segments) qui sont des segments empilés en feuillets β s'appareillant en protofilaments³²³. Contrairement aux steric zippers, les feuillets β des LARKS interagissent faiblement à travers les atomes polaires et les chaînes latérales aromatiques, ce qui expliquerait la réversibilité des contacts entre cellules au sein d'un biofilm lors de la sécrétion de la MEC. En effet, il a été démontré que les LARKS peuvent se dissocier lorsqu'ils sont soumis à une augmentation de la température³²³. Quoi qu'il en soit, les résidus impliqués dans ces motifs sont 205-AGVVTSE-211 pour Omp-Pst1 et 283-LGNY-286 pour Omp-Pst2 (*El Khatib., Nasrallah., Lopes., et al. 2018*¹¹¹). De plus, nous avons résolu une nouvelle structure de DOT d'Omp-Pst2, montrant que la propension à former des DOTs va au-delà d'une séquence spécifique et est plutôt une caractéristique des porines de *P. stuartii*. Puisque la force motrice menant à la formation de DOT est principalement l'attraction électrostatique¹¹¹, le steric zipper – ou le LARKS – servirait uniquement à verrouiller l'interaction porine-porine. Le fait que les porines soient capables d'interagir entre elles à travers différents motifs semble confirmer cette hypothèse.

1- Objectif n°1 : Etude du rôle des porines dans l'établissement et la résistance des communautés microbiennes de *P. stuartii*

Au début de cette thèse, plusieurs questions étaient en suspens : comment *P. stuartii* résiste-t-elle aux conditions stressantes du tractus urinaire, son principal habitat chez l'Homme ? Est-ce que les porines sont impliquées dans cette résistance ? Si oui, comment le sont-elles ? Des expériences réalisées en amont de cette thèse ont montré que la délétion de la porine majoritaire Omp-Pst1 n'est pas tolérée par les bactéries, démontrant qu'elle est indispensable à la survie de *P. stuartii*. La délétion d'Omp-Pst2, quant à elle, a mis en évidence son importance dans les premières phases de croissance de *P. stuartii*²⁰⁴. Ainsi, le **premier objectif** de la thèse a été de mieux comprendre le rôle de ces deux porines 1) dans

l'établissement des communautés flottantes et des biofilms adhérents, et 2) dans la résistance de ces derniers lorsque *P. stuartii* est soumise à diverses conditions mimant – ou exagérant – celles rencontrées dans le tractus urinaire (*i.e.* de fortes concentrations en urée, ammonium, bicarbonate, créatinine, et des variations soudaine de pH).

A. Socialisation microbienne : un moyen de survie pour *P. stuartii*

Nos travaux ont montré que le développement des communautés flottantes et des biofilms adhérents est un mode de socialisation qui confère aux cellules de *P. stuartii* une plus grande résistance aux conditions environnantes stressantes. En effet, les deux types de communautés bactériennes résistent à des concentrations de métabolites bien supérieures (de 2 à 40 fois) à celles rencontrées dans le tractus urinaire. Cette socialisation forte de *P. stuartii* semble être une réponse des bactéries pour se protéger des agressions de l'environnement.

B. Porines : rôles dans la résistance de *P. stuartii* aux métabolites du tractus urinaire, ainsi que dans l'établissement des deux types de communautés microbiennes

Nos résultats suggèrent que la porine majoritaire Omp-Pst1 constitue la principale passerelle permettant l'influx de l'urée, de l'ammonium et du bicarbonate du milieu extérieur vers le périplasme, tandis qu'Omp-Pst2 est impliquée dans la résistance de ces métabolites, assurant une meilleure survie aux bactéries de *P. stuartii*. Dans ces conditions environnementales, la socialisation des bactéries en communautés flottantes, et par la suite en biofilms adhérents, est assurée par la capacité d'auto-association d'Omp-Pst1 en DOTs. Dans les cas où l'expression d'Omp-Pst1 est réduite, Omp-Pst2 compense en fournissant un échafaudage alternatif de ces communautés microbiennes grâce à sa propension plus élevée à former des DOTs¹¹¹.

C. Protection des bactéries de *P. stuartii* : l'importance d'une MEC ?

Pour rappel, les communautés flottantes sont à l'origine de la formation des biofilms adhérents par sédimentation²⁰⁴. Ces derniers sont enrobés d'une MEC, mais nous ignorons à l'heure actuelle si sa synthèse débute dès les premiers stades de développement des bactéries en communautés flottantes ou si elle est concomitante à l'accrochage des cellules à une surface. Néanmoins, nos résultats suggèrent qu'il n'existe probablement pas de MEC autour des communautés flottantes. En effet, nous observons une régulation à la baisse des porines

face aux conditions expérimentales uniquement dans ces suprastructures cellulaires contrairement au sein des biofilms adhérents, dans lesquels les bactéries semblent être protégées par la MEC. Ainsi, elles ne nécessiteraient donc pas cette modification dans l'expression des porines pour résister.

La MEC est spécifique à chaque espèce bactérienne. Ainsi, déterminer sa composition est cruciale pour élucider les relations structure-fonction qui aideront au développement de nouvelles stratégies capables de perturber les biofilms. Chez *P. stuartii*, la caractérisation de la MEC aiderait à comprendre les différences phénotypiques et transcriptomiques entre les communautés flottantes et les biofilms adhérents observées au cours de la thèse. Au cours de la thèse, nous avons tenté de marquer la MEC des biofilms adhérents et potentiellement des communautés flottantes de *P. stuartii* en utilisant des marqueurs couplés à des lectines, celle de Wheat Germ Agglutinin (WGA) et celle de concanavaline A – qui reconnaissent spécifiquement des motifs saccharidiques présents dans la MEC et s'y fixent – ainsi qu'un marqueur des biofilms, FilmTracer™ SYPRO™ Ruby Biofilm Matrix. Cependant, ces tentatives n'ont pas apporté les résultats espérés et nous n'avons pas réussi à marquer spécifiquement la MEC de *P. stuartii*, suggérant une composition particulière de celle-ci qui n'est pas détectée par ces approches.

Dans la littérature, plusieurs autres stratégies de caractérisation sont évoquées. Par exemple, en 2013, McCrate *et al.* ont présenté une approche intégrant de la microscopie électronique, de la biochimie et de la spectroscopie RMN à l'état solide afin de définir la composition chimique de la MEC d'une souche d'*E. coli* uropathogène³²⁴. En 2015, Reichhardt *et al.* ont développé une autre approche de RMN à l'état solide pour déterminer et quantifier spectroscopiquement les réservoirs de carbone de la MEC de *Vibrio cholerae*³²⁵. Cette méthode a également été mise en œuvre pour surveiller les changements de la MEC face à des variations environnementales et des facteurs de stress. En 2017, Mohammed *et al.* ont analysé la composition en protéines de la MEC de *Fusobacterium nucleatum* et *Porphyromonas gingivalis*, deux pathogènes Gram-négatif formant des biofilms dentaires, par spectrométrie de masse couplé à de la chromatographie liquide³²⁶. Les auteurs ont pu identifier des niveaux relativement élevés de plusieurs protéines présentes dans la MEC ; ces protéines pourraient constituer de futures cibles dans la lutte contre les biofilms formés par ces espèces.

En conclusion de ce premier objectif de thèse, nos résultats fournissent de nouvelles informations sur la socialisation et la résistance de *P. stuartii* dans des conditions qui imitent

son environnement physiopathologique. Cette souche infecte des patients immunodéprimés ou subissant une cathétérisation longue. La gravité de ces infections résulte de sa forte résistance intrinsèque aux antibiotiques mais également du caractère hautement social des bactéries, leur conférant une résistance accrue aux stress environnementaux (*Lopes et al., 2019a, en soumission*), aux antibiotiques et potentiellement au système immunitaire^{43,327}. Nos données suggèrent que les futurs traitements contre *P. stuartii* doivent être évalués sur les communautés flottantes et les biofilms adhérents, ainsi que dans des conditions mimant celles rencontrées dans le tractus urinaire. Cela est indispensable pour prendre en considération l'importante adaptabilité de la réponse de la bactérie en fonction de son état social et de son environnement afin de prédire avec précision leur efficacité dans le contexte clinique.

2- Objectif n°2 : Inhibition des DOTs de porines pour lutter contre le caractère social de *P. stuartii*

La résistance aux antibiotiques étant très élevée chez *P. stuartii*, nous nous sommes demandé comment nous pouvons améliorer l'efficacité de ces derniers sur les communautés microbiennes de *P. stuartii*. Est-ce qu'une inhibition du caractère social de *P. stuartii* est une stratégie envisageable à des fins thérapeutiques ? Et si oui, comment arriver à cette inhibition ? Ainsi, le **second objectif** de la thèse a été de tester la stratégie d'une inhibition de la formation des communautés flottantes pour éviter l'établissement des biofilms adhérents. A dessein, nous avons synthétisés une batterie de peptides et molécules peptidomimétiques avec pour but de cibler les motifs d'interaction clé au sein des DOTs de porines. Certains de ces peptides synthétisés ont ensuite été combinés à des antibiotiques afin d'observer un potentiel effet synergique. Trois antibiotiques ont été étudiés, deux utilisés en milieu hospitalier pour lutter contre les infections à *P. stuartii* (céfépime et méropénème) et un troisième envers lequel *P. stuartii* est naturellement très résistante (tétracycline).

A. Lien direct entre la formation de DOTs et la socialisation bactérienne chez *P. stuartii*

Les cavités inter-DOTs sont très fortement chargées négativement¹¹¹. Nous avons montré que la présence de l'arginine, un acide aminé chargé positivement, provoque une répulsion électrostatique au sein des porines, les empêchant de s'auto-associer efficacement en DOTs. Ce phénomène a pour conséquence l'inhibition de la formation des communautés flottantes,

conduisant à une réduction de la quantité de biofilms adhérents. Nous avons ainsi démontré que l'auto-association des porines en DOTs joue un rôle moteur dans la socialisation bactérienne de *P. stuartii*. Nous avons par ailleurs confirmé que la force motrice permettant l'établissement de DOTs est l'attraction électrostatique. Enfin, nos résultats suggèrent qu'en présence de polyamine, ces DOTs ne pourront plus se former. Nous supposons ainsi que c'est le mécanisme qui serait à l'œuvre dans les biofilms adhérents de *P. stuartii*, au sein desquels les cellules ne sont plus en contact et les dimères de porines sont donc dissociés.

Dans la littérature, il a été montré que lorsque qu'un biofilm est mature, les cellules produisent naturellement des composants qui induisent sa dispersion pour permettre la colonisation d'autres niches. Les biofilms de *B. subtilis* produisent en effet des acides aminés en configuration D, déclenchant la dispersion des cellules⁸¹. Il serait ainsi intéressant d'étudier ce mécanisme interne aux biofilms bactériens, ainsi que l'effet des polyamines sur les porines et les bactéries de *P. stuartii*. Ces informations pourraient en effet être utiles pour la conception de nouvelles molécules pouvant éradiquer les biofilms par ces mêmes mécanismes. Cependant, d'autres recherches ont montré qu'un phénomène de dispersion des biofilms à grande échelle dans un hôte vivant pouvait submerger le système immunitaire et provoquer la dissémination de l'infection et éventuellement une septicémie mortelle³²⁸. Les traitements antibiofilms doivent ainsi être utilisés en complément d'autres approches pour limiter ces risques et améliorer les stratégies de lutte systémique et curative.

B. Intégration d'un fragment de coumarine au sein des peptides synthétisés : Une stratégie prometteuse pour le développement d'outils diagnostiques contre les infections à *P. stuartii*

Au cours de cette thèse, des peptides mimant les interfaces des DOTs de porines et couplés à de l'arginine ont été synthétisés dans le but d'inhiber leur propension à s'auto-associer et ainsi empêcher la socialisation bactérienne de *P. stuartii*. Aucun de ces peptides n'étant efficaces, nous avons intégré un fragment de coumarine afin de suivre leur progression au sein des bactéries. De manière surprenante, nous avons observé que l'ajout de ce fragment a conféré à deux peptides la capacité de co-précipiter et de tuer les cellules au sein des communautés flottantes. Les deux peptides LGNY-cou et L-tr-NYRK(tr-cou) co-agrègent en effet avec les bactéries, entraînant la mort des cellules, sans pour autant avoir le même impact sur les biofilms adhérents. Le premier peptide n'a aucune incidence sur le développement de ces derniers, tandis qu'en présence du second, ce sont les communautés flottantes agrégées

sédimentées qui sont observées au fond des puits. Au vu de l'impact fort de L-tr-NYRK(tr-cou) sur les communautés flottantes et les biofilms adhérents de *P. stuartii*, ce peptide pourrait ainsi être utilisé pour le développement d'outils diagnostiques contre les infections de *P. stuartii*. De plus, la sensibilité élevée des communautés flottantes en présence de L-tr-NYRK(tr-cou) suggère une fois encore que ces dernières ne sont pas enrobées d'une MEC assurant leur protection. Ce peptide n'inhibant pas les DOTs de porines, nous suggérons que : (i) soit le contact cellule-cellule au sein des communautés flottantes n'est pas uniquement dû à l'auto-association des porines en DOTs, (ii) soit, malgré l'établissement de ces derniers, le peptide lie si fortement les bactéries entre elles qu'elles ne peuvent se socialiser en communautés flottantes uniformes, (iii) soit le peptide se lie à la surface des communautés flottantes et empêchent ainsi l'ajout de cellules à la périphérie. Pour la suite, des expériences de co-cristallisation entre porines et le peptide restent à envisager dans le but d'étudier l'interaction porines/peptide (si interaction il y a) ce qui permettrait de mieux comprendre le mécanisme d'action des peptides synthétisés.

C. Combinaison des peptides avec les antibiotiques à des buts thérapeutiques ?

Une stratégie alternative envisagée dans la thèse pour lutter contre les infections urinaires chroniques de *P. stuartii* a été de combiner des antibiotiques à nos peptides synthétisés. Nous avons montré que les bactéries de *P. stuartii*, pourtant résistantes à la tétracycline, ne survivaient plus à l'antibiotique en présence du peptide RL-tr-NYRK(tr-cou). En revanche, les bactéries de *P. stuartii*, qui ne sont pas censées survivre à la présence de méropénème dans le milieu, deviennent résistante à l'antibiotique en présence des peptides LGNY et L-tr-NYR.

Ainsi, un des résultats forts de la thèse a été de montrer que la tétracycline pouvait tuer les bactéries pathogènes de *P. stuartii* mais seulement lorsqu'elle est combinée à certains peptides synthétisés. Il est évident que d'autres expérimentations sur *P. stuartii* sont à envisager afin de comprendre au mieux cette synergie inhibitrice. Actuellement, les concentrations peptidiques testées sont beaucoup trop élevées (de l'ordre du millimolaire) pour envisager des traitements thérapeutiques en combinaison avec la tétracycline. Il est nécessaire de diminuer cette concentration peptidique à l'ordre du micromolaire tout en conservant cet effet inhibiteur sur les bactéries. De plus, dans la nature, les biofilms poly-espèces sont prédominants, dans lesquels des interactions inter et intra-espèces complexes s'établissent³²⁹. Par conséquent, les mêmes expériences devront être réalisées sur d'autres

souches bactériennes dans l'espoir d'observer ces résultats prometteurs, pour *in fine* envisager des solutions thérapeutiques nouvelles.

En conclusion de ce second objectif de thèse, nos travaux valident qu'une stratégie thérapeutique envisageable pour lutter contre la socialisation bactérienne de *P. stuartii* est le ciblage des DOTs de ces porines. De plus, ils proposent également que des peptides synthétisés bio-inspirés, tel que L-tr-NYRK(tr-cou), peuvent être des candidats intéressants pour le développement d'outils diagnostiques des infections à *P. stuartii*. Enfin, la combinaison de ces peptides avec des antibiotiques s'avère être une approche thérapeutique à approfondir, puisque nous avons découvert que la tétracycline, un antibiotique peu actif contre *P. stuartii*, peut devenir efficace lorsqu'administré en combinaison avec le peptide RL-tr-NYRK (tr-cou) (Lopes *et al.*, 2019b, *en préparation*). D'autres études seront nécessaires pour améliorer l'activité de ces composés et notamment améliorer leur affinité pour leur site de liaison sur les porines. Il est également tentant d'évaluer l'activité du composé sur d'autres bactéries formant des biofilms, afin de vérifier si les peptides pourraient représenter des molécules actives contre différentes espèces. En effet, les biofilms bactériens sont généralement composés de différentes souches, nécessitant que les molécules présentent un large spectre pour être actives dans le contexte biologique.

3- Perspectives

A. Porines et pompes à efflux : implication corrélée dans la résistance élevée des biofilms aux antibiotiques ?

Les porines ne sont pas les seules protéines membranaires à être impliquées dans la résistance aux antibiotiques. Les pompes à efflux, protéines de transport membranaire des bactéries Gram-positif et négatif, se distinguent également dans cette résistance grâce à leur capacité à extraire une variété d'antibiotiques, cliniquement pertinents, des cellules vers l'environnement extracellulaire^{319,330,331}. Ce faisant, ces protéines réduisent la concentration d'antibiotique intracellulaire, permettant aux bactéries de survivre à des concentrations d'antibiotiques plus élevées. Etant donné que leur surexpression peut entraîner des niveaux de résistance extrêmes chez les pathogènes Gram-négatif³³², l'inhibition de l'efflux s'avère être une stratégie également prometteuse pour lutter contre la multi-résistance de ces derniers. L'analyse d'une

relation entre les porines et les pompes à efflux chez *P. stuartii* serait alors à réaliser afin d'approfondir la compréhension des mécanismes de résistance des bactéries de *P. stuartii* face aux antibiotiques.

B. Les phages : une alternative aux antibiotiques ?

Etant donné l'expansion des bactéries pathogènes multi-résistantes et le manque criant de nouveaux antibiotiques susceptibles de les combattre, il est indispensable d'explorer d'autres approches thérapeutiques, telles que la phagothérapie³³³. Cette technique utilise des virus de l'environnement infectant naturellement les bactéries, les bactériophages (*bacterio-* pour bactéries et *-phage* pour mangeur ; également appelés phages), et représente une alternative prometteuse aux antibiotiques³³⁴. Contrairement à ces derniers qui attaquent un spectre large de bactéries sans distinction entre les « bonnes » et les « mauvaises », les bactériophages sont spécifiques à un type de bactérie particulier à détruire. Une propriété remarquable de ces phages réside dans leur capacité à hydrolyser les polysaccharides bactériens qui composent les biofilms³³⁵, leur conférant un avantage spécifique comparé aux antibiotiques, dont nous connaissons les limites en matière de pénétration dans les biofilms³³⁶.

Pourtant découverte en France en 1917 par le franco-canadien Félix d'Hérelle³³⁷, la phagothérapie est tombée dans l'abandon après la découverte de la pénicilline par Alexander Fleming en 1928 et notamment à cause de la seconde guerre mondiale, qui a généré des besoins immenses en traitements anti-infectieux³³⁸. Néanmoins, en 2019, l'Agence Nationale de Sécurité du Médicament et des produits de santé (ANSM) a décidé de délivrer des autorisations temporaires d'utilisation des bactériophages, considéré comme une première étape avant l'autorisation de mise sur le marché³³⁹. Il faudra cependant éviter de reproduire les mêmes erreurs qu'avec les antibiotiques car une bactérie peut également devenir phago-résistante. En effet, la résistance aux phages peut évoluer très rapidement dans des cultures de bactéries où coexistent des cellules sensibles et résistantes, comme c'est le cas dans les biofilms, et sous attaque de phages³⁴⁰⁻³⁴². Ce processus a été étudié pendant des décennies, mais l'évolution de la résistance aux phages n'a guère retenu l'attention dans le contexte des biofilms³⁴³. À titre d'exemple, en février 2019, Simmons *et al.* ont mis en avant l'inefficacité des phages dans la dispersion des biofilms d'une souche d'*E. coli*³⁴⁴. Les auteurs ont observés que lorsque les bactéries résistantes aux phages deviennent rares au sein d'un biofilm, les phages introduits éliminent la quasi-totalité des cellules sensibles, ce qui laisse aux cellules résistantes résiduelles un nouvelle espace à coloniser. La repopulation de cet espace laisse

place à un biofilm constitué uniquement de bactéries résistantes. En revanche, lorsque les bactéries résistantes aux phages sont déjà abondantes au sein d'un biofilm, ces dernières créent des barrières entre les phages et les cellules sensibles. Ces dernières s'agglomèrent au centre du biofilm et sont ainsi protégées par les bactéries résistantes situées autour. Ainsi, l'optimisation des phages, y compris la compréhension de l'évolution de la résistance de ces derniers chez les bactéries hôtes, nécessite un examen approfondi des interactions phage-biofilm^{345,346}.

VII – Références

VII – Références

1. Gould, S. J. Planet of the bacteria. *PhilPapers* (1996).
2. Mossio, M., Montévil, M. & Longo, G. Theoretical principles for biology: Organization. *Prog. Biophys. Mol. Biol.* **122**, 24–35 (2016).
3. Koch, A. L. Bacterial wall as target for attack: past, present, and future research. *Clin. Microbiol. Rev.* **16**, 673–687 (2003).
4. Rajagopal, M. & Walker, S. Envelope Structures of Gram-Positive Bacteria. *Curr. Top. Microbiol. Immunol.* **404**, 1–44 (2017).
5. Costerton, J. W., Ingram, J. M. & Cheng, K. J. Structure and function of the cell envelope of gram-negative bacteria. *Bacteriol. Rev.* **38**, 87–110 (1974).
6. Terashima, H., Kojima, S. & Homma, M. Flagellar motility in bacteria structure and function of flagellar motor. *Int. Rev. Cell Mol. Biol.* **270**, 39–85 (2008).
7. O’Toole, G., Kaplan, H. B. & Kolter, R. Biofilm formation as microbial development. *Annu. Rev. Microbiol.* **54**, 49–79 (2000).
8. Percival, S. L., Malic, S., Cruz, H. & Williams, D. W. Introduction to Biofilms. in *Biofilms and Veterinary Medicine* (eds. Percival, S., Knottenbelt, D. & Cochrane, C.) **6**, 41–68 (Springer Berlin Heidelberg, 2011).
9. Zobell, C. E. The Effect of Solid Surfaces upon Bacterial Activity. *J. Bacteriol.* **46**, 39–56 (1943).
10. Costerton, J. W., Geesey, G. G. & Cheng, K. J. How bacteria stick. *Sci. Am.* **238**, 86–95 (1978).
11. Lappin-Scott, H., Burton, S. & Stoodley, P. Revealing a world of biofilms--the pioneering research of Bill Costerton. *Nat. Rev. Microbiol.* **12**, 781–787 (2014).
12. Harty, D. W. S. & Handley, P. S. Expression of the Surface Properties of the Fibrillar Streptococcus salivarius HB and Its Adhesion Deficient Mutants Grown in Continuous Culture under Glucose Limitation. *Microbiology* **135**, 2611–2621 (1989).
13. Vlamakis, H., Chai, Y., Beaugregard, P., Losick, R. & Kolter, R. Sticking together: building a biofilm the Bacillus subtilis way. *Nat. Rev. Microbiol.* **11**, 157–168 (2013).
14. Wilson *et al.* The Quantitative Assessment of Pseudomonas aeruginosa (PA)14 Biofilm Surface Coverage on Slippery Liquid Infused Polymer Surfaces (SLIPS). *International Journal of Nanotechnology in Medicine & Engineering* (2018).
15. Schwartz, K., Syed, A. K., Stephenson, R. E., Rickard, A. H. & Boles, B. R. Functional amyloids composed of phenol soluble modulins stabilize Staphylococcus aureus biofilms. *PLoS Pathog.* **8**, e1002744 (2012).
16. Davey, M. E. & O’toole, G. A. Microbial Biofilms: from Ecology to Molecular Genetics. *Microbiol. Mol. Biol. Rev.* **64**, 847–867 (2000).
17. Hall-Stoodley, L., Costerton, J. W. & Stoodley, P. Bacterial biofilms: from the natural environment to infectious diseases. *Nat. Rev. Microbiol.* **2**, 95–108 (2004).
18. Nicolle, L. E. Resistant pathogens in urinary tract infections. *J. Am. Geriatr. Soc.* **50**, S230-235 (2002).
19. Taraszkievicz, A., Fila, G., Grinholc, M. & Nakonieczna, J. Innovative Strategies to Overcome Biofilm Resistance. *BioMed Res. Int.* **2013**, 1–13 (2013).
20. Król, J. E. *et al.* Invasion of E. coli biofilms by antibiotic resistance plasmids. *Plasmid* **70**, 110–119 (2013).

21. Burmølle, M. *et al.* Enhanced biofilm formation and increased resistance to antimicrobial agents and bacterial invasion are caused by synergistic interactions in multispecies biofilms. *Appl. Environ. Microbiol.* **72**, 3916–3923 (2006).
22. Flemming, H.-C. & Wuertz, S. Bacteria and archaea on Earth and their abundance in biofilms. *Nat. Rev. Microbiol.* **17**, 247–260 (2019).
23. Neu, T. Development and structure of microbial biofilms in river water studied by confocal laser scanning microscopy. *FEMS Microbiol. Ecol.* **24**, 11–25 (1997).
24. Rasmussen, B. Filamentous microfossils in a 3,235-million-year-old volcanogenic massive sulphide deposit. *Nature* **405**, 676–679 (2000).
25. Thomas, D. N. & Dieckmann, G. S. Antarctic Sea ice--a habitat for extremophiles. *Science* **295**, 641–644 (2002).
26. Declerck, P. Biofilms: the environmental playground of *Legionella pneumophila*. *Environ. Microbiol.* **12**, 557–566 (2010).
27. Lee, H.-J. *et al.* Enhancing ATP-based bacteria and biofilm detection by enzymatic pyrophosphate regeneration. *Anal. Biochem.* **399**, 168–173 (2010).
28. Rogers, J., Dowsett, A. B., Dennis, P. J., Lee, J. V. & Keevil, C. W. Influence of temperature and plumbing material selection on biofilm formation and growth of *Legionella pneumophila* in a model potable water system containing complex microbial flora. *Appl. Environ. Microbiol.* **60**, 1585–1592 (1994).
29. van der Kooij, D., Veenendaal, H. R. & Scheffer, W. J. H. Biofilm formation and multiplication of *Legionella* in a model warm water system with pipes of copper, stainless steel and cross-linked polyethylene. *Water Res.* **39**, 2789–2798 (2005).
30. Bixler, G. D. & Bhushan, B. Biofouling: lessons from nature. *Philos. Transact. A Math. Phys. Eng. Sci.* **370**, 2381–2417 (2012).
31. Nudleman, E. & Kaiser, D. Pulling Together with Type IV Pili. *J. Mol. Microbiol. Biotechnol.* **7**, 52–62 (2004).
32. Pratt, L. A. & Kolter, R. Genetic analysis of *Escherichia coli* biofilm formation: roles of flagella, motility, chemotaxis and type I pili. *Mol. Microbiol.* **30**, 285–293 (1998).
33. O'Toole, G. A. & Kolter, R. Flagellar and twitching motility are necessary for *Pseudomonas aeruginosa* biofilm development. *Mol. Microbiol.* **30**, 295–304 (1998).
34. Davies, D. G. & Geesey, G. G. Regulation of the alginate biosynthesis gene *algC* in *Pseudomonas aeruginosa* during biofilm development in continuous culture. *Appl. Environ. Microbiol.* **61**, 860–867 (1995).
35. Jamal, M. *et al.* Bacterial biofilm and associated infections. *J. Chin. Med. Assoc. JCMA* **81**, 7–11 (2018).
36. Flemming, H.-C. & Wingender, J. The biofilm matrix. *Nat. Rev. Microbiol.* **8**, 623–633 (2010).
37. Stewart, P. S. & Franklin, M. J. Physiological heterogeneity in biofilms. *Nat. Rev. Microbiol.* **6**, 199–210 (2008).
38. Branda, S. S., Vik, S., Friedman, L. & Kolter, R. Biofilms: the matrix revisited. *Trends Microbiol.* **13**, 20–26 (2005).
39. Latasa, C., Solano, C., Penadés, J. R. & Lasa, I. Biofilm-associated proteins. *C. R. Biol.* **329**, 849–857 (2006).
40. Whitchurch, C. B., Tolker-Nielsen, T., Ragas, P. C. & Mattick, J. S. Extracellular DNA required for bacterial biofilm formation. *Science* **295**, 1487 (2002).
41. Sutherland, I. The biofilm matrix – an immobilized but dynamic microbial

- environment. *Trends Microbiol.* **9**, 222–227 (2001).
42. Azeredo, J. *et al.* Critical review on biofilm methods. *Crit. Rev. Microbiol.* **43**, 313–351 (2017).
 43. Leid, J. G. *et al.* The exopolysaccharide alginate protects *Pseudomonas aeruginosa* biofilm bacteria from IFN-gamma-mediated macrophage killing. *J. Immunol. Baltim. Md 1950* **175**, 7512–7518 (2005).
 44. Mah, T. F. & O’Toole, G. A. Mechanisms of biofilm resistance to antimicrobial agents. *Trends Microbiol.* **9**, 34–39 (2001).
 45. Lawrence, D. *et al.* Species interactions alter evolutionary responses to a novel environment. *PLoS Biol.* **10**, e1001330 (2012).
 46. O’Toole, G. A. *et al.* Genetic approaches to study of biofilms. *Methods Enzymol.* **310**, 91–109 (1999).
 47. Lee, K. & Yoon, S. S. *Pseudomonas aeruginosa* Biofilm, a Programmed Bacterial Life for Fitness. *J. Microbiol. Biotechnol.* **27**, 1053–1064 (2017).
 48. Jackson, K. D., Starkey, M., Kremer, S., Parsek, M. R. & Wozniak, D. J. Identification of *psl*, a locus encoding a potential exopolysaccharide that is essential for *Pseudomonas aeruginosa* PAO1 biofilm formation. *J. Bacteriol.* **186**, 4466–4475 (2004).
 49. Friedman, L. & Kolter, R. Two genetic loci produce distinct carbohydrate-rich structural components of the *Pseudomonas aeruginosa* biofilm matrix. *J. Bacteriol.* **186**, 4457–4465 (2004).
 50. Yang, L. *et al.* Distinct roles of extracellular polymeric substances in *Pseudomonas aeruginosa* biofilm development. *Environ. Microbiol.* **13**, 1705–1717 (2011).
 51. Yang, L. *et al.* Polysaccharides serve as scaffold of biofilms formed by mucoid *Pseudomonas aeruginosa*. *FEMS Immunol. Med. Microbiol.* **65**, 366–376 (2012).
 52. Vasseur, P., Vallet-Gely, I., Soscia, C., Genin, S. & Filloux, A. The *pel* genes of the *Pseudomonas aeruginosa* PAK strain are involved at early and late stages of biofilm formation. *Microbiol. Read. Engl.* **151**, 985–997 (2005).
 53. Evans, L. R. & Linker, A. Production and characterization of the slime polysaccharide of *Pseudomonas aeruginosa*. *J. Bacteriol.* **116**, 915–924 (1973).
 54. Wozniak, D. J. *et al.* Alginate is not a significant component of the extracellular polysaccharide matrix of PA14 and PAO1 *Pseudomonas aeruginosa* biofilms. *Proc. Natl. Acad. Sci. U. S. A.* **100**, 7907–7912 (2003).
 55. Govan, J. R. & Deretic, V. Microbial pathogenesis in cystic fibrosis: mucoid *Pseudomonas aeruginosa* and *Burkholderia cepacia*. *Microbiol. Rev.* **60**, 539–574 (1996).
 56. Sauer, K. The genomics and proteomics of biofilm formation. *Genome Biol.* **4**, 219 (2003).
 57. Zarnowski, R. *et al.* Novel entries in a fungal biofilm matrix encyclopedia. *mBio* **5**, e01333-1314 (2014).
 58. Reichhardt, C. & Cegelski, L. Solid-State NMR for Bacterial Biofilms. *Mol. Phys.* **112**, 887–894 (2014).
 59. Moscoso, M., García, E. & López, R. Biofilm formation by *Streptococcus pneumoniae*: role of choline, extracellular DNA, and capsular polysaccharide in microbial accretion. *J. Bacteriol.* **188**, 7785–7795 (2006).
 60. Rice, K. C. *et al.* The *cidA* murein hydrolase regulator contributes to DNA release and biofilm development in *Staphylococcus aureus*. *Proc. Natl. Acad. Sci. U. S. A.* **104**, 8113–8118 (2007).

61. Harmsen, M., Lappann, M., Knöchel, S. & Molin, S. Role of extracellular DNA during biofilm formation by *Listeria monocytogenes*. *Appl. Environ. Microbiol.* **76**, 2271–2279 (2010).
62. Mayer, C. *et al.* The role of intermolecular interactions: studies on model systems for bacterial biofilms. *Int. J. Biol. Macromol.* **26**, 3–16 (1999).
63. Allison, D. G. & Sutherland, I. W. The Role of Exopolysaccharides in Adhesion of Freshwater Bacteria. *Microbiology* **133**, 1319–1327 (1987).
64. Watnick, P. I. & Kolter, R. Steps in the development of a *Vibrio cholerae* El Tor biofilm. *Mol. Microbiol.* **34**, 586–595 (1999).
65. Romero, D., Aguilar, C., Losick, R. & Kolter, R. Amyloid fibers provide structural integrity to *Bacillus subtilis* biofilms. *Proc. Natl. Acad. Sci. U. S. A.* **107**, 2230–2234 (2010).
66. Shaw, T., Winston, M., Rupp, C. J., Klapper, I. & Stoodley, P. Commonality of Elastic Relaxation Times in Biofilms. *Phys. Rev. Lett.* **93**, (2004).
67. Romeo, T. Bacterial biofilms. Preface. *Curr. Top. Microbiol. Immunol.* **322**, v (2008).
68. Sauer, K., Camper, A. K., Ehrlich, G. D., Costerton, J. W. & Davies, D. G. *Pseudomonas aeruginosa* displays multiple phenotypes during development as a biofilm. *J. Bacteriol.* **184**, 1140–1154 (2002).
69. Lebeaux, D., Ghigo, J.-M. & Lucet, J.-C. [Implanted medical device-related infections: pathophysiology and prevention]. *Rev. Prat.* **64**, 620–625 (2014).
70. Banerjee, G. & Ray, A. K. The talking language in some major Gram-negative bacteria. *Arch. Microbiol.* **198**, 489–499 (2016).
71. Irie, Y. *et al.* Self-produced exopolysaccharide is a signal that stimulates biofilm formation in *Pseudomonas aeruginosa*. *Proc. Natl. Acad. Sci. U. S. A.* **109**, 20632–20636 (2012).
72. Steinberg, N. & Kolodkin-Gal, I. The Matrix Reloaded: Probing the Extracellular Matrix Synchronizes Bacterial Communities. *J. Bacteriol.* **197**, 2092–2103 (2015).
73. Tseng, B. S. *et al.* A Biofilm Matrix-Associated Protease Inhibitor Protects *Pseudomonas aeruginosa* from Proteolytic Attack. *mBio* **9**, (2018).
74. Pearson, J. P., Feldman, M., Iglewski, B. H. & Prince, A. *Pseudomonas aeruginosa* cell-to-cell signaling is required for virulence in a model of acute pulmonary infection. *Infect. Immun.* **68**, 4331–4334 (2000).
75. Borlee, B. R. *et al.* *Pseudomonas aeruginosa* uses a cyclic-di-GMP-regulated adhesin to reinforce the biofilm extracellular matrix. *Mol. Microbiol.* **75**, 827–842 (2010).
76. Jennings, L. K. *et al.* Pel is a cationic exopolysaccharide that cross-links extracellular DNA in the *Pseudomonas aeruginosa* biofilm matrix. *Proc. Natl. Acad. Sci. U. S. A.* **112**, 11353–11358 (2015).
77. Legoux, R. *et al.* N-acetyl-heparosan lyase of *Escherichia coli* K5: gene cloning and expression. *J. Bacteriol.* **178**, 7260–7264 (1996).
78. Schiller, N. L., Monday, S. R., Boyd, C. M., Keen, N. T. & Ohman, D. E. Characterization of the *Pseudomonas aeruginosa* alginate lyase gene (*algL*): cloning, sequencing, and expression in *Escherichia coli*. *J. Bacteriol.* **175**, 4780–4789 (1993).
79. hughes. Bacterial biofilms and their exopolysaccharides. (1997).
80. Sutherland, I. W. Polysaccharases for microbial exopolysaccharides. *Carbohydr. Polym.* **38**, 319–328 (1999).
81. Kolodkin-Gal, I. *et al.* D-Amino Acids Trigger Biofilm Disassembly. *Science* **328**, 627–629 (2010).

82. Otto, M. Staphylococcal Infections: Mechanisms of Biofilm Maturation and Detachment as Critical Determinants of Pathogenicity. *Annu. Rev. Med.* **64**, 175–188 (2013).
83. Stoodley, P., Boyle, J. D., DeBeer, D. & Lappin-Scott, H. M. Evolving perspectives of biofilm structure. *Biofouling* **14**, 75–90 (1999).
84. Davies, D. G. *et al.* The involvement of cell-to-cell signals in the development of a bacterial biofilm. *Science* **280**, 295–298 (1998).
85. Liu, J. *et al.* Metabolic co-dependence gives rise to collective oscillations within biofilms. *Nature* **523**, 550–554 (2015).
86. Prindle, A. *et al.* Ion channels enable electrical communication in bacterial communities. *Nature* **527**, 59–63 (2015).
87. Sifri, C. D. Healthcare epidemiology: quorum sensing: bacteria talk sense. *Clin. Infect. Dis. Off. Publ. Infect. Dis. Soc. Am.* **47**, 1070–1076 (2008).
88. Lee, D.-Y. D., Prindle, A., Liu, J. & Suel, G. M. SnapShot: Electrochemical Communication in Biofilms. *Cell* **170**, 214–214.e1 (2017).
89. Xavier, J. B. Social interaction in synthetic and natural microbial communities. *Mol. Syst. Biol.* **7**, 483 (2011).
90. Liu, J. *et al.* Coupling between distant biofilms and emergence of nutrient time-sharing. *Science* **356**, 638–642 (2017).
91. Di Pippo, F., Di Gregorio, L., Congestri, R., Tandoi, V. & Rossetti, S. Biofilm growth and control in cooling water industrial systems. *FEMS Microbiol. Ecol.* **94**, (2018).
92. Trueba, A., García, S., Otero, F. M., Vega, L. M. & Madariaga, E. Influence of flow velocity on biofilm growth in a tubular heat exchanger-condenser cooled by seawater. *Biofouling* **31**, 527–534 (2015).
93. Lebeaux, D. & Ghigo, J.-M. Infections associées aux biofilms: Quelles perspectives thérapeutiques issues de la recherche fondamentale ? *médecine/sciences* **28**, 727–739 (2012).
94. Percival, S. L. & Kite, P. Intravascular catheters and biofilm control. *J. Vasc. Access* **8**, 69–80 (2007).
95. Donlan, R. M. Biofilms and device-associated infections. *Emerg. Infect. Dis.* **7**, 277–281 (2001).
96. Daniau, Léon, Blanchard, Bernet & Caillet-Vallet. Enquête nationale de prévalence des infections nosocomiales et des traitements anti-infectieux en établissements de santé, France, mai-juin 2017. (2018).
97. Colomb-Cotinat, Maugat, Berger-Carbonne & Colgnard. Infections associées aux soins, résistance aux antibiotiques et consommation d'antibiotiques : données des réseaux de surveillance Raisin. (2018).
98. Santé Publique. CONSOMMATION D'ANTIBIOTIQUES ET RÉSISTANCE AUX ANTIBIOTIQUES EN FRANCE: UNE INFECTION ÉVITÉE, C'EST UN ANTIBIOTIQUE PRÉSERVÉ ! (2018).
99. Costerton, J. W. Bacterial Biofilms: A Common Cause of Persistent Infections. *Science* **284**, 1318–1322 (1999).
100. Kuwae, T. *et al.* Biofilm grazing in a higher vertebrate: the western sandpiper, *Calidris mauri*. *Ecology* **89**, 599–606 (2008).
101. Singh, R., Paul, D. & Jain, R. K. Biofilms: implications in bioremediation. *Trends Microbiol.* **14**, 389–397 (2006).
102. Odegaard, H. Innovations in wastewater treatment: the moving bed biofilm process.

- Water Sci. Technol. J. Int. Assoc. Water Pollut. Res.* **53**, 17–33 (2006).
103. Wanner & Bauchowitz. Les biofilms sont omniprésents. *EAWAG News* **60** (2006).
104. Mishra, B., Golla, R. M., Lau, K., Lushnikova, T. & Wang, G. Anti-Staphylococcal Biofilm Effects of Human Cathelicidin Peptides. *ACS Med. Chem. Lett.* **7**, 117–121 (2016).
105. Ostrowska, K., Kamysz, W., Dawgul, M. & Różalski, A. Synthetic amphibian peptides and short amino-acids derivatives against planktonic cells and mature biofilm of *Providencia stuartii* clinical strains. *Pol. J. Microbiol.* **63**, 423–431 (2014).
106. Saiman, L. *et al.* Azithromycin in patients with cystic fibrosis chronically infected with *Pseudomonas aeruginosa*: a randomized controlled trial. *JAMA* **290**, 1749–1756 (2003).
107. Abraham, W.-R. Going beyond the Control of Quorum-Sensing to Combat Biofilm Infections. *Antibiot. Basel Switz.* **5**, (2016).
108. Korea, C.-G., Ghigo, J.-M. & Beloin, C. The sweet connection: Solving the riddle of multiple sugar-binding fimbrial adhesins in *Escherichia coli*: Multiple *E. coli* fimbriae form a versatile arsenal of sugar-binding lectins potentially involved in surface-colonisation and tissue tropism. *BioEssays News Rev. Mol. Cell. Dev. Biol.* **33**, 300–311 (2011).
109. Rodrigues, L. R. Inhibition of bacterial adhesion on medical devices. *Adv. Exp. Med. Biol.* **715**, 351–367 (2011).
110. Fey, P. D. Modality of bacterial growth presents unique targets: how do we treat biofilm-mediated infections? *Curr. Opin. Microbiol.* **13**, 610–615 (2010).
111. El-Khatib, M. *et al.* Porin self-association enables cell-to-cell contact in *Providencia stuartii* floating communities. *Proc. Natl. Acad. Sci.* **115**, E2220–E2228 (2018).
112. Cowan, S. W. *et al.* Crystal structures explain functional properties of two *E. coli* porins. *Nature* **358**, 727–733 (1992).
113. Nakae, T. Outer membrane of *Salmonella*. Isolation of protein complex that produces transmembrane channels. *J. Biol. Chem.* **251**, 2176–2178 (1976).
114. Coico, R. Gram staining. *Curr. Protoc. Microbiol.* **Appendix 3**, Appendix 3C (2005).
115. Hobot, J. A., Carlemalm, E., Villiger, W. & Kellenberger, E. Periplasmic gel: new concept resulting from the reinvestigation of bacterial cell envelope ultrastructure by new methods. *J. Bacteriol.* **160**, 143–152 (1984).
116. Beveridge, T. J. & Graham, L. L. Surface layers of bacteria. *Microbiol. Rev.* **55**, 684–705 (1991).
117. Stock, J. B., Rauch, B. & Roseman, S. Periplasmic space in *Salmonella typhimurium* and *Escherichia coli*. *J. Biol. Chem.* **252**, 7850–7861 (1977).
118. Prouvost, A.-F. Rôle du périplasme dans la perception par la bactérie de son environnement. (2008).
119. Koebnik, R., Locher, K. P. & Van Gelder, P. Structure and function of bacterial outer membrane proteins: barrels in a nutshell. *Mol. Microbiol.* **37**, 239–253 (2000).
120. Whitfield, C. & Trent, M. S. Biosynthesis and export of bacterial lipopolysaccharides. *Annu. Rev. Biochem.* **83**, 99–128 (2014).
121. Lång, H. Outer membrane proteins as surface display systems. *Int. J. Med. Microbiol. IJMM* **290**, 579–585 (2000).
122. Jarosławski, S., Duquesne, K., Sturgis, J. N. & Scheuring, S. High-resolution architecture of the outer membrane of the Gram-negative bacteria *Roseobacter denitrificans*. *Mol. Microbiol.* **74**, 1211–1222 (2009).
123. Castón, J. R., Berenguer, J., de Pedro, M. A. & Carrascosa, J. L. S-layer protein from *Thermus thermophilus* HB8 assembles into porin-like structures. *Mol. Microbiol.* **9**, 65–75

- (1993).
124. Akira, S. TLR signaling. *Curr. Top. Microbiol. Immunol.* **311**, 1–16 (2006).
 125. Akira, S. Mammalian Toll-like receptors. *Curr. Opin. Immunol.* **15**, 5–11 (2003).
 126. Akira, S. & Takeda, K. Toll-like receptor signalling. *Nat. Rev. Immunol.* **4**, 499–511 (2004).
 127. Rietschel, E. T. & Brade, H. Bacterial endotoxins. *Sci. Am.* **267**, 54–61 (1992).
 128. Lüderitz, O. *et al.* Lipopolysaccharides: structural principles and biologic activities. *Rev. Infect. Dis.* **6**, 428–431 (1984).
 129. Erridge, C., Bennett-Guerrero, E. & Poxton, I. R. Structure and function of lipopolysaccharides. *Microbes Infect.* **4**, 837–851 (2002).
 130. Tzeng, Y.-L., Datta, A., Kolli, V. K., Carlson, R. W. & Stephens, D. S. Endotoxin of *Neisseria meningitidis* composed only of intact lipid A: inactivation of the meningococcal 3-deoxy-D-manno-octulosonic acid transferase. *J. Bacteriol.* **184**, 2379–2388 (2002).
 131. Alexander, C. & Rietschel, E. T. Bacterial lipopolysaccharides and innate immunity. *J. Endotoxin Res.* **7**, 167–202 (2001).
 132. Gao, J. & Guo, Z. Progress in the synthesis and biological evaluation of lipid A and its derivatives. *Med. Res. Rev.* **38**, 556–601 (2018).
 133. Van Amersfoort, E. S., Van Berkel, T. J. C. & Kuiper, J. Receptors, mediators, and mechanisms involved in bacterial sepsis and septic shock. *Clin. Microbiol. Rev.* **16**, 379–414 (2003).
 134. Hershberger, C. & Binkley, S. B. Chemistry and metabolism of 3-deoxy-D-manno-octulosonic acid. I. Stereochemical determination. *J. Biol. Chem.* **243**, 1578–1584 (1968).
 135. Nikaido, H. & Vaara, M. Molecular basis of bacterial outer membrane permeability. *Microbiol. Rev.* **49**, 1–32 (1985).
 136. Lee, B. *et al.* Heterogeneity of biofilms formed by nonmucoid *Pseudomonas aeruginosa* isolates from patients with cystic fibrosis. *J. Clin. Microbiol.* **43**, 5247–5255 (2005).
 137. Maldonado, R. F., Sá-Correia, I. & Valvano, M. A. Lipopolysaccharide modification in Gram-negative bacteria during chronic infection. *FEMS Microbiol. Rev.* **40**, 480–493 (2016).
 138. Raetz, C. R. H. *et al.* Discovery of new biosynthetic pathways: the lipid A story. *J. Lipid Res.* **50 Suppl**, S103-108 (2009).
 139. Nikaido, H. Molecular basis of bacterial outer membrane permeability revisited. *Microbiol. Mol. Biol. Rev. MMBR* **67**, 593–656 (2003).
 140. Navedryk, E., Garavito, R. M. & Breton, J. The orientation of beta-sheets in porin. A polarized Fourier transform infrared spectroscopic investigation. *Biophys. J.* **53**, 671–676 (1988).
 141. Engel, A., Massalski, A., Schindler, H., Dorset, D. L. & Rosenbusch, J. P. Porin channel triplets merge into single outlets in *Escherichia coli* outer membranes. *Nature* **317**, 643–645 (1985).
 142. Chalcraft, J. P., Engelhardt, H. & Baumeister, W. Structure of the porin from a bacterial stalk. *FEBS Lett.* **211**, 53–58 (1987).
 143. Fernández, C., Hilty, C., Wider, G., Güntert, P. & Wüthrich, K. NMR structure of the integral membrane protein OmpX. *J. Mol. Biol.* **336**, 1211–1221 (2004).
 144. Garavito, R. M., Jenkins, J., Jansonius, J. N., Karlsson, R. & Rosenbusch, J. P. X-ray

- diffraction analysis of matrix porin, an integral membrane protein from *Escherichia coli* outer membranes. *J. Mol. Biol.* **164**, 313–327 (1983).
145. Garavito, R. M. & Rosenbusch, J. P. Three-dimensional crystals of an integral membrane protein: an initial x-ray analysis. *J. Cell Biol.* **86**, 327–329 (1980).
 146. Schirmer, T., Keller, T. A., Wang, Y. F. & Rosenbusch, J. P. Structural basis for sugar translocation through maltoporin channels at 3.1 Å resolution. *Science* **267**, 512–514 (1995).
 147. Forst, D., Welte, W., Wacker, T. & Diederichs, K. Structure of the sucrose-specific porin ScrY from *Salmonella typhimurium* and its complex with sucrose. *Nat. Struct. Biol.* **5**, 37–46 (1998).
 148. Karshikoff, A., Spassov, V., Cowan, S. W., Ladenstein, R. & Schirmer, T. Electrostatic Properties of Two Porin Channels from *Escherichia coli*. *J. Mol. Biol.* **240**, 372–384 (1994).
 149. Nikaido, H. Porins and specific diffusion channels in bacterial outer membranes. *J. Biol. Chem.* **269**, 3905–3908 (1994).
 150. Zachariae, U., Klühspies, T., De, S., Engelhardt, H. & Zeth, K. High resolution crystal structures and molecular dynamics studies reveal substrate binding in the porin Omp32. *J. Biol. Chem.* **281**, 7413–7420 (2006).
 151. Yildiz, O., Vinothkumar, K. R., Goswami, P. & Kühlbrandt, W. Structure of the monomeric outer-membrane porin OmpG in the open and closed conformation. *EMBO J.* **25**, 3702–3713 (2006).
 152. Ye, J. & van den Berg, B. Crystal structure of the bacterial nucleoside transporter Tsx. *EMBO J.* **23**, 3187–3195 (2004).
 153. Zeth, K. & Thein, M. Porins in prokaryotes and eukaryotes: common themes and variations. *Biochem. J.* **431**, 13–22 (2010).
 154. Im, W. & Roux, B. Ion permeation and selectivity of OmpF porin: a theoretical study based on molecular dynamics, Brownian dynamics, and continuum electrodiffusion theory. *J. Mol. Biol.* **322**, 851–869 (2002).
 155. Im, W. & Roux, B. Ions and counterions in a biological channel: a molecular dynamics simulation of OmpF porin from *Escherichia coli* in an explicit membrane with 1 M KCl aqueous salt solution. *J. Mol. Biol.* **319**, 1177–1197 (2002).
 156. Delcour, A. H. Outer membrane permeability and antibiotic resistance. *Biochim. Biophys. Acta BBA - Proteins Proteomics* **1794**, 808–816 (2009).
 157. Alcaraz, A., Nestorovich, E. M., Aguilera-Arzo, M., Aguilera, V. M. & Bezrukov, S. M. Salting out the ionic selectivity of a wide channel: the asymmetry of OmpF. *Biophys. J.* **87**, 943–957 (2004).
 158. Galdiero, S. *et al.* Microbe-host interactions: structure and role of Gram-negative bacterial porins. *Curr. Protein Pept. Sci.* **13**, 843–854 (2012).
 159. Rebière-Huët, J. *et al.* Porins of *Pseudomonas fluorescens* MFO as fibronectin-binding proteins. *FEMS Microbiol. Lett.* **215**, 121–126 (2002).
 160. Akira, S., Uematsu, S. & Takeuchi, O. Pathogen recognition and innate immunity. *Cell* **124**, 783–801 (2006).
 161. Faulstich, M. *et al.* Neutral sphingomyelinase 2 is a key factor for PorB-dependent invasion of *Neisseria gonorrhoeae*. *Cell. Microbiol.* **17**, 241–253 (2015).
 162. Groves, J. T. & Kuriyan, J. Molecular mechanisms in signal transduction at the membrane. *Nat. Struct. Mol. Biol.* **17**, 659–665 (2010).
 163. Housden, N. G. *et al.* Directed epitope delivery across the *Escherichia coli* outer

- membrane through the porin OmpF. *Proc. Natl. Acad. Sci. U. S. A.* **107**, 21412–21417 (2010).
164. Tommassen, J., Overduin, P., Lugtenberg, B. & Bergmans, H. Cloning of *phoE*, the structural gene for the *Escherichia coli* phosphate limitation-inducible outer membrane pore protein. *J. Bacteriol.* **149**, 668–672 (1982).
165. Dedieu, L., Pagès, J.-M. & Bolla, J.-M. Environmental regulation of *Campylobacter jejuni* major outer membrane protein porin expression in *Escherichia coli* monitored by using green fluorescent protein. *Appl. Environ. Microbiol.* **68**, 4209–4215 (2002).
166. Pagès, J.-M. Porines bactériennes et sensibilité aux antibiotiques. *médecine/sciences* **20**, 346–351 (2004).
167. Pagès, J.-M., James, C. E. & Winterhalter, M. The porin and the permeating antibiotic: a selective diffusion barrier in Gram-negative bacteria. *Nat. Rev. Microbiol.* **6**, 893–903 (2008).
168. Fernández, L. & Hancock, R. E. W. Adaptive and mutational resistance: role of porins and efflux pumps in drug resistance. *Clin. Microbiol. Rev.* **25**, 661–681 (2012).
169. Munita, J. M. & Arias, C. A. Mechanisms of Antibiotic Resistance. *Microbiol. Spectr.* **4**, (2016).
170. Jeanteur, D., Lakey, J. H. & Pattus, F. The bacterial porin superfamily: sequence alignment and structure prediction. *Mol. Microbiol.* **5**, 2153–2164 (1991).
171. Dé, E. *et al.* A new mechanism of antibiotic resistance in Enterobacteriaceae induced by a structural modification of the major porin. *Mol. Microbiol.* **41**, 189–198 (2001).
172. Thiolas, A., Bornet, C., Davin-Régli, A., Pagès, J.-M. & Bollet, C. Resistance to imipenem, cefepime, and ceftazidime associated with mutation in Omp36 osmoporin of *Enterobacter aerogenes*. *Biochem. Biophys. Res. Commun.* **317**, 851–856 (2004).
173. Pangon, B. *et al.* In vivo selection of a cephamycin-resistant, porin-deficient mutant of *Klebsiella pneumoniae* producing a TEM-3 beta-lactamase. *J. Infect. Dis.* **159**, 1005–1006 (1989).
174. Martínez-Martínez, L. *et al.* In vivo selection of porin-deficient mutants of *Klebsiella pneumoniae* with increased resistance to cefoxitin and expanded-spectrum-cephalosporins. *Antimicrob. Agents Chemother.* **40**, 342–348 (1996).
175. Doménech-Sánchez, A., Hernández-Allés, S., Martínez-Martínez, L., Benedí, V. J. & Albertí, S. Identification and characterization of a new porin gene of *Klebsiella pneumoniae*: its role in beta-lactam antibiotic resistance. *J. Bacteriol.* **181**, 2726–2732 (1999).
176. Finelli, A., Gallant, C. V., Jarvi, K. & Burrows, L. L. Use of in-biofilm expression technology to identify genes involved in *Pseudomonas aeruginosa* biofilm development. *J. Bacteriol.* **185**, 2700–2710 (2003).
177. Yoon, S. S. *et al.* *Pseudomonas aeruginosa* anaerobic respiration in biofilms: relationships to cystic fibrosis pathogenesis. *Dev. Cell* **3**, 593–603 (2002).
178. Cattelan, N. *et al.* Outer membrane protein OmpQ of *Bordetella bronchiseptica* is required for mature biofilm formation. *Microbiol. Read. Engl.* **162**, 351–363 (2016).
179. Buttiaux, R., Osteux, R., Fresnoy, R. & Moriamez, J. [The characteristic biochemical properties of the genus *Proteus*; desirable inclusion of the *Providencia* in this group]. *Ann. Inst. Pasteur* **87**, 375–386 (1954).
180. Stock, I. & Wiedemann, B. Natural antibiotic susceptibility of *Providencia stuartii*, *P. rettgeri*, *P. alcalifaciens* and *P. rustigianii* strains. *J. Med. Microbiol.* **47**, 629–642 (1998).
181. Chamberland, R. R., McElvania TeKippe, E., Burnham, C.-A. D. & Kennedy, D. J. Renal abscess caused by a *Providencia stuartii* isolate biochemically misidentified as

- Pasteurella. *J. Clin. Microbiol.* **51**, 2775–2777 (2013).
182. Krake, P. R. & Tandon, N. Infective endocarditis due to *Providencia stuartii*. *South. Med. J.* **97**, 1022–1023 (2004).
183. Simon, C. *et al.* Images in cardiovascular medicine. Bacterial pericarditis due to *Providencia stuartii*: an atypical case of relapsing pericarditis. *Circulation* **122**, e401–403 (2010).
184. Unverdi, S. *et al.* Peritonitis due to *Providencia stuartii*. *Perit. Dial. Int. J. Int. Soc. Perit. Dial.* **31**, 216–217 (2011).
185. Warren, J. W. *Providencia stuartii*: a common cause of antibiotic-resistant bacteriuria in patients with long-term indwelling catheters. *Rev. Infect. Dis.* **8**, 61–67 (1986).
186. Tumbarello, M. ESBL-producing multidrug-resistant *Providencia stuartii* infections in a university hospital. *J. Antimicrob. Chemother.* **53**, 277–282 (2004).
187. Aubert, D., Naas, T., Lartigue, M.-F. & Nordmann, P. Novel genetic structure associated with an extended-spectrum beta-lactamase bla_{VEB} gene in a *Providencia stuartii* clinical isolate from Algeria. *Antimicrob. Agents Chemother.* **49**, 3590–3592 (2005).
188. De Vecchi, E. *et al.* Aetiology and antibiotic resistance patterns of urinary tract infections in the elderly: a 6-month study. *J. Med. Microbiol.* **62**, 859–863 (2013).
189. Leitner, L. *et al.* Bacteriophages for treating urinary tract infections in patients undergoing transurethral resection of the prostate: a randomized, placebo-controlled, double-blind clinical trial. *BMC Urol.* **17**, 90 (2017).
190. Dandekar, A. A., Chugani, S. & Greenberg, E. P. Bacterial quorum sensing and metabolic incentives to cooperate. *Science* **338**, 264–266 (2012).
191. Jacobsen, S. M., Stickler, D. J., Mobley, H. L. T. & Shirliff, M. E. Complicated Catheter-Associated Urinary Tract Infections Due to *Escherichia coli* and *Proteus mirabilis*. *Clin. Microbiol. Rev.* **21**, 26–59 (2008).
192. Stickler, D. J. Bacterial biofilms in patients with indwelling urinary catheters. *Nat. Clin. Pract. Urol.* **5**, 598–608 (2008).
193. Jones, G. L., Muller, C. T., O'Reilly, M. & Stickler, D. J. Effect of triclosan on the development of bacterial biofilms by urinary tract pathogens on urinary catheters. *J. Antimicrob. Chemother.* **57**, 266–272 (2006).
194. Stickler, D. J. Susceptibility of antibiotic-resistant Gram-negative bacteria to biocides: a perspective from the study of catheter biofilms. *J. Appl. Microbiol.* **92** Suppl, 163S–70S (2002).
195. Stickler, D. J. & Morgan, S. D. Modulation of crystalline *Proteus mirabilis* biofilm development on urinary catheters. *J. Med. Microbiol.* **55**, 489–494 (2006).
196. Tran, Q.-T. *et al.* Implication of Porins in β -Lactam Resistance of *Providencia stuartii*. *J. Biol. Chem.* **285**, 32273–32281 (2010).
197. Schindler, H. & Rosenbusch, J. P. Matrix protein from *Escherichia coli* outer membranes forms voltage-controlled channels in lipid bilayers. *Proc. Natl. Acad. Sci. U. S. A.* **75**, 3751–3755 (1978).
198. Song, W. *et al.* Understanding Voltage Gating of *Providencia stuartii* Porins at Atomic Level. *PLOS Comput. Biol.* **11**, e1004255 (2015).
199. Prilipov, A., Phale, P. S., Gelder, P., Rosenbusch, J. P. & Koebnik, R. Coupling site-directed mutagenesis with high-level expression: large scale production of mutant porins from *E. coli*. *FEMS Microbiol. Lett.* **163**, 65–72 (1998).
200. Hajjar, E. *et al.* Bridging timescales and length scales: from macroscopic flux to the

- molecular mechanism of antibiotic diffusion through porins. *Biophys. J.* **98**, 569–575 (2010).
201. Nestorovich, E. M., Danelon, C., Winterhalter, M. & Bezrukov, S. M. Designed to penetrate: time-resolved interaction of single antibiotic molecules with bacterial pores. *Proc. Natl. Acad. Sci. U. S. A.* **99**, 9789–9794 (2002).
202. Danelon, C., Suenaga, A., Winterhalter, M. & Yamato, I. Molecular origin of the cation selectivity in OmpF porin: single channel conductances vs. free energy calculation. *Biophys. Chem.* **104**, 591–603 (2003).
203. Bajaj, H. *et al.* Antibiotic Uptake through Membrane Channels: Role of *Providencia stuartii* OmpPst1 Porin in Carbapenem Resistance. *Biochemistry (Mosc.)* **51**, 10244–10249 (2012).
204. El Khatib, M. *et al.* *Providencia stuartii* form biofilms and floating communities of cells that display high resistance to environmental insults. *PLOS ONE* **12**, e0174213 (2017).
205. Uversky, V. N. & Fink, A. L. Conformational constraints for amyloid fibrillation: the importance of being unfolded. *Biochim. Biophys. Acta* **1698**, 131–153 (2004).
206. Kyle, R. A. Amyloidosis: a convoluted story. *Br. J. Haematol.* **114**, 529–538 (2001).
207. Sawaya, M. R. *et al.* Atomic structures of amyloid cross-beta spines reveal varied steric zippers. *Nature* **447**, 453–457 (2007).
208. Knowles, T. P. J., Vendruscolo, M. & Dobson, C. M. The amyloid state and its association with protein misfolding diseases. *Nat. Rev. Mol. Cell Biol.* **15**, 384–396 (2014).
209. Pulawski, W., Ghoshdastider, U., Andrisano, V. & Filipek, S. Ubiquitous Amyloids. *Appl. Biochem. Biotechnol.* **166**, 1626–1643 (2012).
210. Toyama, B. H. & Weissman, J. S. Amyloid structure: conformational diversity and consequences. *Annu. Rev. Biochem.* **80**, 557–585 (2011).
211. Lorenz, T. C. Polymerase chain reaction: basic protocol plus troubleshooting and optimization strategies. *J. Vis. Exp. JoVE* e3998 (2012). doi:10.3791/3998
212. Chien, A., Edgar, D. B. & Trela, J. M. Deoxyribonucleic acid polymerase from the extreme thermophile *Thermus aquaticus*. *J. Bacteriol.* **127**, 1550–1557 (1976).
213. Abu Al-Soud, W. & Rådström, P. Capacity of nine thermostable DNA polymerases To mediate DNA amplification in the presence of PCR-inhibiting samples. *Appl. Environ. Microbiol.* **64**, 3748–3753 (1998).
214. VanGuilder, H. D., Vrana, K. E. & Freeman, W. M. Twenty-five years of quantitative PCR for gene expression analysis. *BioTechniques* **44**, 619–626 (2008).
215. Bustin, S. & Nolan, T. Talking the talk, but not walking the walk: RT-qPCR as a paradigm for the lack of reproducibility in molecular research. *Eur. J. Clin. Invest.* **47**, 756–774 (2017).
216. Arya, M. *et al.* Basic principles of real-time quantitative PCR. *Expert Rev. Mol. Diagn.* **5**, 209–219 (2005).
217. Page, R. B. & Stromberg, A. J. Linear methods for analysis and quality control of relative expression ratios from quantitative real-time polymerase chain reaction experiments. *ScientificWorldJournal* **11**, 1383–1393 (2011).
218. Taylor, S. C. & Mrkusich, E. M. The state of RT-quantitative PCR: firsthand observations of implementation of minimum information for the publication of quantitative real-time PCR experiments (MIQE). *J. Mol. Microbiol. Biotechnol.* **24**, 46–52 (2014).
219. Dheda, K. *et al.* Validation of housekeeping genes for normalizing RNA expression in real-time PCR. *BioTechniques* **37**, 112–114, 116, 118–119 (2004).
220. Bustin, S. A. *et al.* The MIQE guidelines: minimum information for publication of

- quantitative real-time PCR experiments. *Clin. Chem.* **55**, 611–622 (2009).
221. Huang, T., Böhlenius, H., Eriksson, S., Parcy, F. & Nilsson, O. The mRNA of the Arabidopsis gene FT moves from leaf to shoot apex and induces flowering. *Science* **309**, 1694–1696 (2005).
222. Wakefield, A. J. *et al.* Ileal-lymphoid-nodular hyperplasia, non-specific colitis, and pervasive developmental disorder in children. *Lancet Lond. Engl.* **351**, 637–641 (1998).
223. Bustin, S. A. & Nolan, T. Pitfalls of quantitative real-time reverse-transcription polymerase chain reaction. *J. Biomol. Tech. JBT* **15**, 155–166 (2004).
224. Cronin, M. *et al.* Universal RNA reference materials for gene expression. *Clin. Chem.* **50**, 1464–1471 (2004).
225. Ståhlberg, A., Kubista, M. & Pfaffl, M. Comparison of reverse transcriptases in gene expression analysis. *Clin. Chem.* **50**, 1678–1680 (2004).
226. Gutierrez, L. *et al.* The lack of a systematic validation of reference genes: a serious pitfall undervalued in reverse transcription-polymerase chain reaction (RT-PCR) analysis in plants. *Plant Biotechnol. J.* **6**, 609–618 (2008).
227. Huggett, J., Dheda, K., Bustin, S. & Zumla, A. Real-time RT-PCR normalisation; strategies and considerations. *Genes Immun.* **6**, 279–284 (2005).
228. Vandesompele, J. *et al.* Accurate normalization of real-time quantitative RT-PCR data by geometric averaging of multiple internal control genes. *Genome Biol.* **3**, RESEARCH0034 (2002).
229. Taylor, S., Wakem, M., Dijkman, G., Alsarraj, M. & Nguyen, M. A practical approach to RT-qPCR-Publishing data that conform to the MIQE guidelines. *Methods San Diego Calif* **50**, S1-5 (2010).
230. Barber, R. D., Harmer, D. W., Coleman, R. A. & Clark, B. J. GAPDH as a housekeeping gene: analysis of GAPDH mRNA expression in a panel of 72 human tissues. *Physiol. Genomics* **21**, 389–395 (2005).
231. Schmittgen, T. D. & Zakrajsek, B. A. Effect of experimental treatment on housekeeping gene expression: validation by real-time, quantitative RT-PCR. *J. Biochem. Biophys. Methods* **46**, 69–81 (2000).
232. Thellin, O. *et al.* Housekeeping genes as internal standards: use and limits. *J. Biotechnol.* **75**, 291–295 (1999).
233. Tricarico, C. *et al.* Quantitative real-time reverse transcription polymerase chain reaction: normalization to rRNA or single housekeeping genes is inappropriate for human tissue biopsies. *Anal. Biochem.* **309**, 293–300 (2002).
234. Bustin, S. A. Quantification of mRNA using real-time reverse transcription PCR (RT-PCR): trends and problems. *J. Mol. Endocrinol.* **29**, 23–39 (2002).
235. Koh, C. J. & Atala, A. Therapeutic cloning and tissue engineering. *Curr. Top. Dev. Biol.* **60**, 1–15 (2004).
236. Mummery, C. L. & Roelen, B. A. J. Stem cells: Cloning human embryos. *Nature* **498**, 174–175 (2013).
237. Ashwini, M., Murugan, S. B., Balamurugan, S. & Sathishkumar, R. [Advances in Molecular Cloning]. *Mol. Biol. (Mosk.)* **50**, 3–9 (2016).
238. Tolmachov, O. Designing plasmid vectors. *Methods Mol. Biol. Clifton NJ* **542**, 117–129 (2009).
239. Qi, H., Lu, H., Qiu, H.-J., Petrenko, V. & Liu, A. Phagemid vectors for phage display: properties, characteristics and construction. *J. Mol. Biol.* **417**, 129–143 (2012).

240. Chauthaiwale, V. M., Therwath, A. & Deshpande, V. V. Bacteriophage lambda as a cloning vector. *Microbiol. Rev.* **56**, 577–591 (1992).
241. Maruyama, I. N. & Brenner, S. A selective lambda phage cloning vector with automatic excision of the insert in a plasmid. *Gene* **120**, 135–141 (1992).
242. Collins, J. & Hohn, B. Cosmids: a type of plasmid gene-cloning vector that is packageable in vitro in bacteriophage lambda heads. 1978. *Biotechnol. Read. Mass* **24**, 193–197 (1992).
243. Chen, C., Zhao, X., Jin, Y., Zhao, Z. K. & Suh, J.-W. Rapid construction of a Bacterial Artificial Chromosomal (BAC) expression vector using designer DNA fragments. *Plasmid* **76**, 79–86 (2014).
244. Emanuel, S. L., Cook, J. R., O’Rear, J., Rothstein, R. & Pestka, S. New vectors for manipulation and selection of functional yeast artificial chromosomes (YACs) containing human DNA inserts. *Gene* **155**, 167–174 (1995).
245. Kakeda, M. *et al.* Human artificial chromosome (HAC) vector provides long-term therapeutic transgene expression in normal human primary fibroblasts. *Gene Ther.* **12**, 852–856 (2005).
246. Cohen, S. N., Chang, A. C., Boyer, H. W. & Helling, R. B. Construction of biologically functional bacterial plasmids in vitro. 1973. *Biotechnol. Read. Mass* **24**, 188–192 (1992).
247. Danna, K. & Nathans, D. Specific cleavage of simian virus 40 DNA by restriction endonuclease of *Hemophilus influenzae*. *Proc. Natl. Acad. Sci. U. S. A.* **68**, 2913–2917 (1971).
248. Gibson, D. G. *et al.* Enzymatic assembly of DNA molecules up to several hundred kilobases. *Nat. Methods* **6**, 343–345 (2009).
249. Grewer, C., Gameiro, A., Mager, T. & Fendler, K. Electrophysiological characterization of membrane transport proteins. *Annu. Rev. Biophys.* **42**, 95–120 (2013).
250. Coleman, J. L. J., Ngo, T. & Smith, N. J. The G protein-coupled receptor N-terminus and receptor signalling: N-terminus a new era. *Cell. Signal.* **33**, 1–9 (2017).
251. Foster, T. J., Geoghegan, J. A., Ganesh, V. K. & Höök, M. Adhesion, invasion and evasion: the many functions of the surface proteins of *Staphylococcus aureus*. *Nat. Rev. Microbiol.* **12**, 49–62 (2014).
252. Los, D. A. & Murata, N. Regulation of enzymatic activity and gene expression by membrane fluidity. *Sci. STKE Signal Transduct. Knowl. Environ.* **2000**, pe1 (2000).
253. Wallin, E. & Heijne, G. V. Genome-wide analysis of integral membrane proteins from eubacterial, archaean, and eukaryotic organisms. *Protein Sci.* **7**, 1029–1038 (2008).
254. Bakheet, T. M. & Doig, A. J. Properties and identification of human protein drug targets. *Bioinforma. Oxf. Engl.* **25**, 451–457 (2009).
255. Yildirim, M. A., Goh, K.-I., Cusick, M. E., Barabási, A.-L. & Vidal, M. Drug-target network. *Nat. Biotechnol.* **25**, 1119–1126 (2007).
256. Fagerberg, L., Jonasson, K., von Heijne, G., Uhlén, M. & Berglund, L. Prediction of the human membrane proteome. *Proteomics* **10**, 1141–1149 (2010).
257. Babcock, J. J. & Li, M. Deorphanizing the human transmembrane genome: A landscape of uncharacterized membrane proteins. *Acta Pharmacol. Sin.* **35**, 11–23 (2014).
258. Seddon, A. M., Curnow, P. & Booth, P. J. Membrane proteins, lipids and detergents: not just a soap opera. *Biochim. Biophys. Acta* **1666**, 105–117 (2004).
259. Linke, D. Detergents: an overview. *Methods Enzymol.* **463**, 603–617 (2009).

260. Allen, T. M., Romans, A. Y., Kercret, H. & Segrest, J. P. Detergent removal during membrane reconstitution. *Biochim. Biophys. Acta* **601**, 328–342 (1980).
261. Daraee, H., Etemadi, A., Kouhi, M., Alimirzalu, S. & Akbarzadeh, A. Application of liposomes in medicine and drug delivery. *Artif. Cells Nanomedicine Biotechnol.* **44**, 381–391 (2016).
262. Rigaud, J. L., Pitard, B. & Levy, D. Reconstitution of membrane proteins into liposomes: application to energy-transducing membrane proteins. *Biochim. Biophys. Acta* **1231**, 223–246 (1995).
263. Klein, R. A. The detection of oxidation in liposome preparations. *Biochim. Biophys. Acta* **210**, 486–489 (1970).
264. Tsai, F.-C., Stuhmann, B. & Koenderink, G. H. Encapsulation of active cytoskeletal protein networks in cell-sized liposomes. *Langmuir ACS J. Surf. Colloids* **27**, 10061–10071 (2011).
265. Colletier, J.-P., Chaize, B., Winterhalter, M. & Fournier, D. Protein encapsulation in liposomes: efficiency depends on interactions between protein and phospholipid bilayer. *BMC Biotechnol.* **2**, 9 (2002).
266. Bloomfield, V. A. Quasi-Elastic Light Scattering Applications in Biochemistry and Biology. *Annu. Rev. Biophys. Bioeng.* **10**, 421–450 (1981).
267. Lorber, B., Fischer, F., Bailly, M., Roy, H. & Kern, D. Protein analysis by dynamic light scattering: Methods and techniques for students. *Biochem. Mol. Biol. Educ.* **40**, 372–382 (2012).
268. Mainard, M. & Jacob, D. Comprendre. La mesure de taille de nanoparticules par diffusion dynamique de la lumière. *Photoniques* 40–44 (2016). doi:10.1051/photon/20168340
269. Renz, M. Fluorescence microscopy-a historical and technical perspective. *Cytom. Part J. Int. Soc. Anal. Cytol.* **83**, 767–779 (2013).
270. Zernike, F. How I discovered phase contrast. *Science* **121**, 345–349 (1955).
271. Bozzola, J. J. Conventional specimen preparation techniques for scanning electron microscopy of biological specimens. *Methods Mol. Biol. Clifton NJ* **1117**, 133–150 (2014).
272. Paddock, S. W. & Eliceiri, K. W. Laser scanning confocal microscopy: history, applications, and related optical sectioning techniques. *Methods Mol. Biol. Clifton NJ* **1075**, 9–47 (2014).
273. Yashiro, W. Hard X-ray imaging microscopy with self-imaging phenomenon. *Microsc. Oxf. Engl.* **67**, 303–316 (2018).
274. Piontek, M. C. & Roos, W. H. Atomic Force Microscopy: An Introduction. *Methods Mol. Biol. Clifton NJ* **1665**, 243–258 (2018).
275. Abbe, E. Beiträge zur Theorie des Mikroskops und der mikroskopischen Wahrnehmung: I. Die Construction von Mikroskopen auf Grund der Theorie. *Arch. Für Mikrosk. Anat.* **9**, 413–418 (1873).
276. Shimomura, O., Johnson, F. H. & Saiga, Y. Extraction, purification and properties of aequorin, a bioluminescent protein from the luminous hydromedusan, Aequorea. *J. Cell. Comp. Physiol.* **59**, 223–239 (1962).
277. Hoffman, R. M. Strategies for In Vivo Imaging Using Fluorescent Proteins. *J. Cell. Biochem.* **118**, 2571–2580 (2017).
278. Jablonski, A. Efficiency of Anti-Stokes Fluorescence in Dyes. *Nature* **131**, 839–840 (1933).
279. Shampo, M. A. & Kyle, R. A. Ernst Ruska--inventor of the electron microscope. *Mayo*

Clin. Proc. **72**, 148 (1997).

280. Harris, J. R. Transmission electron microscopy in molecular structural biology: A historical survey. *Arch. Biochem. Biophys.* **581**, 3–18 (2015).
281. Fischer, E. R., Hansen, B. T., Nair, V., Hoyt, F. H. & Dorward, D. W. Scanning electron microscopy. *Curr. Protoc. Microbiol.* **Chapter 2**, Unit 2B.2. (2012).
282. McGregor, J. E., Staniewicz, L. T. L., Guthrie Neé Kirk, S. E. & Donald, A. M. Environmental scanning electron microscopy in cell biology. *Methods Mol. Biol. Clifton NJ* **931**, 493–516 (2013).
283. Prins, F. A., Velde, I. C. & de Heer, E. Reflection contrast microscopy: The bridge between light and electron microscopy. *Methods Mol. Biol. Clifton NJ* **319**, 363–401 (2006).
284. Miao, null & Sayre, null. On possible extensions of X-ray crystallography through diffraction-pattern oversampling. *Acta Crystallogr. A* **56 (Pt 6)**, 596–605 (2000).
285. Miao, J., Ishikawa, T., Robinson, I. K. & Murnane, M. M. Beyond crystallography: diffractive imaging using coherent x-ray light sources. *Science* **348**, 530–535 (2015).
286. Seibert, M. M. *et al.* Single mimivirus particles intercepted and imaged with an X-ray laser. *Nature* **470**, 78–81 (2011).
287. Dumetz, A. C., Chockla, A. M., Kaler, E. W. & Lenhoff, A. M. Protein phase behavior in aqueous solutions: crystallization, liquid-liquid phase separation, gels, and aggregates. *Biophys. J.* **94**, 570–583 (2008).
288. McPherson, A. Crystallization of proteins from polyethylene glycol. *J. Biol. Chem.* **251**, 6300–6303 (1976).
289. Faham, S. & Bowie, J. U. Bicelle crystallization: a new method for crystallizing membrane proteins yields a monomeric bacteriorhodopsin structure. *J. Mol. Biol.* **316**, 1–6 (2002).
290. Landau, E. M. & Rosenbusch, J. P. Lipidic cubic phases: a novel concept for the crystallization of membrane proteins. *Proc. Natl. Acad. Sci. U. S. A.* **93**, 14532–14535 (1996).
291. Powell, H. R. X-ray data processing. *Biosci. Rep.* **37**, (2017).
292. Blundell, T. L & Johnson, L. N. Protein Crystallography. (1976).
293. Weiss, M. S. Global indicators of X-ray data quality. (2001).
294. Diederichs, K. & Karplus, P. A. Improved R-factors for diffraction data analysis in macromolecular crystallography. *Nat. Struct. Biol.* **4**, 269–275 (1997).
295. Rahman, N. A. A course in theoretical statistics; for sixth forms, technical colleges, colleges of education, universities. (1968).
296. Taylor, G. The phase problem. *Acta Crystallogr. D Biol. Crystallogr.* **59**, 1881–1890 (2003).
297. Rose, J. P. & Wang, B.-C. SAD phasing: History, current impact and future opportunities. *Arch. Biochem. Biophys.* **602**, 80–94 (2016).
298. Ogata, C. M. MAD phasing grows up. *Nat. Struct. Biol.* **5 Suppl**, 638–640 (1998).
299. Ke, H. [25] Overview of isomorphous replacement phasing. *Methods Enzymol.* **276**, 448–461 (1997).
300. Abergel, C. Molecular replacement: tricks and treats. *Acta Crystallogr. D Biol. Crystallogr.* **69**, 2167–2173 (2013).
301. Richardson, J. S., Prisant, M. G. & Richardson, D. C. Crystallographic model validation: from diagnosis to healing. *Curr. Opin. Struct. Biol.* **23**, 707–714 (2013).
302. Ramachandran, G. N. & Sasisekharan, V. Conformation of polypeptides and proteins. *Adv. Protein Chem.* **23**, 283–438 (1968).

303. Morris, A. L., MacArthur, M. W., Hutchinson, E. G. & Thornton, J. M. Stereochemical quality of protein structure coordinates. *Proteins* **12**, 345–364 (1992).
304. Datsenko, K. A. & Wanner, B. L. One-step inactivation of chromosomal genes in *Escherichia coli* K-12 using PCR products. *Proc. Natl. Acad. Sci. U. S. A.* **97**, 6640–6645 (2000).
305. R. Novy & B. Morris. Use of glucose to control basal expression in the pET System. (2001).
306. Dubendorff, J. W. & Studier, F. W. Creation of a T7 autogene. Cloning and expression of the gene for bacteriophage T7 RNA polymerase under control of its cognate promoter. *J. Mol. Biol.* **219**, 61–68 (1991).
307. Rocha, D. J. P., Santos, C. S. & Pacheco, L. G. C. Bacterial reference genes for gene expression studies by RT-qPCR: survey and analysis. *Antonie Van Leeuwenhoek* **108**, 685–693 (2015).
308. Johnson, G., Nour, A. A., Nolan, T., Huggett, J. & Bustin, S. Minimum information necessary for quantitative real-time PCR experiments. *Methods Mol. Biol. Clifton NJ* **1160**, 5–17 (2014).
309. de Jong, I. G., Beilharz, K., Kuipers, O. P. & Veening, J.-W. Live Cell Imaging of *Bacillus subtilis* and *Streptococcus pneumoniae* using Automated Time-lapse Microscopy. *J. Vis. Exp.* (2011). doi:10.3791/3145
310. Scarff, C. A., Fuller, M. J. G., Thompson, R. F. & Iadaza, M. G. Variations on Negative Stain Electron Microscopy Methods: Tools for Tackling Challenging Systems. *J. Vis. Exp.* 57199 (2018). doi:10.3791/57199
311. Hempelmann, E. & Krafts, K. The mechanism of silver staining of proteins separated by SDS polyacrylamide gel electrophoresis. *Biotech. Histochem.* **92**, 79–85 (2017).
312. Kabsch, W. Automatic processing of rotation diffraction data from crystals of initially unknown symmetry and cell constants. *J. Appl. Crystallogr.* **26**, 795–800 (1993).
313. McCoy, A. J. *et al.* Phaser crystallographic software. *J. Appl. Crystallogr.* **40**, 658–674 (2007).
314. Emsley, P. & Cowtan, K. Coot: model-building tools for molecular graphics. *Acta Crystallogr. D Biol. Crystallogr.* **60**, 2126–2132 (2004).
315. Murshudov, G. N. *et al.* REFMAC5 for the refinement of macromolecular crystal structures. *Acta Crystallogr. D Biol. Crystallogr.* **67**, 355–367 (2011).
316. Adams, P. D. *et al.* PHENIX: a comprehensive Python-based system for macromolecular structure solution. *Acta Crystallogr. D Biol. Crystallogr.* **66**, 213–221 (2010).
317. Réseau d’alerte, d’investigation et de surveillance des infections nosocomiales (Raisin). Enquête nationale de prévalence des infections nosocomiales et des traitements anti-infectieux en établissements de santé, France, mai-juin 2012. (2013).
318. Stickler, D. J. Bacterial biofilms and the encrustation of urethral catheters. *Biofouling* **9**, 293–305 (1996).
319. Nikaido, H. Multidrug Resistance in Bacteria. *Annu. Rev. Biochem.* **78**, 119–146 (2009).
320. Davin-Regli, A. *et al.* Membrane permeability and regulation of drug ‘influx and efflux’ in enterobacterial pathogens. *Curr. Drug Targets* **9**, 750–759 (2008).
321. Sauer, K. & Camper, A. K. Characterization of phenotypic changes in *Pseudomonas putida* in response to surface-associated growth. *J. Bacteriol.* **183**, 6579–6589 (2001).

322. Whiteley, M. *et al.* Gene expression in *Pseudomonas aeruginosa* biofilms. *Nature* **413**, 860–864 (2001).
323. Hughes, M. P. *et al.* Atomic structures of low-complexity protein segments reveal kinked β sheets that assemble networks. *Science* **359**, 698–701 (2018).
324. McCrate, O. A., Zhou, X., Reichhardt, C. & Cegelski, L. Sum of the parts: composition and architecture of the bacterial extracellular matrix. *J. Mol. Biol.* **425**, 4286–4294 (2013).
325. Reichhardt, C., Fong, J. C. N., Yildiz, F. & Cegelski, L. Characterization of the *Vibrio cholerae* extracellular matrix: a top-down solid-state NMR approach. *Biochim. Biophys. Acta* **1848**, 378–383 (2015).
326. Mohammed, M. M. A., Pettersen, V. K., Nerland, A. H., Wiker, H. G. & Bakken, V. Quantitative proteomic analysis of extracellular matrix extracted from mono- and dual-species biofilms of *Fusobacterium nucleatum* and *Porphyromonas gingivalis*. *Anaerobe* **44**, 133–142 (2017).
327. Khoury, A. E., Lam, K., Ellis, B. & Costerton, J. W. Prevention and control of bacterial infections associated with medical devices. *ASAIO J. Am. Soc. Artif. Intern. Organs* **1992** **38**, M174-178 (1992).
328. Koo, H., Allan, R. N., Howlin, R. P., Stoodley, P. & Hall-Stoodley, L. Targeting microbial biofilms: current and prospective therapeutic strategies. *Nat. Rev. Microbiol.* **15**, 740–755 (2017).
329. Sutherland, I. W. Biofilm exopolysaccharides: a strong and sticky framework. *Microbiology* **147**, 3–9 (2001).
330. Blair, J. M. A., Richmond, G. E. & Piddock, L. J. V. Multidrug efflux pumps in Gram-negative bacteria and their role in antibiotic resistance. *Future Microbiol.* **9**, 1165–1177 (2014).
331. Okusu, H., Ma, D. & Nikaido, H. AcrAB efflux pump plays a major role in the antibiotic resistance phenotype of *Escherichia coli* multiple-antibiotic-resistance (Mar) mutants. *J. Bacteriol.* **178**, 306–308 (1996).
332. Li, X. Z., Livermore, D. M. & Nikaido, H. Role of efflux pump(s) in intrinsic resistance of *Pseudomonas aeruginosa*: resistance to tetracycline, chloramphenicol, and norfloxacin. *Antimicrob. Agents Chemother.* **38**, 1732–1741 (1994).
333. Dufour, N. & Debarbieux, L. La phagothérapie: Une arme crédible face à l'antibiorésistance. *médecine/sciences* **33**, 410–416 (2017).
334. Nobrega, F. L., Costa, A. R., Kluskens, L. D. & Azeredo, J. Revisiting phage therapy: new applications for old resources. *Trends Microbiol.* **23**, 185–191 (2015).
335. Pires, D. P., Oliveira, H., Melo, L. D. R., Sillankorva, S. & Azeredo, J. Bacteriophage-encoded depolymerases: their diversity and biotechnological applications. *Appl. Microbiol. Biotechnol.* **100**, 2141–2151 (2016).
336. Stewart, P. S. Mechanisms of antibiotic resistance in bacterial biofilms. *Int. J. Med. Microbiol. IJMM* **292**, 107–113 (2002).
337. D'Herelle, F. Sur un microbe invisible antagoniste des bacilles dysentériques. (1917).
338. Ravat, F., Jault, P. & Gabard, J. Bactériophages et phagothérapie: utilisation de virus naturels pour traiter les infections bactériennes. *Ann. Burns Fire Disasters* **28**, 13–20 (2015).
339. ANSM. Phagothérapie: L'ANSM annonce la création d'un comité scientifique spécialisé temporaire (CSST) intitulé 'Phagothérapie – Retour d'expérience et perspectives'. (2019). Available at: <https://ansm.sante.fr/S-informer/Points-d-information-Points-d->

information/Phagothérapie-L-ANSM-annonce-la-creation-d-un-comite-scientifique-specialise-temporaire-CSST-intitule-Phagothérapie-Retour-d-experience-et-perspectives.

340. Koskella, B. & Brockhurst, M. A. Bacteria-phage coevolution as a driver of ecological and evolutionary processes in microbial communities. *FEMS Microbiol. Rev.* **38**, 916–931 (2014).
341. Levin, B. R. & Bull, J. J. Population and evolutionary dynamics of phage therapy. *Nat. Rev. Microbiol.* **2**, 166–173 (2004).
342. Weitz, J. S. *et al.* Phage-bacteria infection networks. *Trends Microbiol.* **21**, 82–91 (2013).
343. Nadell, C. D., Ricaurte, D., Yan, J., Drescher, K. & Bassler, B. L. Flow environment and matrix structure interact to determine spatial competition in *Pseudomonas aeruginosa* biofilms. *eLife* **6**, (2017).
344. Simmons, M., Bond, M. C., Drescher, K., Bucci, V. & Nadell, C. D. *Evolutionary dynamics of phage resistance in bacterial biofilms*. (Microbiology, 2019). doi:10.1101/552265
345. Sutherland, I. W., Hughes, K. A., Skillman, L. C. & Tait, K. The interaction of phage and biofilms. *FEMS Microbiol. Lett.* **232**, 1–6 (2004).
346. Azeredo, J. & Sutherland, I. W. The use of phages for the removal of infectious biofilms. *Curr. Pharm. Biotechnol.* **9**, 261–266 (2008).

VIII – Annexes

RESEARCH ARTICLE

Providencia stuartii form biofilms and floating communities of cells that display high resistance to environmental insults

Mariam El Khatib¹, Que-Tien Tran², Chady Nasrallah^{1*}, Julie Lopes¹, Jean-Michel Bolla³, Michel Vivaudou¹, Jean-Marie Pagès³, Jacques-Philippe Colletier^{1*}

1 Institut de Biologie Structurale, Université Grenoble Alpes – Commissariat à l'Énergie Atomique – Centre National de la Recherche Scientifique, Grenoble, France, **2** School of Biophysics, Jacobs University of Bremen, Bremen, Germany, **3** Équipe Transporteurs Membranaires, Chimiorésistance et Drug-Design, Université Aix-Marseille – Institut de Recherche Biomédicale des Armées, Marseille, France

* Current address: Department of Neuroscience, Institut de Génomique Fonctionnelle, Montpellier, France
* colletier@ibs.fr



OPEN ACCESS

Citation: El Khatib M, Tran Q-T, Nasrallah C, Lopes J, Bolla J-M, Vivaudou M, et al. (2017) *Providencia stuartii* form biofilms and floating communities of cells that display high resistance to environmental insults. PLoS ONE 12(3): e0174213. <https://doi.org/10.1371/journal.pone.0174213>

Editor: Surajit Das, National Institute of Technology Rourkela, INDIA

Received: November 22, 2016

Accepted: March 6, 2017

Published: March 23, 2017

Copyright: © 2017 El Khatib et al. This is an open access article distributed under the terms of the [Creative Commons Attribution License](https://creativecommons.org/licenses/by/4.0/), which permits unrestricted use, distribution, and reproduction in any medium, provided the original author and source are credited.

Data Availability Statement: All relevant data are within the paper and its Supporting Information files.

Funding: This work used the platforms of the Grenoble Instruct Center (ISBG: UMS 3518 CNRS-CEA-UGA-EMBL; <http://www.isbg.fr>) with support from GRAL (ANR-10-LABX-49-01; <http://www.labex-gral.fr>) within the Grenoble Partnership for Structural Biology (PSB). Financial support by the Agence Nationale de la Recherche (ANR-15-CE18-0005-02;

Abstract

Biofilms are organized communities of bacterial cells that are responsible for the majority of human chronic bacterial infections. *Providencia stuartii* is a Gram-negative biofilm-forming bacterium involved in high incidence of urinary tract infections in catheterized patients. Yet, the structuration of these biofilms, and their resistance to environmental insults remain poorly understood. Here, we report on planktonic cell growth and biofilm formation by *P. stuartii*, in conditions that mimic its most common pathophysiological habitat in humans, *i.e.* the urinary tract. We observed that, in the planktonic state, *P. stuartii* forms floating communities of cells, prior to attachment to a surface and subsequent adoption of the biofilm phenotype. *P. stuartii* planktonic and biofilm cells are remarkably resistant to calcium, magnesium and to high concentrations of urea, and show the ability to grow over a wide range of pHs. Experiments conducted on a *P. stuartii* strain knocked-out for the Omp-Pst2 porin sheds light on the role it plays in the early stages of growth, as well as in the adaptation to high concentration of urea and to varying pH.

Introduction

Bacteria are known to live as organized community of cells termed biofilms. In humans, these supra-cellular structures are responsible for the majority of chronic bacterial infections [1,2]. Prominent examples of biofilm-related infections include catheter-associated infections, the leading cause of secondary nosocomial bacteremia (20%) [3], and cystic fibrosis [4], a genetic disorder that favours the colonisation of aerial tissues by *P. aeruginosa*. The chronic nature of biofilm-related infections originates from their increased resistance to the immune system and antibiotherapy. The current model for biofilm formation includes five different stages [5], *viz.* i/ the initial attachment of cells on a biotic or abiotic surface; ii/ the formation of a monolayer of cells; iii/ the migration of cells into a multi-layered colony; iv/ the synthesis of an

<http://www.agence-nationale-recherche.fr>) is acknowledged, as well as from the CEA (www.cea.fr), the CNRS (www.cnrs.fr) and the University Grenoble Alpes (<http://www.univ-grenoble-alpes.fr>). M.E.K. is supported by a joint CEA-GRAL (<http://www.labex-gral.fr>) doctoral fellowship. The funders had no role in study design, data collection and analysis, decision to publish, or preparation of the manuscript.

Competing interests: The authors have declared that no competing interests exist.

extracellular matrix around the cells; and v/ the maturation of the biofilm into a characteristic 3D ensemble, composed of cells flapping in a self-produced polymeric matrix [5]. A sixth stage would be the release and dispersion of biofilm cells to colonize other niches. Depending on species, the biofilm polymeric matrix may be composed of extra-cellular polysaccharides [1], amyloid fibers [6] and DNA [7]. The versatile and adaptable nature of the matrix allows bacteria to attach on, and thus colonize, a range of disparate (biotic or abiotic) surfaces. It also affects antibiotic efficiency through a variety of mechanisms, including reduced diffusion of drugs within the biofilm, masking or alteration of drug targets by the biofilm environment, or the adoption by some cells of a dormant—and therefore less drug-susceptible—phenotype [8,9].

Providencia stuartii is an opportunistic biofilm-forming pathogen from the *Enterobacteriaceae* family [10] that is ubiquitous in the environment [11]. A recent study reported an incidence rate of 4 per 100,000 hospital admissions, suggesting a low rate of prevalence in the general population [11]. *P. stuartii* is yet responsible for ≈ 9% of urinary tract infections, in patients undergoing long-term catheterization [11–15]. These patients are often nursing home (NH) or intensive care unit (ICU) residents; hence this contingent is bound to increase with aging of the population. The in-hospital mortality rate of *P. stuartii* infections is around 30% [11], in part due to its high intrinsic multidrug resistance (MDR) phenotype conferred by the presence of an inducible chromosomal AmpC [16]. This MDR phenotype can be further exaggerated in clinical isolates, a majority of which were shown to feature plasmid-encoded extended-spectrum β-lactamases (ESBLs) [17]. More recently, clinical isolates presenting carbapenemase activities were isolated in Afghanistan [18] and Portugal [19]. *P. stuartii* is adept at biofilm dispersion, explaining that infections sometimes migrate from the urinary tract to other organs, causing endocarditis [20], pericarditis [21], peritonitis [22] or meningitis [23]. These facts, together with the now established ability of *P. stuartii* to disseminate amidst patients in hospital settings [24,25], explain the growing concern among health professionals [11]. As yet, however, studies remain scarce on *P. stuartii* and on the nature and resistance of its biofilms to environmental cues [26–28]. More investigations are needed to characterize how *P. stuartii* biofilms form, and what their specifics are in terms of extracellular matrix composition, cell sub-types and behaviour, and mechanisms of adherence-to and detachment-from surfaces or other cells. Such information is crucial to eventually prevent or manage chronic infections by *P. stuartii*, and the high toll they take on NH and ICU residents [11,29].

In urine, the metabolite urea is found at a concentration of 150 mM, at which it displays a strong anti-microbial effect. Thus, bacteria that colonize the urinary tract must find means to evade this stress. One of these is to feature (or acquire) a urease activity, that will hydrolyze urea into two ammoniums and an carbonate [30]. Calcium and magnesium are generally found at normal serum concentration (2 and 2.5 mM) but may reach higher concentrations in pathological conditions, e.g. in patients presenting bladder stones whose formation correlates with a 2-fold increase in the calcium-concentration/osmolarity ratio of urine [31,32]. The pH of urine is usually acidic but may vary from 6 to 8 depending on diet or pre-conditions. For example, infection by *P. mirabilis* is known to raise urine pH above 8, due to its strong urease activity that degrades urea into carbon monoxide and ammonia [29]. Some clinical isolates of *P. stuartii* feature a plasmid-encoded urease activity, but this activity is generally too weak to induce alkalinisation of urine [33]. Therefore alternative mechanisms, which allow *P. stuartii* cells to evade detrimental effects of urea, must exist. One of these is co-infection with species that have a strong urease activity such as *P. mirabilis*, whose presence was shown to increase *P. stuartii* colonization and bacteremia incidence [34]. Another efficient mechanism could be the limited diffusion of urea across the extracellular matrix of *P. stuartii* biofilms, which would result in reducing the effective concentration of urea in cells, thence preserving these. Access

to the periplasm is mainly controlled by general-diffusion porins, which are water-filled channels sprinkling the outer-membrane thence allowing passive diffusion of nutrients and ions into the periplasm. Porins are the most abundantly expressed outer-membrane (OM) proteins (up to 100,000 copies/cell), with a single porin often accounting for up to 70% of the OM proteinaceous content [35]. Current interest in porins mostly stems from their involvement in antibiotic uptake [36] and in the emergence of antibiotic resistance [37]. But as the first door opened toward the exterior, they also play a number of additional roles in bacterial survival, homeostasis and pathogenesis, adhesion to surfaces and host cells [38], and sometimes penetration into these [39]. Porins are therefore good candidates for playing a role in limiting excessive urea accumulation in the periplasm.

The genome of *P. stuartii* features two porins, Omp-Pst1 and Omp-Pst2 [40]. When grown in rich medium (*per se*, Luria-Bertani or LB), *P. stuartii* predominantly expresses Omp-Pst1, and it was proposed that Omp-Pst1 is the major porin of the bacterium [40]. Electrophysiology measurements revealed that Omp-Pst2 is highly cation-selective and prone to voltage-gating (critical voltage $V_c = 20\text{--}90$ mV), whereas Omp-Pst1 channel gates normally ($V_c > 199$ mV), is mildly anion selective and comparatively more permissive to β -lactam antibiotics [40,41]. MD simulations suggested that Omp-Pst2 atypical voltage-gating behaviour is asymmetric and triggered by the influx of cations from the extracellular to the periplasmic side of the porin. Efflux of cations, on the other hand, would be facilitated, suggesting a potential role for this porin in the regulation of charge distribution across the OM [42].

Here, we report on *P. stuartii* growth and biofilm formation under environmental conditions that mimic its most common habitat in humans, *i.e.* the urinary tract. We used the methodology of Mishra *et al.* [43] to characterize the effect of pH, urea, calcium and magnesium on biofilm genesis, attachment and consolidation. We found that *P. stuartii* growth is independent on pH in the viability range (pH 6 to 9), yet biofilm genesis and attachment onto the surface are favoured at $\text{pH} \geq 8$. We observed that *P. stuartii* biofilms survive in high concentrations of urea (up to 500 mM), calcium and magnesium (up to 50 mM), and that these environmental stresses trigger the consolidation of *P. stuartii* biofilms. Magnesium and calcium both inhibit the attachment of new cells onto surfaces in a dose-dependent manner, but magnesium activates biofilm genesis. Epifluorescence micrographs were taken at various stages of growth, of cells both in the planktonic (floating cells) and in the biofilm state (adherent cells). Most unexpectedly, we observed that planktonic *P. stuartii* cells exhibit a highly social behaviour, whereby cell-to-cell contact occurs prior to attachment of cells onto the surface, resulting in floating communities of cells that precede—and later coexist—with surface-attached biofilms. This observation suggested cell-to-cell contact as the primary mechanism by which *P. stuartii* cells form a community, and prompted us to examine whether or not porins—as the main proteinaceous component of the outer membrane—are involved. A knock-out strain for Omp-Pst2, *P. stuartii* $\Delta P2$, was obtained (*P. stuartii* ATCC 29914 $\Delta\text{ompPst2}::\text{Cm}$) that formed more biofilms (+70%) but displayed retarded growth, higher sensitivity to urea and cations, and a clear dependence of the lag-time on pH. Results suggest that Omp-Pst2 is an important actor in the early stages of *P. stuartii* growth and in adaptation to alkalinity.

Materials and methods

Strains and materials

Escherichia coli BL21 DE3 strain was used as a negative control strain and the wild type *Providencia stuartii* ATCC 29914 strain was obtained from the Pasteur Institute (Paris, France). All fluorescent dyes were from Thermo Fischer Scientific. Unless specified otherwise, chemicals were from Sigma-Aldrich. Polystyrene-bottom 96-well plates were from Greiner.

Generation of the *omp-pst2* knock out strain, *P. stuartii* $\Delta P2$

The disruption of the *omp-Pst2* gene in *P. stuartii* ATCC 29914 was carried out by adapting the protocol described by Datsenko and Wanner [44], based on the use of phage lambda Red recombinase [44]. The PCR primers were *OmpPst2_XbaI* 5' – GTG TCT AGA CAC TTA GTT AGT AAA TGG C –3' (forward) and *OmpPst2_BamHI* 5' – GTT GGA TCC GGA TAA TTG CGT ATG ATG G –3' (reverse). The *ompPst2* PCR amplicon was cloned into pGem-T-Easy vector and the construct was transferred by electroporation into *E. coli* DH5 α for plasmid maintenance and amplification. The plasmid was digested with HindIII enzyme and the subsequent protruding ends were filled in by Klenow enzyme. The construct was then ligated to chloramphenicol-resistance (Cm) cassette making *omp-Pst2::Cm* knockout construct. pCAM-MSU suicide vector for *Enterobacteriaceae* was then used to bring the *omp-Pst2::Cm* into *E. coli* S17-1 λ pir. Biparental mating with *P. stuartii* was then carried out by homology conjugation. Selection of *P. stuartii* ATCC 29914 *omp-Pst2::Cm* mutants was performed in the presence of chloramphenicol at 33 μ g/mL concentration. The resulting genetic modification of *P. stuartii* ATCC 29914 *omp-Pst2::Cm* was finally confirmed by both colony PCR and sequencing, using primers flanking the *omp-Pst2* gene in the *P. stuartii* genome.

Bacterial growth studies

E. coli and *P. stuartii* bacteria were grown in Luria-Bertani (LB) growth medium without antibiotics. LB medium was supplemented with 33 μ g/ml chloramphenicol for the growth of the *P. stuartii* $\Delta P2$ bacteria. Control experiments showed that chloramphenicol at this concentration has no effect on cell-growth and biofilm formation by *P. stuartii*- $\Delta P2$ (data not shown). For each experiment, a single bacterial colony was inoculated in standard LB or pH-specific LB medium for 2 h, yielding cells in their lag phase. These were then distributed into a 96-wells plates supplemented with 0–1 M urea, 0–50 mM Ca²⁺ or 0–50 mM Mg²⁺, and incubated at 37°C and under 100 rpm agitation overnight, to form biofilms. Bacterial growth was monitored in terms of absorbance at 600 nm for 24 h (10 minutes interval between time points) using a Biotek Synergy H4 microplate reader (Winooski, VT, USA)

Environmental stresses impact on biofilm genesis and attachment onto surface

For each experiment, a single bacterial colony was used to inoculate 25 mL of standard LB medium (37°C). A large flask was used, that was maintained under constant shaking at 200 rpm on the rotatory platform, thence preventing bacterial attachment onto the surface and subsequent formation of adherent biofilms. After 2 hours, aliquots of this culture (cells in the lag phase) were transferred in a 96-well plate (see below), serving to study the effect of environmental stresses on biofilm genesis. After 24 h, another set of aliquots was transferred in the 96-well plate, with view to study the effect of environmental stresses on the attachment of cells onto the well surfaces (see below). Cells were confronted with environmental insults after transfer into the 96-well plate. Briefly, above-mentioned aliquots were distributed into wells containing 150 μ L LB medium buffered at increasing pH (4 to 9) or supplemented with increasing concentrations of urea (0–1 M), Ca²⁺ or Mg²⁺ (0–0.05 M). Cells were then incubated at 37°C under constant shaking at 100 rpm. Biofilms were revealed after 24-hours incubation in the 96-well plate.

Environmental stresses impact on established biofilms

For each experiment, a single bacterial colony was used to inoculate 25 mL of standard LB medium (37°C). A large flask was used, that was maintained under constant shaking at 200 rpm on the rotatory platform, thence preventing bacterial attachment onto the surface and subsequent formation of adherent biofilms. After 2 hours, aliquots of this culture (cells in the lag phase) were transferred in a 96-well plate and incubated for 24 hours at 37°C under constant shaking at 100 rpm, resulting in the formation of biofilms at the bottom of the wells. The medium was then removed to discard planktonic bacteria and replaced by fresh LB medium buffered at increasing pH (4 to 9) or supplemented with urea (0–1 M), Ca²⁺ or Mg²⁺ (0–0.05 M). The plate was then incubated at 37°C and 100 rpm overnight. Biofilms were revealed after an additional 24-hours incubation in this plate.

Imaging

Epifluorescence micrographs were taken on an IX81 Olympus inverted microscope; samples were magnified through 20 or 60X objectives (Plan APON60XO, Olympus). SYTO[®] 9 Green fluorescent nucleic acid stain and propidium iodide solution were used at 5 and 20 µM concentration to stain live and dead cells respectively. Bacterial membranes were stained by the fluorescent dye FM1-43FX at 5 µg/mL. Bacterial biofilms were grown in a 96-wells plates as described above. For the imaging of planktonic bacteria, 10 µL of the culture were spread on LB-Gelzan[™] cover slides prepared as previously described [45] and imaged directly afterwards. For biofilm imaging, wells were washed twice with phosphate-buffered saline (PBS) to remove all planktonic bacteria; the remaining adherent bacteria forming the biofilm were then imaged.

Biofilm quantification

Well plates incubated overnight were washed extensively with PBS to remove all planktonic bacteria. Adherent biofilms were then stained with PrestoBlue[®] cell viability reagent. For each plate, fluorescence emission was measured at 590 nm, upon excitation at 560 nm. All experiments were performed at least in triplicate and biofilm formation was quantified with respect to *P. stuartii* cells grown in the absence of environmental stresses.

Results

P. stuartii form floating communities of cells prior to adherent biofilm

In order to characterize *P. stuartii* growth and its ability to form biofilms, we compared it to one of the most common *E. coli* strains used in laboratories, BL21 DE3. This *E. coli* strain is known not to form biofilms [46] and was therefore used as a negative control. When cultivated in LB medium, both *P. stuartii* and *E. coli* show a typical growth curve that can be divided into three phases: (1) a lag phase, (2) an exponential phase, and (3) a stationary phase (Fig 1A). *E. coli* and *P. stuartii* have similar lag phase duration and the same growth rate in the beginning of the exponential phase (Fig 1B). After five hours, however, *E. coli* cells decline whereas *P. stuartii* cells continue to exhibit a positive rate of growth.

Micrographic examination of attached *P. stuartii* cells reveals that no biofilm forms before the stationary phase (Fig 2A–2C), in agreement with the idea that bacteria form biofilms when faced with an environmental stress. After five hours of growth, the well is covered with a large biofilm, presumably as a result of starvation (Fig 2D). Examination of planktonic cells at the exponential and stationary phases reveals that floating communities of cells form by cell-to-cell contact in solution (Fig 2E–2G and S1 Movie), prior to the attachment of cells on the

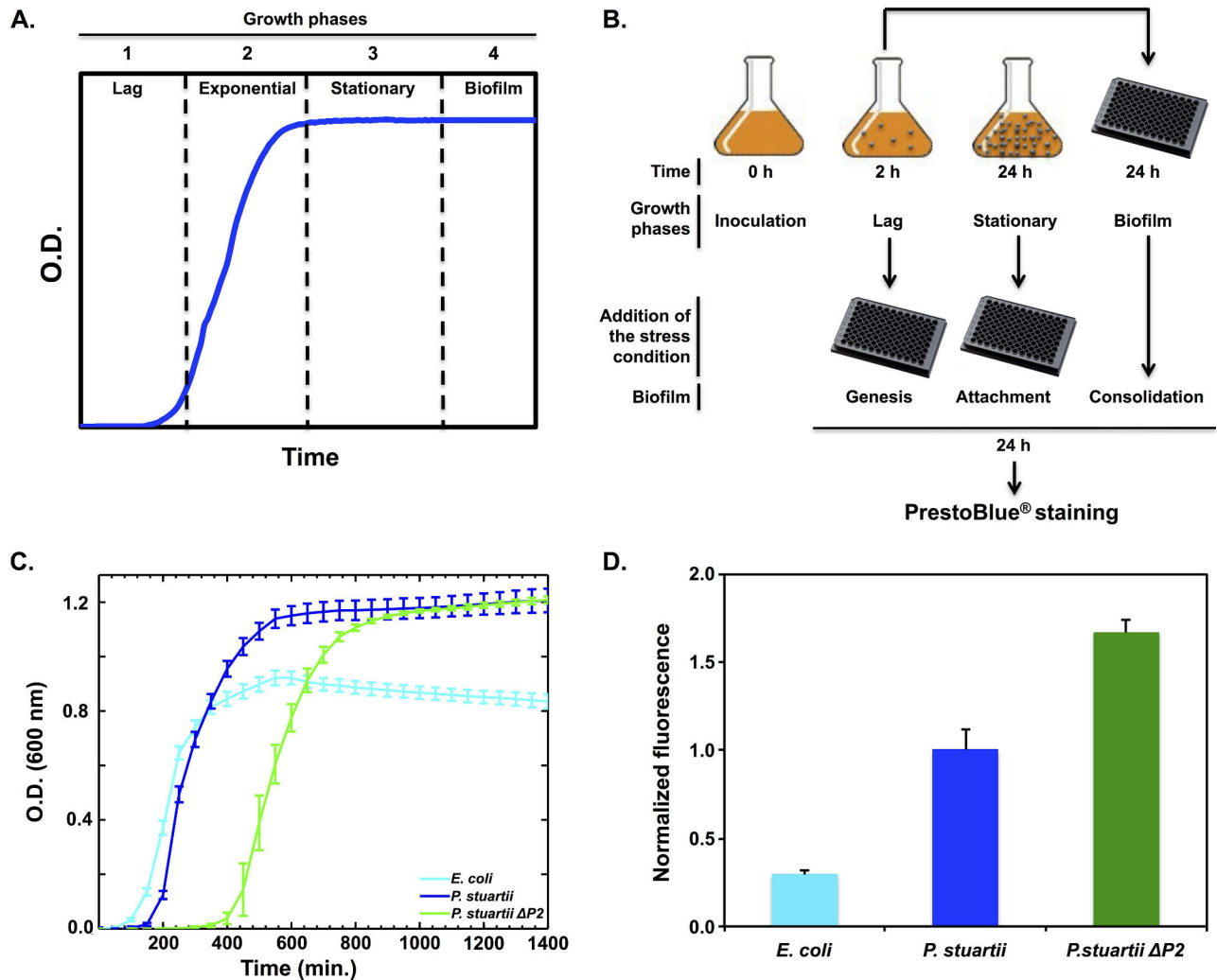


Fig 1. Planktonic bacterial growth and biofilm formation. (A) Bacterial growth can be divided into 4 main phases: (1) the lag phase, (2) the exponential phase, (3) the stationary phase and (4) the biofilm establishment phase. (B) Growth curves of *E. coli* BL21, *P. stuartii* and *P. stuartii*-ΔP2. (C) Experimental protocol designed to challenge the effect of various environmental stresses on the different stages of biofilm formation (genesis, attachment, consolidation) by *P. stuartii*. (D) Biofilm quantification after 24h of growth in 96-wells plates, as revealed by of adherent cells using PrestoBlue. Data are normalized with respect to measurements performed on *P. stuartii*.

<https://doi.org/10.1371/journal.pone.0174213.g001>

surface (Fig 2A–2C)—that is, prior to the formation of canonical biofilms. After five hours of growth, these floating communities of cells are multi-layered and coexist with surface-attached biofilms (Fig 2D–2H).

The viable adherent biomass formed by *P. stuartii* was 3-fold greater than that formed by *E. coli* (Fig 1C), with virtually all cells being alive in *P. stuartii* biofilms (Fig 3A). In contrast, *E. coli* adherent biomass amounted to only few dispersed cells, roughly the half of which were dead (Fig 3A). Phenotypic differences between *P. stuartii* and *E. coli* cells were also clear at the planktonic level, where the dispersion of *E. coli* cells contrasted with the highly gregarious behaviour of *P. stuartii* floating communities (Fig 3B).

We examined whether *Omp-Pst2* could play a role in biofilm formation by repeating these experiments on the *P. stuartii* ATCC 29914 $\Delta ompPst2::Cm$ strain (*P. stuartii* ΔP2). The growth rate of *P. stuartii* ΔP2 in the exponential and stationary phases was identical to that of the wild-

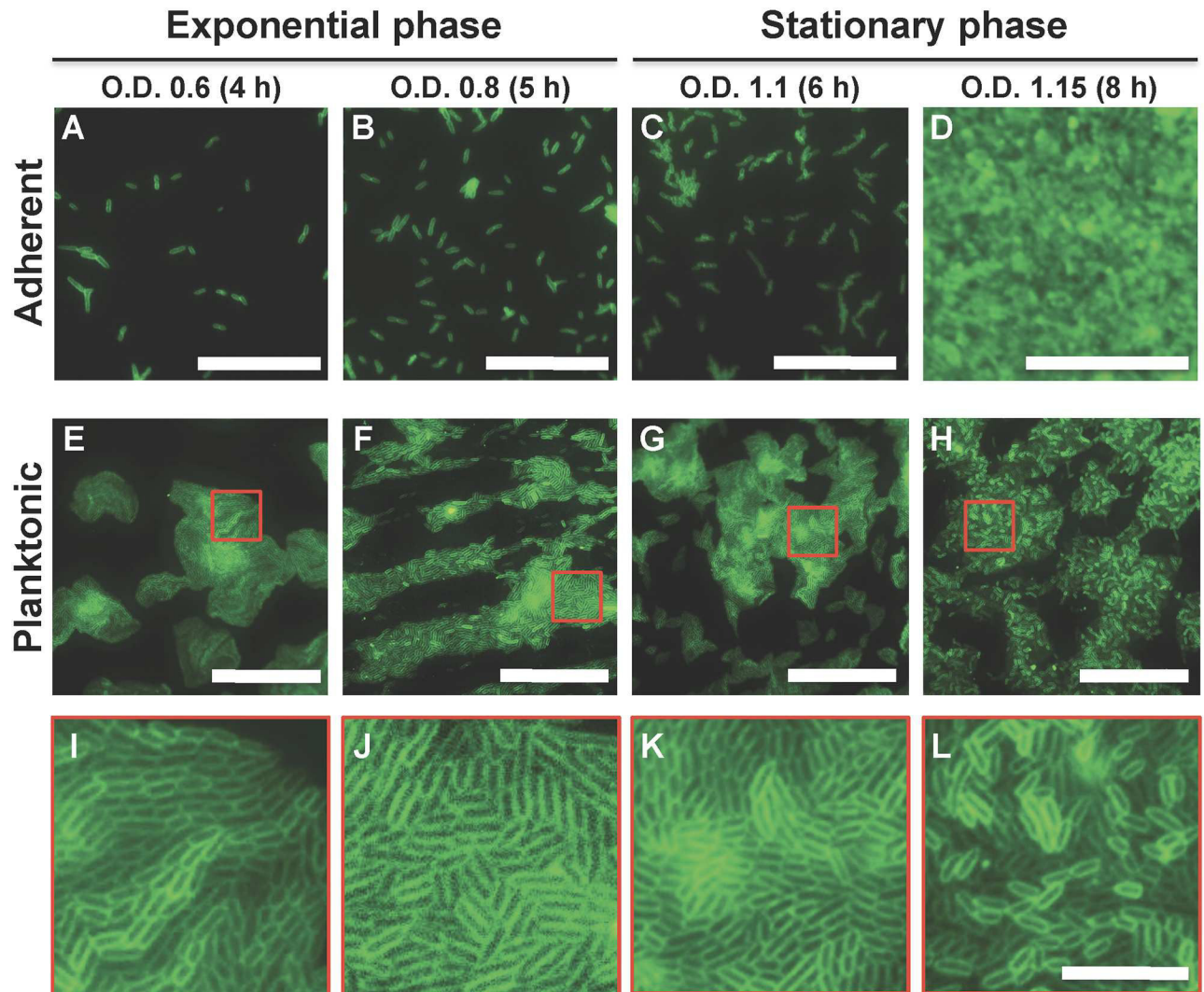


Fig 2. *P. stuartii* form floating-communities of planktonic-cells prior to adherent biofilms. (A-D) Micrographs of bacteria that remain bound to the well surface, after discard of planktonic cells by PBS washes. (E-H) Micrographs of planktonic bacteria. Cells were pipetted from the LB medium, spreaded on LB-Gelzan and imaged immediatly. (I-L) Close-up views of the red-delineated regions in panels E-H showing close contact between the membrane of adjacent cells. Bacterial membranes were stained using FM1-43FX. Scale bars: 50 μ m (A-H) and 10 μ m (I-L).

<https://doi.org/10.1371/journal.pone.0174213.g002>

type strain, showing a rapid adaptation to Omp-Pst2 depletion (Fig 1B). However, cells devoid of Omp-Pst2 displayed retarded growth (+ 60% increase in lag time; Fig 1B) and a 70% increase in biofilm formation (Fig 1C). *P. stuartii* Δ P2 biofilms were comparatively denser, but the lack of Omp-Pst2 did not perturb the microscopic appearance of *P. stuartii* cells—in either planktonic (Fig 3A) or biofilm (Fig 3B) states. Increased biofilm formation by *P. stuartii* Δ P2 could underlie a pathway undertaken by this K.O. strain to overcome the stress induced by the lack of Omp-Pst2 in the early stages of growth.

P. stuartii is resistant to urea and forms biofilm over a large range of pH

Inasmuch as urea is the principal component of urine, we set to determine the effect of this metabolite on *P. stuartii* planktonic cell growth as well as on biofilm genesis, attachment and

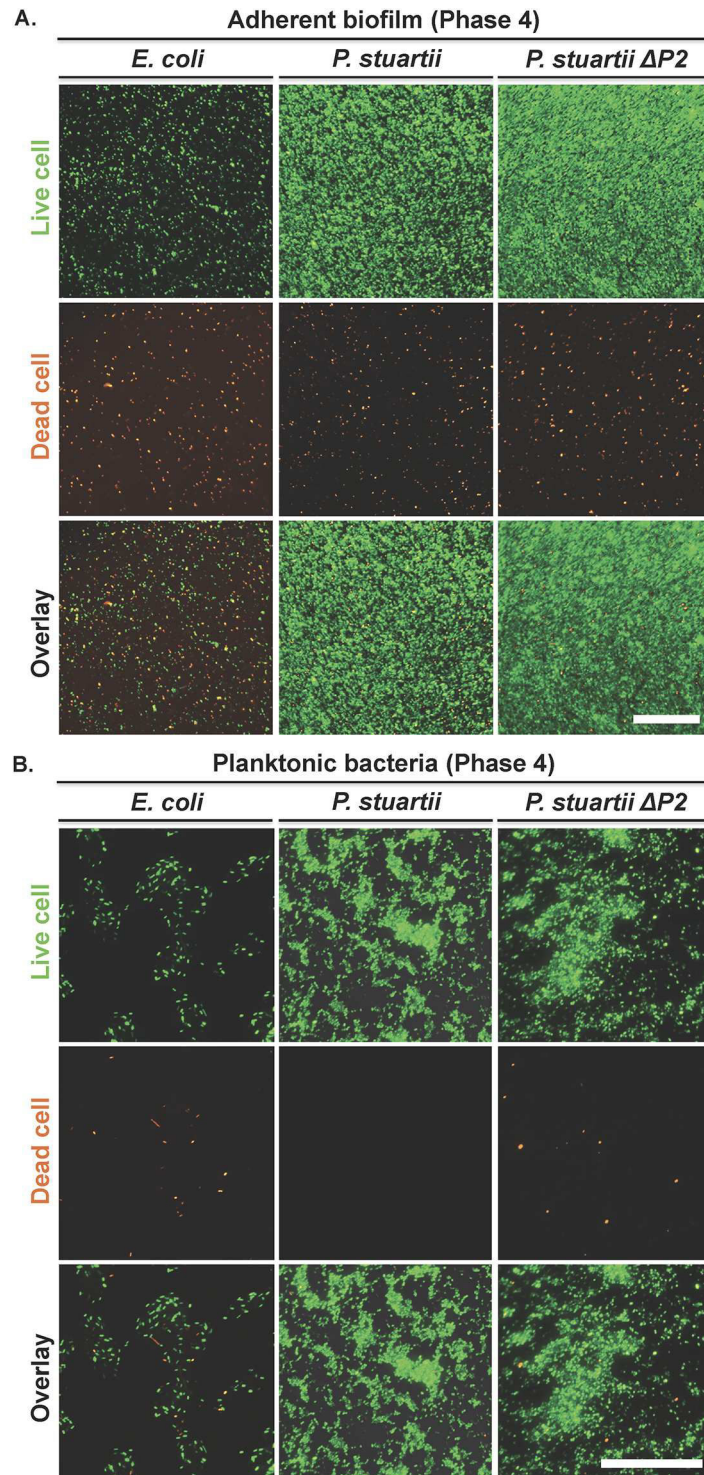


Fig 3. *P. stuartii* is adept at forming large biofilms mainly composed of living cells. (A) Micrographs of bacteria adherent to the wells surface after discard of planktonic cells by PBS washes. (B) Micrographs of planktonic bacteria. Cells were pipetted from the LB medium, spreaded on LB-Gelzan® and imaged immediatly. Live and dead cells were stained with SYTO9 Green and propidium iodide, respectively. Scale bars are 100 and 50 μm in panels (A) and (B), respectively.

<https://doi.org/10.1371/journal.pone.0174213.g003>

consolidation. We used to this end the methodology recently introduced by Mishra *et al.* [43]. Briefly, cells were submitted to increasing urea concentration at various phases of their growth (lag, stationary and biofilm phases), grown overnight (ON) under this environmental pressure, and the viable biofilm mass was then quantified using Presto Blue (Fig 1D). We found that *P. stuartii* planktonic cells sustain normal growth up to 500 mM urea but display an 85% decrease in growth at 1 M urea (Fig 4A). Exposure of cells to urea in the lag and stationary phases reveals that biofilm genesis and attachment to surfaces are unaffected by concentrations of urea up to 200 and 500 mM, respectively (Fig 4B and S1 Fig). Exposure to urea furthermore consolidates pre-formed *P. stuartii* biofilms, in the viability range (0–500 mM) (Fig 4B and S2 Fig). Clearly, ATCC 29914 is a urease-positive *P. stuartii* strain, sustaining urea concentrations ≥ 4 -fold higher than that encountered in its human habitat (150 mM). The urease activity of *P. stuartii* is cytoplasmic and produces 2 ammoniums and 1 carbonate per hydrolysed molecule of urea [30].

We then investigated how *P. stuartii* responds to changes in pH. Using the approach summarized above—and further detailed in the Methods section—we found that *P. stuartii* is unable to grow at pH 4 and 5, but viable between pH 6 and 9 (Fig 4C). Within this range, neither planktonic cells (Fig 4C) nor cells from preformed biofilms are affected by pH variations, although alkalinity favours biofilm genesis and attachment of cells onto the surface (Fig 4D and S1 Fig). While partially destroyed at pH 4, preformed *P. stuartii* biofilms consolidate at pH 5 (Fig 4D and S2 Fig) underlining their resistance to extreme environmental conditions.

Omp-Pst2 is involved in urea uptake and in the regulation of pH in the periplasm

We examined the impact of urea on planktonic growth and biofilm formation by the Δ Omp-Pst2 strain of *P. stuartii*. *P. stuartii* Δ P2 showed normal growth in urea up to 200 mM, but an increased lag time at 500 mM. At 1M, the strain could not grow, suggesting that Omp-Pst2 participates in alleviating urea toxicity in parental cells (Fig 4E). The fitness loss induced by lack of Omp-Pst2 was also visible at the biofilm level, with biofilm genesis, attachment and consolidation all being negatively impacted by urea in a dose-dependent manner (Fig 4F and S1 and S2 Figs).

We also investigated the sensitivity of *P. stuartii* Δ P2 to variations in pH. At the planktonic level, we observed a clear dependency on pH of the lag time of *P. stuartii* Δ P2 growth. The K. O. strain remains unable to grow at pH 4 and 5, but displays a faster and more productive planktonic growth at pH 6 than at pH 9 (Fig 4G). In strong contrast, the growth of the parental strain is equally favoured from pH 6 to 9 (Fig 4C). At the biofilm level, *P. stuartii* Δ P2 cells show reduced biofilm genesis and attachment to the surface at pH 9, resulting in a shift of the optimal pH for biofilm formation from pH 9 to 8 (Fig 4H and S1 Fig). Absence of Omp-Pst2 also lowers biofilm consolidation at pH5, as compared to the parental strain (Fig 4D and 4H and S2 Fig). Altogether, these results indicate a role for Omp-Pst2 in the regulation of periplasmic pH.

P. stuartii biofilms benefit from the presence of Ca^{2+} and Mg^{2+}

Calcium and magnesium are the most abundant divalent-cations in the urine. Therefore, their effect on the growth and fitness of *P. stuartii* cells was investigated, at the planktonic and biofilm levels. Upon addition of 50 mM of calcium and magnesium into the growth medium, *P. stuartii* growth level increased by 17 and 25% respectively (Fig 5A and 5C). Addition of calcium had an inhibitory effect on biofilm genesis as well and on cell attachment onto the surface, but triggered the consolidation of preformed-biofilms (Fig 5B) and a drastic

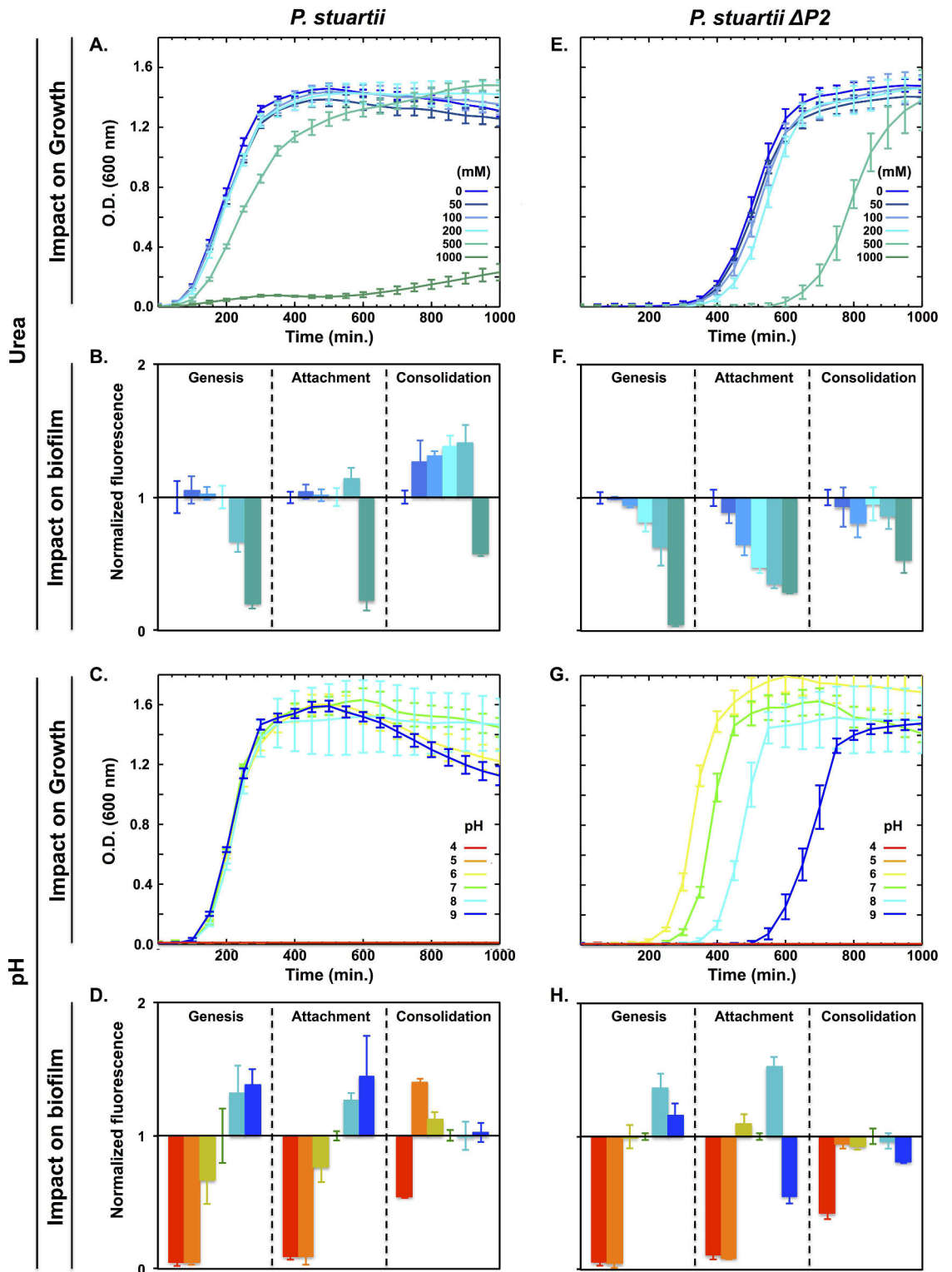


Fig 4. Resistance of *P. stuartii* and *P. stuartii* $\Delta P2$ cells to high concentrations of urea and to pH variations. Effect of urea (A and E) and pH (C and G) on bacterial growth, as judged from the O.D. of cultures at 600 nm. The impact on biofilm genesis, attachment and consolidation was evaluated by adding urea (B and F) or changing the pH (D and H) during the lag, stationary and preformed biofilm phases, respectively. Biofilm formation was quantified 24 h later, by PrestoBlue staining. Fluorescence values were normalized with respect to the control wells containing no urea and buffered at pH7.

<https://doi.org/10.1371/journal.pone.0174213.g004>

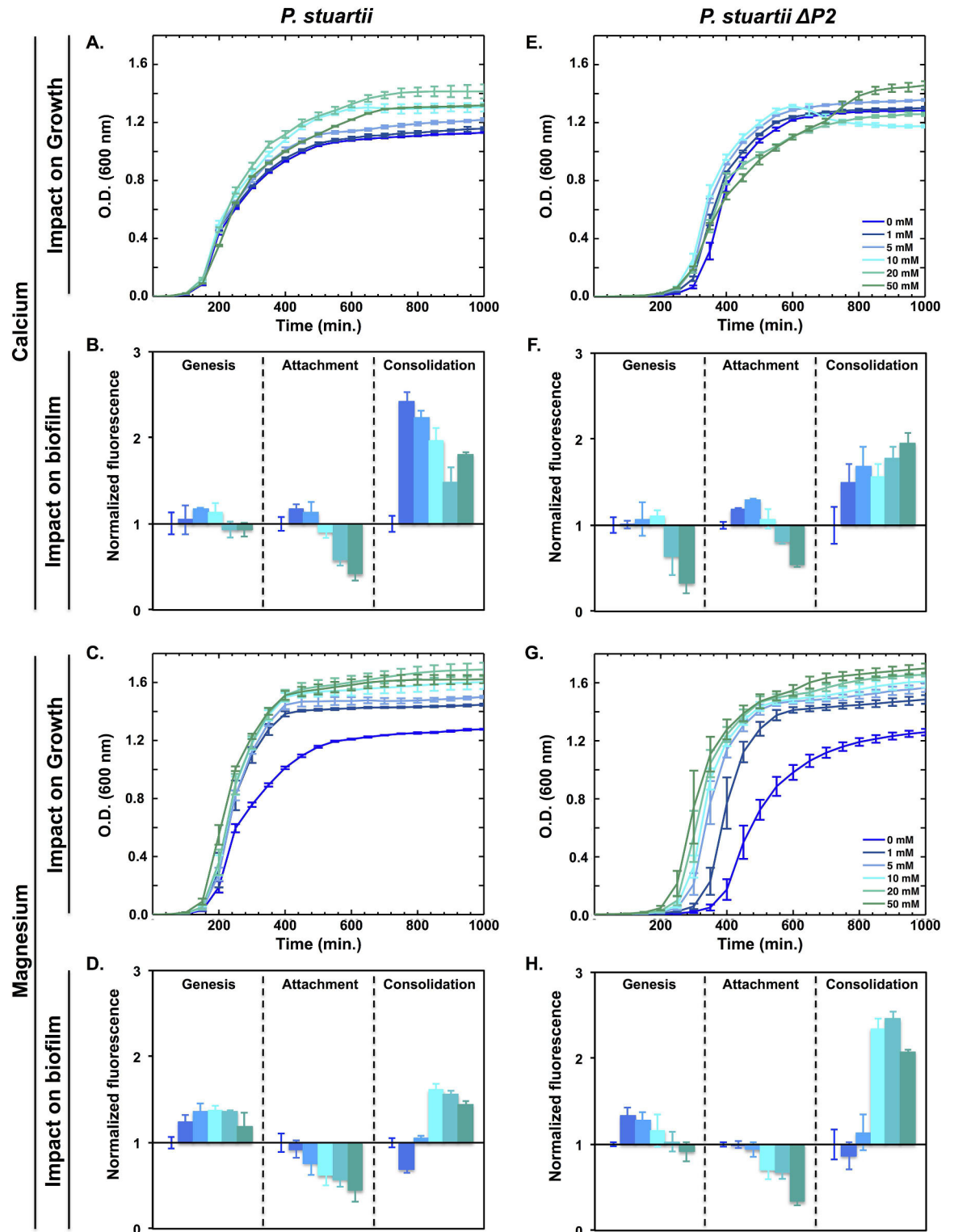


Fig 5. Resistance of *P. stuartii* and *P. stuartii*- Δ P2 cells to high concentrations of calcium and magnesium. Effect of calcium (A and E) and magnesium (C and G) on bacterial growth, as judged from the O.D. of cultures at 600 nm. The impact on biofilm genesis, attachment and consolidation was evaluated by adding calcium (B and F) or magnesium (D and H) during the lag, stationary and preformed biofilm phases, respectively. Biofilm formation was quantified 24 h later, by PrestoBlue staining. Fluorescence values were normalized with respect to the control wells buffered at pH7 and devoid of urea.

<https://doi.org/10.1371/journal.pone.0174213.g005>

reorganisation of their supracellular structure. Micrographs indeed reveal that *P. stuartii* biofilms change shape, forming compact assemblies of tightly aggregated cells (S2 Fig), upon exposure to high calcium concentration. Magnesium also inhibited cell attachment to surfaces, but was beneficial to biofilm genesis and consolidation (Fig 5D) and did not affect the shape of pre-formed biofilms, even at the highest concentrations tested.

Deletion of Omp-Pst2 reproduced or enhanced the impact of the two divalent cations on *P. stuartii* $\Delta P2$ cells, planktonic and biofilm alike. The beneficial effect of calcium on planktonic growth was preserved, and likewise for its inhibitory effect on biofilm genesis and cell attachment onto the surface (Fig 5B and 5F). Pre-formed biofilms of *P. stuartii* $\Delta P2$ also displayed more sensitivity to high calcium concentrations, as exposed by the observation of more compact cell-assemblies characterized by a higher mortality level (S2 Fig), in epifluorescence micrographs. The beneficial effect of magnesium on planktonic growth was also preserved in *P. stuartii* $\Delta P2$ cells, while that on biofilm consolidation was further potentiated (Fig 5H).

Discussion

P. stuartii is a biofilm-forming pathogen (Fig 1B), mainly involved in urinary tract infections in elderly patients [11,15]. It is occasionally implicated in others types of infections [47], including endocarditis [20], pericarditis [21], peritonitis [22] and meningitis [23]. Notwithstanding that the prevalence of infections is increasing alarmingly, knowledge regarding the species and its biofilms remains scarce.

Here, we aimed at studying *P. stuartii* growth and biofilm formation in conditions that mimic its most common habitat in humans, *i.e.* the urinary tract. Our study demonstrated the ability of the microbe to form biofilms in a variety of insulting conditions. Furthermore, it shed light on the highly gregarious behaviour of *P. stuartii* planktonic cells, which associate from the early stages of growth through cell-to-cell contact, forming floating community of cells prior to formation of canonical—per say, adherent—biofilms (Fig 2 and S1 Movie). Cell-to-cell contact in the planktonic state could provide a means to maximize cell density, inter-communication and resistance to environmental cues, before formation of the mature biofilm. We observed that the floating communities of cells could attach altogether to surfaces, allowing biofilms to start from a critical mass.

Planktonic and biofilm cells of *P. stuartii* adapt well to changes in pH, in the pH 6 to 9 range. Alkaline pH furthermore activates *P. stuartii* biofilm genesis and attachment to surfaces (Fig 4A–4D). This fitness suggests the existence of periplasmic pH regulators, which would support the swift adaptation of *P. stuartii* to pH variation. *P. stuartii* $\Delta P2$, plagued by delayed growth, displays a clear dependence of the lag time on pH, suggesting that Omp-Pst2 contributes to the ability of the parental strain to immediately grow regardless of pH (Fig 4C and 4G). Thus Omp-Pst2 could play a role in regulating/buffering periplasmic pH, thereby supporting the adaptation of wild-type *P. stuartii* to changes in environmental pH. In the absence of this presumed regulator, *P. stuartii* $\Delta P2$ cells would take longer to adapt to increasing pH, hence explaining their retarded growth (+300 min at pH 9, compared to pH 7, Fig 4G).

The urease activity of *P. stuartii* ATCC 29914 was uncovered by its ability to grow normally in mediums containing up to 500 mM urea. The species furthermore survives (15%) in 1 M urea (Fig 4A) demonstrating that it would be able to grow in the urinary tract. *P. stuartii* $\Delta P2$ is nevertheless more sensitive to urea, displaying an increased lag time at 500 mM urea (+ 250 min) and showing no growth at 1M urea (Fig 4E). Accordingly, biofilm genesis, attachment and consolidation by this strain are affected by urea in a dose-dependent manner (Fig 4F). This mechanism of toxicity is not detectable in the parental strain. It appears unlikely that Omp-Pst2 absence would effect in increasing urea concentration in the periplasm. Rather,

Omp-Pst2 is involved in a process downstream of the penetration of urea into cells, such as efflux of urea or of its hydrolytic products. We see at least three possible explanations for the reduced resistance to urea of the *P. stuartii* $\Delta P2$ strain. (i) Omp-Pst2 could contribute to the efflux of urea from the periplasm, hence reducing the actual periplasmic (and thus cytoplasmic) concentration of urea. Given the large excess present in the surrounding growth medium, it nevertheless appears unlikely that this efflux activity would significantly affect the periplasmic concentration in urea. (ii) Omp-Pst2 could facilitate the influx of anions neutralizing the periplasmic ammonium generated by urea degradation—but again, given the strong cation-selectivity of Omp-Pst2, however, this hypothesis also appears unlikely. (iii) Omp-Pst2 could be involved in the direct efflux of periplasmic ammonium and in limiting its re-penetration into the periplasm; this is the only hypothesis that fits the prior knowledge on Omp-Pst2. Indeed, MD simulations have suggested that Omp-Pst2 could be involved in the facilitated transport of cations from the periplasm to the extracellular side of the OM [42]. They furthermore highlighted that Omp-Pst2 channel would respond by gating to a massive transit of cations from the external medium to the periplasm [42]. Thus, we favour the hypothesis that Omp-Pst2 alleviates the toxic effects of urea on *P. stuartii* cells by mitigating the toxic accumulation of ammonium in their periplasm. Of note, rough calculations indicate that accumulation of 10 μ M ammonium would raise the periplasmic pH from 7 to 9. Thus, the delayed growth displayed by *P. stuartii* $\Delta P2$ cells in the presence of 500 mM urea could result from increased periplasmic pH, due to reduced efflux of ammonium. More generally, Omp-Pst2 could act on periplasmic pH by regulating the cationic content of the periplasm; this hypothesis will have to be confirmed by electrophysiology.

Elevated calcium and magnesium consolidate preformed *P. stuartii* biofilms, activate planktonic cell growth (Fig 5A and 5C), and reduce cell attachment onto surfaces (Fig 5B and 5D). Calcium at 50 mM induces changes in the macroscopic appearance of biofilms, leading to their compaction (S2 Fig), whereas magnesium slightly activates their genesis. These effects are further exaggerated in *P. stuartii* $\Delta P2$ (Fig 5F and 5H), again supporting that the absence of Omp-Pst2 could lead to accumulation of cations in the periplasm, aggravating the effect of these on cellular metabolism.

Altogether, our results suggest that *P. stuartii* exploits sociability as a means to foster cellular growth and resist to environmental stress, before formation of a canonical—per say, surface-attached—biofilm. Our work also points out that Omp-Pst2 plays a crucial role in the early stages of *P. stuartii* growth (Fig 1A). Data show that Omp-Pst2 is involved in pH regulation (Fig 4G) and could be in charge of ammonium clearance/neutralization from/in the periplasm, a hypothesis supported by electrophysiology data [40] and more recently molecular dynamics simulations on the porin [42]. Our data add to the growing body of evidence that suggests an implication of OM components in biofilm formation and regulation [48,49]. Further studies are needed to understand how *P. stuartii* cells are riveted to one another in floating communities of planktonic cells, and how this phenotype influences the ability of the species to form biofilms.

Supporting information

S1 Movie. *P. stuartii* forms floating communities of cells. Bacteria were grown to an O.D. of 0.5 at 600 nm and imaged by conventional microscopy without washing. The movie shows a Z-scan acquisition of the whole well (bottom-to-top). Planktonic cells assemble into a floating community, wherein cells appear to be attached to one another and are presumably in close contact.
(M4V)

S1 Fig. Impact of urea and pH impact on biofilm genesis. Effect of urea (B-C and H-I) and pH (D-F and J-L) on the genesis of *P. stuartii* (A-F) and *P. stuartii* $\Delta P2$ (G-L) biofilms. Cells were subjected to environmental stresses for 24 h and bacteria adherent to the well surface were imaged after discard of planktonic cells by PBS washes. Live and dead cells were stained with SYTO9 Green and propidium iodide, respectively. Scale bar: 100 μm . (TIF)

S2 Fig. Impact of urea, pH and divalent cations on consolidation of pre-formed biofilms. Effect of urea (B, H), calcium (E, K), magnesium (F, L) and pH (C- D, I-J) on the consolidation of *P. stuartii* (A-F) and *P. stuartii* $\Delta P2$ (G-L) biofilms. Cells were subjected to environmental stresses for 24 h and bacteria adherent to the well surface were imaged after discard of planktonic cells by PBS washes. Live and dead cells were stained with SYTO9 Green and propidium iodide, respectively. Scale bar: 100 μm . (TIF)

Acknowledgments

We are indebted to Martin Weik for continuous support and fruitful discussions. We are grateful to Jean-Philippe Kleman and Françoise Lacroix for their technical support and advices during epifluorescence microscopy experiments. We thank Alexandre Dos Santos Martins and Coline Burnet-Merlin for technical support. This work used the platforms of the Grenoble Instruct Center (ISBG: UMS 3518 CNRS-CEA-UGA-EMBL) within the Grenoble Partnership for Structural Biology (PSB).

Author Contributions

Conceptualization: MEK JPC.

Formal analysis: MEK.

Funding acquisition: JPC.

Investigation: MEK CN JL.

Methodology: MEK JPC.

Project administration: JPC.

Resources: MEK QTT JMB MV JMP JPC.

Software: n/a.

Supervision: JPC.

Validation: MEK, JPC.

Visualization: MEK.

Writing – original draft: MEK, JPC.

Writing – review & editing: MEK, MV, JPC.

References

1. Costerton J. W., Stewart P. S. & Greenberg E. P. Bacterial biofilms: a common cause of persistent infections. *Science* 284, 1318–1322 (1999). PMID: [10334980](https://pubmed.ncbi.nlm.nih.gov/10334980/)

2. Hall-Stoodley L. & Stoodley P. Evolving concepts in biofilm infections. *Cell. Microbiol.* 11, 1034–1043 (2009). <https://doi.org/10.1111/j.1462-5822.2009.01323.x> PMID: 19374653
3. Gould C. V. et al. Guideline for prevention of catheter-associated urinary tract infections 2009. *Infect. Control Hosp. Epidemiol.* 31, 319–326 (2010). <https://doi.org/10.1086/651091> PMID: 20156062
4. Chapman C. M. C., Gibson G. R. & Rowland I. Effects of single- and multi-strain probiotics on biofilm formation and in vitro adhesion to bladder cells by urinary tract pathogens. *Anaerobe* 27, 71–76 (2014). <https://doi.org/10.1016/j.anaerobe.2014.02.001> PMID: 24583095
5. Branda S. S., Vik S., Friedman L. & Kolter R. Biofilms: the matrix revisited. *Trends Microbiol.* 13, 20–26 (2005). <https://doi.org/10.1016/j.tim.2004.11.006> PMID: 15639628
6. Chapman M. R. et al. Role of *Escherichia coli* curli operons in directing amyloid fiber formation. *Science* 295, 851–855 (2002). <https://doi.org/10.1126/science.1067484> PMID: 11823641
7. Whitchurch C. B., Tolker-Nielsen T., Ragas P. C. & Mattick J. S. Extracellular DNA required for bacterial biofilm formation. *Science* 295, 1487–1487 (2002). <https://doi.org/10.1126/science.295.5559.1487> PMID: 11859186
8. Stewart P. S. & William Costerton J. Antibiotic resistance of bacteria in biofilms. *The Lancet* 358, 135–138 (2001).
9. Lebeaux D., Ghigo J.-M. & Beloin C. Biofilm-related infections: bridging the gap between clinical management and fundamental aspects of recalcitrance toward antibiotics. *Microbiol. Mol. Biol. Rev. MMBR* 78, 510–543 (2014). <https://doi.org/10.1128/MMBR.00013-14> PMID: 25184564
10. Manos J. & Belas R. in *The Prokaryotes* (eds Dworkin M., Falkow S., Rosenberg E., Schleifer K.-H. & Stackebrandt E.) 245–269 (Springer New York, 2006).
11. Wie S.-H. Clinical significance of *Providencia* bacteremia or bacteriuria. *Korean J. Intern. Med.* 30, 167–169 (2015).
12. McHale P. J., Walker F., Scully B., English L. & Keane C. T. *Providencia stuartii* infections: a review of 117 cases over an eight year period. *J. Hosp. Infect.* 2, 155–165 (1981). PMID: 6174578
13. Warren J. W. *Providencia stuartii*: A Common Cause of Antibiotic-Resistant Bacteriuria in Patients with Long-Term Indwelling Catheters. *Rev. Infect. Dis.* 8, 61–67 (1986). PMID: 3081988
14. Stickler D. J. Bacterial biofilms in patients with indwelling urinary catheters. *Nat. Clin. Pract. Urol.* 5, 598–608 (2008). <https://doi.org/10.1038/ncpuro1231> PMID: 18852707
15. De Vecchi E. et al. Aetiology and antibiotic resistance patterns of urinary tract infections in the elderly: a 6-month study. *J. Med. Microbiol.* 62, 859–863 (2013). <https://doi.org/10.1099/jmm.0.056945-0> PMID: 23475904
16. Aubert D., Naas T., Lartigue M.-F. & Nordmann P. Novel Genetic Structure Associated with an Extended-Spectrum β -Lactamase bla_{VEB} Gene in a *Providencia stuartii* Clinical Isolate from Algeria. *Antimicrob. Agents Chemother.* 49, 3590–3592 (2005). <https://doi.org/10.1128/AAC.49.8.3590-3592.2005> PMID: 16048993
17. Tumbarello M. et al. ESBL-producing multidrug-resistant *Providencia stuartii* infections in a university hospital. *J. Antimicrob. Chemother.* 53, 277–282 (2004). <https://doi.org/10.1093/jac/dkh047> PMID: 14688041
18. Mc Gann P. et al. Complete Sequence of a Novel 178-Kilobase Plasmid Carrying bla_{NDM-1} in a *Providencia stuartii* Strain Isolated in Afghanistan. *Antimicrob. Agents Chemother.* 56, 1673–1679 (2012). <https://doi.org/10.1128/AAC.05604-11> PMID: 22290972
19. Manageiro V. et al. Draft Genome Sequence of the First NDM-1-Producing *Providencia stuartii* Strain Isolated in Portugal. *Genome Announc.* 3, (2015).
20. Krake P. R. & Tandon N. Infective endocarditis due to *Providencia stuartii*. *South. Med. J.* 97, 1022–1023 (2004).
21. Simon C. et al. Images in cardiovascular medicine. Bacterial pericarditis due to *Providencia stuartii*: an atypical case of relapsing pericarditis. *Circulation* 122, e401–403 (2010). <https://doi.org/10.1161/CIRCULATIONAHA.110.943118> PMID: 20660810
22. Unverdi S. et al. Peritonitis due to *Providencia stuartii*. *Perit. Dial. Int. J. Int. Soc. Perit. Dial.* 31, 216–217 (2011).
23. Sipahi O. R. et al. Meningitis due to *Providencia stuartii*. *J. Clin. Microbiol.* 48, 4667–4668 (2010). <https://doi.org/10.1128/JCM.01349-10> PMID: 20980575
24. Bret L. & Di Martino P. Effect of Ceftazidime, Amikacin and Ciprofloxacin on Biofilm Formation by Some Enterobacterial Clinical Isolates. *Chemotherapy* 50, 255–259 (2004). <https://doi.org/10.1159/000081947> PMID: 15528892

25. Lahlaoui H. et al. Nosocomial dissemination of extended-spectrum β -lactamase VEB-1a-producing *Providencia stuartii* isolates in a Tunisian hospital. *Eur. J. Clin. Microbiol. Infect. Dis.* 30, 1267–1270 (2011).
26. Sturgill G., Toutain C. M., Komperda J., O'Toole G. A. & Rather P. N. Role of CysE in Production of an Extracellular Signaling Molecule in *Providencia stuartii* and *Escherichia coli*: Loss of cysE Enhances Biofilm Formation in *Escherichia coli*. *J. Bacteriol.* 186, 7610–7617 (2004). <https://doi.org/10.1128/JB.186.22.7610-7617.2004> PMID: 15516574
27. Kateete D. P. et al. Rhomboids of Mycobacteria: Characterization Using an *aarA* Mutant of *Providencia stuartii* and Gene Deletion in *Mycobacterium smegmatis*. *PLoS ONE* 7, e45741 (2012). <https://doi.org/10.1371/journal.pone.0045741> PMID: 23029216
28. Ostrowska K., Kamysz W., Dawgul M. & Róžalski A. Synthetic amphibian peptides and short amino-acids derivatives against planktonic cells and mature biofilm of *Providencia stuartii* clinical strains. *Pol. J. Microbiol. Pol. Tow. Mikrobiol. Pol. Soc. Microbiol.* 63, 423–431 (2014).
29. Stickler D. J. Clinical complications of urinary catheters caused by crystalline biofilms: something needs to be done. *J. Intern. Med.* 276, 120–129 (2014). <https://doi.org/10.1111/joim.12220> PMID: 24635559
30. Isaacson L. C. Urinary composition in calcific nephrolithiasis. *Invest. Urol.* 6, 356–363 (1969). PMID: 5773520
31. Raman A. & Sreenevasan G. A. Urinary Osmolarity and Excretion of Sodium, Calcium and Magnesium in Patients with Renal Calculi. *Br. J. Urol.* 44, 537–540 (1972). PMID: 4628536
32. Broomfield R. J., Morgan S. D., Khan A. & Stickler D. J. Crystalline bacterial biofilm formation on urinary catheters by urease-producing urinary tract pathogens: a simple method of control. *J. Med. Microbiol.* 58, 1367–1375 (2009). <https://doi.org/10.1099/jmm.0.012419-0> PMID: 19556373
33. Armbruster C. E., Smith S. N., Yep A. & Mobley H. L. T. Increased Incidence of Urolithiasis and Bacteremia During *Proteus mirabilis* and *Providencia stuartii* Coinfection Due to Synergistic Induction of Urease Activity. *J. Infect. Dis.* 209, 1524–1532 (2014). <https://doi.org/10.1093/infdis/jit663> PMID: 24280366
34. Zeth K. & Thein M. Porins in prokaryotes and eukaryotes: common themes and variations. *Biochem. J.* 431, 13–22 (2010). <https://doi.org/10.1042/BJ20100371> PMID: 20836765
35. Pagès J.-M., James C. E. & Winterhalter M. The porin and the permeating antibiotic: a selective diffusion barrier in Gram-negative bacteria. *Nat. Rev. Microbiol.* 6, 893–903 (2008). <https://doi.org/10.1038/nrmicro1994> PMID: 18997824
36. Delcour A. H. Outer membrane permeability and antibiotic resistance. *Biochim. Biophys. Acta BBA—Proteins Proteomics* 1794, 808–816 (2009). <https://doi.org/10.1016/j.bbapap.2008.11.005> PMID: 19100346
37. Hemery G., Chevalier S., Bellon-Fontaine M.-N., Haras D. & Orange N. Growth temperature and OprF porin affect cell surface physicochemical properties and adhesive capacities of *Pseudomonas fluorescens* MF37. *J. Ind. Microbiol. Biotechnol.* 34, 49–54 (2006). <https://doi.org/10.1007/s10295-006-0160-x> PMID: 16932888
38. Galdiero S. et al. Microbe-host interactions: structure and role of Gram-negative bacterial porins. *Curr. Protein Pept. Sci.* 13, 843–854 (2012). <https://doi.org/10.2174/138920312804871120> PMID: 23305369
39. Tran Q.-T. et al. Implication of Porins in β -Lactam Resistance of *Providencia stuartii*. *J. Biol. Chem.* 285, 32273–32281 (2010). <https://doi.org/10.1074/jbc.M110.143305> PMID: 20667831
40. Bajaj H. et al. Antibiotic Uptake through Membrane Channels: Role of *Providencia stuartii* *OmpPst1* Porin in Carbapenem Resistance. *Biochemistry (Mosc.)* 51, 10244–10249 (2012).
41. Song W. et al. Understanding Voltage Gating of *Providencia stuartii* Porins at Atomic Level. *PLoS Comput Biol* 11, e1004255 (2015). <https://doi.org/10.1371/journal.pcbi.1004255> PMID: 25955156
42. Mishra B., Golla R. M., Lau K., Lushnikova T. & Wang G. Anti-Staphylococcal Biofilm Effects of Human Cathelicidin Peptides. *ACS Med. Chem. Lett.* (2015).
43. Datsenko K. A. & Wanner B. L. One-step inactivation of chromosomal genes in *Escherichia coli* K-12 using PCR products. *Proc. Natl. Acad. Sci.* 97, 6640–6645 (2000). <https://doi.org/10.1073/pnas.120163297> PMID: 10829079
44. de Jong I. G., Beilharz K., Kuipers O. P. & Veening J.-W. Live Cell Imaging of *Bacillus subtilis* and *Streptococcus pneumoniae*; using Automated Time-lapse Microscopy. *J. Vis. Exp.* (2011).
45. Zalewska-Piatek B. M., Wilkanowicz S. I., Piatek R. J. & Kur J. W. Biofilm formation as a virulence determinant of uropathogenic *Escherichia coli* Dr+ strains. *Pol. J. Microbiol. Pol. Tow. Mikrobiol. Pol. Soc. Microbiol.* 58, 223–229 (2009).

46. MOBLEY H. L., CHIPPENDALE G. R., TENNEY J. H. & WARREN J. W. Adherence to uroepithelial cells of *Providencia stuartii* isolated from the catheterized urinary tract. *Microbiology* 132, 2863–2872 (1986).
47. Frey K. G. et al. Full-Genome Assembly of Reference Strain *Providencia stuartii* ATCC 33672. *Genome Announc.* 2, e01082–14 (2014). <https://doi.org/10.1128/genomeA.01082-14> PMID: 25342690
48. Gaddy J. A., Tomaras A. P. & Actis L. A. The *Acinetobacter baumannii* 19606 OmpA Protein Plays a Role in Biofilm Formation on Abiotic Surfaces and in the Interaction of This Pathogen with Eukaryotic Cells. *Infect. Immun.* 77, 3150–3160 (2009). <https://doi.org/10.1128/IAI.00096-09> PMID: 19470746
49. Phillips N. J. et al. Proteomic Analysis of *Neisseria gonorrhoeae* Biofilms Shows Shift to Anaerobic Respiration and Changes in Nutrient Transport and Outer membrane Proteins. *PLOS ONE* 7, e38303 (2012). <https://doi.org/10.1371/journal.pone.0038303> PMID: 22701624



Porin self-association enables cell-to-cell contact in *Providencia stuartii* floating communities

Mariam El-Khatib^{a,1}, Chady Nasrallah^{a,1,2}, Julie Lopes^a, Que-Tien Tran^b, Guillaume Tetreau^a, Hind Basbous^a, Daphna Fenel^a, Benoit Gallet^a, Mathilde Lethier^a, Jean-Michel Bolla^c, Jean-Marie Pagès^c, Michel Vivaudou^{a,d}, Martin Weik^a, Mathias Winterhalter^b, and Jacques-Philippe Colletier^{a,3}

^aInstitut de Biologie Structurale (IBS), University of Grenoble Alpes (UGA), Centre National de la Recherche Scientifique (CNRS), Commissariat à l'énergie atomique et aux énergies alternatives (CEA), 38000 Grenoble, France; ^bLife Sciences & Chemistry, Jacobs University, 28759 Bremen, Germany; ^cUMR MD1, Aix-Marseille University, Institut de Recherche Biomédicale des Armées, Marseille, F-13385 Marseille, France; and ^dLaboratories of Excellence, Ion Channel Science and Therapeutics, 06560 Valbonne, France

Edited by Robert M. Stroud, University of California, San Francisco, CA, and approved January 31, 2018 (received for review August 18, 2017)

The gram-negative pathogen *Providencia stuartii* forms floating communities within which adjacent cells are in apparent contact, before depositing as canonical surface-attached biofilms. Because porins are the most abundant proteins in the outer membrane of gram-negative bacteria, we hypothesized that they could be involved in cell-to-cell contact and undertook a structure-function relationship study on the two porins of *P. stuartii*, Omp-Pst1 and Omp-Pst2. Our crystal structures reveal that these porins can self-associate through their extracellular loops, forming dimers of trimers (DOTs) that could enable cell-to-cell contact within floating communities. Support for this hypothesis was obtained by studying the porin-dependent aggregation of liposomes and model cells. The observation that facing channels are open in the two porin structures suggests that DOTs could not only promote cell-to-cell contact but also contribute to intercellular communication.

biofilms | porins | intercellular communication | cell adhesion | steric zippers

The opportunistic pathogen *Providencia stuartii*, from the Enterobacteriaceae family (1), is involved in increasingly frequent infections in burn victims and patients undergoing long-term catheterization (2–5). Treatment of infections by *P. stuartii* is complicated by its intrinsically strong resistance to a wide range of antibiotics (4, 6–8) and by its ability to form biofilms. The latter may attach and grow on indwelling catheters (3, 9, 10) and on uroepithelial cells (11). Recently, we reported the microscopic characterization of *P. stuartii* plankton and biofilms and the unexpected finding that this species forms floating communities of cells in solution before its deposition as a surface-attached biofilm (12). Within floating communities, cells are in apparent contact and presumably stick to one another via protein–protein interactions (12). Inasmuch as the general diffusion porins are the most abundant proteins in the outer membrane (OM) of gram-negative bacteria, with a major porin often accounting for up to 70% of the OM protein content (up to 10⁵ copies per cell) (13), we set out to verify whether *P. stuartii* porins could partake in the formation of floating communities.

Porins are water-filled channels spanning the OM of gram-negative bacteria (14) and constitute the principal entry route for hydrophilic nutrients, ions, and antibiotics into the periplasm. They are generally assembled as trimers, within which each monomer displays a conserved β -stranded architecture that delineates a hydrophilic channel. Substrate-specific porins are barrels of 18 β -strands, while porins governed by general diffusion (referred to as porins throughout the manuscript) feature 16 β -strands. In both cases, sifting properties are determined by the amino acid distribution at their constriction zone, contributed by the folding of extracellular loop L3 into the channel lumen. The genome of *P. stuartii* encodes two porins, Omp-Pst1 and Omp-Pst2. The uptake of β -lactams (cephalosporins and carbapenems, in particular), quinolones, and fluoroquinolones is mainly due to their passive diffu-

sion through Omp-Pst1 (6, 7). Omp-Pst1 is essential to *P. stuartii* survival, while Omp-Pst2 promotes rapid growth, possibly through regulation of the cationic content of the periplasm (12).

To obtain insight into how Omp-Pst1 and Omp-Pst2 could be linked to the pathogenicity of *P. stuartii*, we first determined their 3D structures. These reveal the molecular basis for the distinct ion selectivity of Omp-Pst1 and Omp-Pst2, while that of a complex with maltose suggests an involvement of Omp-Pst1 in carbohydrate harvesting and uptake. Analysis of crystal-packing interactions led to the discovery of an oligomeric assembly common to both porins and formed by the face-to-face association of two porin trimers through their extracellular loops. These dimers of trimers (DOTs) assemble through steric zipper interactions between homo-specific segments. Incorporation of either of the porins into liposomes results in proteoliposome aggregation, while their ectopic expression in a porin-devoid *Escherichia coli* strain induces a shift from the state of isolated plankton to that of floating communities. Thus, our results support the hypothesis that porins contribute to cell-to-cell contact in floating communities of *P. stuartii* (12). We propose that DOTs are the biological assemblies at the basis of

Significance

We report that porins, the main gateway for hydrophilic nutrients and ions into bacterial cells, assemble face-to-face in crystals, yielding dimers of trimers (DOTs). Further investigation suggests that DOTs could support cell-to-cell contact in the floating communities formed by *Providencia stuartii*, and could enable direct communication between adjacent cells. Self-matching steric zipper interactions are observed at the dimer interface, suggesting a means by which DOT formation could be restricted to cells of the same clonal origin.

Author contributions: M.E.-K., C.N., and J.-P.C. designed research; M.E.-K., C.N., J.L., Q.-T.T., G.T., H.B., D.F., B.G., M.L., and J.-P.C. performed research; Q.-T.T., G.T., J.-M.B., J.-M.P., M.V., M. Weik, and M. Winterhalter contributed new reagents/analytic tools; M.E.-K., C.N., J.L., G.T., M.V., M. Weik, and J.-P.C. analyzed data; and M.V. and J.-P.C. wrote the paper with input from M.E.-K., C.N., J.L., Q.-T.T., G.T., J.-M.P., M. Weik, and M. Winterhalter.

The authors declare no conflict of interest.

This article is a PNAS Direct Submission.

Published under the PNAS license.

Data deposition: The atomic coordinates and structure factors have been deposited in the Protein Data Bank, www.wwpdb.org, under the following PDB accession codes: Omp-Pst1 type-A (4d64), Omp-Pst1 type-B (5nxx), maltose complex with Omp-Pst1 type-B (5nxy), Omp-Pst2 (4d65), 283-LGNY-286 (5n9i), 206-GVVTSE-211 (5n9h), and Omp-Pst1- Δ 207-216-N293G (5nxx).

¹M.E.-K. and C.N. contributed equally to this work.

²Present address: UMR 5203, Institut de Génomique Fonctionnelle, F-34094 Montpellier, France.

³To whom correspondence should be addressed. Email: colletier@ibs.fr.

This article contains supporting information online at www.pnas.org/lookup/suppl/doi:10.1073/pnas.1714582115/-DCSupplemental.

Published online February 23, 2018.

the cell-to-cell contact property and that they could provide a means of direct communication between cells.

Results

Structures of Omp-Pst1 and Its Complex with Maltose. The structure of native Omp-Pst1 was solved in two space groups: C2 (type A; 3.2 Å resolution) and P2₁2₁2₁ (type B; 2.7 Å resolution) (*SI Appendix, Table S1*). In both crystal forms, the asymmetric unit contains a single trimer. In type A crystals, dimerization of trimers along the crystallographic twofold axis results in a DOT, assembled through steric zipper interactions between homologous segments in facing extracellular loops (Fig. 1*A*). In type B crystals, contact is also observed between extracellular loops but does not involve self-matching interactions. In both types of crystals, no contact is observed between intracellular turns, and

complementary contact is established between transmembrane regions. The trimeric structures of Omp-Pst1 in type A and type B crystals are similar, superimposing with an rmsd of 0.356 Å over 1,056 residues. While extracellular loops of Omp-Pst1 are mostly folded as α -helices, the L5 extracellular loop of each monomer contributes a β -hairpin that is positioned over the channel's extracellular vestibule and complicates access to the pore (*SI Appendix, Fig. S1A*). In type A crystals, the L5 β -hairpins are additionally involved in the crystal-packing interactions that underlie DOT assembly, at the unit cell level (Fig. 1*A* and *B*).

Compared with the canonical porins OmpF, OmpC, and PhoE from *E. coli*, Omp-Pst1 displays a similar pattern of charge distribution. In particular, the Omp-Pst1 channel is positively charged (+5e in Omp-Pst1 vs. +3e, +3e, and +6e in OmpF, OmpC, and PhoE, respectively) (Fig. 1*I* and *SI Appendix, Fig. S24*), with a net

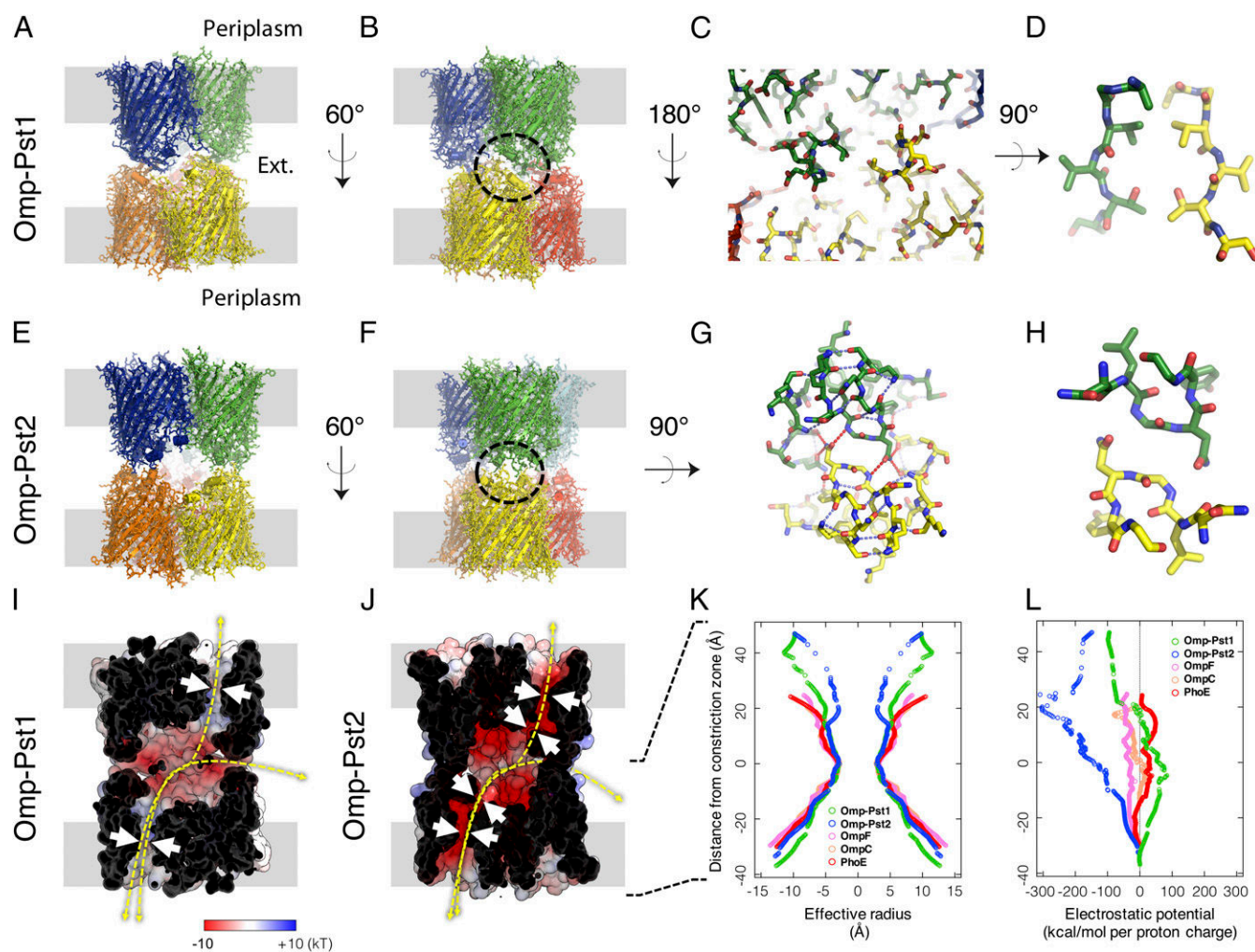


Fig. 1. Omp-Pst1 and Omp-Pst2 form DOTs. (*A*) Lateral view of the Omp-Pst1 DOT. The presumed positions of OMs are shown in gray. (*B*) Same view after 60° vertical rotation. (*C*) Interaction region (circled in *B*) between facing monomers. (*D*) Enlarged view of the center of *C* showing a symmetry class III steric zipper that is buried in the core of the DOT structure. (*E–H*) Equivalent views of the Omp-Pst2 DOT. Main differences are the ellipsoidal fenestrations evident in *E* and the presence of a symmetry class I steric zipper in *H*. (*I*) The dimerization interface of the Omp-Pst1 DOT, viewed as in *B*, delineates a large negatively charged cavity. The electrostatic potential is mapped on the solvent-accessible surface. (*J*) Equivalent representation of Omp-Pst2. In *I* and *J*, white arrows indicate constrictions along the porin channels, whereas yellow arrows indicate possible translocation pathways across porin DOTs: between the periplasm of two adjacent cells, along porin channels, or between the periplasmic space of each cell and the external medium, through fenestrations of the DOTs. (*K*) Effective radii measured along Omp-Pst1 (green), Omp-Pst2 (blue), and *E. coli* porin channels using a 1-Å positively charged rolling probe (equivalent to a proton). The y axis indicates vertical position along the channels from periplasmic (positive y values) to extracellular (negative y values) ends, with reference to the central constriction zone ($z = 0$) contributed by L3. Channels of Omp-Pst1, Omp-Pst2, and *E. coli* porins all display similar radii at their central constriction zone, but the Omp-Pst2 channel features an additional constriction zone in its extracellular vestibule. (*L*) Equivalent plots of electrostatic potentials associated with the translocation of a proton, indicating that Omp-Pst1 is mildly anion selective, while Omp-Pst2 is strongly cation selective. The energy profile of Omp-Pst2 further suggests a facilitated transport of cations from the periplasm to the external medium.

charge of +1e at the constriction zone (0e, -2e, and 0e in OmpF, OmpC, and PhoE, respectively) (Fig. 1 *K* and *L* and *SI Appendix, Fig. S2B*). The electrostatic potential profile calculated along the channel of Omp-Pst1 indicates mild anion selectivity (Fig. 1*L*), in line with electrophysiology measurements and with molecular dynamics (MD) simulations based on this structure (15). Nevertheless, the Omp-Pst1 channel features more charged residues than *E. coli* porins (48%, 35%, and 20% more charged residues than OmpF, OmpC, and PhoE, respectively), suggesting higher translocation selectivity. The extracellular vestibule of Omp-Pst1 is negatively charged (Fig. 1 *I* and *L*).

In an attempt to determine whether or not Omp-Pst1 is involved in translocation of uncharged nutrients into the periplasm, a structure of a complex with maltose was obtained by soaking type B crystals in a mother liquor solution containing 100 mM maltose. The structure of the complex indicates electron density for three maltose molecules, that is, one per monomer, at an identical binding site. Specifically, residues from extracellular loops L1 (K31, E33), L3 (Q121), L6 (R251, G253), L7 (L300), and L8 (G337, N339) form a groove above the constriction zone within which each maltose establishes six to eight H-bonds (depending on the monomer), burying around 70% of its accessible surface (*SI Appendix, Fig. S1B*). The presence of a tight binding site at the channel entrance could underlie a role for Omp-Pst1 in the facilitated translocation of carbohydrates. Ensemble refinement of the maltose-bound Omp-Pst1 structure reveals increased dynamics in L3 residue D117, positioned below the maltose binding site and above the channel constriction zone (*SI Appendix, Fig. S1B*). Hence, D117 could participate in the translocation of maltose from its binding site in the extracellular vestibule to the periplasmic side. Moreover, in all Omp-Pst1 structures, a Ca^{2+} ion could be modeled at the interfacial cavity between the three monomers of the trimer, stabilized by cation- π interaction with the side chain of Trp62 from each monomer (*SI Appendix, Fig. S3 A and B*). Interestingly, this central cavity is opened to the intracellular side but is closed at the extracellular side by symmetrical interactions between Asn75 side chains from the three monomers. Substitution of Ca^{2+} by exposure of the porin to high Zn^{2+} concentrations leads to a dissociation of the trimer, suggesting that this channel-buried ion binding site could be involved in the regulation of Omp-Pst1 oligomerization (*SI Appendix, Fig. S3C*).

Structure of Omp-Pst2. The structure of Omp-Pst2 was solved in the $P2_1$ space group at 2.2 Å resolution (*SI Appendix, Table S1*). A DOT is observed in the asymmetric unit formed by the face-to-face, self-matching interaction of two trimers through their extracellular loops (Fig. 1 *E* and *F*). Hence, Omp-Pst2 and type A Omp-Pst1 crystals reveal a similar biological assembly (Fig. 1 *A*, *B*, *E*, and *F*). The extracellular loops of Omp-Pst2 are mostly folded as α -helices (*SI Appendix, Fig. S1C*), thus contributing an additional constriction zone at the entrance of the channel, which could affect the diffusion of large solutes across Omp-Pst2 (Fig. 1 *J* and *K*). Compared with *E. coli* OmpF, OmpC, and PhoE, the Omp-Pst2 channel features a similar amount of charged residues (20% more charged residues than OmpF, and 8% and 4% less than OmpC and PhoE, respectively) but has a characteristic pronounced acidic nature (Fig. 1*L* and *SI Appendix, Fig. S2C*). The net charge of Omp-Pst2 channel is indeed -4e at the constriction zone, suggesting a strong cation selectivity (Fig. 1*L* and *SI Appendix, Fig. S2D*), which has been verified by electrophysiology measurements (15). Calculation of the electrostatic potential along the Omp-Pst2 channel furthermore suggests a facilitated transport of cations from the intracellular to the extracellular side of the porin (Fig. 1 *J* and *L*), in line with recent MD simulations based on the structure (15). We note that as in Omp-Pst1 crystals, no contact is observed between intracellular turns of Omp-Pst2, and a cavity is apparent at the center of the trimeric complex. This cavity is open at its intracellular end but insulated from the extracellular bulk by

symmetrical interactions between Asn72 (equivalent to Omp-Pst1 Asn75) side chains from the three monomers. At the top of this cavity, an SO_4^{2-} was modeled which appears to be stabilized by an anion- π interaction with the side chain of Trp59 from each monomer (*SI Appendix, Fig. S3 E and F*). Similar to Omp-Pst1, exposure of Omp-Pst2 to high Zn^{2+} concentrations leads to a dissociation of the trimer, suggesting a critical role for this central ion binding site in the regulation of Omp-Pst2 oligomerization (*SI Appendix, Fig. S3 C and D*). Furthermore, it shows that the central channel of Omp-Pst2 can accommodate both positively charged and negatively charged divalent ions.

Omp-Pst1 and Omp-Pst2 Form DOTs Assembled Through Steric Zipper Interactions. In Omp-Pst2 and in type A Omp-Pst1 crystals, packing is supported by the face-to-face interaction of two trimers via their extracellular loops, yielding DOTs (Fig. 1 *A*, *B*, *E*, and *F*). In both DOTs, the dimerization interface delineates a large negatively charged cavity (volumes of 30,610 and 37,959 Å³ for Omp-Pst1 and Omp-Pst2, respectively) (Fig. 1 *I* and *J*). The cavity of Omp-Pst2 is accessible from the bulk via three ellipsoidal fenestrations of 17 × 29 Å (Fig. 1 *E*, *F*, and *J*), while that of Omp-Pst1 is shielded from the bulk and presumably only accessible to water (Fig. 1 *A*, *B*, and *J*). The buried surface areas per facing trimer are 921 Å² for Omp-Pst1 and 1,215 Å² for Omp-Pst2 DOTs—that is, values above the threshold of 856 Å² that has been proposed to discriminate between artificial and biological dimers in crystal structures (16). In comparison, the buried surface area per facing trimer is 350 Å² in type B Omp-Pst1 crystals. The surface complementarity between facing trimers of the DOT is 0.40 for Omp-Pst1 and 0.64 for Omp-Pst2. The latter value is close to that displayed by antibody-antigen complexes, namely 0.65 (17).

The DOTs formed by Omp-Pst1 and Omp-Pst2 are singular in that they appear to be supported by steric zipper interactions—a structural motif that has, to date, been observed only in prions and amyloid fibers. Steric zippers form from the tight interdigitation of side chains emanating from equivalent residues in short self-matching sequences (4–11 residues) and they are, by nature, highly self-selective. In amyloid and prion assemblies, steric zippers associate β -sheets into highly ordered fibers (18, 19), but the steric zipper interfaces that form between facing monomers of Omp-Pst1 and Omp-Pst2 trimers are single layered. Thus, perhaps, neither Omp-Pst1 nor Omp-Pst2 would, if monomeric, be able to dimerize face-to-face through these motifs.

The steric zipper interfaces differ in the two porins. In Omp-Pst1, the three single-layered steric zipper interfaces are contributed by residues 206-GVVTSE-211 from extracellular loop L5 and would belong to the symmetry class III of steric zippers (face-to-face, up-down) (18) (Fig. 1 *C* and *D*), with a 15° tilt between the two facing β -strands. This interface is reinforced only by weak electrostatic interaction (distance between nonhydrogen atoms ≥ 3.5 Å) between K28 and D213 from facing extracellular loops L1 and L5, respectively (*SI Appendix, Fig. S4A*). The formation of Omp-Pst1 DOT thus appears fully governed by extracellular loop L5. In Omp-Pst2, residues 282-NLGNYG-287 from facing extracellular loops L7 interact via three single-layered nontilted steric zippers that would correspond to the symmetry class I of steric zippers (face-to-face, up-up) (18) (Fig. 1 *G* and *H*). Each steric zipper interface, centered around residues G284 and N285, is complemented by a network of H-bonds which fastens extracellular loops L5, L7, and L8 from facing monomers (Fig. 1*G* and *SI Appendix, Fig. S5A*). Of note, Omp-Pst1 features a 290-NLGNGY-295 sequence in its extracellular loop L7, similar to the 282-NLGNYG-287 sequence of Omp-Pst2. However, the L5 β -hairpin protrusion that contributes the 206-GVVTSE-211 steric zipper interface renders L7 inaccessible in Omp-Pst1 (*SI Appendix, Fig. S1A*). Nonetheless, N293, equivalent to Omp-Pst2 N285, plays an important role in Omp-Pst1 DOT formation, contributing two H-bonds to Y216 at the base of

the L5 β -hairpin which stabilize the latter and, therefore, the steric zipper interface (*SI Appendix, Fig. S4A*).

To evaluate the steric zipper propensity of Omp-Pst1 and Omp-Pst2 segments involved in their dimerization into DOTs, we crystallized the corresponding peptides. For each, we chose the smallest fragment hypothetically involved in the interaction: 206-GVVTSE-211 from Omp-Pst1, and 283-LGNY-286 from Omp-Pst2. Both peptides produced urchinlike microcrystals from which their structures were solved at 1.7 and 1.0 Å resolution, respectively (Fig. 2 and *SI Appendix, Table S1*). The two peptides display canonical cross- β structures, characterized by the in-register stacking of strands into β -sheets and by the mating of these sheets via a steric zipper, perpendicular to the fiber axis. Thus, both 206-GVVTSE-211 and 283-LGNY-286 have a high propensity to form steric zippers (Fig. 2) in isolation of their respective parent proteins. The 3D profile method (20) also identified these segments as highly prone to form steric zippers, with scores of -26.2 and -22.1 kcal/mol, respectively (*SI Appendix, Fig. S6*). They accordingly form fibrils in vitro (*SI Appendix, Fig. S6 A and B*).

Omp-Pst1 and Omp-Pst2 Self-Interact in Vitro. We investigated whether Omp-Pst1 and Omp-Pst2 can have adhesion properties in vitro. If so, incorporation of either porin into liposomes should lead to proteoliposome aggregation—a process we monitored by dynamic light scattering (DLS). We first examined phosphatidylcholine (PC) liposomes, whose surfaces are neutral at physiological pH. We used the direct-dilution method to incorporate porins into liposomes, enabling real-time monitoring of the process. Using centrifugation on sucrose gradient (21), we confirmed insertion of Omp-Pst1 and Omp-Pst2 into preformed liposomes, and observed that this process is favored at acidic pH (*SI Appendix, Fig. S7*). We then used DLS to monitor the average hydrodynamic radius of the proteoliposome aggregates which form, upon incorporation of Omp-Pst1 or Omp-Pst2 at increasing concentrations, into preformed liposomes (60-nm starting radius). We found that insertion of either porin into liposomes results in a fast (~ 30 to 45 s) and porin-concentration-dependent aggregation of proteoliposomes (Fig. 3 and *SI Appendix, Fig. S8A*). In contrast, incorporation of *E. coli* OmpF into PC liposomes by the same method had

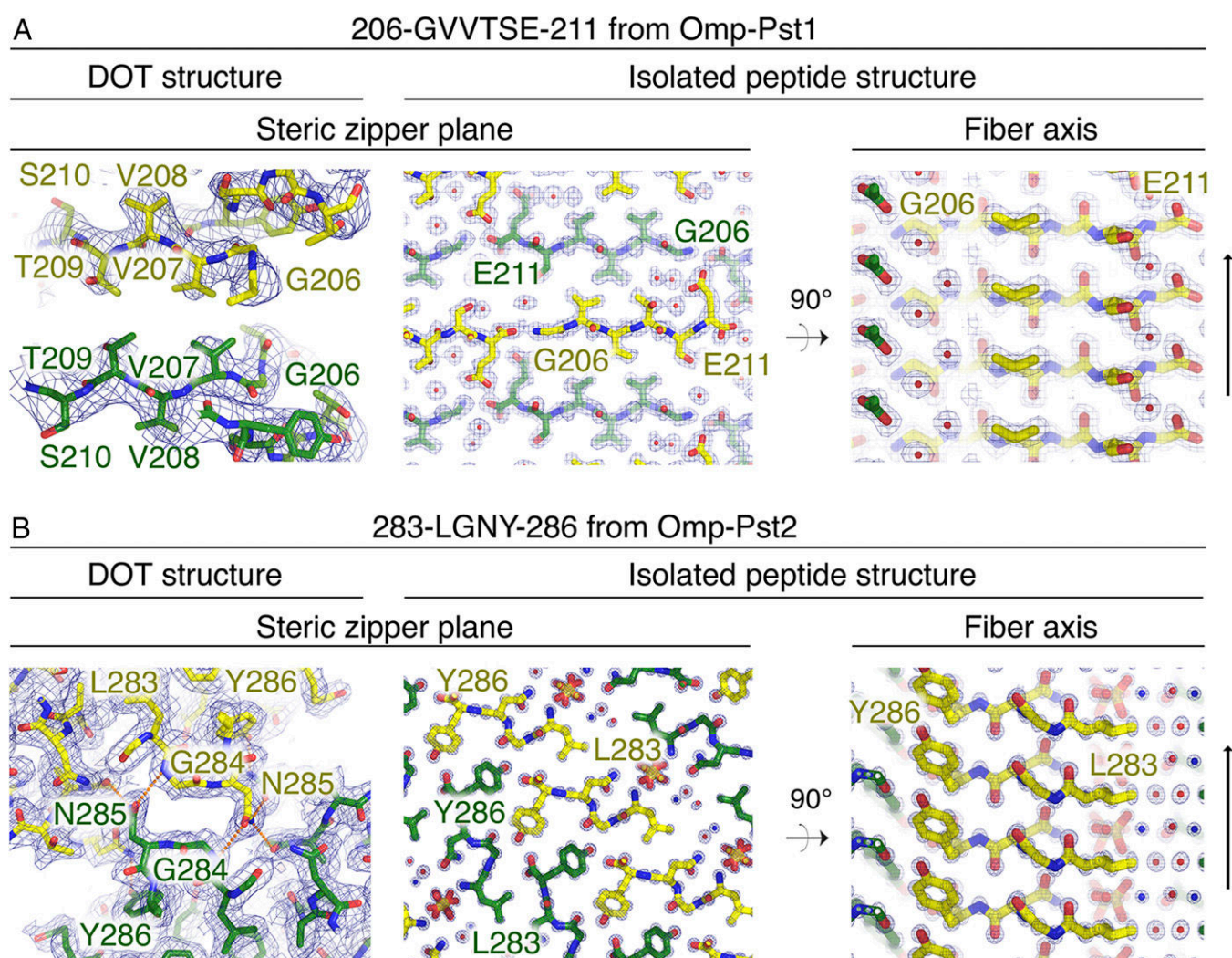


Fig. 2. The segments involved in the formation of the Omp-Pst1 and Omp-Pst2 DOTs also form steric zippers in isolation from their parent protein. (*A and B*) Both 206-GVVTSE-211 from Omp-Pst1 (*A*) and 283-LGNY-286 from Omp-Pst2 (*B*) form single-layered steric zippers in the DOT structures of Omp-Pst1 and Omp-Pst2, respectively (*Left*). The 206-GVVTSE-211 and 283-LGNY-286 steric zippers would belong to symmetry classes III and I, respectively. In isolation, the GVVTSE and LGNY peptides also form steric zippers (*Middle and Right*), as revealed by their crystal structures solved at 1.7 and 1.0 Å resolution, respectively. (*Middle*) Steric zipper interfaces. (*Right*) A view of 90° apart revealing that both GVVTSE and LGNY adopt a canonical cross- β structure, whereby the steric zipper repeats itself every 4.8 Å through hydrogen bonding along a fiber axis. In the peptide structures, GVVTSE and LGNY form steric zippers that belong to symmetry classes I and III, respectively. Thus, symmetry classes are inverted in the porin and steric zipper structures. In all panels, the corresponding refined 2mFo-DFc electron density map is contoured at 1σ .

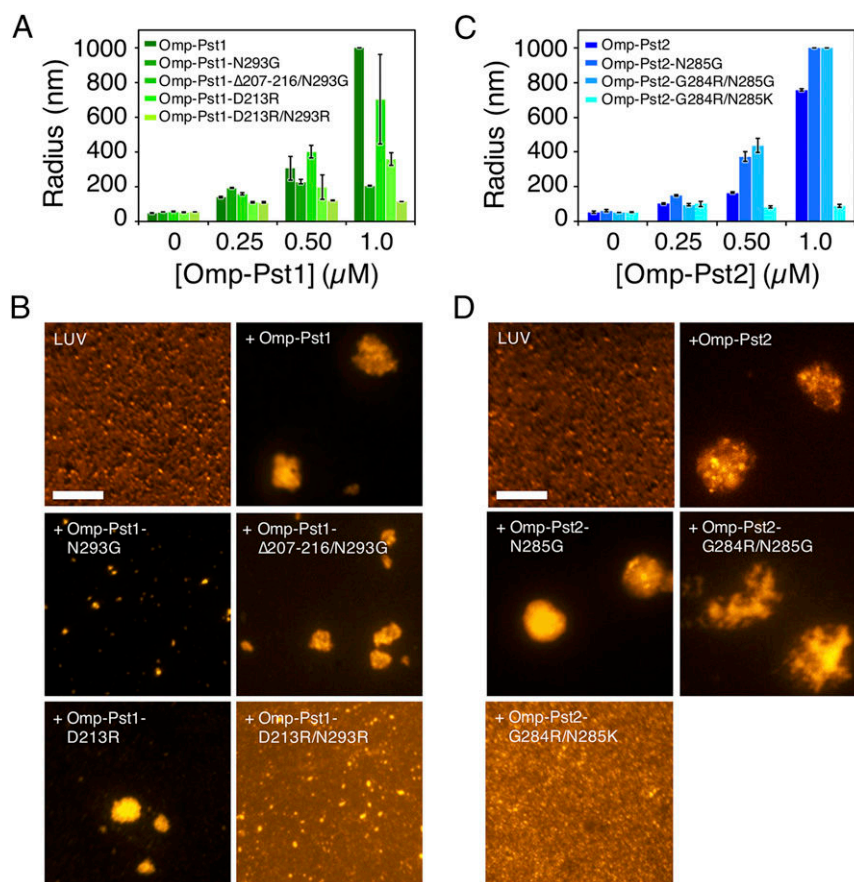


Fig. 3. Altering charge distribution at the DOT interface reduces aggregation properties of Omp-Pst1 and Omp-Pst2 in vitro. (A) DLS was used to measure the hydrodynamic radii of proteoliposomes formed 24 h after the addition of increasing concentrations of Omp-Pst1 and its specified mutants (colored in shades of green) to a monodispersed 60-nm liposome solution. (B) Proteoliposomes formed at 1 μM porin were spread onto an agarose-coated cover slide for epifluorescence imaging. Large unilamellar vesicles (LUVs) were labeled using rhodamine-derivatized lipids. (C and D) Same as in A and B, but for Omp-Pst2. (B and D scale bars: 20 μm ; magnification: 60 \times .)

comparatively no effect on their average size distribution (*SI Appendix, Fig. S8A*). The proteoliposome aggregation induced by Omp-Pst1 and Omp-Pst2 is visible in the pH 4 to 8 range, although it was reduced (smaller liposomes aggregates) at pH 7 and 8, either due to a suboptimal incorporation of porins into liposomes at these pH values or to a reduced self-affinity (*SI Appendix, Fig. S7*). To increase the stringency of further measurements, we nonetheless worked at pH 7, which avoided the formation of proteoliposome aggregates too large (>1 μm) and too polydisperse (>50%) to be resolved by our DLS instrument.

We ascertained the presence of Omp-Pst1 and Omp-Pst2 in proteoliposome aggregates by labeling lipids and porins specifically, and then by examining porin-induced proteoliposome aggregation using epifluorescence microscopy (*SI Appendix, Fig. S8B*). Omp-Pst1 and Omp-Pst2 were specifically labeled by engineering of a cysteine (Omp-Pst1-K221C and Omp-Pst2-K211C) at the C-terminal extremity of their L5 loop (*SI Appendix, Figs. S4B and S5B*, respectively), followed by derivatization of the resulting mutants with a maleimide-coupled green fluorophore (Alexa488). Fluorescent liposomes were prepared by introduction of a red fluorescent lipid (rhodamine derivative) in the bilayer composition. Both Omp-Pst1-K221C and Omp-Pst2-K211C retained the ability to induce proteoliposome aggregation in DLS experiments (*SI Appendix, Fig. S8A*). Furthermore, in epifluorescence micrographs, we observed a colocalization of the fluorescence signals arising from the lipids and the porins. The observation that the Omp-Pst1-K221C mutant can still self-associate indicates that the

interface revealed by type B crystals is not relevant for proteoliposome aggregation, as the H-bond between K221(NZ) and N293(O) is central to this interface (*SI Appendix, Fig. S4*). Aggregates of proteoliposomes formed at 2 μM porin concentration were examined by transmission electron microscopy, revealing stacks of lipid bilayers (*SI Appendix, Fig. S9*). Those aggregates display periodic order, further exemplifying the strong tendency of Omp-Pst1 and Omp-Pst2 porin to self-associate, both laterally and axially.

Additional DLS data were collected on liposomes composed of palmitoyl-oleyl (PO)PC and PO phosphatidylserine (POPS), in the presence and absence of rough and smooth lipopolysaccharides (LPSs). Data were collected at pH 7, at two liposome concentrations (0.125 and 1.25 mg/mL, corresponding to \sim 2 and \sim 20 nM of 60-nm liposomes in *SI Appendix, Figs. S10 and S11*, respectively), and at two LPS-to-phospholipid mass ratios (1:10 and 1:100), before and after the removal of the detergent using biobeads.

The data show that *P. stuartii* porin self-association is hindered by electrostatic repulsion between (overall negatively charged) POPS liposomes. Omp-Pst2 self-association is inhibited in the presence of rough and smooth LPSs (*SI Appendix, Figs. S10 C and D and S11 C-F*), additional to those already copurified with the protein (*SI Appendix, Fig. S12 A and B*). Omp-Pst1 self-association is not affected by inclusion of rough LPSs (which lack O-antigen but possess shorter core oligosaccharides and lipid A) in (overall neutral) POPC liposome bilayers, even at an LPS-to-phospholipid mass ratio of 1:10 (*SI Appendix, Figs. S10 C and D and S11 C and D*), whereas it is reduced by the inclusion of smooth LPSs (which possess O-antigen,

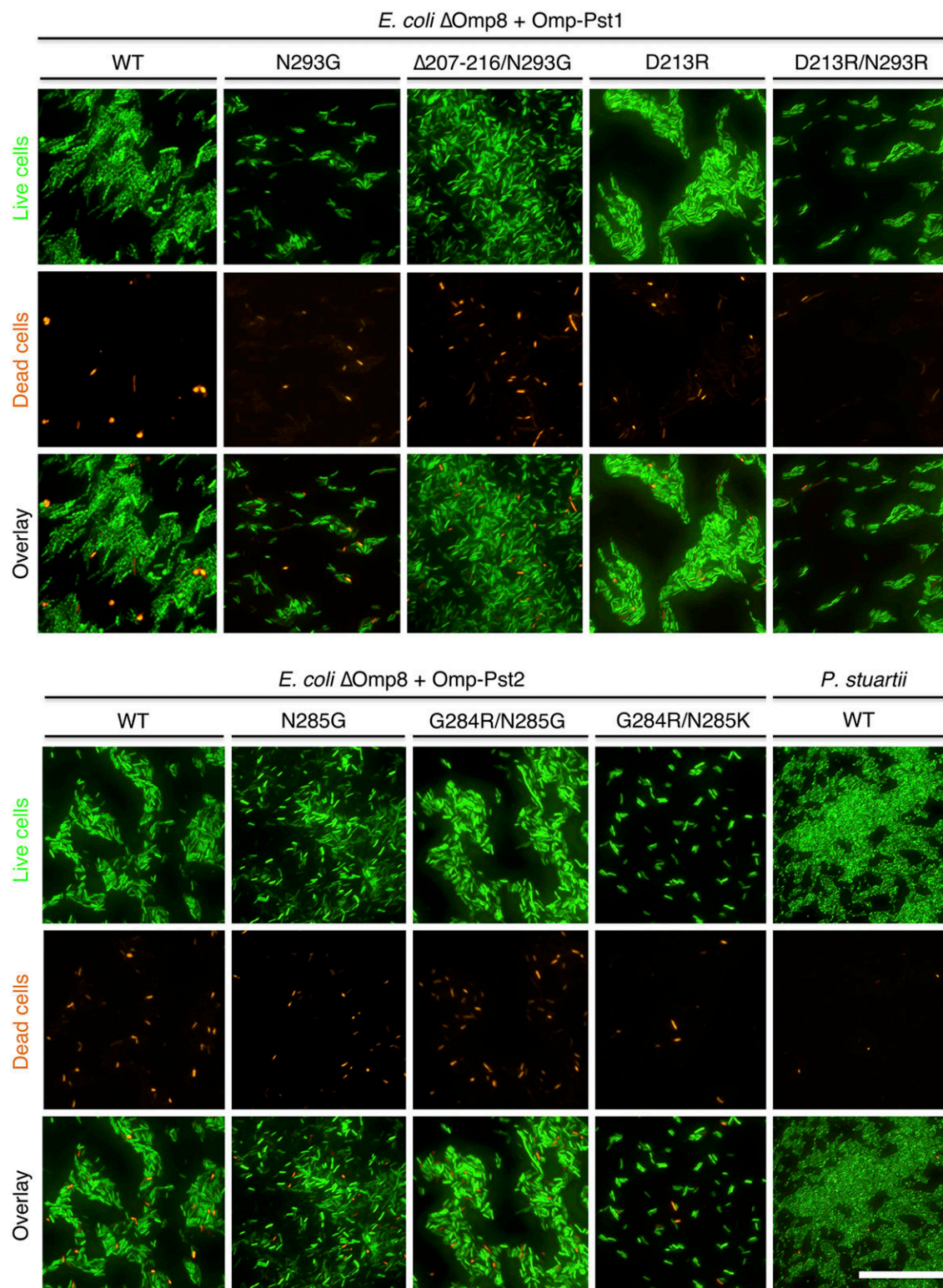


Fig. 4. Omp-Pst1 and Omp-Pst2 mutations affect the formation of floating communities of cells by transformed *E. coli* Δ Omp8 cells. Bacterial strains were grown for 24 h in 96-well plates. Subsequently, live and dead cells were stained with SYTO9 Green and propidium iodide, respectively. Planktonic cells were harvested by direct pipetting from the LB medium, spread on LB-Gelzan, and imaged immediately afterward. For comparison, the floating communities natively formed by *P. stuartii* cells are also shown. (Scale bar: 50 μ m for all images; magnification: 60 \times .)

complete core oligosaccharides, and the lipid A) at an LPS-to-phospholipid mass ratio of 1:100 (*SI Appendix, Fig. S10 I and J*) and suppressed at 1:10 (*SI Appendix, Fig. S11 E and F*).

The data also show that detergent does not promote proteoliposome aggregation. First, removal of detergent hardly affects the size of proteoliposome aggregates when phospholipid-only

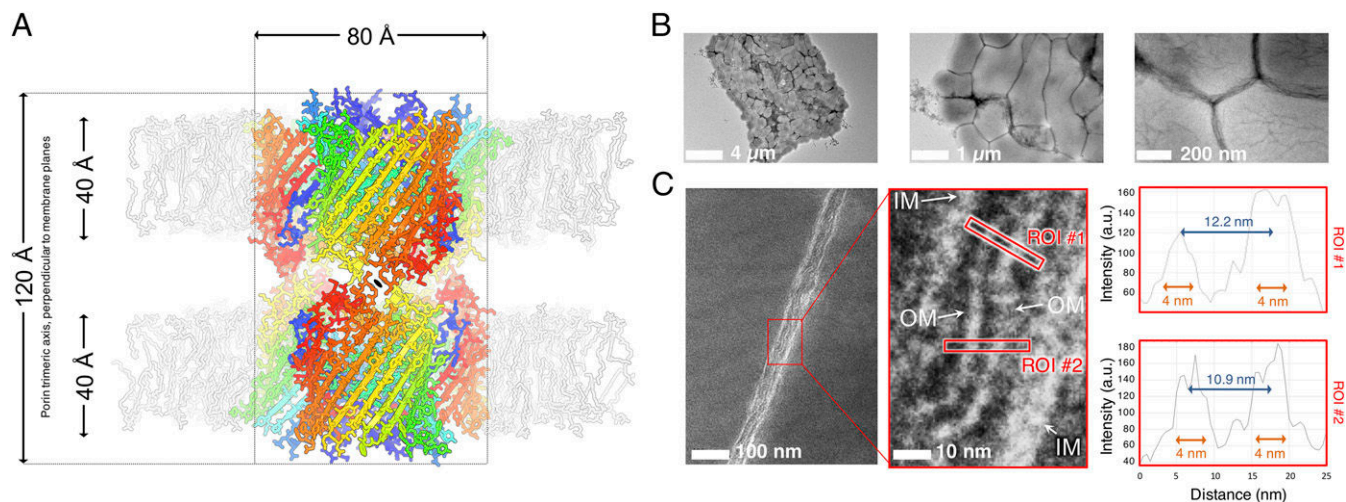


Fig. 5. The distance between adjacent cells in *P. stuartii* floating communities is compatible with the formation of a porin DOT. (A) Lateral and longitudinal extent of a porin DOT. The Omp-Pst2 DOT is shown as sticks and ribbons, colored sequence-wise from cold (N-ter) to hot (C-ter) color. A phospholipid bilayer was reconstituted around each trimer in the DOT at the presumed positions of OMs; phospholipids are depicted as gray sticks. (B and C) Negatively stained transmission electron micrographs of *P. stuartii* floating communities. (B) *P. stuartii* floating communities can incorporate hundreds of closely connected cells. Empty spaces with cellular debris are sometimes observed within floating communities, suggesting that cellular death could play a role in the regulation of cell-to-cell contacts of these floating communities. (C) A close contact is observed between the OMs of adjacent cells in floating communities (Left). In the close-up view (Middle), OMs are ~10 nm apart, a distance that would allow a DOT to form between two OMs. (Right) Integrated intensity plots for the two regions of interest (ROIs) highlighted by the red squares depicted in Middle. IM, inner membrane.

liposomes are used (SI Appendix, Fig. S10 A, B, E, and F). Second, the detergent, at concentrations much higher than used in our study, reduces the size of liposomes (SI Appendix, SI Methods and Fig. S13A), whereas incorporation of porins augments it. Additionally, smaller proteoliposome aggregates are observed when higher concentrations of liposomes are used (SI Appendix, Figs. S10 and S11 show data at 0.125 and 1.25 mg/mL), supporting the hypothesis that proteoliposome aggregation depends on the number of porins inserted per liposome (SI Appendix, Figs. S10 and S11).

We also investigated the effect of high concentrations of salt and chaotropes (urea, NH_4Cl , NaCl, and NaSCN). Efforts to investigate the effects of CaCl_2 , MgCl_2 , and ZnCl_2 were thwarted by the aggregating effect of these ions on liposomes. We found that Omp-Pst1-induced aggregation of phospholipid-only liposomes is reduced, albeit to different extents, in the presence of urea, NH_4Cl , NaCl, and NaSCN. In contrast, Omp-Pst2-induced aggregation of such liposomes is prevented by urea, promoted by NH_4Cl and NaCl, and unaffected by NaSCN. The presence of LPS changes these patterns, restoring self-association for Omp-Pst1 in the presence of NaCl, although still inhibiting Omp-Pst2 self-association. We note that biobeads and LPSs are incompatible, as LPSs strongly interact with both biobeads and porins, resulting in the extraction of the latter from liposome bilayers (SI Appendix, Figs. S10 C, D, I, and J and S14). Finally, we used DLS to measure the dissociation constants for lauryldimethylamine *N*-oxide-solubilized Omp-Pst1 and Omp-Pst2 DOTs (SI Appendix, SI Methods and Fig. S13B). Fitting of these data suggests dissociation constants of 0.6 and 0.4 μM for Omp-Pst1 and Omp-Pst2, respectively, at pH 7.

Self-Association of Omp-Pst1 and Omp-Pst2 Is Driven by Electrostatic Interactions. We used site-directed mutagenesis to further characterize self-association of Omp-Pst1 and Omp-Pst2 in vitro. First, we targeted the steric zipper interface observed in Omp-Pst1 DOTs (SI Appendix, Fig. S4), either by introduction of point mutations in L5 and L7 (Omp-Pst1-D213R, Omp-Pst1-N293G, and Omp-Pst1-D213R/N293R) or by deletion of the full L5 β -hairpin that supports this interface (Omp-Pst1- Δ 207–216/N293G)

(SI Appendix, Fig. S4D). The charge-altering mutations D213R (SI Appendix, Fig. S4E) and D213R/N293R (SI Appendix, Fig. S4F) respectively reduced and suppressed the ability of Omp-Pst1 to induce proteoliposome aggregation (Fig. 3 A and B). The L7 mutant Omp-Pst1-N293G (SI Appendix, Fig. S4C), designed to destabilize extracellular loop L5—thereby inhibiting steric zipper formation—through suppression of the two H-bonds between N293 and Tyr216, was unable to promote proteoliposome aggregation (Fig. 3 A and B and SI Appendix, Fig. S4). The inability of Omp-Pst1-N293G to induce proteoliposome aggregation was yet fully reversed by deletion of the entire L5 β -hairpin, namely, Omp-Pst1- Δ 207–216/N293G (SI Appendix, Fig. S4D). Hence, the self-association properties of Omp-Pst1 are impacted by electrostatic repulsion or destabilization of the steric zipper interface, but not by the complete suppression of the L5 β -hairpin (Fig. 3 A and B). Likewise, two Omp-Pst2 mutants aimed at disrupting the 282-NLGNYG-287 steric zipper interface, namely, Omp-Pst2 N285G and Omp-Pst2-G284R/N285G (SI Appendix, Fig. S5 C and D), showed increased ability to induce proteoliposome aggregation (Fig. 3 C and D). Again, only the Omp-Pst2-G284R/N285K mutant with two positive charges added side-by-side (SI Appendix, Fig. S5E) displayed a reduced ability to induce proteoliposome aggregation, reminiscent of Omp-Pst1-D213R/N293R. Hence, the main driving force behind Omp-Pst1 and Omp-Pst2 self-association appears to be electrostatic attraction, while single-layered steric zipper interaction between facing monomers could underlie a slotting mechanism that regulates DOT formation. In that case, Omp-Pst1- Δ 207–216/N293G should form DOTs that solely assemble through electrostatic interactions, since both steric zipper interfaces available at the surface of Omp-Pst1 should be disrupted in that mutant.

To verify this hypothesis, we crystallized Omp-Pst1- Δ 207–216/N293G and solved its structure at 3.2 Å resolution (SI Appendix, Fig. S15 and Table S1). Reminiscent of type A Omp-Pst1 crystals, those of Omp-Pst1- Δ 207–216/N293G belong to the C2 space group and reveal the presence of a DOT at the unit cell level (SI Appendix, Fig. S4 A and B). The buried surface area per facing trimer is 1,126 Å², and the dimerization interface delineates a large negatively charged cavity characterized by a volume of 24,540 Å³

(*SI Appendix, Fig. S15C*). As proposed, electrostatic interactions between extracellular loops are at the basis of this DOT, which is not supported by steric zipper interactions and wherein facing channels do not join at their extracellular ends—another difference with the DOTs formed by wild-type Omp-Pst1 and Omp-Pst2. Rather, one monomer from each trimer plugs into the center of the facing trimer and establishes contact with the three facing monomers through extracellular loops L7 (to L4 in a first monomer), L8 (to L6 and L8 in a second monomer), and L5 (to L5 in the third monomer). The first two interaction zones are polar, featuring H-bonds between Asp296(OD2) and Met168(N) and between the NZ atom K334 and the main chain carbonyl oxygen of Asp254, respectively (*SI Appendix, Fig. S15D*). The unnatural Omp-Pst1- Δ 207–216/N293G DOT is nevertheless characterized by a more accessible central cavity, showing reduced surface complementarity between facing trimers (0.37) and featuring six large ellipsoidal fenestrations (up to $7 \times 20 \text{ \AA}$) (*SI Appendix, Fig. S15*).

Omp-Pst1 and Omp-Pst2 Support Cell-To-Cell Contact in *P. stuartii* Floating Communities. *P. stuartii* is highly social, forming floating communities of cells before depositing as surface-attached biofilms (12). We thus asked whether a correlation would exist between expression of *P. stuartii* porins and the formation of such floating communities. Omp-Pst1 is the major porin of *P. stuartii* (*SI Appendix, Fig. S12C*) and essential to its survival; hence, a knockout strategy was unsuited to challenge our hypothesis (12). Rather, we opted for an ectopic expression strategy, using as a surrogate for *P. stuartii* a strain of *E. coli* BL21 deleted of its major porins OmpF, OmpC, OmpA, and LamB: *E. coli* Δ Omp8 (22) (*SI Appendix, SI Methods*). Like BL21, the Δ Omp8 strain does not form detectable floating or surface-attached biofilms (*SI Appendix, Fig. S16*). However, this strain displays reduced growth and fitness and a longer lag-phase (*SI Appendix, Fig. S17A*). Ectopic expression of either Omp-Pst1 or Omp-Pst2 in Δ Omp8 cells restores normal growth and reduces the lag phase (*SI Appendix, Fig. S17A*). Furthermore, it confers to *E. coli* Δ Omp8 cells the ability to form floating communities similar to those formed by *P. stuartii* (Figs. 4 and 5 and *SI Appendix, Fig. S16*). Formation of these is independent of that of surface-attached biofilms, which recombinant Δ Omp8 strains remain unable to form (*SI Appendix, Fig. S16*).

We then set to verify whether mutants unable to induce aggregation of proteoliposomes would also fail at forming floating communities. Δ Omp8 cells expressing mutated versions of Omp-Pst1 (D213R, N293G, D213R/N293R, and Δ 207–216/N293G) or Omp-Pst2 (N285G, G284R/N285G, and G284R/N285K) display similar growth and lag phases as cells expressing wild-type Omp-Pst1 and Omp-Pst2, demonstrating that the mutants are well-expressed and folded, and that their diffusive properties are not affected (*SI Appendix, Fig. S17 B and C*). Strikingly, however, Δ Omp8 cells expressing porin mutants that are able to induce aggregation of proteoliposomes in vitro form floating communities, whereas those expressing mutants unable to self-associate in vitro do not (Figs. 3 and 4). Thus, our data show that the expression of self-associating *P. stuartii* porins is sufficient to enable formation of communities of cells by a non-biofilm-forming *E. coli* strain (Fig. 4 and *SI Appendix, Fig. S16*). We therefore propose that this mechanism is at play in the formation of *P. stuartii* floating communities (Fig. 5), wherein cell-to-cell contacts are observed. As the formation of floating communities precedes that of surface-attached biofilms (12) (Fig. 5 and *SI Appendix, Fig. S18*), porins could also be involved in the cell-to-cell contacts observed within the core of surface-attached biofilms (*SI Appendix, Fig. S19*).

Discussion

The crystallographic structures of Omp-Pst1 and Omp-Pst2 reveal that, within crystals, these porins are able to form DOTs through self-matching interaction of homologous segments in their extracellular loops (Figs. 1 and 2). Using liposome-based assays, we

found that Omp-Pst1 and Omp-Pst2 display self-association properties in vitro (Fig. 3), while by means of ectopic expression in Δ Omp8 (a porin-devoid strain of *E. coli*), we showed that the sole expression of Omp-Pst1 or Omp-Pst2 endows these model cells with the capability to form floating communities (Fig. 4). Thus, our data suggest that the self-association of porins from adjacent cells can sustain contact between these cells. Based on buried surface area statistics, the DOTs revealed by type A crystals of Omp-Pst1 and by crystals of Omp-Pst2 and Omp-Pst1- Δ 207–216/N293G are compatible with the adhesive properties of these porins, but the side-by-side DOTs observed in type B crystals of Omp-Pst1 are not. We thus propose that the DOT structures are the biological assemblies that contribute to rivet cells one to another in *P. stuartii* floating communities (Fig. 5), possibly in parallel with other adhesion mechanisms. Our observation that DOT formation is impaired by smooth LPSs suggests that DOTs may be specific to “rough” colonies.

Floating communities of cells associated through DOTs could provide a scaffold for biofilm genesis, allowing the building of a critical biomass before deposition onto a surface and secretion of an extracellular matrix. In line with this hypothesis, cells within the core layers of *P. stuartii* surface-attached biofilms (*SI Appendix, Fig. S19 A and B*) display the same phenotype as those in floating communities; that is, a close contact is observed between their OMs (Figs. 4 and 5 and *SI Appendix, Fig. S19 A and B*). Hence, Omp-Pst1 and Omp-Pst2 DOTs could be targeted to inhibit socialization of *P. stuartii* in its early stages—that is, before formation of a canonical biofilm, when only cell-to-cell contact is at play. We showed that a simple disruption or removal of the steric zipper interface does not suppress the self-associating properties of the porins, but that they can be abolished in vitro and in vivo through destabilization of the steric zipper interface or by electrostatic repulsion (Figs. 3 and 4). In yeast, steric zippers promote the selection of strains based on self-templating prions, while in amyloid diseases (19), they allow the formation of a variety of fiber polymorphs which differ in toxicity and shape. In *P. stuartii* porins, steric zippers could serve to avoid interspecies DOT formation, thus restricting contact to cells of the same strain only.

Within crystallographic DOTs, facing channels are opened, suggesting that they could provide, in vivo, an effective conduit for the exchange of signaling solutes or nutrients by passive diffusion (Fig. 1)—irrespective of whether or not they are at the origin of the cell-to-cell contact phenotype. It is known that within biofilms, cells exchange chemical information through a mechanism termed “quorum sensing” (QS), which orchestrates the phenotypic adaptation undergone by bacteria as they morph from the planktonic isolated state to the multicellular biofilm state (23). QS is also involved in the adaptation of biofilm cells to local environmental changes (23), in metabolic codependence (24) and time-sharing processes (25), and in the release of cells from the biofilm (23). As yet, however, it had remained unclear how soluble QS effectors could mediate intercellular communication in the first stages of biofilm formation—that is, when the cell density is low and no surrounding matrix is present. The DOT structures hint at a direct intercellular communication mechanism, which would be effective regardless of the cell density or the diffusion volume. Such a mechanism would be well adapted to enable cell cross talk in the floating communities that form before attachment on a surface.

The crystallographic structures show that Omp-Pst1 forms more hermetic DOTs (virtually no fenestrations) than Omp-Pst2, suggesting that intercellular solute translocation would be more efficient across Omp-Pst1 DOTs (Fig. 1 B and F). Also, the presence of an additional constriction zone in Omp-Pst2 channel would limit large solute exchange across Omp-Pst2 DOTs (Fig. 1 J and K). Hence, Omp-Pst1 DOTs are better candidates than Omp-Pst2 DOTs for the exchange of signaling solutes (23) and nutrients (24, 25) between *P. stuartii* cells. The structure of maltose-bound Omp-Pst1 is particularly interesting in this context, because it reveals not

only that this porin could be involved in the harvesting of maltose (and other di-glycosides) at the surface of the OM (*SI Appendix, Fig. S1B*), but also that the binding site for maltose is not affected by the oligomerization into a DOT. Hence, *Omp-Pst1* DOTs could permit equilibration of di-glycoside concentrations between adjacent cells. In contrast, the protrusion contributed by the longer L6 loop of *Omp-Pst2* would prevent the binding of a solute at this locus. Furthermore *Omp-Pst2* is highly cation selective, and the electrostatic potential developed along its channel is suggestive of a facilitated transport of cations from the periplasm to the bulk (Fig. 1*L*). MD simulations have revealed the propensity of *Omp-Pst2* to become nonconductive when cations translocate toward the periplasm, while recent experimental work highlighted the essential role it plays in the resistance to high urea concentrations and the regulation of the cationic content of the periplasm (12). In pathophysiological conditions where *P. stuartii* cells encounter high urea concentrations (2–5), e.g., in the urinary tract, *Omp-Pst2* could facilitate the export of the ammonium that accumulates in the periplasm (12) due to *P. stuartii* urease activity (12). *Omp-Pst2* DOTs could therefore function as check valves, allowing adjacent cells to expel cationic waste through fenestrations at the dimerization interface, while not reabsorbing it. The observation that *Omp-Pst2* self-association is promoted by high concentrations of ammonium chloride is in favor of this hypothesis.

In conclusion, our results suggest a previously uncharacterized role for porins, namely, to form primitive junctions between *P. stuartii* cells. These junctions could foster the formation of floating communities (Figs. 4 and 5) and support intercellular communications. Porin DOTs could thus represent new targets for diagnosis, disruption, and eradication of *P. stuartii* biofilms and associated chronic infections. It remains unclear if biofilm-forming species other than *P. stuartii* also form floating communities before surface-attached biofilms, and, if so, whether or not porin DOTs do support the formation of these floating communities. Examination of porin structures deposited in the Protein Data Bank, and of their crystal-packing interactions, reveals that many crystallize as DOTs associated through their extracellular loops. Thus, some porins may need to be reexamined for their putative propensity to self-associate, in light of the DOTs they form in crystals (e.g., 2j4u, 2xe1, 2xe2, 2xe5, 2y0h, 3poq, 3pou, 3pox, 3t0s, 3t24, 3wi4, 3wi5, 4aui, 4ftr, 4fso, 4gey, and 4gf4). Further work will be needed to examine the occurrence of porin DOTs in other

gram-negative biofilm-forming bacteria, and the extent to which these DOTs are supported by steric zipper interactions.

Methods

A full description of methods is given in *SI Appendix, Materials and Methods*. Briefly, *E. coli* strain BL21 (DE3) Δ Omp8 (Δ lamB ompF::Tn5 Δ ompA Δ ompC) was used to generate recombinant strains. Expression of *Omp-Pst1* and *Omp-Pst2* in *P. stuartii* and *E. coli* Δ Omp8 strains was monitored using qRT-PCR. Crystallization conditions were screened using standard crystallization screens and improved manually. Porin crystals were grown by the sitting drop method, and peptide crystals by the hanging drop method. X-ray data were collected at European Synchrotron Radiation Facility (ESRF) beamlines ID14-EH4, ID23-EH2, and ID30B; processed and scaled using standard software; and phased either by molecular replacement with homology models or by direct methods. Large unilamellar liposomes were produced by the standard film hydration method and their average hydrodynamic radius was determined using DLS; epifluorescence imaging was performed using an inverted microscope. Floating and surface-attached biofilms of *E. coli* and *P. stuartii* were prepared and imaged by epifluorescence microscopy as described in ref. 12. Electron micrographs of *P. stuartii* floating communities were obtained by sedimentation (30 min) of fixated planktonic cells, followed by negative staining with phosphotungstic acid (Fig. 5) or sodium silicotungstic acid (*SI Appendix, Fig. S19*).

ACKNOWLEDGMENTS. We thank E. Kandiah, D. Cascio, M. R. Sawaya, I. Silman, and J. Zaccà for critically reading the manuscript; C. Breyton and D. Levy for suggesting on-column delipidation of porins and sucrose gradient experiments, respectively; and A. Martel, A. Le Roy, A. Flayhan, A. Laganowsky, A. Davin-Regli, E. Moiseeva, M. Zhao, G. Schoehn, and T. Vernet for stimulating discussions. We are indebted to I. Snigireva for scanning electron micrographs and to J.-P. Kleman and F. Lacroix for technical support and advice during epifluorescence microscopy experiments. This work used the platforms of the Grenoble Instruct Center [Integrated Structural Biology Grenoble: Unité mixte de service 3518 CNRS-CEA-UGA-European Molecular Biology Laboratory (EMBL)], with support from the French Infrastructure for Integrated Structural Biology (Grant ANR-10-INSB-05-02) and the Grenoble Alliance for Integrated Structural Cell Biology (GRAL) (Grant ANR-10-LABX-49-01) within the Grenoble Partnership for Structural Biology. The electron microscopy facility is supported by the Rhône-Alpes Region, the Fondation de la Recherche Médicale, the Fonds Européen de Développement Régional, the CNRS, the CEA, the UGA, the EMBL, and the Groupement d'Intérêt Scientifique-Infrastructures en Biologie, Santé et Agronomie. We are grateful to the ESRF for beam time under the long-term projects MX722, MX1464, and MX1583 (IBS beamtime allocation group). We acknowledge financial support from the CEA, the CNRS, the UGA, Agence Nationale de la Recherche Grant ANR-15-CE18-0005-02 (to J.-P.C.), GRAL Grant C7H-LXG11A20-COLLETIER (to J.-P.C.), Laboratory of Excellence "Ion Channel Science and Therapeutics" Grant ANR-11-LABX-0015-01 (to M.V.), and Aix-Marseille University and the Service de Santé des Armées (J.-M.P.). M.E.-K. is supported by a joint CEA-GRAL doctoral fellowship (Grant C7H-LXG11A20-DYNAMOP).

- Manos J, Belas R (2006) The genera *Proteus*, *Providencia*, and *Morganella*. *Prokaryotes* 6:245–269.
- McHale PJ, Walker F, Scully B, English L, Keane CT (1981) *Providencia stuartii* infections: A review of 117 cases over an eight year period. *J Hosp Infect* 2:155–165.
- Stickler DJ (2008) Bacterial biofilms in patients with indwelling urinary catheters. *Nat Clin Pract Urol* 5:598–608.
- Warren JW (1986) *Providencia stuartii*: A common cause of antibiotic-resistant bacteriuria in patients with long-term indwelling catheters. *Rev Infect Dis* 8:61–67.
- Warren JW (1991) The catheter and urinary tract infection. *Med Clin North Am* 75:481–493.
- Tran Q-T, et al. (2010) Implication of porins in β -lactam resistance of *Providencia stuartii*. *J Biol Chem* 285:32273–32281.
- Bajaj H, et al. (2012) Antibiotic uptake through membrane channels: Role of *Providencia stuartii* *OmpPst1* porin in carbapenem resistance. *Biochemistry* 51:10244–10249.
- Stock I, Wiedemann B (1998) Natural antibiotic susceptibility of *Providencia stuartii*, *P. rettgeri*, *P. alcalifaciens* and *P. rustigianii* strains. *J Med Microbiol* 47:629–642.
- Broomfield RJ, Morgan SD, Khan A, Stickler DJ (2009) Crystalline bacterial biofilm formation on urinary catheters by urease-producing urinary tract pathogens: A simple method of control. *J Med Microbiol* 58:1367–1375.
- Hollick GE, et al. (1984) Characterization of endemic *Providencia stuartii* isolates from patients with urinary devices. *Eur J Clin Microbiol* 3:521–525.
- Mobley HL, Chippendale GR, Tenney JH, Warren JW (1986) Adherence to uroepithelial cells of *Providencia stuartii* isolated from the catheterized urinary tract. *J Gen Microbiol* 132:2863–2872.
- El Khatib M, et al. (2017) *Providencia stuartii* form biofilms and floating communities of cells that display high resistance to environmental insults. *PLoS One* 12:e0174213.
- Zeth K, Thein M (2010) Porins in prokaryotes and eukaryotes: Common themes and variations. *Biochem J* 431:13–22.
- Nikaido H (2003) Molecular basis of bacterial outer membrane permeability revisited. *Microbiol Mol Biol Rev* 67:593–656.
- Song W, et al. (2015) Understanding voltage gating of *Providencia stuartii* porins at atomic level. *PLOS Comput Biol* 11:e1004255.
- Ponstingl H, Henrick K, Thornton JM (2000) Discriminating between homodimeric and monomeric proteins in the crystalline state. *Proteins* 41:47–57.
- Lawrence MC, Colman PM (1993) Shape complementarity at protein/protein interfaces. *J Mol Biol* 234:946–950.
- Sawaya MR, et al. (2007) Atomic structures of amyloid cross-beta spines reveal varied steric zippers. *Nature* 447:453–457.
- Eisenberg D, Jucker M (2012) The amyloid state of proteins in human diseases. *Cell* 148:1188–1203.
- Goldschmidt L, Teng PK, Riek R, Eisenberg D (2010) Identifying the amyloids, proteins capable of forming amyloid-like fibrils. *Proc Natl Acad Sci USA* 107:3487–3492.
- Lévy D, Gulik A, Bluzat A, Rigaud JL (1992) Reconstitution of the sarcoplasmic reticulum Ca(2+)-ATPase: Mechanisms of membrane protein insertion into liposomes during reconstitution procedures involving the use of detergents. *Biochim Biophys Acta* 1107:283–298.
- Prilipov A, Phale PS, Van Gelder P, Rosenbusch JP, Koeblnik R (1998) Coupling site-directed mutagenesis with high-level expression: Large scale production of mutant porins from *E. coli*. *FEMS Microbiol Lett* 163:65–72.
- Davies D (2003) Understanding biofilm resistance to antibacterial agents. *Nat Rev Drug Discov* 2:114–122.
- Liu J, et al. (2015) Metabolic co-dependence gives rise to collective oscillations within biofilms. *Nature* 523:550–554.
- Liu J, et al. (2017) Coupling between distant biofilms and emergence of nutrient time-sharing. *Science* 356:638–642.

Résumé de la thèse

Les biofilms bactériens, communautés multicellulaires adhérentes à une surface et enrobées d'une matrice extracellulaire, sont cruciaux pour le maintien de la plupart des écosystèmes de notre planète mais représentent également une menace pour la santé humaine. Leur éradication est un véritable défi pour la microbiologie moderne du fait de leur résistance élevée aux antibiotiques. *Providencia stuartii* est une bactérie Gram-négative connue pour sa forte capacité à former des biofilms dans le tractus urinaire humain, qui est responsable pour environ 10% des infections nosocomiales urinaires chroniques. Nous avons montré que cette souche bactérienne exploite un moyen de socialisation supplémentaire préalable à l'adhésion des cellules aux surfaces et la sécrétion d'une matrice extracellulaire, les communautés flottantes. Les deux porines de *P. stuartii*, Omp-Pst1 et Omp-Pst2, soutiennent la formation des communautés flottantes en s'auto-associant à travers leurs boucles extracellulaires pour former des dimères de trimères (DOTs) intercellulaires. La formation des DOTs, rivetant les cellules adjacentes entre elles, est médiée par des forces électrostatiques et des interactions de type steric zipper.

Les deux grands objectifs de la thèse ont été i) de caractériser les impacts environnementaux sur l'établissement et la survie des deux types de communautés formés par *P. stuartii*, et ii) d'empêcher la socialisation bactérienne par inhibition des DOTs de porines. Nos résultats ont montré que des peptides mimant les résidus impliqués dans les interactions de type stérique zipper des DOTs de porines, et couplés à de la coumarine, sont prometteurs pour diagnostiquer les infections à *P. stuartii*. De plus, nous avons mis en avant qu'une combinaison d'antibiotiques avec certains de ces peptides est une nouvelle approche thérapeutique envisageable pour lutter contre les infections de *P. stuartii*. Nos résultats montrent aussi que les futurs traitements devraient être évalués sur les communautés flottantes et les biofilms adhérents, dans des conditions imitant les voies urinaires, afin d'être efficaces et potentiellement éradiquer *P. stuartii*.

PhD summary

Bacterial biofilms are multicellular communities adherent to surfaces and surrounded by an extracellular matrix. They are crucial for maintaining most of our planet's ecosystems, but also a threat to human health. Biofilm eradication is one of the greatest challenges of modern microbiology due to their high resistance to antibiotics. In this PhD, we focused on *Providencia stuartii*, a Gram-negative pathogen that forms biofilms in the human urinary tract and is responsible for about 10% of hospital-acquired urinary tract infections. *P. stuartii* exploits an additional means of socialization, forming floating communities of cells (FCCs), that later sediment and adhere onto surfaces yielding surface-attached biofilms (SABs). The two porins of *P. stuartii*, Omp-Pst1 and Omp-Pst2, are involved in FCC formation by self-association into intercellular dimers of trimers (DOTs). The main driving force behind DOT formation is electrostatic attraction, yet the DOT structure is locked-in by steric zipper interactions between facing extracellular loops.

The two main objectives of this PhD were (i) to characterize the environmental impacts on the establishment and survival of the two type of socialized communities formed by *P. stuartii*, and (ii) to inhibit bacterial socialization by targeting porin DOTs. Our results reveal that peptides featuring residues involved in the steric zipper interaction of DOTs, and coupled with coumarin, are promising lead compound to diagnose *P. stuartii* infections. In addition, we tested combinations of antibiotics with some of these peptides and results suggest that is was a new therapeutic approach that can be envisaged to fight against *P. stuartii* infections. Future treatments should be evaluated on FCCs and SABs in conditions mimicking urinary tract, to be efficient and potentially eradicate *P. stuartii*.